Advanced Materials for Composite Armour

Zhu, Fuyou

Advanced Materials for Composite Armour

Fuyou Zhu

A thesis submitted for the degree of
Doctor of Philosophy (PhD)

May **2009**

School of Engineering and Materials
Queen Mary, University of London

Acknowledgements

I would like to express my thanks to my supervisor, Professor P. J. Hogg for his comments, suggestions and encouragement, freely offered during the course of this work.

Thansk also to Dr Asa Barber for his advices and help during the final stage of my study.

Thanks also to Mr Bill Godwin, Mr Colin Langdown, Dr. Guogang Ren and Dr Silvano Cauchi-Savona for their occasional advice and help, which is greatly appreciated.

Thanks also to Mrs Sandra Wells, Miss Victoria Wells, all members of the lecturing staff, technicians and fellow students in the Materials Department who helped at one time or another with this work.

Thanks also to Professor Chengyan Zhu and Carr Reinforcements Ltd who provided the materials for work.

Special thanks to my parents and my beloved Shuangwu Li for their continuous support during the course of this study.

Special thanks also to Mr Shuirong Li for his help and encouragement at some crucial stages of my study.

Abstract

Composite integral armour plays an important role in future combat system. Despite numerous experimental studies there are still disadvantages such as complex manufacturing process, relatively big damage area, difficult to repair and limit shape etc. Composite integral armour without all these problems is essential for the success of future main battle tank which has a total weight of only 20 tons.

3D fabrics are seen as potential solution to poor impact damage tolerance of textile composites. Binder yarns in through-thickness direction can bridge cracks and stop crack tip growth resulting very good impact damage tolerance.

The major purple of this work is to incorporate new materials and new configuration into composite integral armour. The underlying premise is that ballistic performance of new armour is judged mainly by single hit ballistic limit followed by damage resistance which in turn followed by energy absorption in high energy low velocity impact. Computer simulation of 3D textile composites and damage mechanism study were used through-out the study for analysing and explaining experimental results.

Judged by these properties, conclusions regarding to ballistic performance of eight 3D texile composties were made. The benefit of the work will be a new explanation of composite armour research. This will help the success of future combat system.

Contents

List of Figures

List of Tables

Glossary

AD_f

areal density of plain woven E-glass fabrics 6.6

E

Young's modulus 2.7

EAD

result of ballistic limit energy divided by areal density 7.3

E_P

perforation energy 6.7

E_{50}

ballistic limit energy 6.6

N_f

number of layers of fabrics 6.6

P_d

characteristic transition point in force versus deformation curve of drop weight impact test where the slope of the curve decrease 9.3

P_i

characteristic transition point in force versus deformation curve of drop weight impact test where initial drop of force occurs 9.3

P_m

characteristic transition point in force versus deformation curve of drop weight impact test where sudden drop of force occurs 9.3

S

two dimentional damage area 7.3

SAD

result of two dimentional damage area divided by areal density 7.3

SI

area of a projectile projected on the front of the textile composites in the through thickness direction 6.7

Tu

fibre sepecific toughness used by Cunniff [26] 2.7

U

fibre property developed by Cunniff [26] 2.7, 6.6, 6.7

UI

material property incorporating the effect of projectiles during ballistic impacts 6.7, 10.2

VS

fibre stress wave velocity used by Cunniff [26] 2.7

V_{50}

ballistic limit velocity 2.1, 2.2, 2.4, 2.10, 3.2, 4.3

δ

displacement of the impactor in drop weight impacts 2.4

ψ

angle between the impacting direction of a projectile and longitudinal axis of the prjectile 0.0, 2.2

ρ

density of glass fibre 2.7

σ

ultimate tensile strength of a fibre 2.7

θ

angle between the impacting direction of a projectile and the direction perpendicular to the surface of a target 0.0, 2.2

ε

ultimate tensile strain of a fibre 2.7

g

gravitational acceleration on the earth 2.4

h

vertical distance between the impactor and the specimen 2.4

m

weight of the impactor 2.4

t

thickness of the composite 6.6

ARL

the United States of American's armys corporate basic and applied research laboratory 1.1

CAI

compression after impact 2.12

CFRP

composite material containing carbon fibres and plastics with carbon fibres being reinforcement and plastics being matrix 2.5

CIA

multi-material armour or multi-functional armour with each component serves a specific purpose and yet combinations of layers provide role-sharing multifunctionality 1.1, 2.14

CT

a non-destructive evaluation technique for tomography studies 2.13, 5.2

E-glass

calcium alumino-borosilicate glass fibre 2.7

EP

epoxy resin 4.1

FSP

cylindrical projectile with a blunt chisel shaped nose and a raised flange at the base[32] 2.5, 2.7

GRP

composite material containing glass fibres and plastics with glass fibres being reinforcement and plastics being matrix 2.8

Kevlar

para-aramide fibre developed at DuPont plc 2.7, 2.15

MEKP

methyl ethyl ketone peroxide 4.1

MMC

Metal-Matrix Composite 1.1

NDE

Non-Destructive Evaluation 2.3

PBO

poly (p-feny-2 6-benzobisoxazol) 2.7, 2.15

PET

polyethylene terephthalate 4.1

PP

polypropylene 4.1

SEM

Scanning Electron Microscope 0.0, 4.3

Spectra

ultra high molecular weight polyethylene fibre 2.7, 2.15

VE

vinyl ester resin 4.1

Chapter 1

Background and Motivation

1.1 Background

1.1.1 Armour

Amour is a protective covering aiming to stop threats against soldiers or vehicles in battle fields. The modern ballistic threats include kinetic energy projectiles and chemical energy weapons. In kinetic energy threat, a projectile penetrates the target because the kinetic energy is sufficient to inactive the target as shown in figure 1.1. While in chemical energy threat, the projectile penetrates the target because it has stored chemical energy in the form of high explosive. Laible [53] suggested that the main ballistic threats to soldiers are fragments from bombs, shells, mortars and grenades, etc. In terms of penetration process, these shell fragments belong to kinetic energy threats.

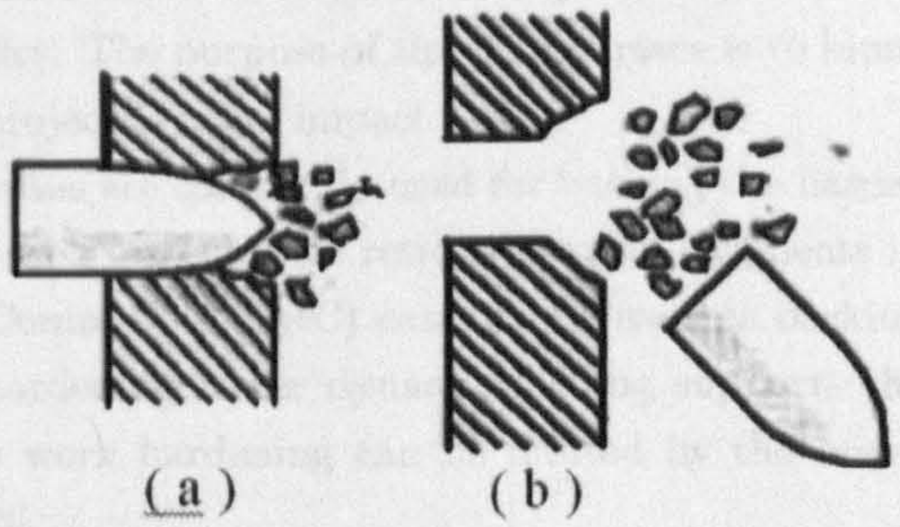

Figure 1.1: **Penetration process of kinetic threats** - (a) partial penetration; (b) complete penetration.

Conventional light amour consisted of metal alloys, ceramics and the like. Amours made from these materials are isotropic, and their capability of stopping ballistic threats is in proportion to the amount of materials used, i.e., thickness. As time went by, the thickness of amour increased due to the advancement of weaponry technology. Military vehicles equipped with these kind amours weigh as such as 70 tones.

Since the end of the Cold war, countries around the world such as USA, UK, and Russia have realized the importance of mobility of army force. For example, the US government is trying to develop a future combat system in which tanks with weight between $10 - 20$ tons can be carried by aircraft such as $C - 130$ Hercules and be quickly deployed anywhere in the world [62].

1.1.2 Composite

A composite is made of two or more materials. Normally one or more components have high strength or stiffness and one is an adhesive binder. The most common composite is fibre reinforced plastic which contains fibres bonded together in plastic matrix. The most common fibre reinforced plastic is glass fibre reinforced polymer.

Composites have high specific strengths and stiffness, good corrosion resistance [20, 89], and good flexibility in design [22, 89]. They have good damage tolerance [22], fatigue properties [20], and excellent thermal and acoustical insulation [89]. They are also easy to fabricate which reduces less cost. And most importantly they have better specific impact resistance than conventional materials such as metals and ceramics [89]. With all these advantages, composites have being highly regarded as potential replacements for traditional amour. Some parts of prototype military combat vehicles such as turrets and hulls have been manufactured using glass-fabric reinforced plastic [80, 91].

1.1.3 Composite Amour

To date, most of the practical composite structures to resist penetration are layered [43]. The simplest composite structure consists of a hard frontal surface and softer backing. The hard frontal materials are typically ceramics or hardened metallics. The purpose of the hard surface is to blunt and to induce a destructive shock wave on to the projectile upon impact.

Aluminium and fibre-reinforced polymer composites are commonly used for backing the harder frontal materials. The softer backing materials act as a 'catcher' for residual broken fragments in preventing target penetration [23]. Metal-Matrix Composite (MMC) can also be used as backing layer. The hypothesis that MMCs exhibit work hardening under dynamic loading supports the observed ballistic performance [92]. However, the work hardening can be limited by the micro structural damage from shock wave interactions [23].

1.1.4 Composite Integral Armour

The multi-material armour scheme described above shows the basic of composite integral armour (CIA) or multi-functional armour, i.e. each component serves a specific purpose, yet combinations of layers provide role-sharing multifunctionality. Often, single layers also serve multifunctional roles (e.g., structural, multi-hit ballistic, ballistic shock) through uniquely designed interactions with adjacent layers [36].

Fig 1.2 shows a CIA developed by US Army Research Laboratory (ARL). It shows a thin protective polymer matrix composite face sheet on the outside of the vehicle to protect the ceramic ballistic tiles from incidental damage and provide through-thickness ceramic confinement; ceramic tiles to absorb most of the kinetic energy of the projectile through a combination of projectile dwell, mixed-mode fracture under high pressure, and erosion/deformation of the projectile; a layer of rubber to prevent premature failure of the composite backing plate, improve multi-hit ballistic performance, and attenuate the propagation of high-frequency stress waves; a thick-section composite plate to provide structural backing for the ballistic tiles and structural properties for the vehicle; and a fire-protective "spall" layer on the inner surface of the vehicle. Additional layers can be incorporated for electromagnetic ground planes, signature control, greater ballistic shock

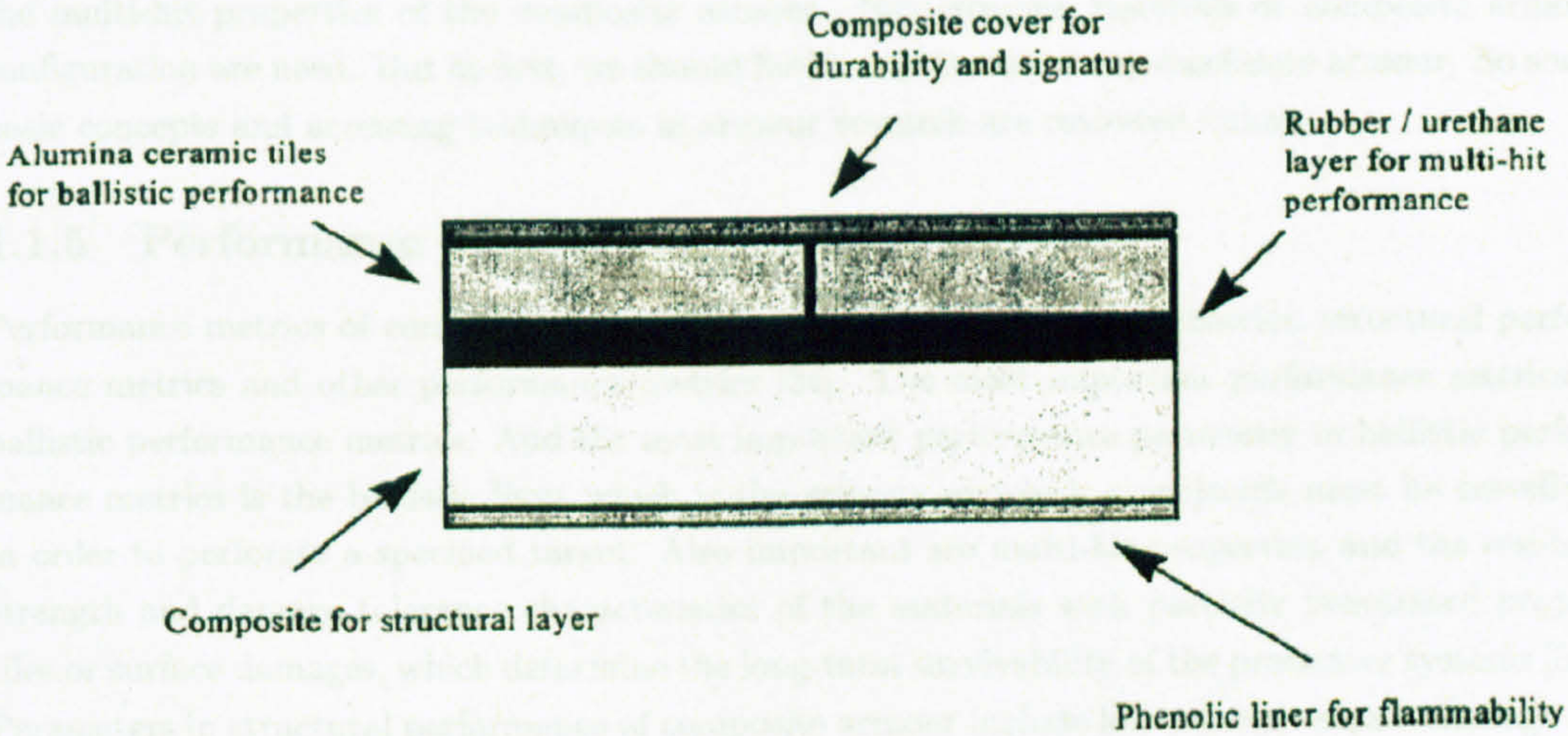

Figure 1.2: **Example of the composite integral armour program** - after Fink [33].

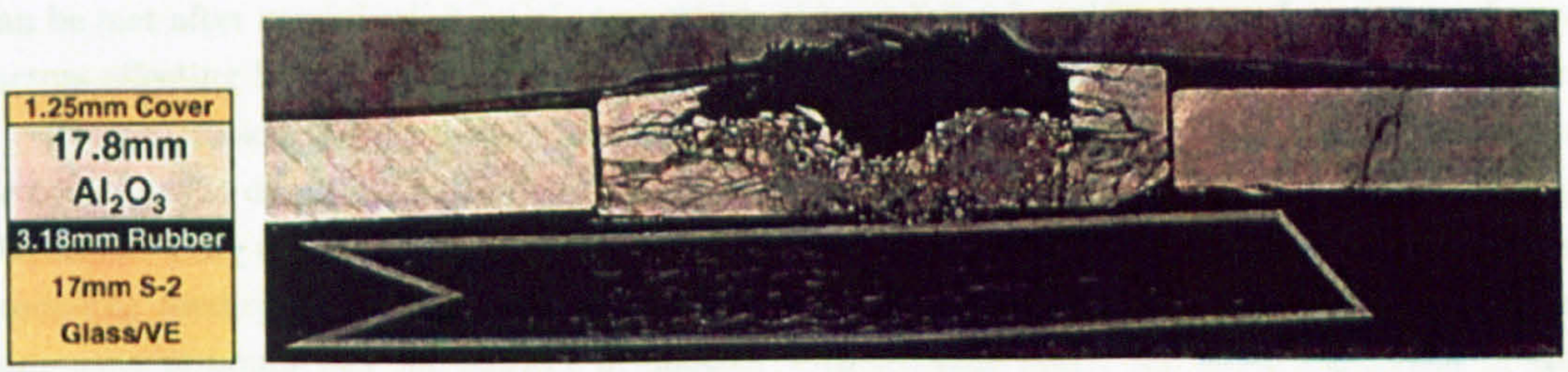

Figure 1.3: **Ballistic impact damage in composite integral armour** - (a) armour configuration; (b) cross-section of armour after ballistic impact [36].

protection, etc. Figure 1.3 shows a CIA sample after ballistic test. It can be seen that the ceramic front suffered local spalling and some cracks present in the faceplate. But huge damage occurs in the polymer matrix composite backing layer.

As stated above, the composite backing layer plays important structural role. So it is necessary to reduce the damage scale in the polymer matrix composite backing layer which also increases the multi-hit properties of the composite armour. New armour materials or composite armour configuration are need. But at first, we should find a way to access any candidate armour. So some basic concepts and accessing techniques in armour research are reviewed below.

1.1.5 Performance Metrics of Composite Amour

Performance metrics of composite amour include ballistic performance metrics, structural performance metrics and other performance metrics [34]. The most important performance metrics is ballistic performance metrics. And the most important performance parameter in ballistic performance metrics is the ballistic limit which is the velocity at which a projectile must be travelling in order to perforate a specified target. Also important are multi-hit properties, and the residual strength and damage tolerance characteristics of the materials with partially penetrated projectiles or surface damages, which determine the long-term survivability of the protective systems [56]. Parameters in structural performance of composite armour include low-velocity impact damage resistance etc. Other performance parameters include area density, manufacturability, reparability, and manufacturing and assemble costs etc.

1.2 Motivation

After introducing a hard front, the problem of the composite being weak under a concentrated force has been solved. The challenge left is to choose a fibre reinforced plastic which has good ballistic performance, structural performance and other properties such as manufacturability. Composites have great flexibility in design. Various fibre and matrix materials and fabric structures are available. In addition, various manufacturing methods are available. It is believed that the challenge can be met after careful selection of components of composites based on in-depth understanding of factors affecting ballistic performance of composite and the development of an assessment system.

The motivation of this work is to find a way to optimise the combination of fibres, resins and architectures to develop effective light weight composite armour to protect people and equipment in the battle. Only experimental methods have been used to achieve the aims of this study. Computer modelling methods have not been used. This was due to the fact that computer modelling of composite armours was the subject of another PhD student under the same supervisor of this study.

Chapter 2

Literature Review

2.1 Introduction

It was stated that in 1.1.5, good composite amour should have high single-hit ballistic limit velocity (V_{50}), good multi-hit properties, and good low velocity impact properties and manufacturability. V_{50} is the most important parameter, and can be assessed by a gas gun test. Multi-hit property is related to damage resistance which can be characterized by measuring the size of the damaged area generated [33]. Low velocity impact properties can be accessed using a drop weight impact test. Microscope studies and ultrasonic C-scan can be used to evaluate manufacturability by identifying voids or resin rich areas. Further discussion of the relevant test methods will be presented in sections following.

2.2 Ballistic Velocity Testing

2.2.1 Introduction

The aim of ballistic testing is to determine single-hit ballistic limit velocity. Ballistic threats are launched by guns using means such as explosive powder charges, pressurized gas, or magnetic field. A ballistic limit criterion is selected before testing. Figure 2.1 lists three ballistic limit criteria. In figure 2.1(a), complete penetration occurs when light is visible through the penetration in the armour or when the nose of the projectile can be seen from the rear of the armour. In figure 2.1(b), a complete penetration requires that the projectile or a major portion of the projectile pass through the plate. In figure 2.1(c), a complete penetration occurs whenever a fragment or fragments from either the impacting projectiles or the armour are caused to be ejected form the back of the armour with sufficient remaining energy to pierce a thin sheet

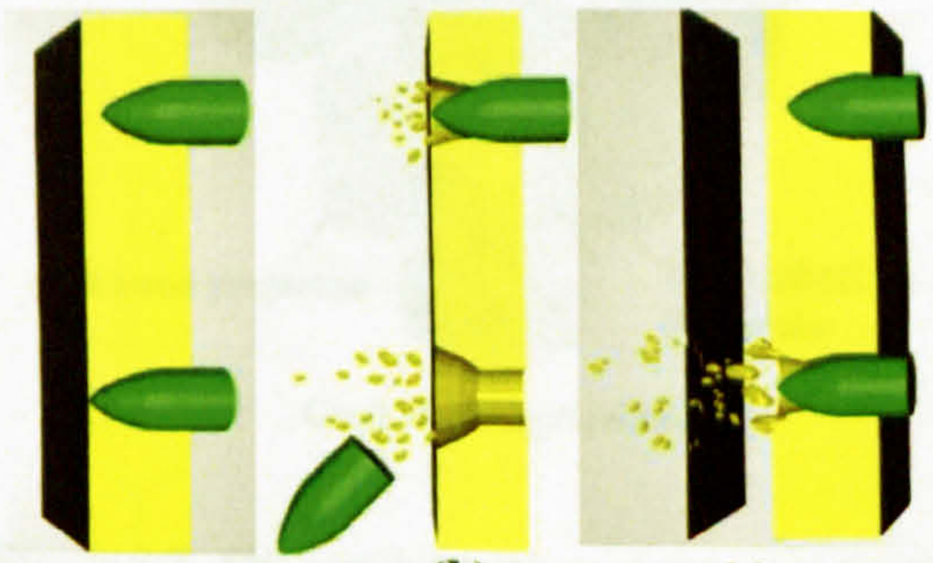

Figure 2.1: **Ballistic limit criteria** - redraw from [78].

of aluminium alloy of 0.05 mm to 0.50 mm thick (witness plate), placed parallel to end 15.24 cm behind the target.

After selection of ballistic limit criteria, ballistic threats with a range of velocities can be studied. Ideally a ballistic limit velocity can be identified with a sufficient number of shots. This is time-consuming and expensive. In addition, the ballistic limit velocity is a function of many variables which includes projectile parameters (i.e., nose shape, cross sectional area, length-diameter ratio, mass and rigidity) and target parameters (i.e., material properties, thickness, lay-up and boundary conditions), among others ([27]). In reality, despite efforts to reproduce experimental conditions, ballistic events repeated several times can yield a number of different results. For this reason, a ballistic limit velocity is defined for a 50% chance of perforating the target. A 'short cut' procedure is therefore normally adopted in which the velocity of the projectile is varied to achieve three complete penetrations and three partial penetrations within a small velocity band. The width of this velocity band varies from specification to specification and is dependent on various parameters of the target such as thickness and areal desnity. These six velocities are then averaged to give a value for V_{50}. Examples can be found in a US patent [24].

2.2.2 Effects of Projectiles at Ballistic Velocity Test

Kinetic energy steel projectiles having a known geometric shape and hardness are the most widely used projectiles in ballistic testing. As stated above, projectile parameters affecting the ballistic limit velocity results include nose shape, cross sectional area, length-diameter ratio, mass and rigidity. Other issues such as projectile deformation and spinning effects will also affect the results [32].

The nose shape of the projectile can be oval, hemispherical etc as shown in figure 2.2. The nose shape of the projectile or penetrator affects testing results in both low velocities and ballistic velocities. But the effects are greater at ballistic velocities. A sharp nosed projectile will penetrate further in the armour than a more blunt projectile of larger diameter with the same mass which may cause significantly more damage to the armour [32]. The momentum transfer to the amour by a blunt projectile is much higher than that of a sharp nosed projectile at ballistic velocities [50].

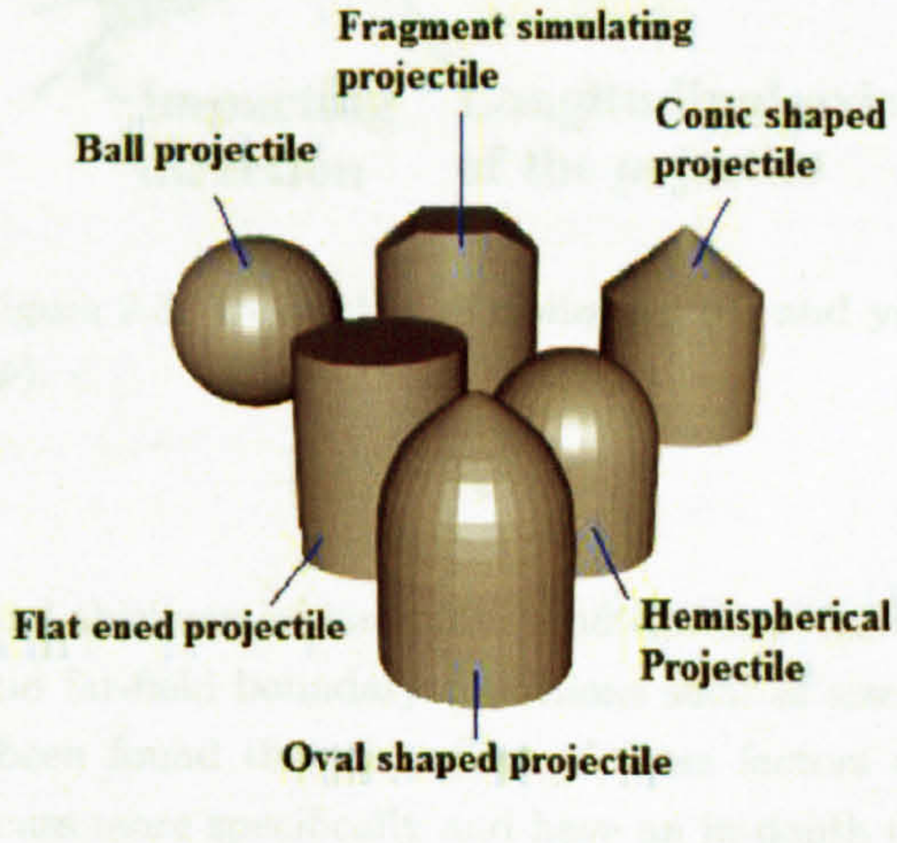

Figure 2.2: **Projectiles with various nose shapes used in ballistic tests** - ball, FSP etc.

Cantwell and Morton [18] studied the effect of mass of the projectile while maintaining the same shape and size and found out that the mass of projectile affects the resulting damage. They suggested that for a given impact energy lighter projectiles are more damaging to the residual properties of the composite materials they tested. This is because the incident energy is dissipated immediately over a small area around the point of impact in the form of shearing the fibres.

Deformation of the projectile can occur in the ballistic test depending on the armour material

and the projectile used. For example, it occurs in ballistic testing of composite armours with a hard front surface. And it also occurs when performing ballistic testing with projectiles commonly used in civilian handguns and rifles. Because the projectile is typically made of lead with a copper outer coating (jacket).

2.2.3 Light Gas Gun Test

A light gas gun is a specially developed apparatus designed to generate very high velocities. Unlike other gun tests using an explosive powder charge, gas gun tests use pressurized gases such as helium and nitrogen to propel projectiles. A sabot acts as a projectile carrier and gas seal which will be captured at the end of gun barrel letting the projectile leaving the gun barrel in free flight. Components of a gas gun include a gas reservoir, a driver chamber, a long barrel, a sabot, a target stage, incident/exit velocity measuring devices such as chronograph, a sabot capturer, firing triggering devices such as high speed solenoid valve. Velocity in a gas gun test can be controlled by changing factors such as firing pressure, weight of projectile, weight of sabot or length of barrel.

Various other devices can be incorporated into gas gun test for different purposes. For example, paper screens can be placed in the projectile's line of flight to check for yaw which is defined in figure 2.3. A laser designator can be used to achieve accurate aiming. And a thick backing of plasticine clay can be mounted to the back of impacted panel to investigate the dynamic deformations of the back face which can also be studied using high-speed photographing.

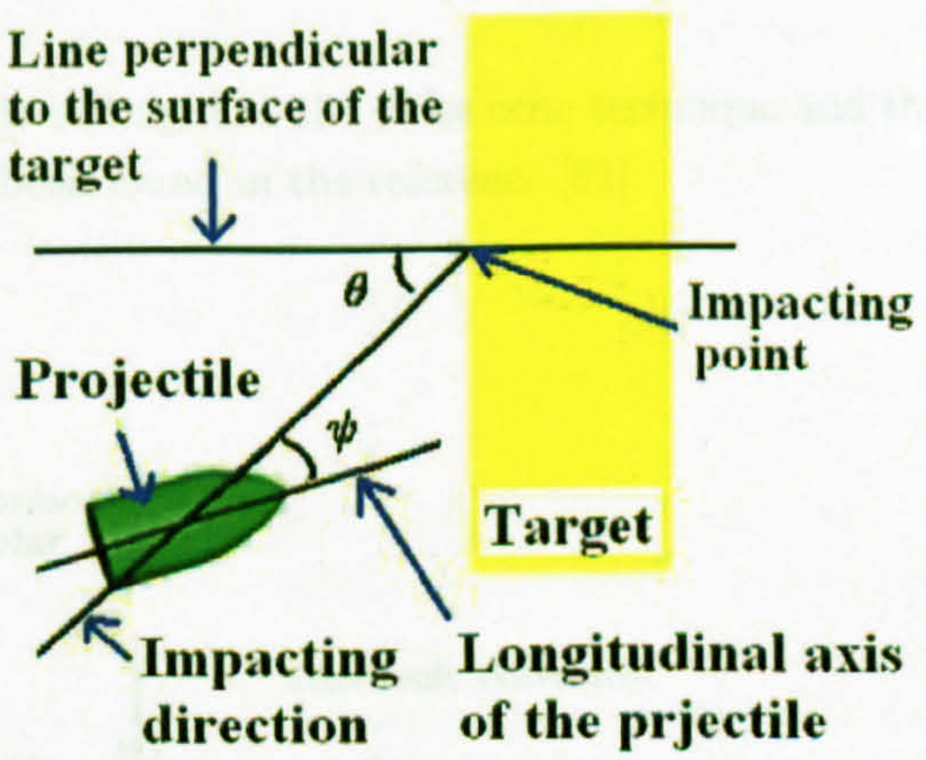

Figure 2.3: **Definition of obliquity (θ) and yaw (ψ).** -

2.2.4 Ballistic Velocity Test of Composites

Factors affecting the ballistic performance of composite amours include intrinsic factors and extrinsic factors. Intrinsic factors include fibre material(s), resin material(s), fabric architecture and thickness of laminate. And extrinsic factors include shape of projectile, weight of projectile, and far-field boundary conditions such as size of specimen and means of fixing specimen. It has been found that the effect of these factors are mutual interdependent. In order to be able to discuss more specifically and have an in-depth understanding, the effect of fabric architecture was used as a first order factor. Other factors would be discussed in the order of fibre material, resin material and shape of projectile.

2.3 Inspection of impact damages in textile composites using Ultrasonic C-scan

2.3.1 Ultrasonic Testing

Ultrasonic testing is one kind of non-destructive evaluation (NDE) techniques. Other NDE techniques include penetrants, eddy current, radiography, acoustic emission, and holography. When a ultrasonic beam (or energy, wave) passes through a objective, it attenuates. Ultrasonic testing is a technique that tries to relate this attenuation to the damage or flaws in the objective. The ultrasonic waves used by ultrasonic testing have frequencies greater than the audible range ($15kHz$). These waves behave in a similar manner to light: they obey the laws of reflection and refraction.

Ultrasonic testing is used both to find imperfections in a component and to measure mechanical moduli. In flaw detection, pulses of ultrasound are reflected from boundaries to build up a picture of the interior of a component. These pulses are produced and received by transducers which are normally piezoelectric crystals. Once the reflected pulse is received from the flaw, it must be displayed to the operator in a convenient form. The method of achieving this are called scans and three most common are termed A, B and C ([81]).

There are two main test techniques for ultrasonic testing, i.e., the pulse echo technique and the through transmission technique. More details can been found in the reference [81].

2.3.2 Ultrasonic C-scan

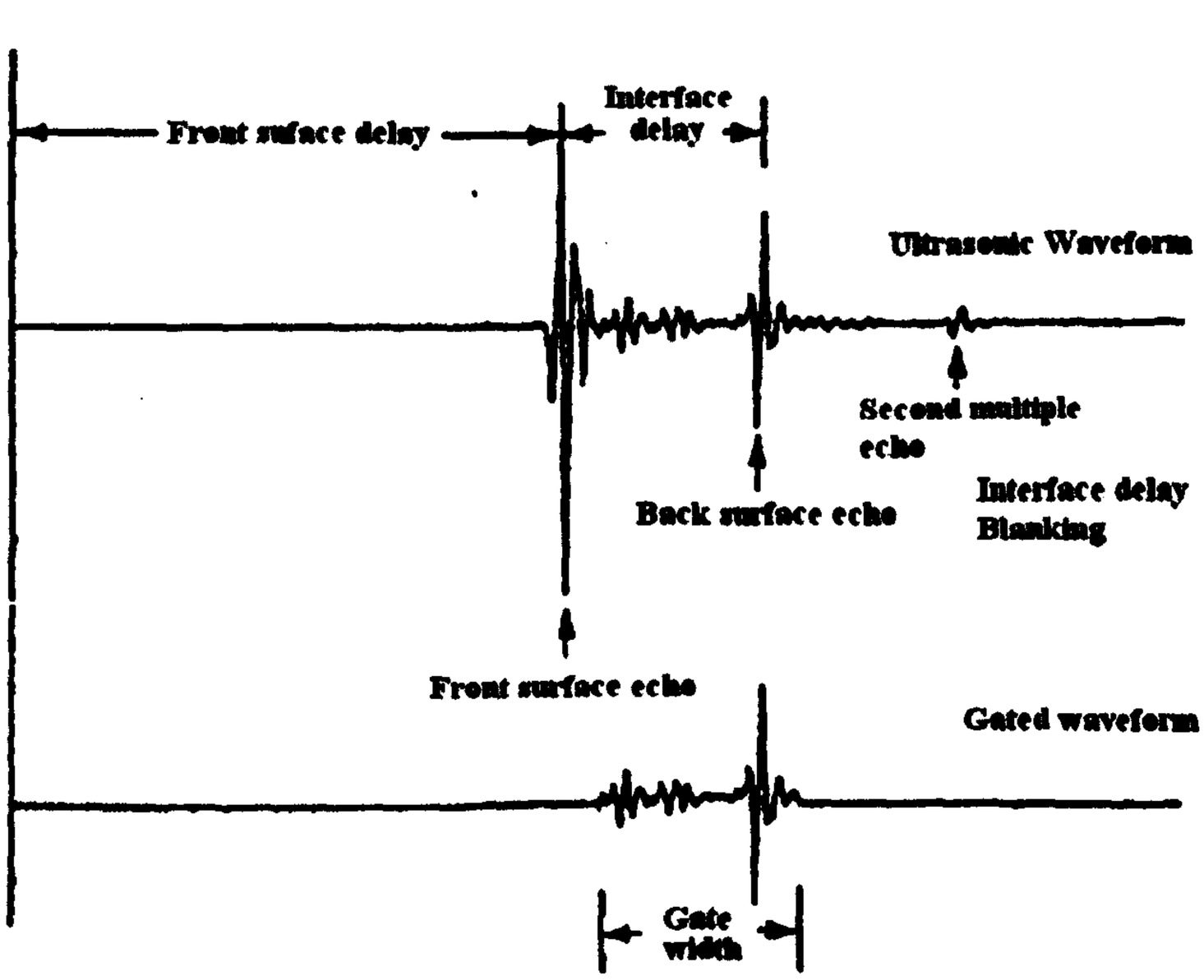

Figure 2.4: **C-scan gate parameters** - [11]

C-scan is two-dimensional views of the interior structure of material. Defects show up as colour variations in the image, i.e., the C-scan collects three values for each point on the sample: x coordinates, y coordinates, and a gray-scale value corresponding to the quality. The specified region

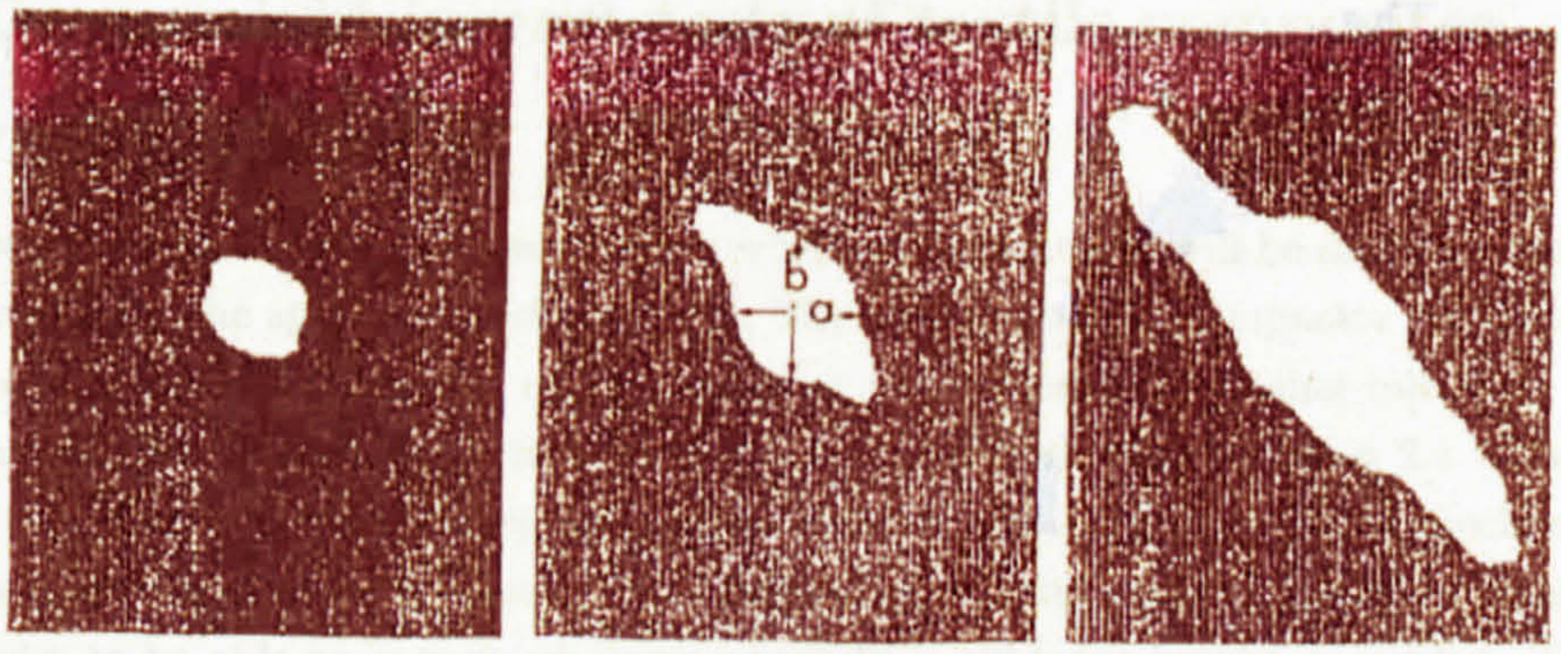

Figure 2.5: **C-scan images of impact damage caused by** - (a) low; (b) medium; (c) high energies [57].

of the total ultrasonic waveform at a particular depth is called the "gated region" and is shown in figure 2.4. The interface delay is a function of speed of sound and thickness of the material, and the front surface delay is a function of the local length of the transducer [11]. The gate width is set by the user to include as much of the waveform as needed. The gate selection determines whether the C-scan will be based upon attenuation or echo-capture data, i.e., the through transmission technique or the pulse echo technique. Generally, the echo characterization is used to capture delamination and interlaminar defects ([33]). In this study, focus is placed on its application in ballistics impact research.

C-scan has been widely used in the field of low velocity impact such as drop weight impact. For example, Lee et al [57] used C-scan to show clearly the damage caused by different impacting energies (fig 2.5). In reference [12], Boll et al used a slightly non-conventional c-scan called (acoustic backscatter c-scan) to study the impact damage of epoxy-matrix carbon-fibre composites. This approach was found to be more sensitive and yields significantly more information about damage distribution.

C-scan has also been used in ballistic impact research. For example, Gillespie and Monib [39] used a $5MHz$ focused transducer to scan an S-2 glass fabric composite after ballistic impact. Three gates were examined, i.e., 10%, 50%, and 80% of the thickness. And the authors pointed out the C-scans are most representative for delamination damage. Before scanning, they scrub the surfaces of the panel while it was immersed in the water tank to remove air bubbles. After scanning, they found an approximately circular damage pattern centred on the impact site.

2.3.3 Ultrasonic C-scan tests of textile composites

In composite laminates, signal attenuation usually results from three sources, i.e. viscoelastic effects in the resin, the heterogeneity and matrix cracking. By selecting the appropriate sound wave frequency the attenuation due to internal damage mechanisms can be maximised allowing an overall assessment of internal damage to be made ([17]).

2.4 Drop weight impact tests of textile composites

2.4.1 Testing apparatus

In drop-weight impact tests, an object impactor with known weight will be dropped from a known height and impact the specimen underneath it. The kinetic energy of impactor just before hitting the specimen is equal to potential energy it has at the beginning assuming initial no losses due to frictional effects. So the impacting energy can be calculated using equation 2.1 where m is the weight of the impactor, h is the vertical distance between the impactor and the specimen, g is the gravitational acceleration on the earth. The impacting velocity can be calculated using equation 2.2. In order to be able to impact specimen precisely, a guidance system is needed. This can be achieved used two vertical guiding bars. The cross-section of the guiding bars can be circular or channel as shown in figure 2.6. The impactor is placed between the guiding bars. A horizontal steel bar is used to connect the impactor to the two steel rods ([4]). The guiding system with channelled guiding bars has smaller friction than the guidance system with steel rods. Because there is not direct contact between the horizontal bar and the guiding bars ([96]). In addition, its friction can be minimized using additional plastic pads engraved on the sides of the impactor ([96]). For guiding systems using steel columns, there are also ways to minimize the friction during falling. Aslan et al ([4]) used two frictionless linear bearings at each end of the horizontal bar to minimize friction. Now equation 2.2 can not be used to calculate the impacting velocity if there is friction between the horizontal steel bar and the two vertical steel bars.

Baucom et al ([7]) used magnetostrictive position sensors to measure the displacement of the impactor during the whole impacting process. They attached a magnetic ring to the impactor. A wire covered with a waveguide and protected by protective tubing was placed along the route of the magnetic ring. A current pulse was launched along the wire generating a magnetic field along the route. This magnetic field interacts with the magnetic field generated by the magnetic ring interact producing a strain pulse which travels at sonic speed along the waveguide. A transducer is placed at the bottom of the wire to detect the strain pulse. The position of the moving magnet, i.e. the impactor, is precisely characterized by measuring the time difference between the launching of the electronic pulse and the arrival of the strain pulse. Thus a curve of displacement versus time can be produced. Velocity of the impactor at the any point during the impacting process can be determined using equation 2.3 where δ is displacement.

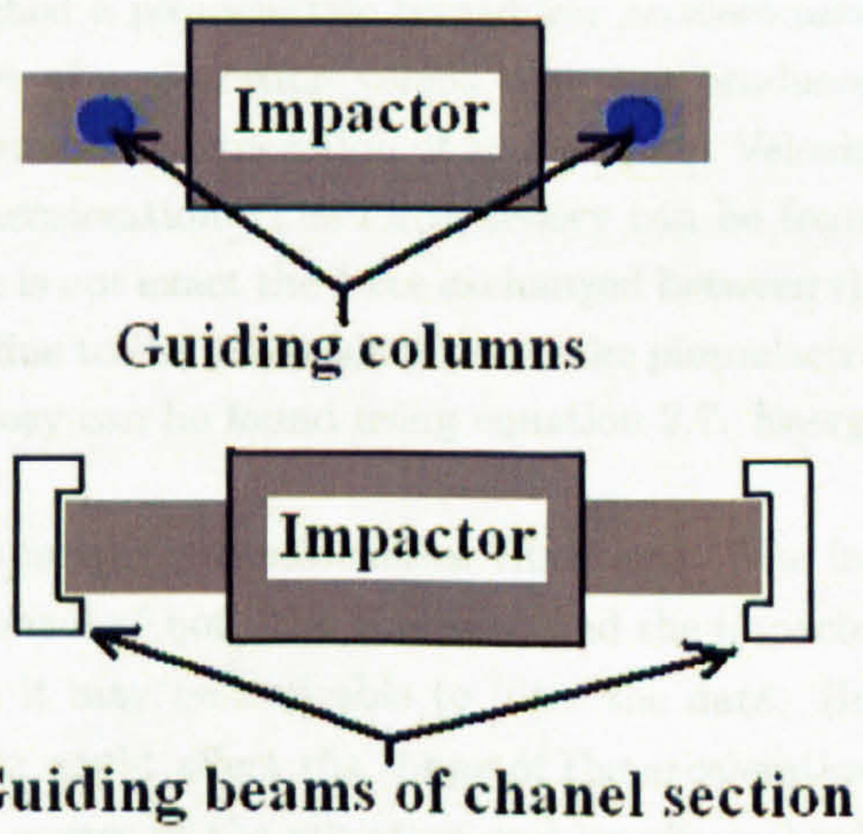

Figure 2.6: **Guiding systems in drop weight impact test machine.** - [96]

$$E = mgh \tag{2.1}$$

$$V = \sqrt{2mgh} \tag{2.2}$$

$$v(t) = \frac{\delta(t)}{dt} \tag{2.3}$$

$$E(t) = \frac{1}{2}m({V_0}^2 - V(t)^2) \tag{2.4}$$

$$V(t) = V_0 - \Delta V = V_0 - \int a(t)dt \tag{2.5}$$

$$F(t) = ma(t) \tag{2.6}$$

$$\delta(t) = \int v(t)dt \tag{2.7}$$

$$E(t) = F(t)d\delta \tag{2.8}$$

Measuring impact velocity using displacement versus time curves works very well up to the point of impact. After this point, the impactor will either rebound or start to perforate the specimen. For the former case, velocity can still be determined easily using the displacement versus time curve. Total energy dissipation can be calculated using equation 2.4 where m is the impacting weight, V_i is the velocity of the impactor just before the impacting, V_r is the residual velocity of the impactor. But for the later case, it is difficult to determine the velocity due to the friction between the impactor and the specimen. Baucom et al ([7]) attached a piezoelectric transducer accelerometer to the impactor to measure its acceleration. A curve of acceleration versus time was produced. The change of velocity after impact is calculated by numerical integration of acceleration. Velocity history can be found using equation 2.5 where a is acceleration. The force history can be found using equation 2.6. It should be noticed that this force is not exact the force exchanged between the specimen and the impactor. There is an inertial force due to the materials between the piezoelectric transducer and the specimen ([8]). Displacement history can be found using equation 2.7. Energy history can be found using equation 2.8.

The rapid variation of acceleration during the impacting process excites vibrations. The frequency of the vibration depends on the stiffness and mass of both the specimen and the impactor ([8]). This interferes with the signal acquisition. So it may be desirable to filter the data. But caution must be taken because the amount of filtering might affect the shape of the acceleration-time history curve and mask important details. The source of the vibration and its effect should be well understood before any data filtering. Experimental modal analysis can be used to filter data. For example, Gelingardi et al ([8]) identified the first axial eigenfrequency of the dart using experimental modal analysis. Later they used a low pass filter with cut off frequency equal to the first axial eigenfrequency of the dart.

The acquisition rate is another important issue in signal acquisition. Gelingardi et al ([8]) suggested that an acquisition rate of 50 kHz is good enough. Because the impacting process lasts approximately 40 milliseconds.

Now it seems that the magnetostrictive position sensor described above is not necessary if there is a way to determine the velocity just before impact. This can be achieved using a sensor such as laser sensor, photodiode etc. For example, Lifeshitz et al [59] attached a flat arm of known width

to the horizontal steel bar mentioned above. This arm passes in front of a photo cell when the impactor falls or rebounds. Then the velocity of the impact or rebound is equal to the width of the arm divided by the time intervals that it takes the fiat arm to pass the photo cell.

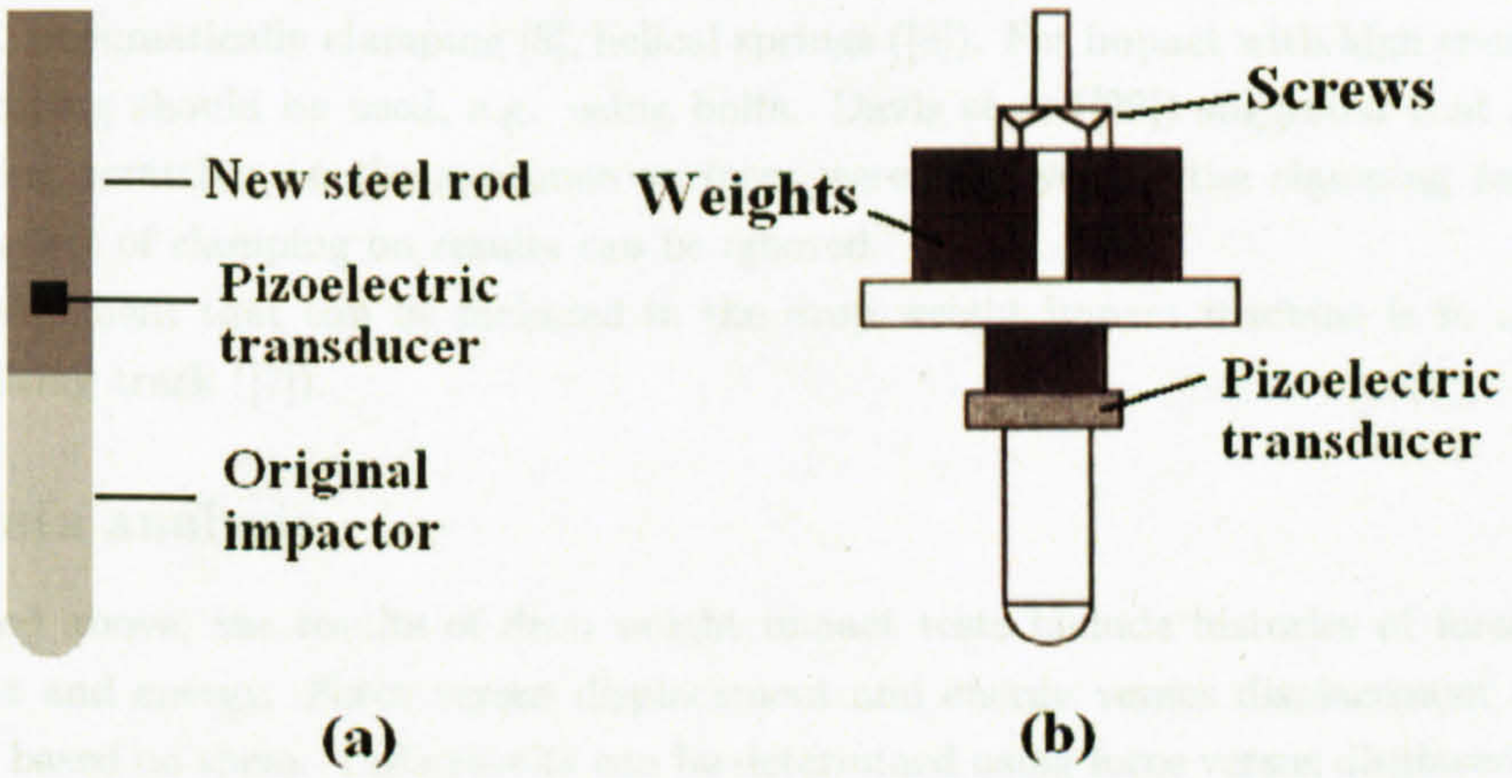

Figure 2.7: **Adding extra weights in drop weight impact test** - (a) extra steel rod; (b) extral weights ([19])

So far three things including a horizontal steel bar, a piezoelectric accelerometer and a magnetic ring have been attached to the original impactor. The original impactor is a short rod made from hard steel with known geometry and weight. The weight of the original impactor is normally small. Zhou ([96]) suggested that this steel rod should have enough length to allow both reflection and penetration of the specimen. This can be achieved by placing another steel rod behind the original impactor as shown in figure 2.7 (a). Extra weight is needed to achieve high energy impact. Figure 2.7 (b) shows a example ways to adding extra weight.

In drop weight impact tests where the impactor doesn't perforate the specimen, there is a possibility of multi-hits due to rebounds which should be avoided. Brakes can be used to prevent multi-hits [63, 73], which can be triggered manually or automatically. A rebound catch mechanisms was used by Davies et al [29] as shown in figure 2.8. It contains two spring-loaded arms, two catch blocks and an aluminium latch bar. The two spring-loaded arms are restrained by the aluminium latch bar before impact. During the impacting process the two spring-loaded arms are released when the latch bar is caught by the catch blocks. When the impactor continues to fail the two arms rub against the inside of the catch blocks until the impactor rebounds back above the catch blocks. Then the two arms are in full stretch. When the impactor fails for the second time the two arms land on the catch blocks and the impactor will be stopped.

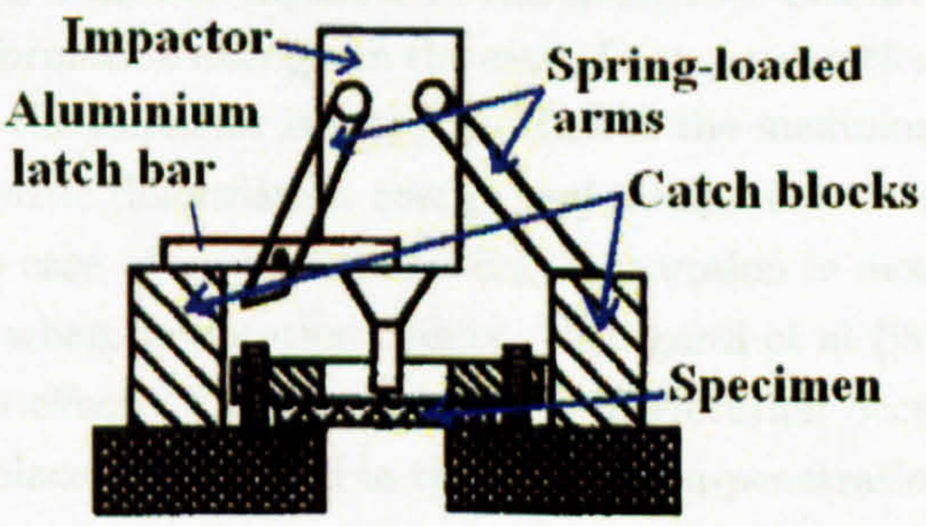

Figure 2.8: **A rebound catch mechanism in drop weight impact test** - Redraw from reference [29]

Not only the movement of the impactor that needs to be restricted, so does the movement of the specimen. A sample stage is normally used to restrict the movement of the specimen. It is mounted to either the ground or a heavy base on which the two vertical guiding bars are mounted. The specimen is clamped to the sample stage. For impact with small energy, weak clamping should be used, e.g. pneumatically clamping [9], helical springs ([8]). For impact with high energies, other ways of clamping should be used, e.g. using bolts. Davis et al ([29]) suggested that if very few friction sliding scratches on the specimen surfaces were observed in the clamping regions after impact the effect of clamping on results can be ignored.

Other refinement that can be included in the drop weight impact machine is to introduce a motorized lifting track ([7]).

2.4.2 Data analysis

As mentioned above, the results of drop weight impact tests include histories of force, velocity, displacement and energy. Force versus displacement and energy versus displacement curves can constructed based on them. Tests results can be determined using force versus displacement curve. There are three possible results, i.e. rebound, stop or perforation as shown in figure 2.9 ([8]). Drop weight impact tests with these three results have been used for researchers for different purposes. For example, in the case of rebound, compression tests of the impacted specimen can be carried out to determine its residual strength. These types of tests are called compression after impact tests. This non-penetration test can also used to assess damage resistance. A full picture of damage in specimen, i.e. 3D in nature, is necessary to make a correct judgment. A parameter called V_{50} drop mass which is similar to ballistic limit velocity can be determined ([2]). In the case perforation, the energy absorption is the main focus. In this study, the last two cases are the main focuses, esp. case where the projectile is stopped. Energy absorbed by composite specimens due to impact damage such as delamination, matrix cracks, fibre fracture, i.e. unrecoverable energy is the key parameter to be measured.

During the impact process, energy is transferred from the impactor to the specimen. The area under the force versus displacement curve is the deformation energy. In the case of non-penetration, the deformation energy reaches a maximum when the impactor is stopped. This is the maximum energy the specimen can store both as internal elastic deformation energy and dissipating it via plastic deformation or fragmentation ([8]). In the case of perforation, energy absorption is more complicated. It is difficult to determine the point where perforation occurs. Gelingardi et al ([8]) determine this point by neglecting the strain rate effect. They assuming that perforation occur suddenly at the instant equal to the maximum displacement defined in the case of non-penetration tests.

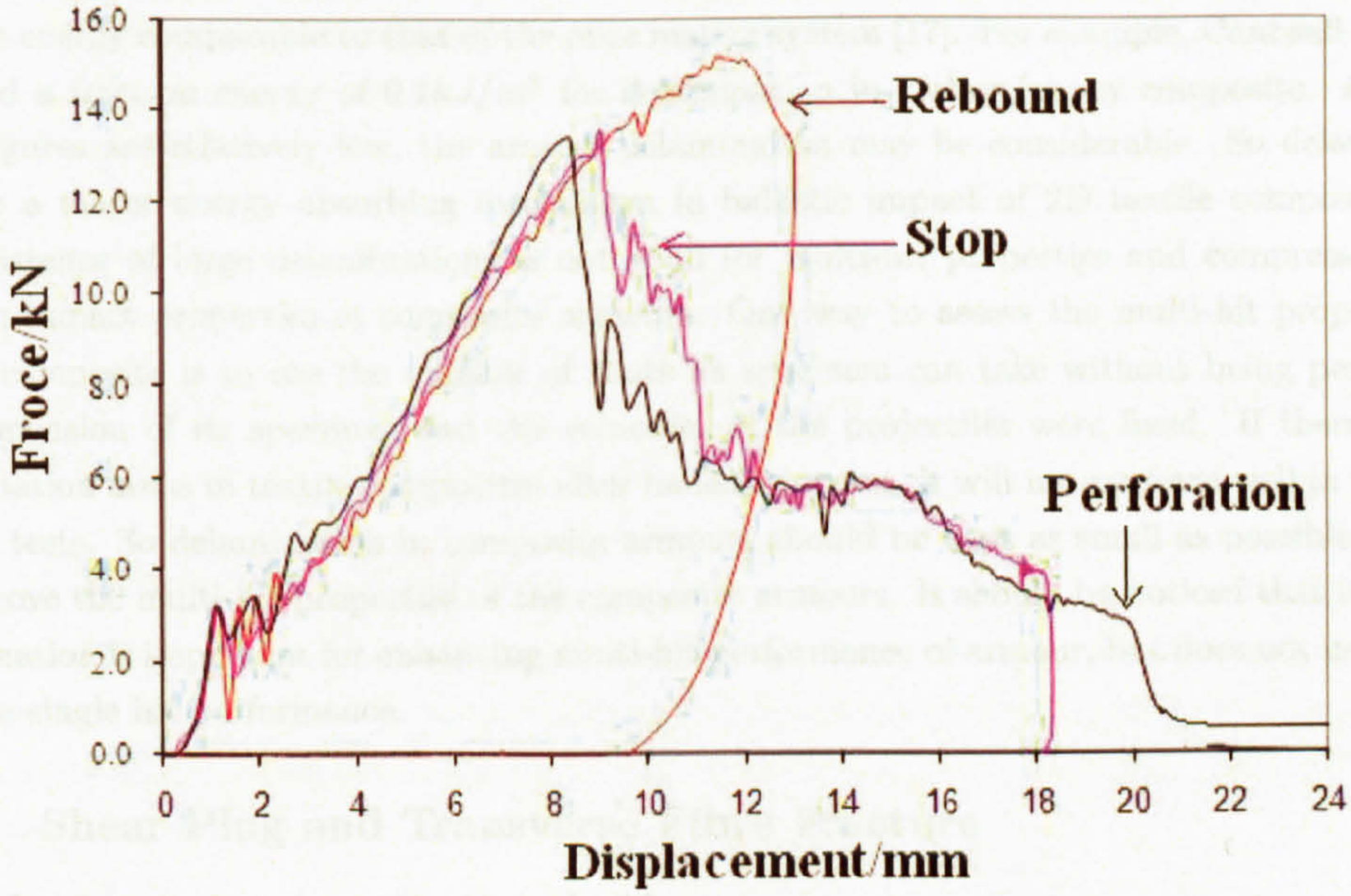

Figure 2.9: **Test results of drop weight impact tests** - contact force versus displacement curves

2.5 Damage Patterns in Ballistic Impacted 2D Textile Composites

2.5.1 Introduction

It is necessary to understand the failure processes and their related energy absorption before identifying the right materials for a composite armour design [68, 94]. 2D preforms used in textile composites have a common feature, i.e. a layered structure. Resin rich areas exist between interlaminar spaces. They only differ with each other in in-plane mechanical properties, crimping of individual yarns etc.

On a macroscopic scale, damage in composite laminate after ballistic impact include delamination, shear plug, matrix cracking, transverse fibre fracture, tensile fibre fracture, and fibre spallation etc. On a microscopic scale, damage involves fibre-matrix debonding and fibre pull-out [17].

2.5.2 Delamination

Delamination is the separation of layers in a composite laminate. It is caused by the fact that there are resin rich regions at the ply interfaces and the occurrence of large interlaminar stresses during ballistic impact. Sierakowski et al [77] suggested that delamination is mainly induced by flexural stress waves. It was observed that the five stress waves will be induced by dynamic impact in composite materials. Two waves related to in-plane motion and three related to flexural plate deformations [28]. But Cantwell [17] described delamination as the result of tensile stresses generated by tensile waves which are the result of reflections of a compressive stress wave at the rear surface of the target. The compressive stress wave is induced by the incident projectile.

In 2D textile composites, since delamination does not involve the destruction of fibres, it displays fracture energy comparable to that of the pure matrix system [17]. For example, Cantwell et al [20] reported a fracture energy of $0.1kJ/m^2$ for delamination in carbon/epoxy composite. Although these figures are relatively low, the area of delamination may be considerable. So delamination may be a major energy absorbing mechanism in ballistic impact of 2D textile composites [17]. The existence of large delaminations is not good for multi-hit properties and compression after ballistic impact properties of composite armours. One way to assess the multi-hit property of a textile composite is to use the number of shots its specimen can take without being penetrated. The dimension of its specimen and the velocities of the projectiles were fixed. If there are big delamination areas in textile composites after ballistic impact, it will not perform well in multi-hit impact tests. So delamination in composite armours should be kept as small as possible in order to improve the multi-hit properties of the composite armours. It should be noticed that inhibiting delamination is important for enhancing multi-hit performance of armour, but does not necessarily improve single hit performance.

2.5.3 Shear Plug and Transverse Fibre Fracture

Shear plug is a distinct damage pattern found in high speed impact. It does not occur in low velocity impact. It is formed due to the high shear stresses created at the point of impact. As shown in figure 2.10 below, the material around the projectile is sheared and pushed foreword [32].

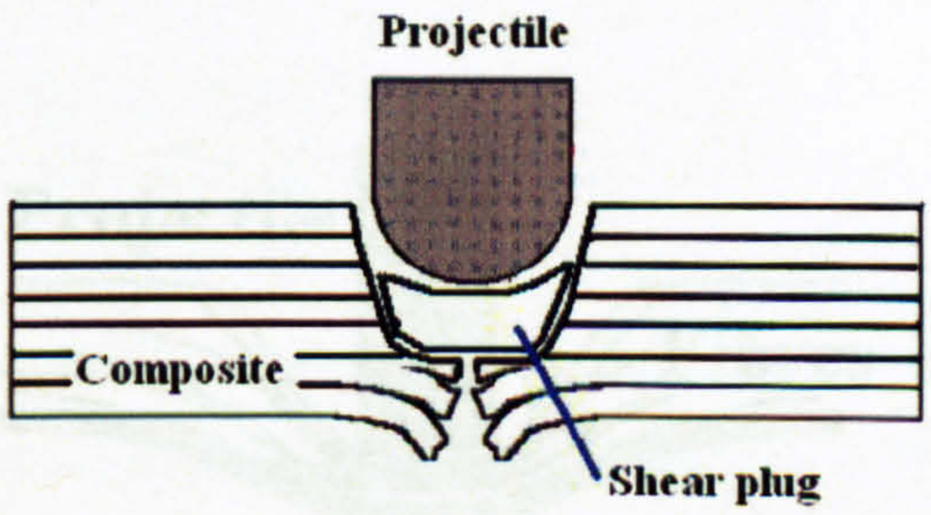

Figure 2.10: **Shear plug damage mechanism** - Redrawn after [32]

Transverse fibre fracture occurs in and near the shear plug region. Transverse fibre fracture energies in CFRP range between $20kJ/m^2$ and $60kJ/m^2$ [20] which is almost 20 times higher than that of delamination. So although transverse fibre fracture is generally limited to regions local to and near shear plug it can be a source of considerable energy absorption [17].

2.5.4 Matrix Cracking

Matrix cracks in damaged composite laminates include intralaminar matrix cracks and interlaminar matrix crack. Intralaminar matrix crack propagates in the region of resin between individual fibres, and interlaminar matrix crack propagates in the resin rich layer between two layers. During the initial crack propagation, matrix cracking exhibits fracture energy similar in magnitude to that of the neat matrix material. However, as the matrix cracks continue to grow they are bridged by local fibres and more energy is needed [17].

2.5.5 Tensile fibre failure

Tensile fibre fracture may occur in both the front and rear side of composite laminate. Tensile fibre failure in the front side of composite laminate occurs specifically for tipped projectiles [25]. For

example, Iremonger observed that fragment simulation projectile cut a plug by shearing the fibres along its right-angled edges and by tensile failure in the oblique faces. Tensile fibre failure in the rear side of composite laminate can be caused by larger loading area that results from delamination [48] and shear plug.

2.5.6 Fibre spallation

Fibre spallation resulted from the reflected tensile waves mentioned in 2.5.2. Attempts to limit damage due to stress wave propagation have centred on using woven fabrics as surface protection or employing through thickness reinforcing fibres [17].

2.5.7 Fibre-matrix debonding

Fibre-matrix debonding occurs when the stress field near the crack tip exceeds the local strength of the local fibre-matrix interface. With continuing crack propagation the fracture surfaces separate causing many fibres to pull out of their surrounding matrix. During this pulling out process energy is extended in overcoming local frictional forces.

2.5.8 Fibre Stretching

Fibre stretching plays an important role in energy absorption in fabric armours. Its effect is restricted in composite armour due to the presence of resin which prevents fibres moving freely. But there is still evidence of fibre stretching in composite armour. Scott [74] observed fibre stretching in the first few layers as show in figure 2.11. Fibres are driven in to the underlying layers before they fail, rebound and form a reverse pyramid on the impact surface.

2.5.9 Melting of Fibres

For some organic fibres such as nylon, melting of fibres may occur during ballistic impact. The melted nylon fibre would partly bind the fibre together [48].

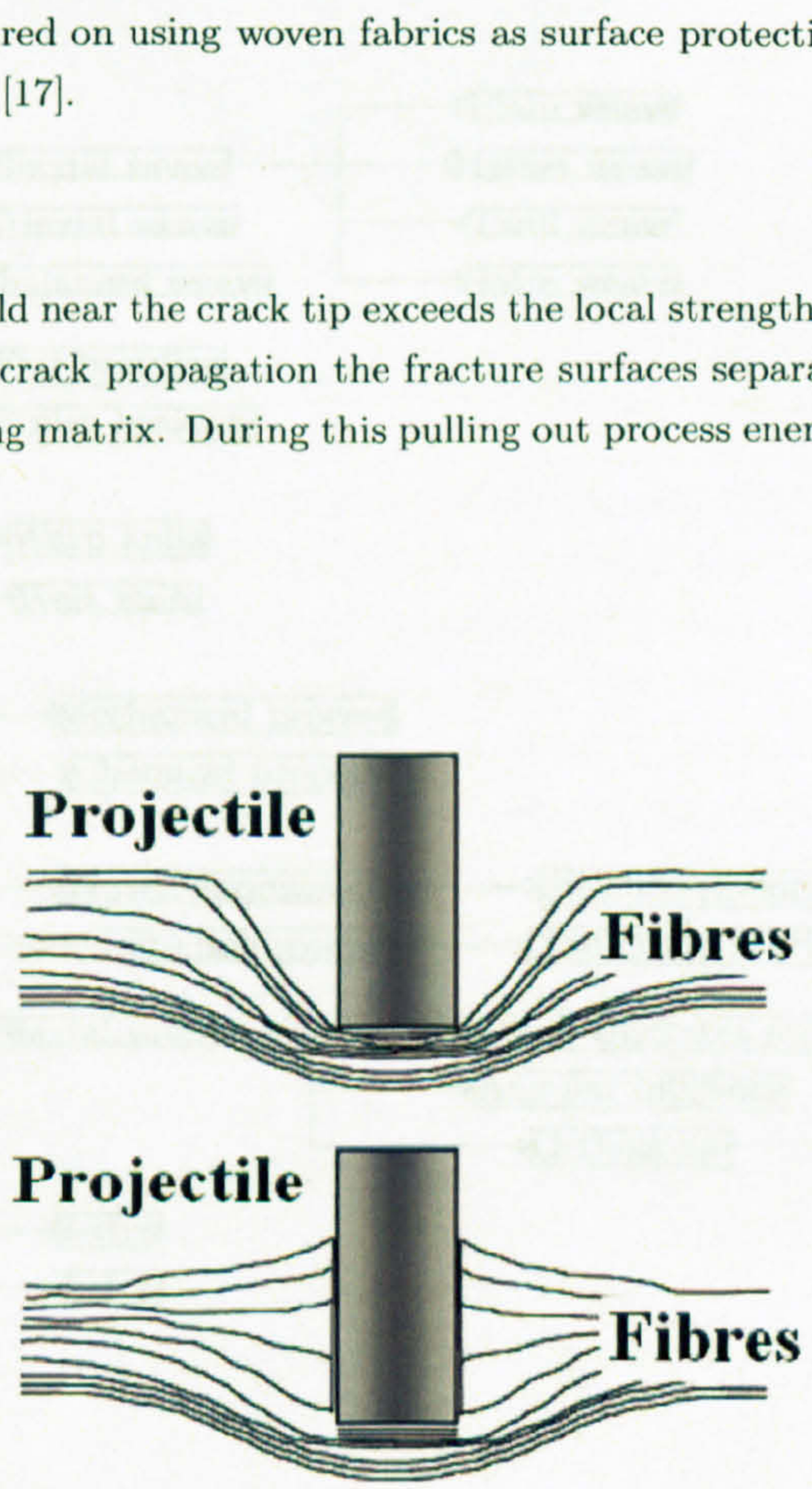

Figure 2.11: **Fibre stretching in ballistic velocity impact of composite.** - after Scott[74]

2.5.10 Damage Process

Different damage mechanisms occur and dominate in different stages in the process of ballistic impact. Cantwell [17] studied ballistic performance of CFRP using ball projectiles. He described the process of damage during ballistic velocity impact as follows: at first, matrix cracking occurs followed by delamination; Then fibre fracture and shear plug occur; During the pushing out of the plug, more fibre fracture occurs, and failure mode changes from a through-thickness shear mode to

fibre failure when the projectile encountered the region of delamination. Similar process of damage development was also observed by Lee et al [55] who used Spectra fibre reinforced composites and FSPs.

2.6 Effect of Fabric Structure on Ballistic Performance of 2D Textile Composite

2.6.1 2D fabrics

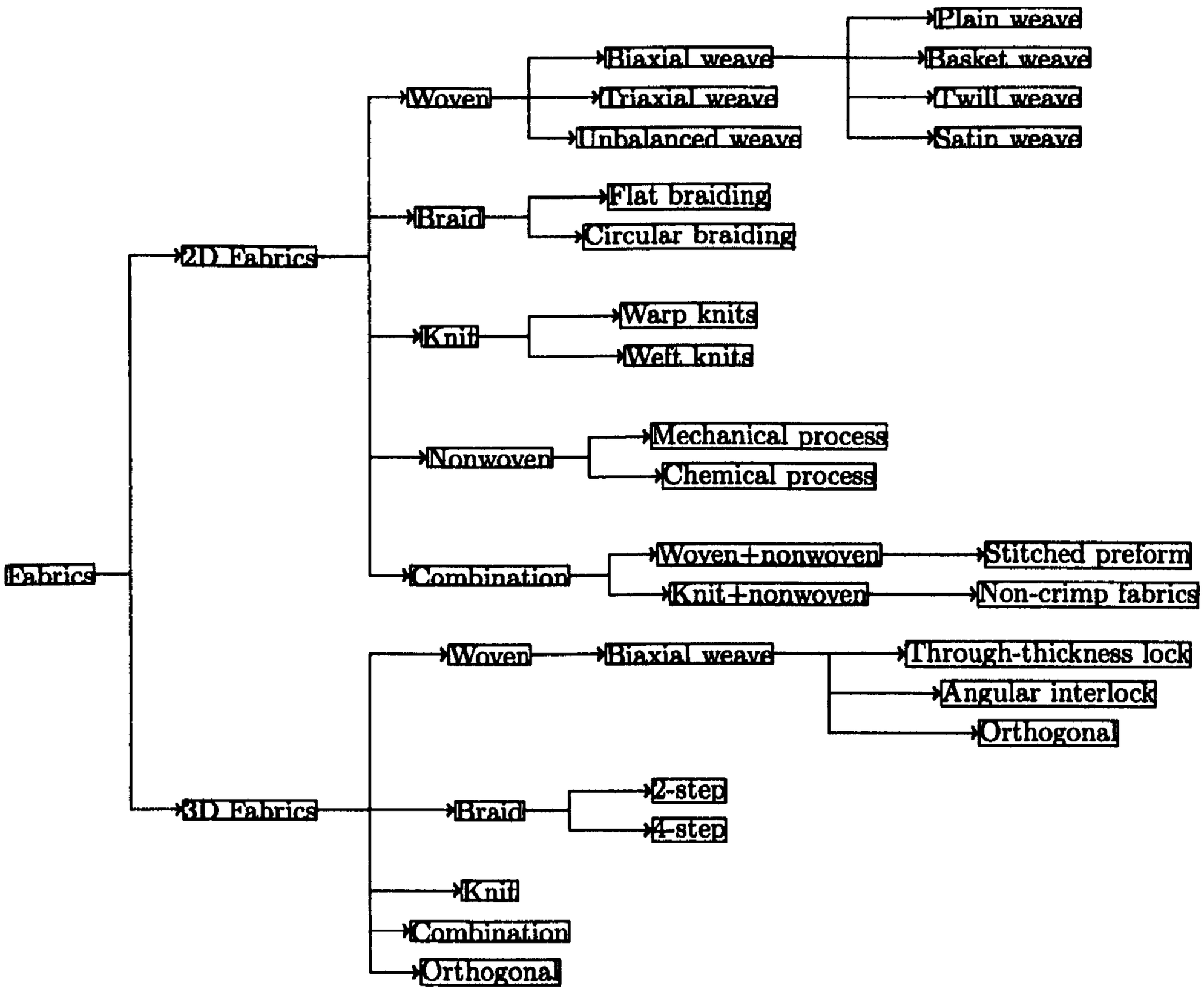

Figure 2.12: **Fabrics currently available ·**

An assembly of fibre or fabrics which is used to fabricate a composite panel is called a preform. Unlike issues such as the effect of properties of its constituent materials on overall properties and effect of ratios of its constituent materials on overall properties, the effect of the architecture of preform is less understood, especially in impact loading conditions [6]. Preforms can be formed by multi-layers of 2D fabrics or 3D fabrics, or a monolithic 3D fabric. Figure 2.12 shows fabrics available nowadays except short fibre reinforcements and random distributed long fibre mats, i.e. 1D preforms. Composites reinforced by these fibres are not suitable for ballistic application due to their non-uniform microstructures.

2.6.2 2D Weaves

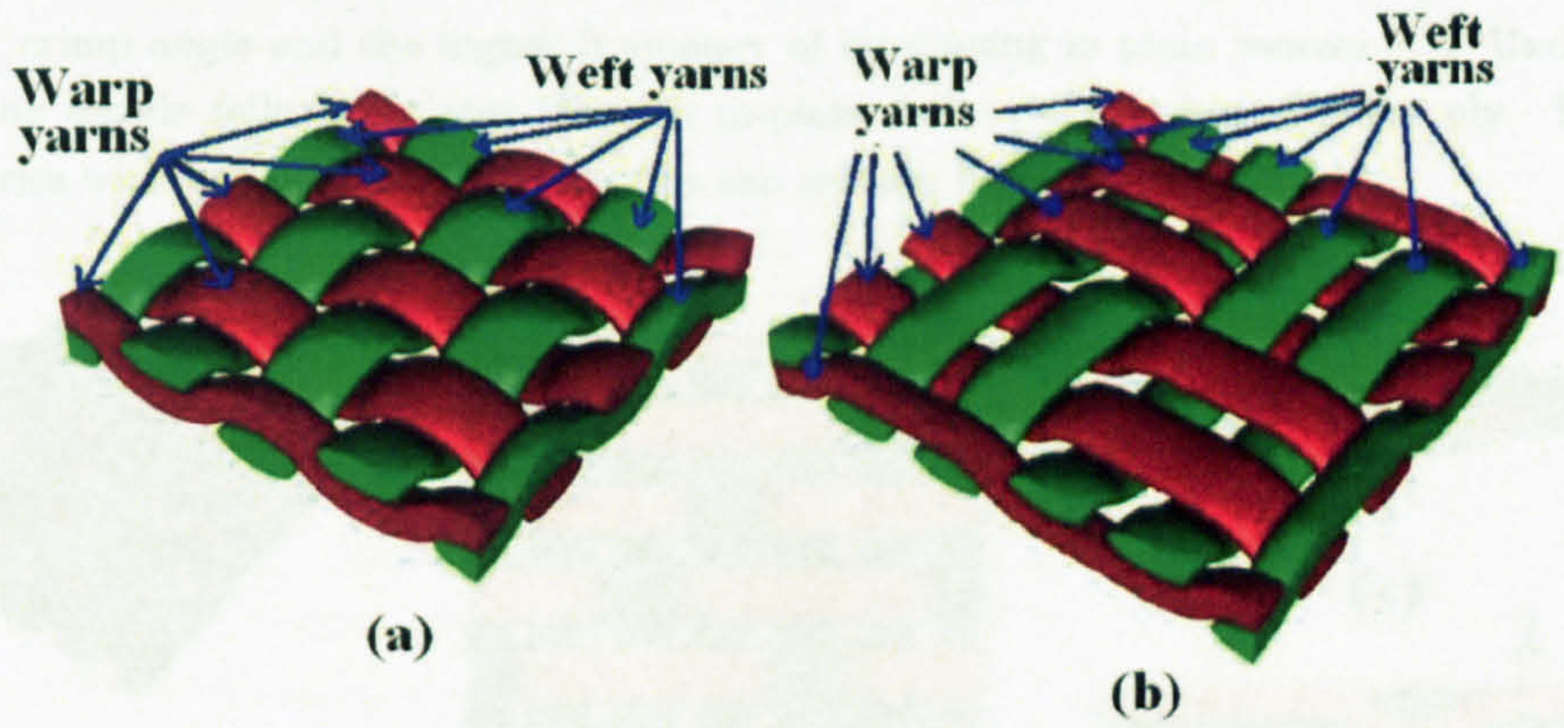

Figure 2.13: **2D woven fabrics** - (a) plain weave; (b) basket weave.

2D woven fabrics are formed by interlacing two or more sets of yarns. When two sets of yarns are used, i.e. in biaxial weaving, they are normally interlaced at right angles. The set of lengthwise yarns are called warp yarns. And another set of yarns which are drawn under and over warp yarns are called weft yarns. Plain woven fabric is the simplest biaxial woven preform. Each weft yarn crosses the warp yarn by going over one, then under the next, and so on as shown in figure 2.13 (*a*). Basket weaves are similar to plain woven but with two or more tows as a unit interlacing with each other as shown in figure 2.13 (*b*). Both plain weave and basket weave are balanced weaves. Twill woven fabric is made by passing the weft yarns over one warp yarns and then under two or more warp threads, over one and under two or more, and so on as show in figure 2.14. The satin weave is characterized by four or more weft yarns floating over a warp yarn or vice versa, four warp yarns floating over a single weft yarn. Two examples of satin weave are shown in figure 2.15 and 2.16. More sets of yarns can also be used, and the resulting fabrics are called triaxial or multiaxial weaves. A single ply of triaxial or mulitaxial weave has approximately isotropic in-plane elasticity [66]. But as show in figure 2.17, fibres in triaxial weave are less compacted. Thus composites made from these fabrics will have lower fibre volume fraction than composites made from biaxial weaves.

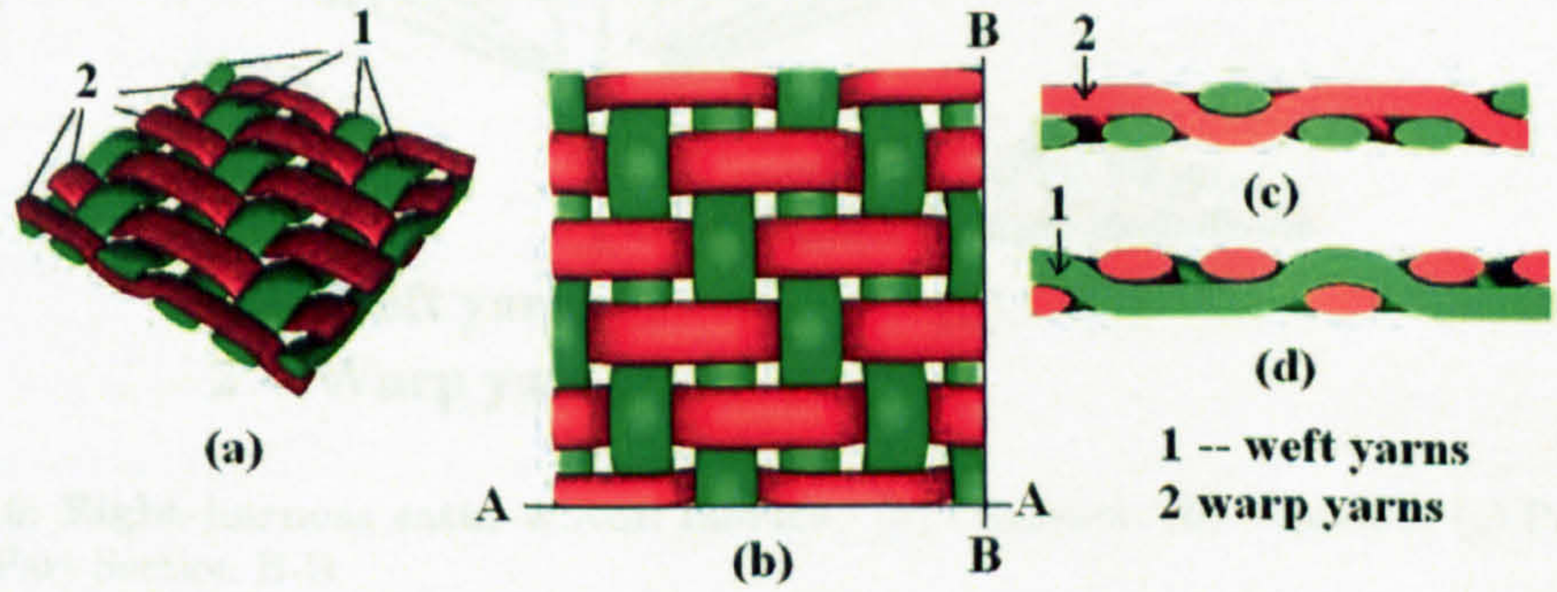

Figure 2.14: **Twill woven fabrics.** - (a) Overview; (b) Top-view; (c) Part section A-A; (d) Part Section B-B

In 2D biaxial weaves, the satin weave has the best drapability and least interlacing. Ulven [85]

observed that it also has better impact properties which was also observed by Hosur et al [47] who used carbon fibres and epoxy resin. Satin laminate has larger damage area [47]. This is due to the bigger crimp angle and the higher frequency of interlacing in plain weaves [47]. Under impact loading, the tensile failure initiates through in-plane failure of the bottommost ply. Thus satin weave fabrics with better in-plane properties can sustain higher stresses.

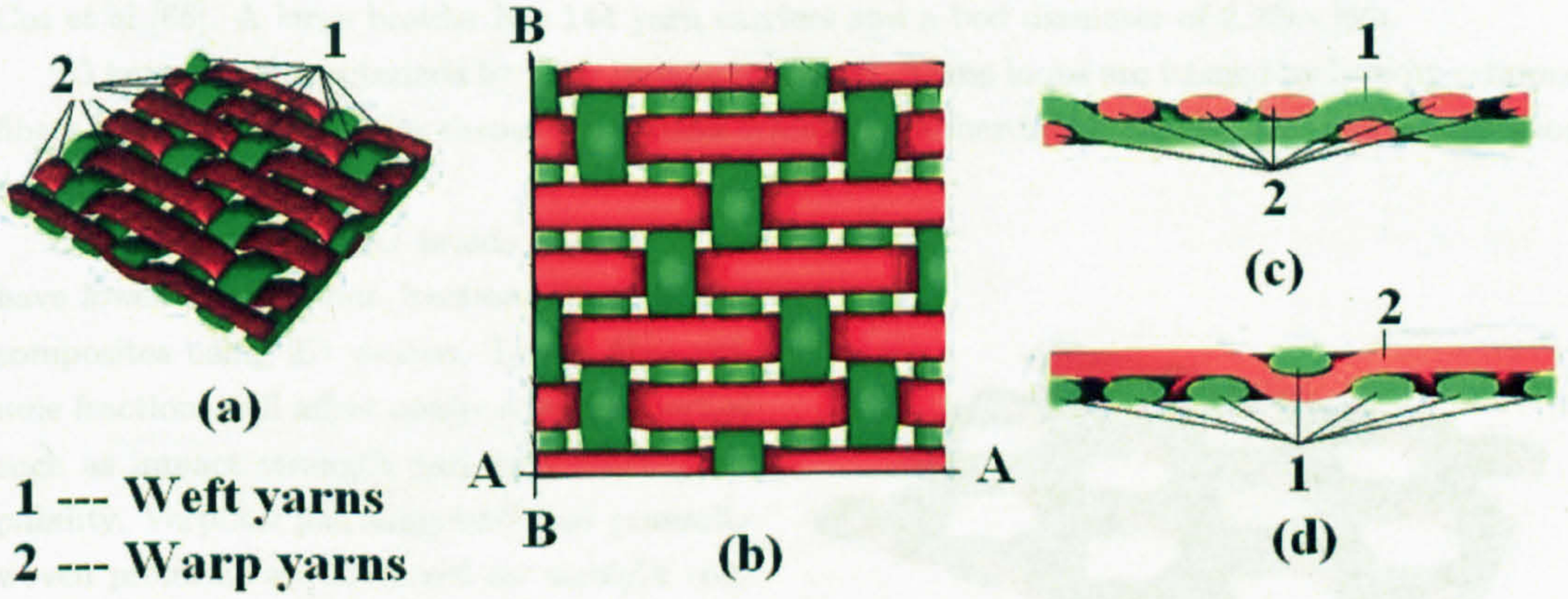

Figure 2.15: **Four-harness satin woven fabrics** - (a) Overview; (b) Top-view; (c) Part section A-A; (d) Part Section B-B

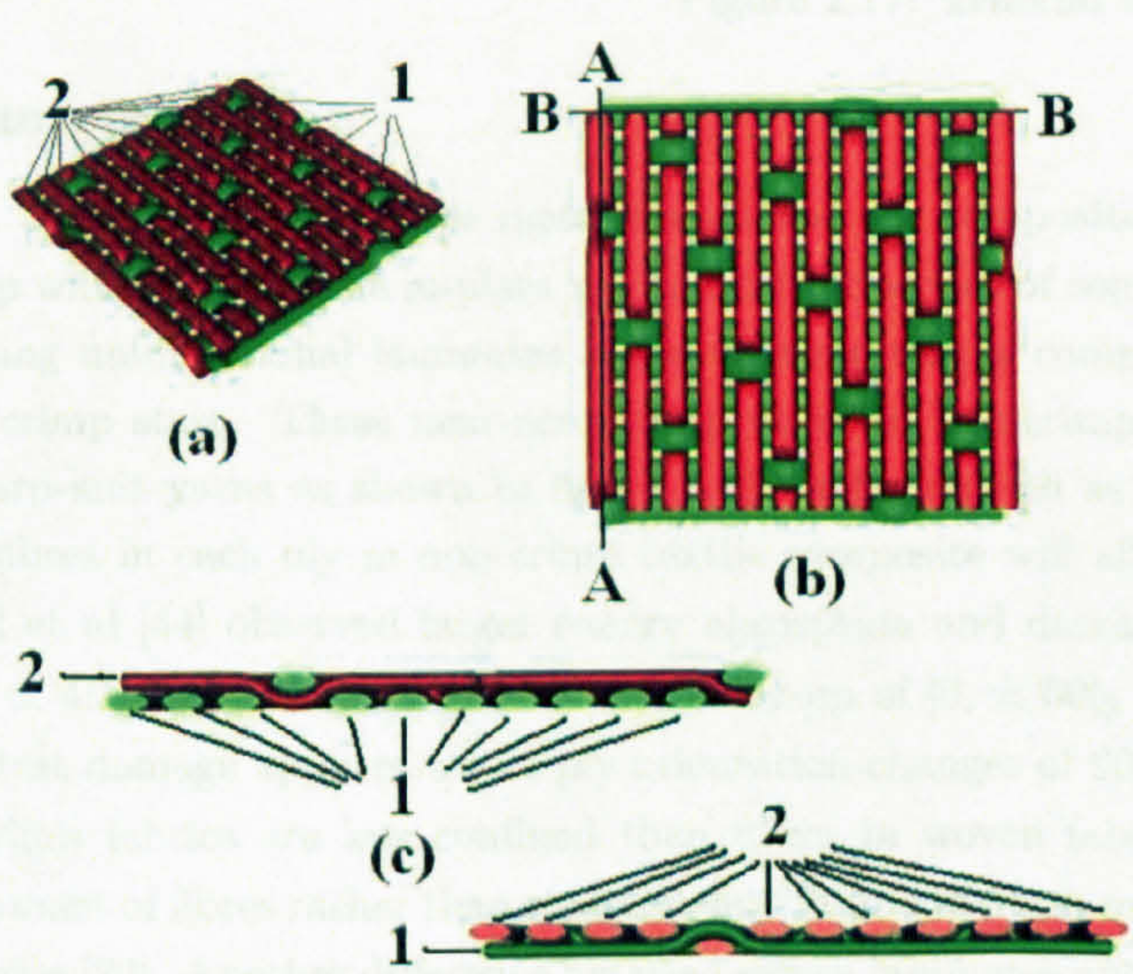

Figure 2.16: **Eight-harness satin woven fabrics** - (a) Overview; (b) Top-view; (c) Part section A-A; (d) Part Section B-B

2.6.3 2D braids and 2D knits

2D braids are formed by intertwining two or more yarn systems. In terms of structure, 2D braids are almost identical to 2D weaves. The main difference between the two structures is that the angle between the yarn systems in a braid can be less than 90° [86]. Applications for braids as composite armour can be limited by the size of the braiding machines available as described by Cot et al [66]. A large braider has 144 yarn carriers and a bed diameter of $2.25m$ [66].

2D knits are characterized by their interlacing loops. These loops are formed by heavily crimped fibres which results in poor through-thickness strength and hardness. But 2D knits have very good drapability.

Composites using 2D braids and 2D knits have lower fibre volume fractions than that of composites using 2D weaves. Lower fibre volume fractions will affect composites' properties such as impact strength and load bearing capability. Verpoest [86] suggested that generally woven preforms are preferred for straight contoured shapes while braided and knitted preforms are selected for more complex shapes but are often confined to non-load bearing applications.

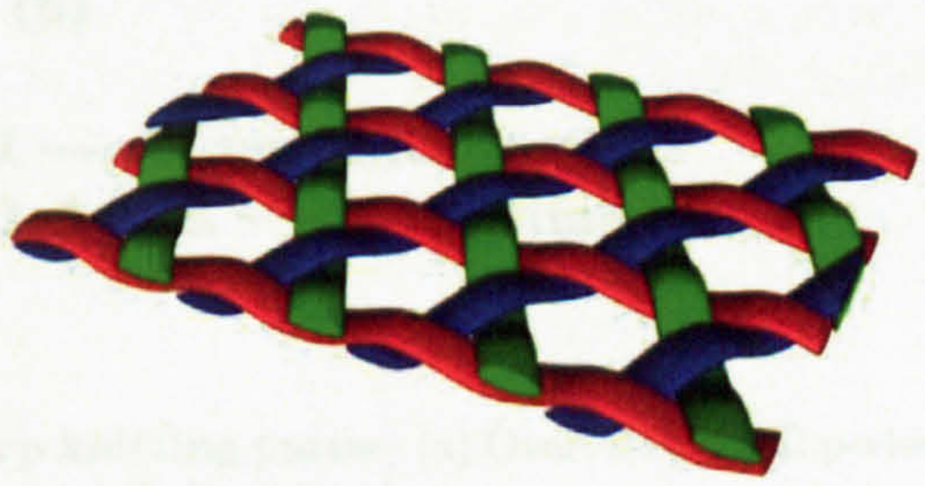

Figure 2.17: **Triaxial woven fabrics.**

2.6.4 Non-crimp fabrics

So far it seems that biaxial weaves are best materials suitable for composite amour. But there is the problem of crimp which reduces the in-plain mechanical properties of composite. This problem can be solved by using unidirectional laminates and non-crimp textile composites in which fibres have the near-zero crimp state. These near-zero crimp fibres in non-crimp fabrics are normally held together by warp-knit yarns as shown in figure 2.18, or by z-stitch as shown in figure 2.19. The orientation of fibres in each ply in non-crimp textile composite will affect the damage. For example, Hammond et al [44] observed larger energy absorption and damage area for laminates with a lay-up of $[0, \pm 45, 90]_2$ s than laminates with a lay-up of $[0, \pm 60]_3$ s. Cantwell et al [20] found that the greatest damage appears where ply orientation changes of 90° occur.

Fibres in non-crimp fabrics are less confined than fibres in woven fabrics. During ballistic impact, planar movement of fibres rather than straining and failure of fibres may occur. Composites may fail at low energies [20]. Another difference between woven laminates and non-crimp laminates is a phenomena called generator strip reported by Ellis et al [32] which occurs in non-crimp laminate but not in woven laminate. The generator strip phenomenon can be described as follows: (a) upon impact the projectile pushed a strip of the first layer of the laminate toward the real of the panel inducing shear cracks in the resin matrix parallel to the fibres; (b) this strip, in turn, applied a transverse load to the second ply and resulted in a separation between the first two laminae [55] as shown in figure 2.20. In addition, delamination in non-crimp fabrics has more anisotropic pattern. This is because of the presence of resin-rich areas between the reinforcing fabric layers and the greater constraint to matrix crack propagation parallel to the fibres in woven laminate.

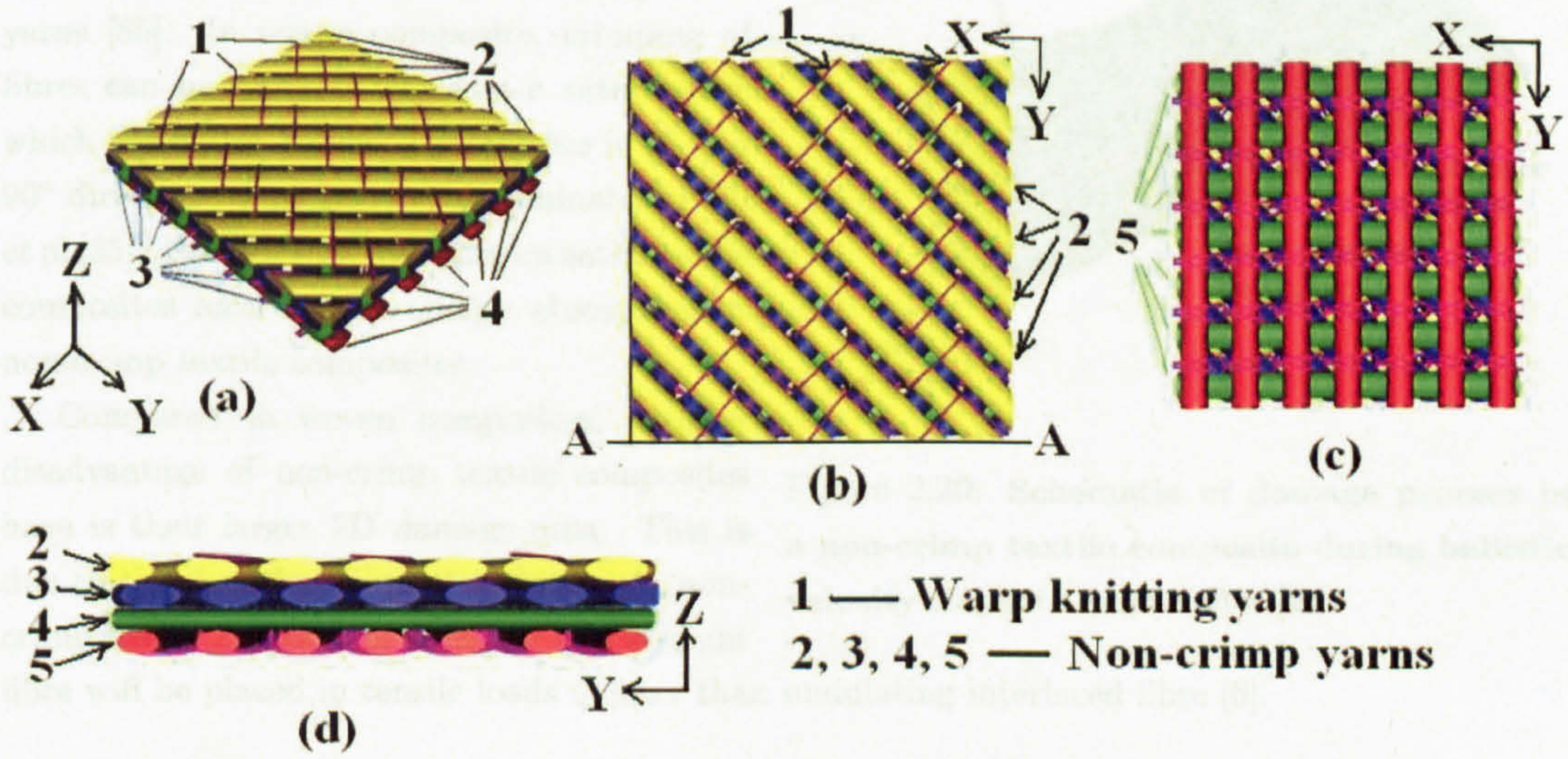

Figure 2.18: **Non-crimp fabrics containing warp knitting yarns** - (a) Overview; (b) Top-view; (c) Bottom-view; (d) Part section A-A; (e) Part section B-B.

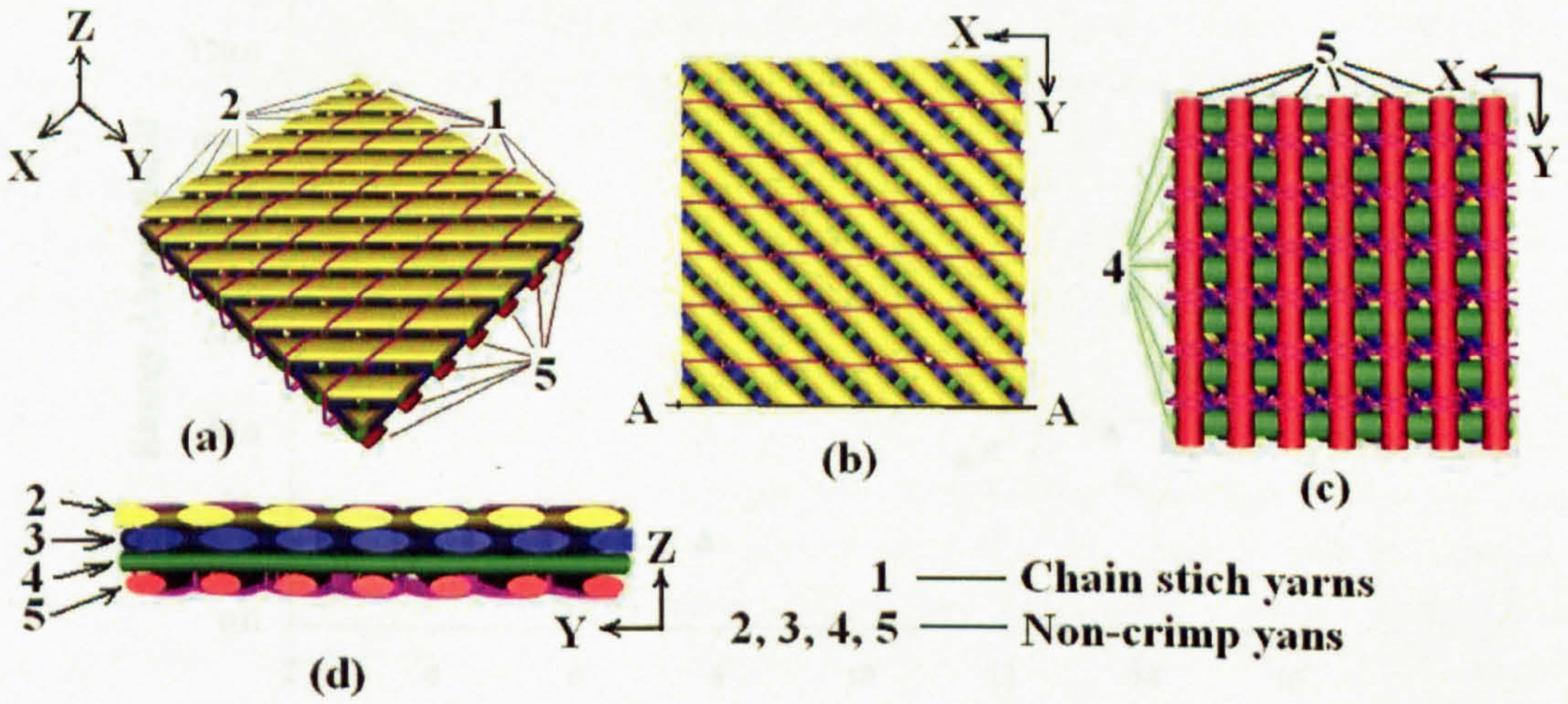

Figure 2.19: **Non-crimp fabrics containing stitch yarns** - (a) Overview; (b) Top-view; (c) Bottom-view; (d) Part section A-A; (e) Part section B-B.

Woven composites also have higher strain to failure values in impact loads than non-crimp textile composites due to the interlacing of the yarns [85]. In woven composite, crimping of fibres can be reduced by using a satin weave which has better balanced properties in 0° and 90° directions than non-crimp laminates. Fujii et al [35] observed that five-harness satin textile composites have similar energy absorption as non-crimp textile composites.

Compared to woven composites, another disadvantage of non-crimp textile composites have is their larger 2D damage area. This is due to the fact that fibre straightness in non-crimp textile composites is higher and straight fibre will be placed in tensile loads quicker than undulating interlaced fibre [6].

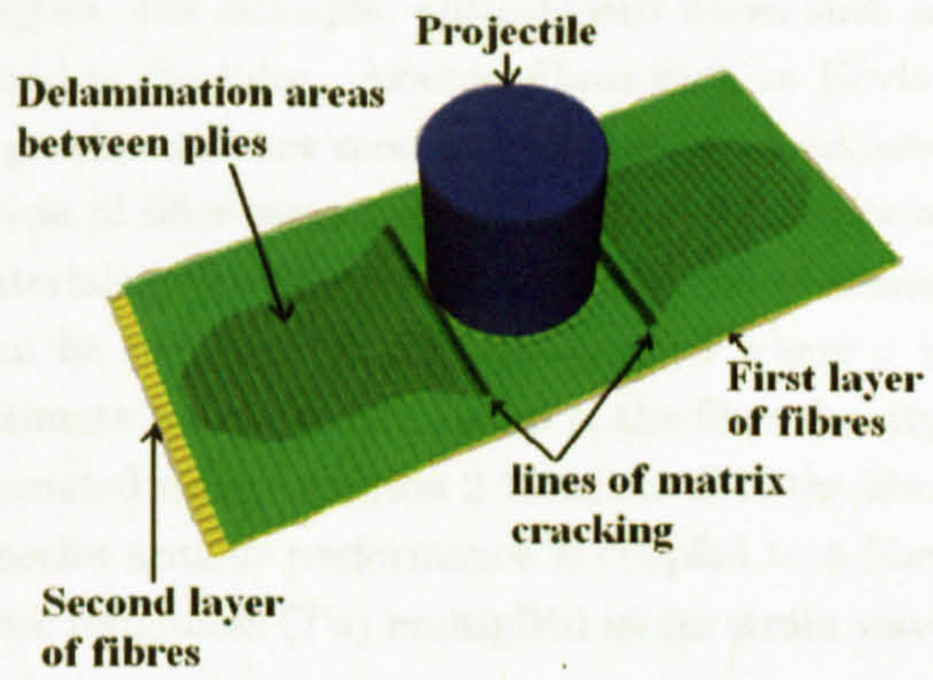

Figure 2.20: **Schematic of damage process in a non-crimp textile composite during ballistic velocity impact** - redraw after [32]

2.7 Effect of Materials on Ballistic Performance of 2D Textile Composite

2.7.1 Biaxial Woven textile composites

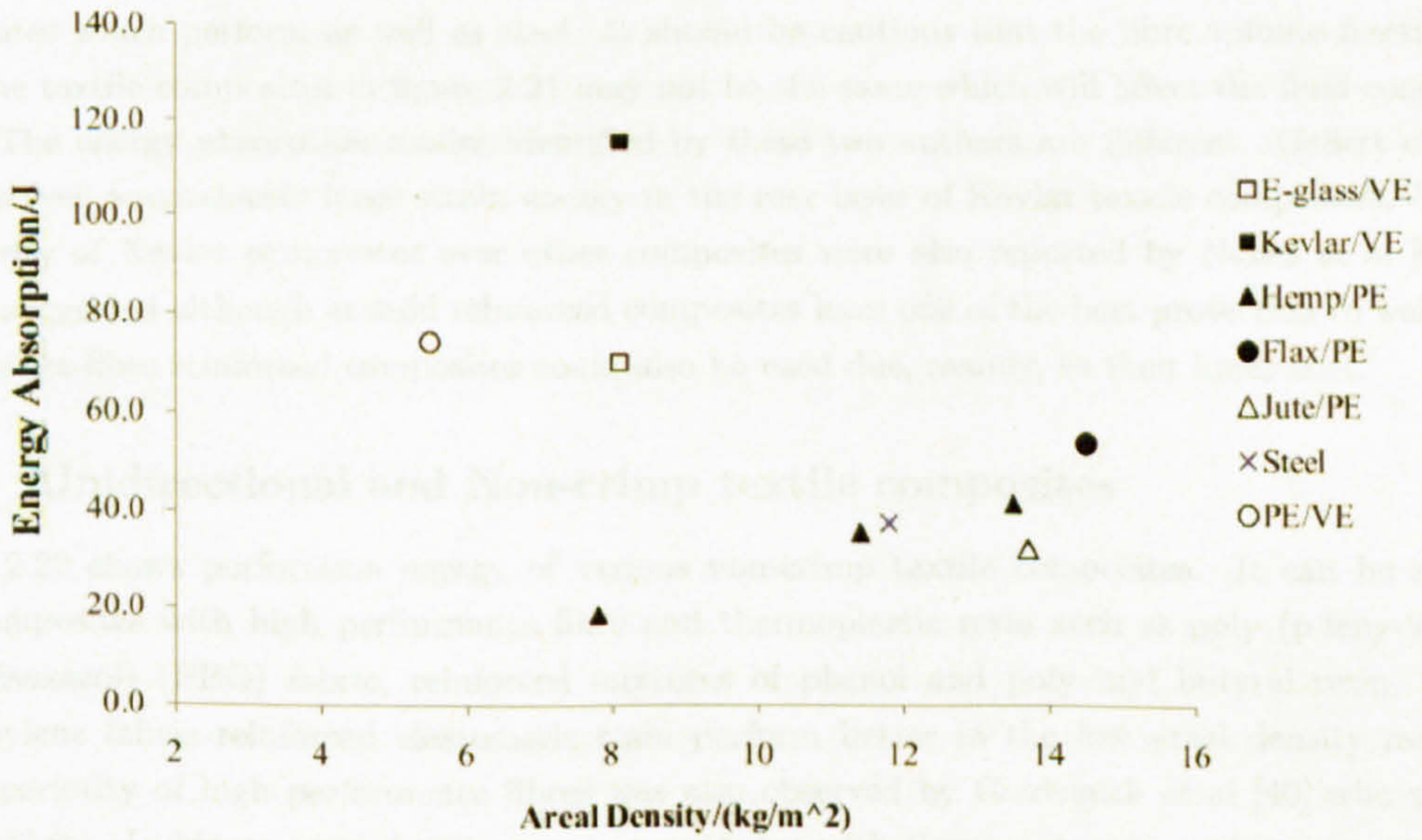

Figure 2.21: **Perforation energy of plain woven textile composites** - Datas for Hemp/PE, Flax/PE, and Jute/PE composites are from [88] and dates for E-glass/VE, Kevlar/VE, and PE/VE composites are from [37]

Different fibres have different mechanical properties. For example, polyethylene fibres such as Specatra-900 have high strength, high ductility and low modulus. Aramid fibres such as Kevlar have high strength, medium ductility and specific gravity and low modulus. Graphite fibres have high tensile modulus and low ductility [95]. The type of fibre materials will affect the transfer of stress wave in composite which is a function of materials properties. If we assume a linear elastic fibre, the specific toughness ((Tu)) of the fibre can be calculated using equation 2.9 where σ is the fibre ultimate tensile strength, ϵ is the fibre ultimate tensile strain, and ρ is the fibre density. The stress wave velocity of the fibre VS can be calculated using equation 2.10 where E is the fibre Young's modulus. Cunniff [26] observed that composite armour performance is coupled to a fibre property U defined as the product of the specific fibre toughness (Tu) multiplied by its strain wave velocity VS. Equations 2.11 below defined the property.

$$Tu = \frac{\sigma\epsilon}{2\rho} \tag{2.9}$$

$$VS = \sqrt{\frac{E}{\rho}} \tag{2.10}$$

$$U = Tu \times VS = \frac{\sigma\epsilon}{2\rho}\sqrt{\frac{E}{\rho}} \tag{2.11}$$

Gellert et al [37] did ballistic tests on E-glass/vinyl ester, Kevlar/vinyl ester, and Spectra/vinyl ester textile composites using FSPs. With the same FSPs, Wambua [88] studied the ballistic performance of flax/polypropylene, hemp/polypropylene, and jute/polypropylene textile composites. Perforation energies of these textile composites are shown in figure 2.21. Composites with high strength fibres such as , Spectra and E-glass fibres perform better than low strength natural fibre composites which perform as well as steel. It should be cautious that the fibre volume fractions of all the textile composites in figure 2.21 may not be the same which will affect the final conclusions. The energy absorption modes identified by these two authors are different. Gellert et al [37] observed anomalously large strain energy in the rear layer of Kevlar textile composites. The superiority of Kevlar composites over other composites were also reported by Nunes et al [67]. But he suggested although aramid reinforced composites have one of the best protection to weight ratios, glass-fibre reinforced composites could also be used due, mainly, to their lower cost.

2.7.2 Unidirectional and Non-crimp textile composites

Figure 2.22 shows perforation energy of various non-crimp textile composites. It can be seen that composites with high performance fibre and thermoplastic resin such as poly (p-feny-2, 6-benzobisoxazol) (PBO) fabric, reinforced mixtures of phenol and polyvinyl butyral resin, and polyethylene fabric reinforced elastomeric resin perform better in the low areal density range. The superiority of high performance fibres was also observed by Goldsmith et al [40] who used Kevlar fibres. In bigger areal density range, composites with thermoset resin perform are not as good as composites with thermoplastic resin (based on trendline). This is because of the fact that epoxy matrix is rigid and this does not allow PBO and Spectra fibres to move relative to each other during penetration. These movements are necessary for PBO and Spectra fibres to store energy by tensioning which is more efficient than delamination in terms of energy absorption. So in order

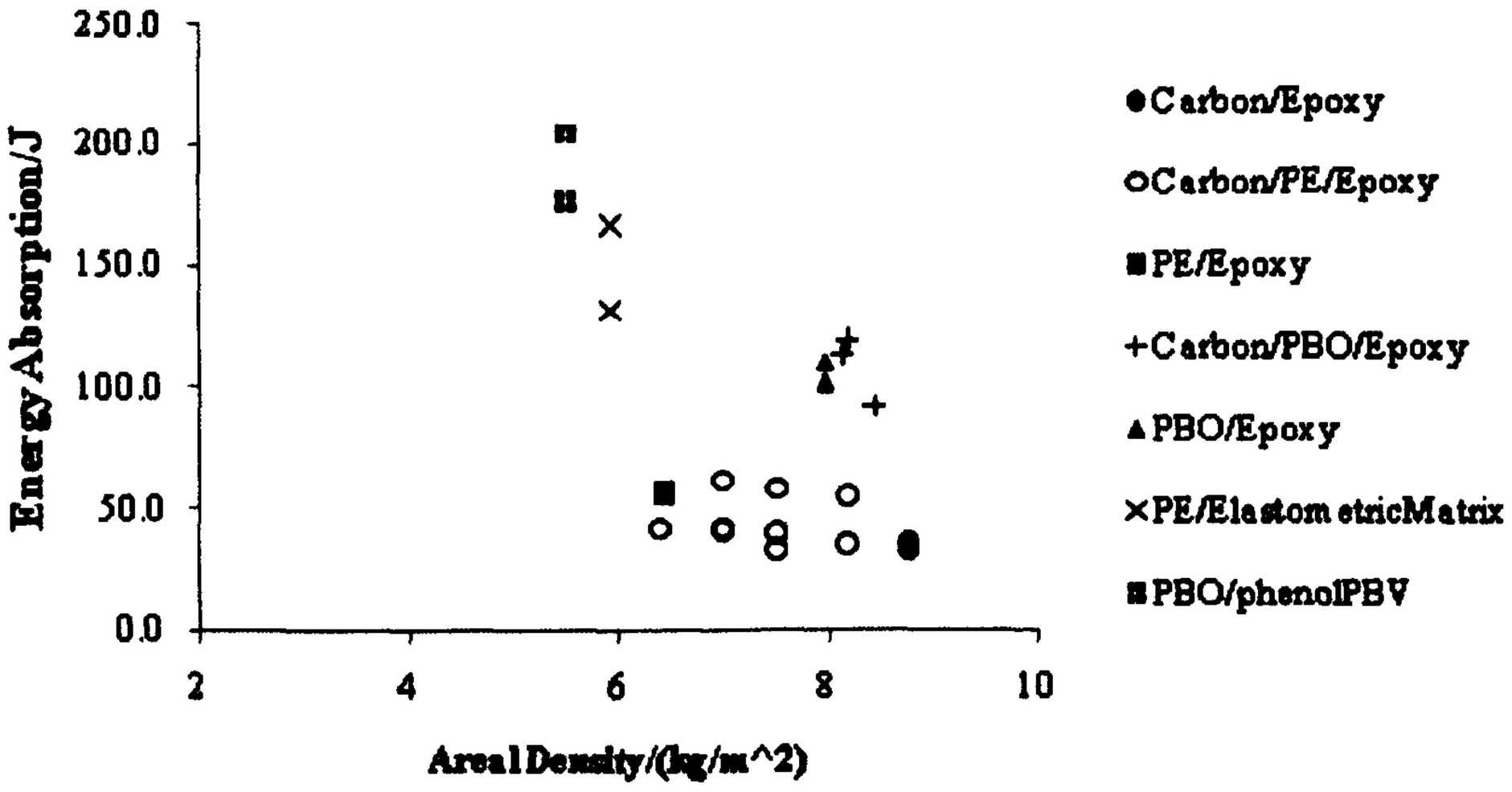

Figure 2.22: **Perforation energy of plain woven textile composites.** - redraw from [54]

to utilise the inherent potential of the fibres, the matrix should be adapted to take account of the different fibres, which means a rigid matrix for the stabilization of the carbon fibres and a weak matrix for the organic fibres allowing them to move relative to each other under impact penetration [54]. It should be cautious that the fibre volume fractions of all textile composites in figure 2.22 may not be the same which will affect the final conclusions.

In high area density range, composites with PBO fibres and Spectra fibres still perform better than composites with carbon fibre. The delamination areas at velocities near the ballistic limit of Spectra and PBO composites are twice as bigger as that of carbon composites. The properties of carbon fibre composites were improved by, hybridizing carbon with PBO fibres, putting PBO fibre at the back of the laminate. The resulting composite even performs slightly better than PBO composites.

2.8 Effect of Shape of Projectile on Ballistic Performance of 2D Textile Composite

The shape of a projectile has a significant effect on the ballistic performance of composite laminates. Different projectile geometries can cause different damage modes. For example, hemispherical projectiles cause smooth perforations, cone projectiles cause sharp edge penetrations, and flat projectiles cause intense shear failures. Montgomery et al [64] found that pointed bullets were not decelerated as quickly as blunt bullets. But they also reported that effect of the bullet geometry decreases as the number of plies increases, which has also been observed by Lim et al [83].

Gellert et al [38] studied ballistic performance of glass fibre reinforced plastics (GRP) using flat ended and conic projectiles. They found that less energy is needed to perforate thick composite laminates when conic projectiles were used. They also found that perforation energies are independent of projectile nose shape for thin composite laminates.

2.9 Effect of Interface Property on Ballistic Performance of 2D Textile Composite

Interface properties in composite laminates are also important for its ballistic performance. The damage patterns that occur in ballistic impacts such as fibre debonding are dependent on interface properties, and strong a fibre/matrix adhesion may result in shear plug [21].

Interface properties can be improved by using fibre surface treatments. For example, Tanabe [84] observed that surface treatments were effective in improving ballistic performance in a certain range of impact velocities.

2.10 Effect of Target Thickness on Ballistic Performance of 2D Textile Composite

Gellert et al [38] studied the effect of the target thicknesses on perforation energies of woven glass fibre textile composites in ballistic velocity impacts. They used flat ended steel projectile and conic projectiles. Target thicknesses in the range from $4.5mm$ to $20mm$ have been tested. Bilinear relationships were found between perforation energies and target thickness. Perforation energies were calculated using equation 2.12 where V_{50} is the ballistic limit velocity. They suggested that although the bilinear relationships between perforation energies and target thicknesses are new, the bilinear relationships between damage area and target thickness are not which have been observed in [72, 75]. Cross-sections of their perforated samples are shown in figure 2.23. These cross-sections indicate two characteristics of damage and delamination. They suggested that the transition of the relationship between perforation energy and thickness was due to change in perforation mechanisms from largely dishing in thin panels to a combination of indentation and dishing. The authors also suggested that the bilinear relationships can be easily mistaken as non-linear or even linear if sufficient wide range of target thickness were not studied.

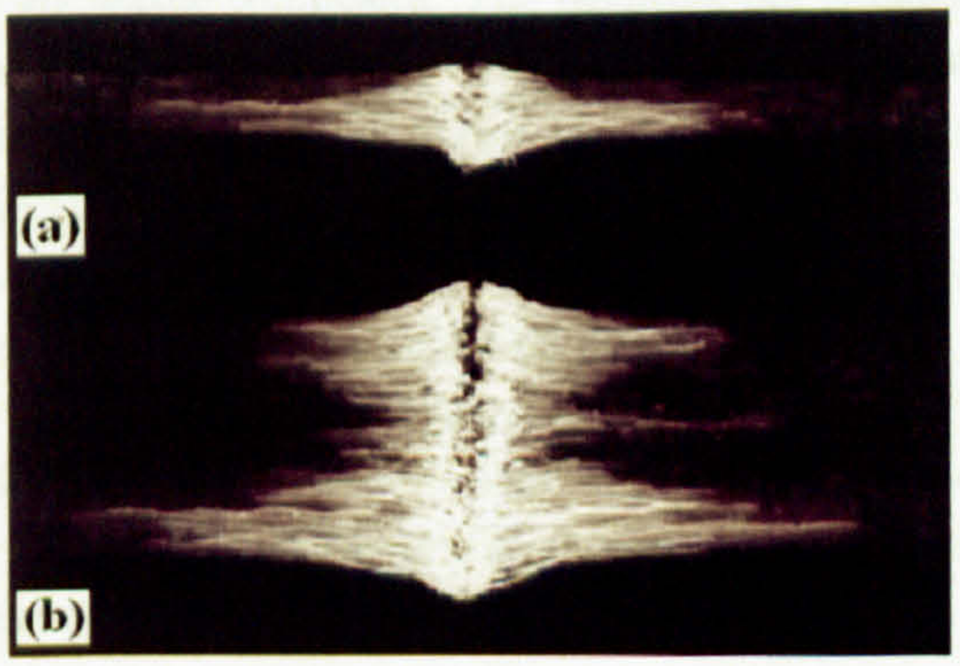

Figure 2.23: **Cross-sections of textile composites that have been impacted by cone projectiles :** - (a) 4.5 mm thickness; (b) 20 mm thickness. The impact face is upper edge of each target. [38]

$$E_P = \frac{1}{2} m V_{50}^2 \tag{2.12}$$

It has been stated that factors affecting ballistic performances of composites are mutual-interdependent. Target thickness may affect the influence of architecture of preforms on ballistic performance of composites. For example, Hosur et al [47] found that the influence of architectures of weaves on the ballistic limits is more significant for thick samples than thin ones.

2.11 Capability of typical energy absorption of various damage modes

Cantwell et al [20] summarized typical values of the energy absorbing capabilities of various damage mechanisms in carbon fibre textile composites. The carbon/epoxy composite has a fracture energy of $0.1kJ/m^2$ for delamination and $60kJ/m^2$ fracture energy for transverse fibre fracture. As we know, fibres are strong in longitudinal direction and weak in the transverse direction. It can be imagined that the fracture energy of tensile fibre fracture is higher than shear fracture energy. This was also reported by Prevorsek et al [68]. They suggested that because current high performance fibres have outstanding tensile properties but are relatively weak in compression and shear, the enhancement of penetration resistance would be achieved by design structures where penetration involves as much as possible straining and breaking of fibres in tension. The superiority of energy absorption is even more obvious when compared with energy absorption in delamination.

With such a low capability for energy absorption, a huge delamination area is needed to absorb the kinetic energy of the travelling projectile in a 2D textile composite. The resulting big damage area reduces the multi-hit property as mentioned in section 2.5.2 and the damage tolerance of composite panel. For a conventional 2D woven composites discussed above, large delamination is unavoidable, and may be the dominant energy absorption mechanisms in some cases.

So far, it can be concluded that there are two requirements for successful candidate fabric architecture for composite armours with both good single-hit and multi-hit properties, i.e. (1) promoting tensile fibre failures; (2) reducing large delamination area. Delamination can be reduced by using toughened resin systems and through-thickness stitching. Another way to reduce large delamination damage is to use 3D fabrics. In the sections below, 3D textile composite composites were reviewed in search of a textile composite meeting the two requirements mentioned above.

2.12 Ballistic Velocity Impact Performances of 3D textile composites

2.12.1 Unit Cell of 3D fabric preforms

The unit cell is the smallest repeat entity in a fabric preform ([16]). Fabric preforms are described by translation and reflection of the unit cell pattern. Unit cells of a 2D fabric can be easily identified by looking at their surface. While one 3D fabric preform may have more than one unit cell and some of them may can't be identified by just looking at their surface. By looking at surface of 3D fabric, a repeat unit can still be identified. It is formed by combination of several unit cells and is called macrocell (Byun and Chou, 1996). So knowing macrocell is enough to identify a 3D fabric preform. But identification unit cells and their position in macrocell is necessary if thing such as numerical modelling of composite and testing of composite with strain gage.

2.12.2 3D Woven fabrics

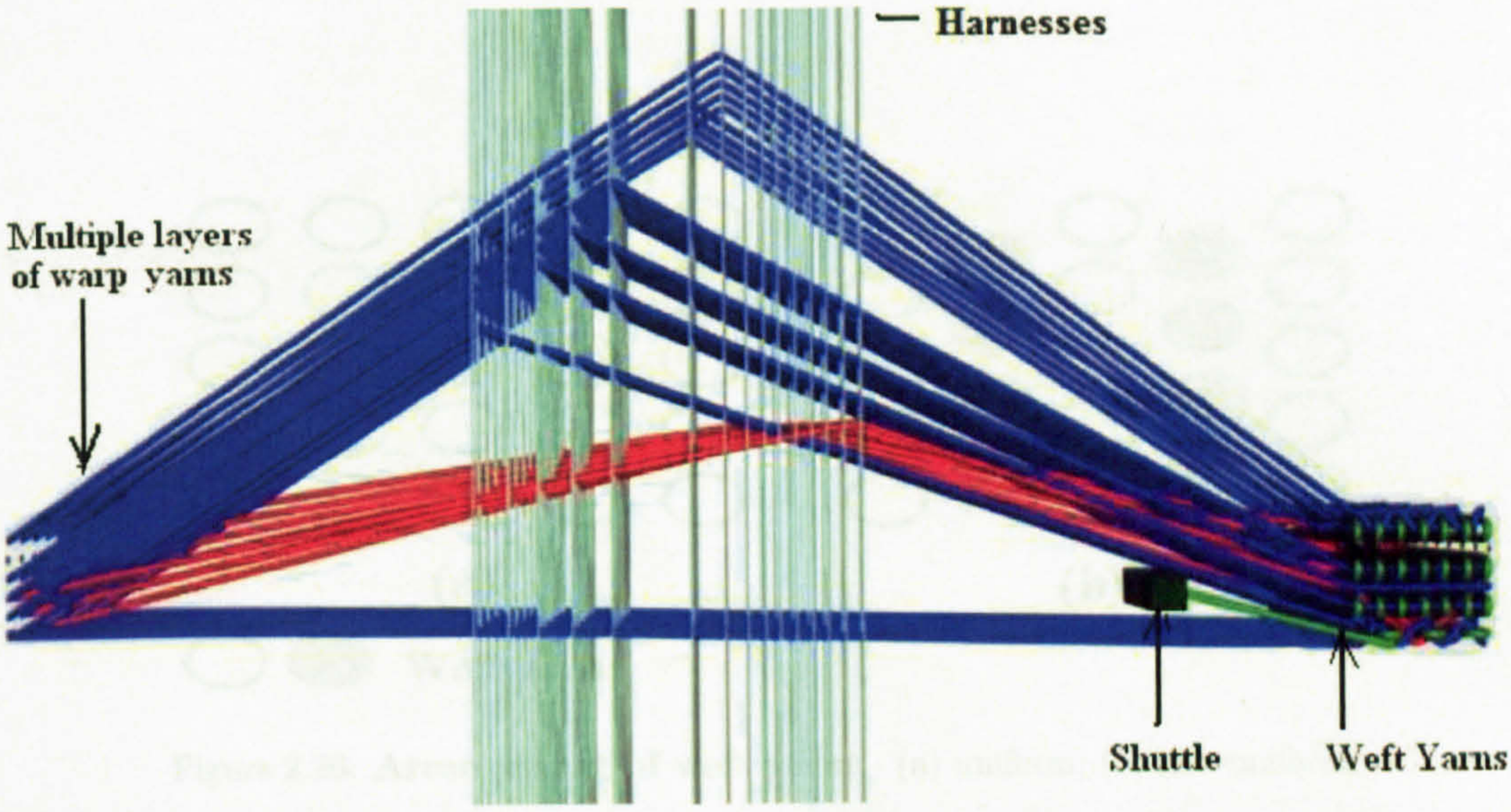

Figure 2.24: **3D weaving process.**

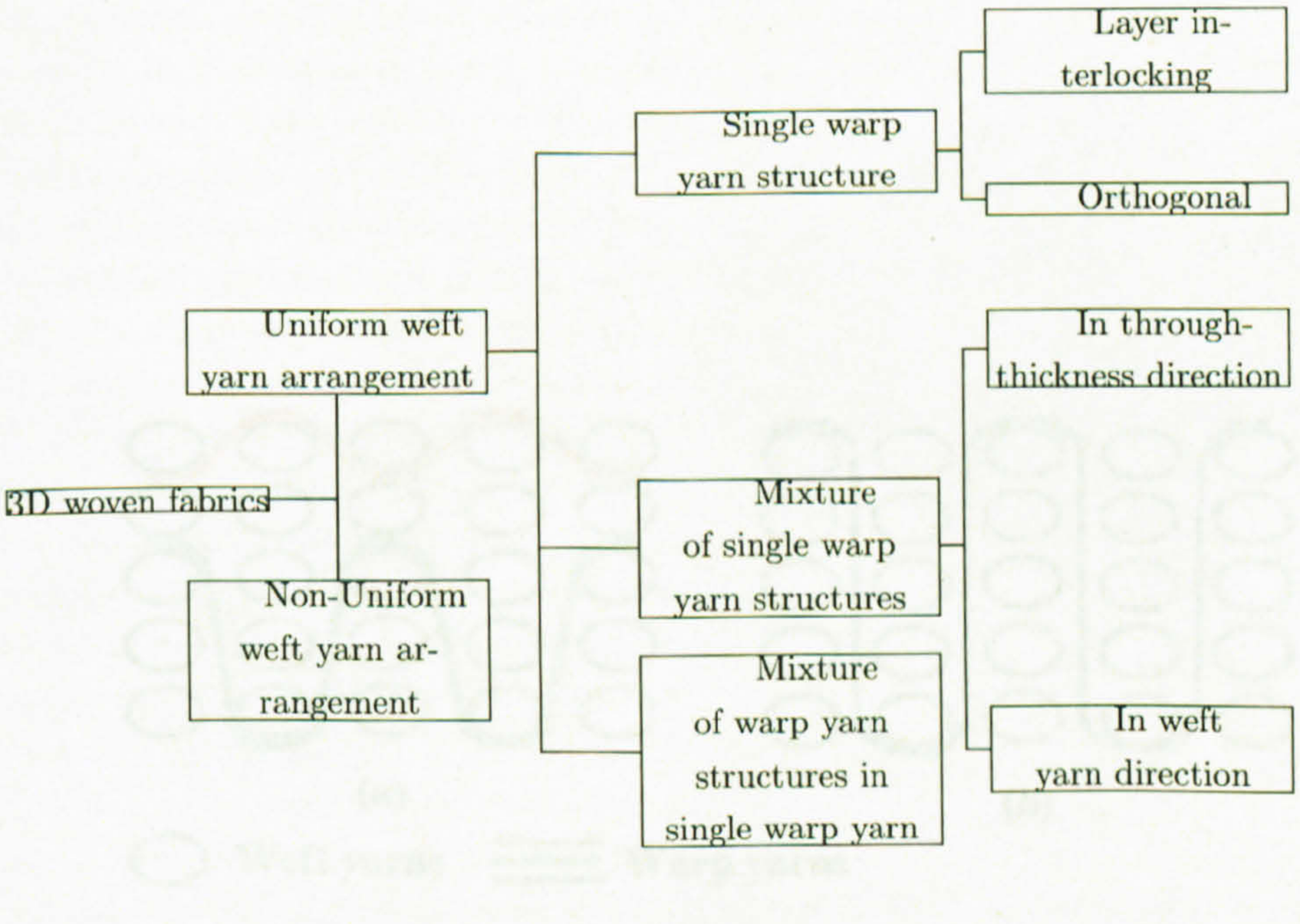

Figure 2.25: **3D woven fabrics .**

3D fabrics can be manufactured by textile techniques such as weaving, braiding, stitching and knitting. For example, figure 2.24 shows a weaving process for 3D woven fabric. Like traditional 2D weaving process, it produces fabric by interlacing of two sets of yarns, i.e. warp and weft yarns which is achieved by using lifting mechanism of warp yarns and insertion mechanism of weft yarns. During the weaving process, warp yarns are picked and lifted creating a space (shed) into which

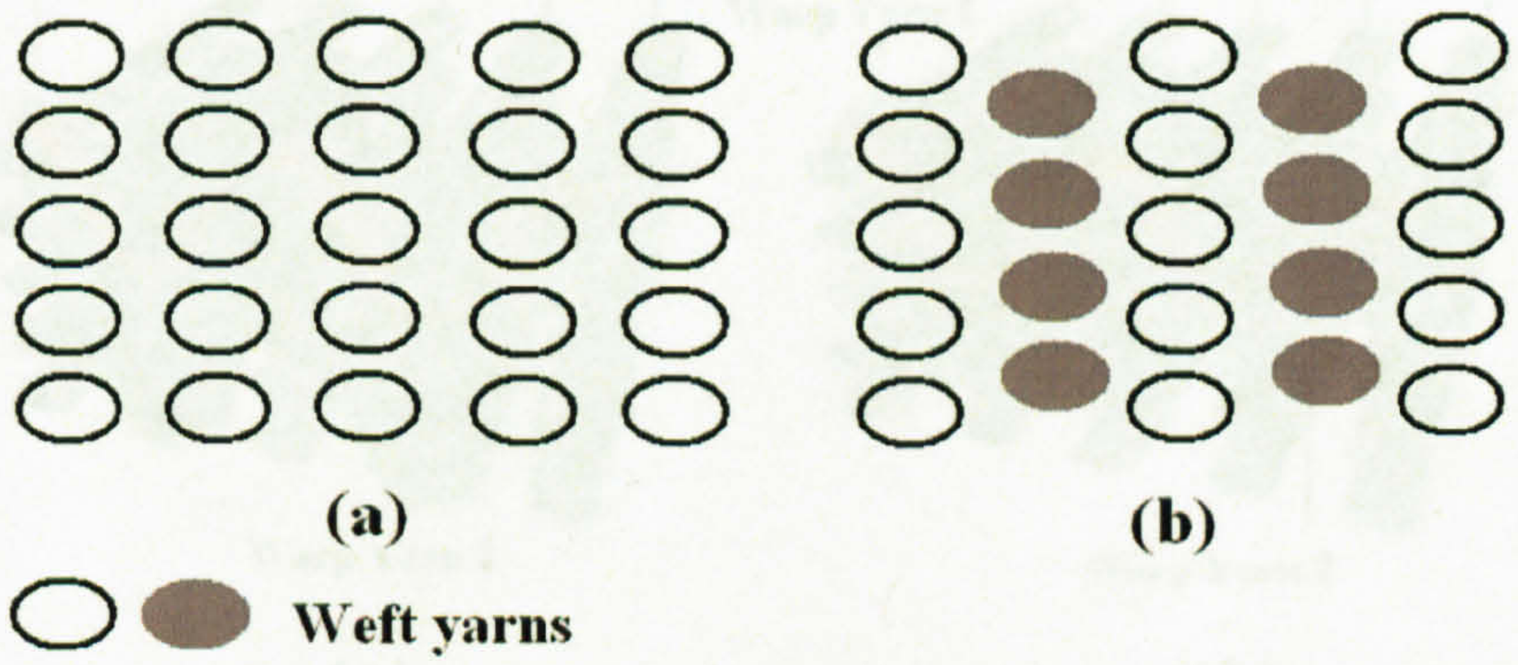

Figure 2.26: **Arrangement of weft yarns** - (a) uniform; (b) non-uniform.

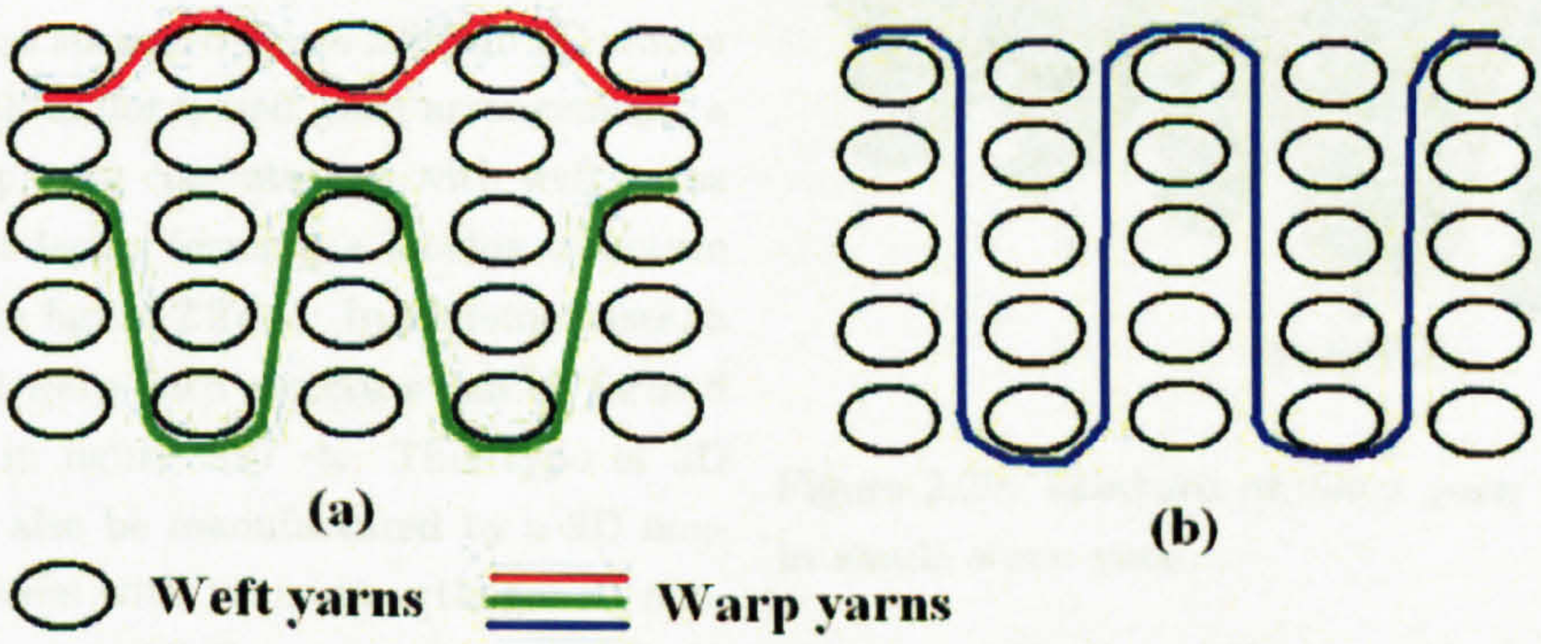

Figure 2.27: **Single warp yarn structures** - (a) two layer interlocking; (b) three layer interlocking; (c) four layer interlocking; (d) orthogonal.

the weft yarns are inserted at right angles to the warp (the 90° direction). Multiple layers of warp yarns are used in 3D weaving. The number of layers of warp yarns used determines the thickness of 3D fabrics. The width of weft yarns determines the width of 3D fabrics.

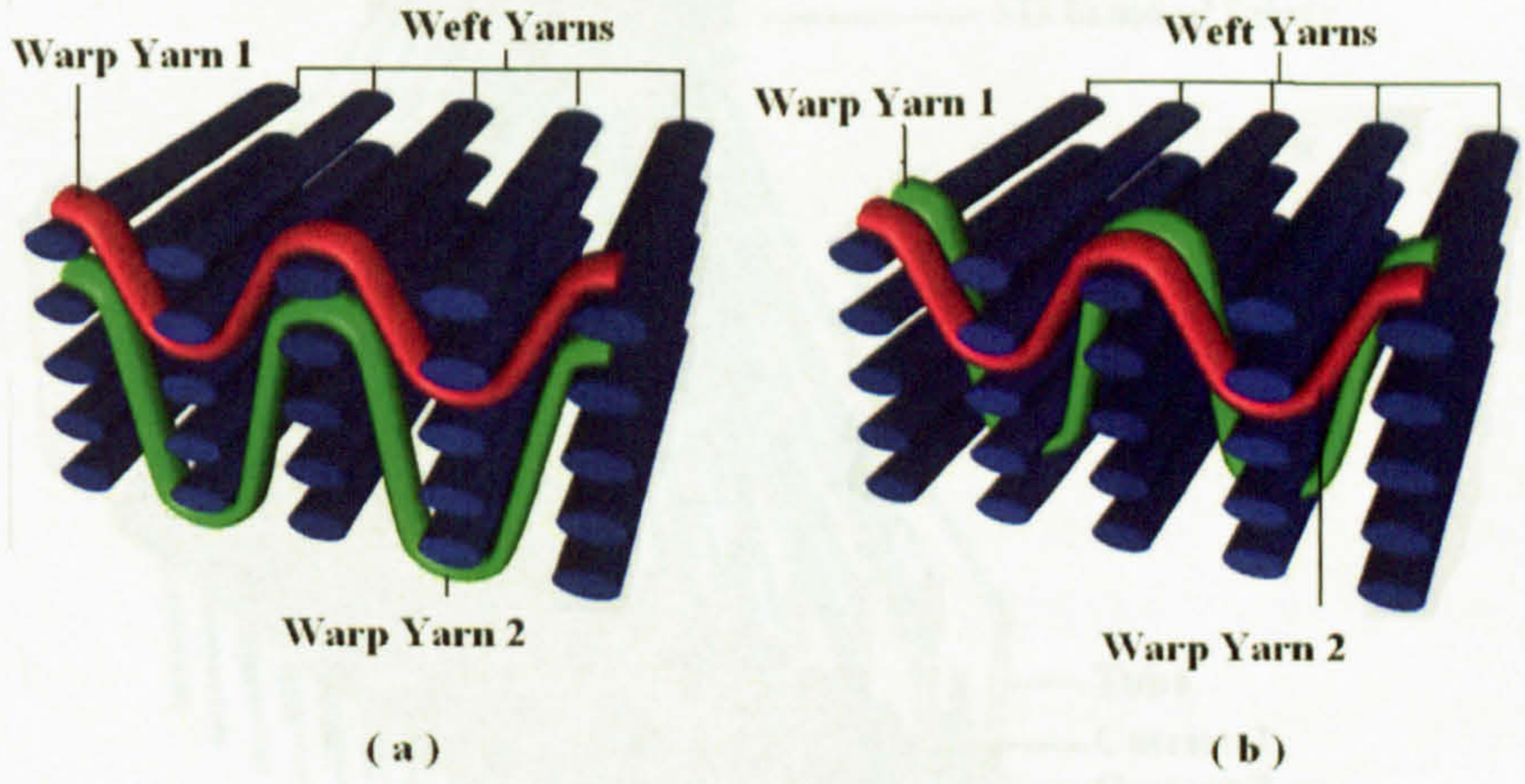

Figure 2.28: **Mixture of single warp yarn structures** - (a) in through-thickness direction; (b) in weft yarn direction.

The architecture of 3D woven fabric is determined by interlinking of warp and weft yarns which is in turn controlled by the sequence by which warp yarns are lifted and the position weft yarns are inserted. Figure 2.25 lists 3D woven fabrics that can be manufactured by 3D weaving machine shown in figure 2.24. Weft yarns can be inserted uniformly or non-uniformly as shown in figure 2.26. In 3D woven fabrics with uniform weft yarn arrangement, a single warp yarn can interlink with weft yarns in different layers forming a locking structure as shown in figure 2.27 -*a*. In extreme cases, a orthogonal warp yarn structure can be formed as shown in figure 2.27 -*b*. This type of 3D fabric can also be manufactured by a 3D non-woven process with yarns in orthogonal, non-interlacing way. All these warp yarns with single structure mentioned above can be mixed in 3D woven fabrics. As shown in figure 2.28, they can be mixed in through-thickness direction and weft yarn direction. Not only warp yarns with a single structure can be mixed, but locking structures in a single warp yarn as shown in figure 2.29. In 3D woven fabrics with a non-uniform weft yarn arrangement, defining the fabric architecture is very complicated and is only possible when the weft yarn arrangement is known.

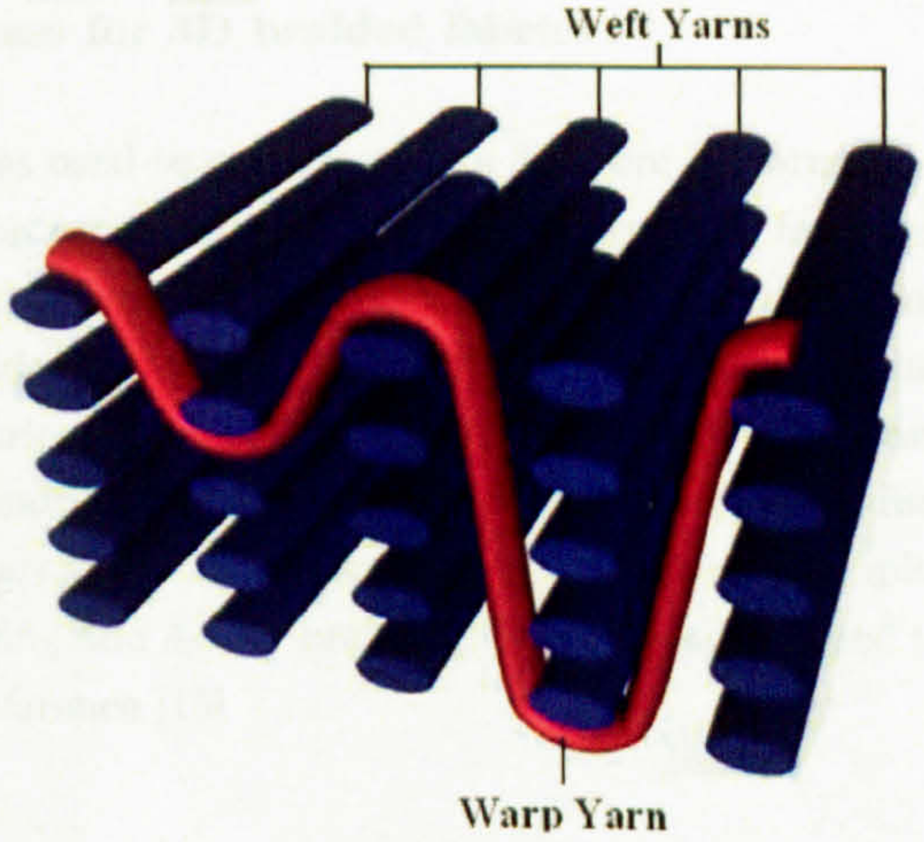

Figure 2.29: **Mixture of warp yarn structures in single warp yarn.**

2.12.3 3D braided fabrics

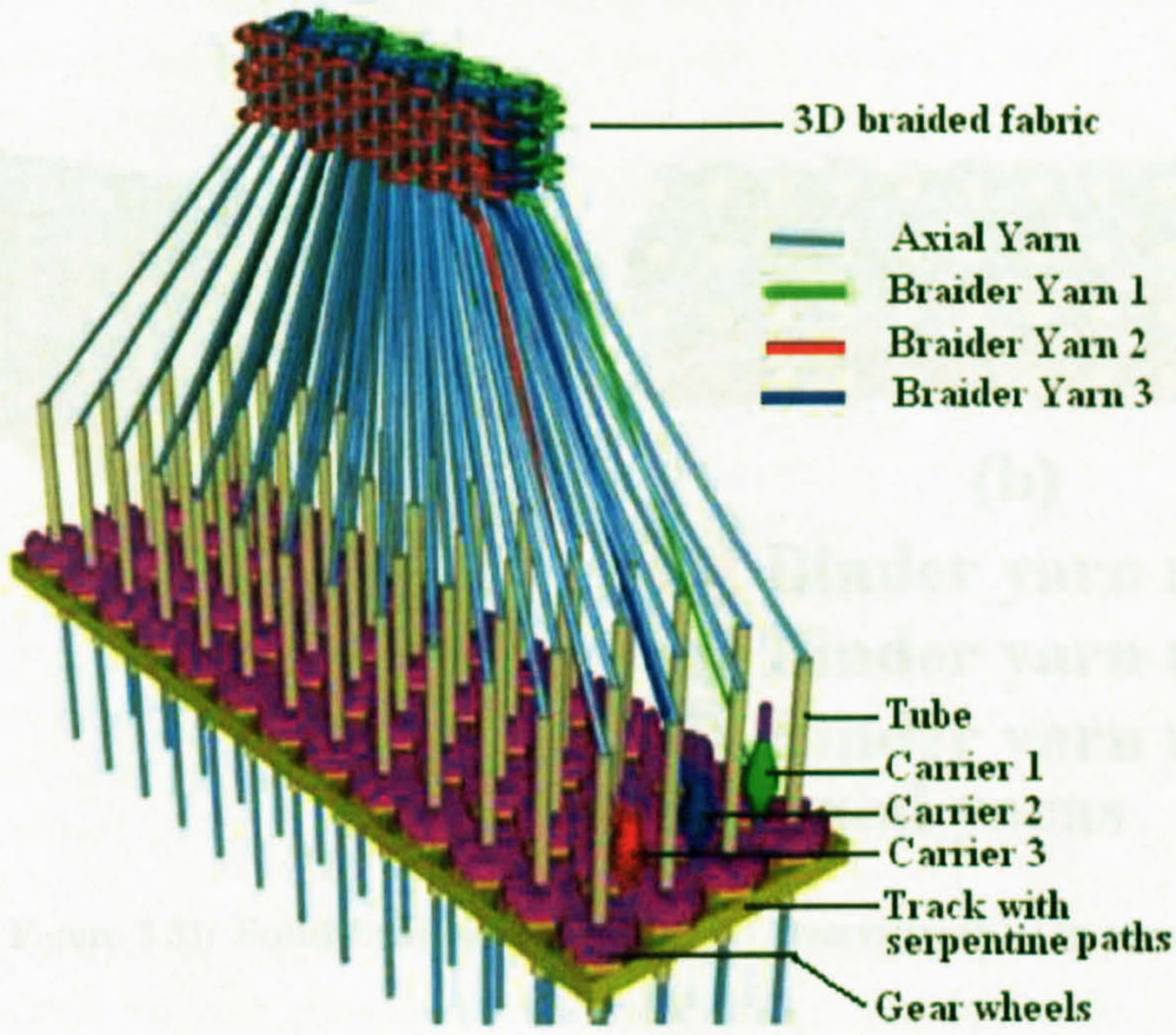

Figure 2.30: **Solid braiding process for 3D braided fabrics .**

Braiding was reported as the first textile process used to manufacture a 3D fibre preform for a composite [65]. As shown in figure 2.12, 3D braiding processes include two-step braiding, four-step braiding and solid braiding or multi-layer interlocking braiding. Figure 2.30 shows a solid braiding process. Driven by gear wheels, carriers carry braider yarns travel along serpentine paths forming a braided structure. Figure 2.31 shows a 3D fabric manufactured using solid braiding process. 2-step braiding is similar to solid braiding except that more braider yarns are used. 4-step braiding is also similar to solid braiding except that there are no axial yarns. Figure 2.32 shows examples of 3D braided fabric manufactured by 2-step braiding and 4-step braiding. More details related to 2-step and 4-steop braiding can be found in the reference [15].

2.12.4 3D knitted fabrics

Similar to 2D knitted fabrics, 3D knitted fabrics are formed by interlooping of yarns. They are manufactured by knitting machines with more than two needle beds and are results of careful stitch control during knitting process [65]. Figure 2.33 shows a spacer fabric which can be manufactured by double needle bed knitting machine.

2.12.5 3D stitched fabrics

3D stitching is a process which involves sewing high tensile strength yarn through an uncured prepreg laminate or dry fabric plies using an industrial sewing machine [65]. Kevlar is the most popular yarn material for high tensile strength yarn.

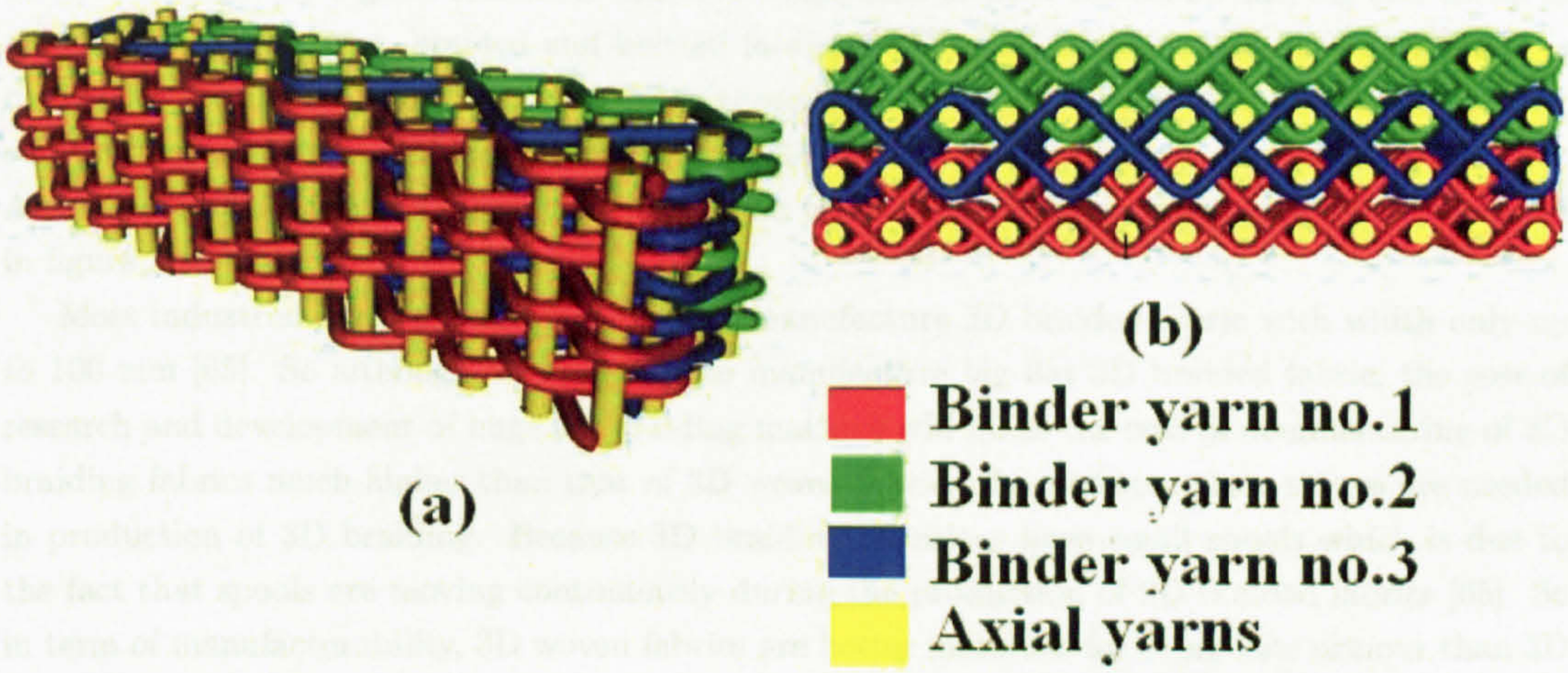

Figure 2.31: **Solid braided fabrics.** - (a) Overview; (b) Top view.

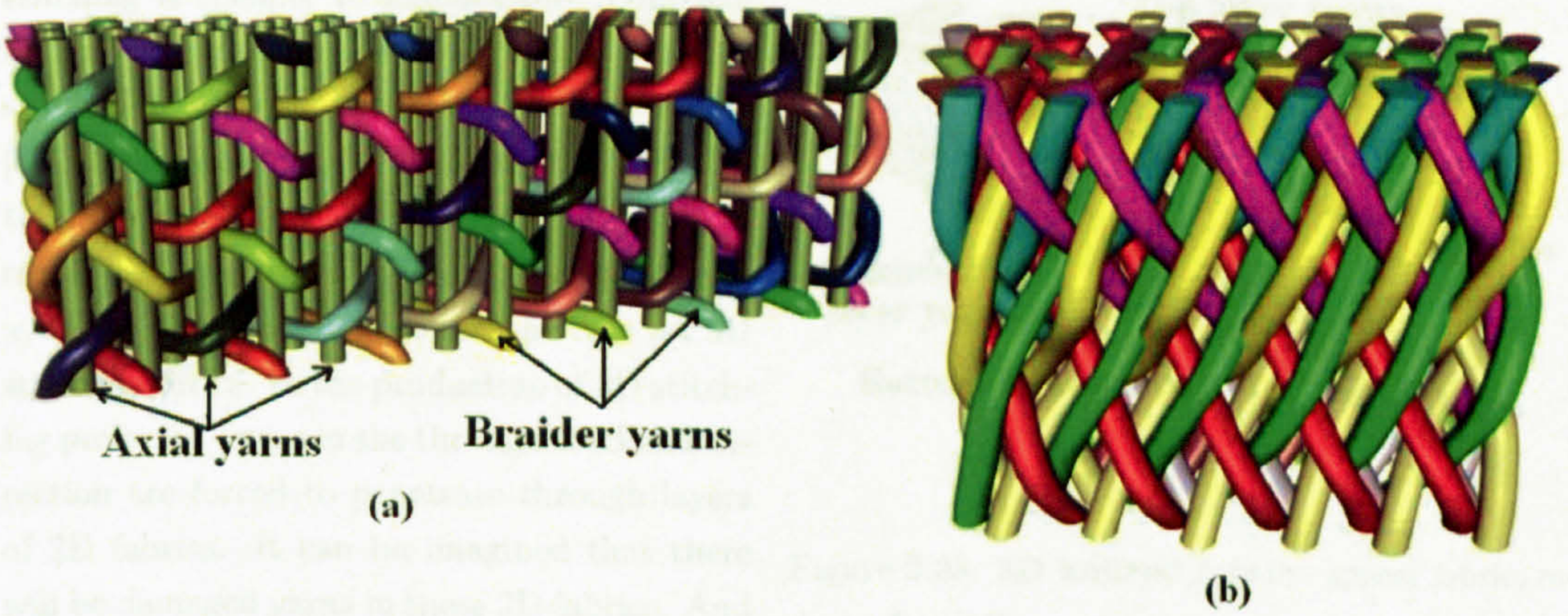

Figure 2.32: **3D braided fabric** - (a) 2-step braided fabric; (b) 4-step braided fabric.

2.12.6 Manufacturability of flat 3D fabrics for composite armour

Manufacturability is a very important issue when choosing fabric for composite armour. Composite armours are normally flat and some of them are big such as composite integral armour for future combat vehicles. So a good candidate fabric for composite armour should be flat, big and cheap to manufacture. 3D woven, braided and knitted fabrics can be flat. The size of a 3D woven fabric is dependent on the width of the harnesses as shown in figure 2.24. The width of 3D knitted fabric can be increased by increasing the number of needles in each needle bed of a knitting machine. And the size of 3D braided fabric is dependent on the number of carriers and gear wheels as shown in figure 2.30.

Most industrial 3D braiding machines can manufacture 3D braided fabric with width only up to 100 mm [65]. So although it is possible to manufacture big flat 3D braided fabric, the cost of research and development of huge 3D braiding machine will make the cost of manufacturing of 3D braiding fabrics much higher than that of 3D woven fabrics. In addition, more setups are needed in production of 3D braiding. Because 3D braiding machines have small spools which is due to the fact that spools are moving continuously during the production of 3D braided fabrics [65]. So in term of manufacturability, 3D woven fabrics are better materials for composite armour than 3D braided fabrics.

3D knitting technology is not as mature as 3D braiding and 3D weaving technologies. It is still in the early stages. The cost of research and development of big knitting machines will be even higher than that of 3D braiding machines. In addition, 3D knitting machines cannot make thick preforms [65]. And 3D knitted fabrics' cover factor which is an indication of gross area covered by fabrics is smaller compared with 3D woven fabrics, i.e. loose fabric. Chitrangad suggested that fabrics used in ballistic applications should have cover factors higher than 0.6. Thus 3D knitted fabrics have the danger of being too loose for ballistic application. So in term of manufacturability, 3D woven fabrics are better materials for composite armour than 3D knitted fabrics.

Compared with 3D woven fabrics, 3D stitching is cheaper to manufacture. But like 3D knitting machines, sewing machines for 3D stitched fabrics cannot make thick preforms [65]. In 3D weaving, 3D braiding and 3D knitting, yarns in the z, i.e. through-thickness direction are inserted at the same time as yarns in x, and y direction. This is not the case for 3D stitched fabrics. In the production of 3D stitching preforms, yarns in the through-thickness direction are forced to penetrate through layers of 2D fabrics. It can be imagined that there will be damaged yarns in these 2D fabrics. And most importantly, compared with 3D weaving and 3D braiding, fewer fibres can be placed in the through-thickness direction. So although compared to 3D woven fabrics, 3D stitched fabrics are cheaper to manufacture, they are not as good as 3D woven fabrics as reinforcement materials for composite armour in term of manufacturability [65].

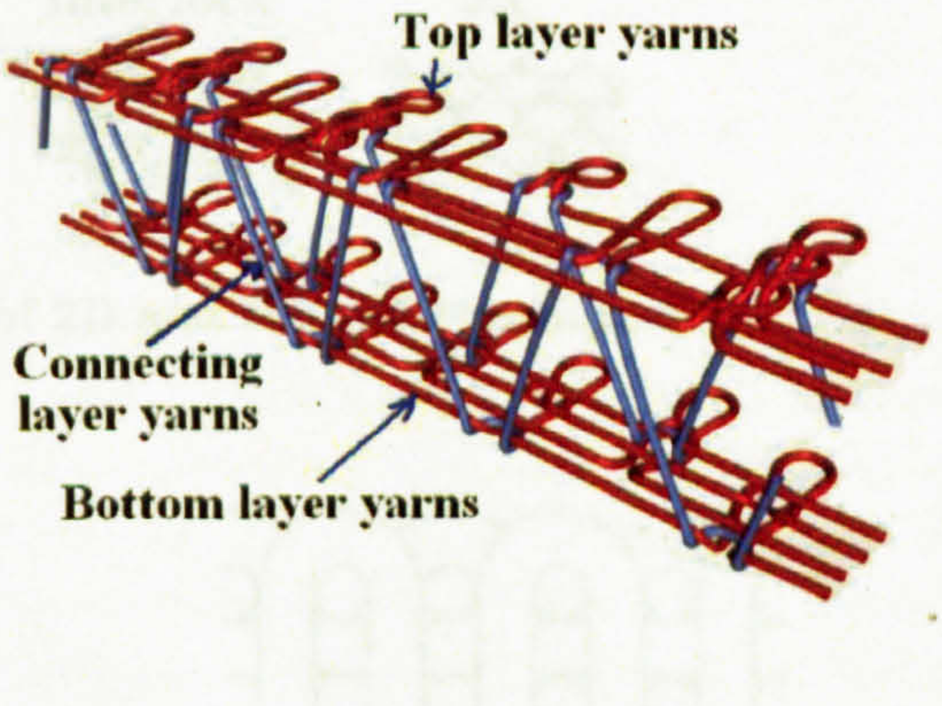

Figure 2.33: **3D knitted fabric** - spacer fabric, redraw after [14]

So far, the discussion was only focusing on manufacturability of 3D fabrics. Issues such as mechanical properties and failure mechanisms in composites made from 3D fabrics are not well characterized and there are no validated methods for predicting properties in their composites. Issues of ballistic impact properties of 3D textile composites are only discussed by a few people such as Lundblad [60]. And there is almost no direct comparison of ballistic impact properties of different 3D textile composites. If manufacturability is the only available criterion for choosing candidate material for reinforcement of composite armour, the 3D woven fabric is the best 3D fabric for composite armour. In the sections below, interlaminar fracture properties, impact properties and failure mechanisms of 3D woven fabrics are reviewed.

2.12.7 Interlaminar fracture properties of 3D woven fabrics

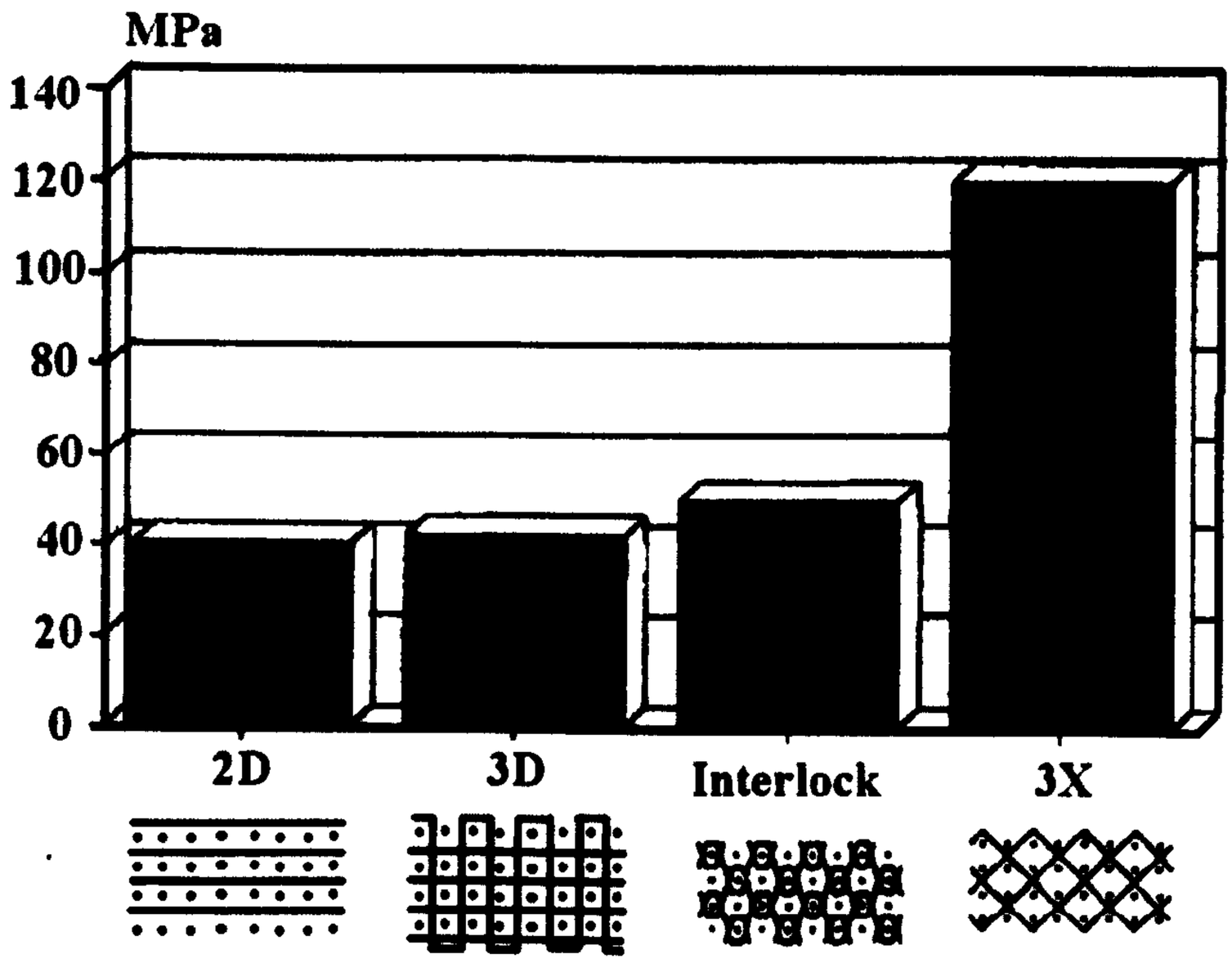

Figure 2.34: **Interlaminar Shear Strength of 2D and 3D textile composites.** - [13]

As expected, many researchers found that the interlaminar fracture properties of 3D woven fabric reinforced polymer matrix composites are better than 2D fabric reinforced polymer matrix composites as shown in figure 2.34. For example, Gunon et al [42] found that the delamination toughness for a 3D woven carbon/epoxy composite with a fibre in through-thicknesses direction content of only 1% was about 14 times higher than a 2D carbon/epoxy prepreg laminate. And the largest reported in-

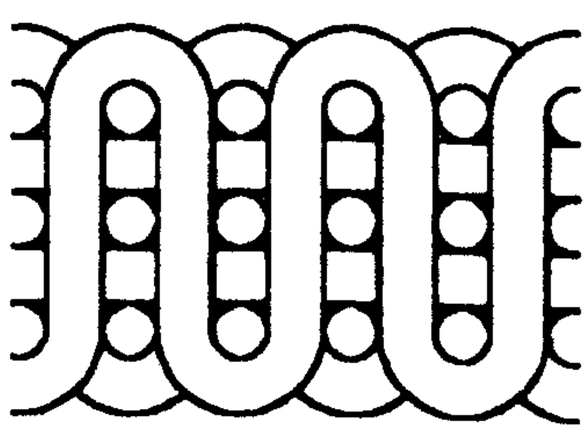

Figure 2.35: **3D woven fabric example 1** - [6]

crease is for a 3D woven composite with an 8% fibres in the through-thickness direction content that has a mode I delamination resistance more than 20 times higher than for 2D laminate [3].

2.12.8 Impact properties of 3D woven textile composites

Although there are few published literatures about ballistic impact tolerance of 3D textile composites, there are lots of papers about low velocity impact damage tolerance of such materials. Although the velocity of a ballistic impact is much greater than that of low-velocity drop-weight impact, the loading conditions of ballistic impact involve variable penetration velocity, as in drop-weight impact, since the penetrator decelerates during the event [56]. In addition, they share some similar damage mechanisms such as matrix cracking, transverse fibre fracture and delamination. Thus low velocity impact properties of 3D multilayer interlocking woven textile composites can give an insight to their ballistic performances.

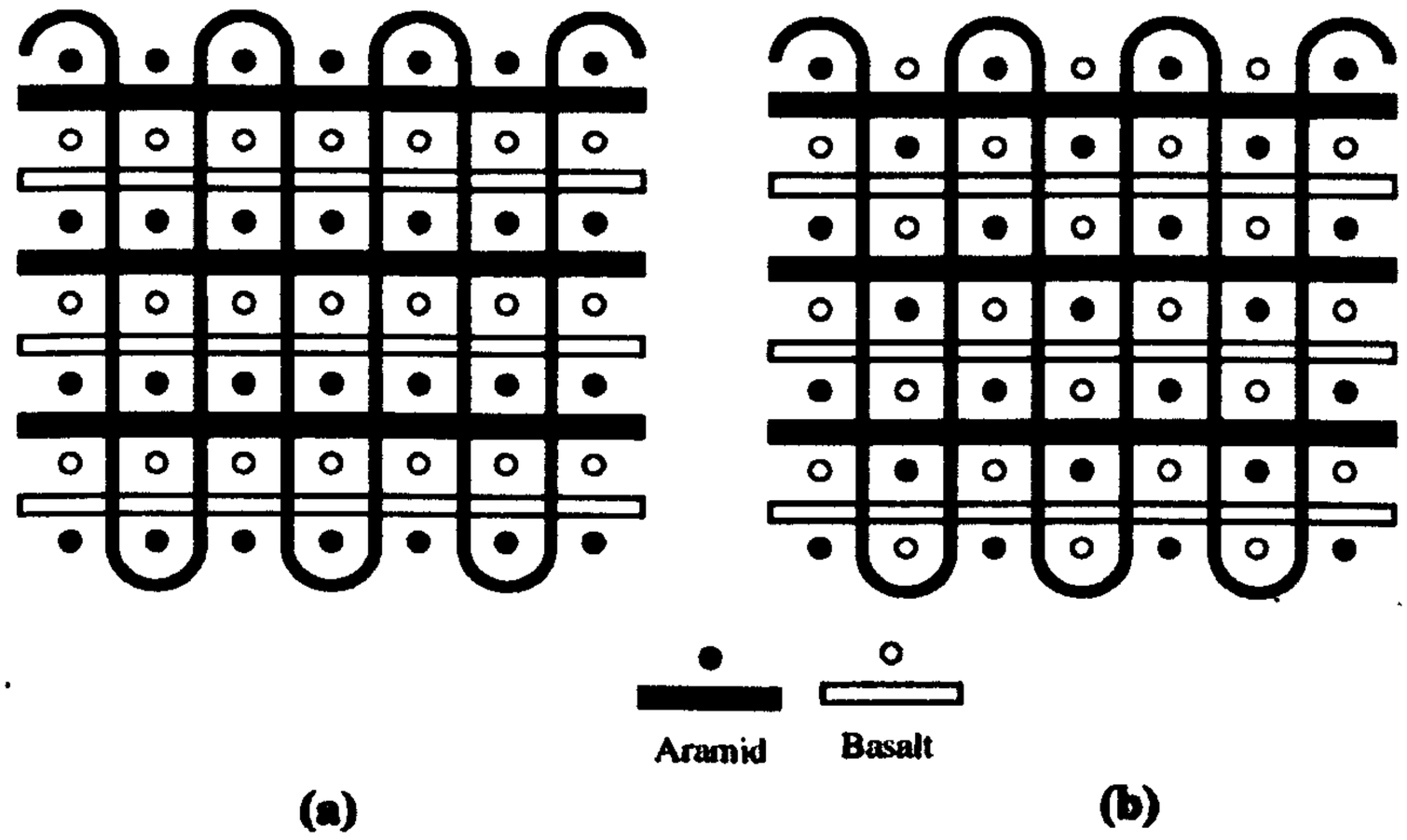

Figure 2.36: **3D woven fabric example 2 -** (a) interply hybrid; (b) intraply hybrid [90].

Impact properties of composites reinforced by a 3D woven architecture called 3D orthogonal were investigated by Baucoma et al [6], and Wang et al[90]. Baucom et al [6] used glass fibres and Wang et al[90] used Basalt fibres and aramid fibres (Kevlar-29) as shown in figure 2.35 and figure 2.36. Impact velocities of 2m/s and 3 m/s were used. Baucoma et al [6] did multiple normal impact tests. And Wang et al [90] did single normal penetration impact test. 2D textile composites reinforced by plain woven fabric and by mixture of non-crimp fabric and chopped-fibre mat are also tested by Baucoma et al [6]. They observed that compared to 2D textile composites, 3D textile composites react differently to low velocity impacts. When subjected to repeating low velocity low energy impacts, 3D textile composites fail gradually [6] which is characterized by sudden drop of peak force. And the 3D woven textile composite has higher total energy absorption during than 2D textile composites which have comparable areal density and thickness. The modes of failure they identified include matrix cracking, delamination or debonding, fibre fracture and the straining and fracture of the rovings in the through-thickness direction. Baucoma et al suggested that the last two modes of failure are unique to 3D woven textile composite and are the reasons of their higher

damage tolerance which they judged by normalization of energy absorption by areal density. A higher energy absorption capability of 3D woven textile composite subjected to low velocity impact was also investigated by Brandt et al [13]. They observed that the 3D textile composite absorbs approximately 2.5 times more energy than the 2D laminate during through-penetration impact tests. In [90], Wang et al focused on the effect of the methods of hybridizing, i.e. interply or intraply as shown in figure 2.36.

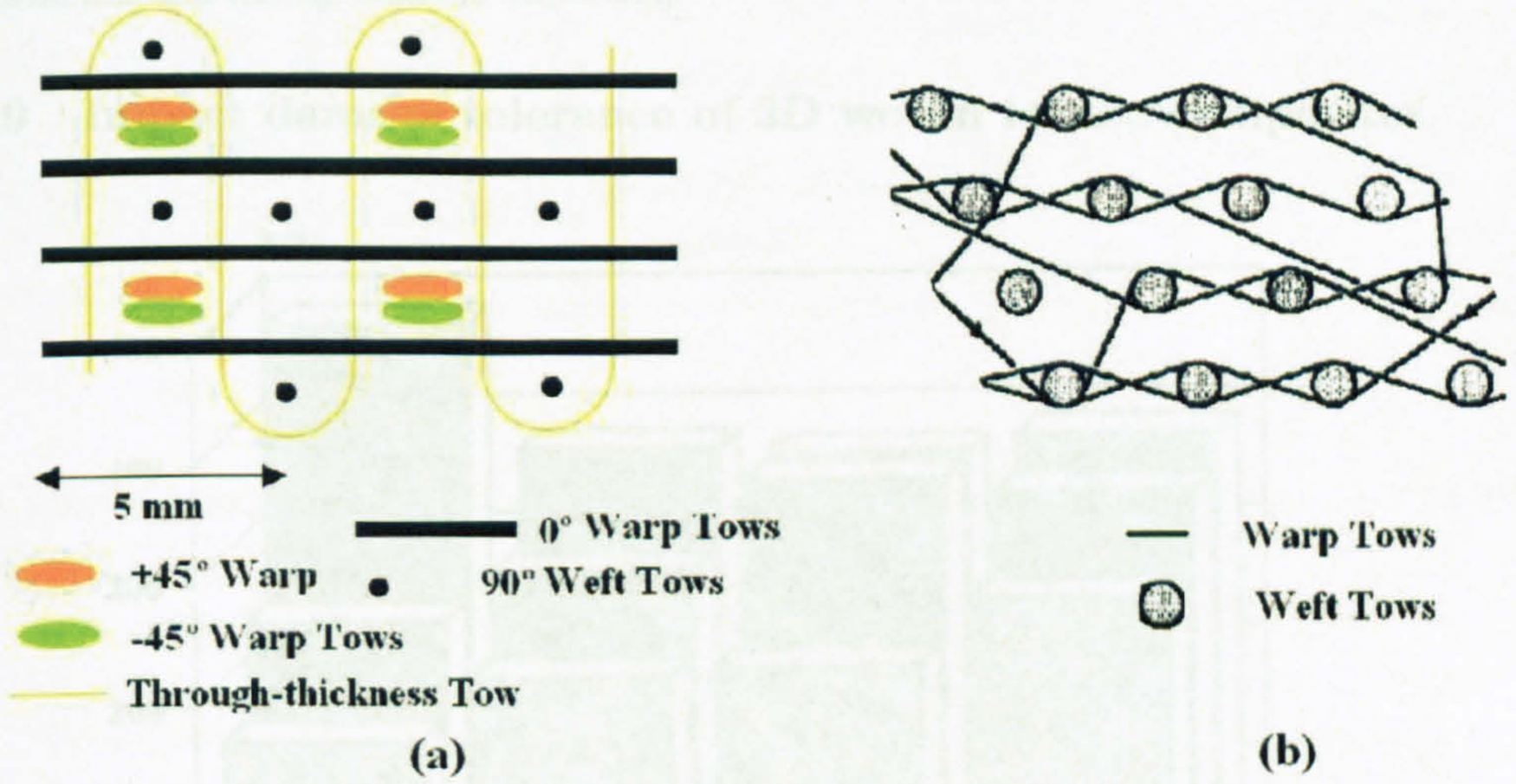

Figure 2.37: **3D woven fabric examples** - (a) example no.3 [61]; (b) example no.4 [1]

Several modified 3D orthogonal preforms were used by McIlhagger et al [61]. These woven preforms had multi-axial weft yarns. One example is shown in figure 2.37 *a*. And they differed from each other in the number and position of 90° and ±45° weft tows and the density of through-thickness tows. Non-penetration impact test of composites reinforced by these woven preform at the velocity of $9m/s$ were carried out. They observed that composites with ±45° weft tows in the outer layers have higher indentation depth and higher delamination areas compared to composites with 90° weft tows in the outer layers. And composites with smaller density of through-thickness yarns have bigger damage.

The low velocity impact properties of another 3D woven textile composite was investigated by Adanur et al [1]. The architecture of the preform is shown in figure 2.37 *b*. Compared with 3D orthogonal fabrics, this preform has no straight warp yarns and weft yarns are interlocked by warp yarns. These kinds of 3D woven fabrics are widely named as 3D interlocked fabrics. Through-penetration tests were carried out at speed of $1.5m/s$ to both 2D textile composites and 3D textile composites. They characterized the impact damage tolerance by using a parameter which is equal to energy absorption/volume of the composite sample. And they observed that 3D textile composites have higher impact damage tolerance at the maximum load. They suggested that this is due to the fact that yarns in the through-thickness direction can hinder crack propagation and increase the impact resistance and damage tolerance. They also compared the failure mechanisms in 2D and 3D textile composites. They observed brittle rupture with edge delamination in 2D textile composites. Breakage during the impact test occurred almost without cracking. In contrast, they identified various failure mechanisms in 3D textile composites. The failure mechanisms include fibre

breakage, fibre debonding and fibre pull-out but no large delamination. They observed that cracks in 3D specimens were nucleated along the layer locking yarns but not across them. And cracks were hindered by layer locking yarns. They concluded that layer locking yarns in 3D multilayer locking woven composites not only can retard the delaminations, but also can change their propagation directions. As a result, the damage and energy-absorption capabilities of the composites were increased. So far, 3D multilayer interlocking textile composite shows great potential of reducing large delamination during ballistic impacting.

2.12.9 Impact damage tolerance of 3D woven textile composites

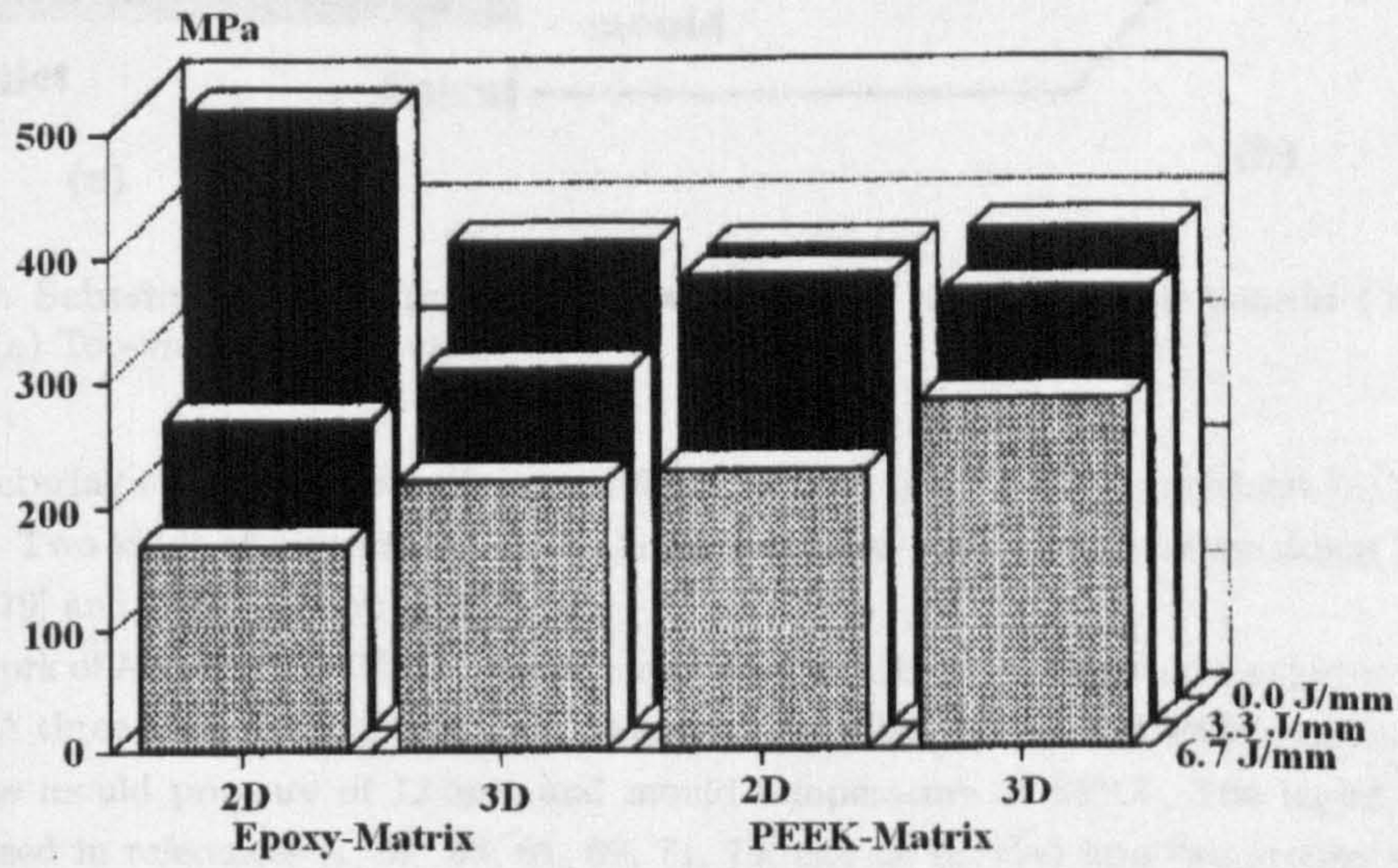

Figure 2.38: **Compression after impact strength of 2D and 3D textile composites** - [13]

The most dangerous mode of quasi-static loads to composite armour structures after they have been subjected to impact is believed to be compression. So compression after impact (CAI) is widely used to characterize damage tolerance of composite armour. The superior impact damage resistance of 3D woven composites usually results in higher post-impact mechanical properties than for 2D laminates [3, 13, 49, 82, 87]. For example, in figure 2.38 it is shown that the CAI strengths of 3D woven composites are significantly higher than for 2D laminates ([3, 87]).

2.13 Manufacturing of 3D woven textile composites

2.13.1 Vacuum assisted resin transfer moulding (VARTM)

Good manufacturability of 3D woven textile composites is essential for their application for composite armour. Good manufacturability means firstly, the real structure fabrics in composites should not be too much different from ideal structure. Secondly, fabrics should have good wet-out properties so that composite panels have a low percentage of voids. And thirdly resin rich area should be small.

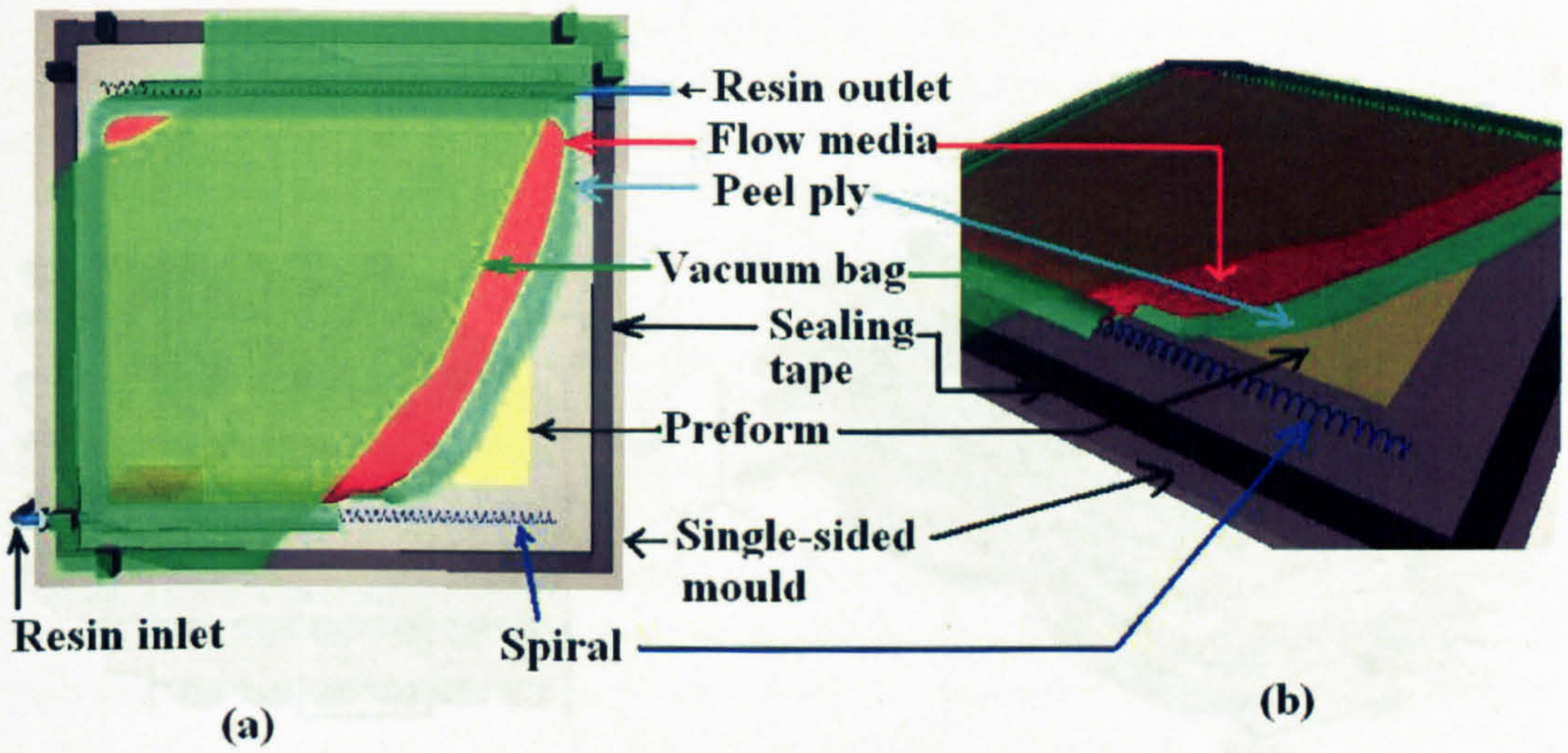

Figure 2.39: **Schematic Diagram of a vacuum assisted resin transfer mould (VARTM) process** - (a) Top-view; (b) over-view

Manufacturing of 3D woven textile composites has been performed in references [1, 52, 58, 61, 69, 71, 79]. Two kinds of manufacturing methods have been used, i.e. liquid moulding [1, 52, 58, 61, 69, 71, 79] and compression moulding [1].

In the work of Adanur et al [1], 3D textile composites have been manufactured using compression moulding. A three-piece aluminium mould was used. Consolidation of 3D textile composites taken place at the mould pressure of $12.5psi$ and mould temperature of $85°C$. The liquid moulding processes used in references [1, 52, 58, 61, 69, 71, 79] can be divided into two groups depending on whether the mould was closed or not. In references [1, 52, 58, 61, 69, 71], the mould used for liquid moulding process include two matched moulds. These two moulds form a closed cavity with fixed dimensions where the resin is injected into to "wet" reinforcements within. In reference [79], a single-side mould was used. Vacuum bagging was used to form a closed cavity for resin infusion.

Vacuum can be used to draw resin into the mould cavity of the two kinds of moulds described above. This kind of liquid moulding process was called vacuum assisted resin transfer moulding (VARTM). Figure 2.39 shows a set-up of VARTM. A porous fabric called as flow media (fine mesh) was used to distribute resin. The flow media is normally placed on the top of preform.

2.13.2 Yarn architectures of 3D woven textile composites

2.13.2.1 Methods

As described in figure 2.25, the architecture of a 3D woven fabric can be very complicated. The architecture of a 3D woven fabric in its textile composite can be even more complicated. Because there are distortions of the architecture of 3D woven fabric during both the manufacturing of the fabric and the composite. The properties of a composite is determined by the architecture of its reinforcements [30]. The more we know about the real architecture of a 3D woven fabric the more accurate we are able to predict mechanical properties of a 3D woven textile composite.

The yarn arrangement of a 3D woven textile composite can be experimentally determined by

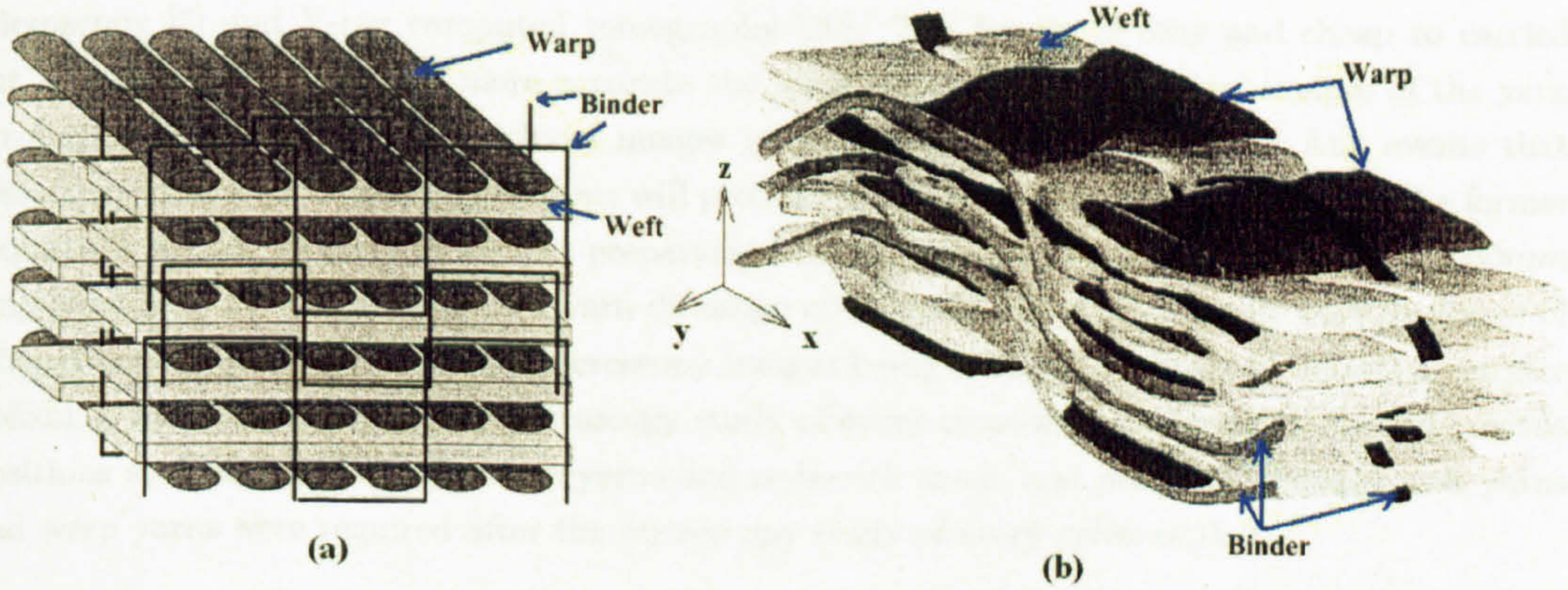

Figure 2.40: **Example 1 of yarn architecture of 3D woven textile composites** - (a) ideal; (b) real [5]

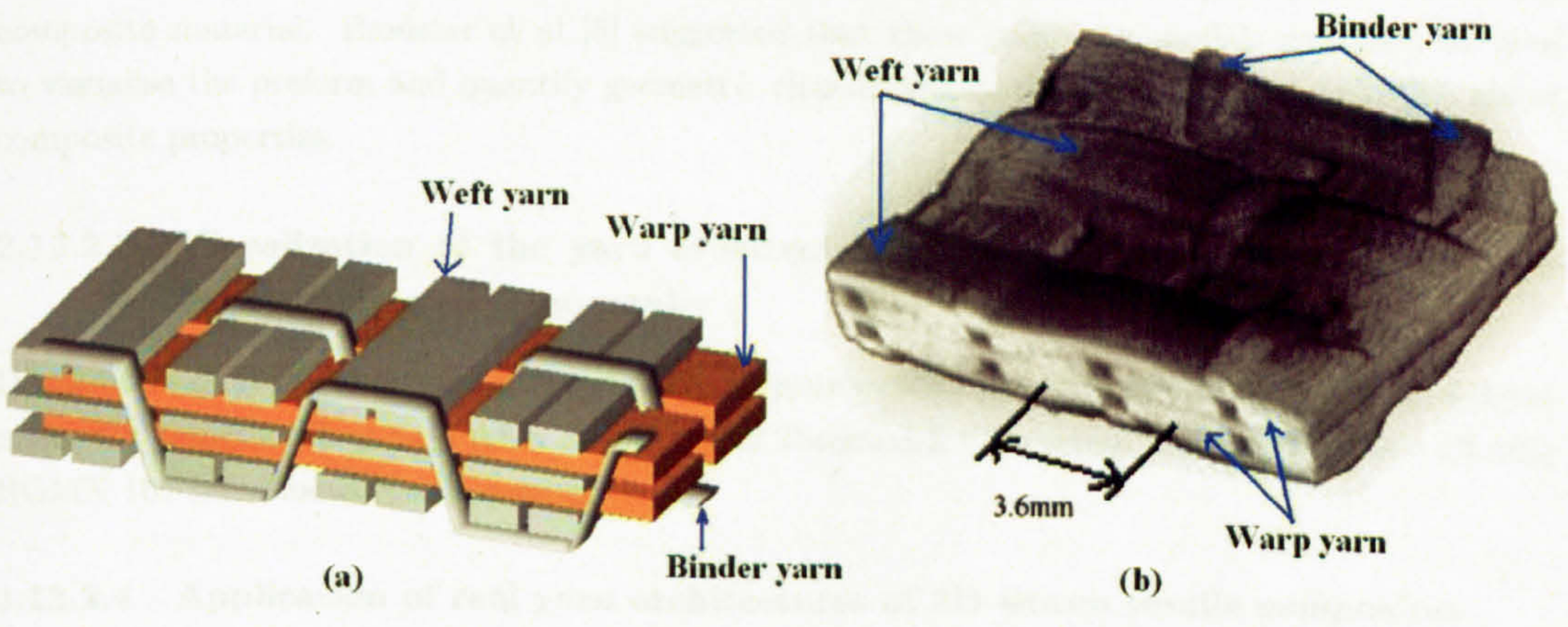

Figure 2.41: **Example 2 of yarn architecture of 3D woven textile composites** - (a) ideal; (b) real [30]

using various imaging techniques. Imaging techniques include destructive techniques and non-destructive techniques. The former includes optical microscopy and the later includes techniques based on laser ranging or ultrasonics and X-ray computed tomography. So far two imaging techniques have been used to determine the yarn arrangement of 3D woven fabrics. They are optical microscopy [5] and X-ray computed tomography [30]. The former is easy and cheap to carried out than the later. It is also more accurate the later. Because it uses actual images of the yarn arrangement while the later produces images indirectly using a X-ray signal. Any events that distort the passways of the X-ray beams will produce artefacts in the gathered images. The former requires a serious amount of sample preparation time [30]. For example, the image of a $30mm$ long cross-section image in the weft yarn direction of a textile composite sample with thickness of $3.5mm$ is the result of around 50 microscopy images being sticked together. In addition, surface polishing was needed before the microscopy study of every cross-section. Drawing lines at various positions such as positions abetween yarns and resin-rich areas, and positions between weft yarns and warp yarns were required after the microscopy study of every cross-section.

2.13.2.2 Visualization of the yarn architecture of 3D woven textile composite by optical microscopy

Banister et al [5] determined the yarn arrangment of 3D woven textile composites by optical microscopy. The procedures they used are described below. After manufacturing, multiple cross-sections of the composite specimens were cut at a number of different positions within the macrocell of the weave architecture. These cross-sections were polished, and then examined under optical microscope. The images obtained from the microscope were directly digitised and closed contours were drawn around each of the yarns through the use of Microstations software. Using the same software, these boundaries, that represent the warp, weft and binder yarns at various positions in the composite, were appropriately linked to form three-dimensional representations of the yarns. The computer model thus generated was an accurate description of the yarn paths within the composite material. Banister et al [5] suggested that these computer models can then be used to visualise the preform and quantify geometric characteristics that can be correlated with global composite properties.

2.13.2.3 Visualization of the yarn architecture of 3D woven textile composite by X-ray computed tomography

Desplentere et al [30] determined the yarn architectures of 3D woven textile composties using X-ray micro CT images. They used AEA Technologies Tomohawk CT system implemented on a Phillips HOMX 161 microfocus X-ray system.

2.13.2.4 Application of real yarn architectures of 3D woven textile composites

Yarn architectures of 3D woven textile composites produced by Banister et al [5] and Desplentere et al [30] are shown in figure 2.40 and figure 2.41 respectively. Banister et al [5] mainly focused on architecture visualisation. In figure 2.40, it can be seen that the real yarn achitecture looks very different from the ideal yarn architecture. The real architecture illustrates resin-rich areas caused by binder yarns and collimation of warp yarns. It also illustrates the crimping of yarns.

Desplentere et al [30] used the real yarn architectures of 3D woven textile composites to measure the properties of the 3D woven textile composites by computer modelling. They predict Young's modulus accurately (with less than 5% deviation).

2.14 Other ways to improve ballistic performance of composite laminate

2.14.1 Hybrid Fabrics

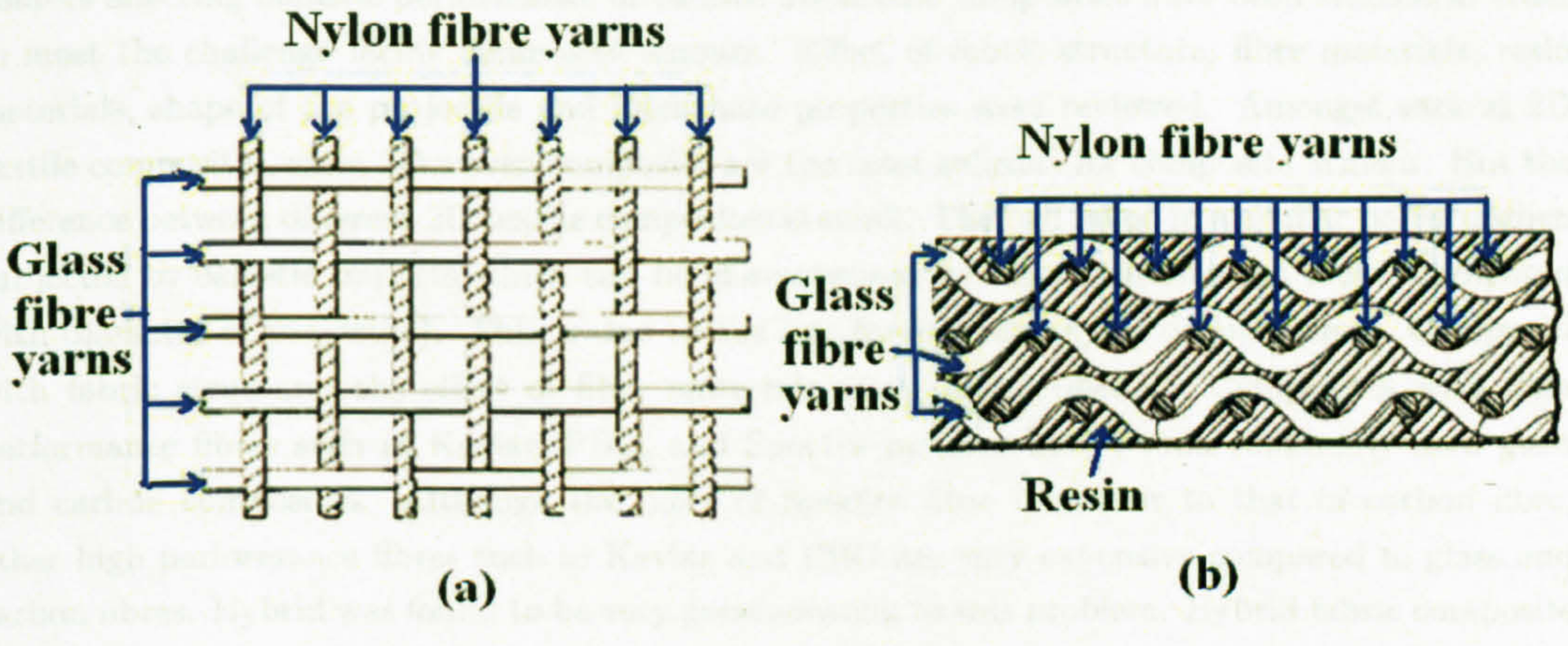

Figure 2.42: **Hybrid fabrics** - (a) A greatly enlarged plain view of a woven fabric comprising a lightweight armour material and including interlaced glass and nylon fibres in accordance with the present invention of Harry et al ([45]); (b) A sectional view of a laminated armour member including a plurality of layers of woven fabric of the type illustrated in (*a*) impregnated with a resin and bonded together into a composite laminate structure

Harry et al [45] found that by interweaving glass and nylon fibres into one fabric, a substantially more projectile-resistant material results which has been found to be better than a fabric woven of either glass fibres or nylon fibres alone (figure 2.42). It is believed that there is an interaction between the two types of fibres comprising the woven fabric. The glass fibre is thought to serve the function of the strong member and preferably is composed of roving, rather than twisted fibres, while the lighter-weight nylon fibre is believed to function as both a supporting structure and elongating or stretching member. The optimum ratio of glass to nylon lies within the range from about 90 parts glass and 10 parts nylon to 10 parts glass and 90 parts nylon, by weight. The resin can be cured polyester or epoxy resin or preferably a rubber-phenolic resin so that resin elongation, between 10 and 400 percent is obtained.

2.14.2 Stress wave management

Lots of methods of improving armour ballistic impact performance by improving stress wave management were reported in recent years. For example, Gupta and Ding [43] found that a target with a single thick high-strength, high-wave-speed layer offered the best penetration resistance. They suggested that the high wave speed of the layers allowed the impact load and energy imparted to

the target to be absorbed more quickly and distributed widely in the substrate. Gama et al [36] replaced rubber with closed-cell aluminium foam in composite integral armour (CIA).

Grujicic et al [41] found that unidirectional fibre reinforced composites had better performance than fabric reinforced composites in terms of stress wave. They suggested that this was due to the fact that shock wave that travelled through fibres was not or less reflected against the yarn cross-overs that were ubiquitous in a woven fabric and that did not occur in the uni-directional product, the energy was distributed faster and more efficiently.

2.15 Conclusions

Factors affecting ballistic performance of various 2D textile composites have been studied in order to meet the challenge facing composite amours. Effect of fabric structure, fibre materials, resin materials, shape of the projectile and interphase properties were reviewed. Amongst various 2D textile composites, satin 2D woven composite are the most suitable for composite armour. But the difference between different 2D textile composites is small. They all failed in a similar pattern when subjected to ballistic impacts which can be characterized by huge delamination areas (compared with diameter of projectile). This is due to the low fracture energy of delamination. Compared with fabric structure, the effect of fibre materials are more significant. Composites with high performance fibres such as Kevlar, PBO, and Spectra perform better than commonly used glass and carbon composites. Although the price of Spectra fibre is similar to that of carbon fibre, other high performance fibres such as Kevlar and PBO are very expensive compared to glass and carbon fibres. Hybrid was found to be very good solution to this problem. Hybrid fabric composite laminates of PBO and carbon fibres have equally good ballistic properties as pure PBO composites. The effect of resin materials was found to be very significant for high performance fabrics.

Fracture energy of delamination was compared with that of transverse and tensile fibre fracture energy. It was observed that the later was $30-60$ times bigger. So it seems that ballistic properties such as multi-hit properties may be improved by designing composite laminate where impact involves as much as possible breaking of fibres in tension and as least as possible delamination.

Methods of reducing delamination include using tough resin, stitching, and 3D fabrics. Using 3D fabrics was found to be the best solution. 3D fabrics such as 3D woven, 3D braids, and 3D knits were studied. 3D braid and 3D knit composites were found to be not as good as 3D woven composite due to their poor compression properties. Within 3D woven fabrics, focus was put on multilayer interlocking fabrics. Its manufacturability was reviewed. Caution should taken when analyzing 3D multilayer interlocking textile composites. Because there is difference between the ideal structure and the real structure. A computer simulation of the real structure is necessary sometimes.

Chapter 3

Experimental Plan and Aims of Project

3.1 Introduction

Because of the fact that large number of issues regarding to the ballistic performance of textile composites have been reviewed in chapter 2 and large number of materials and experimental methods needed to be described in this study, it is believed that a summary of experimental plan and aims of this project can help readers to form a better understanding of the basic structure of this work.

3.2 Experimental Plan

As mentioned in section 2.1 being able to develop an assessment system is also a key task to meet the challenge of composite armour. Initial investigation revealed that there are a large number of variables that affect the choice of materials in composite armour. By setting up databases or drawing "master curves", whether the candidate material for composite armour is good or not can be decided. A flow chart shown in figure 3.1 explains the experimental procedures.

Tests methods mentioned in 2.1 were used. At first, microscopy was used to study the manufacturability. Secondly ballistic gas gun tests were used to determine single hit V_{50}. Thirdly damage area was measured using ultrasonic C-scans or visual examination to quantify the damage resistance. At last the energy absorption in high energy, low velocity impacts was studied using the drop weight impact test.

3.3 Aims of Project

After selection of candidate materials, i.e. 3D multilayer interlocking textile composites and setting-up of assessment procedures, the objectives of this project are clear. They are listed below.

1. To set-up the following databases of 2D textile composites

(a) V_{50}
(b) energy absorption in drop weight impact
(c) 2D damage area

2. To assess 3D multilayer interlocking textile composites
3. To identify the relationships between fabric architecture and ballistic performance in 3D multilayer interlocking textile composites

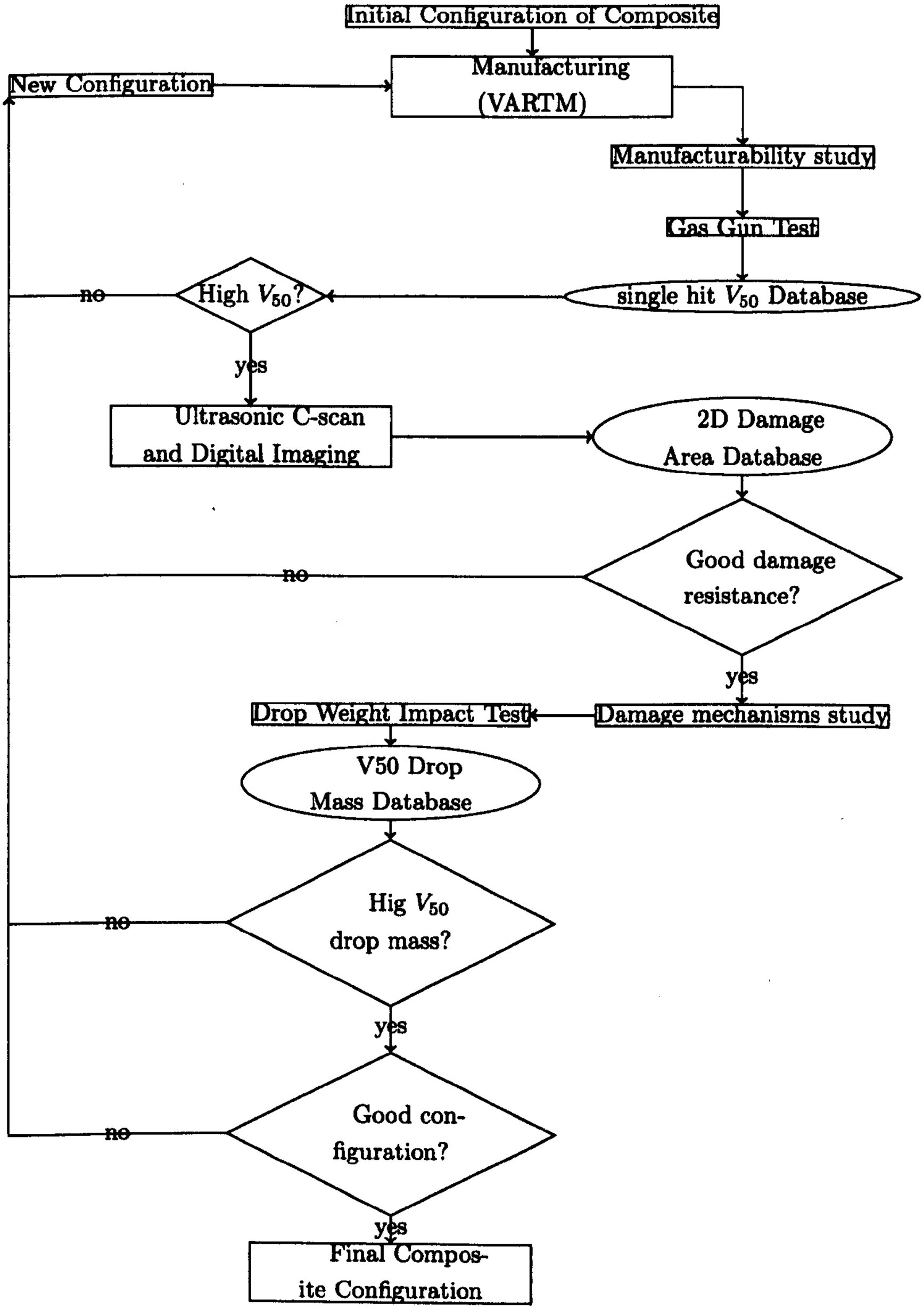

Figure 3.1: **Flow chart shows the experimental procedures armour development .**

Chapter 4

Materials and Experimental Methods

4.1 Materials

4.1.1 Material Identification Codes

To avoid confusion, table 4.1 lists the abbreviations that will be used to identify the materials throughout this report.

4.1.2 Fabrics

The selection of 2D fabrics for baseline studies was based on the availability of the 2D fabrics and the use of 3D fabrics. The main new materials in this study were 3D woven fabrics. Thus 2D woven fabrics were the ideal baseline materials. 3D woven fabrics were manufactured using both E-glass and carbon fibres. Thus 2D woven E-glass and carbon fabrics were selected. Plain woven E-glass fabric and 5-harness satin woven carbon fabric were used as the main baseline materials due to the large amount of these fabrics available during the course of this study. A plain woven carbon fabric and a second plain woven E-glass fabric were used in the later stage of this work when the first plain woven E-glass fabric and the 5-harness satin woven carbon fabric were not available. They were used to study the effect of resin material on the ballistic performance of 2D textile composites. The second plain woven E-glass fabric has a bigger areal density than the first plain woven fabric. Preforms in baseline studies consisted layers of the 2D woven fabrics described above.

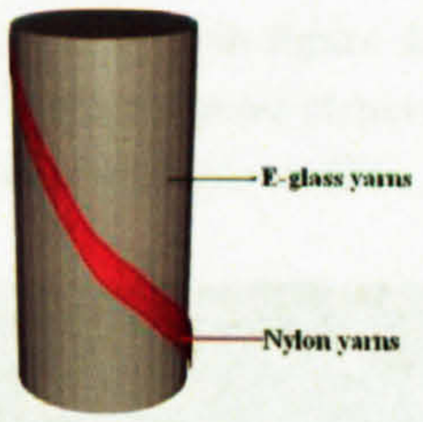

Figure 4.1: **Coating of E-glass yarns by nylon yarns .**

Non-crimp fabrics and fabrics with co-mingled yarns were used in this study as new materials. Two kinds of E-glass non-crimp biaxial $\pm 45°$ fabrics were used. They have different areal densities. The one with lower areal density was used firstly. The one with higher areal density were used

later because of the large amount available. One kind of carbon non-crimp biaxial ±45° fabrics was also used. Preforms of non-crimp textile composites consisted layers of the non-crimp fabrics mentioned above. The following five fibre lay-ups were used to study the effect of fibre lay-up on the ballistic performance of non-crimp textile composites. They are $[\pm 45]_s$, $[\pm 45]_2 s$, $[\pm 45]_2$, $[\pm 45]_4$ and $[+45/-45/0/90]_s$. The selection of fabrics with co-mingled yarns was based on the availability of the materials. Two plain woven carbon/Polyethylene terephthalate (PET) fabrics with different areal densities were used. One plain woven E-glass/Polypropylene (PP) fabric and one twill woven E-glas/Polypropylene (PP) fabric were also used. Preforms of textile composites with co-mingled yarns consisted layers of the 2D woven fabrics with co-mingled yarns described above.

The selection of 3D woven fabrics was more complicated than 2D fabrics. This was due to the enormous large amount of architectures available for 3D woven fabrics. The first 3D woven architecture selected was based on the work of Lundblad et al [60]. It was a through-thickness interlocking architecture. Lundblad et al [60] observed that Kevlar fabrics with this kind of architecture had very good ballistic performance. Two 3D woven fabrics C1 and G7 with this kind of architecture were manufactured by Carr Reinforcements Ltd and Zhejing Sci-Tech Univeristy respectively. The ideal yarn arrangements in these two 3D woven fabrics were illustrated in figure 4.4 to figure 4.7. The visualization of the yarn arrangements in these figures were produced using Blender, a 3D content creating software. Carbon fibres were used for all the yarns in C1. E-glass fibre yarns coated with nylon fibres as shown in figure 4.1 were used for weft and warp yarns in G7. The use of the nylon fibres was to assure good structure integrity and manufacturability of the fabrics. Kevlar yarns were used as binder yarns in G7.

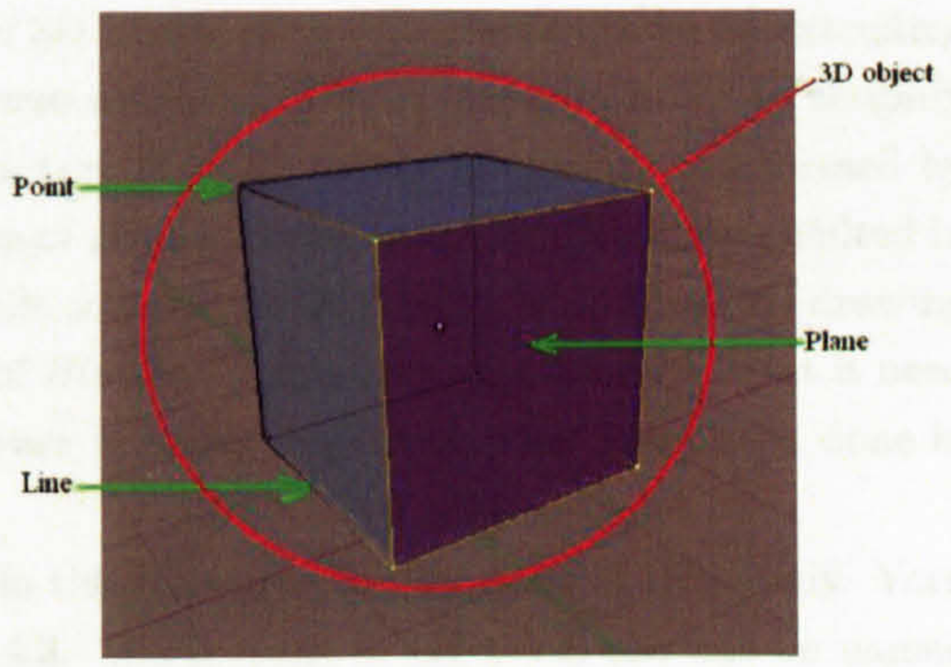

Figure 4.2: **3D object in** *Blender*© .

3D woven fabrics G1 and G2 were designed to study the effect of the position of plain woven style warp yarns on the ballistic performance of 3D woven textile composites. 3D woven fabrics G3, G4, and G5 were designed to study the effect of mix of different multi-layer locking warp yarns on the ballistic performance of 3D woven textile composites. 3D woven fabric G6 was selected to study the effect of the arrangement of weft yarns on the ballistic performance of 3D woven textile composites. 3D woven fabrics G1, G2, G3, G4, G5 and G6 were manufactured by Zhejing Sci-Tech Univeristy. E-glass yarns coated with nylon yarns were used for all yarns in these fabrics. The ideal yarn arrangements in these 3D textiles were illustrated from figure 4.6 to figure 4.17.

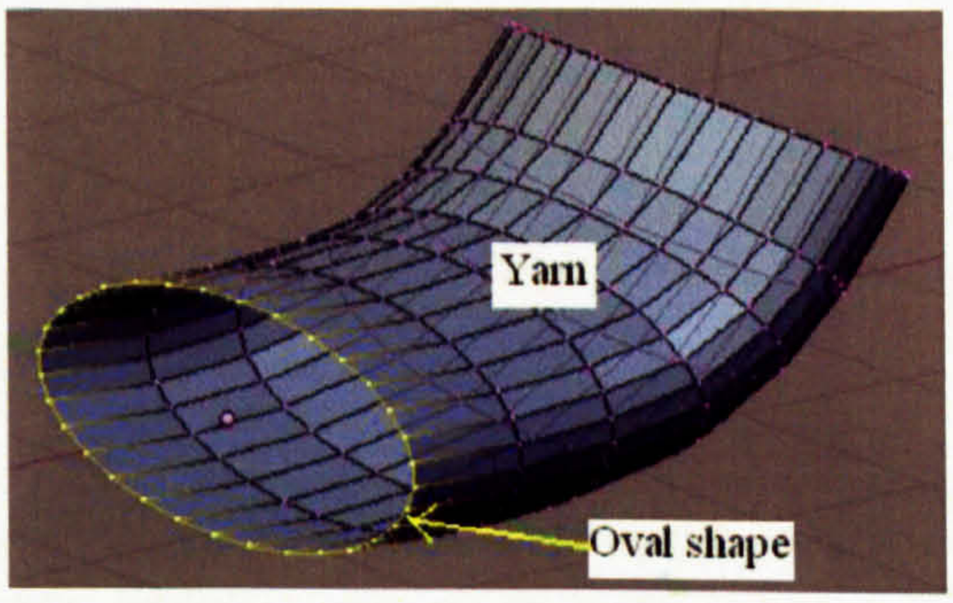

Figure 4.3: **Drawing of yarns in** *Blender*© .

The visualization of the yarn arrangements in the seven 3D woven preform architectures shown

from figure 4.6 to figure 4.17 were produced using *Blender*©, a 3D content creating software. A 3D content or 3D object in *Blender*© is formed by a finite number of trigons and/or tetragons. An example was shown in figure 4.2. 3D objects can also be created by copying and pasting of existing 3D objects. Trigons and tetragons in *Blender*© can be draw upon three or four existing points. Tetragons in *Blender*© can also be draw by extruding existing lines. After drawings, a 3D object in *Blender*© can be viewed in any direction. Images of a 3D object viewed from any direction can be rendered and exported. A 3D object can be divided into several 3D objects, and vice versa. In *Blender*© windows, there are eight viewing layers. Visibility of an object is dependent on the visibility of viewing layer it located. In addition, some points and lines of a 3D object can be hidden.

In this study, yarns in the ideal architectures of 3D textile composites were drawn by extruding oval shapes as shown in figure 4.3. Weft yarns were assumed to be straight in order to simplify the categorization of 3D fabrics. An ideal architecture of a 3D textile composite was formed by putting specific yarns in specific positions. The use of *Blender*© software in this study resulted in better description of yarn arrangements in 3D textile composites than using traditional 2D drawing methods. *Blender*© is a freeware. Thus the use of *Blender*© was very cost effective. But it need time and efforts to learn how to *Blender*© software in order to achieve what have been done in this study.

Table 4.3 summerized the yarn arrangements in the 3D woven fabrics used in this study. Yarn arrangement in G6-1-VE was not listed in table 4.3. Warp yarns in G6-1-VE can not be named based on the number of layers of weft yarns it interlaced with. Because the numbers of the weft yarns in two adjacent rows of weft yarns were different.

Two resin system were used, i.e. vinyl ester resin and epoxy resin as shown in table 4.2. 2% of Methyl ethyl ketone peroxide (MEKP) catalyst was added into vinyl ester resin which results in a pot life of 55 minutes. Epoxy resin was used with hardener with a epxoy:hardener ratio of 100:34. Most composite panels were manufactured using vinyl ester resin. Abbreviations VE and EP were given to vinyl ester resin and epoxy resin respectively as shown in table 4.1.

Table 4.1: Material Identification Codes

Materials	Description	Abbreviation
2D fabrics	Plain woven carbon fabric with areal density of 375 g/m^2	PWC1
	5 harness satin woven carbon fabrics with are areal density of 375 g/m^2	5HSC
	Plain woven E-glass fabric with areal density of 400 g/m^2	PWEG1
	Plain woven E-glass fabric with areal density of 600 g/m^2	PWEG2
	Plain woven hybrid fabric no.1 of carbon fibre and PET fibre	PWCPET1
	Plain woven hybrid fabric no.2 of carbon fibre and PET fibre	PWCPET2
	Plain woven hybrid fabric of E-glass fibre and PP fibre	PWEGPP
	Twill woven hybrid fabric of E-glass fibre and PP fibre	TWEGPP
	Non-crimp biaxial carbon fabric with fibre in $\pm 45°$ direction	NCC
	Non-crimp biaxial E-glass fabric with fibre in $\pm 45°$ direction	NCEG1
	Non-crimp biaxial E-glass fabric with fibre in $\pm 45°$ direction	NCEG2
3D fabrics	3D carbon woven fabric with structure VII in figure 4.4	C1
	3D E-glass fabric with structure I in figure 4.6	G1
	3D E-glass fabric with structure II in figure 4.8	G2
	3D E-glass fabric with structure III in figure 4.10	G3
	3D E-glass fabric with structure VI in figure 4.12	G4
	3D E-glass fabric with structure V in figure 4.14	G5
	3D E-glass fabric with structure VI in figure 4.16	G6
	3D E-glass fabric with structure VII in figure 4.4	G7
Resin	vinyl ester resin	VE
	epoxy resin	EP

Table 4.2: Resins

Name	Manufacturer	Code
Vinyl ester resin	Reichhold	NORPOL DION 9102-500
Epoxy resin	Mouldlife Ltd	Araldite Ly564
Hardener for epoxy resin	Mouldlife Ltd	Araldite XB 3486
Catalyst for Vinyl ester resin	Kerox Chemicals Pvt Ltd	Methyl ethyl ketone peroxide(MEKP)

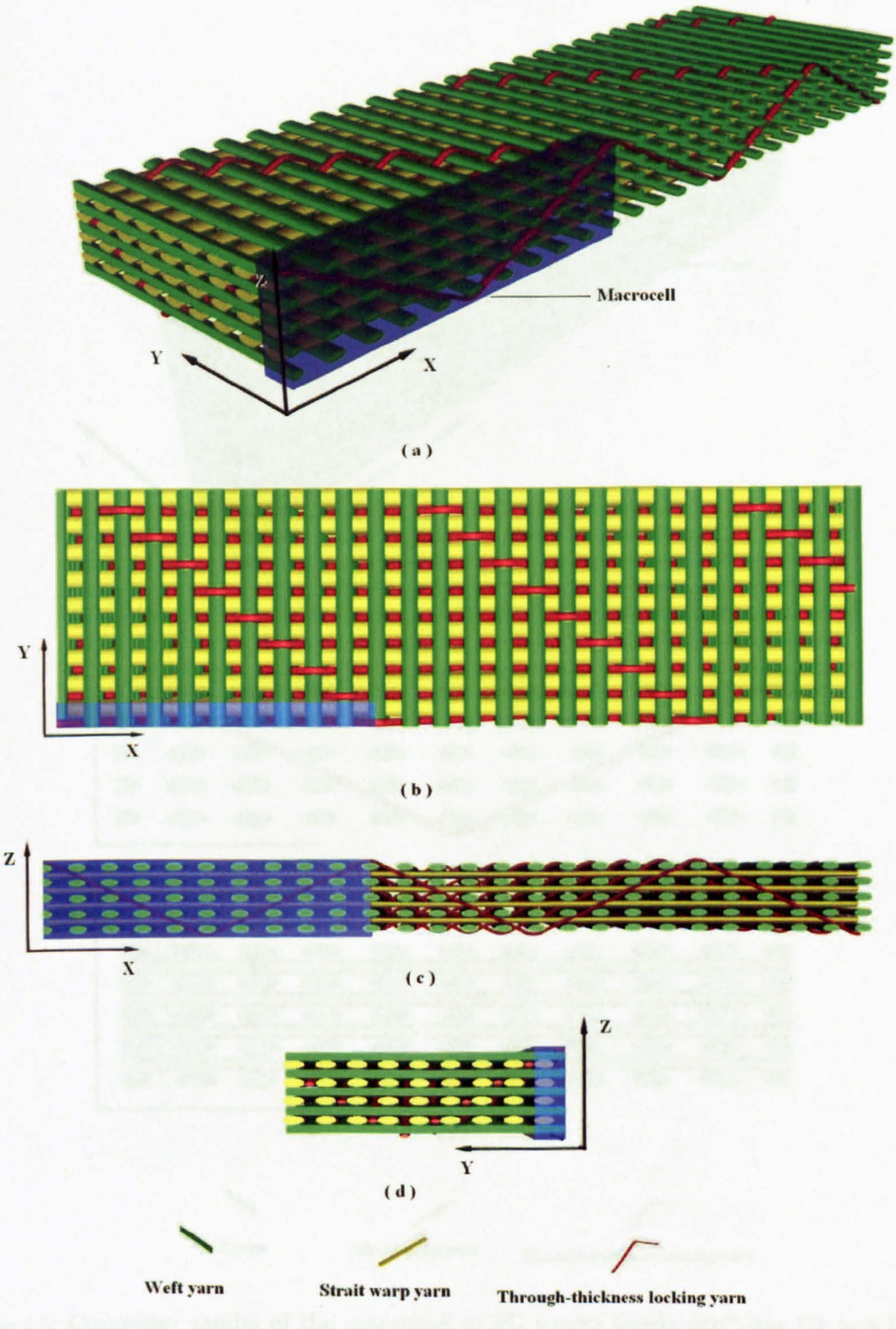

Figure 4.4: **Computer model of the structure of 3D woven fabric preforms C1, G7 and their macrocells:** - (a) overview; (b) top view; (c) side view in weft yarn direction; (d) side view in warp yarn direction.

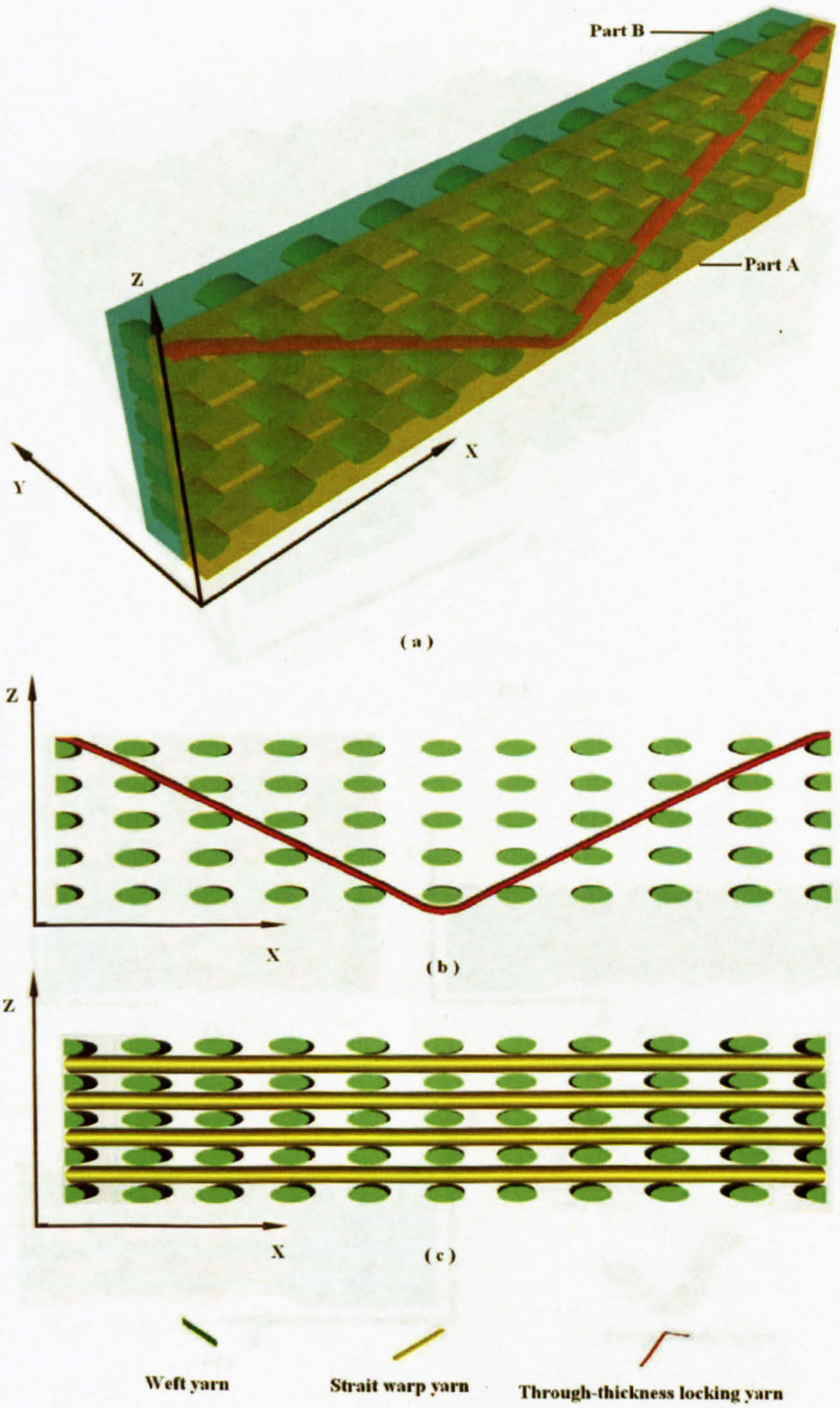

Figure 4.5: **Computer model of the macrocell of 3D woven fabric preforms C1 and G7** - (a) overview; (b) side view in weft yarn direction of part A; (c) side view in weft yarn direction of part B.

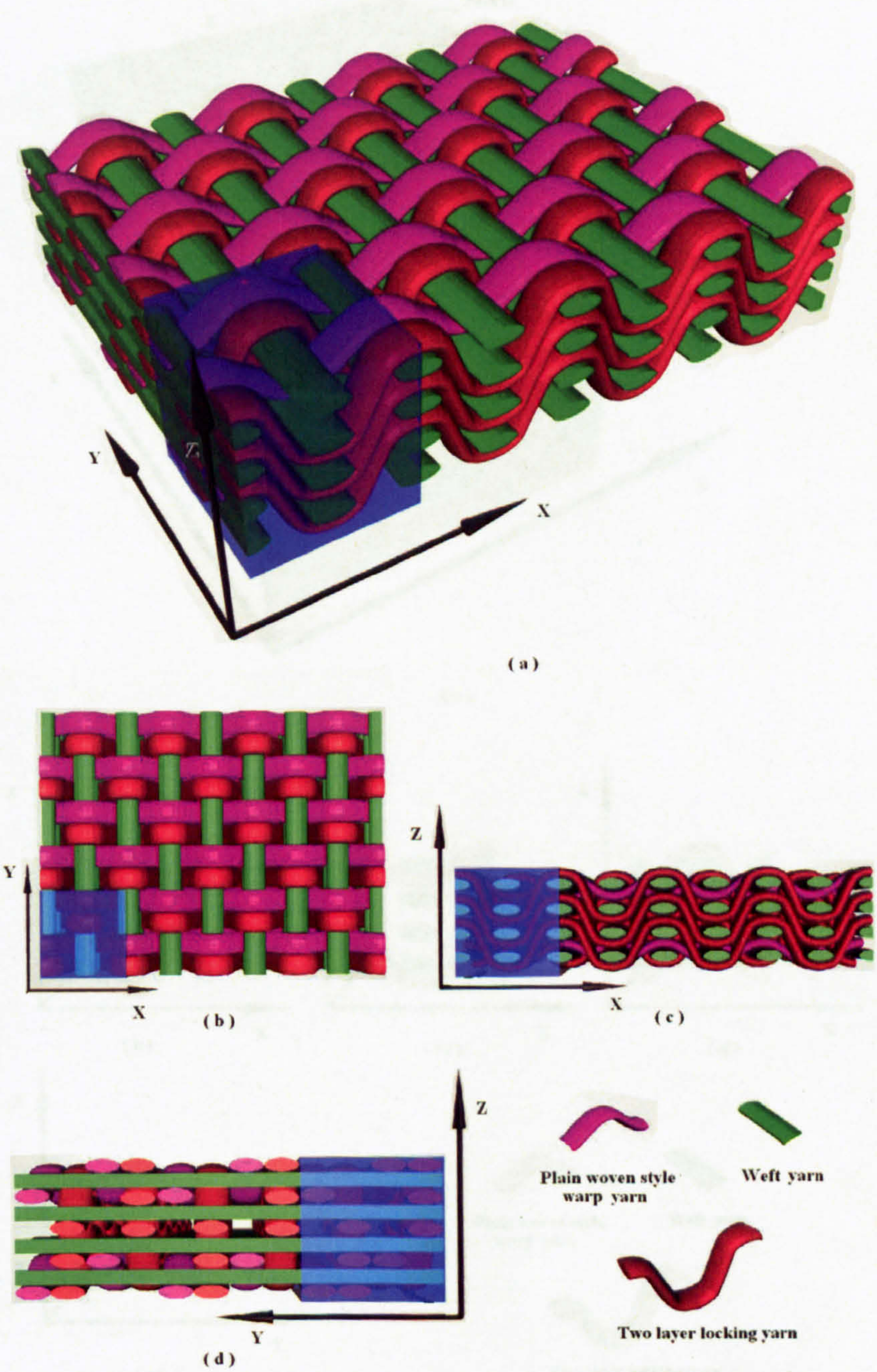

Figure 4.6: **Computer model of the structure of 3D woven fabric preform G1 and its macrocell:** - (a) overview; (b) top view; (c) side view in weft yarn direction; (d) side view in warp yarn direction.

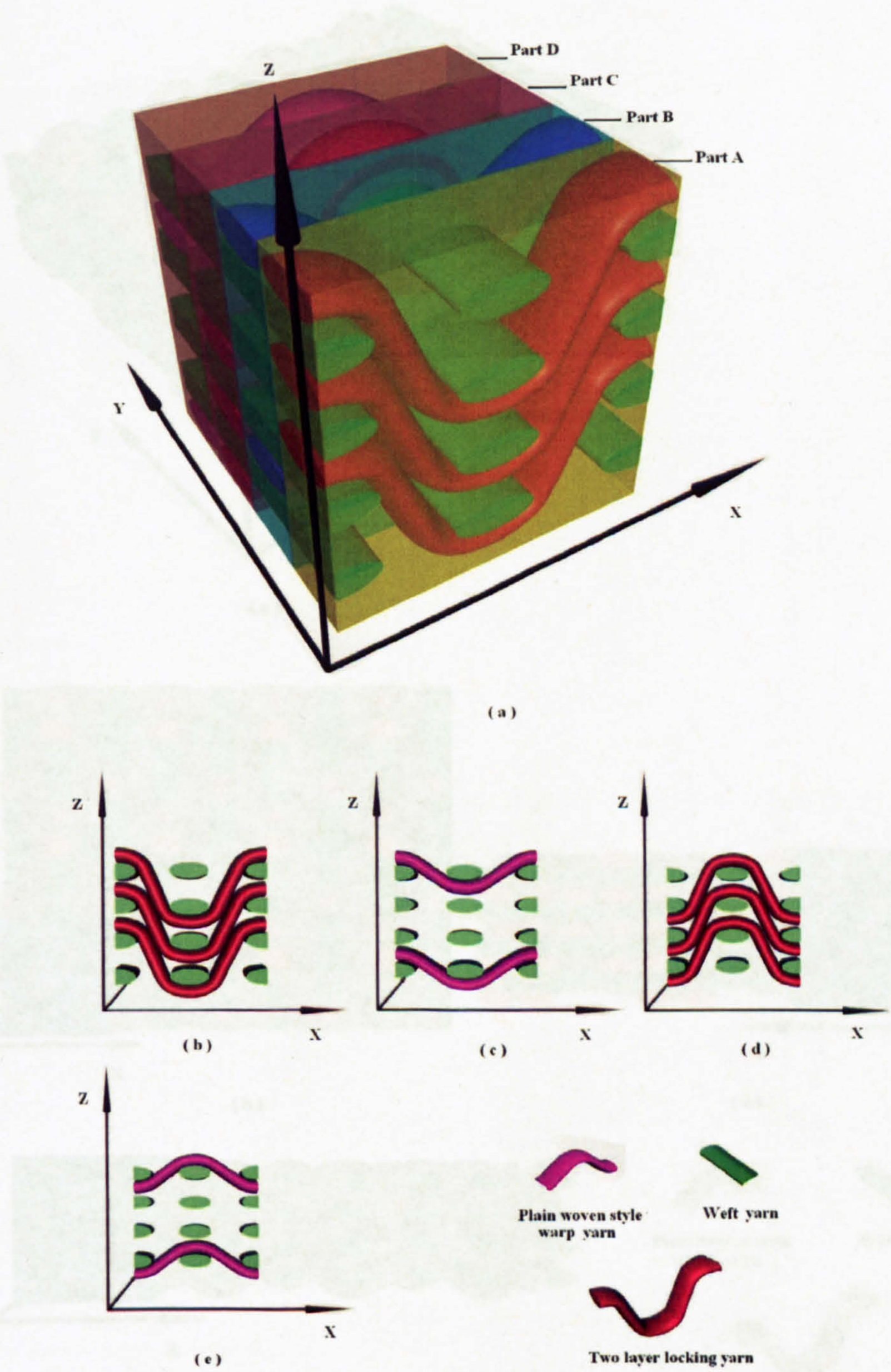

Figure 4.7: **Computer model of the macrocell of 3D woven fabric preform G1** - (a) overview; (b) side view in weft yarn direction of part A; (c) side view in weft yarn direction of part B; (d) side view in weft yarn direction of part C; (e) side view in weft yarn direction of part D;

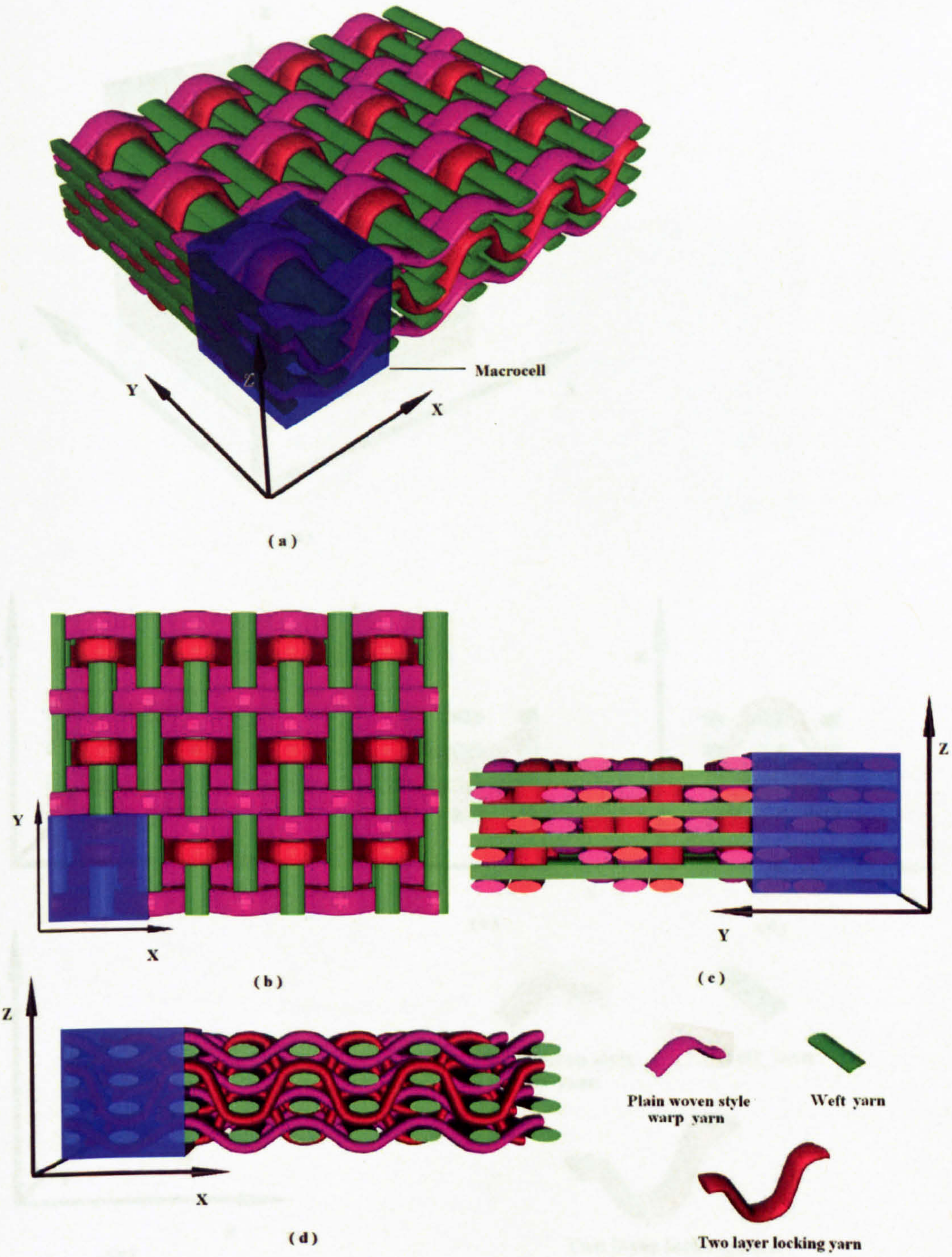

Figure 4.8: **Computer model of the structure of 3D woven fabric preform G2 and its macrocell:** - (a) overview; (b) top view; (c) side view in warp yarn direction; (d) side view in weft yarn direction.

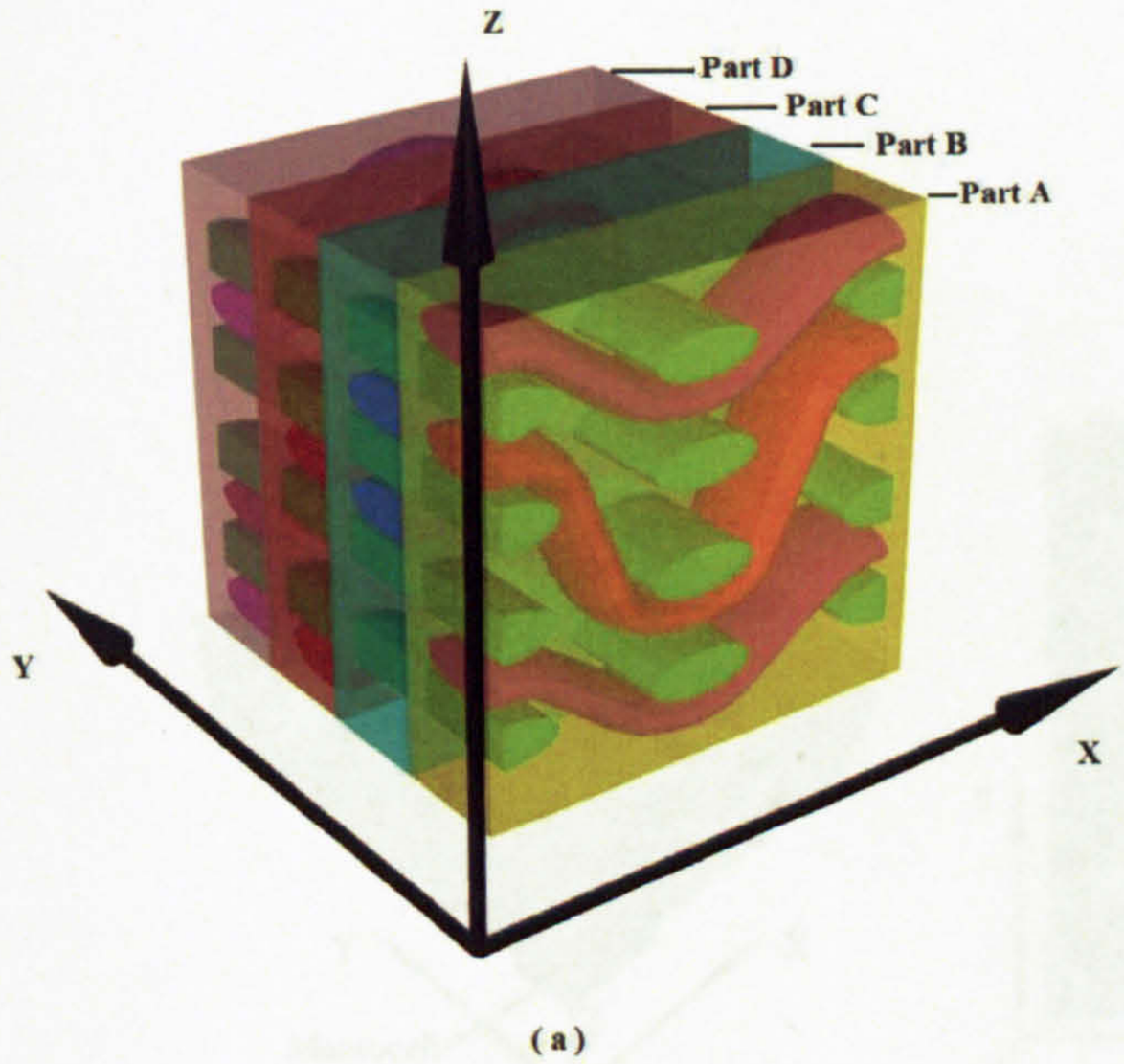

Figure 4.9: **Computer model of the macrocell of 3D woven fabric preform G2** - (a) overview; (b) side view in weft yarn direction of part A; (c) side view in weft yarn direction of part B; (d) side view in weft yarn direction of part C; (e) side view in weft yarn direction of part D.

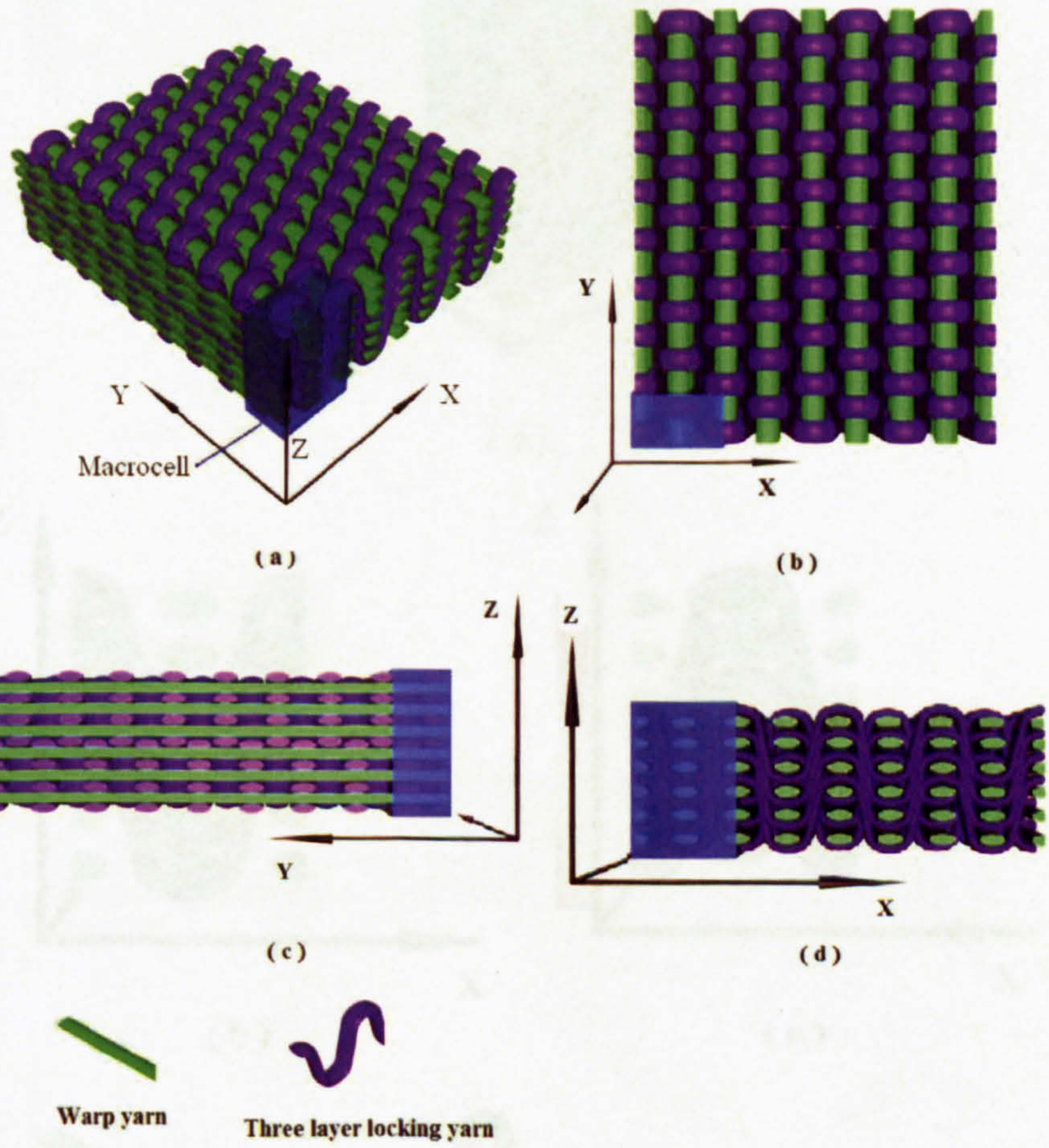

Figure 4.10: **Computer model of the structure of 3D woven fabric preform G3 and its macrocell:** - (a) overview; (b) top view; (c) side view in warp yarn direction; (d) side view in weft yarn direction.

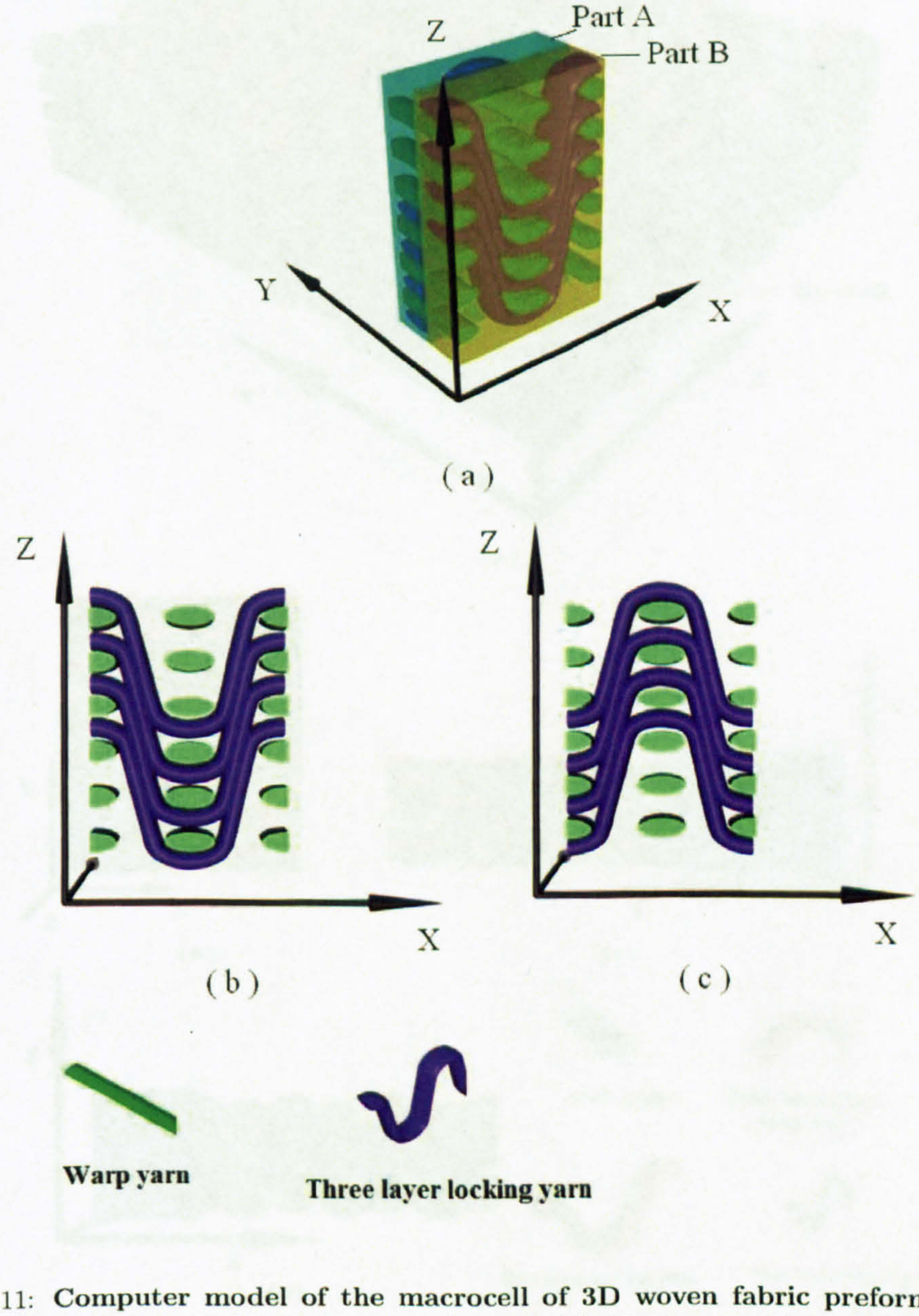

Figure 4.11: **Computer model of the macrocell of 3D woven fabric preform G3** - (a) overview; (b) side view in weft yarn direction of part A; (c) side view in weft yarn direction of part B.

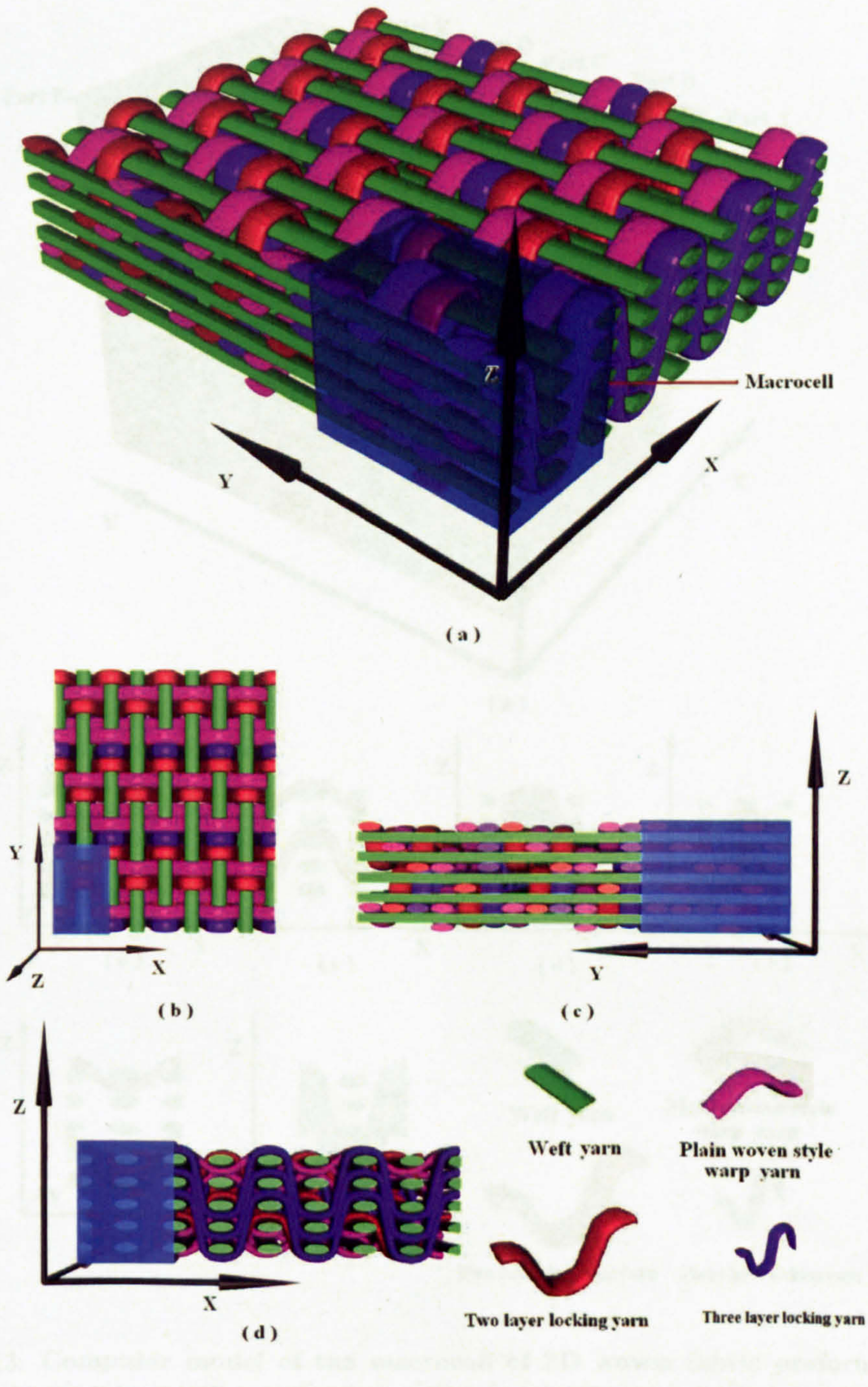

Figure 4.12: **Computer model of the structure of 3D woven fabric preform G4 and its macrocell:** - (a) overview; (b) top view; (c) side view in warp yarn direction; (d) side view in weft yarn direction.

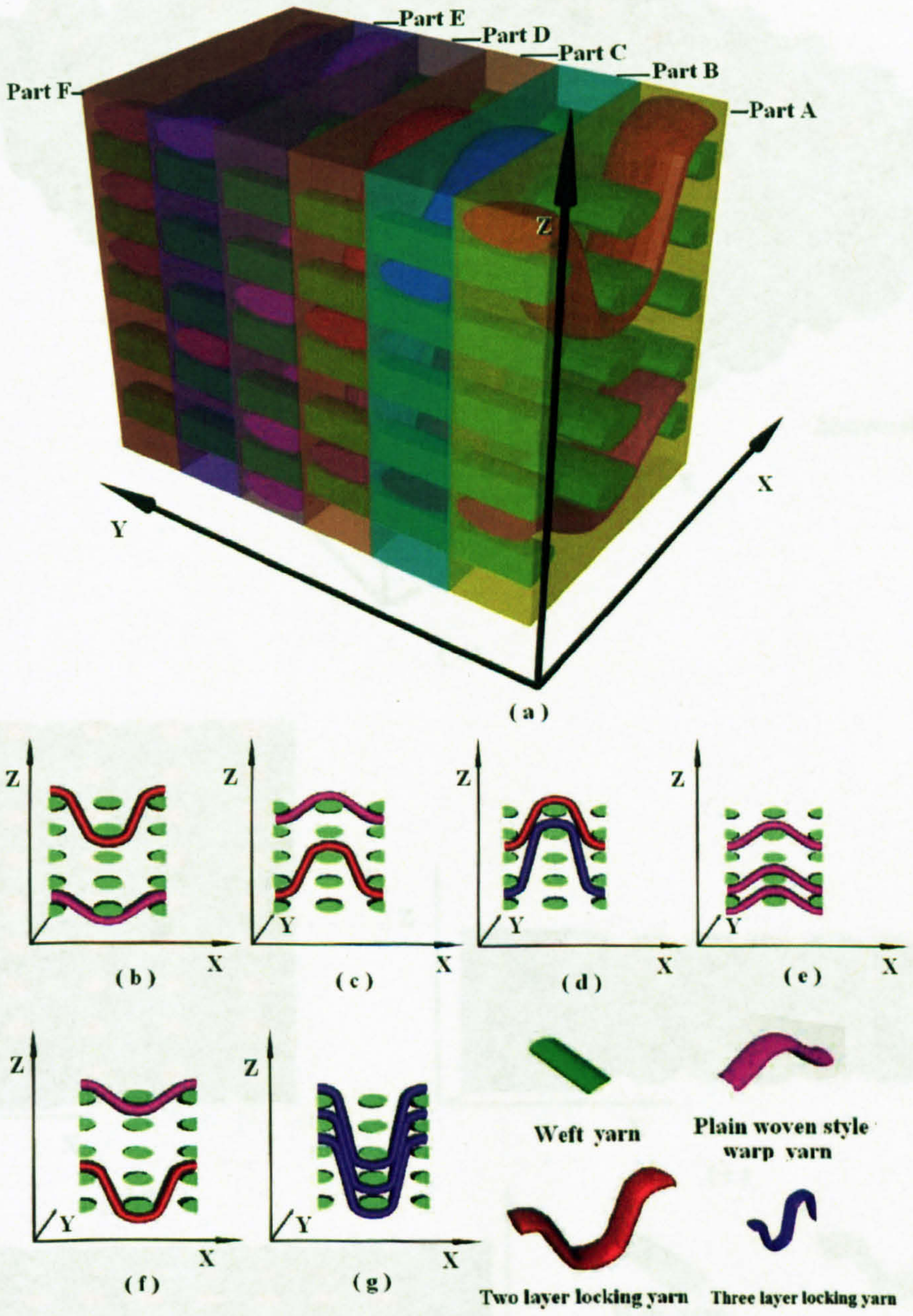

Figure 4.13: **Computer model of the macrocell of 3D woven fabric preform G4** - (a) overview; (b) side view in weft yarn direction of part A; (c) side view in weft yarn direction of part B; (d) side view in weft yarn direction of part C; (e) side view in weft yarn direction of part D; (f) side view in weft yarn direction of part E; (g) side view in weft yarn direction of part F.

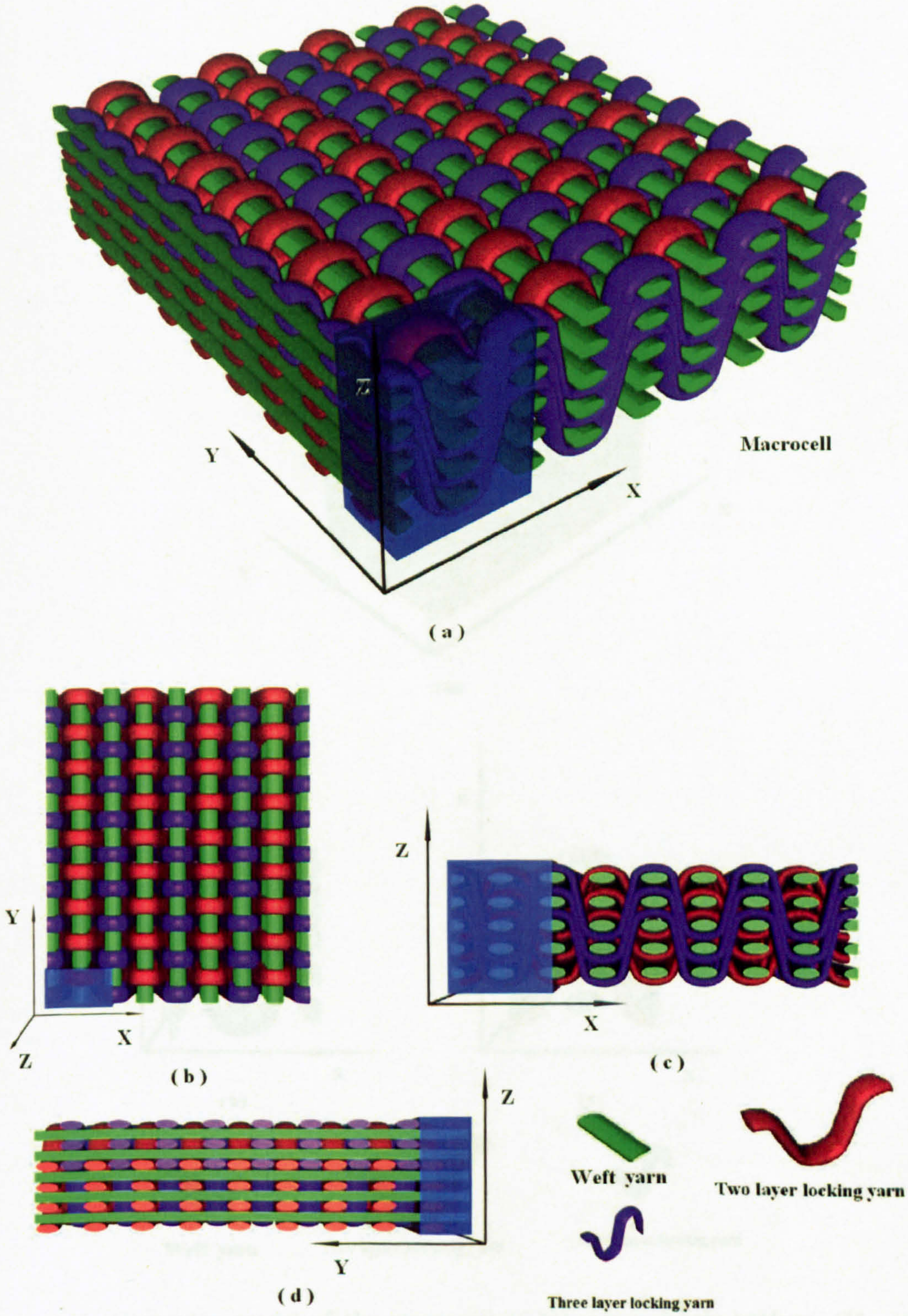

Figure 4.14: **Computer model of the structure of 3D woven fabric preform G5 and its macrocell:** - (a) overview; (b) top view; (c) side view in weft yarn direction; (d) side view in warp yarn direction.

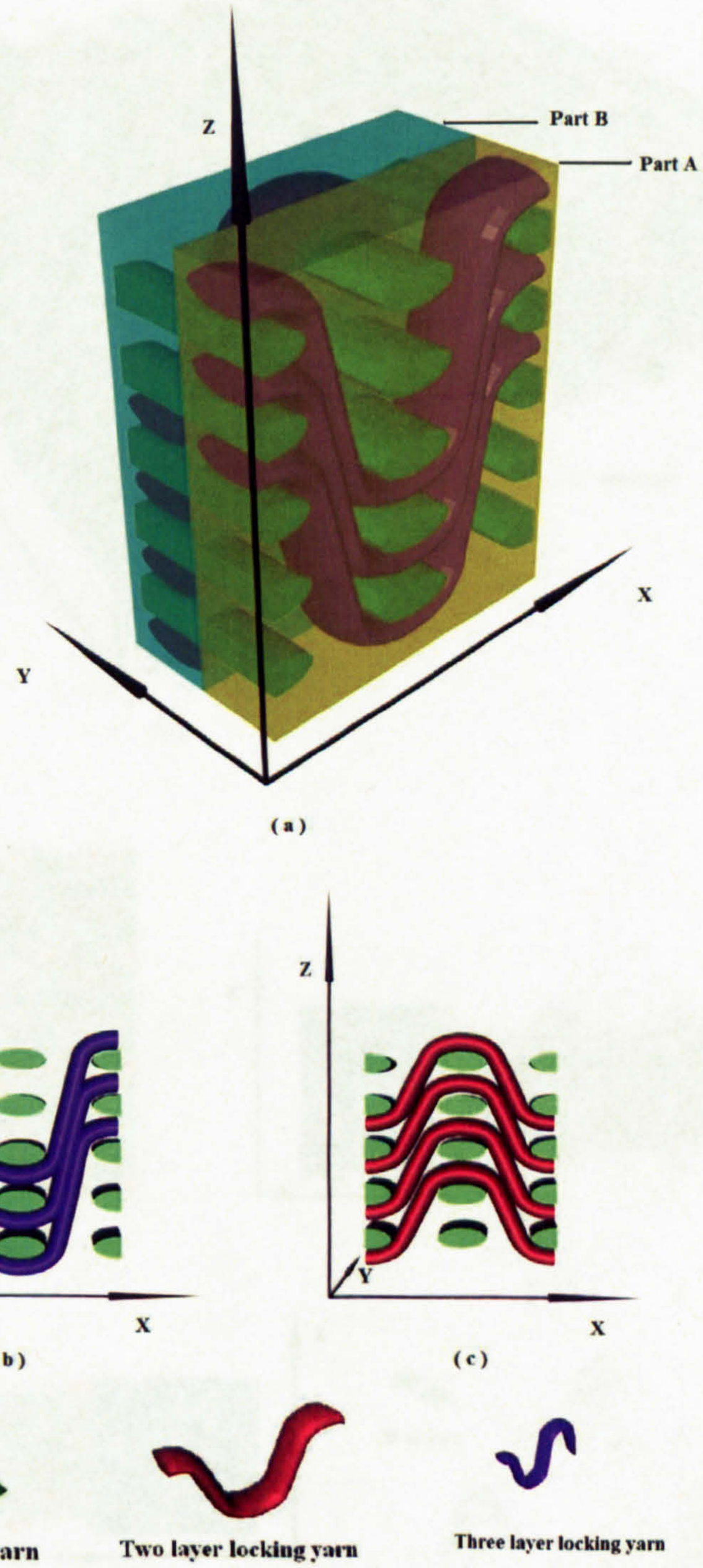

Figure 4.15: **Computer model of the macrocell of 3D woven fabric preform G5** - (a) overview; (b) side view in weft yarn direction of part A; (c) side view in weft yarn direction of part B.

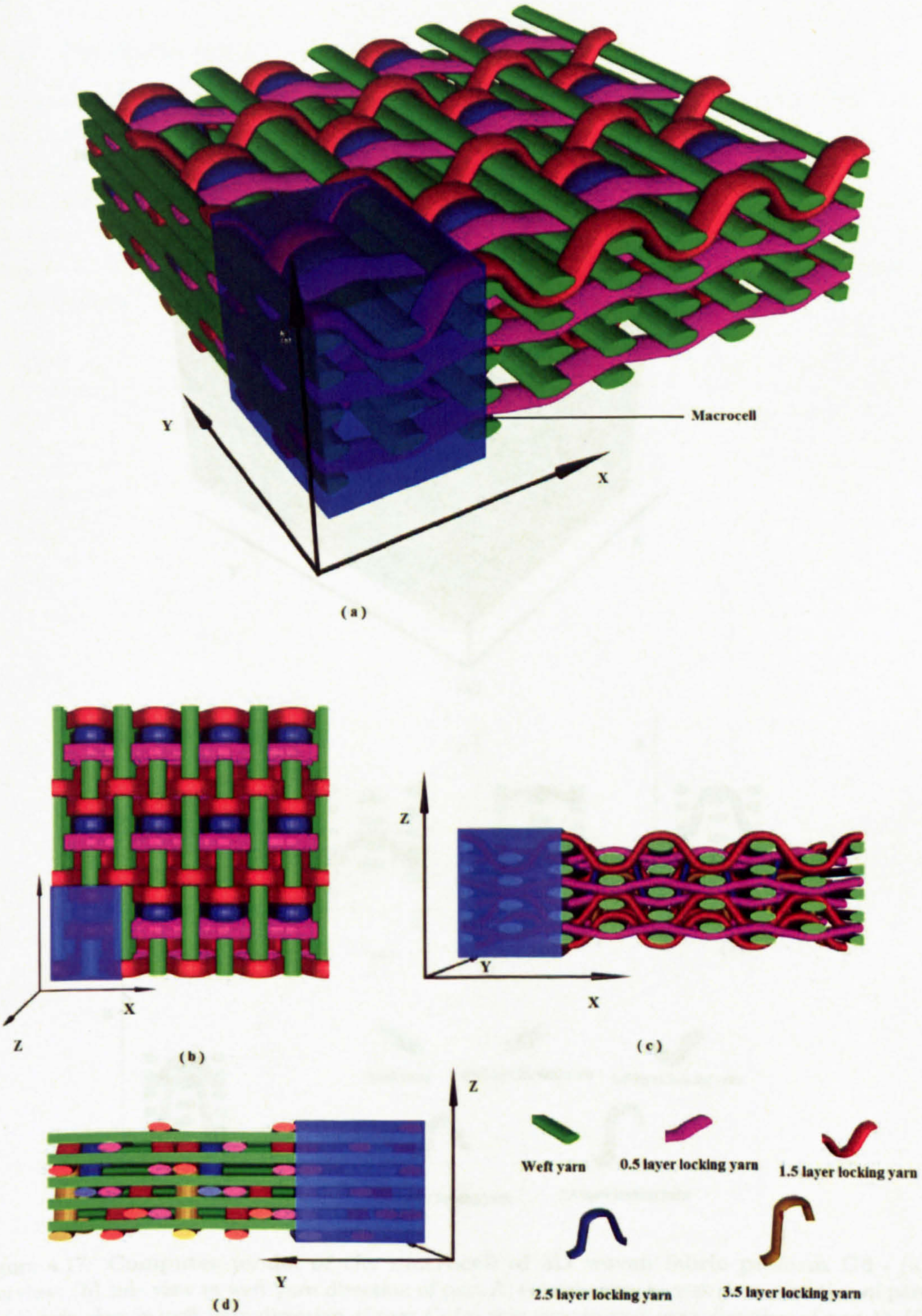

Figure 4.16: **Computer model of the structure of 3D woven fabric preform G6 and its macrocell:** - (a) overview; (b) top view; (c) side view in weft yarn direction; (d) side view in warp yarn direction.

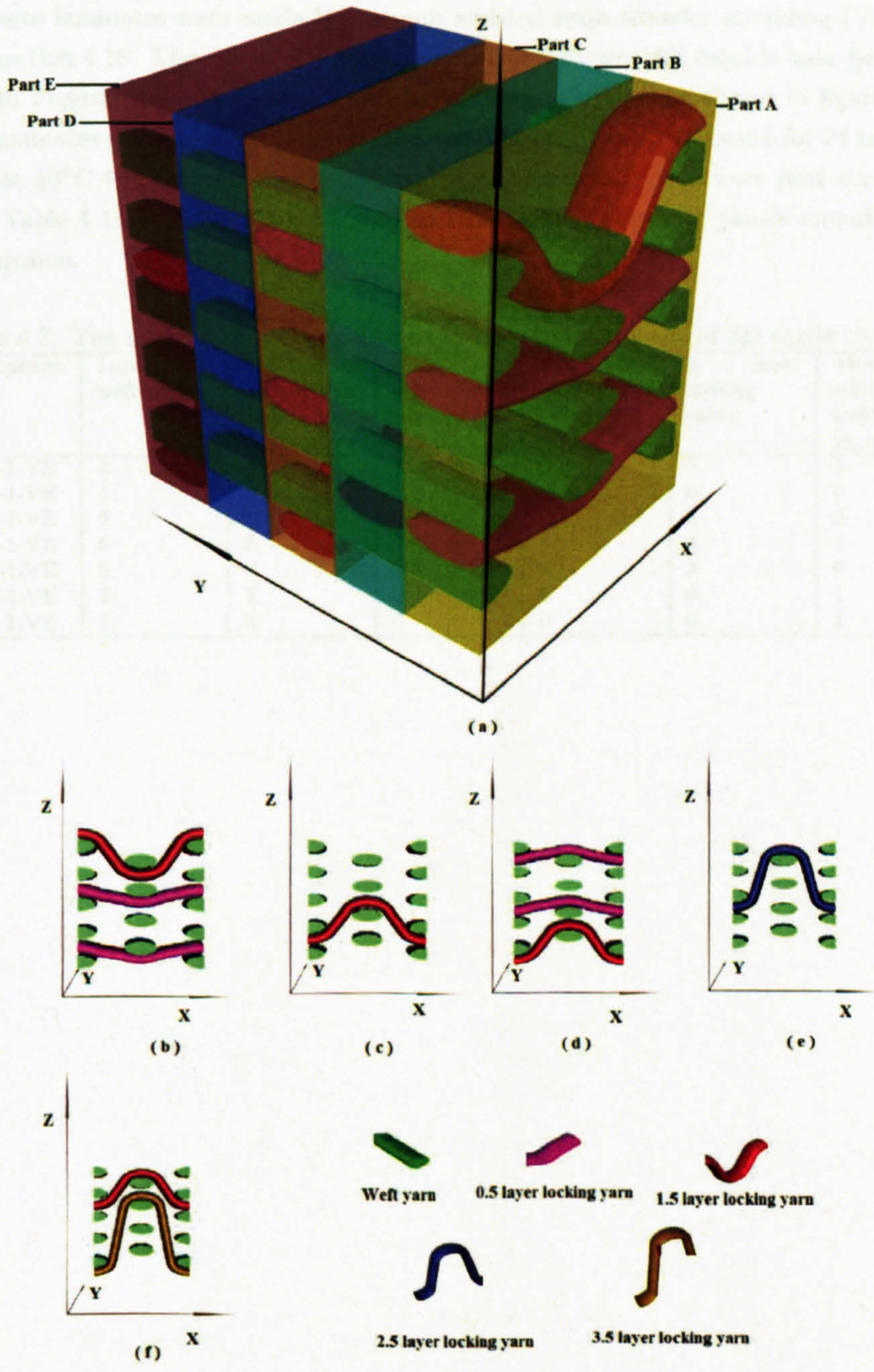

Figure 4.17: **Computer model of the macrocell of 3D woven fabric preform G6** - (a) overview; (b) side view in weft yarn direction of part A; (c) side view in weft yarn direction of part B; (d) side view in weft yarn direction of part C; (e) side view in weft yarn direction of part D; (f) side view in weft yarn direction of part E.

4.2 Processing

4.2.1 Laminate manufacturing

All composite laminates were made by vacuum assisted resin transfer moulding (VARTM) mentioned in section 4.18. The size of the flat mould is $540x540mm$. All moulds have been previously coated with Frekote Release Agent. Set-up of vacuum infusion was shown in figure 4.18. After infusion, laminates containing vinyl ester resin were left in room temperature for 24 hours and then post cure at $80°C$ for 3 hours. And laminates containing epoxy resin were post cure at $50°C$ for 24 hours. Table 4.4 and table 4.5 list all 2D and 3D textile composite panels manufactured using vacuum infusion.

Table 4.3: The number of each kind of warp yarn in macrocells of 3D texile composites

Composite	Layers of weft yarns	Straight warp yarns	Plain woven style warp yarn	2 layer locking yarns	3 layer locking yarns	Through thickness locking yarns
G1-1-VE	4	0	4	6	0	0
G2-1-VE	4	0	6	4	0	0
G3-1-VE	6	0	0	0	8	0
G4-1-VE	5	0	6	4	4	0
G5-1-VE	5	0	0	4	3	0
G7-1-VE	5	4	0	0	0	1
C1-1-VE	5	4	0	0	0	1

Table 4.4: 2D flat textile composites

Fabrics used	Layers of fabrics used	Resin used	Abbreviation	Thickness (mm)
5HSC	4	VE	5HSC-4-VE	1.81
	6	VE	5HSC-6-VE	2.80
	8	VE	5HSC-8-VE	3.40
	12	VE	5HSC-12-VE	4.18
PWEG1	4	VE	PWEG1-4-VE	1.19
	6	VE	PWEG1-6-VE	1.75
	8	VE	PWEG1-8-VE	2.37
	12	VE	PWEG1-12-VE	3.27
	14	VE	PWEG1-14-VE	4.04
PWC	6	VE	PWC-6-VE	
	6	EP	PWC-6-EP	
PWEG2	6	VE	PWEG2-6-VE	
NCC	2 (with fibre lay-up of $[\pm 45]_s$)	VE	NCC-S-VE	
	2 (with fibre lay-up of $[\pm 45]_2$)	VE	NCC-2-VE	
NCEG1	2 (with fibre lay-up of $[\pm 45]_s$)	VE	NCEG1-S-VE	
	4 (with fibre lay-up of $[\pm 45]_{2s}$)	VE	NCEG1-2S-VE	
	4 (with fibre lay-up of $[\pm 45]_4$)	VE	NCEG1-4-VE	
NCEG2	4 (with fibre lay-up of $[+45/-45/0/90]_s$)	VE	NCEG2-4-VE	
PWCPET1	2	VE	PWCPET1-2-VE	
	4	VE	PWCPET1-4-VE	
PWCPET2	4	VE	PWCPET2-2-VE	
PWEGPP	4	EP	PWEGPP-4-EP	
TWEGPP	2	EP	TWEGPP-2-EP	
	4	EP	TWEGPP-4-EP	

Table 4.5: 3D flat textile composites

Fabrics used	Layers of fabrics used	Resin used	Abbreviation	Thickness (mm)
C1	1	VE	C1-1-VE	2.30
	1	EP	C1-1-EP	
G1	1	VE	G1-1-VE	2.85
G2	1	VE	G2-1-VE	3.46
G3	1	VE	G3-1-VE	2.74
G4	1	VE	G4-1-VE	3.84
G5	1	VE	G5-1-VE	2.71
G6	1	VE	G6-1-VE	4.19
G7	1	VE	G7-1-VE	4.42

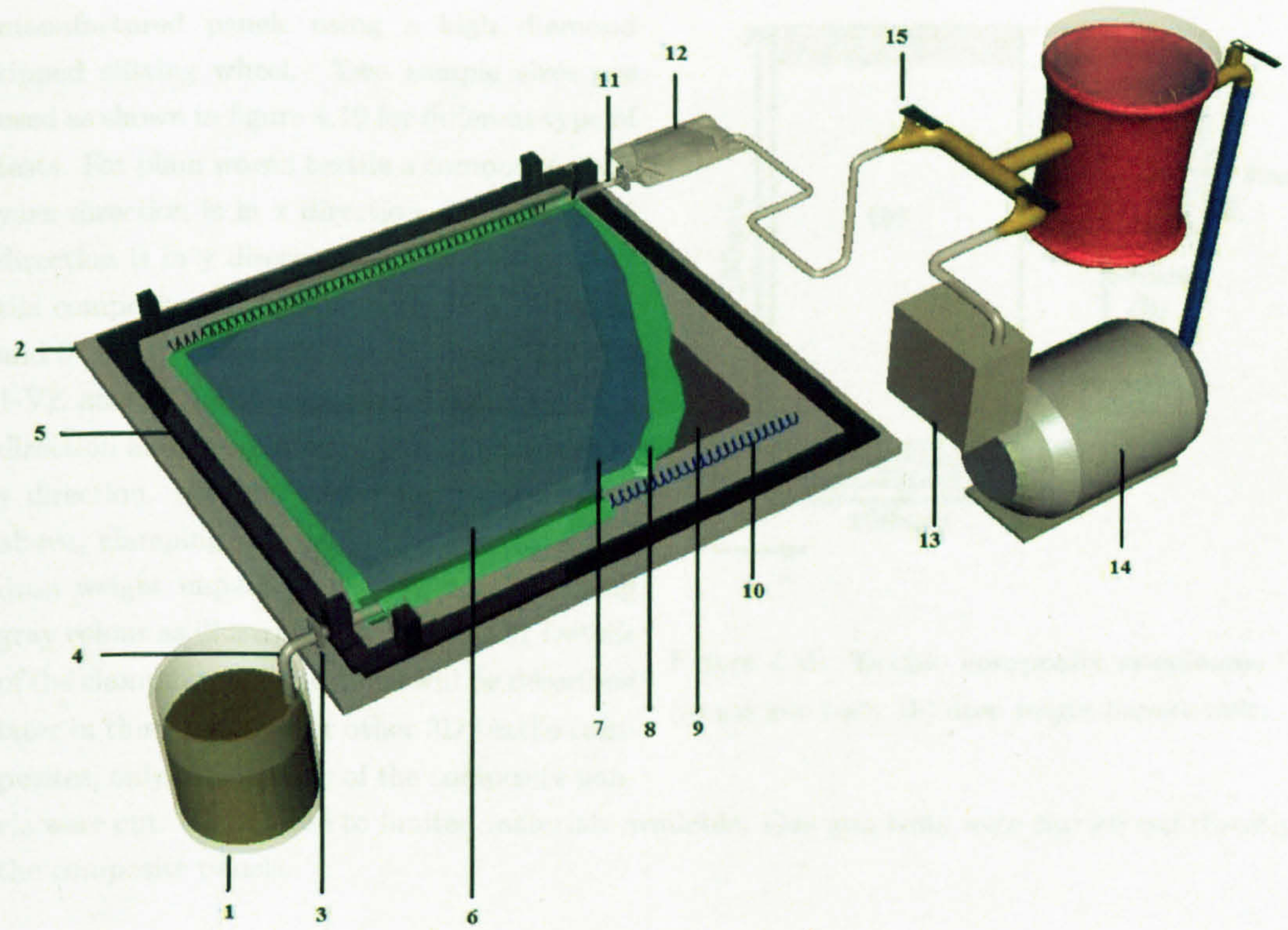

1 -- Resin & Resin pot 2 -- Flat steel plate 3 -- Clamp 4 -- Resin inlet 5 -- Edge sealing taky tape 6 -- Plastic bag film
7 -- Resin distribution media 8 -- Peel ply 9 -- Preform 10 -- Spring 11 -- Resin outlet 12 -- Resin absorption bag
13 -- Pressure meter 14 -- Vacuum pump 15 -- Turn valve

(a)

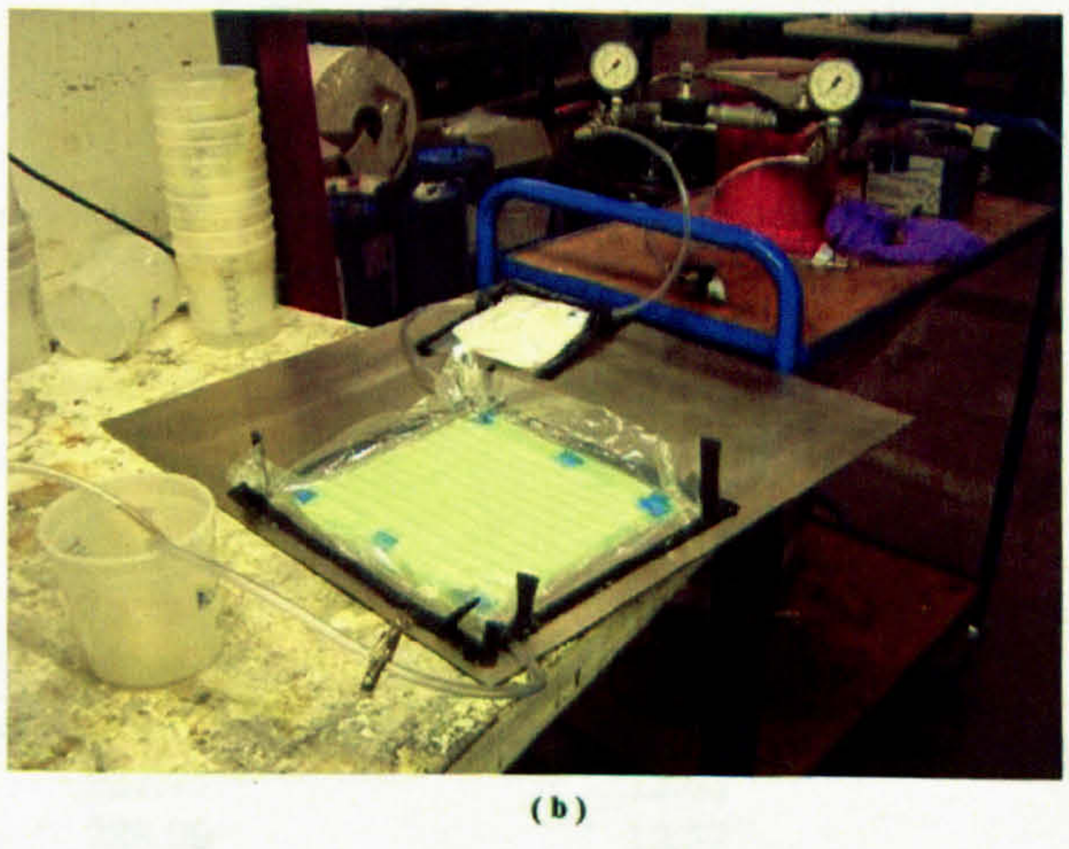

(b)

Figure 4.18: **Vacuum infusion with semi-flexible mould processing of composite laminate** - (a) theoretic lay out; (b) experimental lay out.

4.2.2 Composite test specimen preparation

Individual test specimens were cut from the manufactured panels using a high diamond tipped slitting wheel. Two sample sizes are used as shown in figure 4.19 for different type of tests. For plain woven textile a composite, weft yarn direction is in x direction and warp yarn direction is in y direction. For non-crimp textile composites, 90° direction is in y direction and 0° is in x direction. For 3D composite C1-1-VE and C1-1-EP, weft yarn direction is in x direction and straight warp yarn direction is in y direction. For textile composites mentioned above, clamping regions in gas gun tests and drop weight impact tests were denoted using gray colour as illustrated in figure 4.19. Details of the clamping configurations will be described later in this chapter. For other 3D textile composites, only sharp edges of the composite panels were cut. This is due to limited materials available. Gas gun tests were carried out directly on the composite panels.

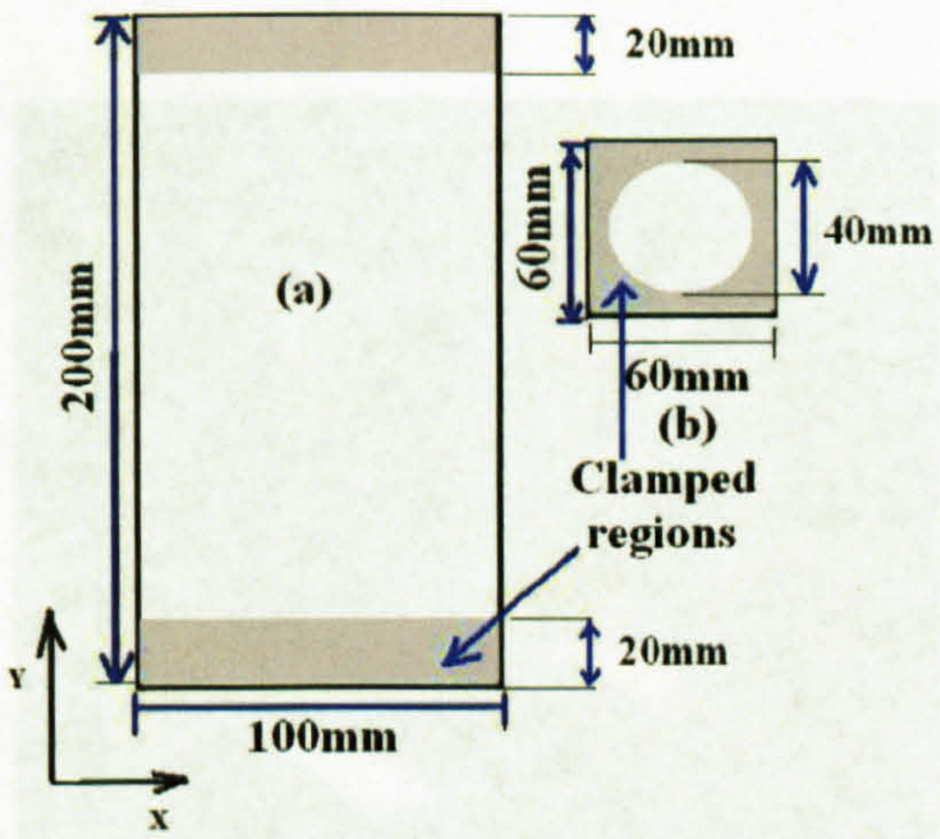

Figure 4.19: **Textile composite specimens for** - (a) gas gun tests; (b) drop weight impact tests.

4.3 Test Methods

4.3.1 The Light Gas Gun Test

Table 4.6: Gas Gun Test Result of PWEG1-8-VE samples impacted by 0.44g steel balls

Shot Number	Impact Velocity V(m/s)	Impact Energy E/J	Status
1	237.71	12.43	Not penetrated
2	238.99	12.57	Not penetrated
3	240.12	12.68	Not penetrated
4	243.26	13.02	Penetrated
5	244.98	13.20	Penetrated
6	245.24	13.23	Penetrated

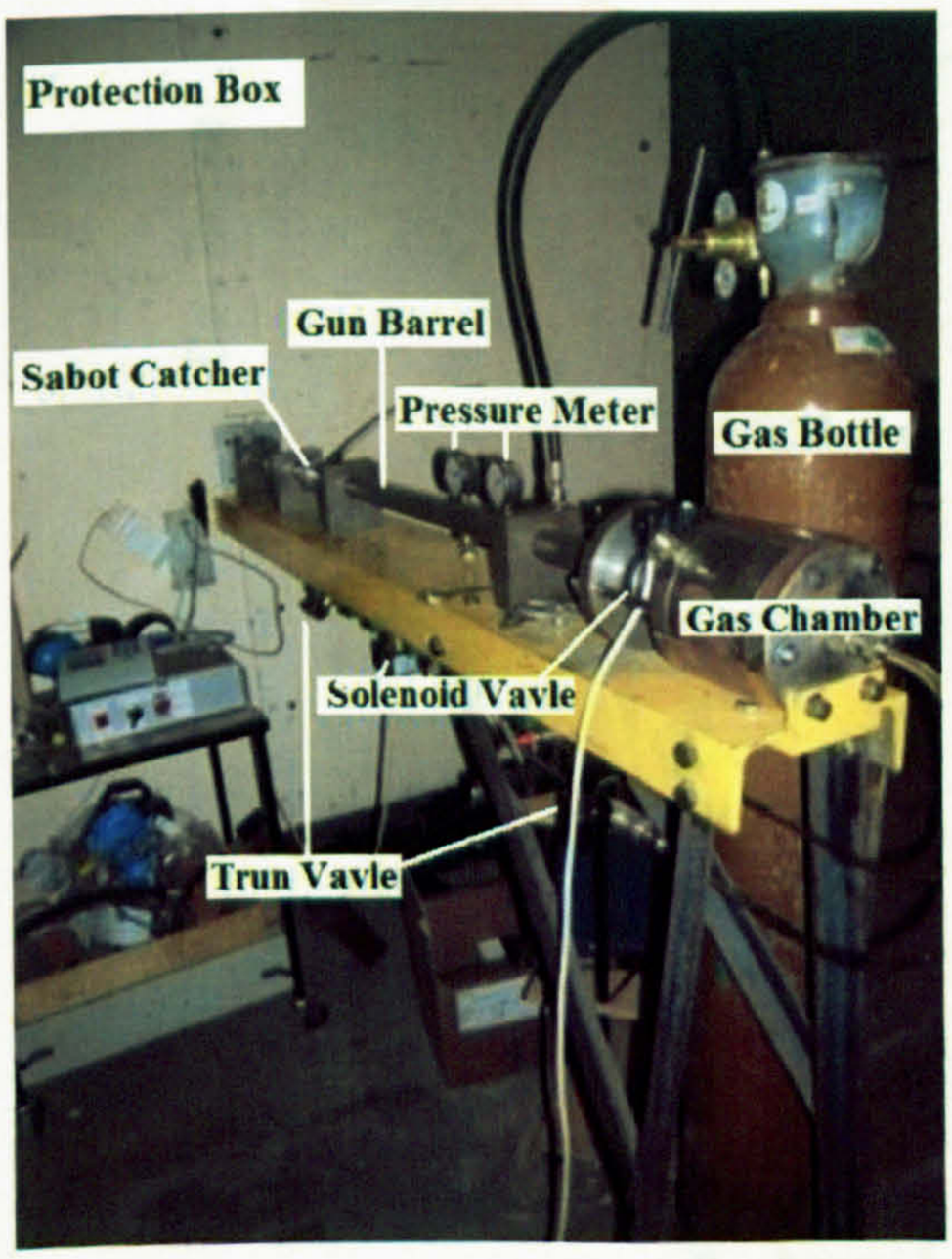

(a)

(b)

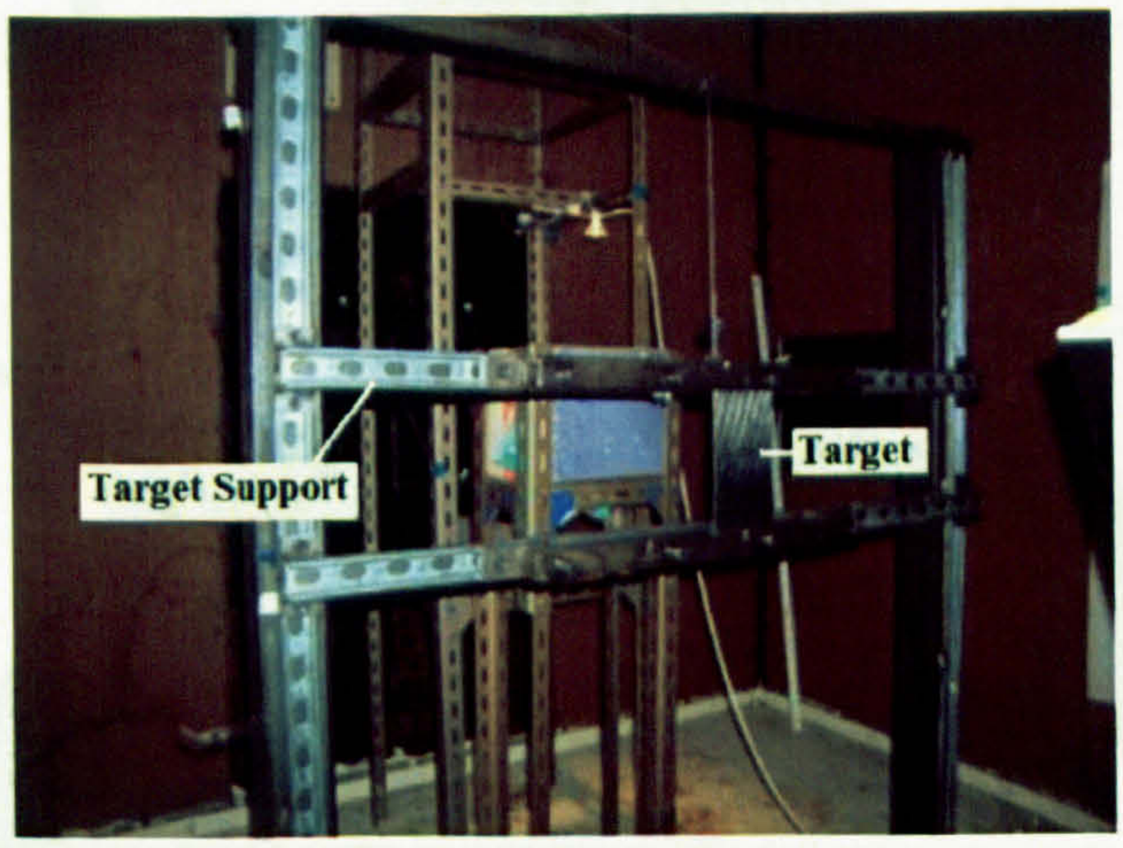

(c)

Figure 4.20: **Gas Gun** - (a) main components; (b) chronograph; (c) sample stage.

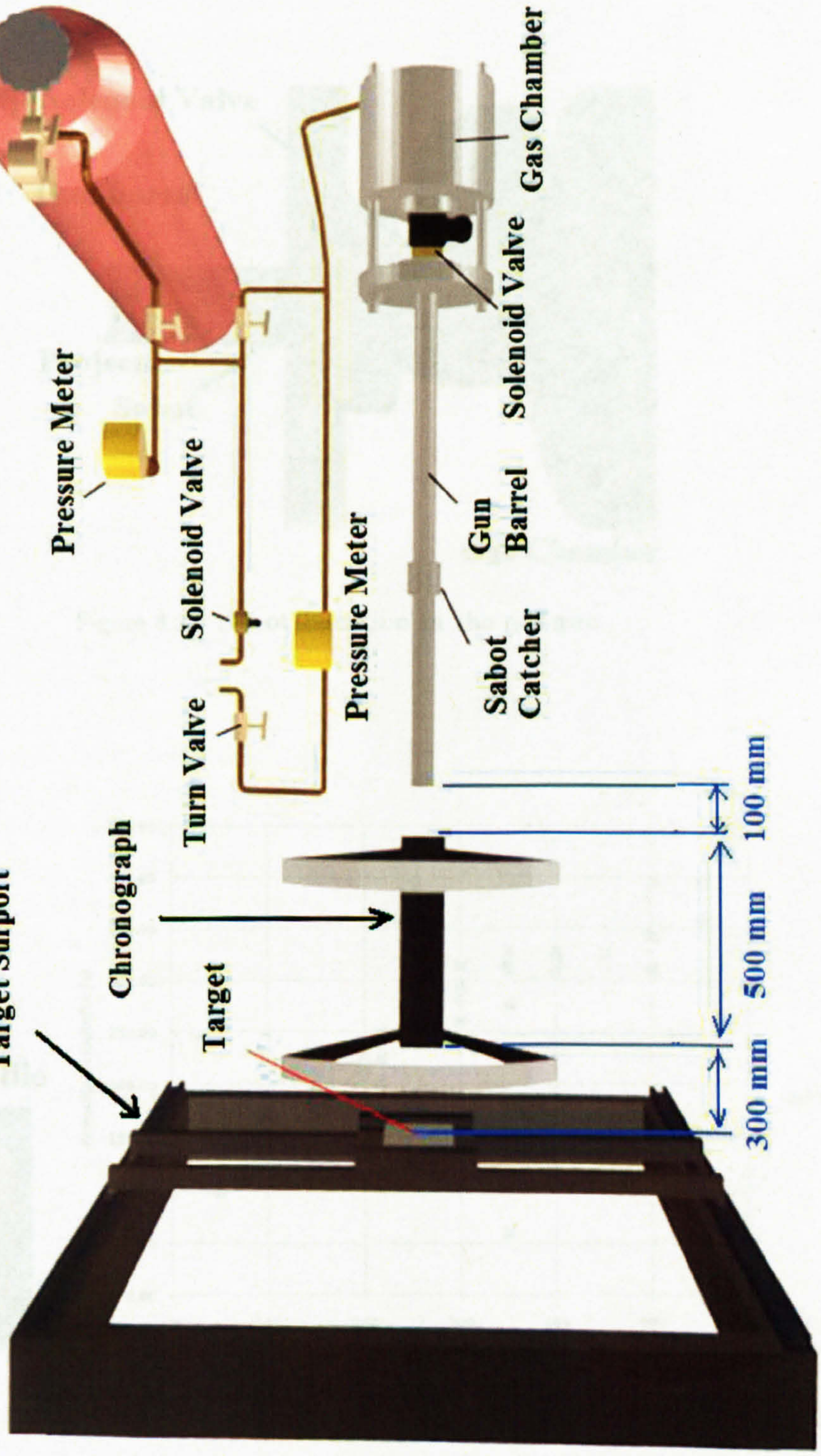

Figure 4.21: **Schematic of gas gun testing .**

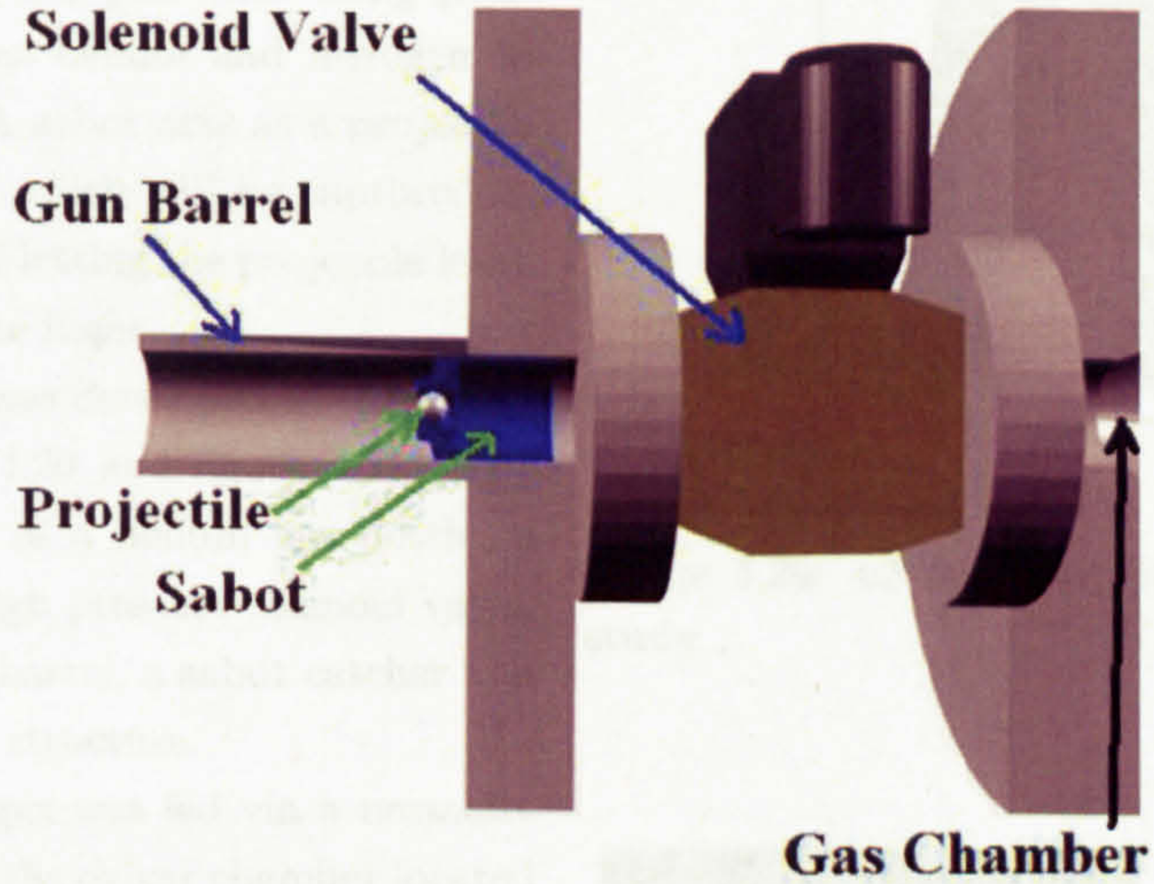

Figure 4.22: **Sabot Location in the gas gun** .

(a)

(b)

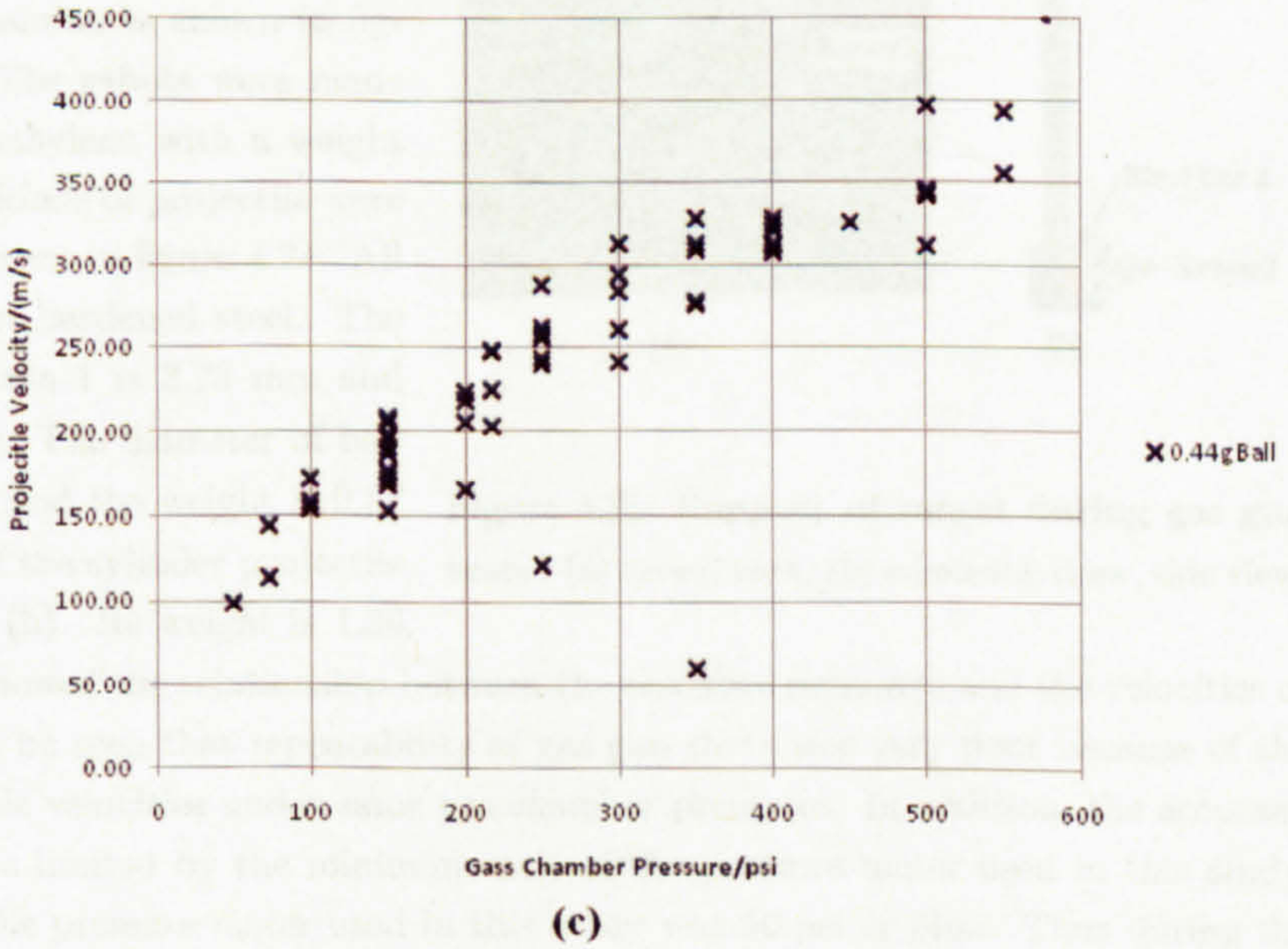

(c)

Figure 4.23: **Sabot Geometry and velocity control in gas gun test** - (a) computer model of geometry of sabot; (b) Sabot with ball projectile; (c) velocity/pressure calibration.

A light gas gun is a specially developed apparatus designed to generate very high velocity. Unlike other gun tests that use an explosive powder charge, gas gun tests using pressurized gases such as helium and nitrogen to propel projectiles. A sabot acts as a projectile carrier and gas seal which will be captured at the end of gun barrel letting the projectile leave the gun barrel in free flight.

A light gas gun was developed in this study as shown in figure 4.20 and figure 4.21. The gun was comprised of a helium gas bottle, a driver chamber, a high pressure solenoid valve, a long and uniform barrel, a sabot catcher and a specimen support structure.

Bottled helium gas was fed via a normally closed turn valve to the driver chamber located at the end of the gun barrel. Here the gas was restrained by a closed solenoid valve which is located between the driver chamber and the barrel. The projectile was placed in a holder, usually termed a "sabot", and positioned in the font of the solenoid valve as shown in figure 4.22. Typical sabot geometry is shown in figure 4.23 (a) and (b). The sabots were made form high density polyethylene with a weight of 2.5 gram. And three kinds of projectile were used in this study as shown in figure 4.24. All projectiles were made of hardened steel. The diameter of ball projectile 1 is 3.78 mm and the weight is 0.44 gram. The diameter of ball projectile 2 is 4.75 mm and the weight is 0.87 gram. The dimension of the cylinder projectile is shown in figure 4.24 (b). Its weight is 1.39 gram. Figure 4.23 (c) showed the relationship between the chamber pressures and the velocities of 0.44g steel balls. It can be seen that repeatability of gas gun shots was very poor because of the big variation of projectile velocities under same gas chamber pressures. In addition, the accuracy of pressure readings was limited by the minimum unit of the pressure meter used in this study. The minimum unit of the pressure meter used in this study was 50 psi or 5bar. Thus during the late stage of this study gas chamber pressures of gas gun shots were not recorded, and chamber pressures were not included in gas gun test results.

As show in the figure 4.21, the distance between the sabot catcher and the chronograph was very small. The distance between the target and the chronograph was also very small. In addition, an additional gun barrel of $300mm$ long was placed after the sabot catcher which reduced the

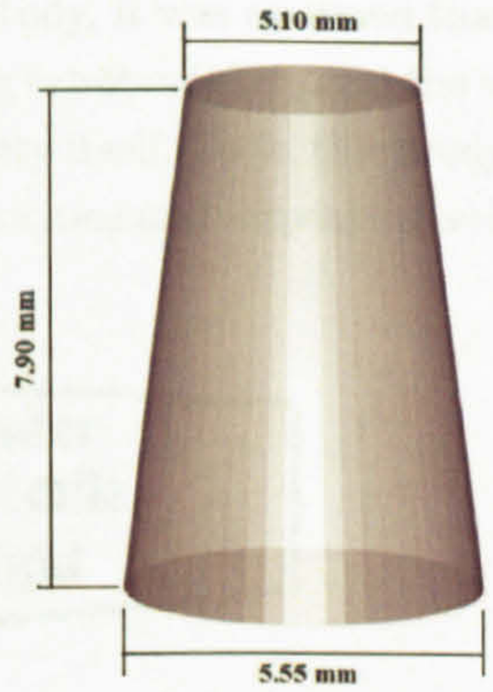

Figure 4.24: **Cylinder projectiles used in this study .**

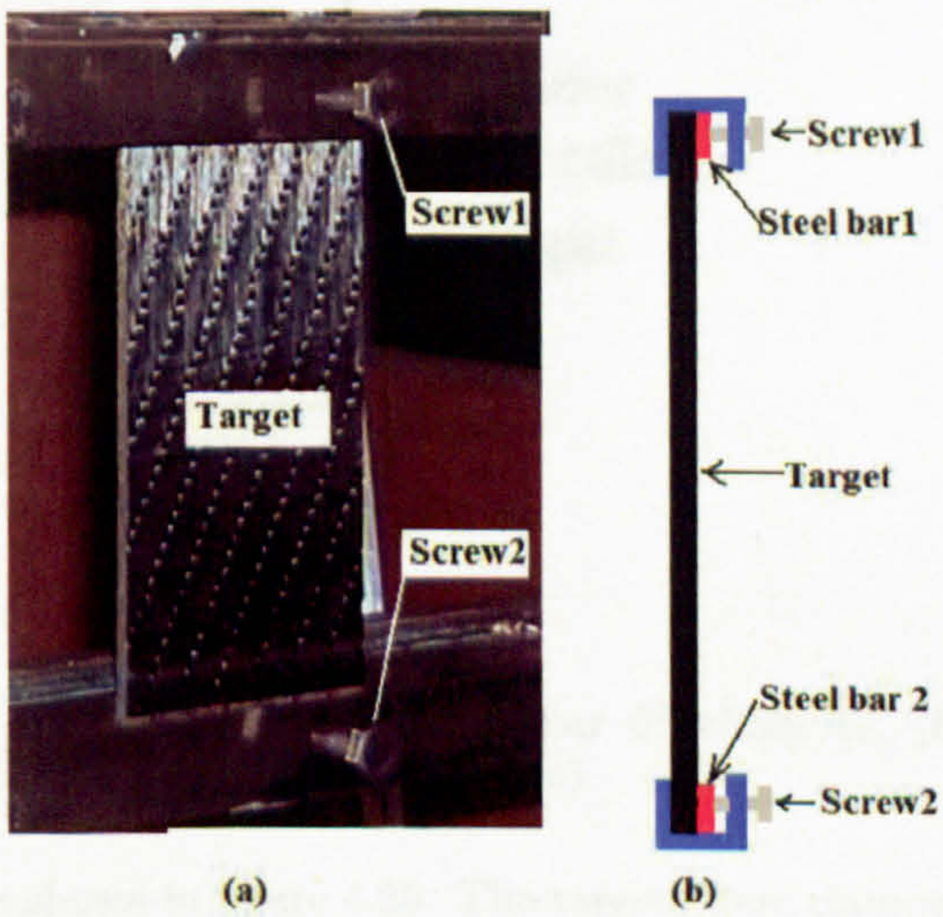

Figure 4.25: **Support of target during gas gun tests** - (a) actual view; (b) schematic draw, side view.

effect of air resistances during gas gun tests. Thus in this study, it was assumed that the difference between the muzzle velocity (projectile velocity after leaving sabot catcher) and the velocity prior to impacting was very small compared to the impacting velocity itself. So in this study, the velocities measured by chronograph may be seen as both muzzle velocities and impacting velocities.

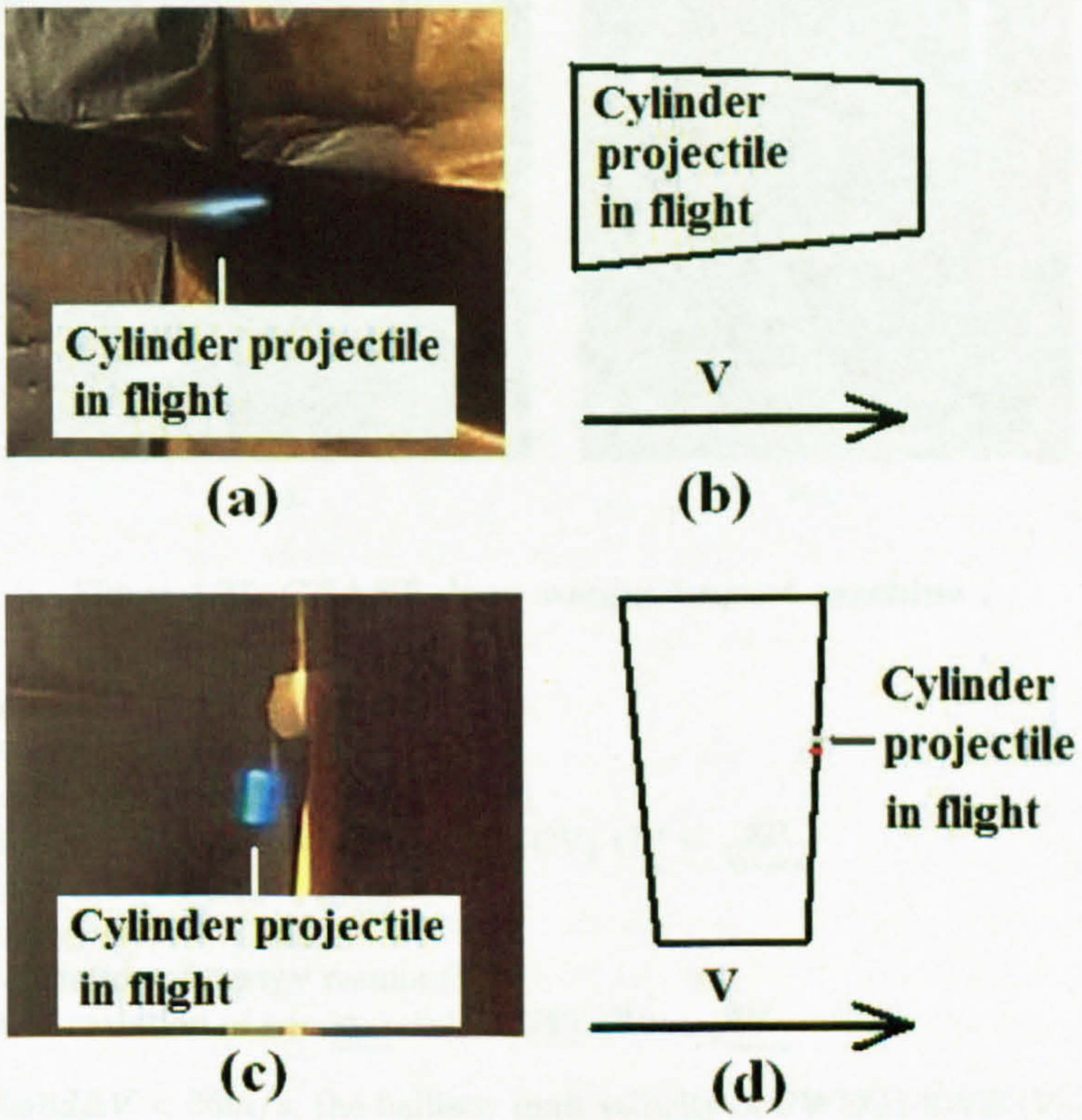

Figure 4.26: **Cylinder projectile in flight** - (a) successful test with near 0° obliquity; (b) illustration of (a); (c) failed test with near 90° obliquity; (d) illustration of (c)

The targets were supported during the tests as shown in figure 4.25. The targets were clamped by two steel bars. The length of the steel bars was similar to the width of the target, and the height of the steel bars was $20mm$. Recall in figure 4.19, the composite specimens for gas gun tests was $200mm$ long in weft yarn direction and $100mm$ wide in warp yarn direction. As shown infigure 4.25, specimens for gas gun were clamped along the short edges. The long edges were not supported. It should be noticed that results of this research were particular to the support conditions used on the laminates in this study. It should also be noticed that the boundary conditions for the low-velocity impacts are very different from the boundary conditions described above. For the purpose of safety, the target and the supporting structure together with the chronograph were housed in a large steel box. Yaw (as defined in figure 2.3) of cylinder projectile was characterized by high speed strobe photography. Figure 4.26 shows a cylinder projectile in flying. According to pictures taken during tests, the yaws of cylinder projectile were mostly near 0°. Ballistic Limits (V_{50}) of all the specimens were calculated as described in 2.2.1. Six shots, three non-penetrated and three penetrated, were used to determine V_{50}. A example results of gas gun tests is shown in table 4.6. The following calculation will be carried out to examine the accuracy of the results:

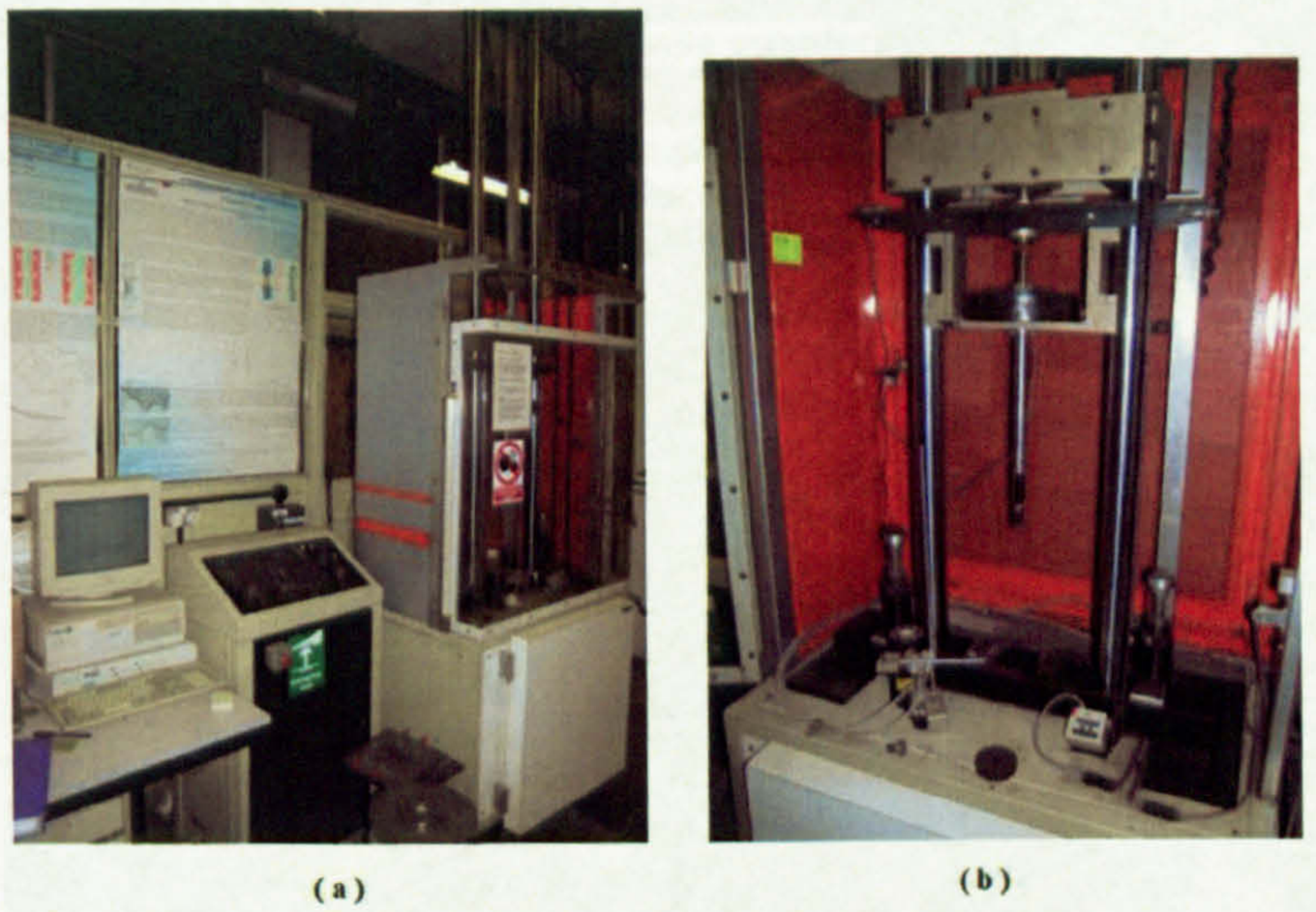

(a) (b)

Figure 4.27: **CEAST drop weight impact machine .**

1. Velocity range $\Delta V = V_{max} - V_{min}$
2. Mean of velocity results V_{mean}
3. Standard deviation of velocity results (SD)
4. Coefficient of variation of velocity resutls (CV) $CV = \frac{SD}{V_{mean}}$
5. Energy range $\Delta E = E_{max} - E_{min}$
6. Mean of energy results E_{mean}
7. Standard deviation of energy results (SD)
8. Coefficient of variation of energy results (CV) $CV = \frac{SD}{V_{mean}}$

If $CV < 10\% and \Delta V < 36 m/s$, the ballistic limit velocity of PWEG1-8-VE (V_{BL}) will be equal to V_{mean}.

4.3.2 The Drop-Weight Impact Test

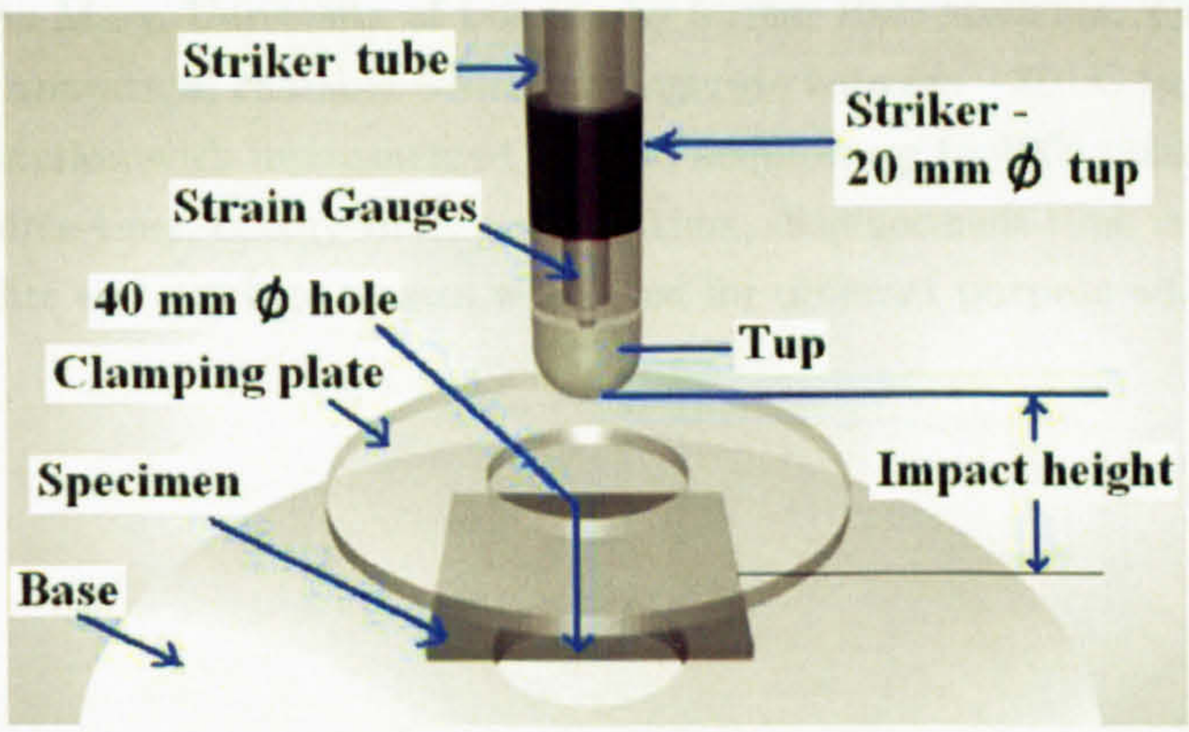

Figure 4.28: **CEAST drop weight impact machine ·**

The drop-weight impact machine is an apparatus designed to determine energy absorption of material samples at low velocity impact (1-7 m/s). The drop-weight machine used in this study

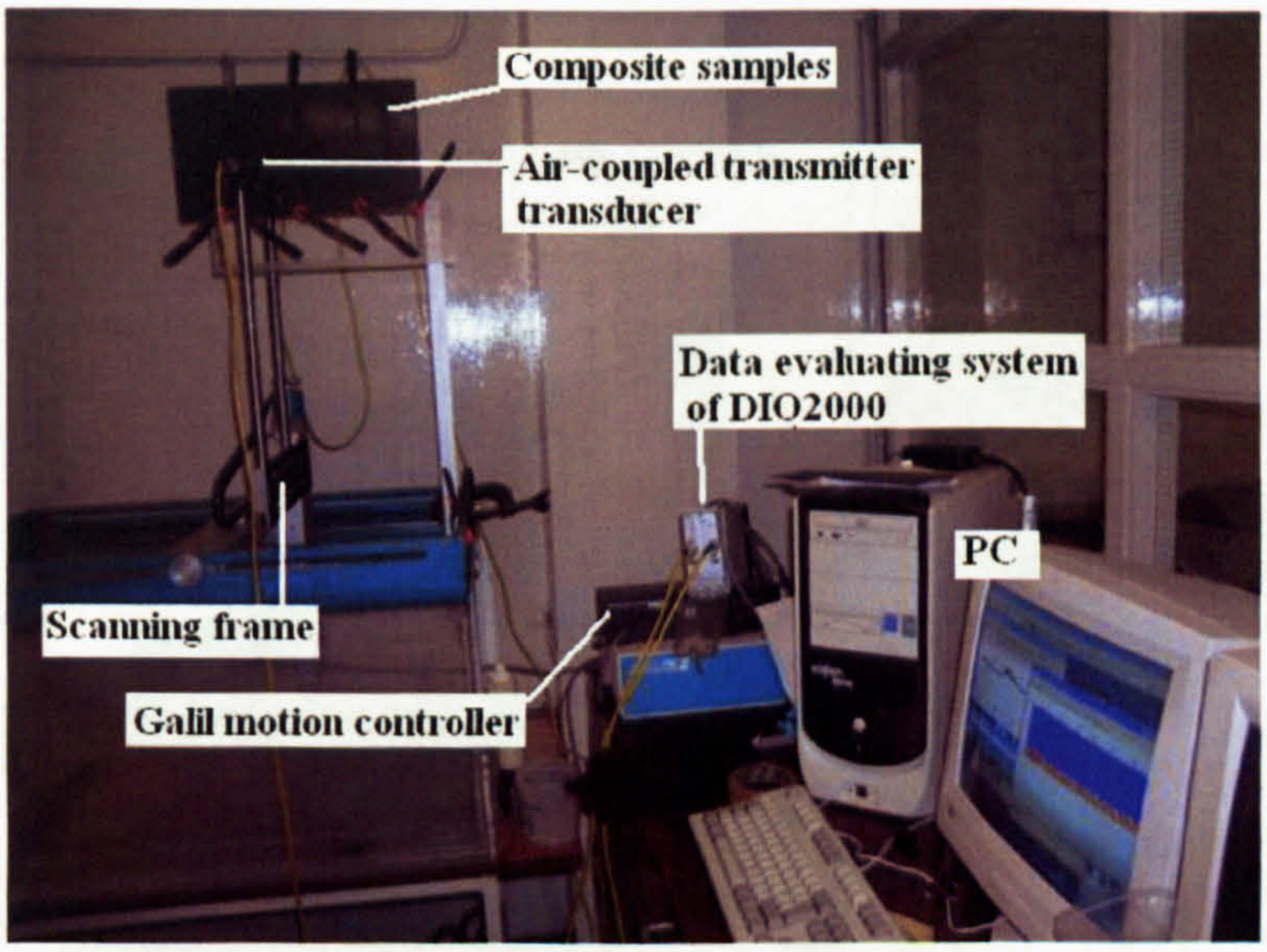

Figure 4.29: **Ultrasonic c-scan machine.** -

consists of a proprietary falling-weight drop tower produced by CEAST of Italy and the DAS 4000/Windows 95 data acquisition system as shown in figure 4.27 (a). The drop tower comprises of a falling carriage of mass which itself includes a striker head (Figure 4.27 (b)), two parallel guide rails, an electronic flag device, a pivoting target support structure and an environmental chamber.

The velocity of impact and the incident energy of the striker are simultaneously varied by adjusting the drop height. The maximum falling height of the machine is 2.4 m which yields a velocity of 6.86 m/s. The velocity immediately prior to impact is measured by the electronic flag device. In accordance with ISO / DISS 6603/1 the specimens were located onto a 40 mm diameter steel ring and were centrally impacted by a hardened hemispherical tip of 20 mm diameter as shown in figure 4.28. The selection of the sample size and impactor in this study were suggested by the supervisor of the author of this work. Because similar sample size and impactor have been used extensively in Queen Mary, University of London by former PhD students. The support assembly is located in an environmental chamber which may operate between $-70°$ C to $+100°$ C. DAS 4000 WIN used in conjunction with instrumented strikers acquires up to 4000 points during an impact event to produce force-time, energy-time, velocity-time, displacement-time curves. In this study, several falling heights and carriage masses were used for different purpose which will discussed in respective section.

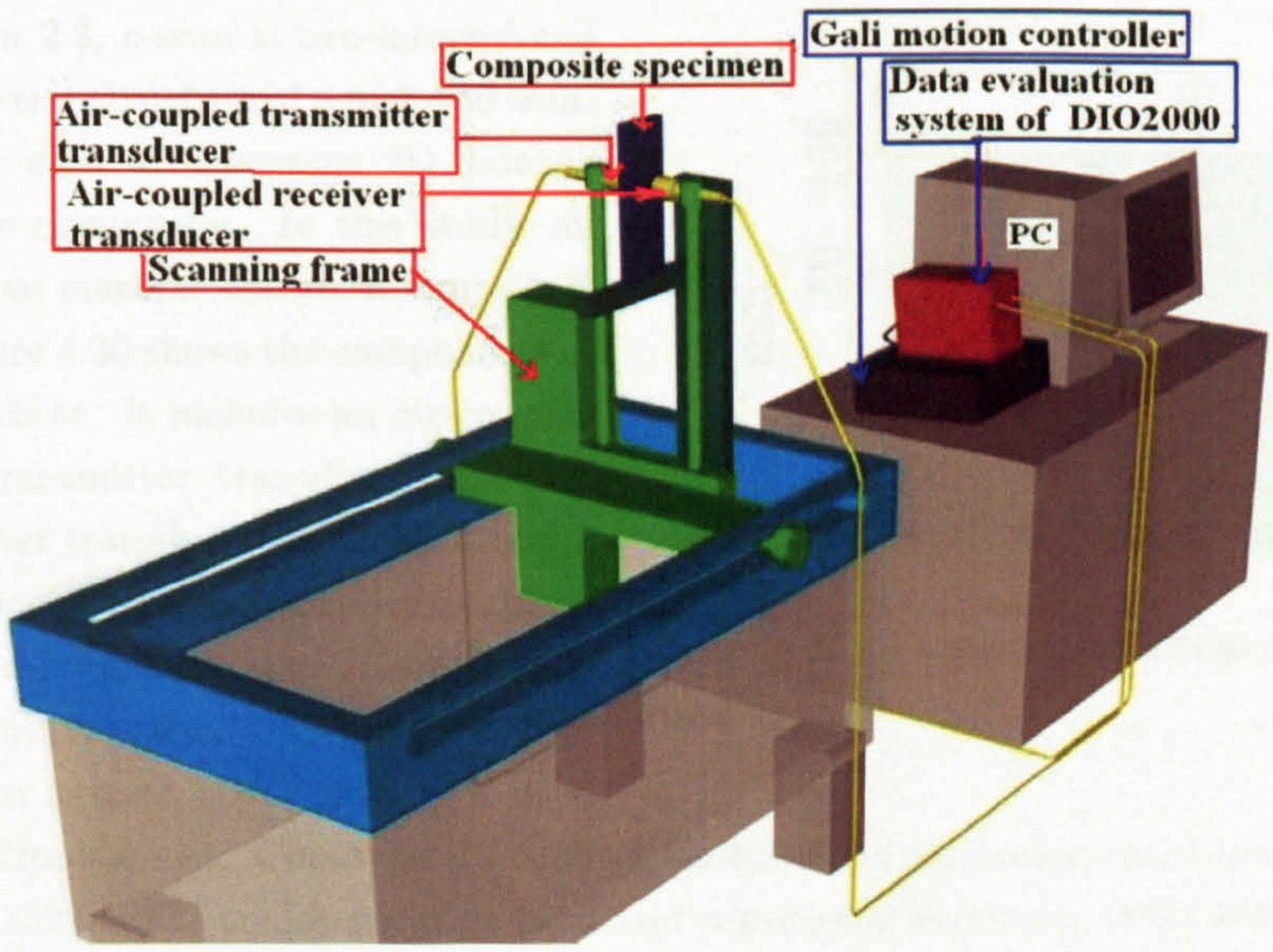

Figure 4.30: **Components of ultrasonic C-scan machine.**

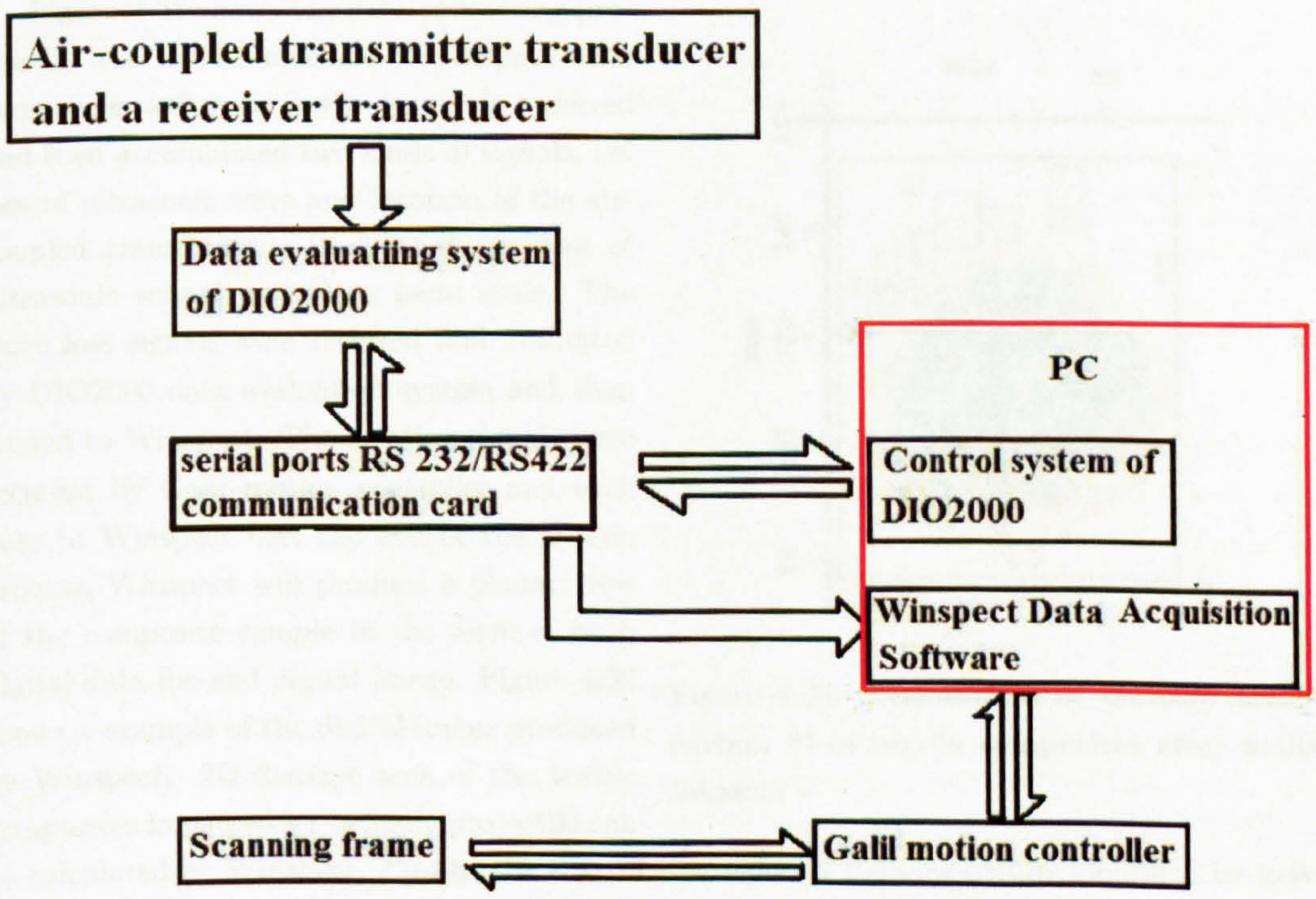

Figure 4.31: **Data flow chart during the ultrasonic C-scan test.**

4.3.3 Ultrasonic C-scan

As described in 2.3, c-scan is two-dimensional view of the interior structure of a material sample. It can be used to determine 2D damage areas of textile composites. In this study, an ultrasonic c-scan machine shown in figure 4.29 was used. Figure 4.30 shows the components of the c-scan machine. It includes an air-coupled 5 MHz flat transmitter transducer and a 5 MHz flat receiver transducer (AIRSTAR incl.), a scanning frame (Physical Acoustics Corporation), a Galil motion controller (Galil Motion Control, Mountain View, USA), a DIO2000 data evaluation system (DIO 2000 S T A R M A N S electronics, Ltd. Computer controlled multichannel electronic real time system), a serial ports RS 232/RS422 communication card and a personal computer (PC) with two software installed. The two software installed in the PC are control system of DIO2000 and Winspect data acquisition software (Winspect Data Acquisition Software, Utex Scientific software Instruments Inc., Mississauga, Canada). The choosing of air-coupled ultrasonics rather than water coupled ultrasonics was due to the lack of expertises of the later in Queen Mary, University of London during the course of this work.

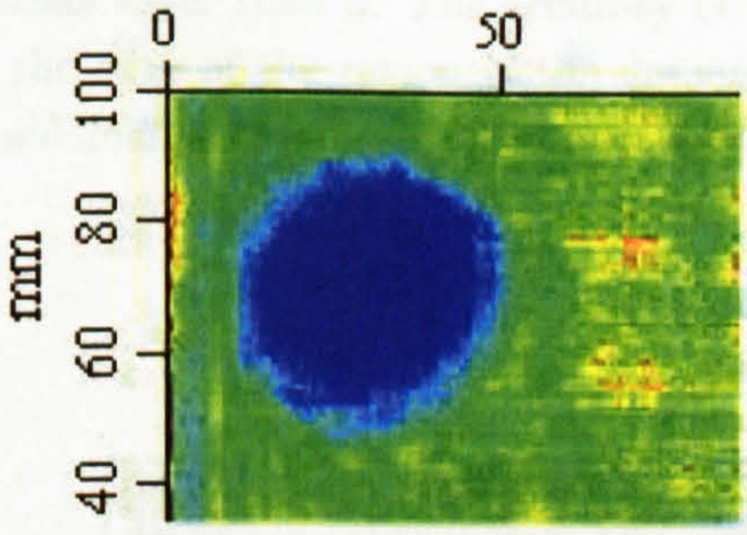

Figure 4.32: **A example of ultrasonic c-scan picture .**

Figure 4.31 shows the data processing process in the c-scan machine. Winspect data acquisition software is the core. It received and then accumulated two kinds of signals, i.e. loss of ultrasonic wave and location of the air-coupled transducers. It denoted any loss of ultrasonic wave by a colour band scale. The wave loss signals were received and evaluated by DIO2000 data evaluation system and then passed to Winspect. The location signals were received by Galil motion controller and then pass to Winspect. At the end of the C-scan process, Winspect will produce a planar view of the composite sample in the form of both digital data file and digital image. Figure 4.32 shows a example of the digital image produced by Winspect. 2D damage area of the textile composites impacted by ballistic projectile can be calculated by Winspect. Firstly, the edge of the region of damage will be identified by looking at the digital image produced by Winspect. Secondly, a colour band scale (p) will be determined. Colours with scales higher than this scale are only present outside the region of damage. Thirdly, the size of the damage area will be calculated based on this colour band scale by Winspect. As

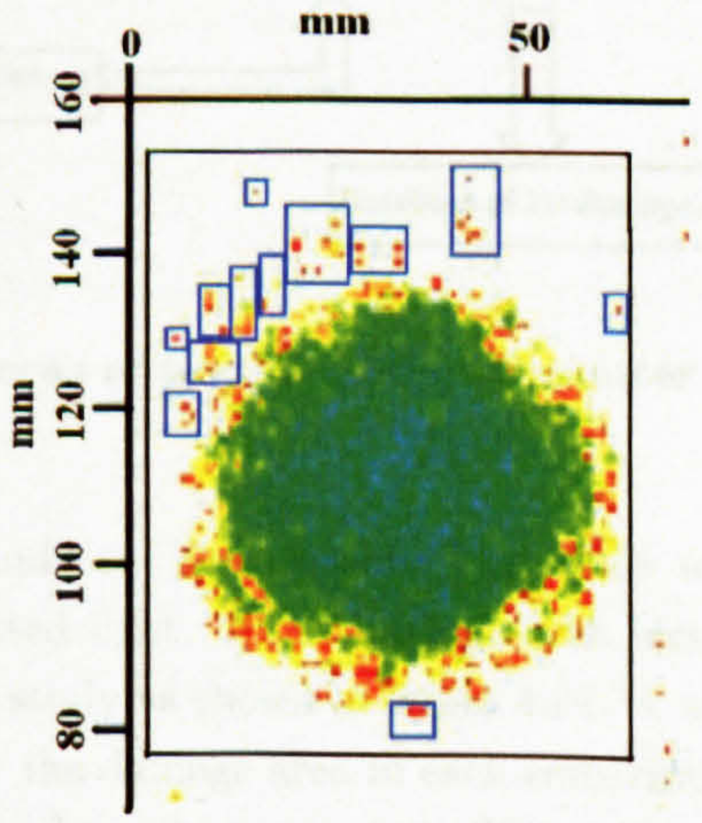

Figure 4.33: **Calculation of damage areas of carbon fibre textile composites after ballistic impacts .**

shown in figure 4.33, 2D damage area of the composite sample (S) can be calculated as the difference between the sum of positions inside the black square with colour scale lower than p and Sum of positions inside the blue squares with colour scale lower than p. The accuracy of the 2D damage area calculated can be judged by looking at the edge of the region of the damage area. The higher the contrast between damaged area and undamaged the higher the accuracy and the less blue squares are needed.

4.3.4 Visual examination

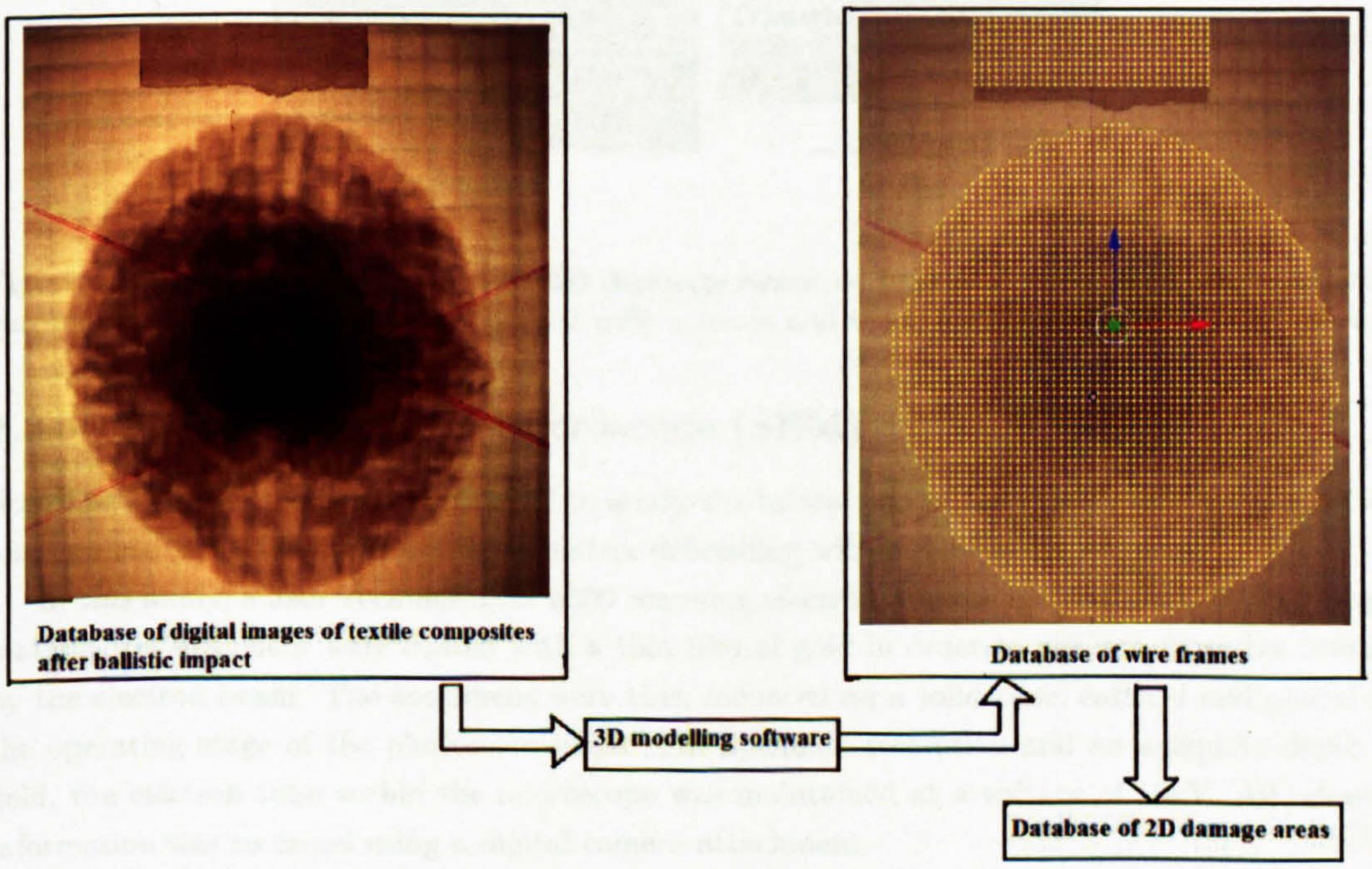

Figure 4.34: **Visual examination of 2D damage areas of textile composites after ballistic impacts .**

The glass fibre textile composites used in this study are translucent. The study of damage in these composites is relatively easy under transmitted light. A 2D damage area identification process based on visual examination was used in this study as shown in figure 4.34. A short strip of paper tape with a width of 25 mm was placed near the damage area in each composite sample. A digital camera was used to capture images of damaged textile composites. The captured images formed a database. Then 3D modelling software was used to draw a square to cover the paper tape. Thus the dimension of the square is $25mm \times 25mm$. This square was then subdivided several times. Finally the paper tape was covered by squares with dimension of $25/32mm \times 25/32mm$, i.e. $\approx 0.61mm^2$. Squares with this dimension were then used to cover the region of damage area. As shown in figure 4.35, half of some squares were cut off in order to improve the accuracy of this measurement. At last, numbers of squares and triangles were counted and the damage area was calculated as the sum of the areas of the squares and the triangles.

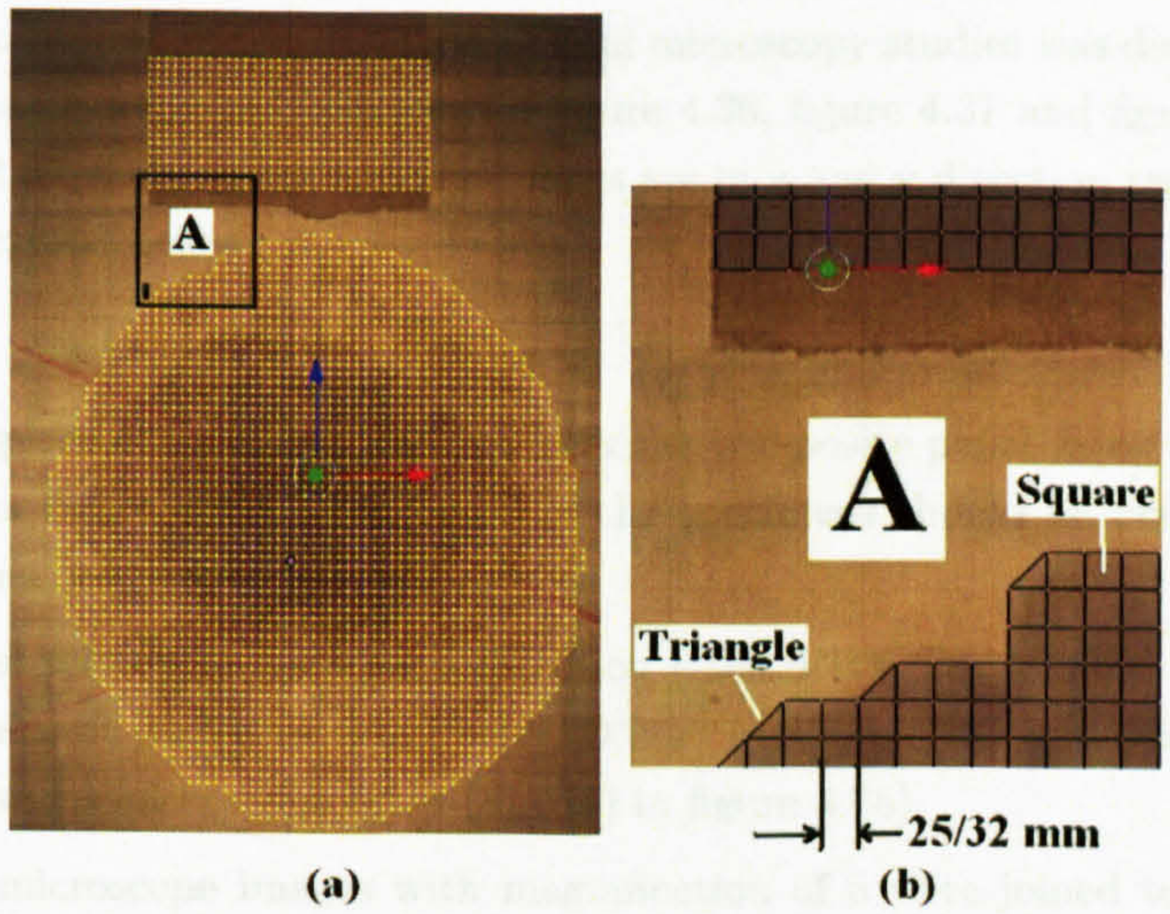

Figure 4.35: **Visual examination of 2D damage areas of textile composites after ballistic impacts** - (a) Region of damage covered with squares and triangles; (b) zoom in of position A.

4.3.5 Scanning Electron Microscope (SEM)

Scanning electron microscope was used to study the interaction of the cracks, wetting properties, and especially fibre pull-out and fibre-matrix debonding within damaged specimens.

In this study, a Jeol Technics JSM 6300 scanning electron microscope was used. Before examination, the specimens were coated with a thin film of gold in order to prevent excessive heating by the electron beam. The specimens were then mounted on a solid base, earthed and placed on the operating stage of the photomicroscope. For optimum resolution and an adequate depth of field, the electron tube within the microscope was maintained at a voltage of 10kV. All relevant information was recorded using a digital camera attachment.

Although not used extensively in this study, the SEM is particularly useful for observing fibre pull-out and fibre matrix debonding, damage mechanisms not readily detected by other techniques.

4.3.6 Optical Microscopy

Optical Microscope was used to give information on, and distinguish between many forms of the damage generated during impact, i.e. matrix cracking, fibre fracture and delamination. It was also used to investigate manufacturability.

In order to examine the specimens under the microscope, the damaged specimens were cut in half and carefully polished with diamond abrasive. The cracking within the composite was subsequently examined by Olympus BX60 optical microscope.

4.3.7 Visualisation of yarn architecture in 3D textile composite

As reviewed in 2.13.2, caution must be taken when discussing the effect of architecture on properties of 3D textile composites. Sometimes the structure of the preform in the composite panel is very different from its ideal structure. Microscope studies can be used to determine the real structure of preforms as mentioned in 2.13.2.

A computer simulation process based on optical microscopy studies was developed in this work. It includes three major steps as illustrated in figure 4.36, figure 4.37 and figure 4.38 respectively. In figure 4.36 and 4.37, warp yarns and weft yarns are in x and y direction respectively. Details of these steps are described below:

1. Identification of repeat unit
   - A small piece of specimen was cut from the composite panel using a diamond saw (step (a) (b) in figure 4.36). The edges of the specimens should be perpendicular to either weft yarns or straight warp yarns.
   - One cross-section in warp yarn direction (face A'B'C'D' in figure 4.36) and one cross-section in weft yarn direction (face C'D'E'F' in figure 4.36) were polished and examined under optical microscope (step (c) - (f) in figure 4.36).
   - Optical microscope images with magnification of 5 were joined together using digital imaging software to form images of face ABCD and CDEF (step (c) - (f) in figure 4.36).
   - Repeat units in both weft and warp yarn direction were identified.
   - From the corner where two cross-sections meet the lengths of repeat units in both weft yarn direction and weft yarn direction were identified and marked. Parts of specimens outside the marks in both weft and warp yarn directions were cut away.
2. Creation of database of cross-section images
   - All warp yarns in one repeat unit in the image of face A'B'C'D' were identified. A number of positions of cross-sections in weft yarn direction were marked. The selection of these cross-sections is based on the position and the shape of warp yarns. Any warp yarn should be in contact with at least one of these cross-sections. The positions of the cross-sections were normally put to where warp yarns change shapes, vanish or start to appear. Because large amounts of images are needed to be taken for each cross-section, the number of cross-section should be kept as small as possible.
   - The marked composite samples were polished to the first position. Cross-section MNKL are now ready to be viewed (step (a) - (b) in figure 4.37).
   - Optical microscope images of cross-section MNKL with magnification of 5 were taken and stored in the database of cross-section images (step (c) - (f) in figure 4.37).
   - Repeating step (a) - (f) in figure 4.37 for each marked position.
3. Creation of computer model of 3D woven preform
   - Images of cross-sections in weft and warp yarns directions were taken out of the database of cross-section images and imported into 3D modelling software *Blender*© used as background images. Outlines of yarns were identified using points and lines. The final result is a wire frame. The wire frame was stored in the database of frames of cross-sections (step (a) - (c) in figure 4.38).
   - All wire frames of one textile composite were taken out of the database of frames of cross-sections and put together in *Blender*©. They were connected to each other to form a computer model of 3D fabric preform (step (d) - (f) in figure 4.38).
   - Finally surfaces and colours were applied (step (g) in figure 4.38)

- Repeating step (a) - (g) in figure 4.38 for each textile composite.

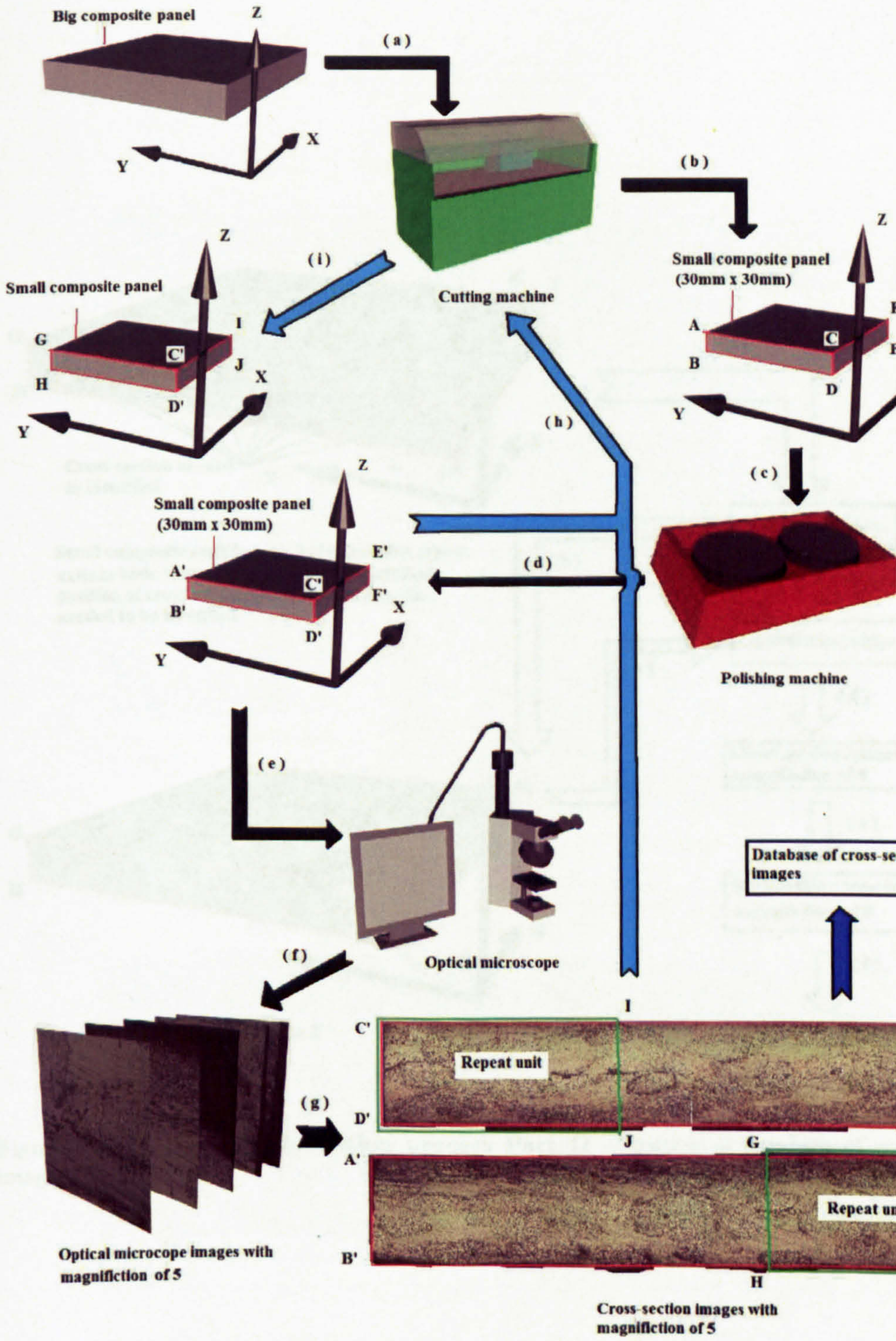

Figure 4.36: **Computer simulation process Part I** - identification of repeat unit .

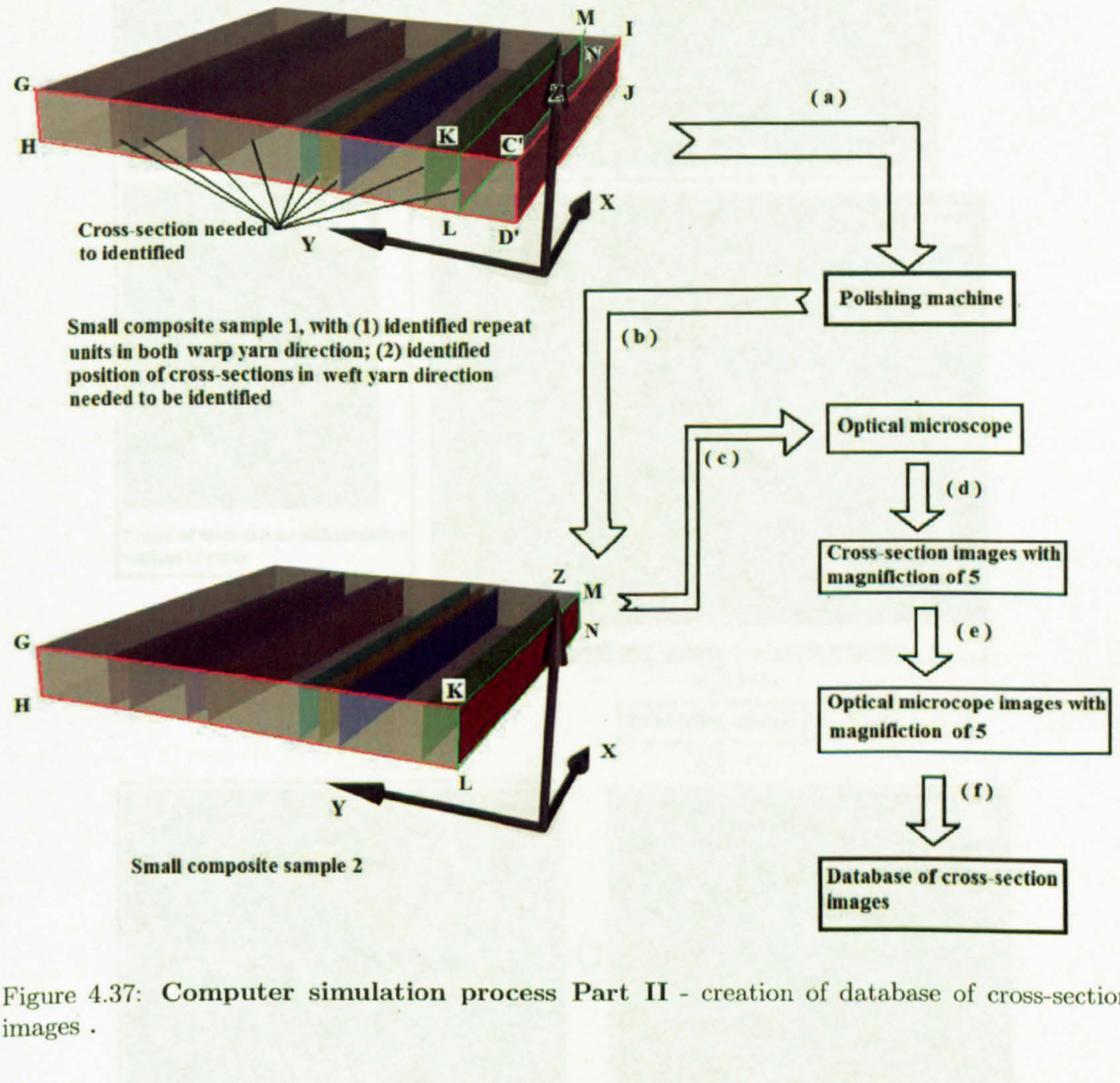

Figure 4.37: **Computer simulation process Part II** - creation of database of cross-section images .

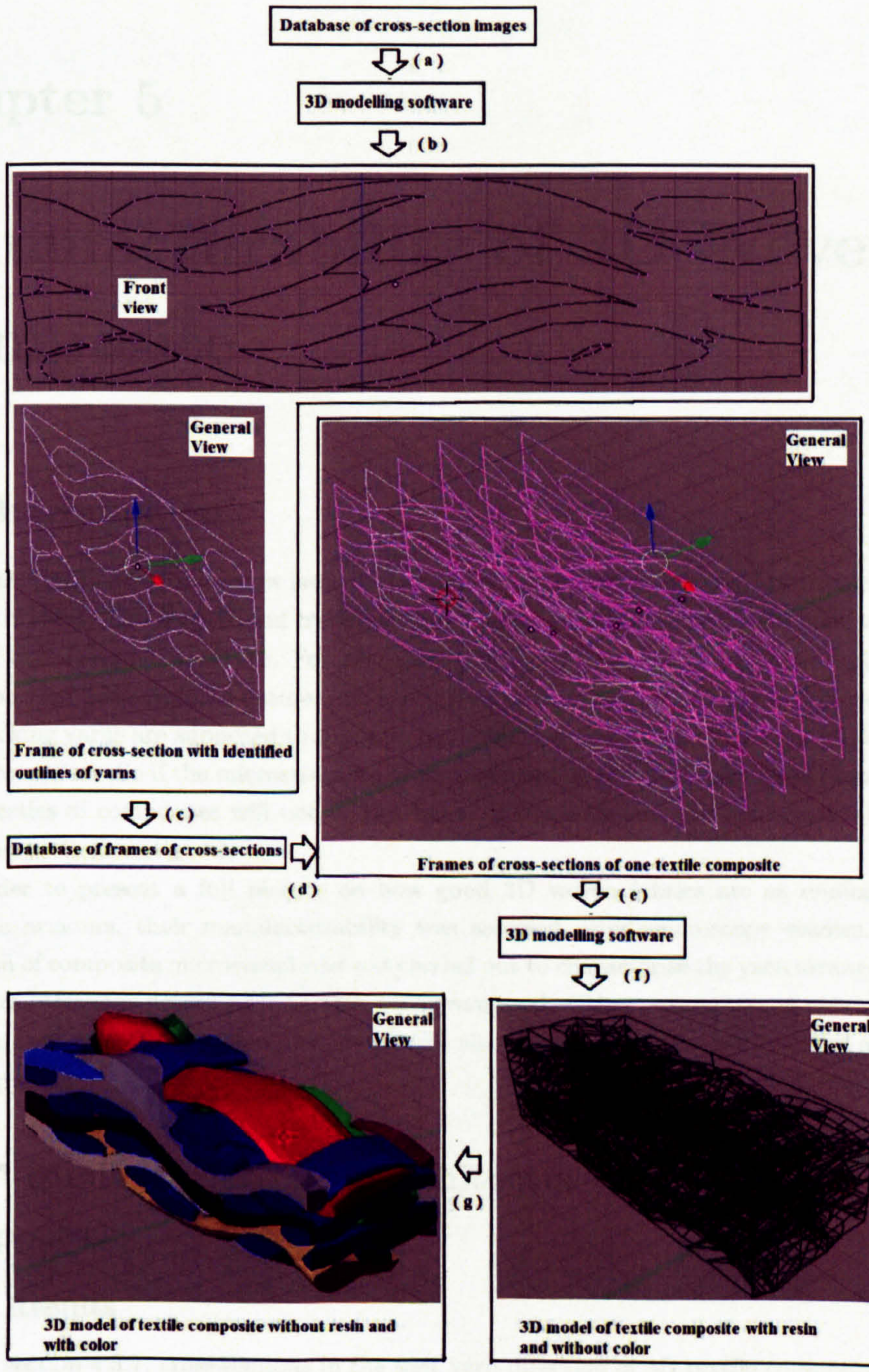

Figure 4.38: **Computer simulation process Part III** - creation of computer model of 3D woven preform .

Chapter 5

Manufacturability of 3D Woven Composite

5.1 Introduction

Manufacturability is an important issue in the application of any materials. For textile composites, manufacturability can be accessed by several parameters, such as wet-out of fibres, void content, degree of distortion of yarns, etc. For 3D fabric reinforced composites, manufacturability is even more important because of its nature, i.e., specific yarns have specific functions. For example, multilayer locking yarns are supposed to suppress delamination and getting more materials involved in energy absorption. So if the microstructure of arrangement of yarns changes during manufacturing, the properties of composites will not be the same. If this happens, the manufacturability of this textile composite is not good.

In order to present a full picture on how good 3D woven fabrics are as reinforcements for composite armours, their manufacturability was assessed using microscopy studies. Computer simulation of composite microstructures was carried out to characterise the yarn arrangement in the composites. Methods described in section 4.3.7 were used. Other parameters of manufacturability such as wet-out properties and void content were also accessed by using both optical and scanning microscopy.

5.2 Visualisation of yarn architectures of 3D fabrics in composites

5.2.1 Results

Recall in section 4.3.7, cross-sections in the weft yarn direction of 3D textile composites were used to form 3D models of the real yarn arrangements of 3D textile composites. The positions of these cross-sections in each 3D textile composites are shown in figure 5.1. The results of 3D simulation of the real yarn arrangements of the eight 3D woven textile composites are shown, and analyzed from figure 5.2 to figure 5.9.

Figure 5.1: **Positions of the cross-sections in weft yarn direction used for 3D simulation of** - (a) G1-1-VE; (b) G2-1-VE, (c) G3-1-VE; (d) G4-1-VE; (e) G5-1-VE; (f) G6-1-VE; (g) G7-1-VE; (h) C-1-VE.

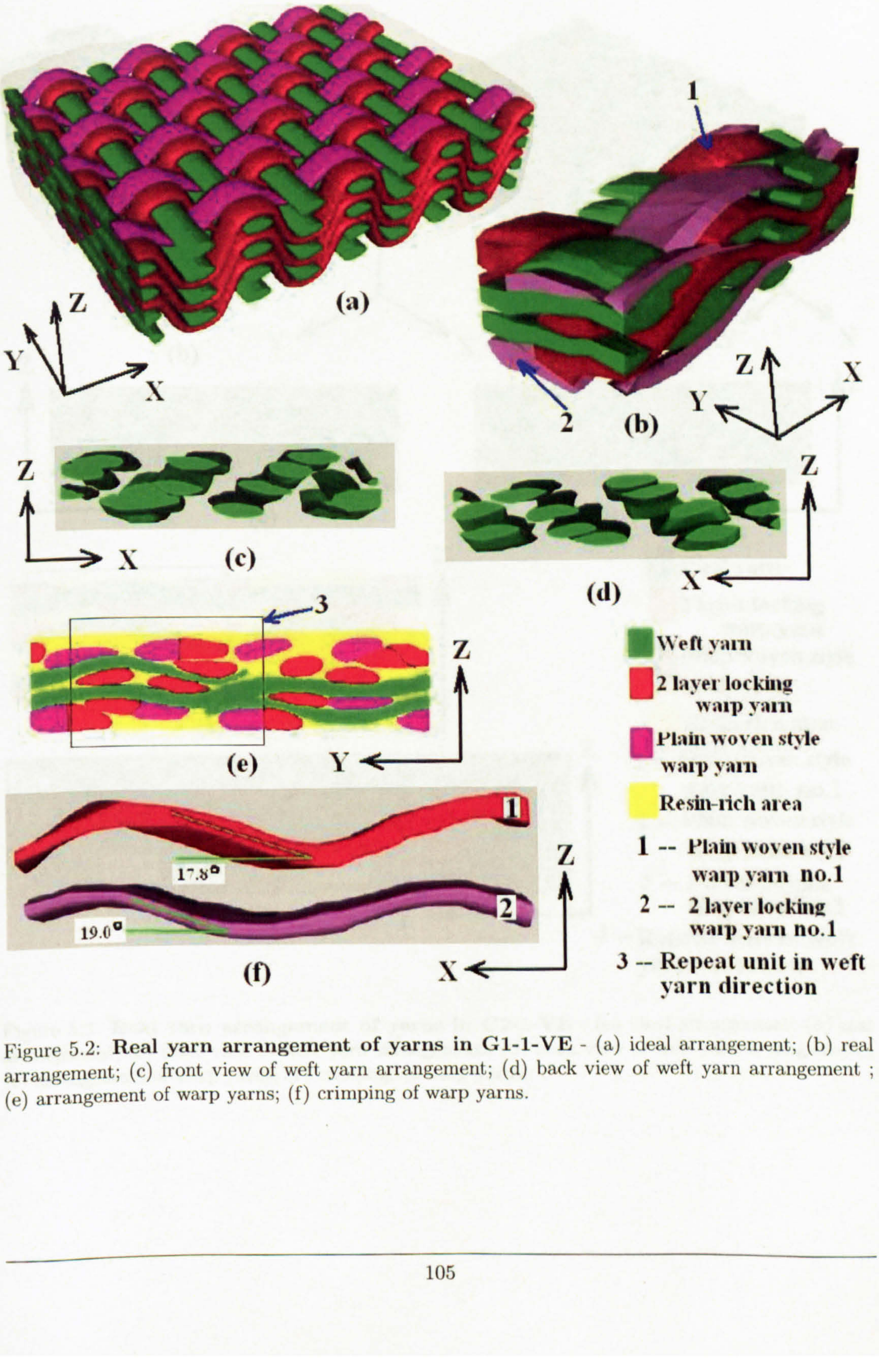

Figure 5.2: **Real yarn arrangement of yarns in G1-1-VE** - (a) ideal arrangement; (b) real arrangement; (c) front view of weft yarn arrangement; (d) back view of weft yarn arrangement ; (e) arrangement of warp yarns; (f) crimping of warp yarns.

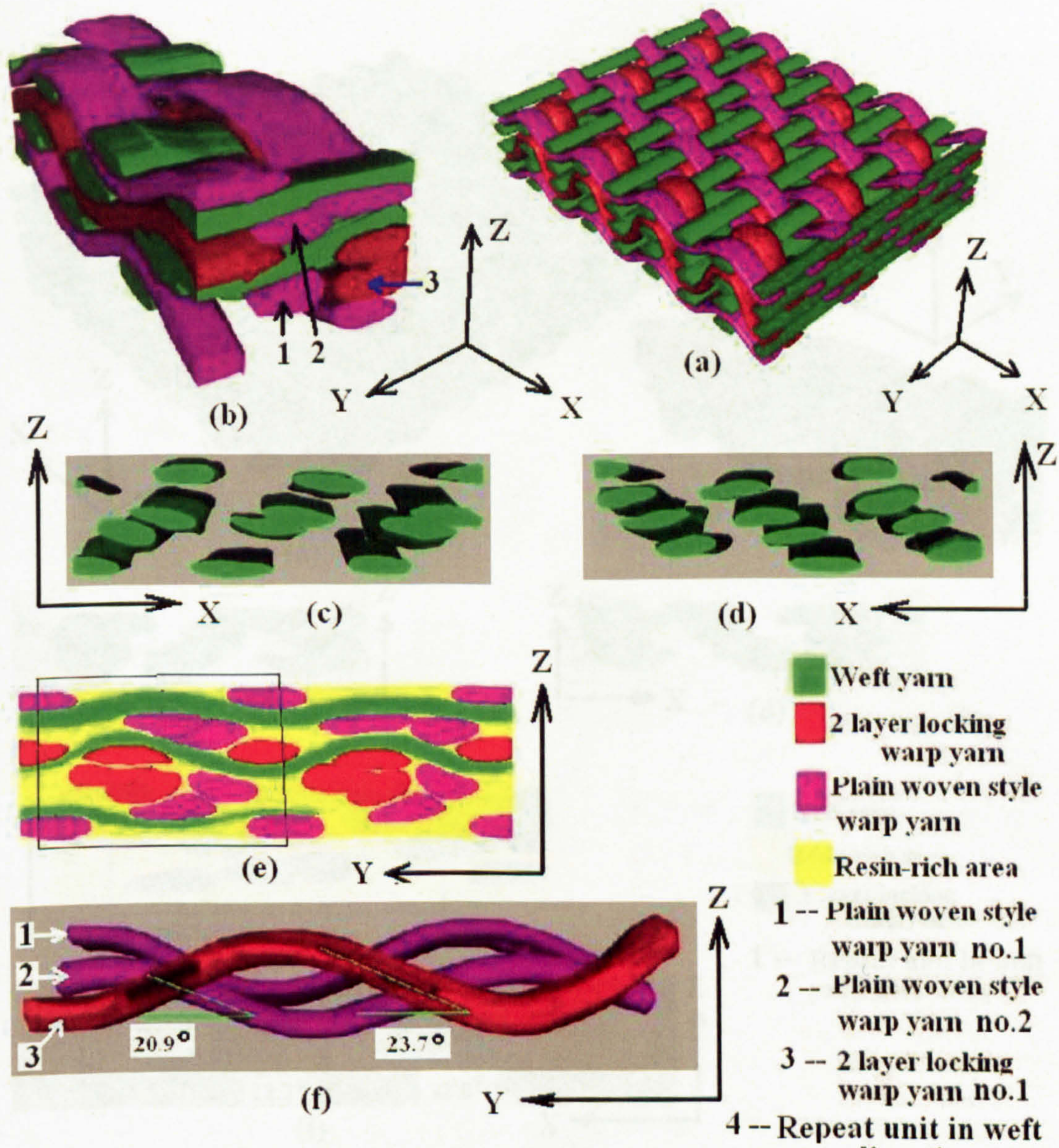

Figure 5.3: **Real yarn arrangement of yarns in G2-1-VE** - (a) ideal arrangement; (b) real arrangement; (c) front view of weft yarn arrangement; (d) back view of weft yarn arrangement ; (e) arrangement of warp yarns; (f) crimping of warp yarns.

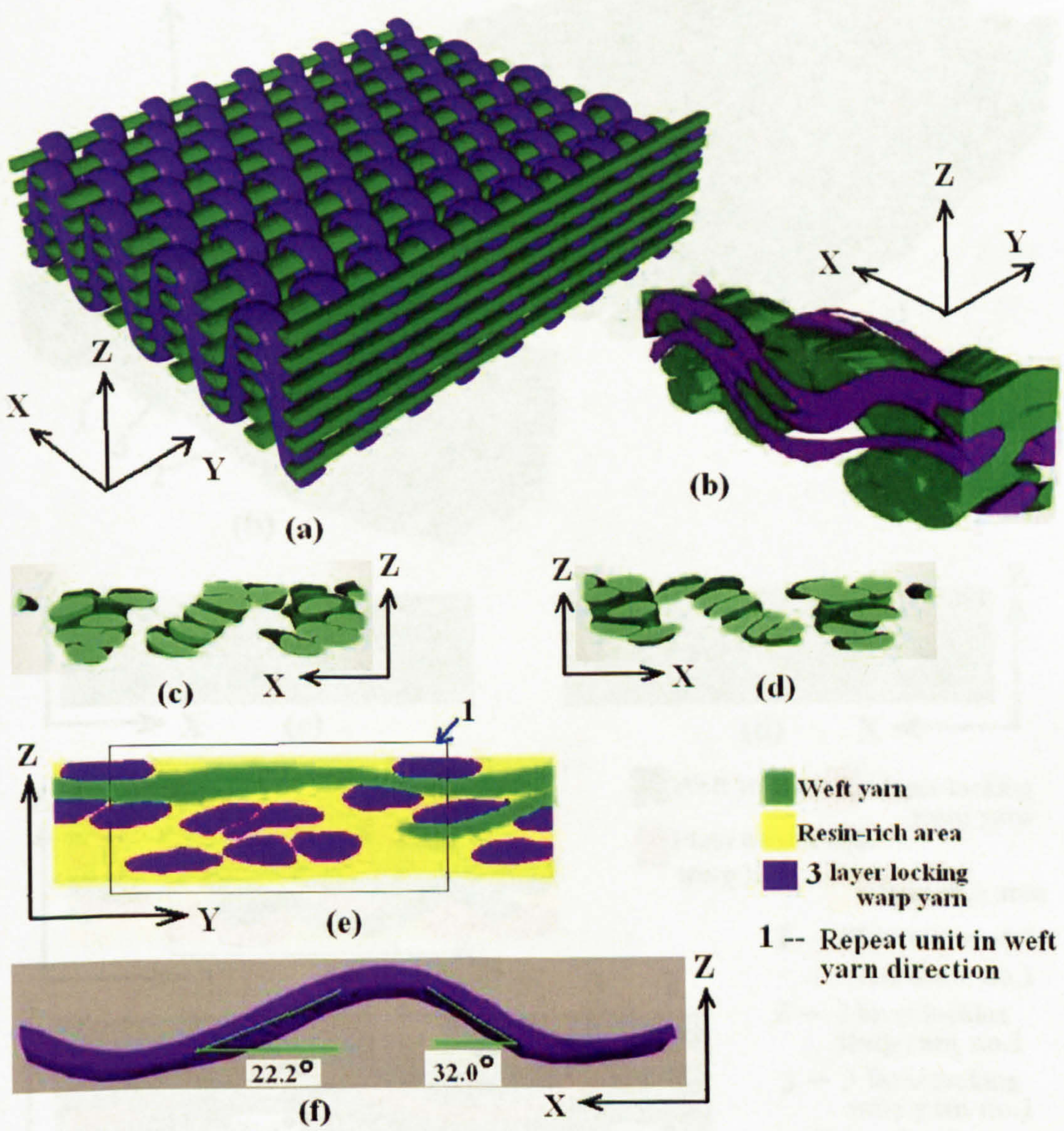

Figure 5.4: **Real yarn arrangement of yarns in G3-1-VE** - (a) ideal arrangement; (b) real arrangement; (c) front view of weft yarn arrangement; (d) back view of weft yarn arrangement ; (e) arrangement of warp yarns; (f) crimping of warp yarns.

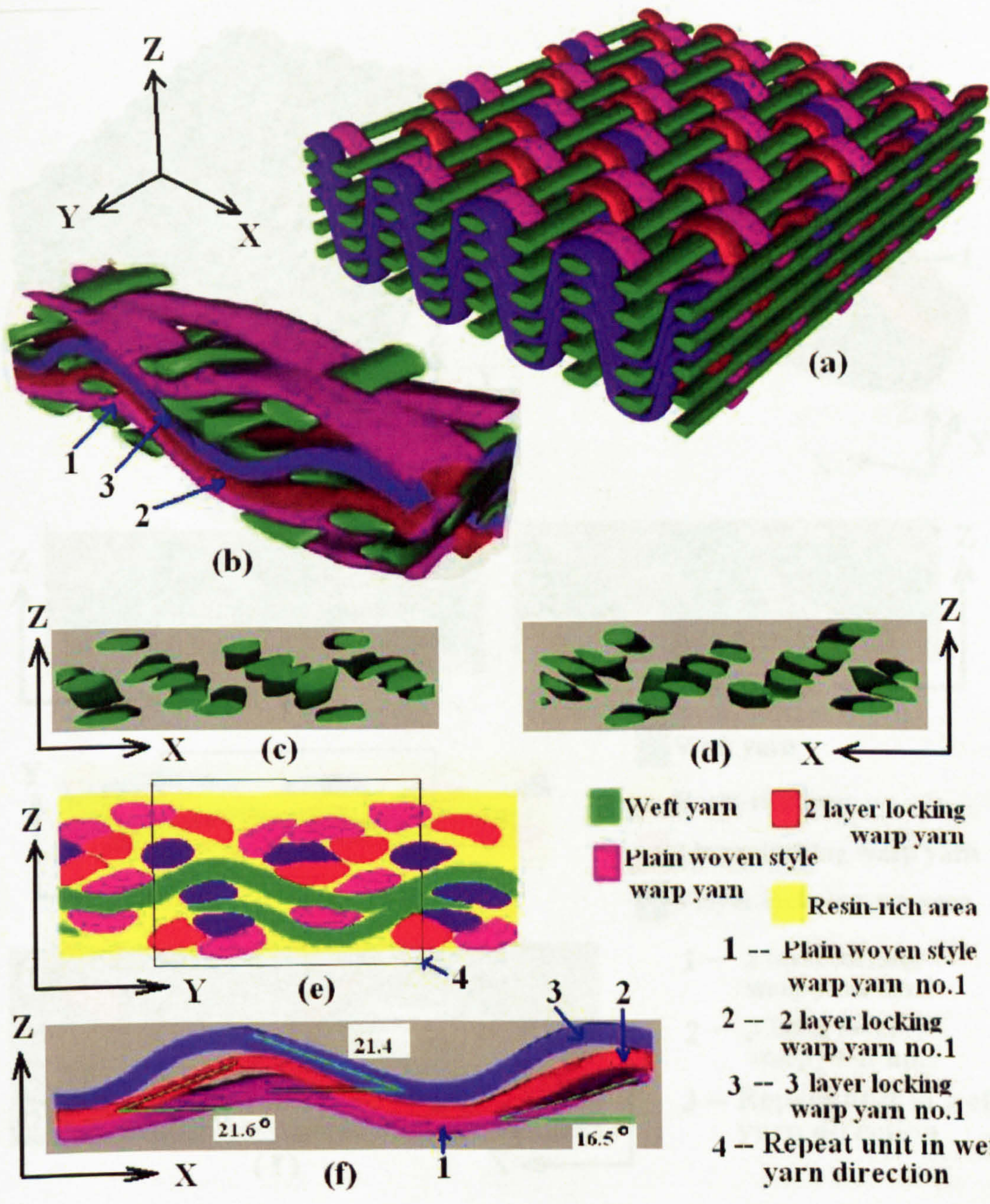

Figure 5.5: **Real yarn arrangement of yarns in G4-1-VE** - (a) ideal arrangement; (b) real arrangement; (c) front view of weft yarn arrangement; (d) back view of weft yarn arrangement ; (e) arrangement of warp yarns; (f) crimping of warp yarns.

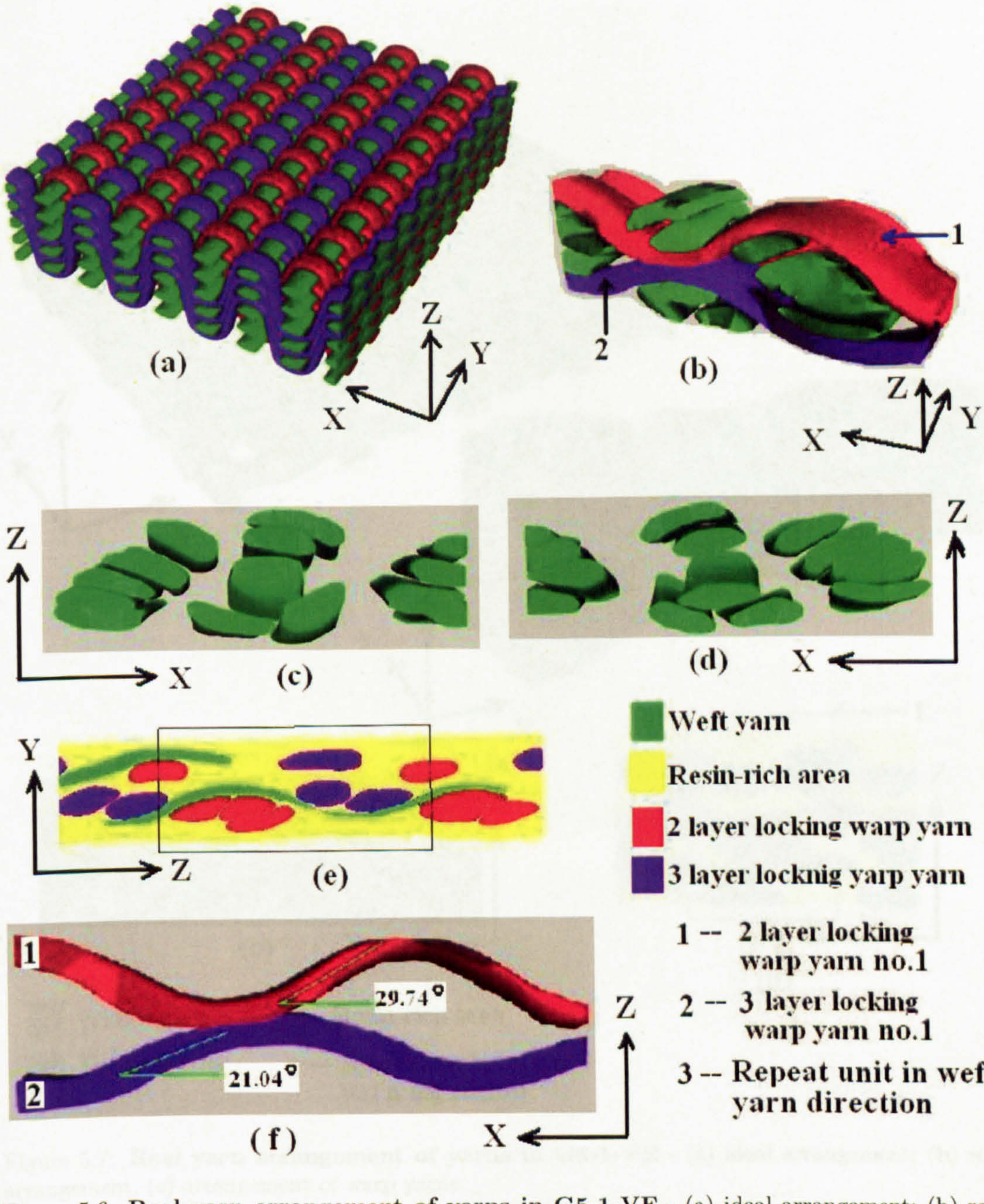

Figure 5.6: **Real yarn arrangement of yarns in G5-1-VE** - (a) ideal arrangement; (b) real arrangement; (c) front view of weft yarn arrangement; (d) back view of weft yarn arrangement ; (e) arrangement of warp yarns; (f) crimping of warp yarns.

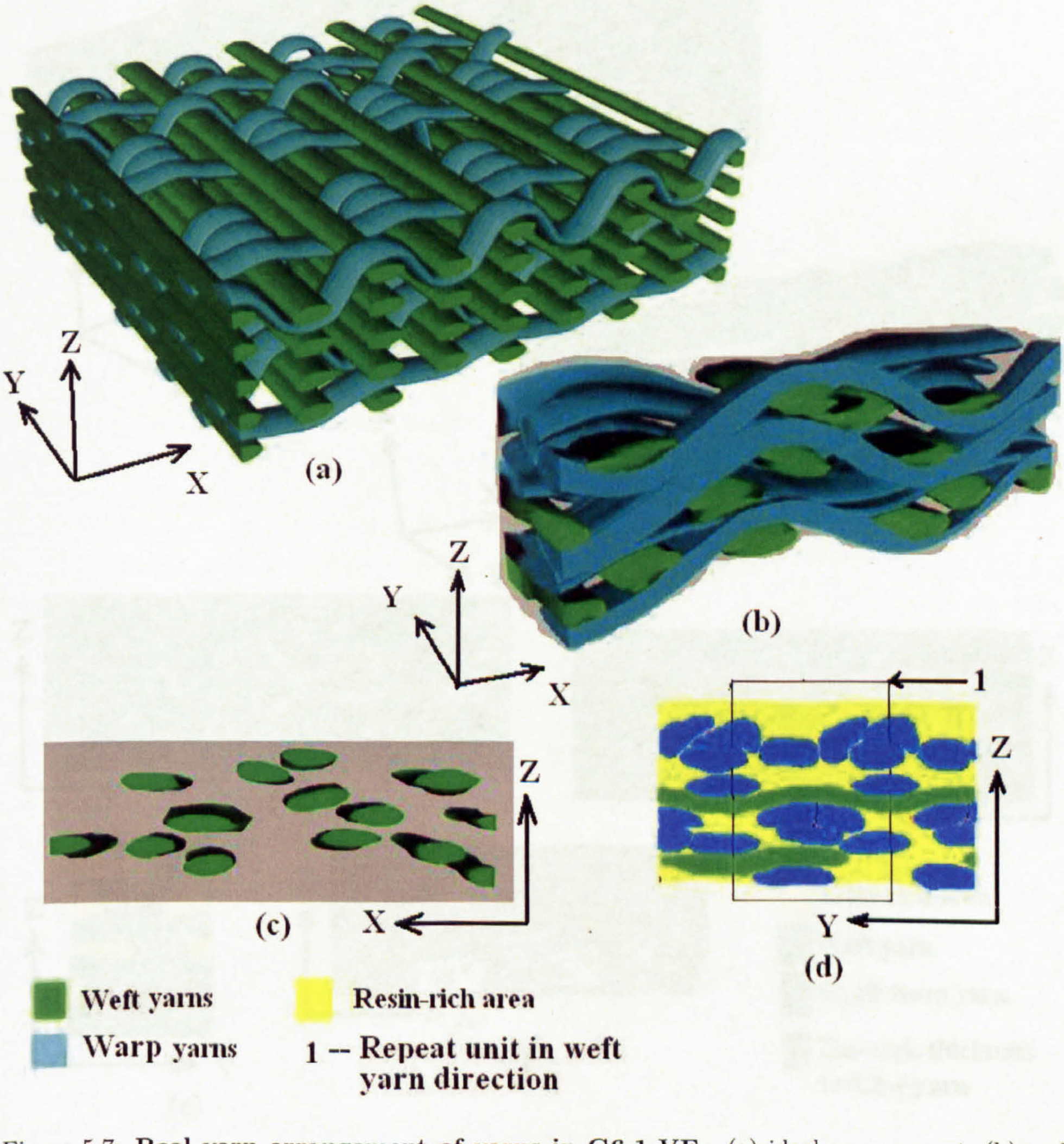

Figure 5.7: **Real yarn arrangement of yarns in G6-1-VE** - (a) ideal arrangement; (b) real arrangement; (c) arrangement of warp yarns.

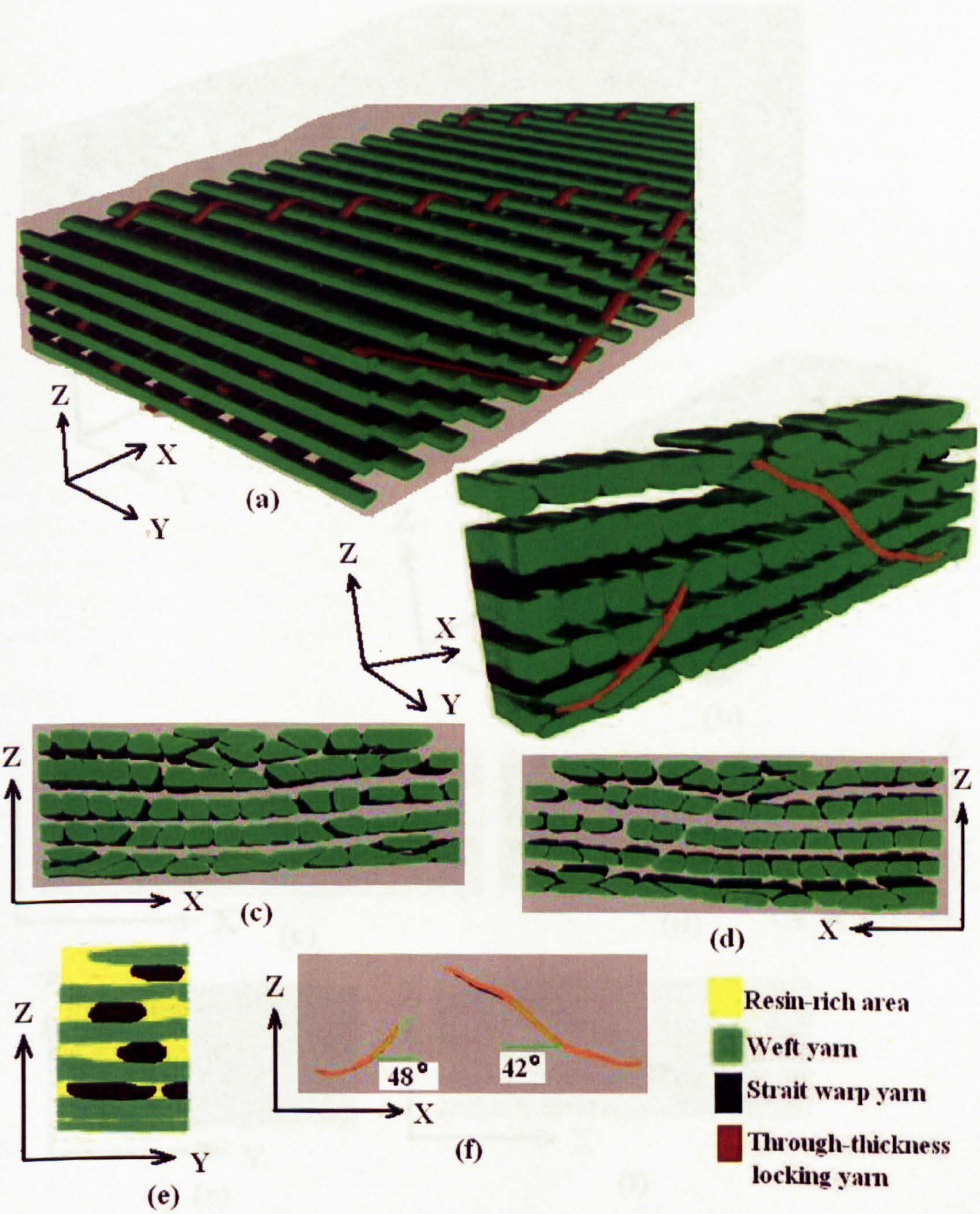

Figure 5.8: **Real yarn arrangement of yarns in G7-1-VE** - (a) ideal arrangement; (b) real arrangement; (c) front view of weft yarn arrangement; (d) back view of weft yarn arrangement ; (e) arrangement of warp yarns; (f) crimping of warp yarns.

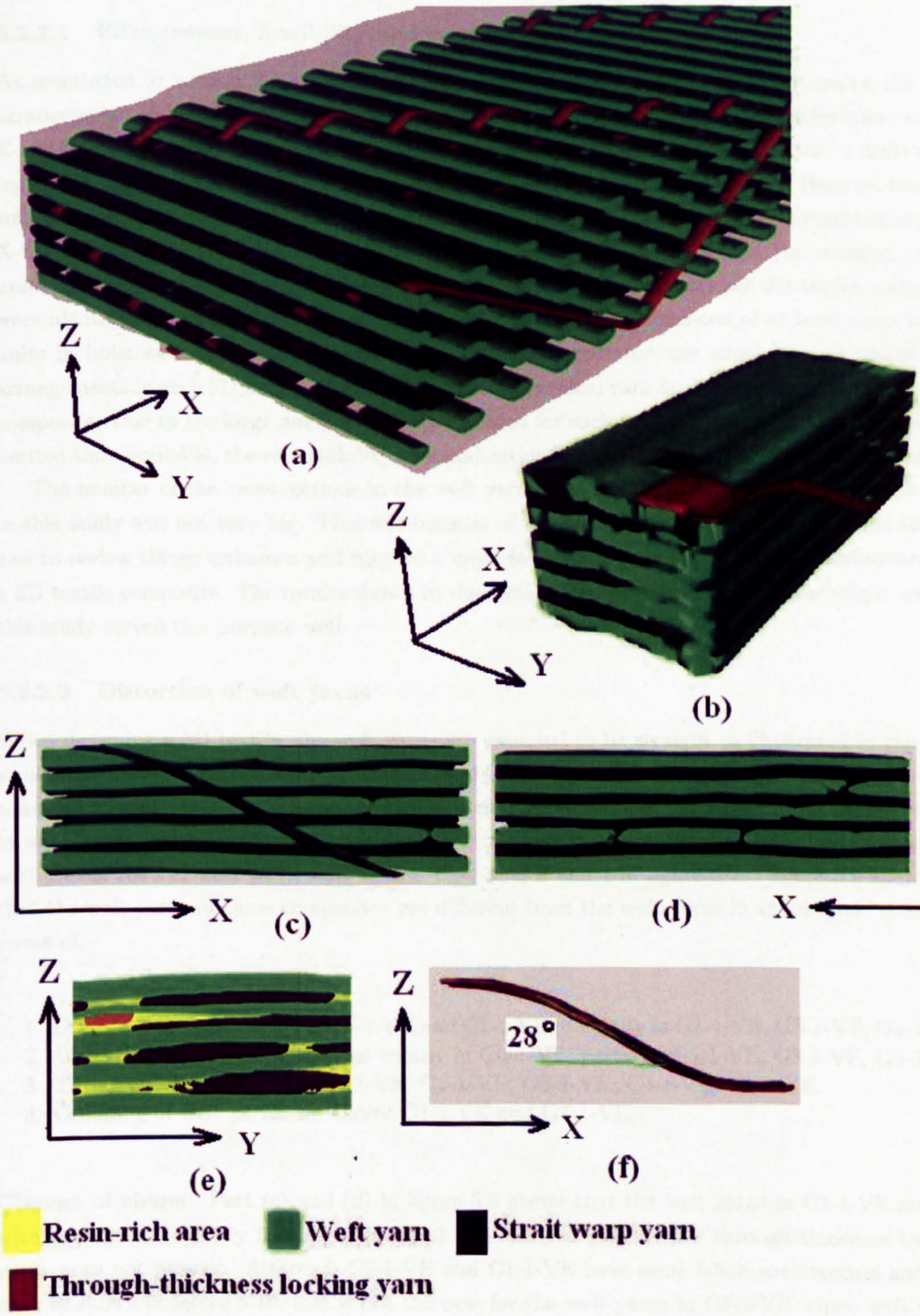

Figure 5.9: **Real yarn arrangement of yarns in C1-1-VE** - (a) ideal arrangement; (b) real arrangement; (c) front view of weft yarn arrangement; (d) back view of weft yarn arrangement ; (e) arrangement of warp yarns; (f) crimping of warp yarns.

5.2.2 Discussion

5.2.2.1 Effectiveness, feasibility and weakness of visualization study

As mentioned in section 2.13.2, various imaging techniques can be used to determine the yarn arrangements of 3D textile composites experimentally. Compared with other techniques such as X-ray CT, the method used in this study was much more time-consuming. It was a destructive technique. Its results were less accurate than the results of X-ray CT study. Because less and smaller specimens were studied in the method used in this study than in other techniques such as X-ray CT. But efforts have been made in this study to increase its accuracy. For example, repeat units of the yarn arrangement in both warp and weft yarn directions of each 3D textile composite were identified carefully. Specimen of each 3D textile composite consisted of at least three repeat units in both weft and weft yarn directions. This ensured that the simulated models of yarn arrangements in each 3D textile composite represented typical yarn arrangements in each 3D textile composite. Due to the large amount of images needed for each model of yarn arrangement and the limited time available, the repeatability of visualization results were not checked experimentally.

The number of the cross-sections in the weft yarn direction of each 3D textile composite used in this study was not very big. This was because of the fact that the main focus of these studies was to review things unknown and may be a must for the analysis of the ballistic performance of a 3D textile composite. The results shown in the sections below proved that the technique used in this study served this purpose well.

5.2.2.2 Distortion of weft yarns

When designing a 3D textile, the weft yarns are assumed to be straight as illustrated in the ideal structures of the 3D textile composites from figure 5.2to figure 5.9. In ideal structures of 3D textile composites, weft yarns are assumed to be (1) oval in cross-section; (2) straight; (3) perpendicular to warp yarns; (4) aligned in a line in through-thickness direction (in the warp yarn direction as well if even rows of weft yarns were used). Part *b*, *c*, *d* and *e* of figure 5.2to figure 5.9 show that that the weft yarns in these composites are different from the weft yarns in the original design in terms of:

1. Change of Shape: totally in G7-1-VE and C1-1-VE; partially in G1-1-VE, G3-1-VE, G5-1-VE.
2. Distortion of rows of weft yarns: totally in G6-1-VE; partially G1-1-VE, G3-1-VE, G5-1-VE.
3. Tilting of weft yarn rows: G1-1-VE, G2-1-VE, G3-1-VE, G4-1-VE, G5-1-VE.
4. Crimping of weft yarns: all except C1-1-VE and G7-1-VE.

Change of shape Part (*c*) and (*d*) in figure 5.9 shows that the weft yarns in C1-1-VE merged with each other laterally forming a block of non-crimped yarns when through-thickness locking yarns were not present. Although C7-1-VE and C1-1-VE have same fabric architecture and tow sizes as shown in figure 5.10, this is not the case for the weft yarns in G7-1-VE where weft yarns were wrapped using nylon fibres as illustrated in figure 4.1. Part *c* and *d* in figure 5.8 shows that although collision of weft yarns took place merging of weft yarns didn't occur which resulting more than twice bigger thickness of G7-1-VE than C1-1-VE. Lateral collision of weft yarns were not observed in other 3D woven textile composites. This is due to the fact that more multi-layer locking

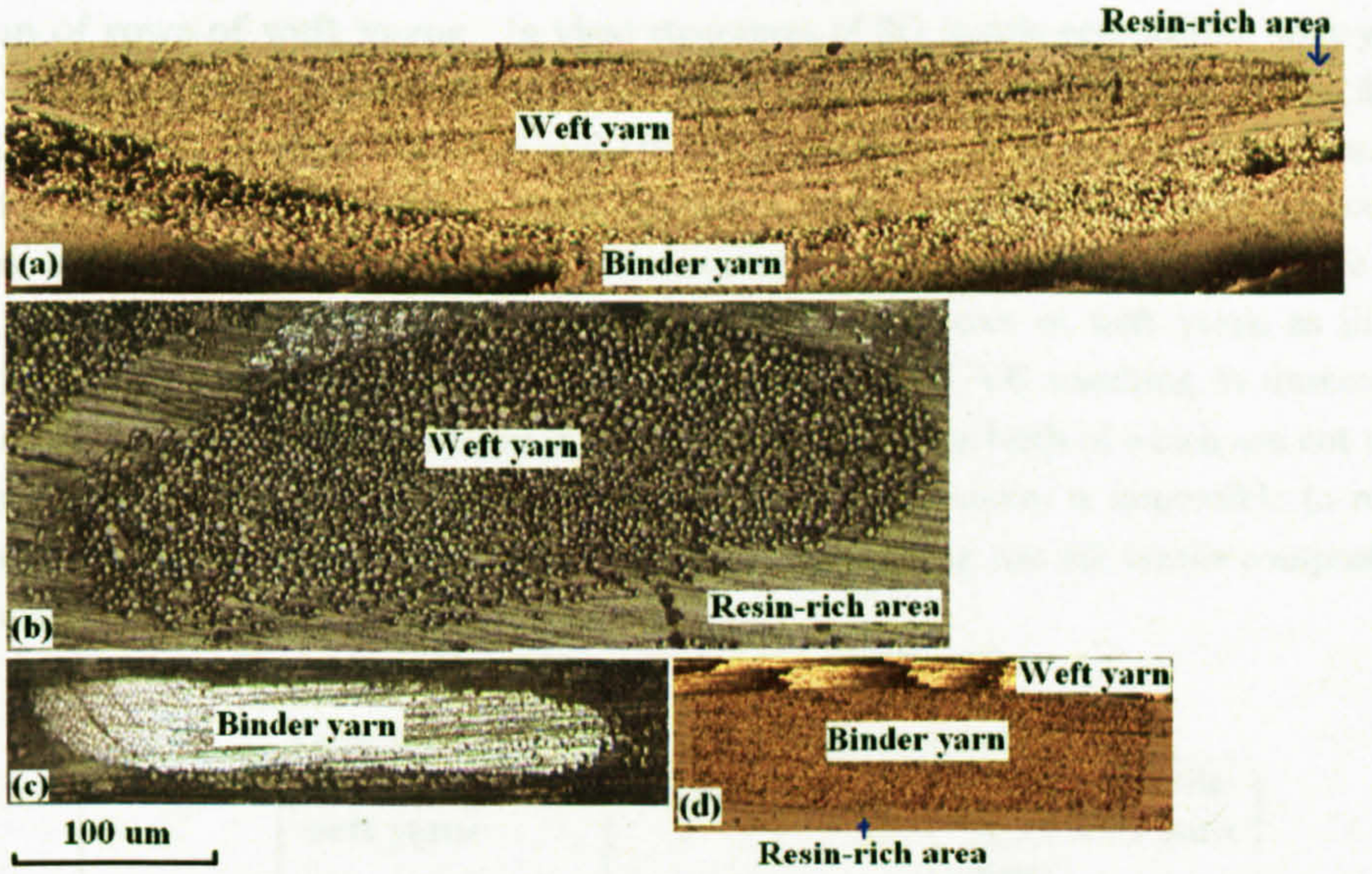

Figure 5.10: **Yarns in C1-1-VE and G7-1-VE** - (a) weft yarn in C1-1-VE; (b) weft yarn in G7-1-VE; (c) binder yarn in G7-1-VE; (d) binder yarn in C1-1-VE.

yarns are used in G1-1-VE et than in G7-1-VE. Vertical collision of weft yarns were observed in G1-1-VE etc except C1-1-VE and G7-1-VE. Because there are large amount of non-crimp warp yarns in C1-1-VE and G7-1-VE between every two layers of weft yarns. It can be seen in part *c* and *d* in figure 5.2 to figure 5.7 that vertical collisions of weft yarns observed in G3-1-VE and G5-1-VE where there are 3 layer locking yarns were more serious than that observed in G1-1-VE, G2-1-VE and G3-1-VE. It was observed that the use of plain woven style warp yarns in G1-1-VE, G2-1-VE and G4-1-VE reduce or prevent the vertical collisions of weft yarns, especially. in G2-1-VE and G4-1-VE where plain woven style yarns were present in locations through-thickness. So far it can be concluded that changes in shape of the weft yarns in 3D woven textile composites is dependent on the confining of individual weft yarn and the collisions of weft yarns. Good confining of fibre in weft yarn can be achieved using yarn coating method as illustrated in figure 4.1. Collisions of weft yarns can be reduced by using non-crimp warp yarns or plain woven style warp yarns in through-thickness locations.

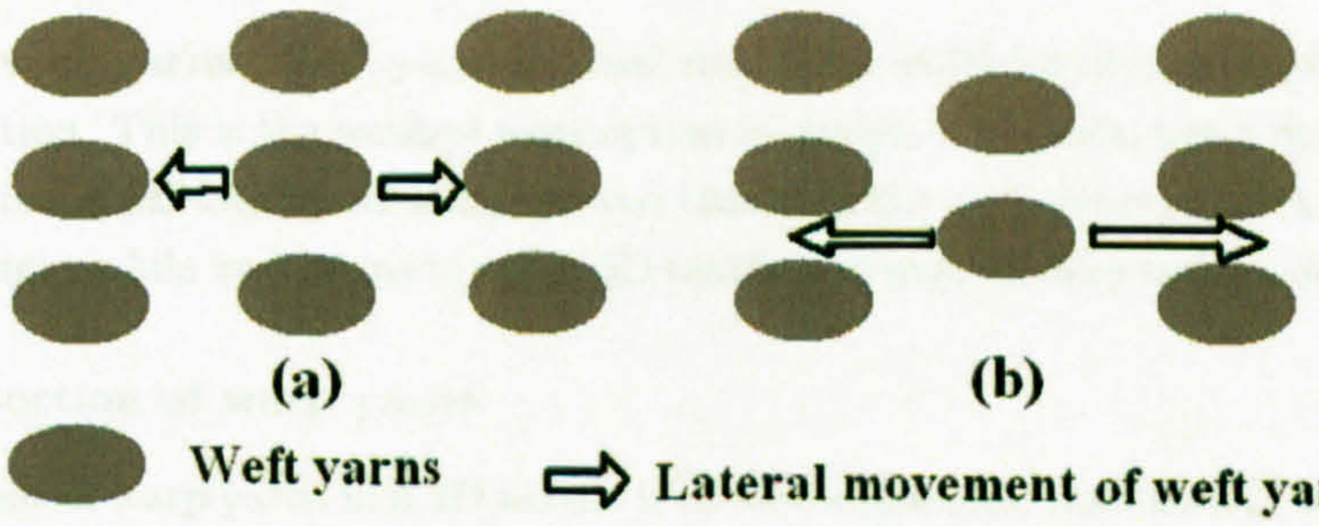

Figure 5.11: **Lateral movement of weft yarns in 3D fabrics with** - (a) even rows of weft yarns; (b) uneven rows of weft yarns

Distortion of rows of weft yarns In ideal structures of 3D textile composites, weft yarns are organized in vertical rows in through-thickness directions. Part *c* and *d* in figure 5.2 to figure 5.9 shows that some weft yarns in G3-1-VE and G5-1-VE are not even align to a single line. This is because of the vertical collisions of weft yarns mentioned above. In G6-1-VE, there is no row of weft yarns. This is because weft yarns in 3D fabrics with uneven rows of weft yarns has more freedom in lateral movement than weft yarns in 3D fabrics with even rows of weft yarns as illustrated in figure 5.11. The serious distortion of weft yarn rows in G6-1-VE resulting in unrecognizable arrangement of weft yarns and very loose distribution of weft yarns both of which are not desirable in manufacturing of 3D textile composites. Because the former makes it impossible to relate the properties of the textile composites to the parameters of designing the 3D textile composites, and the later may result in low fibre volume fraction.

Table 5.1: Thickness of 3D textile composites

Material	No. of layers of weft yarns	Thickness/*mm*	Angle of tilting of weft yarn rows/°
G1-1-VE	4	2.85	55.4
G2-1-VE	4	3.46	49.4
G3-1-VE	6	2.74	50.2
G4-1-VE	5	3.84	59.4
G5-1-VE	5	2.71	55.2
G7-1-VE	5	5.42	
C1-1-VE	5	2.30	

Tilting of weft yarn rows . In ideal structures of 3D woven textile composites, the thicknesses of the 3D textile composites are dependent on the number of layers of weft yarns. As mentioned above, C1-1-VE and G7-1-VE have similar yarn arrangement and tow sizes, but merging of weft yarns results in much smaller thickness of C1-1-VE than G7-1-VE. It was observed that in G1-1-VE, G2-1-VE, G3-1-VE, G4-1-VE, and G5-1-VE, the thickness was reduced due to tilting of weft yarn rows. In ideal structures, the angle between the weft yarn rows and the warp yarn direction is 90°, i.e. 0° tilting. The tilting angles of weft yarn rows in G1-1-VE, G2-1-VE, G3-1-VE, G4-1-VE and G5-1-VE are listed in table 5.1.

Crimping of weft yarns Weft yarns in ideal structures of 3D textile composites are straight in weft yarn direction. This is the weakest assumption in design 3D fabrics, but a must for simplifying the categorization of 3D fabrics. It was observed that that the weft yarns in G7-1-VE and C1-1-VE are almost straight while weft yarns in other 3D textile composites have certain degree of crimping.

5.2.2.3 Distortion of warp yarns

The arrangement of warp yarns in a 3D textile is more complicated than that of weft yarns. Images of cross-sections in the weft yarn direction can only show how the warp yarns interlace with weft yarns. It only shows the positions of warp yarns in the through-thickness direction. It doesn't show the arrangement of warp yarns in weft yarn direction. In order to fully understand the architectures of the 3D textile composites used in this study, one cross-section image in the warp yarn direction

of each 3D textile composites were constructed using microscope images with magnification of 5. Different warp yarns were painted using different colour as shown part (*e*) in figure 5.2 to figure 5.9. Warp yarns in G6-1-VE are painted using the same colour because of the serious distortion of the arrangement of weft yarns.

Part (*b*),(*e*) and (*f*) of figure 5.2to figure 5.9 show that that the weft yarns in these composites are different from the weft yarns in the original design in terms of:

1. degree of packing - high: C1-1-VE ; medium: G1-1-VE, G2-1-VE, G4-1-VE, G7-1-VE; low: G3-1-VE; very low: G5-1-VE.
2. consistence of the degree of crimping - consistent: C1-1-VE, G1-1-VE, G2-1-VE, G4-1-VE, G5-1-VE, G6-1-VE; not consistent: G3-1-VE and G7-1-VE.
3. degree of crimping - proportional to layer of weft yarns locked: G2-1-VE and G4-1-VE; not proportional to layer of weft yarns locked.

degree of packing When design 3D fabrics, mixture of different kinds of multi-layer locking yarns is used increase the degree of packing of warp yarns. Part *e* in figure 5.2, 5.3, 5.4, 5.5, 5.6 and 5.8 show that composites containing mixture of multi-layer locking yarns including G1-1-VE, G2-1-VE and G4-1-VE have higher degree of packing of warp yarns than G3-1-VE which only has 3 layer locking yarns, but the degree of packing of warp yarns in G5-1-VE is lower than G3-1-VE although G5-1-VE contains mixture of 2 and 3 layer locking yarns. This is largely due to the larger amount of weft and warp yarns in G3-1-VE than G5-1-VE. Table 5.1 shows that although G3-1-VE has 1 more layer of weft yarns than G5-1-VE, its thickness is similar to that of G5-1-VE.

Consistence of the degree of crimping In ideal structures of 3D textile composites, the multilayer locking yarns are in sinusoidal shape in weft yarn direction. Part *f* in figure 5.2, 5.3, 5.4, 5.5, 5.6 and 5.8 show that most warp yarns in 3D textile composites used in this study are in sinusoidal shape. But two angles of crimp were observed for one 3-layer locking yarns were observed in G5-1-VE and G7-1-VE. In G7-1-VE, the through-thickness locking yarn is not smooth unlike the through-thickness yarn in C1-1-VE.

Degree of crimping In ideal structures, the angle of crimp of plain woven style warp yarn is smaller than that of 2-layer locking yarn which in turn is smaller than that of 3-layer locking yarn. In real structures, this is only true in G2-1-VE and G4-1-VE.

5.2.3 Conclusions

Based on the discussions above, it can be concluded that the closeness between ideal yarn arrangement and real yarn arrangement of a 3D woven textile composite can be improved by using yarn coating method as illustrated in figure 4.1, more straight and plain woven style warp yarns, even rows of weft yarns, mixture of different kinds of multi-layer locking yarns, less 3 layer or more layer locking yarns. It should be borne in mind that good similarity between ideal yarn arrangement and real yarn arrangement of a 3D woven textile composite may be very important for tasks such as computer modelling of the mechanics of 3D woven textile composites, the assessment of manufacturability is not as important as other experimental assessments in this study. The more valuable aspect of the computer simulations carried out so far is the reviewing of real yarn arrangements in

all eight 3D woven textile composites which may prevent wrongly analysis and explanation of the experimental results acquired later in this study.

5.3 Resin rich area

Resin rich areas exist in both 2D and 3D textile composites. Several factors cause the resin rich area. For example, the size of tows (or yarns), manufacturing methods etc. For woven textile composites esp. 3D textile composites, fabric architecture plays a key role in the occurrence of resin rich area. The crimping of weft and warps in plain woven textile composite cause some resin rich area as shown in figure 5.12. These resin rich areas distribute evenly in composites and play an important role in the occurrence of delamination. They actually improve the energy absorption of composites subjected to impacts. The resin rich areas in 3D textile composites are much bigger than that of 2D textile composites and were not distribute evenly as shown in figure 5.12. In C1-1-VE and G7-1-VE specimens, resin rich areas occur mainly underneath or above through-thickness locking yarns as shown in figure 5.12. The existence of strait warp yarns reduces the amount of resin rich area significantly compared with other 3D textile composites.

5.4 Wet-out

The properties of fibre-matrix interface in composites are largely determined by the ability of the matrix to wet the fibre surface. Thus good manufacturability requires good wet-out of fibres. As shown in figure 5.13 good fibre wet-out and fibre/matrix bonding are obtained in (a) PWC1-12-VE, (b) G1-1-VE, (c) CAR-1-VE specimens, as evident by the flakes of matrix material adhering to the fibres.

5.5 Conclusions

It has been found out that the fabric architectures in composites are distorted to certain degrees for all 3D textile composites. The distortions of ideal structure include merging of weft yarns, tilting of weft yarn rows etc. The use of fibre coating on the surface of yarns and avoiding use of uneven weft yarns rows can reduce distortion of ideal structure. Overall distortion of ideal structure is much more serious in 3D textile composites. In addition, there are more resin rich areas in 3D textile composites than 2D textile composites. In other words, yarns in 3D textile composites are less packed than 2D textile composites although mixture of multilayer locking yarns can be used to reduce resin rich area. So in terms of closeness to ideal structure and resin rich area, the manufacturability of 3D textile composites is not as good as 2D textile composites. But 3D textile composites have wet-out properties as good as that of 2D textile composites. An intraduction of near-net-shape 3D preforms can reduce manufacturing costs through reduced time.

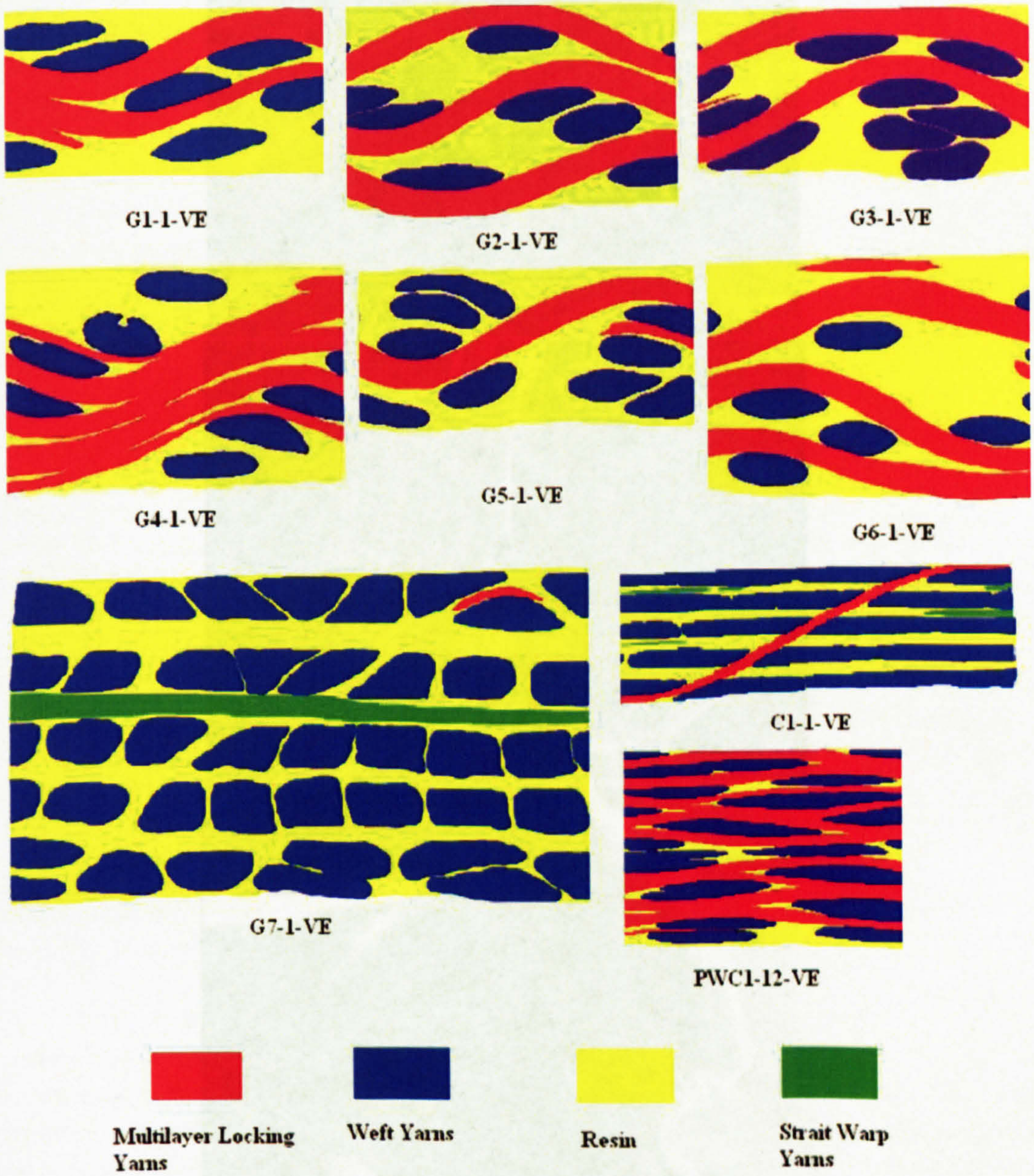

Figure 5.12: **Resin rich area in 2D and 3D textile composites .**

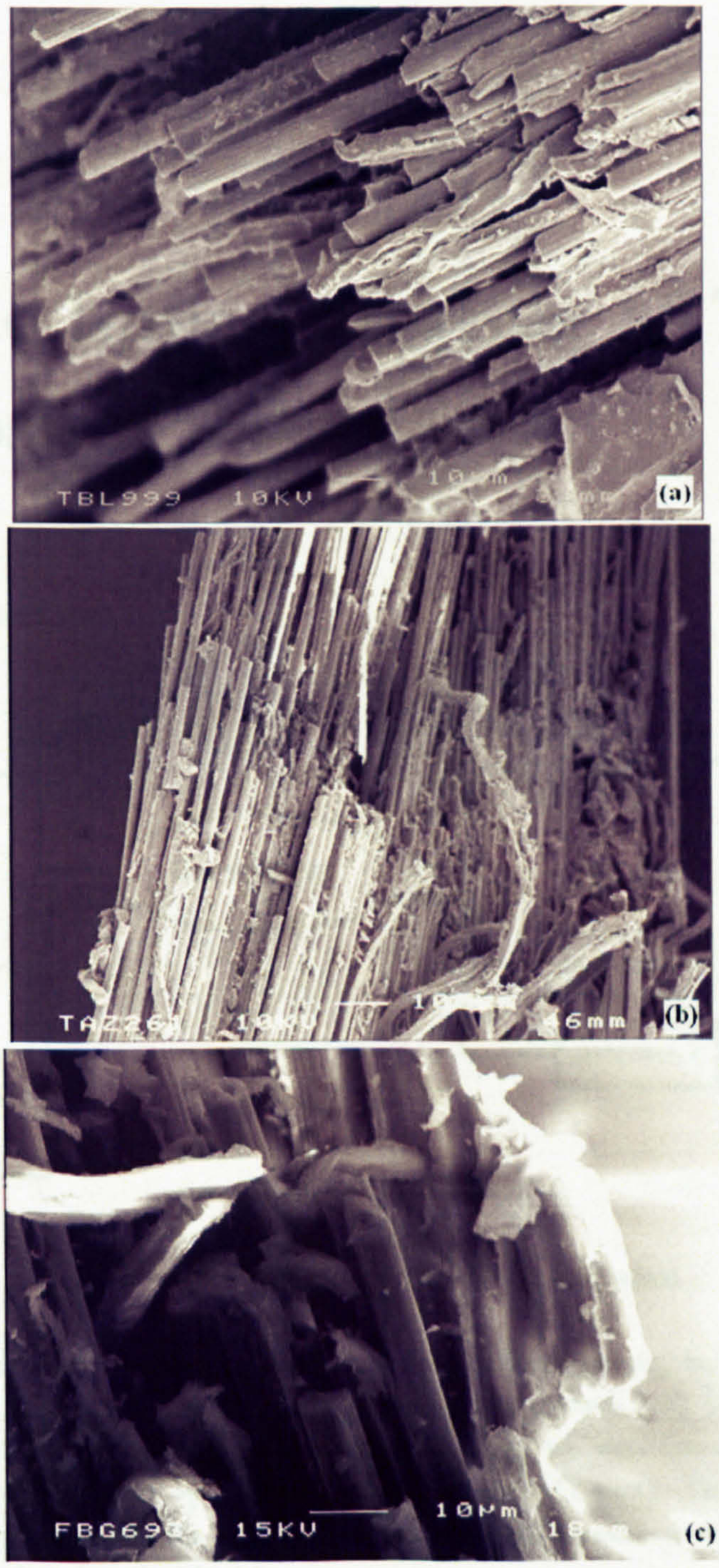

Figure 5.13: **Good fibre wet-out and fibre/matrix bonding are obtained in** - (a) PWC1-12-VE, (b) G1-1-VE, (c) CAR-1-VE specimens, as evident by the fakes of matrix material adhering to the fibres.

Chapter 6

Ballistic Impact Testing of Textile Composites

6.1 Introduction

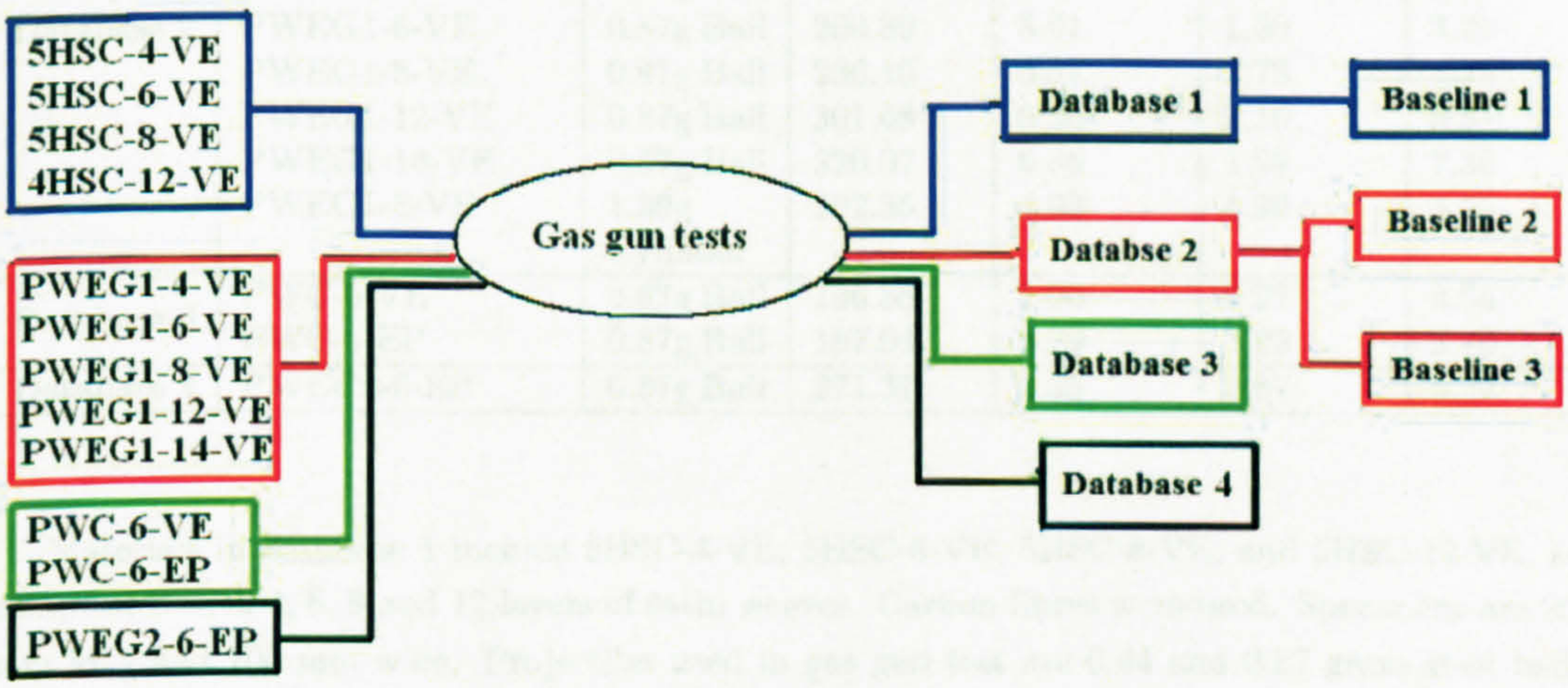

Figure 6.1: **Gas gun tests of baseline materials -**

As shown in figure 3.1 the gas gun test is the first step of assessing ballistic performance of textile composites. Its objective is to identify the single-hit ballistic limit velocities (V_{50}) for all the textile composites listed in table 4.4 and table 4.5. Their V_{50} were identified using a method described in section 2.2.1. Each V_{50} was the average velocity of 6 shots. Three of these six shots were from penetrated tests and the other three were from non-penetrated tests. The precision of the V_{50} was reviewed as described in 4.3.

There were two stages in the process of gas gun tests. The first stage involved gas gun tests of 5 harness satin carbon textile composites and plain woven E-glass textile composites. Its aim is to form V_{50} baselines. Three baselines were formed as shown in figure 6.1. The second stage involves gas gun tests of non-crimp textile composites, commingled textile composites and 3D

woven textile composites. Its aim is to compare V_{50}s of these textile composites against those of baseline materials.

6.2 Gas gun tests of baseline materials

6.2.1 Database 1

Table 6.1: Gas gun test results of materials in databases

Group	Material	Projectile	Average Velocity (V_{50})	Standard deviation (m/s)	Coefficient of variation (%)	Areal density (kg/m^2)
Database 1	5HSC-4-VE	0.44g Ball	186.99	6.84	3.66	2.50
	5HSC-8-VE	0.44g Ball	277.35	12.62	4.55	4.70
	5HSC-12-VE	0.44g Ball	352.69	5.52	1.56	6.66
	5HSC-6-VE	0.87g Ball	202.80	3.87	1.91	3.58
Database 2	PWEG1-4-VE	0.44g Ball	176.56	11.67	6.61	2.08
	PWEG1-8-VE	0.44g Ball	284.93	3.37	1.18	4.23
	PWEG1-12-VE	0.44g Ball	349.68	2.38	0.68	6.31
	PWEG1-4-VE	0.87g Ball	152.72	5.31	3.47	2.08
	PWEG1-6-VE	0.87g Ball	200.89	3.01	1.50	3.21
	PWEG1-8-VE	0.87g Ball	236.10	6.57	2.78	4.23
	PWEG1-12-VE	0.87g Ball	301.68	6.33	2.10	6.31
	PWEG1-14-VE	0.87g Ball	320.07	6.36	1.99	7.36
	PWEG1-8-VE	1.39g Cylinder	202.85	4.03	1.99	4.23
Database 3	PWC-6-VE	0.87g Ball	196.86	1.90	0.97	3.54
	PWC-6-EP	0.87g Ball	187.04	2.29	1.22	3.70
Database 4	PWEG2-6-EP	0.87g Ball	271.37	2.35	0.87	5.22

Materials in database 1 include 5HSC-4-VE, 5HSC-6-VE, 5HSC-8-VE, and 5HSC-12-VE, i.e. composites with 4, 6, 8 and 12 layers of satin weaves. Carbon fibres were used. Specimens are 200 mm long and 100 mm wide. Projectiles used in gas gun test are 0.44 and 0.87 gram steel balls. The following tests have been carried out:

1. 5HSC-4-VE, 5HSC-8-VE, 5HSC-12-VE impacted by 0.44g balls
2. 5HSC-6-VE impacted by 0.87g balls

The final V_{50} results are shown in table 6.1. More details of these ballistic tests can be found in figure A.1 in appendix A and table B.1 and table B.2 in appendix B.

As shown in figure 6.2 (a), 15 shots were fired in the gas gun test of 5HSC-4-VE samples. Because this is the first series of gas gun tests, there was no reference point regarding the relationship between areal density of textile composite and its ballistic limit velocity. At first a random gas pressure was chosen, where the shot was penetrated. In the second shot, gas pressure was reduced by 50 psi. The shot was non-penetrated. In the following shots, gas pressures were controlled between the gas pressures of the first shot and the second shots. The shooting continued until the fulfilment of the following requirements:

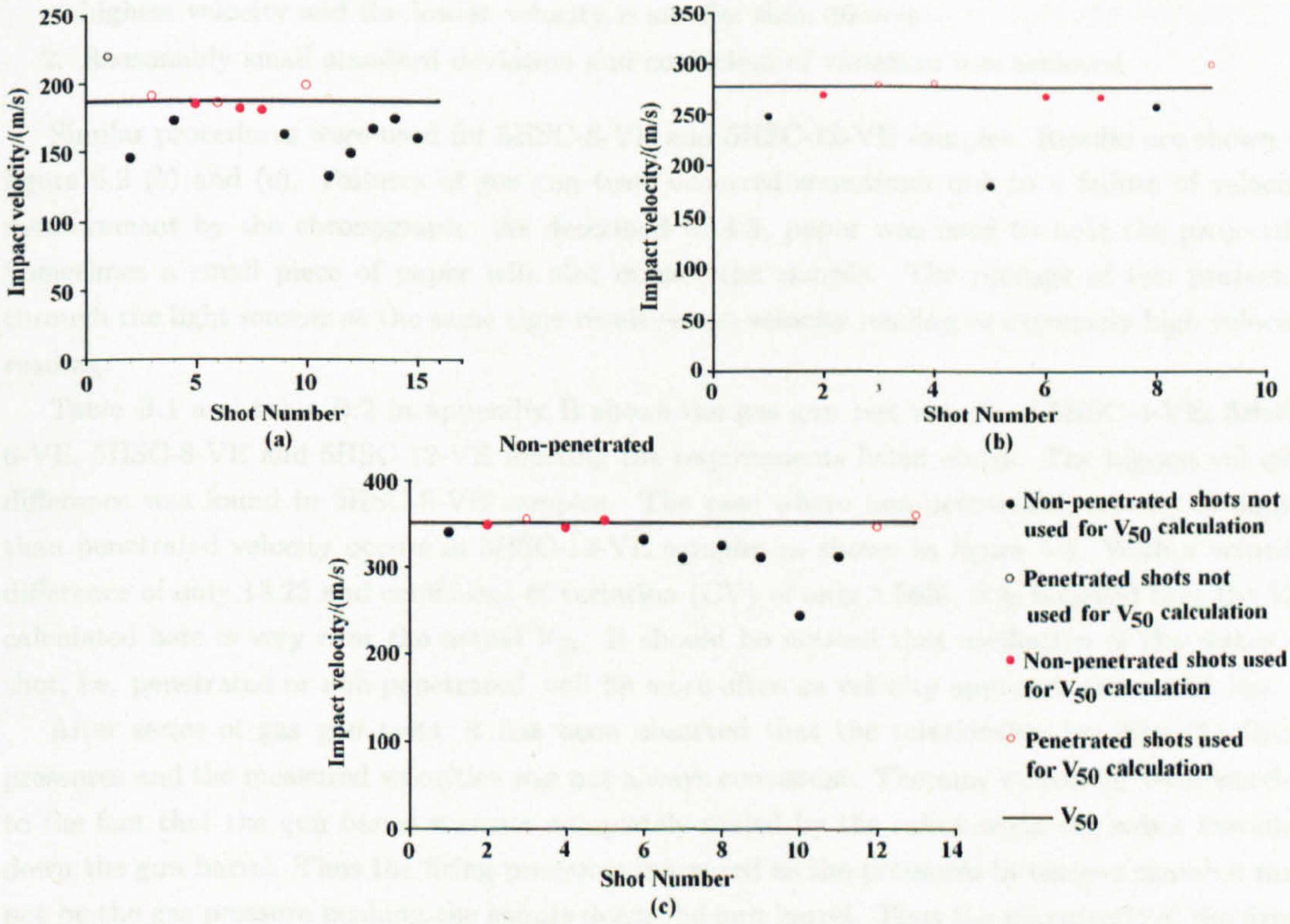

Figure 6.2: **Gas gun test results of materials in database 1 using 0.44g steel balls** - (a) 5HSC-4-VE; (b) 5HSC-8-VE; (c) 5HSC-12-VE.

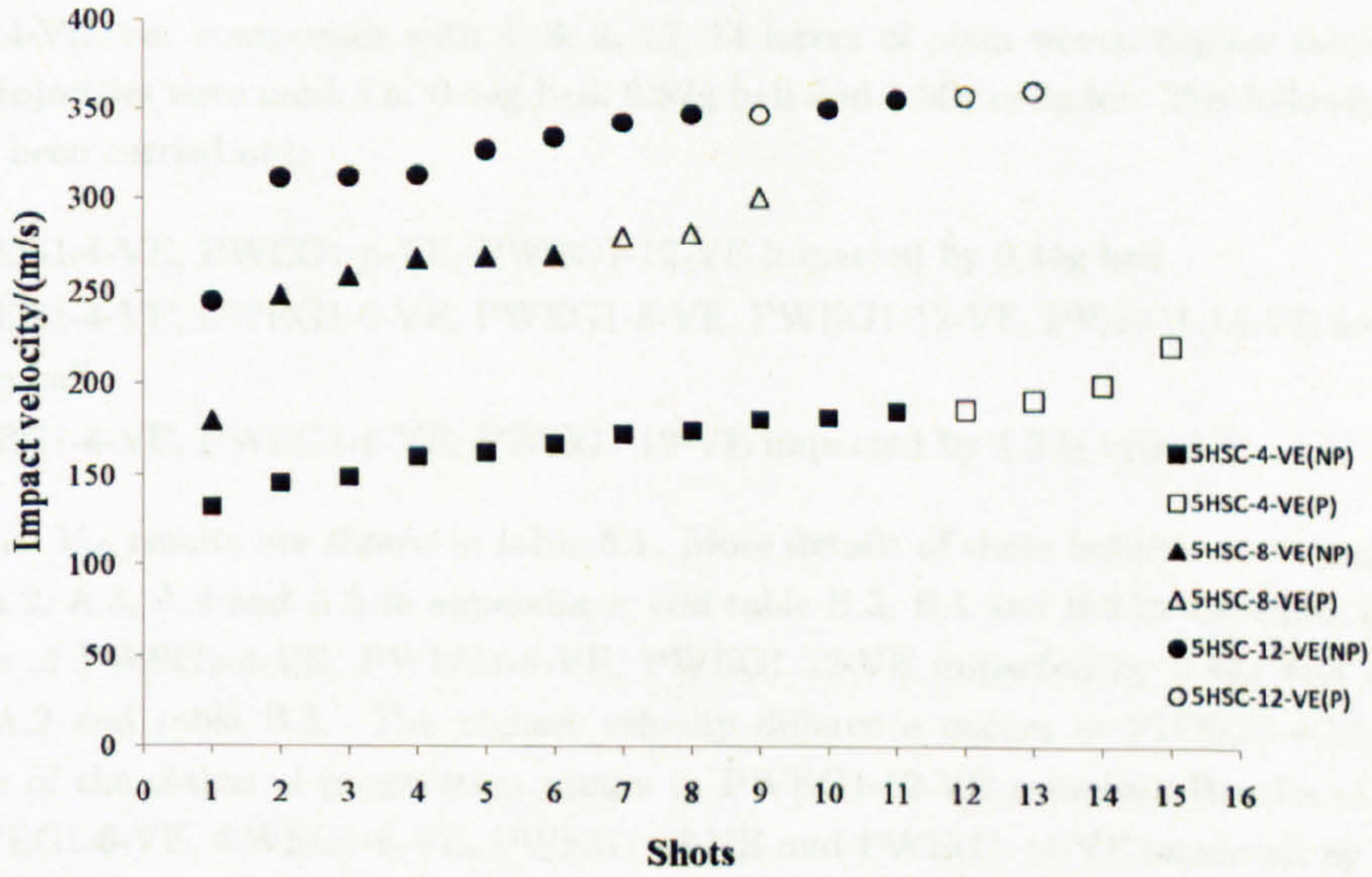

Figure 6.3: **Gas gun test results of baseline 1 materials using 0.44g steel ball** - sequence of penetration and non-penetration; NP=non-penetrated; P=penetrated.

1. Identify 3 penetrated shots and 3 non-penetrated shots where the difference between the highest velocity and the lowest velocity is smaller than 36 m/s
2. Reasonably small standard deviation and coefficient of variation was achieved

Similar procedures were used for 5HSC-8-VE and 5HSC-12-VE samples. Results are shown in figure 6.2 (*b*) and (*c*). Failures of gas gun tests occurred sometimes due to a failure of velocity measurement by the chronograph. As described in 4.3, paper was used to hold the projectile. Sometimes a small piece of paper will also impact the sample. The passage of two projectile through the light sensors at the same time results in no velocity reading or extremely high velocity reading.

Table B.1 and table B.2 in appendix B shows the gas gun test results of 5HSC-4-VE, 5HSC-6-VE, 5HSC-8-VE and 5HSC-12-VE meeting the requirements listed above. The biggest velocity difference was found in 5HSC-8-VE samples. The case where non-penetrated velocity is bigger than penetrated velocity occurs in 5HSC-12-VE samples as shown in figure 6.3. With a velocity difference of only 13.25 and coefficient of variation (CV) of only 1.56%, it is believed that the V_{50} calculated here is very near the actual V_{50}. It should be noticed that oscillation of the status of shot, i.e. penetrated or non-penetrated, will be more often as velocity approach the actual V_{50}.

After series of gas gun tests, it has been observed that the relationship between the firing pressures and the measured velocities was not always consistent. The may reason for that was due to the fact that the gun barrel was not completely sealed by the sabot when the sabot travelled down the gun barrel. Thus the firing pressures measured as the pressures in the gas chamber may not be the gas pressure pushing the sabots down the gun barrel. Thus the magnitude of the firing pressure for each shots were not listed in this work.

6.2.2 Database 2

Materials in database 2 include PWEG1-4-VE, PWEG1-6-VE, PWEG1-8-VE, PWEG1-12-VE and PWEG1-14-VE, i.e. composites with 4, 6, 8, 12, 14 layers of plain woven E-glass fabrics. Three kinds of projectiles were used, i.e. 0.44g ball, 0.87g ball and 1.39g cylinder. The following gas gun tests have been carried out:

1. PWEG1-4-VE, PWEG1-8-VE, PWEG1-12-VE impacted by 0.44g ball
2. PWEG1-4-VE, PWEG1-6-VE, PWEG1-8-VE, PWEG1-12-VE, PWEG1-14-VE impacted by 0.87g ball
3. PWEG1-4-VE, PWEG1-8-VE, PWEG1-12-VE impacted by 1.39g cylinder

The final V_{50} results are shown in table 6.1. More details of these ballistic tests can be found in figure A.2, A.3, A.4 and A.5 in appendix A and table B.3, B.4 and B.2 in appendix B.

Results of PWEG1-4-VE, PWEG1-8-VE, PWEG1-12-VE impacted by 0.44g ball are shown in figure A.2 and table B.3. The highest velocity difference occurs in PWEG1-4-VE samples. Oscillation of the status of penetration occurs in PWEG1-12-VE samples. Results of PWEG1-4-VE, PWEG1-6-VE, PWEG1-8-VE, PWEG1-12-VE and PWEG1-14-VE impacted by 0.87g ball are shown in figure A.3, figure A.4 and table B.4. Results of PWEG1-8-VE impacted by 1.39g cylinder are shown in figure A.5 and table B.5.

During the gas gun tests of these materials, the relationship between V_{50} and areal density in baseline 2 was used as reference. Knowing V_{50}, the highest kinetic energy the composite can stop can be calculated using equation 6.1 where m is the weight of the projectile.

$$E = \frac{1}{2}mV_{50}^2 \tag{6.1}$$

$$V = \sqrt{\frac{2E}{0.87 \times 10^{-3}}} \tag{6.2}$$

Assuming projectile has no effect on the perforation energies of composite PWEG1-4-VE, PWEG1-8-VE and PWEG1-12-VE, the V_{50} of composite PWEG1-4-VE, PWEG1-8-VE and PWEG1-12-VE can be calculated using equation 6.1, 6.2 and V_{50} results in baseline 1. During the gas gun tests of these textile composites, the first impacting velocity for each one of one of PWEG1-4-VE, PWEG1-8-VE and PWEG1-12-VE was controlled near the velocity calculated using equation 6.2. The number of shots used for baseline 3 materials is reduced significantly. Table B.4 lists the velocities used for the calculation of V_{50}. The biggest velocity difference is 17.65 m/s. The highest CV is 7.36. Overall the V_{50} data presented here are more precise than the V_{50} data in baseline 1 and 2.

6.2.3 Database 3

Materials used in database 3 include PWC-6-VE, and PWC-6-EP. They are composites made from plain woven carbon fibres. The final V_{50} results are shown in table 6.1. More details of these ballistic tests can be found in figure A.6 in appendix A and table B.6 in appendix B.

6.2.4 Database 4

The composite materials used in database 4 were PWEG2-6-EP. They were composites made from plain woven E-glass fabrics. The plain woven fabrics used here are different from the one used in database 2 in terms of areal density. The areal density of the plain woven fabrics used in database 2 is $400g/m^2$. The areal density of the plain woven fabric used here is normally $600g/m^2$. An epoxy resin system was used to manufacture PWEG2-6-EP panels. The final V_{50} results are shown in table 6.1. More details of these ballistic tests can be found in figure A.7 in appendix A and table B.7 in appendix B.

6.3 Gas gun tests of 3D woven textile composites

6.3.1 Carbon fibre textile composites

Materials used in this section include C1-1-VE and C1-1-EP. They are manufactured using preform C1. Two resin system were used, i.e. vinyl ester and epoxy. Specimens of C1-1-VE were impacted three kinds of projectiles, i.e. 0.44g steel ball, 0.87g steel ball and 1.39g cylinder. Specimens of C1-1-EP were impacted using 0.87g steel balls. The final V_{50} results are shown in table 6.2. More details of these ballistic tests can be found in figure A.8, A.9, A.10 in appendix A and table B.8, B.10, B.9 in appendix B.

Table 6.2: Gas gun test results of new materials

Group	Material	Projectile	Average Velocity (V_{50})	Standard deviation (m/s)	Coefficient of variation (%)	Areal density (kg/m^2)
3D woven	C1-1-VE	0.44g Ball	254.99	4.79	1.88	3.26
	C1-1-VE	0.87g Ball	224.26	5.29	2.36	3.26
	C1-1-EP	0.87g Ball	225.94	5.19	2.30	3.58
	C1-1-VE	1.39g Cylinder	212.19	3.30	1.55	3.26
	G1-1-VE	0.87g Ball	260.83	5.85	2.24	4.95
	G2-1-VE	0.87g Ball	266.95	4.79	1.80	5.48
	G3-1-EP	0.87g Ball	255.00	3.00	1.18	4.84
	G4-1-EP	0.87g Ball	307.42	2.13	0.69	6.83
	G5-1-EP	0.87g Ball	230.48	11.43	4.96	4.76
	G6-1-EP	0.87g Ball	278.15	3.71	1.33	6.88
	G7-1-EP	0.87g Ball	342.91	5.86	1.71	8.93
Non-crimp	NCC-S-VE	0.87g Ball	255.00	1.92	0.75	4.59
	NCC-2-VE	0.87g Ball	272.84	11.36	4.16	4.59
	NCEG1-S-VE	0.87g Ball	161.07	5.92	3.68	2.19
	NCEG1-2S-VE	0.87g Ball	255.02	7.25	2.84	4.30
	NCEG1-4-VE	0.87g Ball	236.55	15.59	6.59	4.32
	NCEG2-4-VE	0.87g Ball	212.65	9.73	4.57	3.56
Co-mingled	PWCPET1-2-VE	0.44g Ball	146.85	10.69	7.28	2.49
	PWCPET1-4-VE	0.44g Ball	196.44	13.40	6.82	3.65
	PWCPET2-2-VE	0.44g Ball	106.02	10.31	9.72	1.82
	TWEGPP-2-EP	0.87g Ball	193.78	3.66	1.89	2.82
	TWEGPP-4-EP	0.87g Ball	260.43	2.93	1.12	5.52
	PWEGPP-4-EP	0.87g Ball	260.62	1.56	0.60	5.33

6.3.2 Glass fibre textile composites

Materials used in this section include G1-1-VE, G2-1-VE, G3-1-VE, G4-1-VE, G5-1-VE, G6-1-VE and G7-1-VE. Projectiles used are 0.87 g steel balls. The final V_{50} results are shown in table 6.2. More details of these ballistic tests can be found in figure A.11, figure A.12 and figure A.13 in appendix A and table B.11 in appendix B. The highest velocity difference is only 5.43 m/s. Vibration of penetration status occurred in G1-1-VE, G3-1-VE, G4-1-VE, G5-1-VE and G6-1-VE.

6.4 Gas gun tests of non-crimp textile composites

6.4.1 Carbon fibre textile composites

Materials used in this section include NCC-S-VE and NCC-2-VE. Projectiles used are 0.44 g steel balls. The final V_{50} results are shown in table 6.2. More details of these ballistic tests can be found in figure A.14 in appendix A and table B.13 in appendix B.

6.4.2 Glass fibre textile composites

Materials used in this section include NCEG1-S-VE, NCEG1-2S-VE, NCEG1-4-VE, NCEG2-4-VE. Projectiles used are 0.87 g steel balls. The final V_{50} results are shown in table 6.2. More details of these ballistic tests can be found in figure A.15 and figure A.16 in appendix A and table B.14 in appendix B.

6.5 Gas gun tests of comingled textile composites

6.5.1 Carbon fibre and PET fibre

Materials used in this section include PWCPET1-2-VE, PWCPET1-4-VE and PWCPET2-2-VE. Projectiles used are 0.44 g steel balls. The final V_{50} results are shown in table 6.2. More details of these ballistic tests can be found in figure A.17 in appendix A and table B.15 in appendix B.

6.5.2 Glass fibre and polypropylene (PP) fibre

Materials used in this section include TWEGPP-2-EP, TWEGPP-4-EP, PWEGPP-4-EP, PWEG2-6-EP and M1-1-VE. Projectiles used are 0.87 g steel balls. The final V_{50} results are shown in table 6.2. More details of these ballistic tests can be found in figure A.18 in appendix A and table B.16 in appendix B.

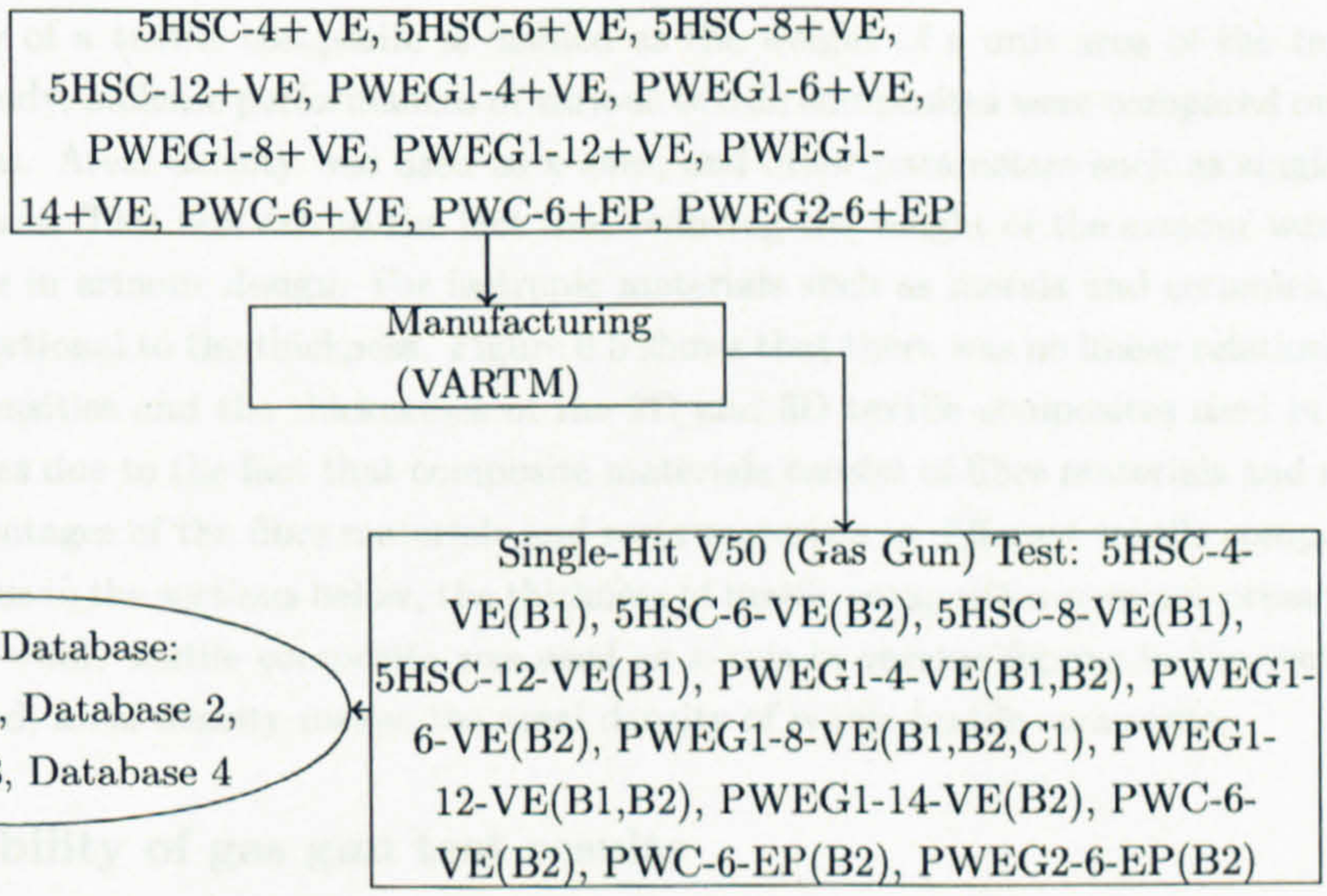

Figure 6.4: **Experimental procedures of contructure of V_{50} databases** - +=together with; B1=tested using 0.44g steel balls; B2=tested using 0.87g steel balls; C1=tested using 1.39g cylinders.

6.6 Discussion of results

6.6.1 Areal densities of textile composites

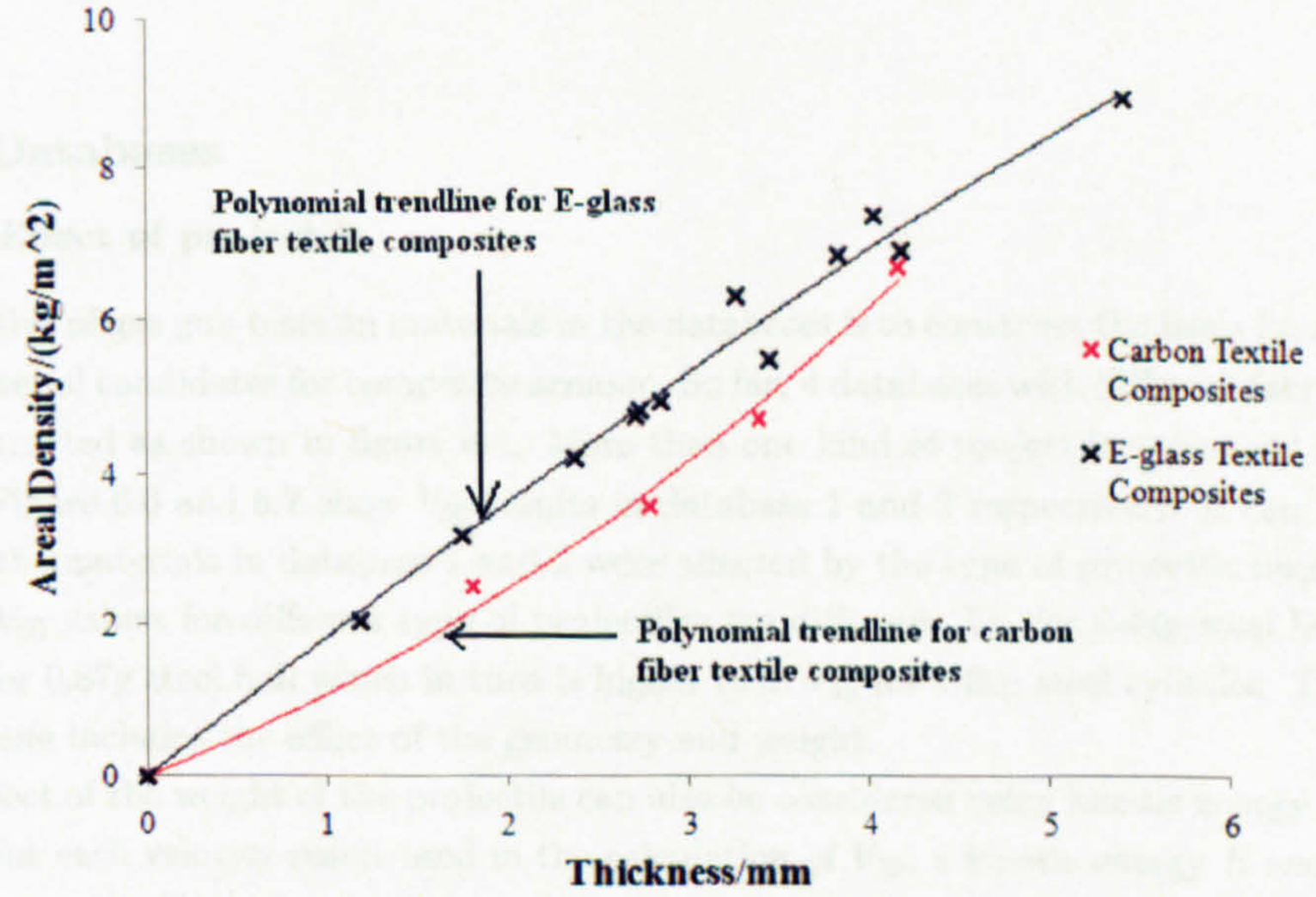

Figure 6.5: **Areal density and thickness values of E-glass and carbon fibre textile composites** .

The areal density of a textile composite is defined as the weight of a unit area of the textile composite. In this study, ballistic performances of various textile composites were compared on the base of areal densities. Areal density was used as x-axes, and other parameters such as single-hit V_{50} were used as y-axes. This was due to the fact that reducing the weight of the armour was the most important issue in armour design. For isotropic materials such as metals and ceramics, the areal density is proportional to the thickness. Figure 6.5 shows that there was no linear relationship between the areal densities and the thicknesses of the 2D and 3D textile composites used in this study. One reason was due to the fact that composite materials consist of fibre materials and resin materials. The percentages of the fibre materials and resin materials in different textile composite may be different. Thus in the sections below, the thickness of textile composites were not presented. Areal density of the whole textile composite was used as x-axis in various figures in the sections below. If not specified, areal density means the areal density of whole textile composite.

6.6.2 Repeatability of gas gun test results

Although the inherent repeatability of gas gun test results is a very important issue, it is very difficult to assess it in this study. The most difficult thing is to achieve two identical ballistic impacts. Firstly, the status of the projectiles in all impacts just before impacting must be same. Secondly, the material structures around the path of the projectile must also be same in these impacts. In this study due to the limitation of the ballistic test facilities, it has been observed that achieving continuous impacts with same velocities and same impacting points was impossible. But ballistic impacts with near identical velocities have been observed after series of gas gun tests. 17 out of 28 pairs of impacts with near identical velocities have same results, i.e. penetrated or non-penetrated. The best inherent repeatability was found in gas gun test results of non-crimped textile composites. The worst inherent repeatability was found in gas gun test results of textile composites with comingled yarns and 3D textile composites without non-crimped yarns such as G1-1-VE.

6.6.3 Databases

6.6.3.1 Effect of projectile

The objective of gas gun tests on materials in the databases is to construct the basis for assessments of new material candidates for composite armour. So far, 4 databases with different fabric materials were constructed as shown in figure 6.4. More than one kind of projectile were used in database 1 and 2. Figure 6.6 and 6.7 show V_{50} results in database 1 and 2 respectively. It can be seen V_{50} results of the materials in database 1 and 2 were affected by the type of projectile used. For same material, V_{50} values for different type of projectiles are different. V_{50} for 0.44g steel ball is higher than V_{50} for 0.87g steel ball which in turn is higher than V_{50} for 1.39g steel cylinder. This effect of the projectile includes the effect of the geometry and weight.

The effect of the weight of the projectile can also be considered using kinetic energy rather than velocity. For each velocity result used in the calculation of V_{50}, a kinetic energy E was calculated using equation 6.1. The average of the six kinetic energies were used as ballistic limit energy (E_{50}) or perforation energy. Figure 6.8 and 6.9 show V_{50} results in database 1 and 2 respectively. It can be seen that the type of projectile also affects E_{50} results. For the same material, E_{50} results of

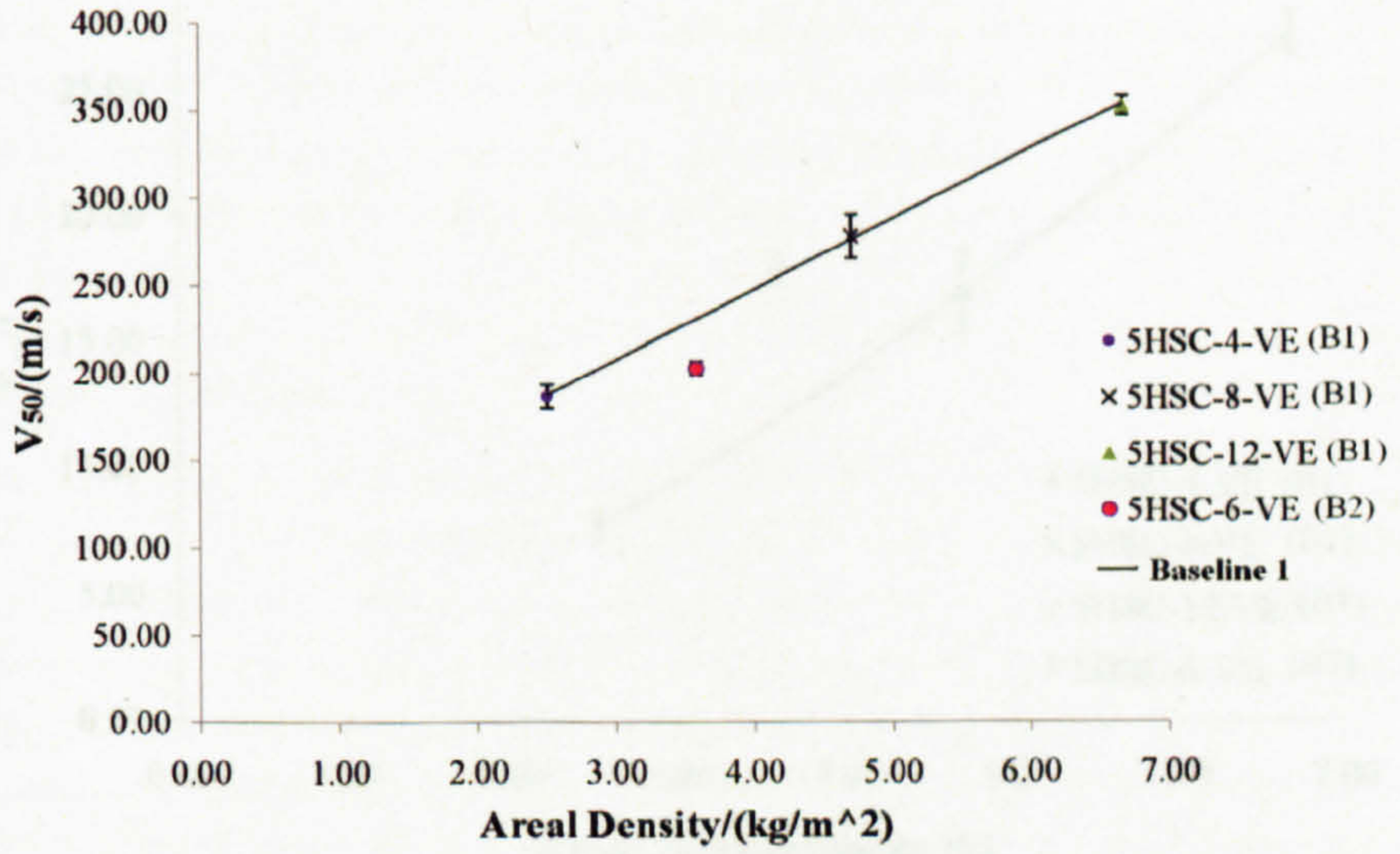

Figure 6.6: V_{50} **results in database 1** - B1=tested using 0.44g steel balls; B2=tested using 0.87g steel balls.

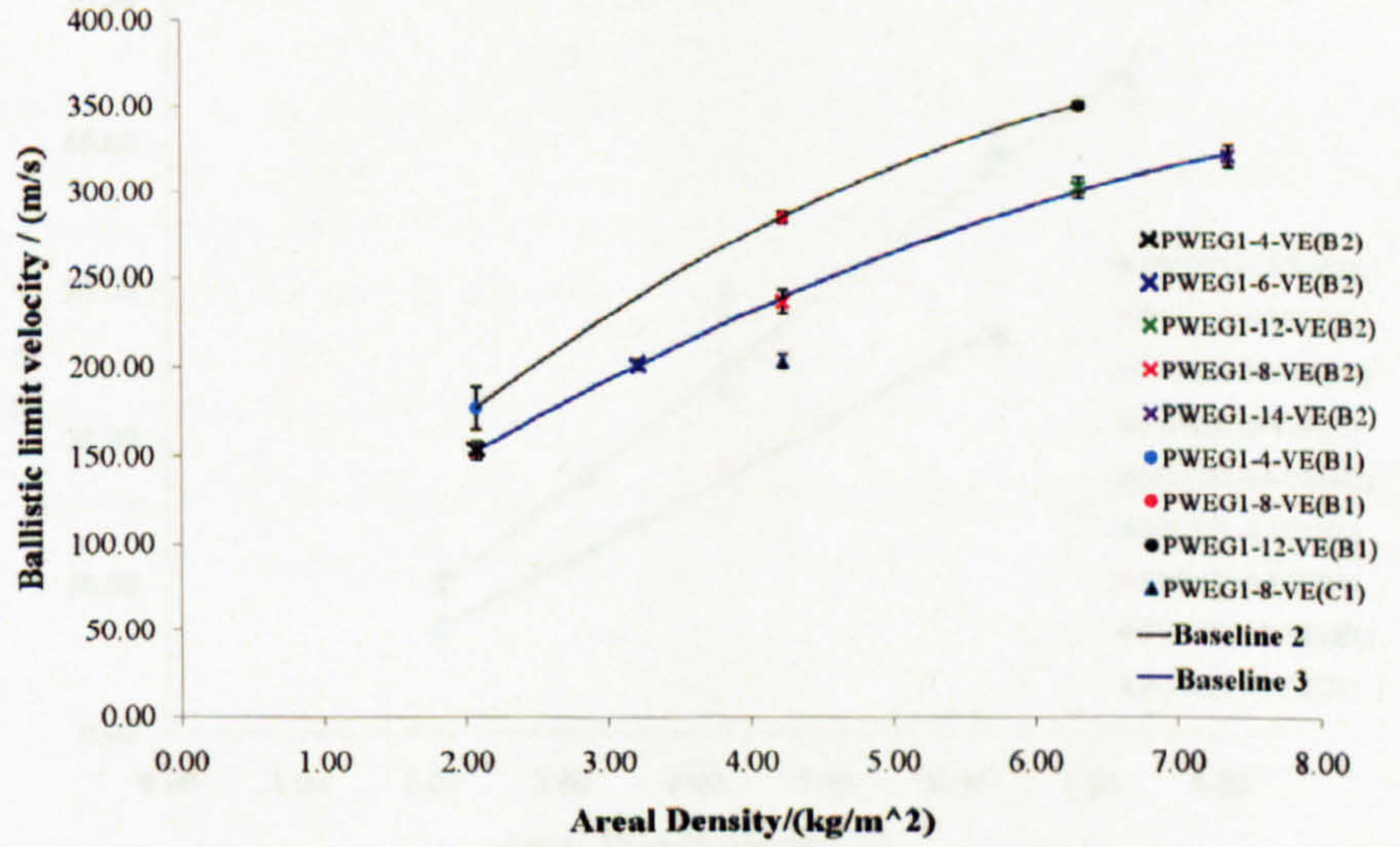

Figure 6.7: V_{50} **results in database 2** - B1=tested using 0.44g steel balls; B2=tested using 0.87g steel balls; C1=tested using 1.39g cylinders.

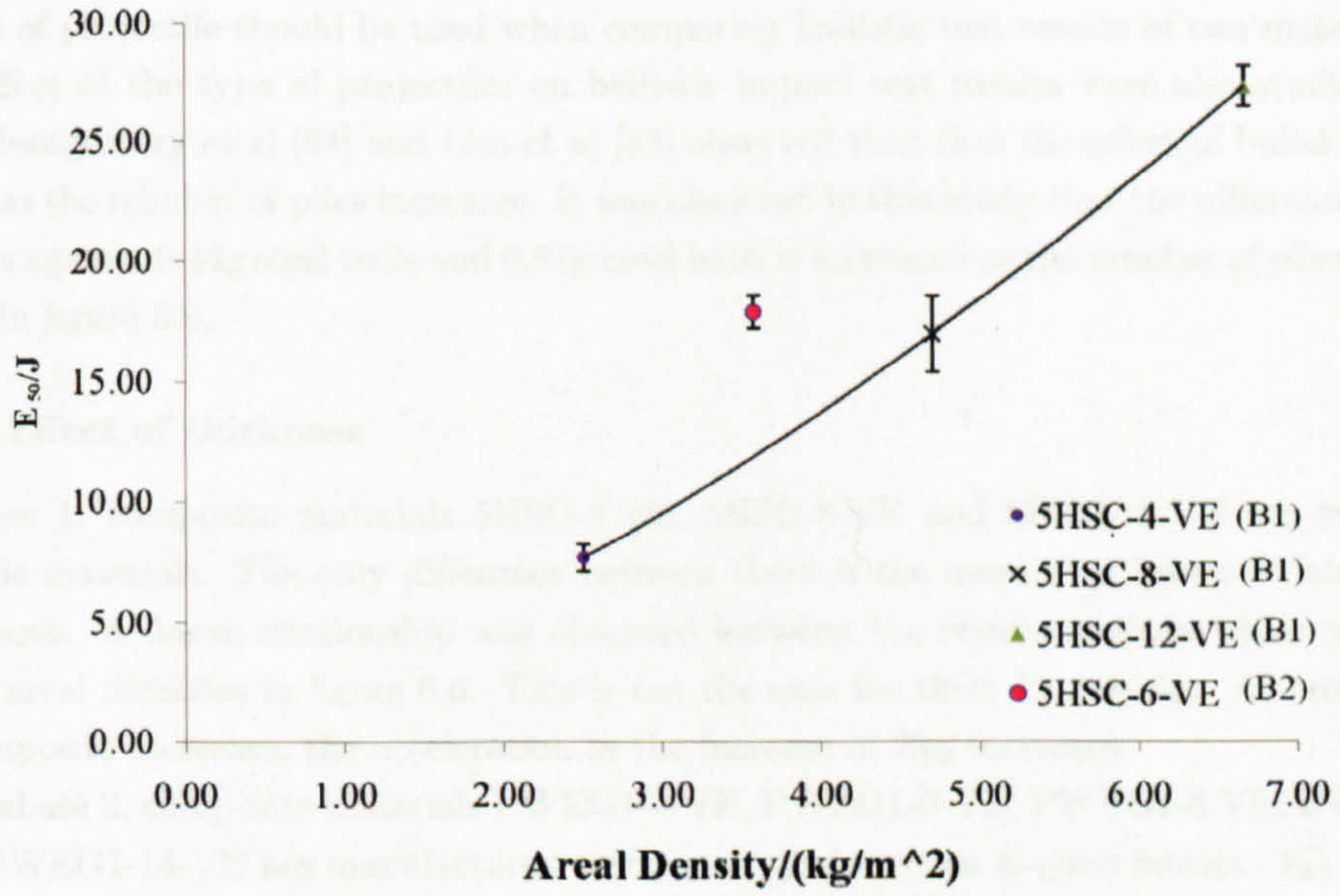

Figure 6.8: E_{50} **results in database 1** - B1=tested using 0.44g steel balls; B2=tested using 0.87g steel balls.

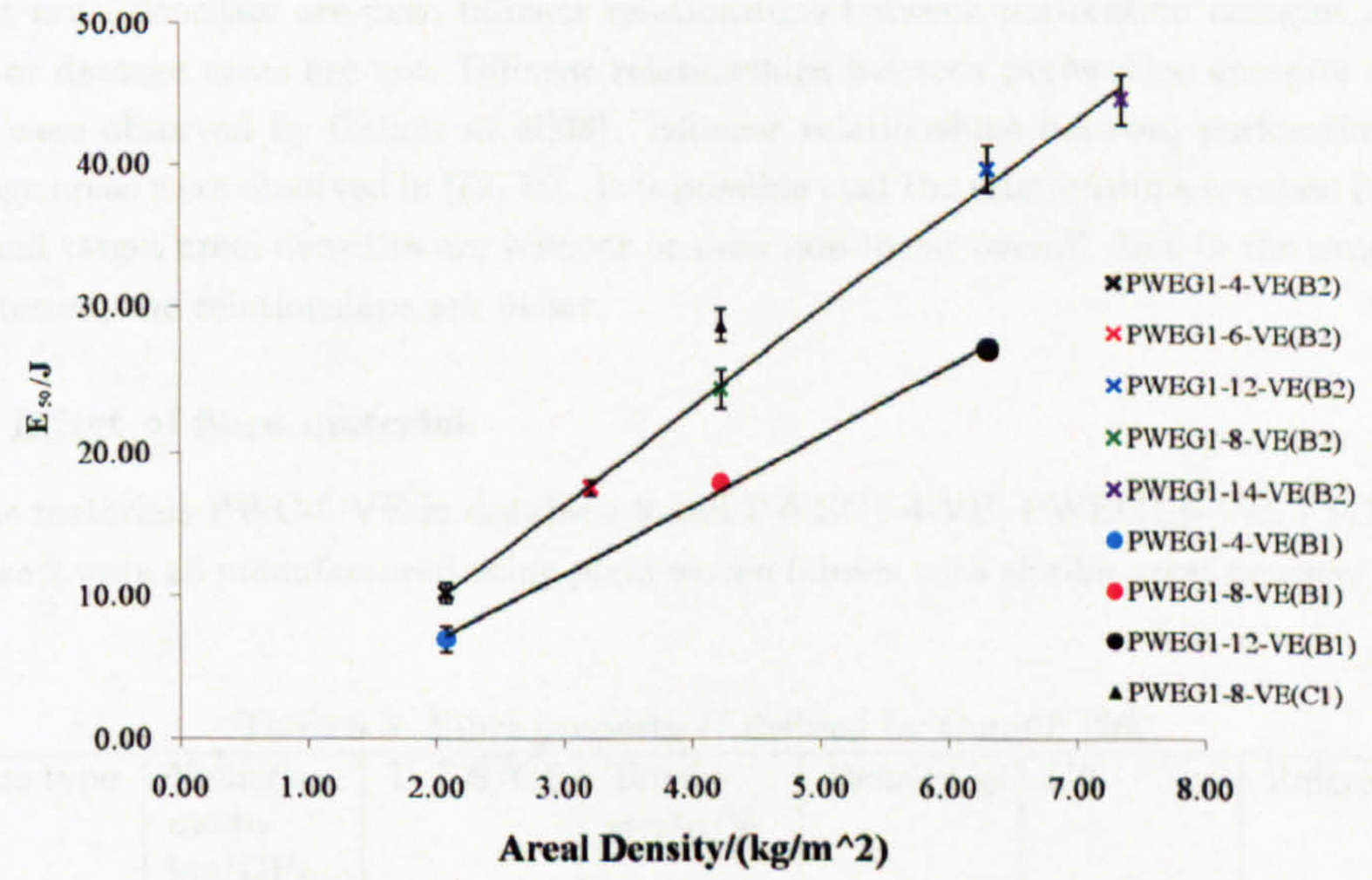

Figure 6.9: E_{50} **results in database 2** - B1=tested using 0.44g steel balls; B2=tested using 0.87g steel balls; C1=tested using 1.39g cylinders.

different type of projectiles are in the order of 1.39g steel cylinder 0.87g steel ball 0.44g steel ball. So far, it can be concluded that the type of projectile used affects ballistic test results. Thus the same type of projectile should be used when comparing ballistic test results of two materials.

The effect of the type of projectiles on ballistic impact test results were also studied in [38, 83, 64]. Montgomery et al [64] and Lim et al [83] observed that that the effect of bullet geometry decreases as the number of plies increases. It was observed in this study that the difference between E_{50} results against 0.44g steel balls and 0.87g steel balls is increased as the number of plies increases as shown in figure 6.9.

6.6.3.2 Effect of thickness

In database 1, composite materials 5HSC-4-VE, 5HSC-8-VE and 5HSC-12-VE are made from same fabric materials. The only difference between them is the number of layers of fabrics used, i.e. thickness. A linear relationship was observed between V_{50} results of these three composites and their areal densities in figure 6.6. This is not the case for their E_{50} results. As areal density of the composite increases, the acceleration in the increase of E_{50} increases.

In database 2, composite materials PWEG1-4-VE, PWEG1-6-VE, PWEG1-8-VE, PWEG1-12-VE and PWEG1-14-VE are manufactured using same plain woven E-glass fabrics. V_{50} results as well as E_{50} results of these materials can be divided into three groups according to projectiles used. In group 1, PWEG1-4-VE, PWEG1-8-VE and PWEG1-12-VE were impacted by 0.44g steel balls. In group 2, PWEG1-4-VE, PWEG1-6-VE, PWEG1-8-VE, PWEG1-12-VE and PWEG1-14-VE were impacted by 0.87g steel balls. There is only one V_{50} result in group 3. Thus no trend line can be applied. It can be seen in figure 6.7 that as areal density increases the rate of the increase of V_{50} increases in both group 1 and 2. Linear relationships were observed between E_{50} results and areal densities in group 1 and 2 in figure 6.7. Although linear relationship between perforation energies and target areal densities are new, bilinear relationships between perforation energies and target thickness or damage areas are not. Bilinear relationships between perforation energies and target thickness were observed by Gellert et al[38]. Bilinear relationships between perforation energies and damage areas were observed in [72, 75]. It is possible that the relationships between perforation energies and target areal densities are bilinear or even non-linear overall. But in the range of areal densities tested, the relationships are linear.

6.6.3.3 Effect of fibre material

Composite materials PWC-6-VE in database 3 and PWEG1-4-VE, PWEG1-6-VE, PWEG1-8-VE in database 2 were all manufactured using plain woven fabrics with similar areal density. The effect

Table 6.3: Fibre property U defined by Cunniff [26]

Fibre type	Young's modulus/GPa	U.T.S/GPa	Tensile strain/%	Density/gcm	UB	Reference
E-glass	72.3	3.445	4.8	2.57	17.06	[31]
Carbon	230	3.650	1.4	1.76	16.60	[76]
Kevlar	130	3.4	2.5	1.45	27.75	[93]

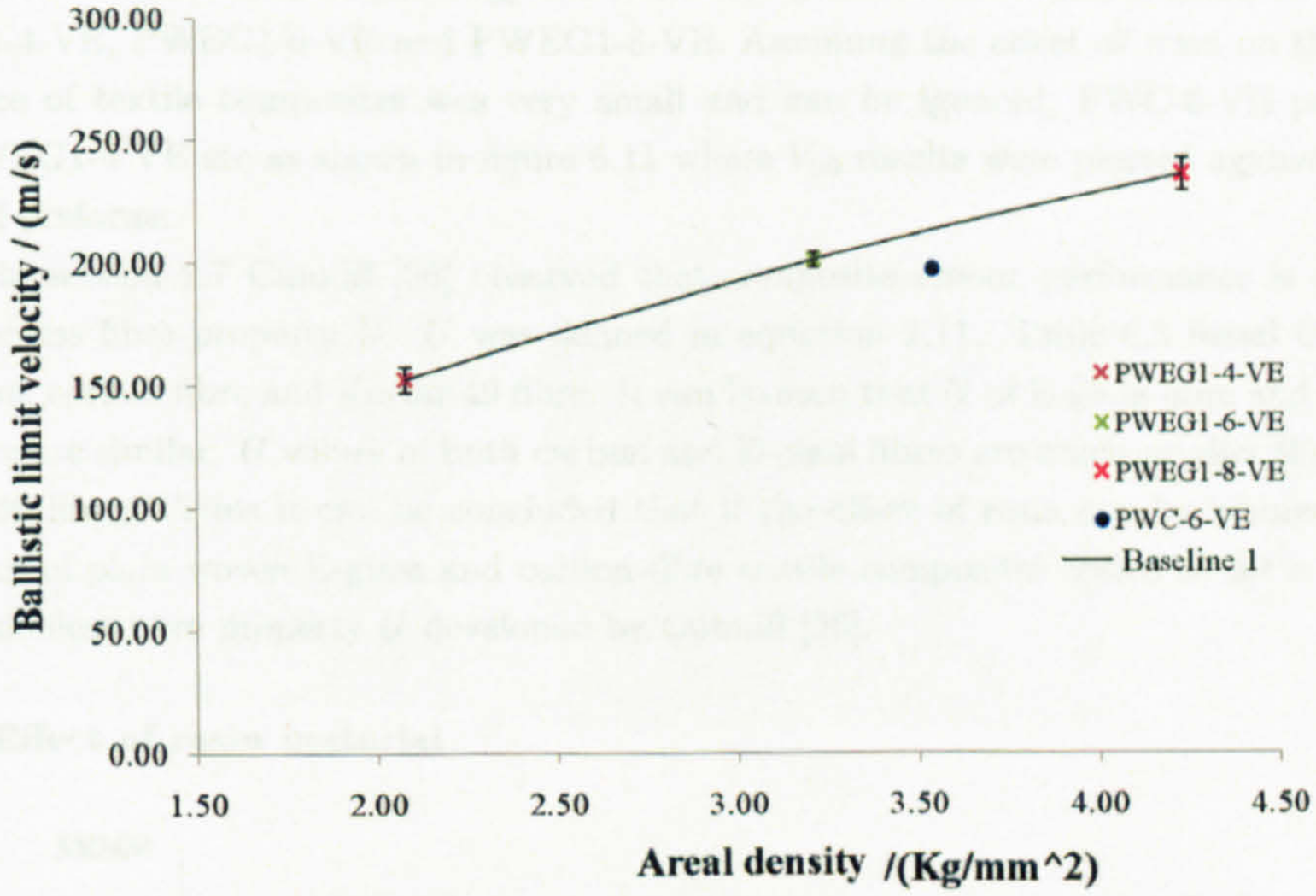

Figure 6.10: **Effect of fibre material on V_{50} results** - V_{50} versus areal density of composite .

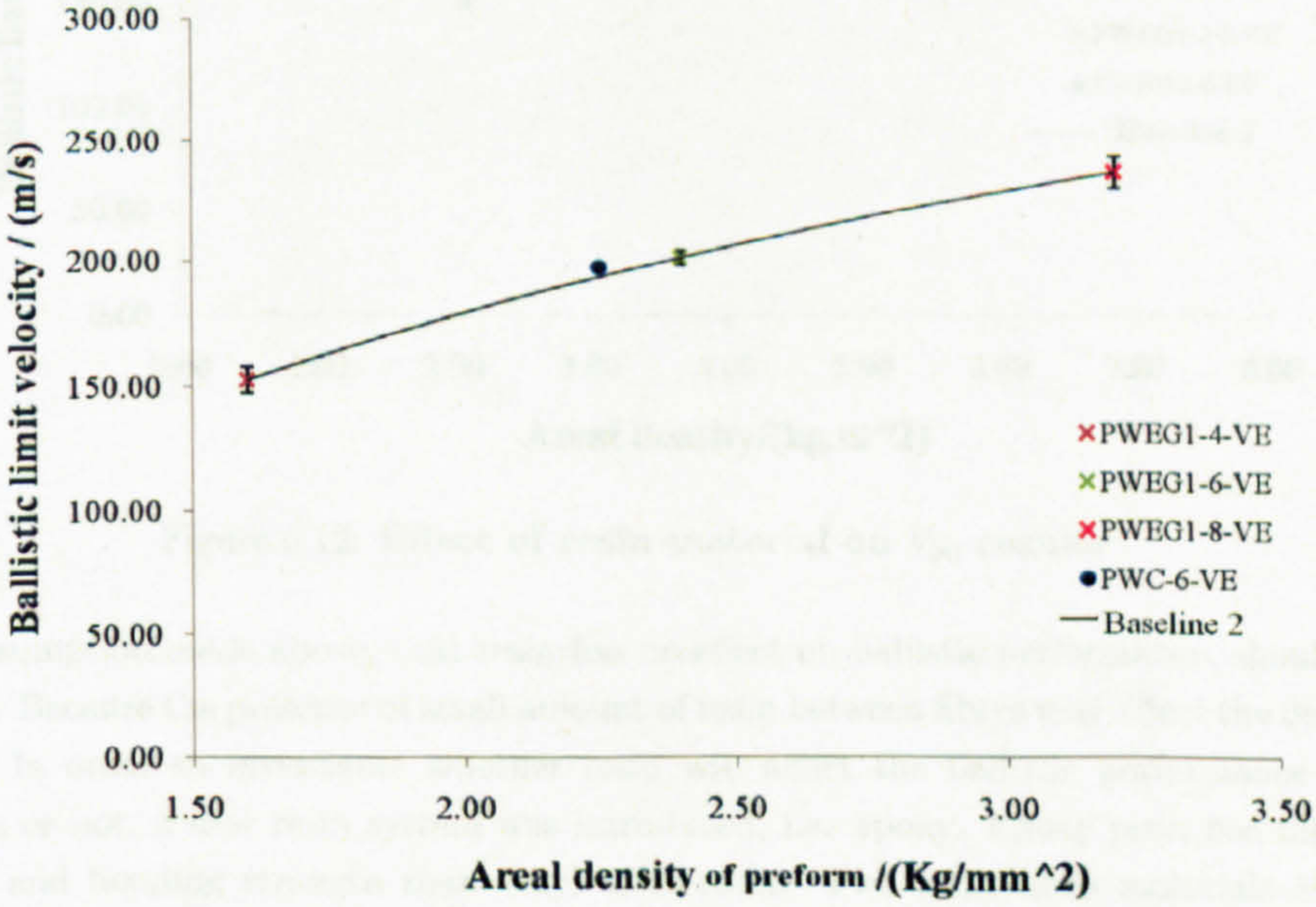

Figure 6.11: **Effect of fibre material on V_{50} results** - V_{50} versus areal density of preform .

of fibre materials on ballistic performance of textile composites can studied by investigating their ballistic performance. V_{50} results of all these composites impacted by 0.87g steel balls are shown in figure 6.10. It can be seen that the V_{50} of PWC-6-VE is below the trendline fitted to the results of PWEG1-4-VE, PWEG1-6-VE and PWEG1-8-VE. Assuming the effect of resin on the ballistic performance of textile composites was very small and can be ignored, PWC-6-VE performs as well as PWEG1-4-VE etc as shown in figure 6.11 where V_{50} results were plotted against the areal densities of preforms.

Recall in section 2.7 Cunniff [26] observed that composite amour performance is coupled to a dimensionless fibre property U. U was defined in equation 2.11. Table 6.3 listed U values of E-glass fibre, carbon fibre and Kevlar 49 fibre. It can be seen that U of E-glass fibre and U value of carbon fibre are similar. U values of both carbon and E-glass fibres are much smaller than U value of Kevlar 49 fibres. Thus it can be concluded that if the effect of resin can be ignored, ballistic performance of plain woven E-glass and carbon fibre textile composites tested so far is related to the dimensionless fibre property U developed by Cunniff [26].

6.6.3.4 Effect of resin material

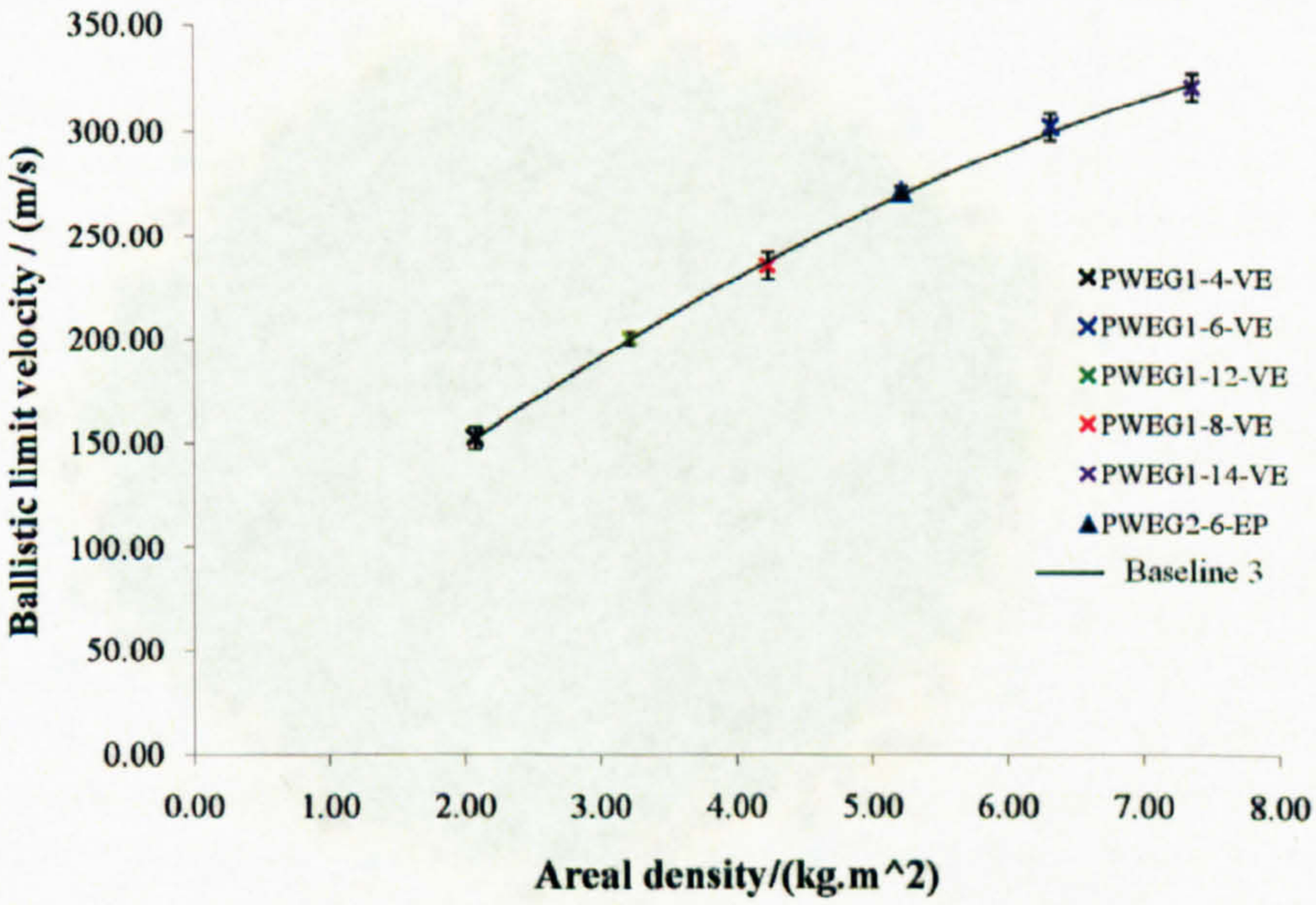

Figure 6.12: **Effect of resin material on V_{50} results .**

The assumption made above, that resin has no effect on ballistic performance, should be used cautiously. Because the presence of small amount of resin between fibres may affect the deformation of fibres. In order to investigate whether resin will affect the ballistic performance of textile composites or not, a new resin system was introduced, i.e. epoxy. Epoxy resin has much better toughness and bonding strength than vinyl ester resin. Two composites materials with epoxy resin and plain woven fabrics were manufactured. They are PWC-6-EP and PWEG2-6-VE. V_{50} value of PWC-6-EP is $187.04 \pm 2.3 m/s$. V_{50} of PWC-6-VE is $196.9 \pm 2.0 m/s$. In addition, the areal density of PWC-6-EP is 3.4% higher than that of PWC-6-VE. Visual observation of the damaged specimens of PWC-6-EP reviews that petalling of composite materials in the rear side

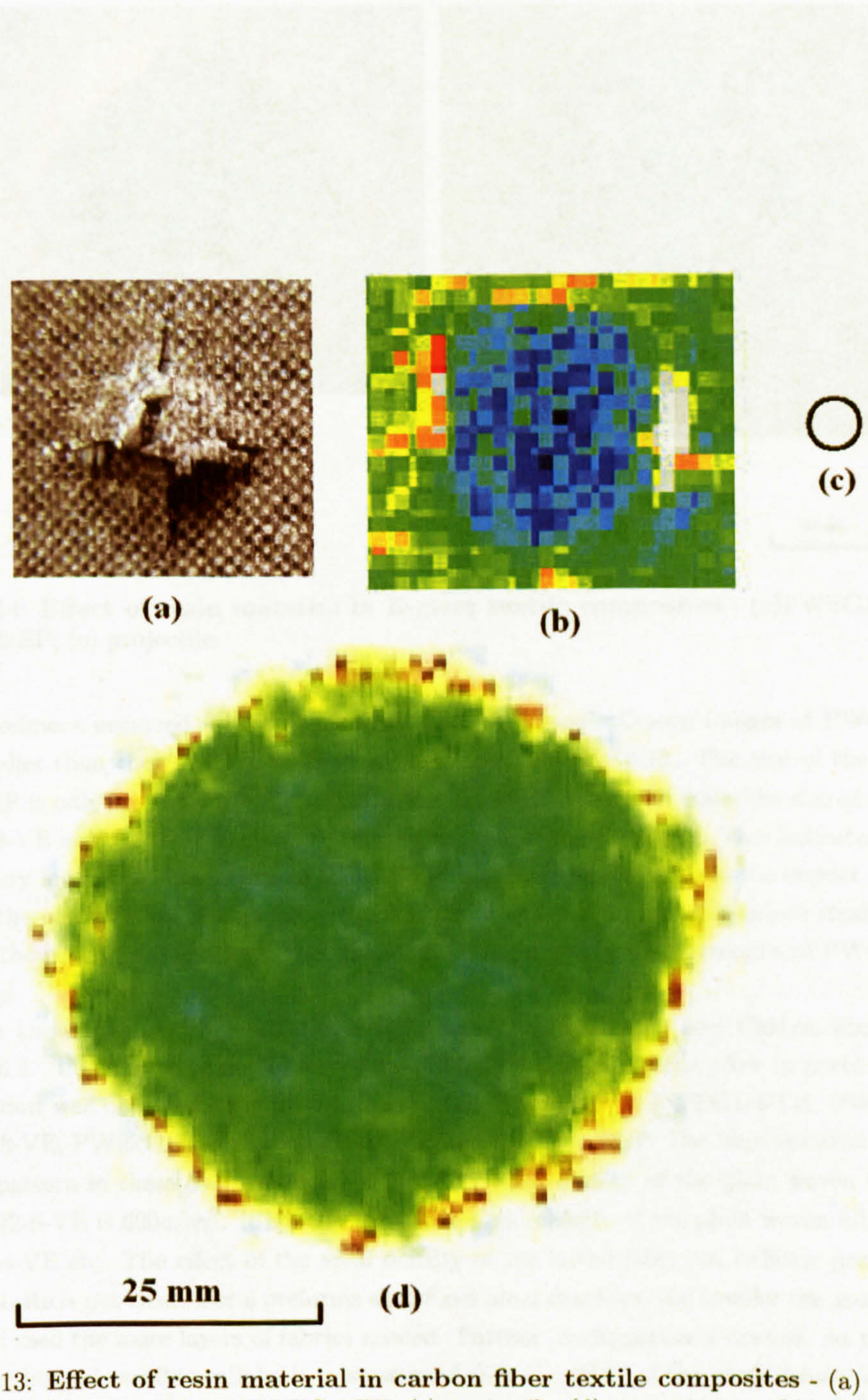

Figure 6.13: **Effect of resin material in carbon fiber textile composites** - (a) petalling in PWC-6-EP; (b) c-scan image of PWC-6-EP; (c) projectile; (d) c-scan image of PWC-6-VE.

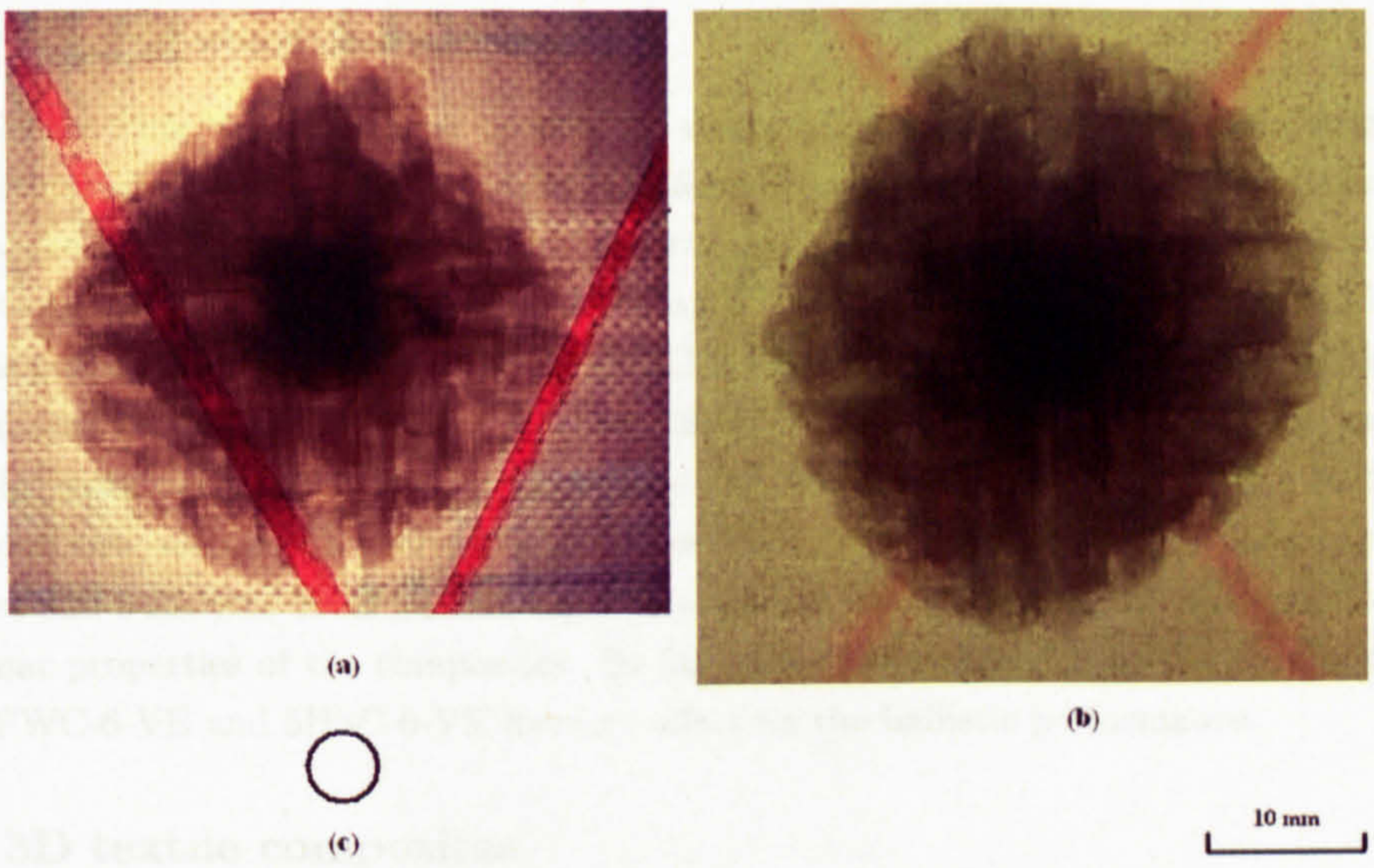

Figure 6.14: **Effect of resin material in E-glass textile composites** - (a)PWEG1-6-VE; (b) PWEG2-6-EP; (c) projectile.

of the specimens occurred as shown in figure 6.13. Ultrasonic C-scan images of PWC-6-EP are much smaller than that of PWC-6-VEP as illustrated in figure 6.13. The size of the damage in PWC-6-EP is only around 4 times the size of the size of the projectile while the size of the damage in PWC-6-VE is more than 10 times the size of the size of the projectile. This indicates that there is no or very few big delaminations in PWC-6-EP specimens resulting from the impact. This is the result of the combination of high bonding strength of epoxy resin and low failure strain of carbon fibre. Without big delaminations, the advantage of high interlaminar strength of PWC-6-EP can be ignored.

As we know, E-glass fibre has higher failure strain than Kvelar and Carbon fibre as shown in table 6.3. Petalling was not observed in PWEG2-6-VE specimens after impacts. Extensive delamination was observed. Figure 6.12 shows the V_{50} values of PWEG1-4-VE, PWEG1-6-VE, PWEG1-8-VE, PWEG1-12-VE, PWEG1-14-VE and PWEG2-6-EP. The fibre material and biaxial weaving pattern in these composites are same. The areal density of the plain woven fabrics used in PWEG2-6-VE is $600g/m^2$. It is bigger than the areal density of the plain woven fabrics used in PWEG1-4-VE etc. The effect of the areal density of the initial fabric on ballistic performance of the composite is not clear. For a preforms with fixed areal densities, the smaller the areal density of the fabric used the more layers of fabrics needed. Further investigation is needed. At the moment, due to the limited results availabe it was assumed that the effect of the areal density of the fabric on ballistic performance of the composite was minor compared to the effect of the areal density of the whole composite. On this basis, figure 6.12 illustrated that the resin material has no effect on the ballistic performance of plain woven E-glass textile composites when impacted 0.87g steel balls.

6.6.3.5 Effect of weaving structure

Two biaxial weaving structures were used in database 1, 2, 3, and 4. They are plain weaving and 5 harness satin weaving. The plain woven carbon fabrics used in PWC-6-VE and the 5 harness satin weaves used in 5HSC-6-VE have same fibre material and areal density. Vinyl ester resin was used for both PWC-6-VE and 5HSC-6-VE. Thus the effect of weaving structure can be studied by looking at ballistic performance of PWC-6-VE and 5HSC-6-VE. V_{50} value of 5HSC-6-VE is $202.8 \pm 3.9 m/s$ which is similar to that of PWC-6-VE which is 196.86 ± 1.90. Thus weaving structure has no effect on ballistic performance here. Both plain weaves and 5 harness satin weaves belong to 2D weaves. Damage patterns such as delamination and fibre fractures will occur in both plain woven textile composites and 5 harness satin weaves, especially delamination. Delamination is dependent on the interlaminar properties of the composites. So far it can be conduced that the crimping angles of yarns in PWC-6-VE and 5HSC-6-VE have no effect on the ballistic performance.

6.6.4 3D textile composites

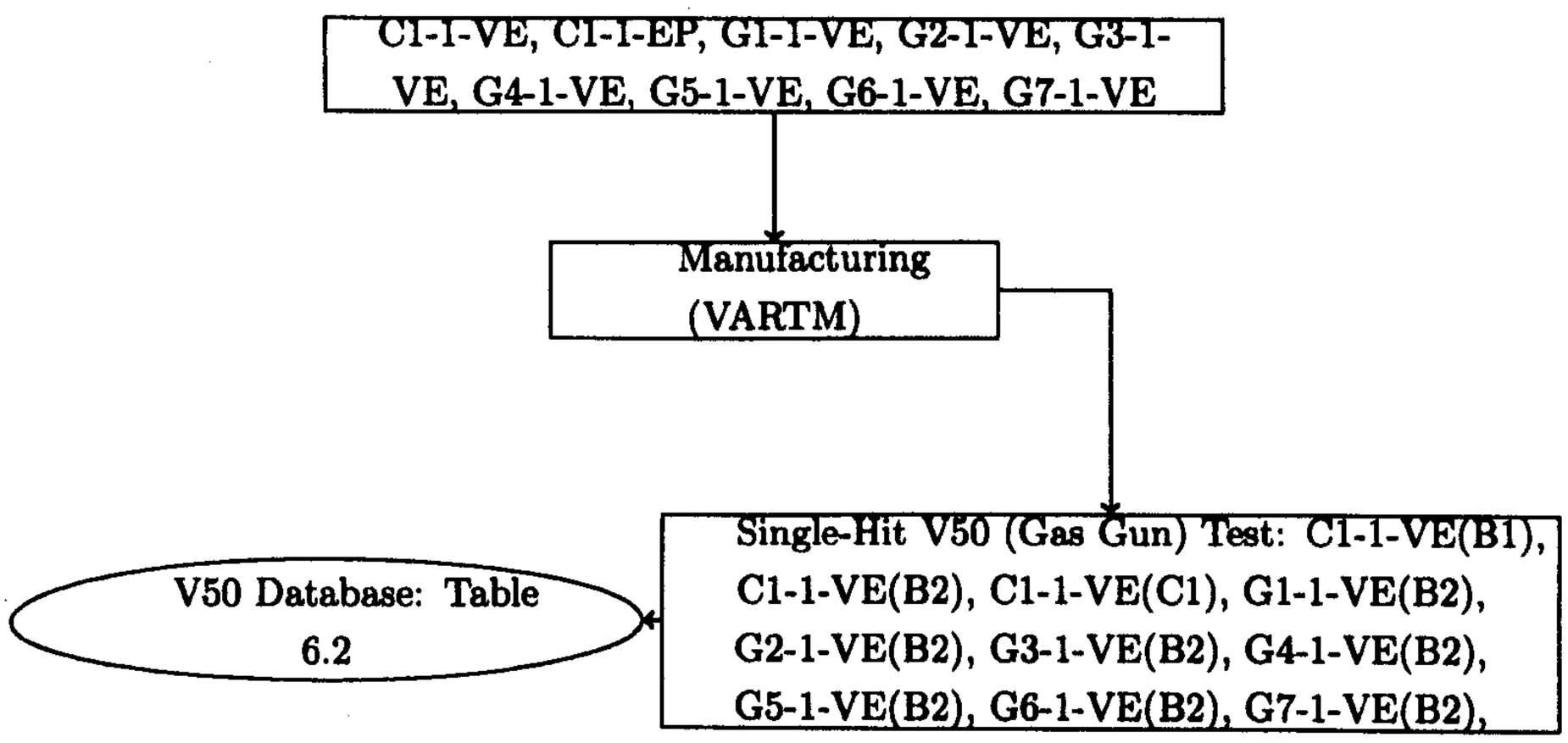

Figure 6.15: **Gas gun tests of 3D woven textile composites** - +=together with; B1=tested using 0.44g steel balls; B2=tested using 0.87g steel balls; C1=tested using 1.39g cylinders.

6.6.4.1 V_{50} results

3D textile composites are the first group of new materials tested. As discussed in section 2.12.8, Brandt et al [13] observed that energy absorption of 3D textile composites during low velocity impact is 2.5 times that of 2D textile composites. The flow chart shown in figure 6.15 illustrates the first stage of the process of assessing 3D textile composites. Table 6.2 lists all the V_{50} results of 3D textile composites. 3D textile composites will be assessed by comparing their V_{50} results to that of 2D textile composites in the V_{50} databases.

Specimens of 3D textile composites C1-1-VE were impacted by three kinds of projectiles, i.e. 0.44g steel ball, 0.87g steel ball, and 1.39g cylinder. The V_{50} value of C1-1-VE tested with 0.44g steel balls was plotted against baseline 1 and baseline 2 in figure 6.16 and figure 6.17 respectively. It can be seen that C1-1-VE performed better than materials in baseline 1 for 5-harness satin,

Table 6.4: Volume fraction of 2D and 3D textile composites

Material	Volume fraction of fibre/%
G1-1-VE	42.6
G2-1-VE	40.9
G3-1-VE	36.6
G4-1-VE	39.2
G5-1-VE	41.4
G6-1-VE	41.7
PWEG1-4-VE	52.5
PWEG1-4-VE	53.2
PWEG1-4-VE	52.4
PWEG1-4-VE	54.1
PWEG1-4-VE	54.0

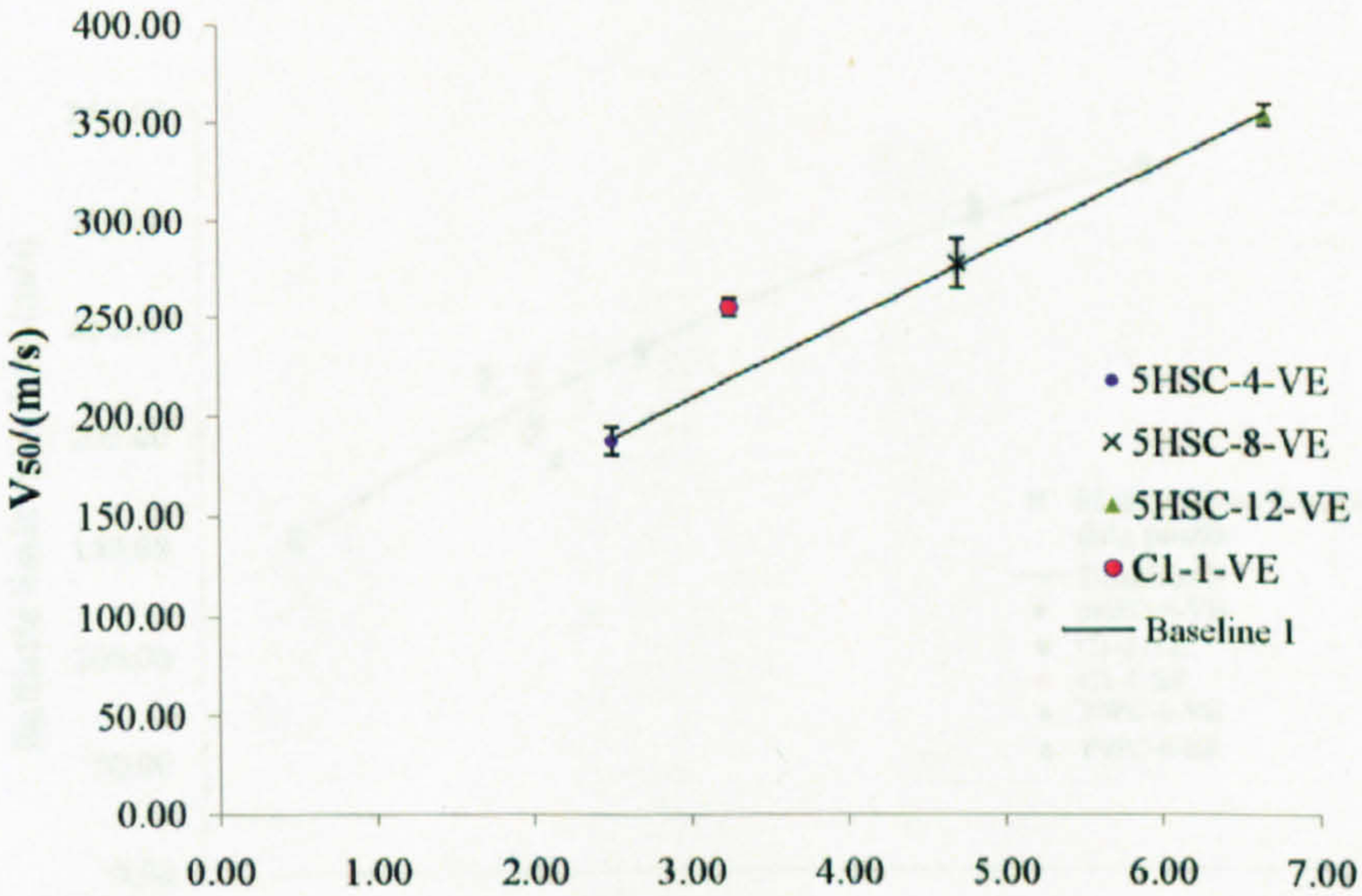

Figure 6.16: V_{50} **result of C1-1-VE against 0.44g steel balls** - C1-1-VE versus baseline 1 .

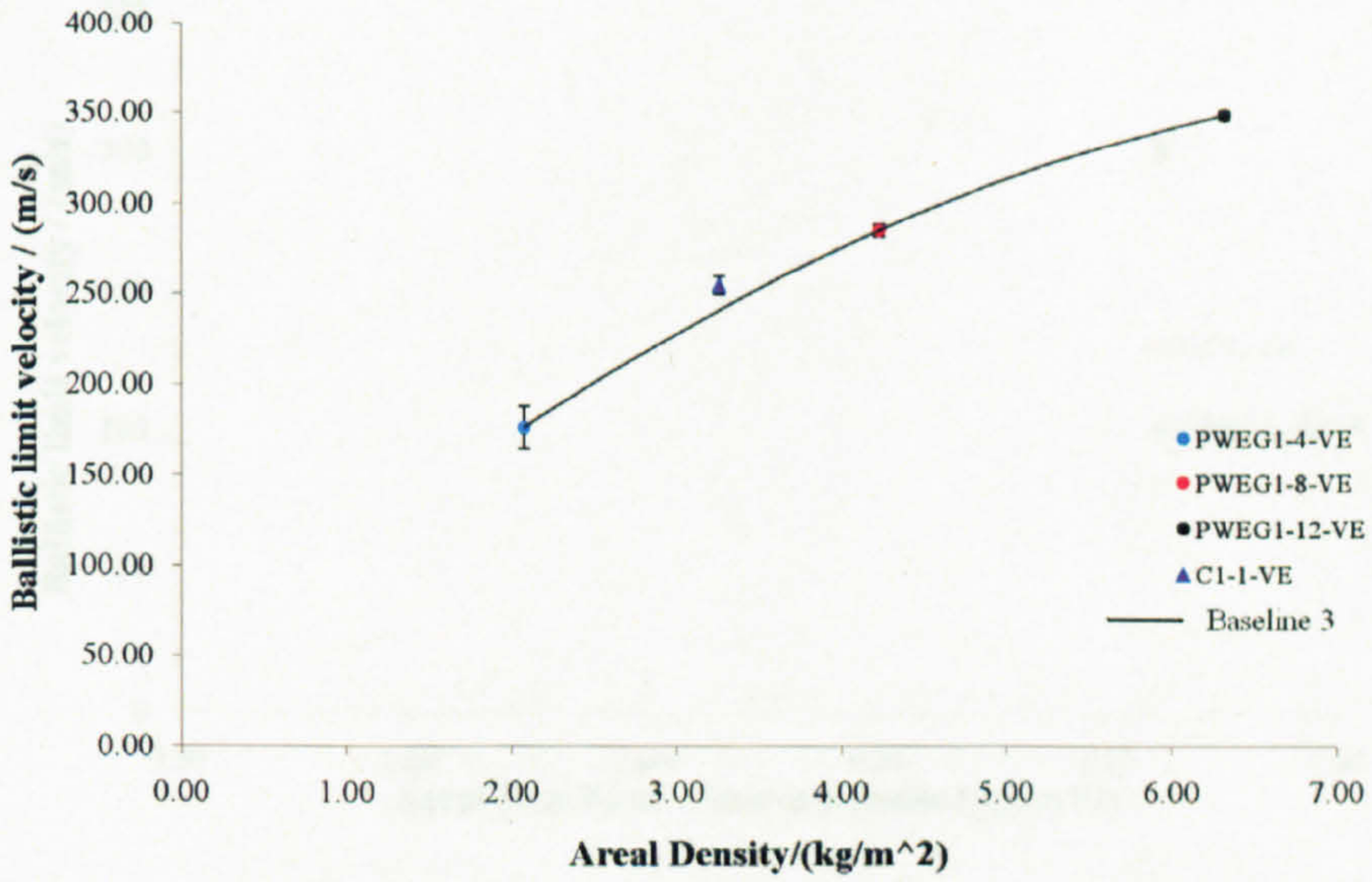

Figure 6.17: V_{50} **result of C1-1-VE against 0.44g steel balls** - C1-1-VE versus baseline 2.

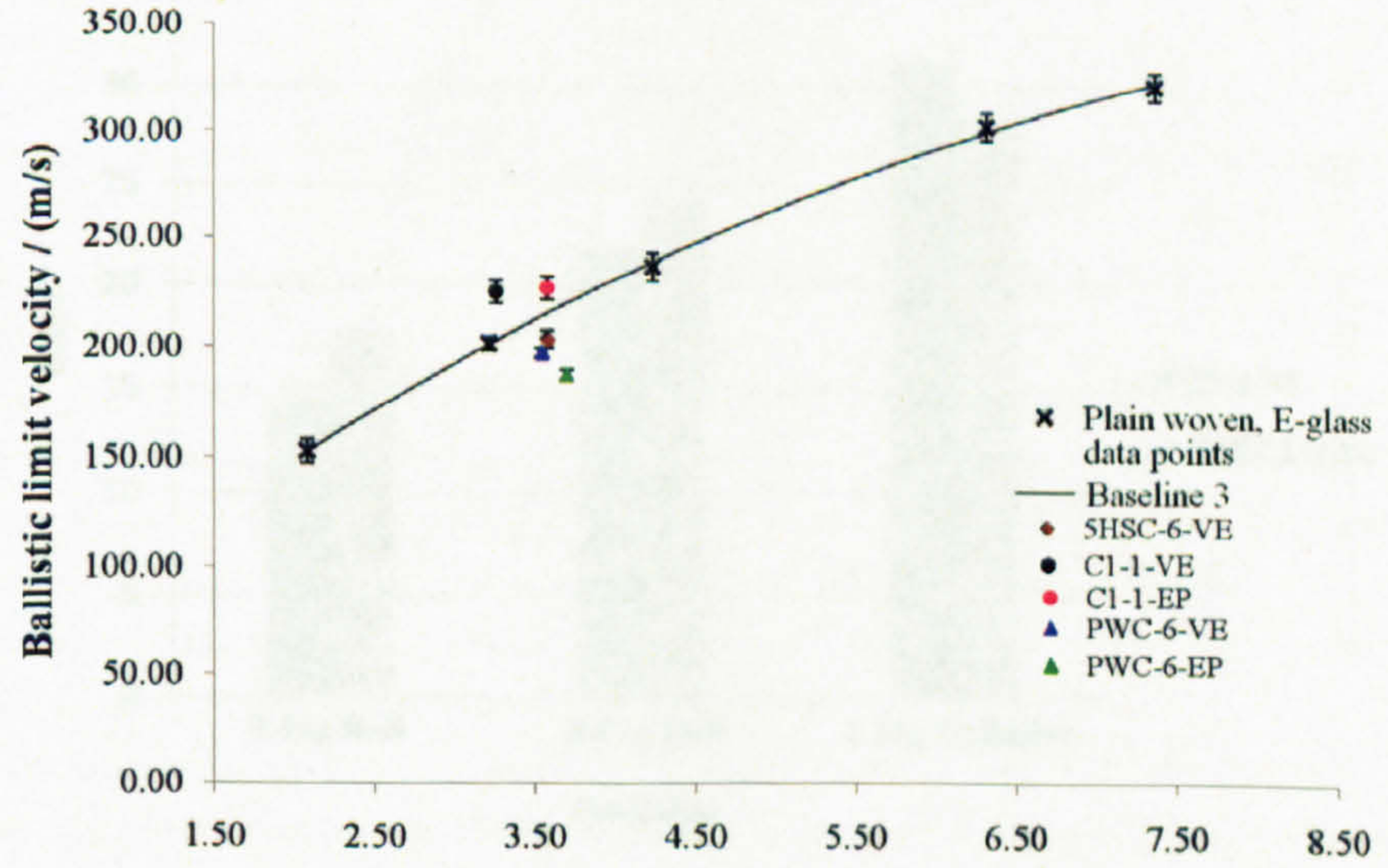

Figure 6.18: V_{50} **result of C1-1-VE against 0.87g steel balls** - C1-1-VE versus baseline 3.

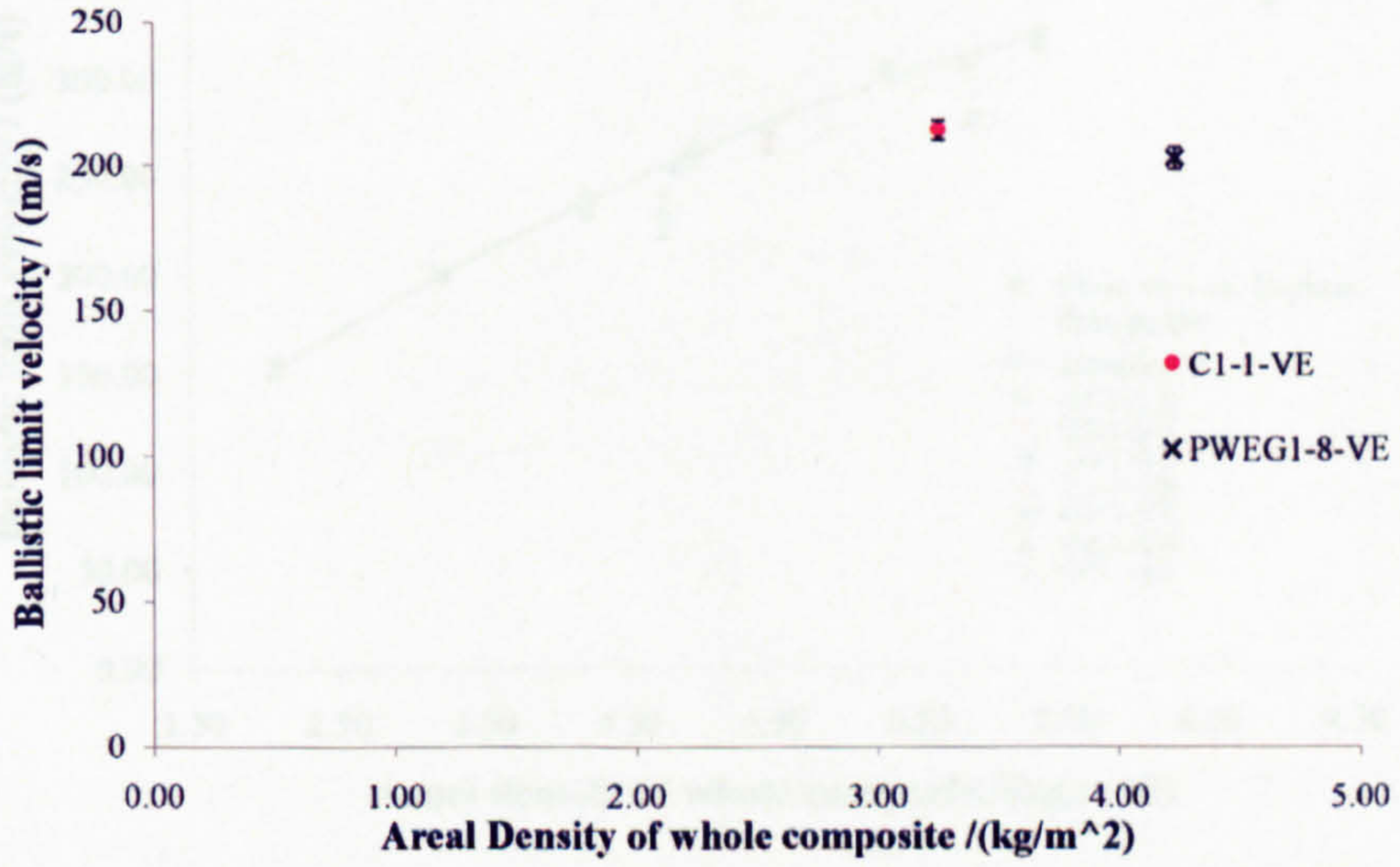

Figure 6.19: V_{50} **result of C1-1-VE against 1.39g cylinder** - C1-1-VE versus PWEG1-8-VE ·

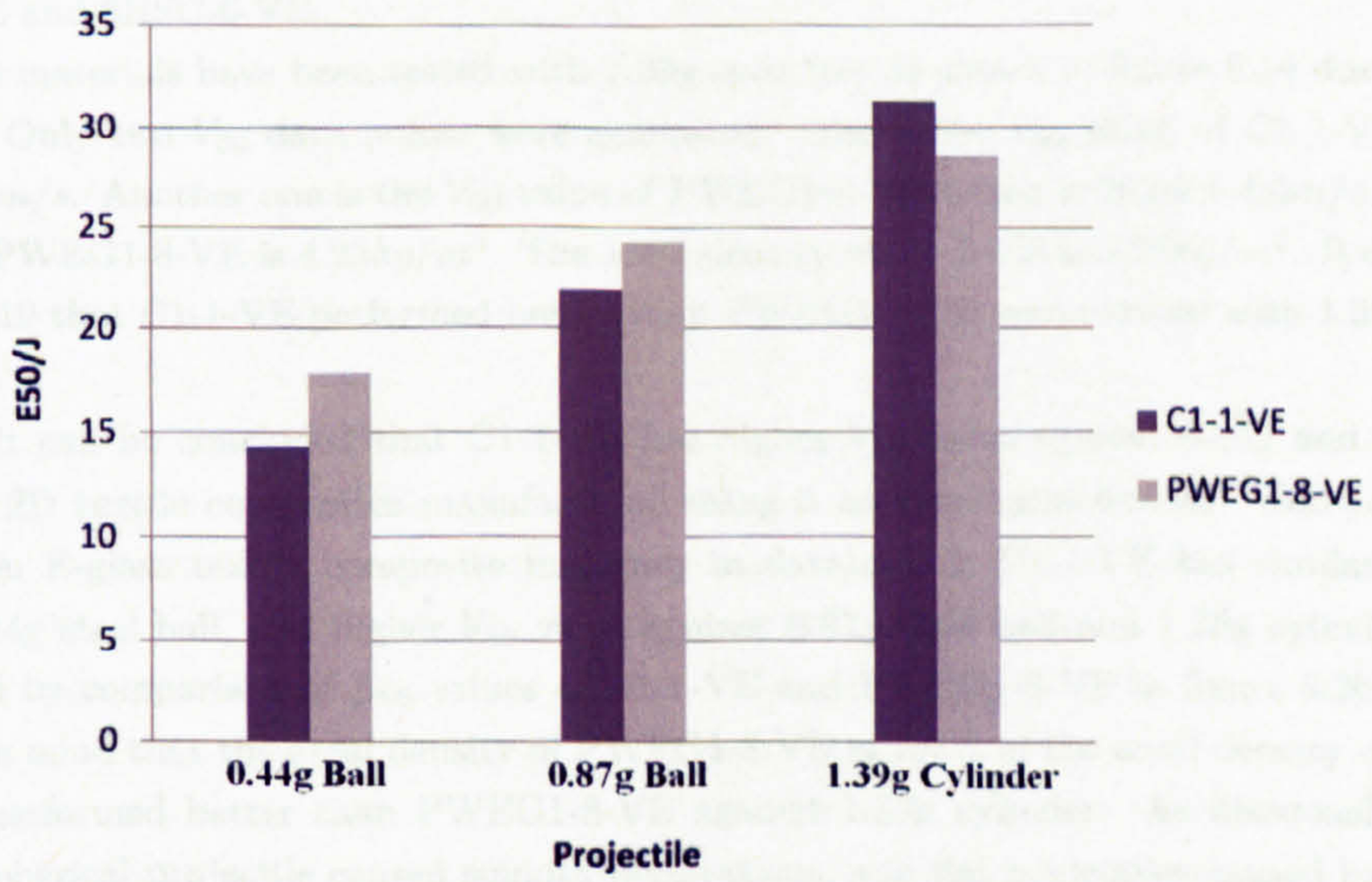

Figure 6.20: V_{50} **result of C1-1-VE and PWEG1-8-VE against three kinds of projectiles** . -

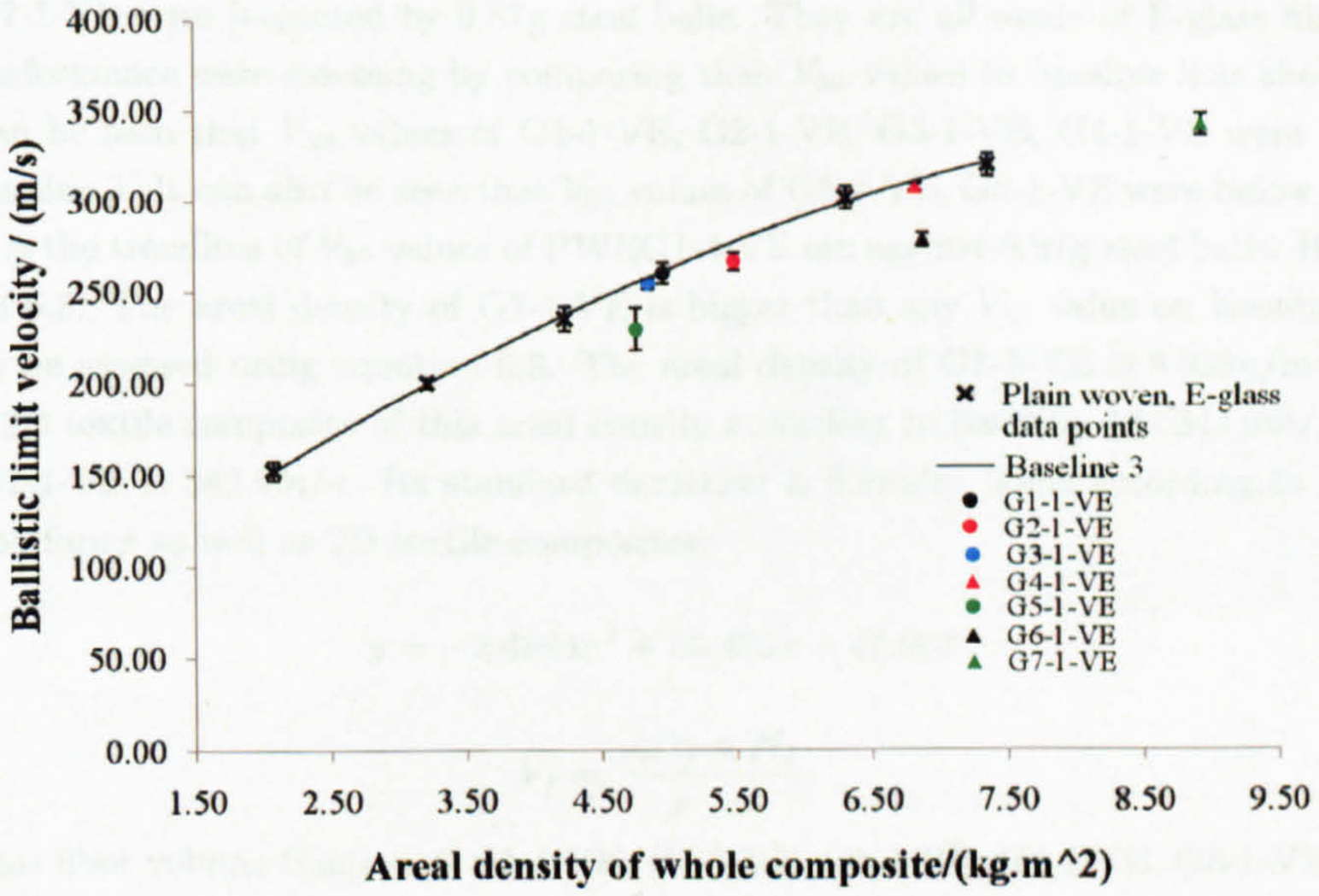

Figure 6.21: V_{50} **results of 3D E-glass woven textile composites .**

carbon fibre laminates, against 0.44g steel balls. It can be seen that C1-1-VE performed as well as materials in baseline 2 for plain woven E-glass laminates, against 0.44g steel balls.

The V_{50} value of C1-1-VE against 0.87g steel balls was plotted against baseline 3 for plain woven E-glass laminates against 0.87g steel balls and V_{50} values of PWC-6-VE and 5HSC-6-VE as shown in figure 6.18. It can be seen that C1-1-VE performed better than materials in baseline 3, PWC-6-VE and 5HSC-6-VE.

Limited materials have been tested with 1.39g cylinders as shown in figure 6.19 due to limited materials. Only two V_{50} data points were generated. One is the V_{50} value of C1-1-VE which is $212.2 \pm 3.3 m/s$. Another one is the V_{50} value of PWEG1-8-VE which is $202.9 \pm 4.0 m/s$. The areal density of PWEG1-8-VE is $4.23 kg/m^2$. The areal density of C1-1-VE is $3.26 kg/m^2$. It can be seen in figure 6.19 that C1-1-VE performed better than PWEG1-8-VE when tested with 1.39g cylinder projectiles.

So far it can be concluded that C1-1-VE has higher V_{50} value against 0.44g and 0.87g steel balls than 2D textile composites manufactured using 5 harness satin weaves. Compared to 2D plain woven E-glass textile composite materials in database 2, C1-1-VE has similar V_{50} value against 0.44g steel ball, and higher V_{50} value against 0.87g steel ball and 1.39g cylinder. This is highlighted by comparison of E_{50} values of C1-1-VE and PWEG1-8-VE in figure 6.20. It should be borne in mind that the areal density of PWEG1-8-VE is 131% of the areal density of C1-1-VE. C1-1-VE performed better than PWEG1-8-VE against 1.39g cylinder. As discussed in section 2.8, hemispherical projectile caused smooth perforations, and flat projectiles caused intense shear failures. The momentum transfer to the amour by a blunt projectile is much high than that of a sharp nosed projectile at ballistic velocities [50]. It seems that the presence of binder yarns in the thought-thickness direction of C1-1-VE increased the ballistic performance of C1-1-VE against 1.39g cylinder projectile more than against a 0.87g ball projectile.

Specimens of 3D textile composites G1-1-VE, G2-1-VE, G3-1-VE, G4-1-VE, G5-1-VE, G6-1-

VE and G7-1-VE were impacted by 0.87g steel balls. They are all made of E-glass fibres. Their ballistic performance were assessing by comparing their V_{50} values to baseline 3 as show in figure 6.21. It can be seen that V_{50} values of G1-1-VE, G2-1-VE, G3-1-VE, G4-1-VE were on or very close to baseline 3. It can also be seen that V_{50} values of G5-1-VE, G6-1-VE were below baseline 3. Baseline 3 is the trendline of V_{50} values of PWEG1-4-VE etc against 0.87g steel balls. Its equation is equation 6.3. The areal density of G7-1-VE is bigger than any V_{50} value on baseline 3. Thus it can only be assessed using equation 6.3. The areal density of G7-1-VE is $8.93kg/m^2$. The V_{50} value of a 2D textile composite of this areal density according to baseline 3 is $344.9m/s$. The V_{50} value of G7-1-VE is $342.9m/s$. Its standard deviation is $5.9m/s$. Thus according to baseline 3, G7-1-VE performs as well as 2D textile composites.

$$y = -2.4894x^2 + 55.485x + 47.907 \tag{6.3}$$

$$V_f = \frac{AD_f \times N_f}{\rho \times t} \tag{6.4}$$

The glass fiber volume fraction of G1-1-VE, G2-1-VE, G3-1-VE, G4-1-VE, G5-1-VE, G6-1-VE were measured by the resin burn-off technique according to ASTM D2584. The results are listed in table 6.4. The fiber volume fraction of C1-1-VE was not characterized. Because ignition loss method is not suitable for caron fiber textile composites. The fiber vloume fraction of G7-1-VE was also not characterized. Because there were Kevlar fibers in G7-1-VE. Ignition loss method is not suitable for Kevlar fiber textile composites. The glass fibre volume fraction of 2D plain woven textile composites such as PWEG1-4-VE were calculated using equation 6.4 where AD_f is the areal density of plain woven E-glass fabrics, N_f is the number of layers of fabrics used, ρ is the density of glass fibre, and t is the thickness of the composite. Results are shown in table 6.4. The reason why burn-off was used is due to the fact that it is difficult to measure the areal density of 3D fabrics accurately.

During the characterization of the fibre volume fraction in both 2D and 3D textile composites, it was assumed that there was no void. Thus the fibre volume fraction results are open to some degree of error. Figure 6.22 shows microscopy images of hand-polished 2D and 3D textile composites used in this study. It can be seen that there are only a few voids. It has been observed that the void content in the selected area of C1-1-VE in figure 6.22 (a) was only 0.1%. The void content in the selected area of G1-1-VE in figure 6.22 (c) was only 0.4%. It can be seen in table 6.4 that the fibre volume fractions of 2D textile composites are around 53%. The fibre volume fractions of 3D textile composites are much smaller than their 2D counterparts. G3-1-VE has the lowest fibre volume fraction of 39.2%. There were significant difference between the volume fraction of 2D textile composites and 3D textile composites. Thus the error caused by the assumption that there were no void consents can be ignored.

Two factors contributed to low fibre volume fraction of 3D textile composites. The first one is the lack of straight warp yarns in G1-1-VE etc. The second one is the much bigger tow size G1-1-VE etc have than plain woven fabrics. Bibo and Hogg [10] studied the energy absorption of various 2D textile composites. They suggested that in through-penetration impact the fibre volume fraction is the dominant factor controlling energy absorption. The specific fibre arrangement is a second-order effect and the resin contributes no noticeable effects at all. The results in section 6.6.3.4 show that resin affect the V_{50} value by varying areal density of the composite.

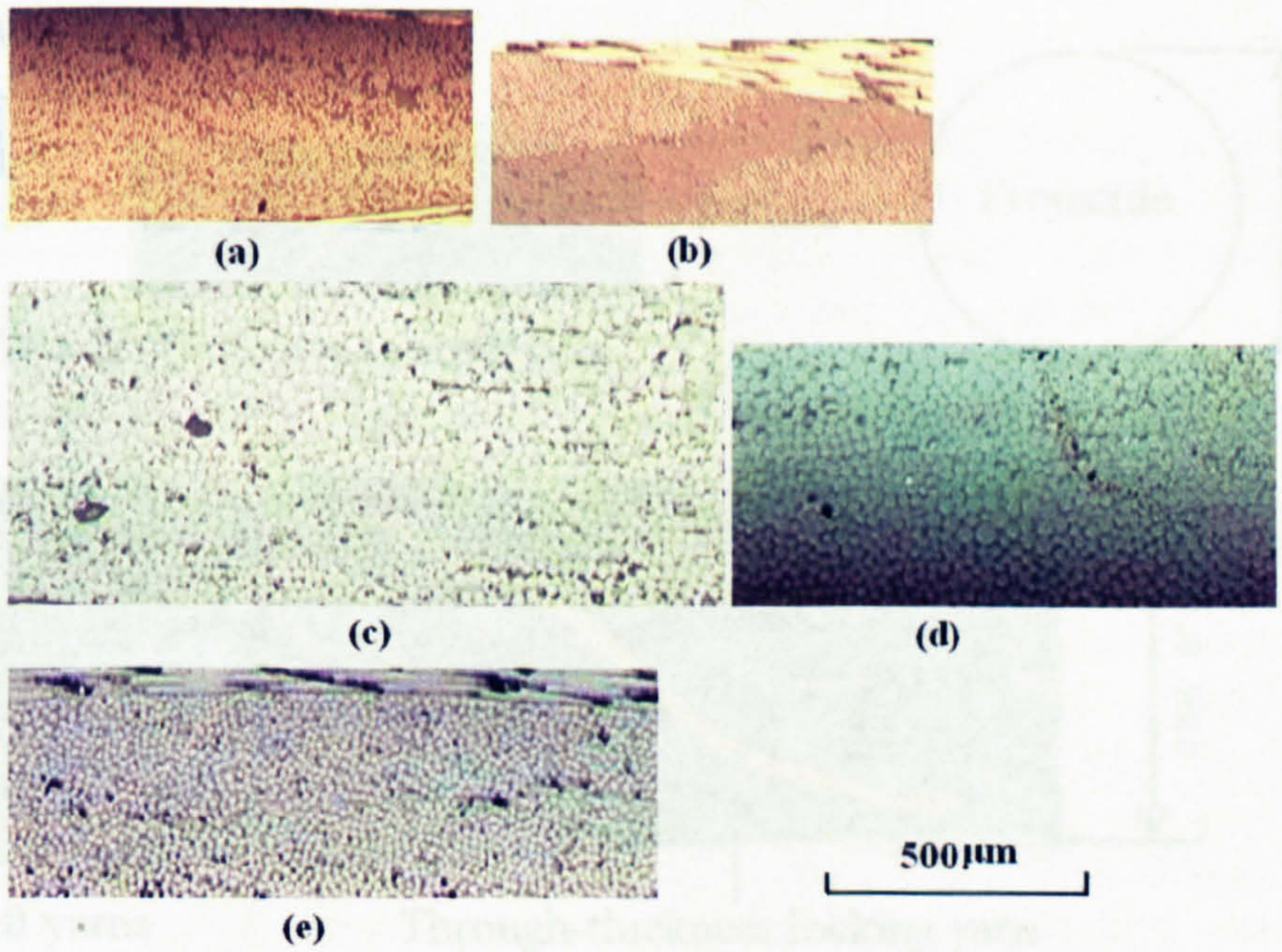

Figure 6.22: **Hand-polished 2D and 3D textile composites by the VARTM process and imaged with optical microscope. Voids (black areas) are present.** - (a)C1-1-VE; (b)5HSC-6-VE; (c)G1-1-VE; (d) G2-1-VE; (e) PWEG1-8-VE.

So far it can be concluded that G1-1-VE, G2-1-VE, G3-1-VE, G4-1-VE and G7-1-VE performed as well as 2D textile composites in baseline 3 while G5-1-VE and G6-1-VE don't. The volume fractions of all 3D textile composites were smaller than that of 2D textile composites. One way to increase the volume fraction is to use smaller yarns. Whether it is possible to increase V_{50} value by increasing fibre volume fraction of 3D textile composites is not clear.

6.6.4.2 Effect of yarn material and architecture of 3D woven fabrics

Recalling in chapter 5, yarn arrangements in all eight 3D woven textile composites were studied. Based on the information obtained in chapter 5, the following comparisons of the ballistic performance of two different 3D woven textile composites were carried out:

- C1-1-VE vs G7-1-VE: same yarn architecture, tow size, different confining of weft yarns
- G1-1-VE vs G2-1-VE: different amount and position of plain woven style yarns
- G3-1-VE vs G4-1-VE: single locking structures versus mixture of locking structures
- G4-1-VE vs G5-1-VE: mixture of locking structures through-out versus mixture of locking yarns only in weft yarn direction
- G1-1-VE, G2-1-VE, G3-1-VE, G4-1-VE, G5-1-VE versus G6-1-VE:uniform weft yarns vs. mixture arrangement of weft yarns

C1-1-VE and G7-1-VE It has been observed in this chapter that C1-1-VE performed better than 2D textile composites in databases, and G7-1-VE performed as well as 2D textile composites.

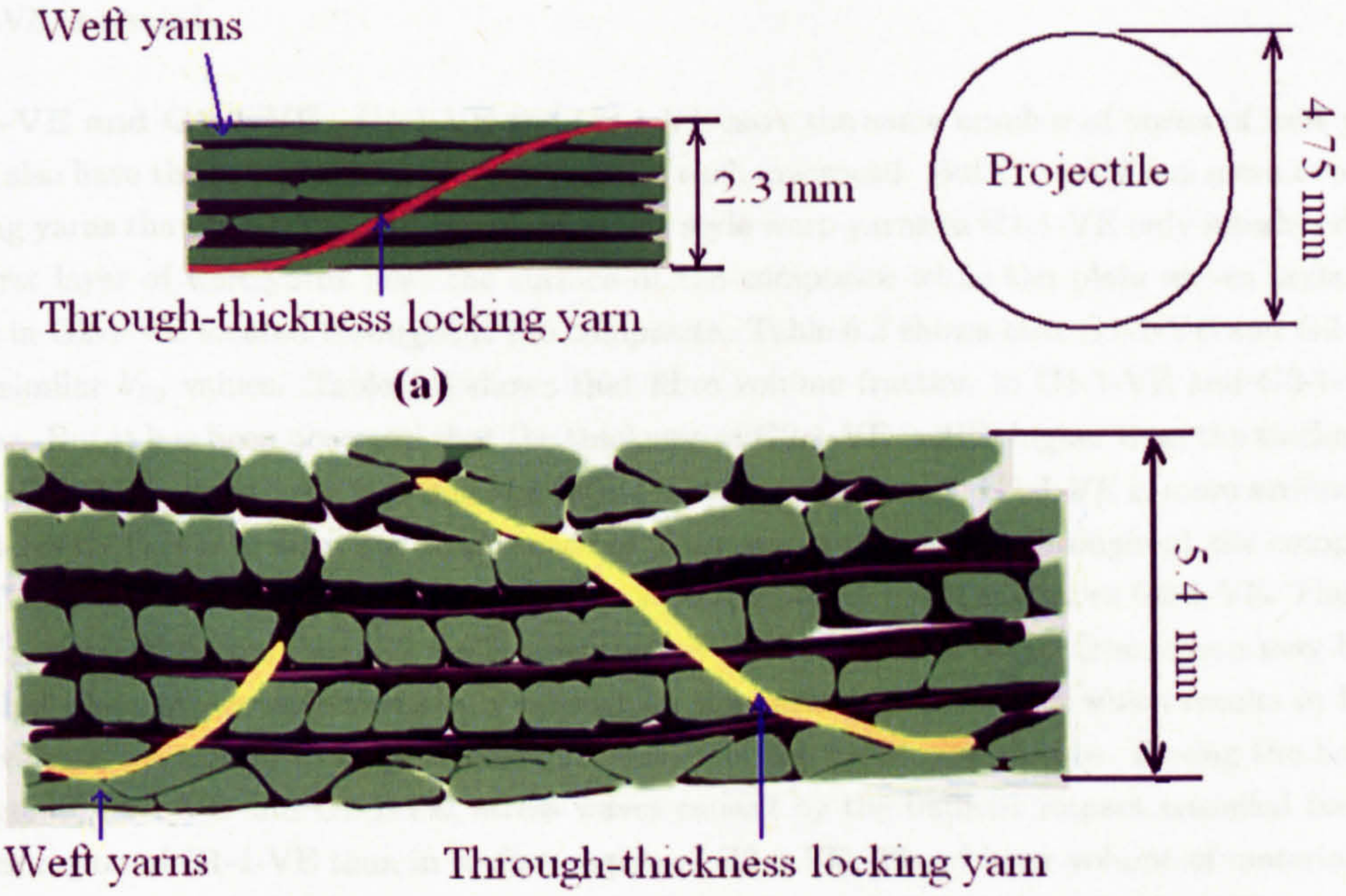

Fiugre 6.23 Thickness of C1-1-VE and G7-1-VE: (a) C1-1-VE; (b) G7-1-VE.

Recall in section 5.2.2.2, visualisation of yarn arrangements in C1-1-VE and G7-1-VE reviewed that weft yarns in C1-1-VE merged with each, and weft yarns in G7-1-VE were wrapped with nylon yarns. Thus although lateral collisions of weft yarns occurred, merging of weft yarns didn't. This resulted in much bigger thickness of G7-1-VE than C1-1-VE as shown in figure 6.23. In C1-1-VE and G7-1-VE, the majority of the yarns are non-crimp yarns. Thus it can be imagined that delaminations could occur when C1-1-VE and G7-1-VE were subjected to ballistic impacts, and may even be the dominant damage mechanism. The areal density of G7-1-VE is $8.93kg/m^2$, and the areal density of C1-1-VE is $3.26kg/m^2$. 2D woven textile composites 5HSC-6-VE and PWEG1-17-VE have areal densities similar to C1-1-VE and G7-1-VE respectively. There are five weft yarn layers and four straight warp yarn layers in both C1-1-VE and G7-1-VE, i.e. 9 layers. There are six and 17 layers in 5HSC-6-VE and PWEG1-17-VE respectively. Much smaller number of layers exists in G7-1-VE compared to PWEG1-17-VE which results in low volume fraction and much less delamination. This is one reason why G7-1-VE has not performed better than 2D textile composites when tested with 0.87g ball. The bigger thickness of G7-1-VE compared with C1-1-VE means that the ratio of the diameter of the projectile to the thickness of the composite is smaller for G7-1-VE compared with C1-1-VE, i.e. the 0.87g steel balls are relatively small compared to G7-1-VE but relatively big compared to C1-1-VE. Recall in figure 6.20, it has been observed that the bigger the projectile the better the ballistic performance of C1-1-VE when compared with 2D textile composites. Thus it can be imagined that G7-1-VE may perform better than 2D textile composites when tested with projectiles that are bigger than 0.87g balls. The last but not the least reason may be the different binder yarn materials used in C1-1-VE and G7-1-VE. Further investigation regarding to the effect of binder yarns on the ballistic performance of C1-1-VE and

G7-1-VE is needed.

G1-1-VE and G2-1-VE G1-1-VE and G2-1-VE have the same number of layers of weft yarns. They also have the same amount of warp yarns in each macrocell. But G1-1-VE has more two-layer locking yarns than G2-1-VE, and the plain woven style warp yarns in G1-1-VE only interlaced with the first layer of weft yarns near the surface of the composite while the plain woven style warp yarns in G2-1-VE located throughout the composite. Table 6.2 shows that G1-1-VE and G2-1-VE have similar V_{50} values. Table 6.4 shows that fibre volume fraction in G1-1-VE and G2-1-VE is similar. But it has been observed that the thickness of G2-1-VE is 21% higher than the thickness of G1-1-VE. This is due to the fact that the tilting of weft yarns rows in G1-1-VE is more serious than in G2-1-VE. This is in turn due to presence of plain woven style yarns throughout the composite. With lower areal density than G2-1-VE, G1-1-VE absorbed as much energy as G2-1-VE. Thus G1-1-VE performed better than G2-1-VE when tested with 0.87g steel balls. One reason may be the fact that plain woven style yarns only present on the surface of the fabric which results in higher fibre volume fraction in the region near the surface of the textile composites. During the ballistic impacts of G1-1-VE and G2-1-VE, stress waves caused by the ballistic impact travelled faster in surface region of G1-1-VE than in surface region of G2-1-VE. Thus bigger volume of materials will be involved in absorbing kinetic energies of the prjectiles in G1-1-VE than in G2-1-VE.

G3-1-VE, G4-1-VE and G5-1-VE There are three-layer locking yarns in G3-1-VE, G4-1-VE and G5-1-VE. In addition, G4-1-VE also has plain woven style warp yarns and 2 layer locking yarns, and G5-1-VE also has two-layer locking yarns, i.e. G4-1-VE and G5-1-VE have mixture of locking yarns. In G4-1-VE, different locking yarns are mixed throughout the composite, i.e. in both through-thickness direction and weft yarn direction. It was observed that although G3-1-VE has more layers of weft yarns than G4-1-VE, the areal density of G4-1-VE is 41% higher than that of G3-1-VE. Table 6.4 shows that G3-1-VE has very low fibre volume fraction. The low fibre volume fraction of G3-1-VE results in small area density of G3-1-VE which should at least similar to that of G4-1-VE. Computer simulation of yarn arrangements in 3D textile composites in chapter 5 reviewed that vertical collisions of weft yarns in G3-1-VE are more serious than in G4-1-VE. Although figure 6.21 shows that both G3-1-VE and G4-1-VE performed as well as 2D textile composites when tested with 0.87g balls, but the distortion of its ideal structure reduces its thickness greatly. Thus if assessed based on both single hit V_{50} and manufacturability, G4-1-VE performed better than G3-1-VE. It was observed that G5-1-VE performed not as well as 2D textile composites in databases. Computer simulation of yarn arrangements in 3D textile composites in chapter 5 revealed that G5-1-VE has much looser distribution of warp yarns than G3-1-VE and G4-1-VE, i.e. lower degree of packing. This results in lower degree of lateral covering of fibres in G5-1-VE than in G3-1-VE and G4-1-VE which may be the reason for the poor ballistic performance of G5-1-VE.

G1-1-VE etc vs G6-1-VE It has been observed that G6-1-VE performed not as well as 2D textile composites in databases. Computer simulation of yarn arrangements in 3D textile composites in chapter 5 reviewed that G6-1-VE has much looser distribution of warp yarns than other 3D textile composites. This results in lower degree of lateral covering of fibres in G6-1-VE than other 3D textile composites which may be the reason for the poor ballistic performance of G6-1-VE.

So far it can be concluded that although the use of nylon coating yarns as illustrated in figure 4.1 is good for the manufacturability of 3D textile composites, it is not good for single-hit ballistic impact performance of 3D textile composites. Because 3D textile composites with nylon coating yarns may have bigger thickness and lower fibre volume fraction than 3D textile composites with same yarn arrangement but without nylon coating yarns. It can also be concluded that the arrangements of warp yarns in 3D textile composites affect the single-hit ballistic impact performance of 3D textile composites. Placing more plain woven style warp yarns in the surface region is good for single-hit ballistic impact performance of 3D textile composites. Mixture of different kinds of multi-layer locking yarns in both weft yarn direction and through-thickness direction in 3D textile composites results in good packing of warp yarns and higher fibre volume fraction than 3D textile composites with only one kind of multilayer locking yarns both of which are good for single-hit ballistic impact performance of 3D textile composites. Mixture of different kinds of multi-layer locking yarns in only weft yarn direction may not achieve good packing of warp yarns. Low degree of packing of yarns in 3D textile composites may also be caused by the use uneven rows of weft yarns. Thus it can be concluded that not only 3D textile composites with uneven rows of weft yarns have poor manufacturability, they also have poor single-hit ballistic performance.

6.6.4.3 Effect of resin materials

In order to investigate the effect of the resin material on ballistic performance, the V_{50} value of C1-1-EP against a 0.87g steel ball was compared with that of C1-1-VE against a 0.87g steel ball. Both samples have identical number of carbon fibre plies in the initial preforms. The V_{50} value of C1-1-EP is $225.9m/s$ with standard deviation of $5.2m/s$. The V_{50} value of C1-1-VE is $224.3m/s$ with standard deviation of $5.3m/s$. On this bases the resin materials has no effect on V_{50} values. But it was observed that the areal density of C1-1-EP is 10% higher than that of C1-1-VE, suggesting that the amount of fibre breaking is the key parameter in this case.

Recall in section 6.6.3.4, large delamination was not observed in specimens of PWC-6-EP after impacts. C-scan images of specimens of C1-1-EP show delamination. But the size of delamination of C1-1-EP is smaller than that of C1-1-VE. It seems that the increase in energy absorption due to the increase of interlaminar strength and the decrease of energy absorption due to decreases in delamination area are balanced.

6.6.5 Non-crimp textile composites

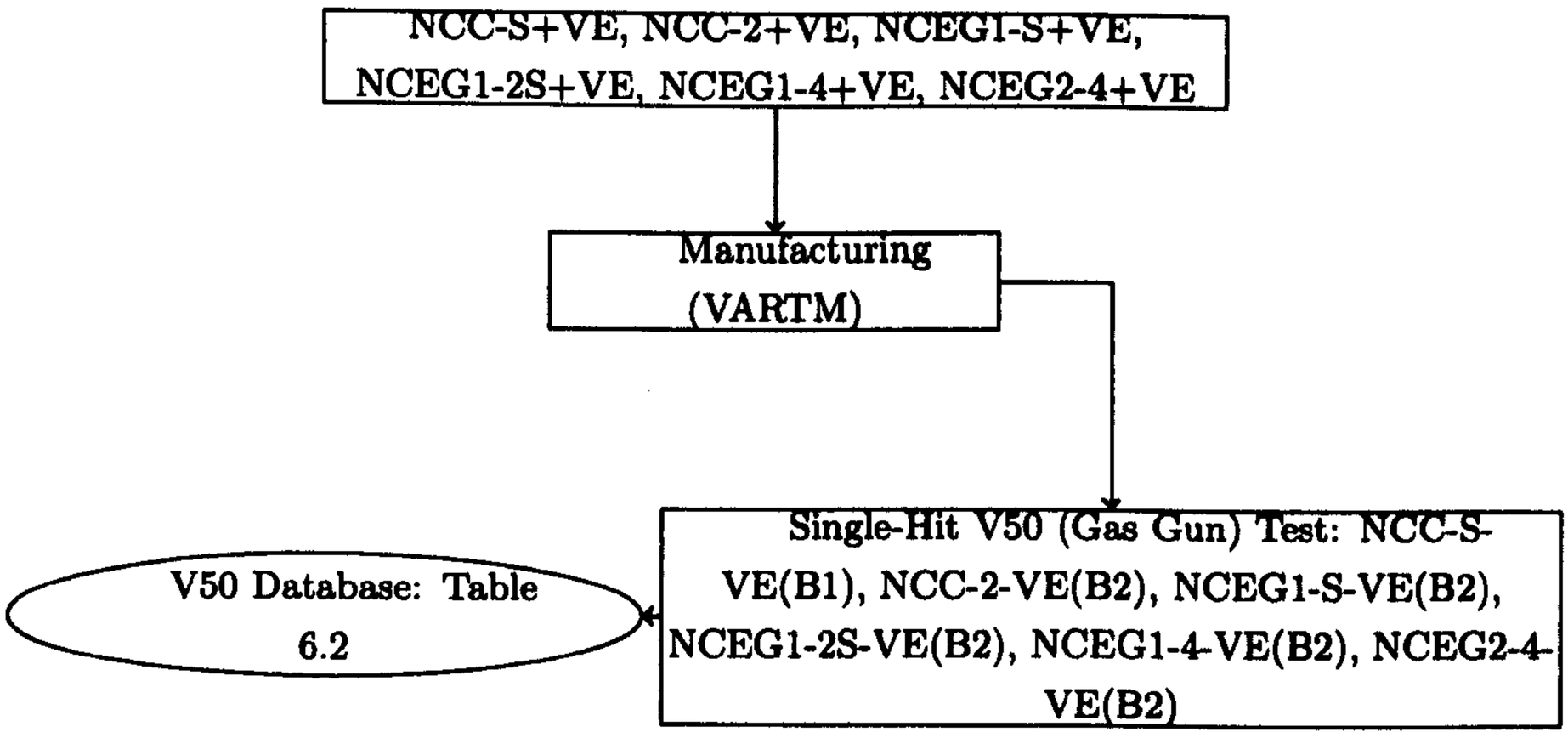

Figure 6.24: **Gas gun tests of 3D woven textile composites** - +=together with; B1=tesed using 0.44g steel balls; B2=tested using 0.87g steel balls.

6.6.5.1 V_{50}

Six non-crimp textile composites were tested using 0.44g and 0.87g steel ball as shown in figure 6.24. These non-crimp textile composites were manufactured using three kinds of biaxial fabrics as described in table 4.1. One is made from carbon fibres and two are made from E-glass fibres. Two non-crimp E-glass fabrics EBX-800 and EBX-602 are manufactured by COTECH. The former has higher areal density. The reason why two non-crimp E-glass fabrics were used was due to the availability of the mateirals. Non-crimp E-glass EBX-602 fabrics were used orginally. But the amount available was limited. Non-crimp E-glass EBX-800 fabrics were used after non-crimp E-glass EBX-602 fabrics were not available. The lay-up of fibres in all six non-crimp textile composites are listed in table 6.5.

Non-crimp textile composites were assessed by comparing their V_{50} to baseline 1 or 3 as shown in figure 6.25 and 6.26. It was observed that V_{50} values of all non-crimp textile composites are either on the baseline or very close to the baseline. This further suggests that fibre and resin materials control ballistic performance of 2D textile composites and not fabric structure. In terms of energy, fibre material properties control energy absorption in forms of fibre fractures. Resin

Table 6.5: Fibre lay-up of non-crimp textile composites

Material	Lay-up
NCC-2-VE	$[\pm 45]_2$
NCC-S-VE	$[\pm 45]_s$
NCEG1-S-VE	$[\pm 45]_s$
NCEG1-2S-VE	$[\pm 45]_{2s}$
NCEG1-4-VE	$[\pm 45]_4$
NCEG2-4-VE	$[90/0/-45/+45]_s$

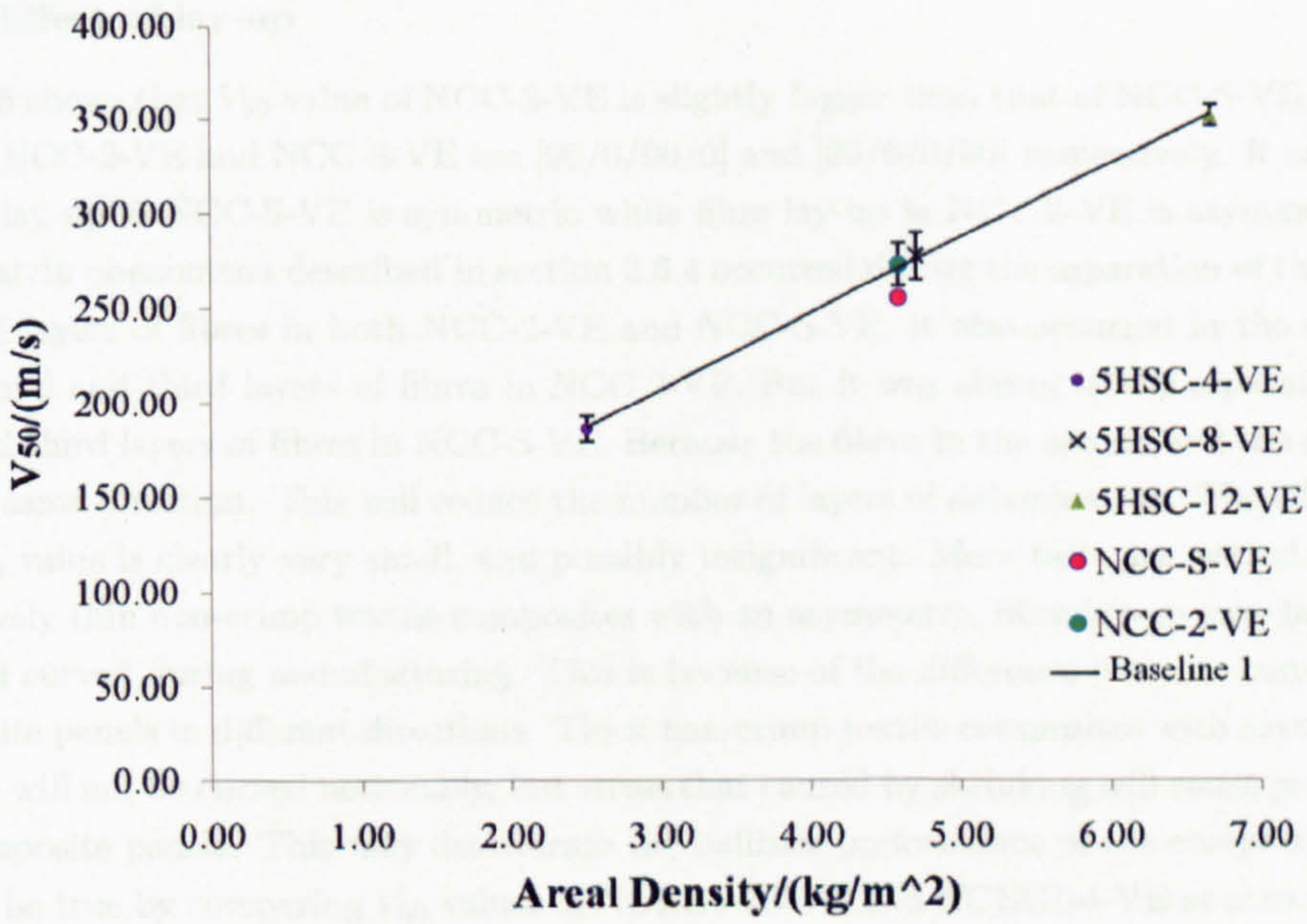

Figure 6.25: V_{50} **results of non-crimp carbon fibre textile composites .**

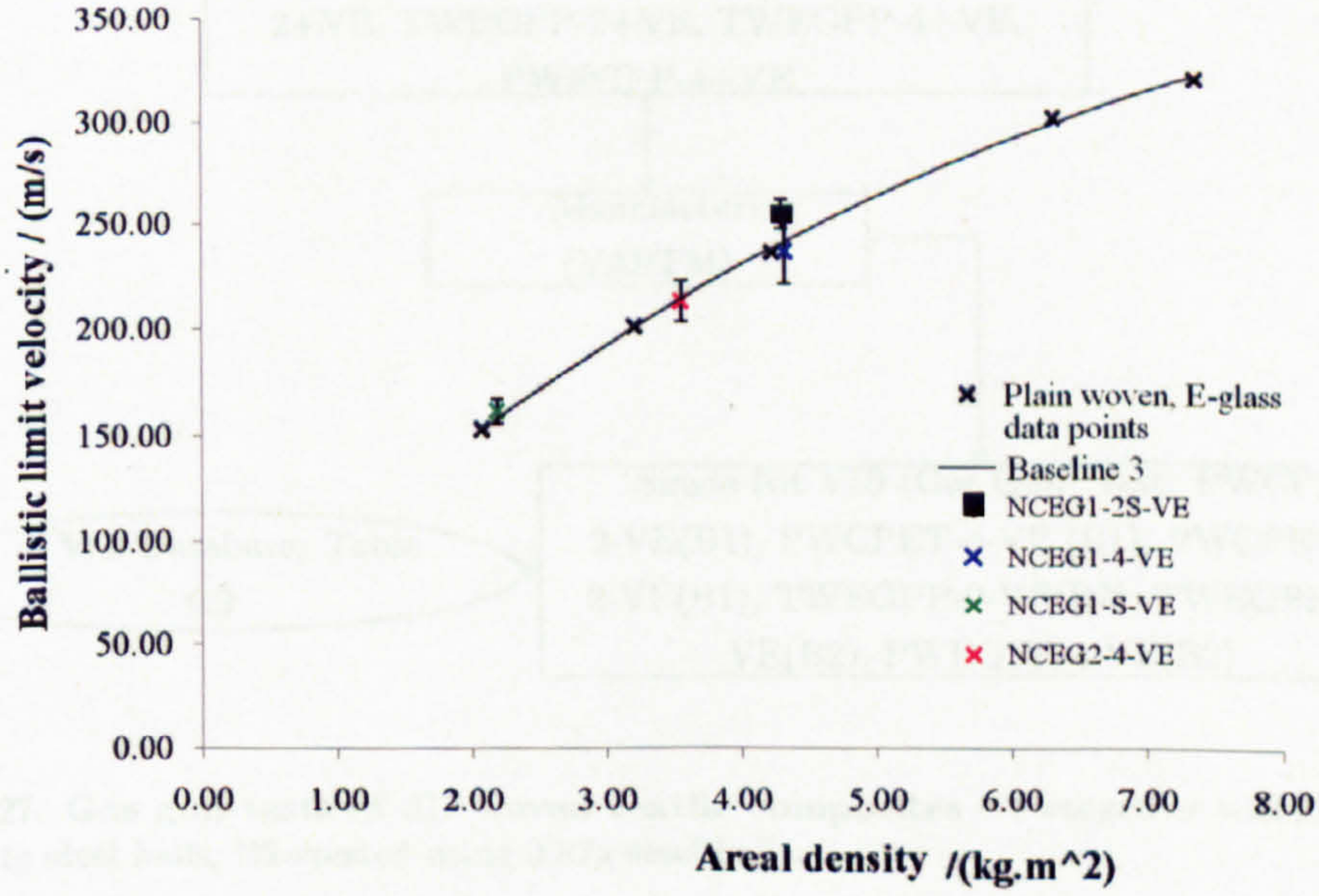

Figure 6.26: V_{50} **results of non-crimp E-glass fibre textile composites .**

material properties control energy absorption in forms of delaminations.

6.6.5.2 Effect of lay-up

Figure 6.25 shows that V_{50} value of NCC-2-VE is slightly bigger than that of NCC-S-VE. The fibre lay-out in NCC-2-VE and NCC-S-VE are [90/0/90/0] and [90/0/0/90] respectively. It can be seen that fibre lay-up in NCC-S-VE is symmetric while fibre lay-up in NCC-2-VE is asymmetric. The generator strip phenomena described in section 2.6.4 occurred during the separation of the first and the second layers of fibres in both NCC-2-VE and NCC-S-VE. It also occurred in the separation of the second and third layers of fibres in NCC-2-VE. But it was absent in the separation of the second and third layers of fibres in NCC-S-VE. Because the fibres in the second and the third layer are in the same direction. This will reduce the number of layers of delamination. The effect of this on the V_{50} value is clearly very small, and possibly insignificant. More tests are needed.

Relatively thin non-crimp textile composites with an asymmetric fibre lay-up may become distorted and curved during manufacturing. This is because of the difference between cure-shrinking of composite panels in different directions. Thick non-crimp textile composites with asymmetric fibre lay-up will not be curved noticeably, but stress that caused by shrinking will cause pre-stressing of the composite panels. This may deteriorate the ballistic performance of the composite. This is proved to be true by comparing V_{50} values of NCEG1-2S-VE and NCEG1-4-VE as shown in figure 6.26 although the difference is not significant. More tests are needed. Fibre lay-up in NCEG1-2S-VE and NCEG1-4-VE are [90/0/90/0/0/90/0/90] and [90/0/90/0/90/0/90/0] respectively. V_{50} values of NCEG1-2S-VE is bigger than that of NCEG1-4-VE.

6.6.6 Co-mingled textile composites

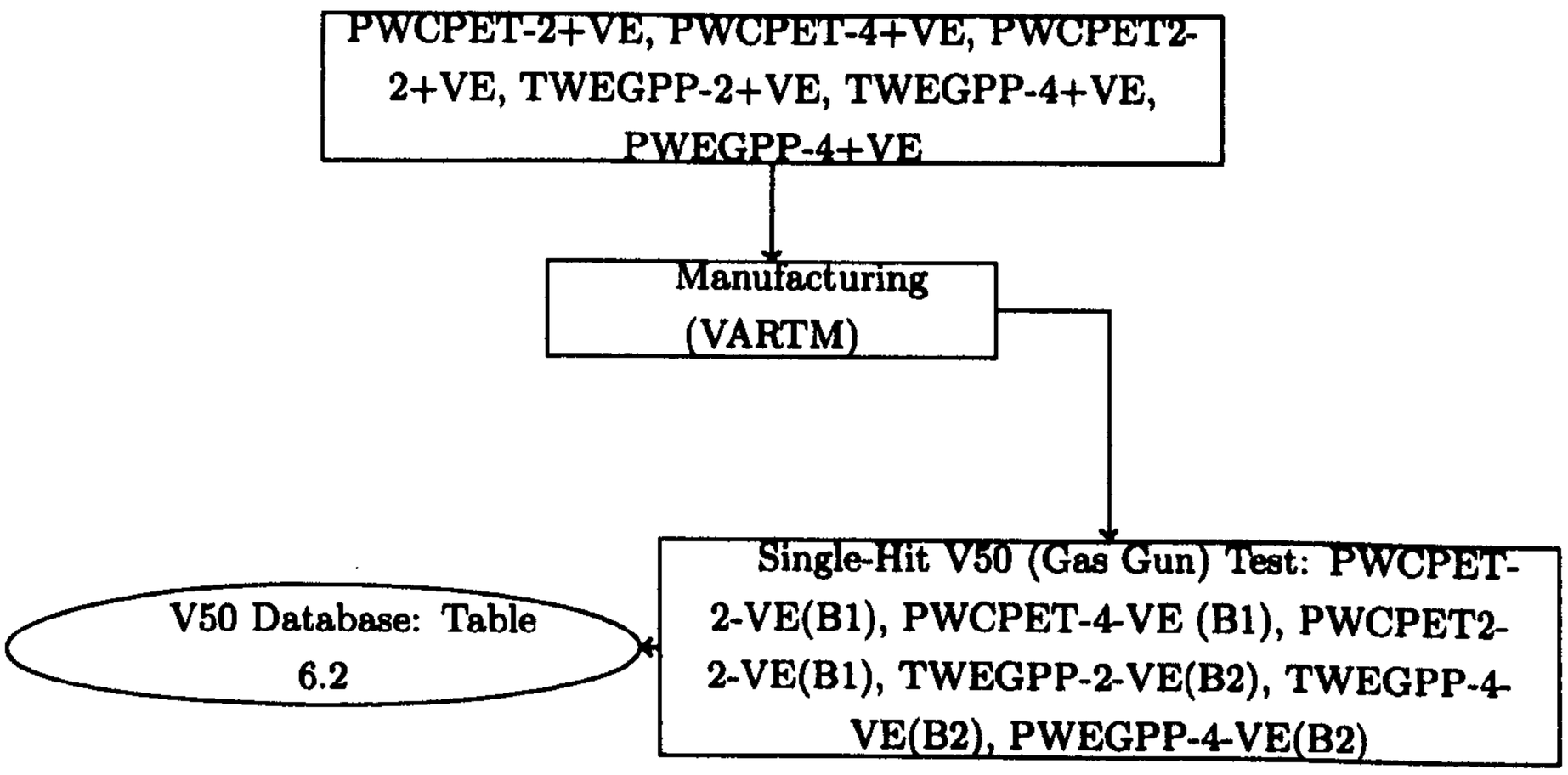

Figure 6.27: **Gas gun tests of 3D woven textile composites** - +=together with; B1=tested using 0.44g steel balls; B2=tested using 0.87g steel balls.

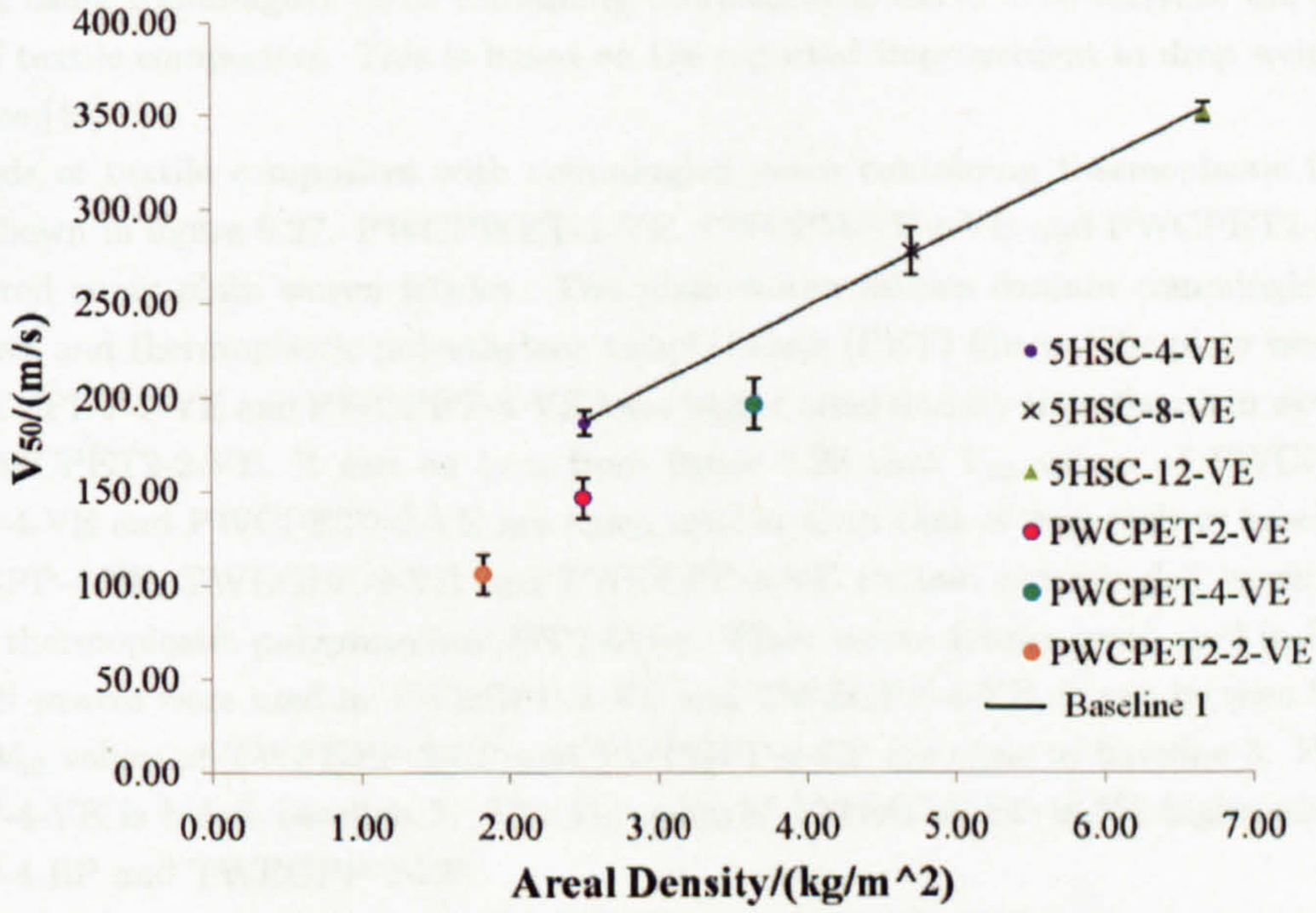

Figure 6.28: V_{50} **results of textile composites with comingled yarns impacted by 0.44g steel balls .**

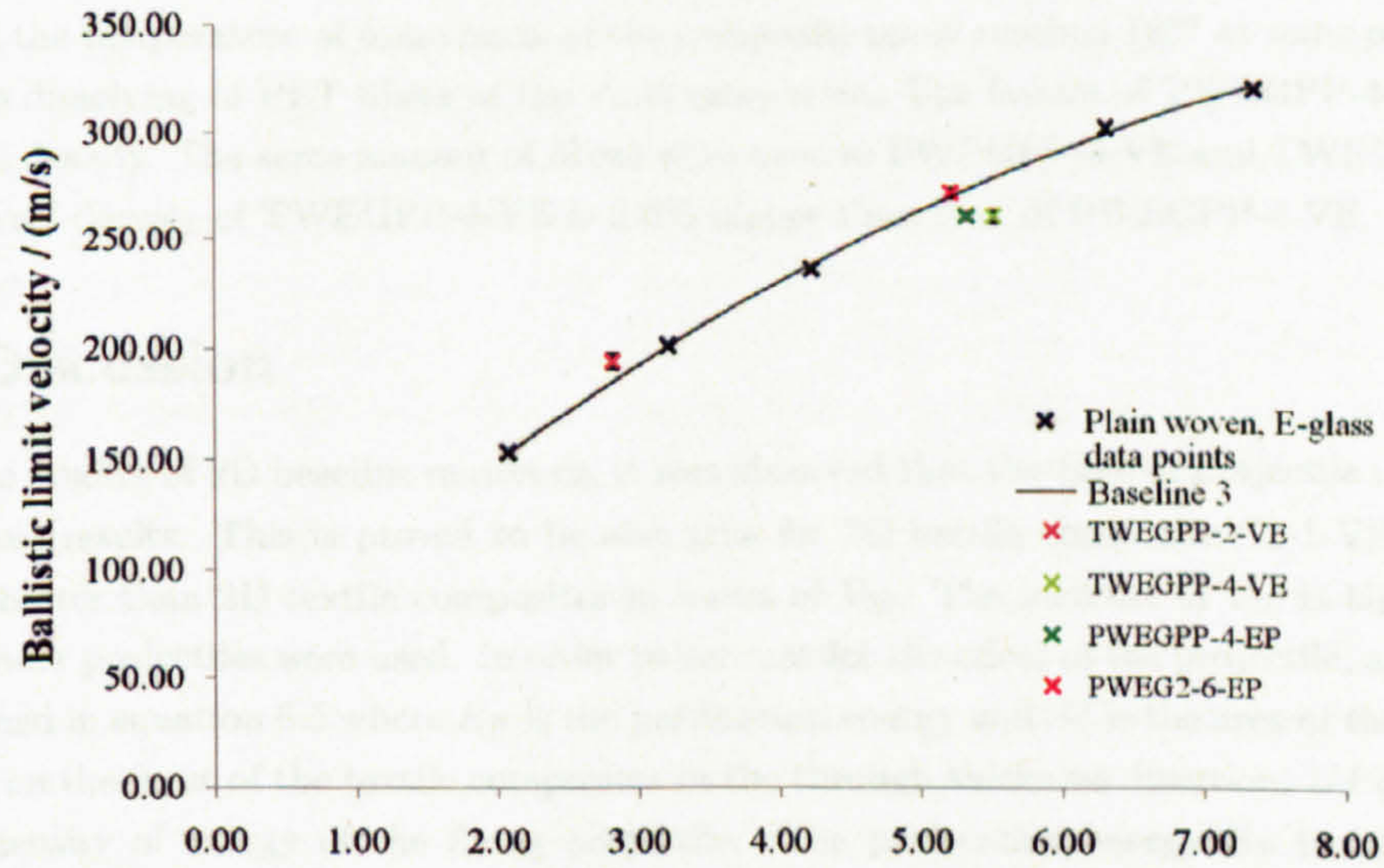

Figure 6.29: V_{50} **results of textile composites with comingled yarns impacted by 0.87g steel balls .**

6.6.6.1 V_{50}

The aim of using commingled yarns containing thermoplastic fibres is to increase the energy absorption of textile composites. This is based on the reported improvement in drop weight impact performance [46].

Six kinds of textile composites with commingled yarns containing thermoplastic fibres were tested as shown in figure 6.27. PWCPWET-2-VE, PWCPWET-4-VE and PWCPET2-2-VE were manufactured using plain woven fabrics. The plain woven fabrics contain commingled yarns of carbon fibres and thermoplastic polyethylene terephthalate (PET) fibres. The plain woven fabrics used in PWCPET-2-VE and PWCPET-4-VE have bigger areal density than the plain woven fabrics used in PWCPET2-2-VE. It can be seen from figure 6.28 that V_{50} values of PWCPET-2-VE, PWCPET-4-VE and PWCPET2-2-VE are much smaller than that of materials in baseline 1.

PWEGPP-4-EP, TWEGPP-2-VE and TWEGPP-4-VE contain commingled yarns of E-glass fibres and thermoplastic polypropylene (PP) fibres. Plain woven fabrics were used in PWEGPP-4-EP. Twill weaves were used in TWEGPP-2-VE and TWEGPP-4-VE. It can be seen from figure 6.29 that V_{50} values of TWEGPP-2-EP and PWEGPP-4-EP are close to baseline 3. V_{50} value of TWEGPP-4-VE is below baseline 3. The V_{50} value of PWEG2-6-EP is 5% higher than that of PWEGPP-4-EP and TWEGPP-2-EP.

It can be concluded that only TWEGPP-2-VE and PWEGPP-4-VE performed as well as materials in database 2 against 0.87g steel balls. Similar PET fibres were used by Hogg [46]. He observed that the PET fibres were dissolved in the epoxy resins during cure. It is very likely that PET fibres were dissolved in the vinyl ester resins during cure. The fabrics with comingled PET fibres were manufactured by Carr Reinforcements Ltd as thermoplastic pre-preg fabrics. They suggested that these fabrics can be moulded at a temperature as low as 180°. During the VARTM processes, it has been observed that the panel was very hot during the cure of vinyl ester resin. It was very likely that the temperature of some parts of the composite panel reached 180° at some point which resulted in dissolving of PET fibres in the vinyl ester resins The failure of TWEGPP-4-VE is due to its areal density. The same amount of fibres were used in PWEGPP-4-VE and TWEGPP-4-VE. But the areal density of TWEGPP-4-VE is 3.6% higher than that of PWEGPP-4-VE.

6.7 Discussion

During the studies of 2D baseline materials, it was observed that the type of projectile used affects ballistic test results. This is proved to be also true for 3D textile composite C1-1-VE. C1-1-VE performs better than 2D textile composites in terms of V_{50}. The increase of V_{50} is biggest when 1.39g cylinder projectiles were used. In order to account for the effect of the projectile, a parameter UI is defined in equation 6.5 where E_P is the perforation energy and SI is the area of the projectile projected on the front of the textile composites in the through thickness direction. UI can be seen as areal density of energy of the flying projectile. The perforation energy E_P is calculated as $\frac{1}{2}mV_{50}{}^2$. The projected areas of all three types of projectiles have a circular shape. In figure 6.31 *b*, UI results were plotted against the areal densities of composites where data points were identified by the projectile used in ballistic impact test and the fabrics used in manufacturing. For example, ball1-PWEG1 means the V_{50} or UI values of textile composites manufactured using fabrics PWEG1, i.e. PWEG1-4-VE, PWEG1-6-VE etc. It can be seen that the apparent effect of

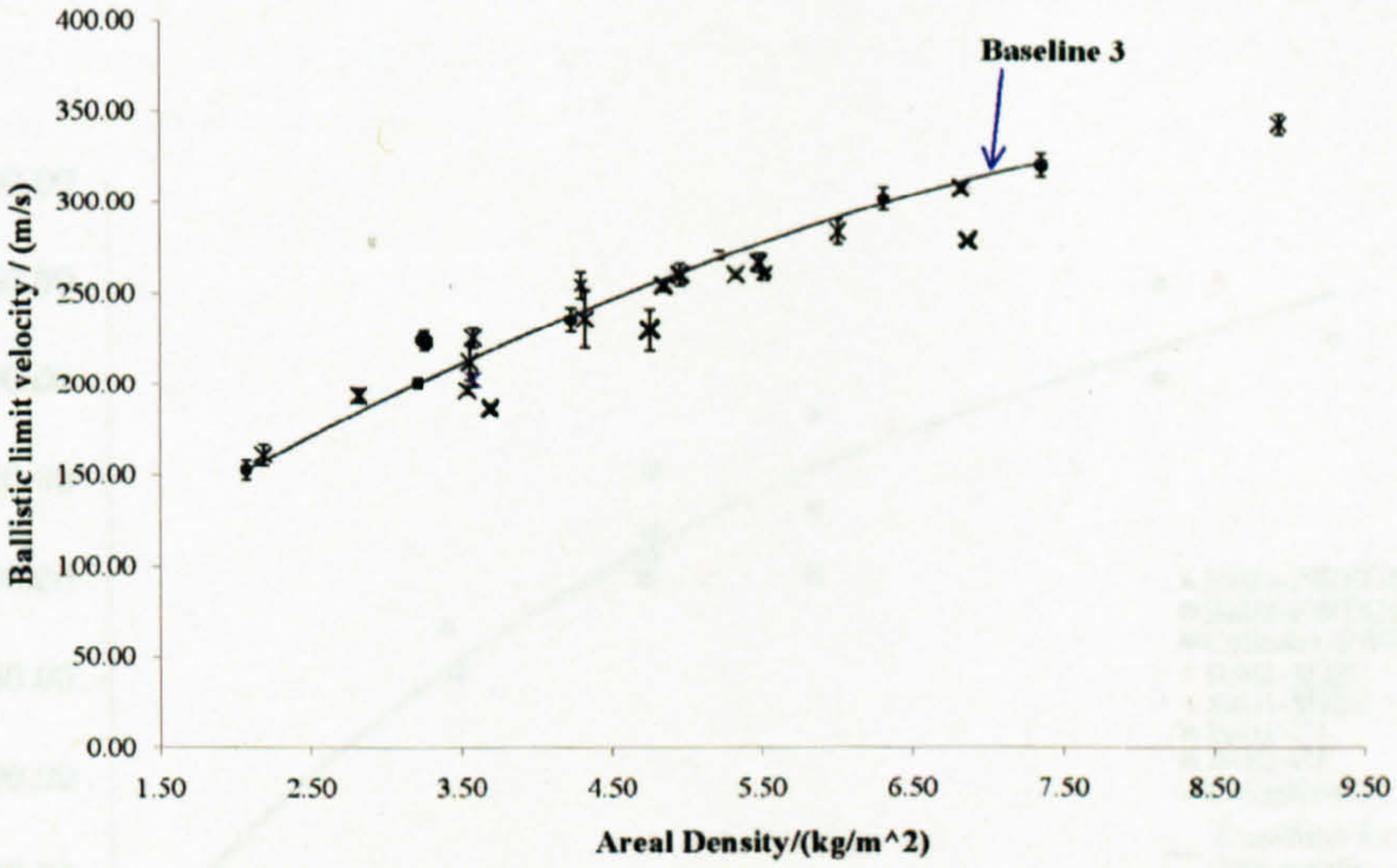

Figure 6.30: **Ballistic limit velocities (V_{50}) of 2D and 3D textile composites against 0.87g steel ball.**

the projectile was reduced, especially for 3D textile composite C1-1-VE. A linear master curve can be applied to all data points.

$$UI = \frac{E_P}{SI} \tag{6.5}$$

The effect of resin materials was studied. It was observed that in both 2D and 3D carbon textile composites, replacing vinyl ester resin with epoxy resin did not increase V_{50}. It actually decreased the V_{50} value slightly in 2D carbon textile composites. This may be caused by a combination of high bonding strength epoxy resin and the low failure strain of carbon fibres. The use of epoxy resin also increased the areal densities of the composites, by reducing fibre volume fraction and increasing the densities. It has been observed that it took more time for epoxy resin to impregnate the preforms than vinyl ester resin during the VARTM processes. This was due to the higher viscosity of the epoxy resin than the vinyl ester resin used in this study. In addition, the epoxy resin has higher density than the vinyl ester resin used in this study. It has also observed that composites manufactured using plain woven and five harness satin woven carbon fibre fabrics have similar ballistic performances.

Although there is an effect of resin on V_{50} value, it was observed that when replacing areal density of the whole composite with areal density of the preform V_{50} values of textile composites are related to the dimensionless fibre property U developed by Cunniff [26]. The importance of the effect of fibre materials on V_{50} values of textile composites were highlighted by comparing figure 6.30. It can be seen that most data points are located near baseline 3. Thus it can be concluded that fibre materials is the primary factors affecting V_{50} values of textile composites.

Among all the new materials tested, only 3D carbon textile composite C1-1-VE performed better than the baseline materials. Materials that performed worse than baseline materials include PWCPET-2-VE, PWCPET-3-VE, PWCPET2-2-VE, G5-1-VE and G6-1-VE. Other new materials performed as well as the baseline materials. The volume fractions of all 3D textile composites are

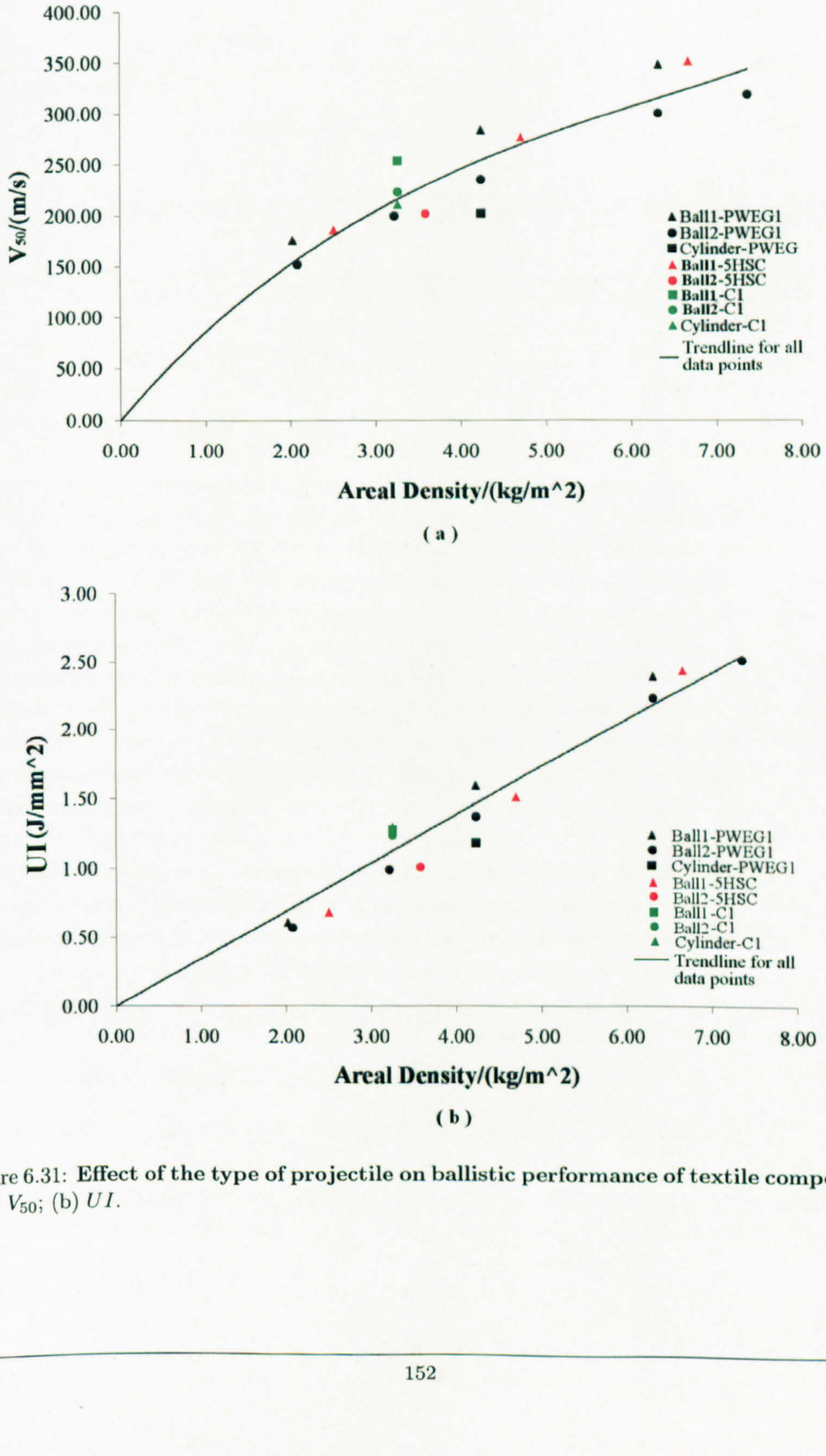

Figure 6.31: **Effect of the type of projectile on ballistic performance of textile composites** - (a) V_{50}; (b) UI.

smaller than that of 2D textile composites. One way to increase the volume fraction is to use smaller yarns. Whether it is possible to increase V_{50} value by increasing fibre volume fraction of 3D textile composites is not clear.

Chapter 7

Ballistic impact damage resistance of 2D and 3D textile composites

7.1 Introduction

Damage resistance of composite material can be evaluated as the dependence of the damage area on the impact energy ([70]). When impacted by same energy, the smaller the damage area the better the damage resistance of the textile composite. E_{50} values of various textile composites were identified in chapter 6. Thus damage resistance of these textile composites can be compared if their damage areas were known. Damage area of textile composites can be determined using ultrasonic c-scan machine or visual examination method described in section 4.3.4.

Determination of two dimensional damage areas is not only necessary for analysing damage resistance properties, but also important in the interpretation of absorbed energy (AE) when there is lack of information on 3-D distribution of damage. Determination of two dimensional damage areas is particularly important in the case of low-velocity impact. Because absorbed energy is a second-order compound parameter whose accuracy completely depends on the accuracy of impact force in the low-velocity impacts.

In the sections below, the damage areas of the V_{50} samples of all the baseline materials and all the new materials that performed at least as well as baseline materials were characterized. The aim is to compare the damage resistance of baseline materials and new materials.

7.2 Results - Damage areas of V_{50} Samples

7.2.1 C-scan and visual examination

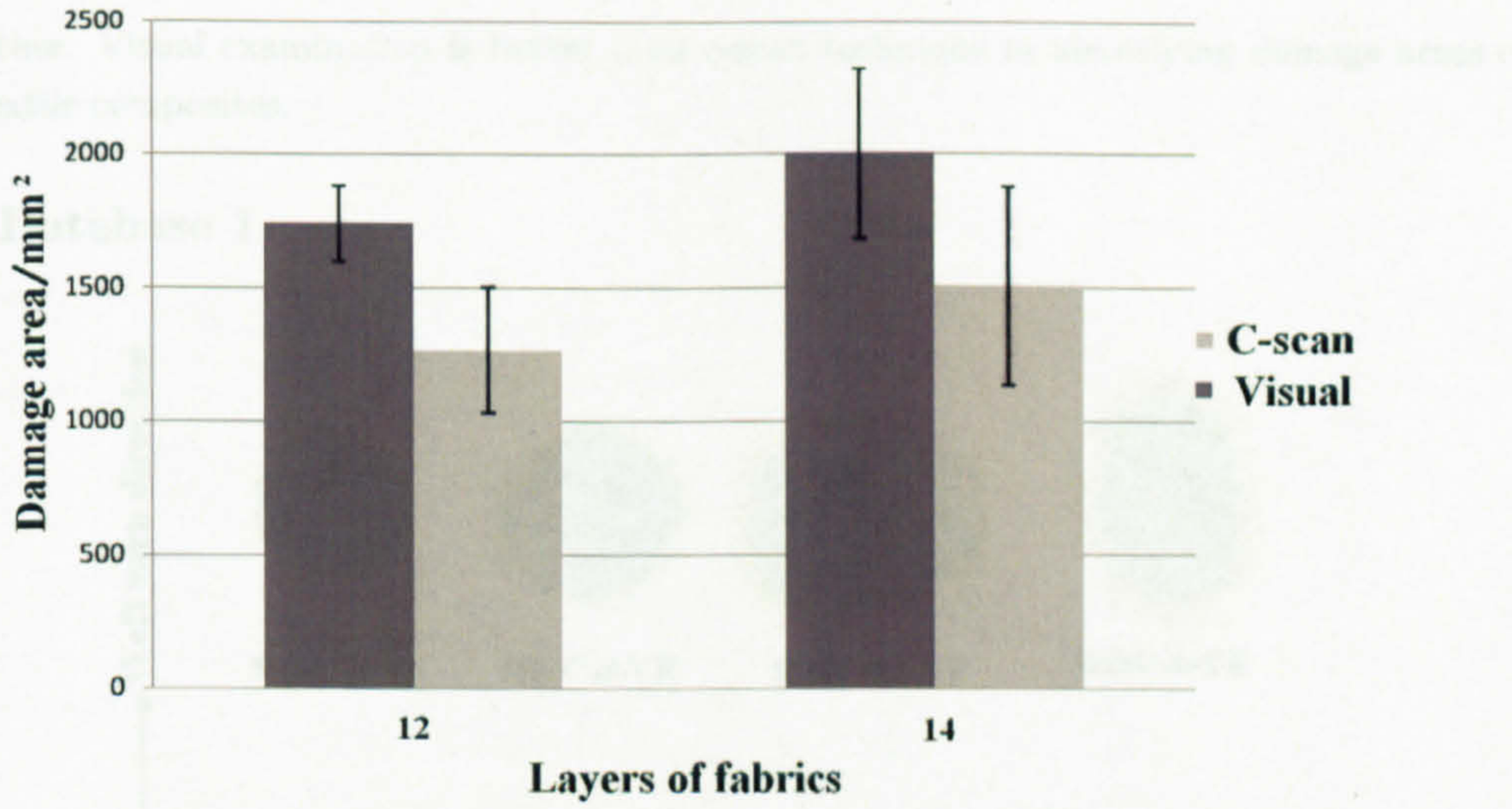

Figure 7.1: **2D damage areas of PWEG1-12-VE and PWEG1-14-VE impacted by 0.87g steel balls** - by ultrasonic c-scan and visual examination

The aim of the study of 2D damage areas of materials in databases is to construct a reference base for assessing new material candidates for composite armour. 2D damage areas of all 2D textile composites database 1, 2, 3, and 4 in figure 6.4 have been identified except for that of PWC-6-EP. Because ultrasonic c-scan tests of PWC-6-EP samples failed to generate any damage images. Damage areas of 2D textile composites manufactured containing carbon fibres were identified using ultrasonic c-scan technique, while visual examination method was used for all 2D textile composites containing E-glass fibres.

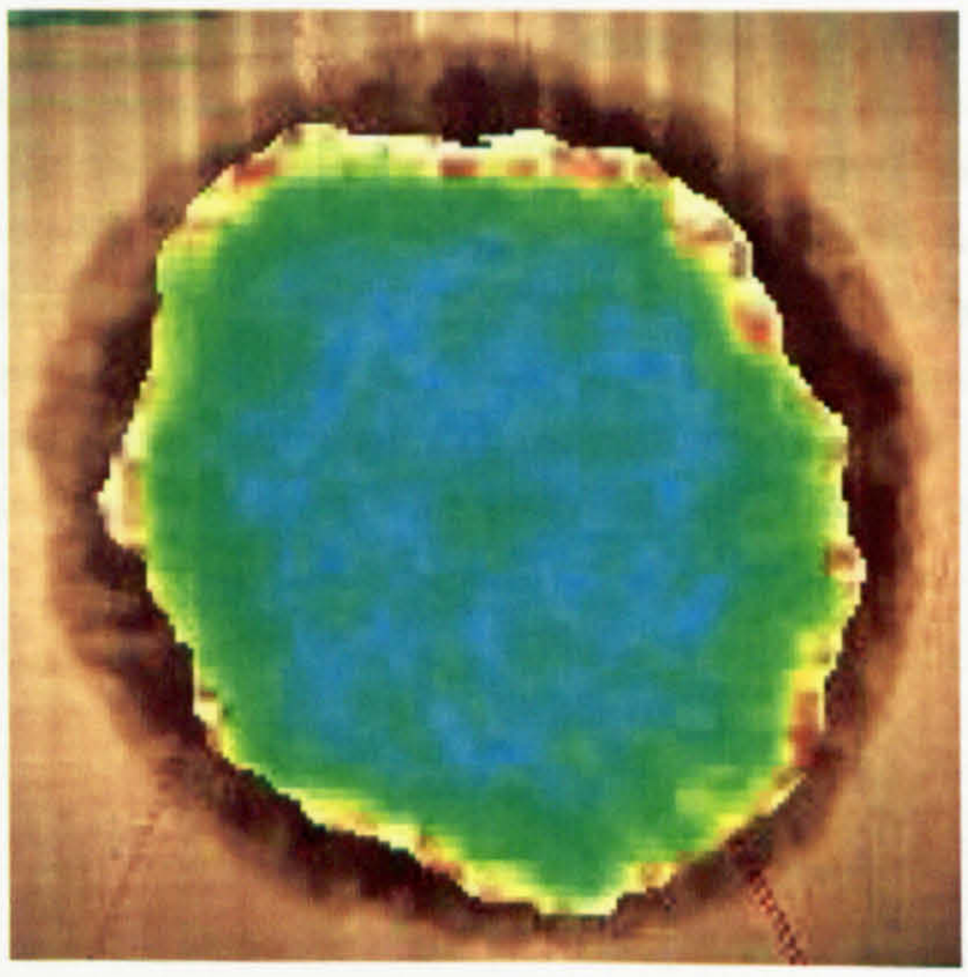

Figure 7.2: **2D damage areas obtained by using** - ultrasonic C-scan (colour) and visual examination (background)

In order to investigate the possibility of using 2D damage area results from both c-scan tests and visual examination tests, damage areas of PWEG1-12-VE and PWEG1-14-VE impacted by 0.87g balls were studied using both c-scan and visual examination techniques. Damage area results from both techniques were compared in figure 7.1. In figure 7.2, 2D damage images obtained by using c-scan and visual examination were put together. It can be seen that damage area results from visual examination are bigger that the damage area results from c-scan tests. This may due to the fact that only 5 MHz transmitter and receiver transducers were used in this study. The frequency of 5MHz may be too high for ultrasonic scanning of the textile composites used in this study. So far it can be concluded that damage areas results from c-scan tests and visual examination tests can not directly compared

to each other. Visual examination is better than c-scan technique in identifying damage areas of E-glass textile composites.

7.2.2 Database 1

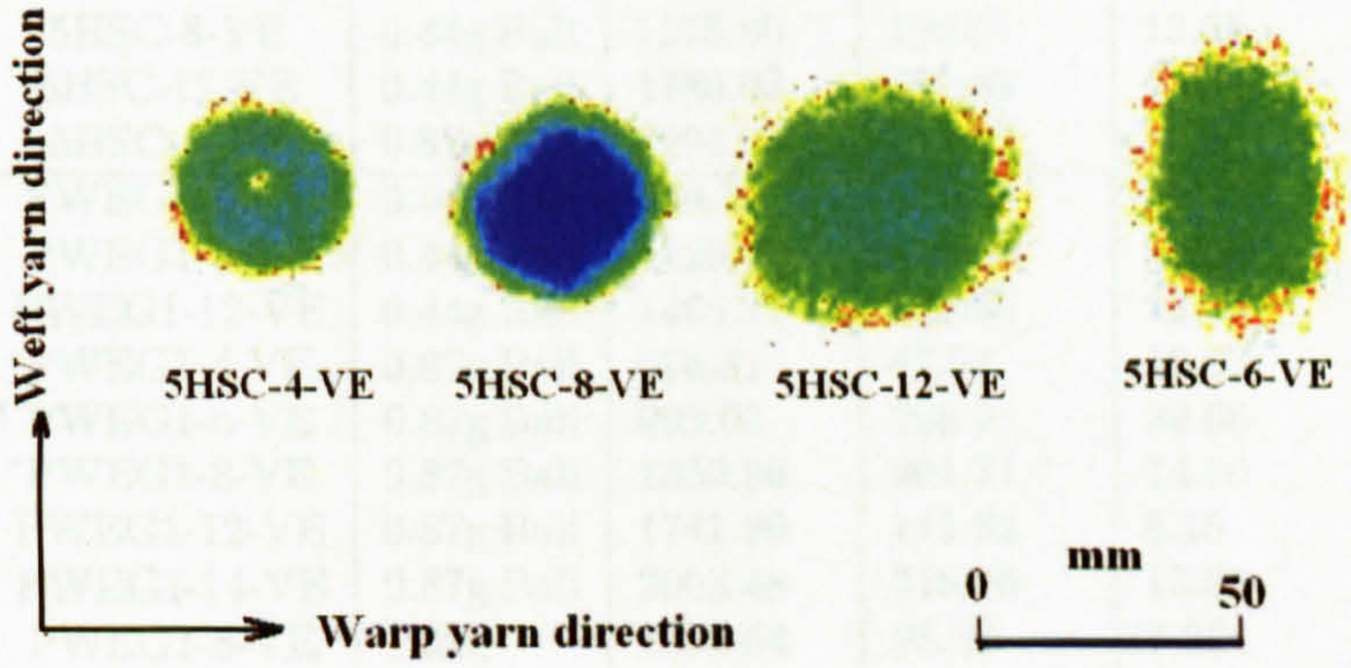

Figure 7.3: **Outlines of damages of V_{50} samples in database 1 -**

As described in section 6.2.1, gas gun test results of 6 samples of each kind of composite material were used to calculate its ballistic limit velocity. Composite materials used in database 1 include 5HSC-4-VE, 5HSC-6-VE, 5HSC-8-VE, and 5HSC-12-VE. 24 samples were used for V_{50} calculation. In this section, damage areas of these 24 samples were identified using the ultrasonic C-scan facility mentioned in section 4.3.3. Damage areas results are listed in table 7.1. More details can be found in table B.1 and table B.2 in appendix B. Examples of the outlines of the damage areas of 5HSC-4-VE, 5HSC-6-VE, and 5HSC-12-VE are shown in figure 7.3. More can be found in figure C.1 in appendix C.

Table 7.1: Damage areas of V_{50} samples in databases

Group	Material	Projectile	Average damage areas (mm^2)	Standard deviation (mm^2)	Coefficient of variation (%)	Areal density (kg/m^2)
Database 1	5HSC-4-VE	0.44g Ball	737.31	107.44	14.57	2.50
	5HSC-8-VE	0.44g Ball	1375.80	190.61	13.85	4.70
	5HSC-12-VE	0.44g Ball	1789.03	400.63	22.39	6.66
	5HSC-6-VE	0.87g Ball	1294.00	293.53	22.68	3.58
Database 2	PWEG1-4-VE	0.44g Ball	540.15	36.14	6.69	2.02
	PWEG1-8-VE	0.44g Ball	1020.70	123.29	12.08	4.06
	PWEG1-12-VE	0.44g Ball	1468.71	183.45	12.49	6.16
	PWEG1-4-VE	0.87g Ball	376.31	47.54	12.63	2.08
	PWEG1-6-VE	0.87g Ball	999.03	296.35	29.66	3.21
	PWEG1-8-VE	0.87g Ball	1350.96	201.31	14.90	4.23
	PWEG1-12-VE	0.87g Ball	1741.99	141.92	8.15	6.31
	PWEG1-14-VE	0.87g Ball	2003.48	318.76	15.91	7.36
	PWEG1-8-VE	1.39g Cylinder	1355.64	98.39	7.26	4.23
Database 3	PWC-6-VE	0.87g Ball	1572.31	477.58	30.37	3.54
Database 4	PWEG2-6-EP	0.87g Ball	1030.88	113.94	11.05	5.22

7.2.3 Database 2

Composite materials used in baseline 2 include PWEG1-4-VE, PWEG1-6-VE, PWEG1-8-VE, PWEG1-12-VE and PWEG1-14-VE. 36 samples were used for V_50 calculation. In this section, 2D damage areas of these 36 samples were identified using the visual examination method mentioned in section 4.3.4. The results are shown in table 7.1. More details can be found in table B.3, table B.4 and table B.5 in appendix B. Examples of the outlines of the damage areas of all the textile composites in database 2 were shown in figure 7.4. More examples can be found in figure C.3, figure C.4 and figure C.5 in appendix C.

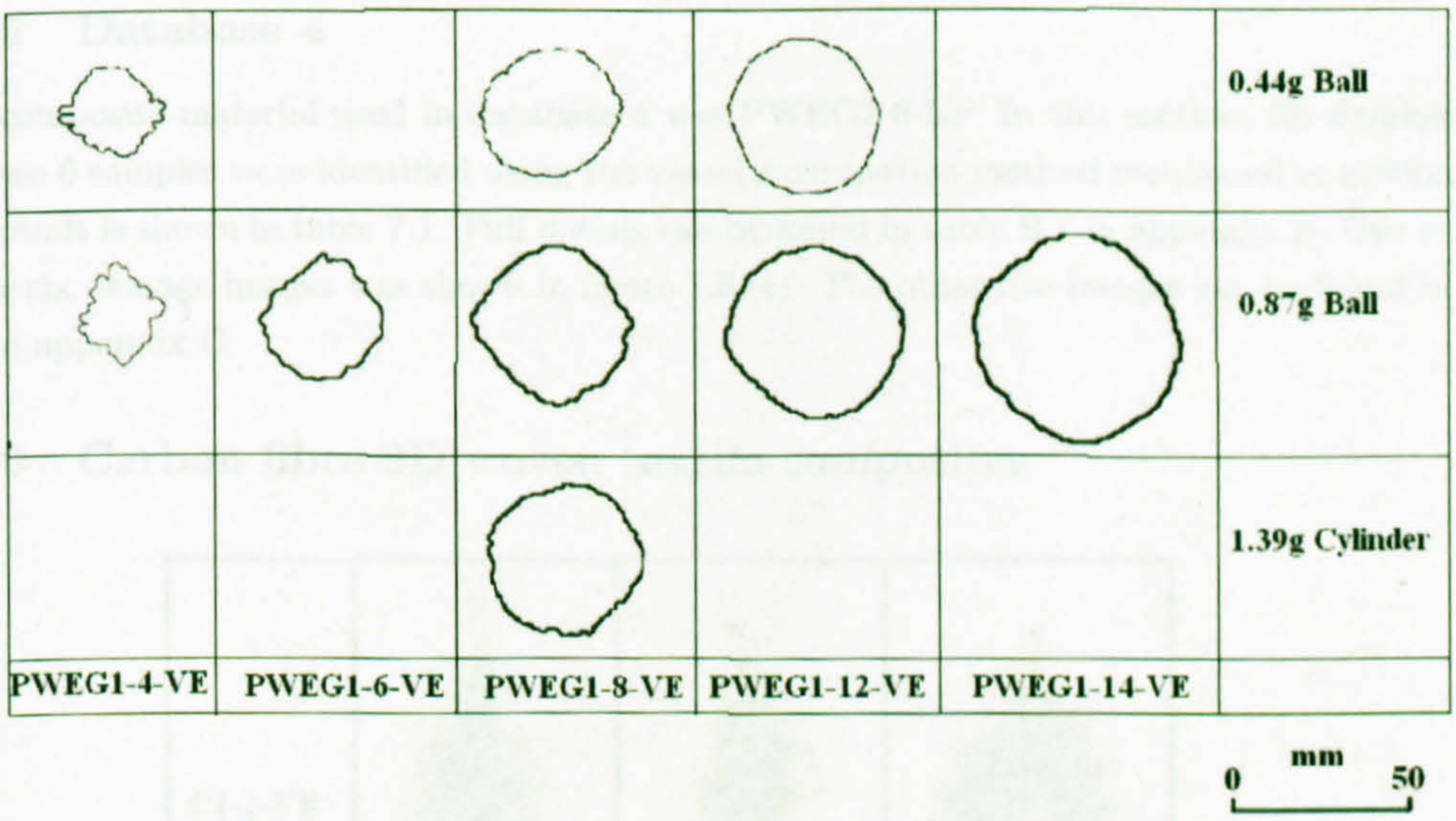

Figure 7.4: **Outlines of damages of V_{50} samples in database 2 -**

7.2.4 Database 3

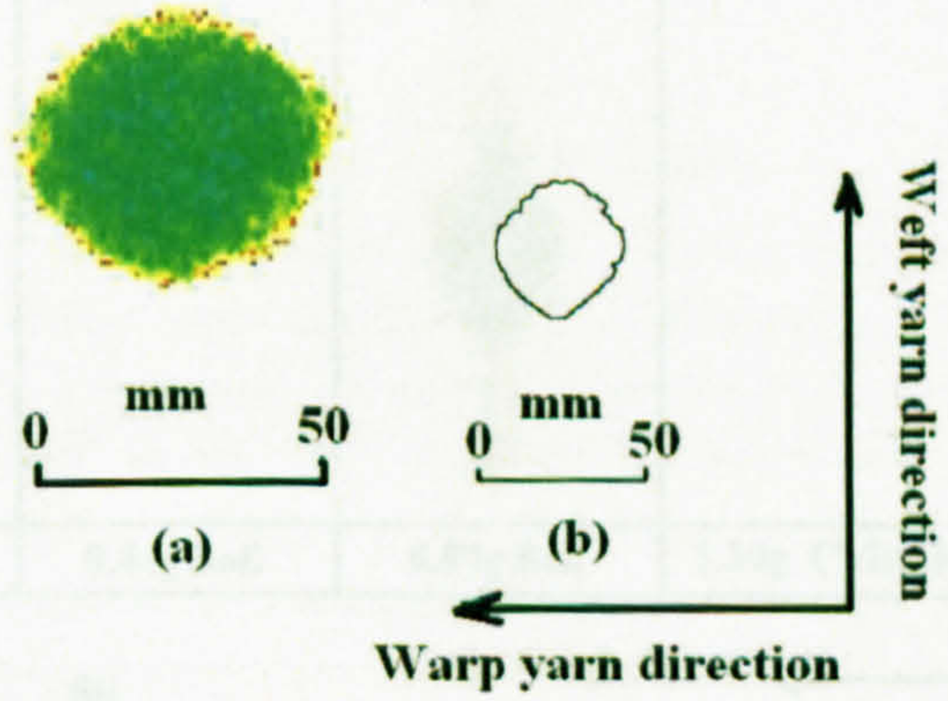

Figure 7.5: **Outline of damage of V_{50} sample in database 3 and 4 -** (a) database 3; (b) database 4.

Materials used in database 3 include PWC-6-VE, and PWC-6-EP. They are composites made from plain woven carbon fibres. In this section, only damage areas of these PWC-6-VE samples were studied using the ultrasonic C-scan facility mentioned in section 4.3.3. As described in section 6.6.3.4, PWC-6-EP has lower V_{50} than PWC-6-VE due to the combination of high bonding strength of epoxy resin and low failure strain of carbon fibres. The result was shown in table 7.1. More details can be found in table B.6 in appendix B. One example of the six damage images was shown in figure 7.5 (a). The other five images can be found in figure C.6 in appendix C.

7.2.5 Database 4

The composite material used in database 4 was PWEG2-6-EP. In this section, 2D damage areas of these 6 samples were identified using the visual examination method mentioned in section 4.3.4. The result is shown in table 7.1. Full details can be found in table B.7 in appendix B. One example of the six damage images was shown in figure 7.5 (*b*). The other five images can be found in figure C.7 in appendix C.

7.2.6 Carbon fibre 3D woven textile composites

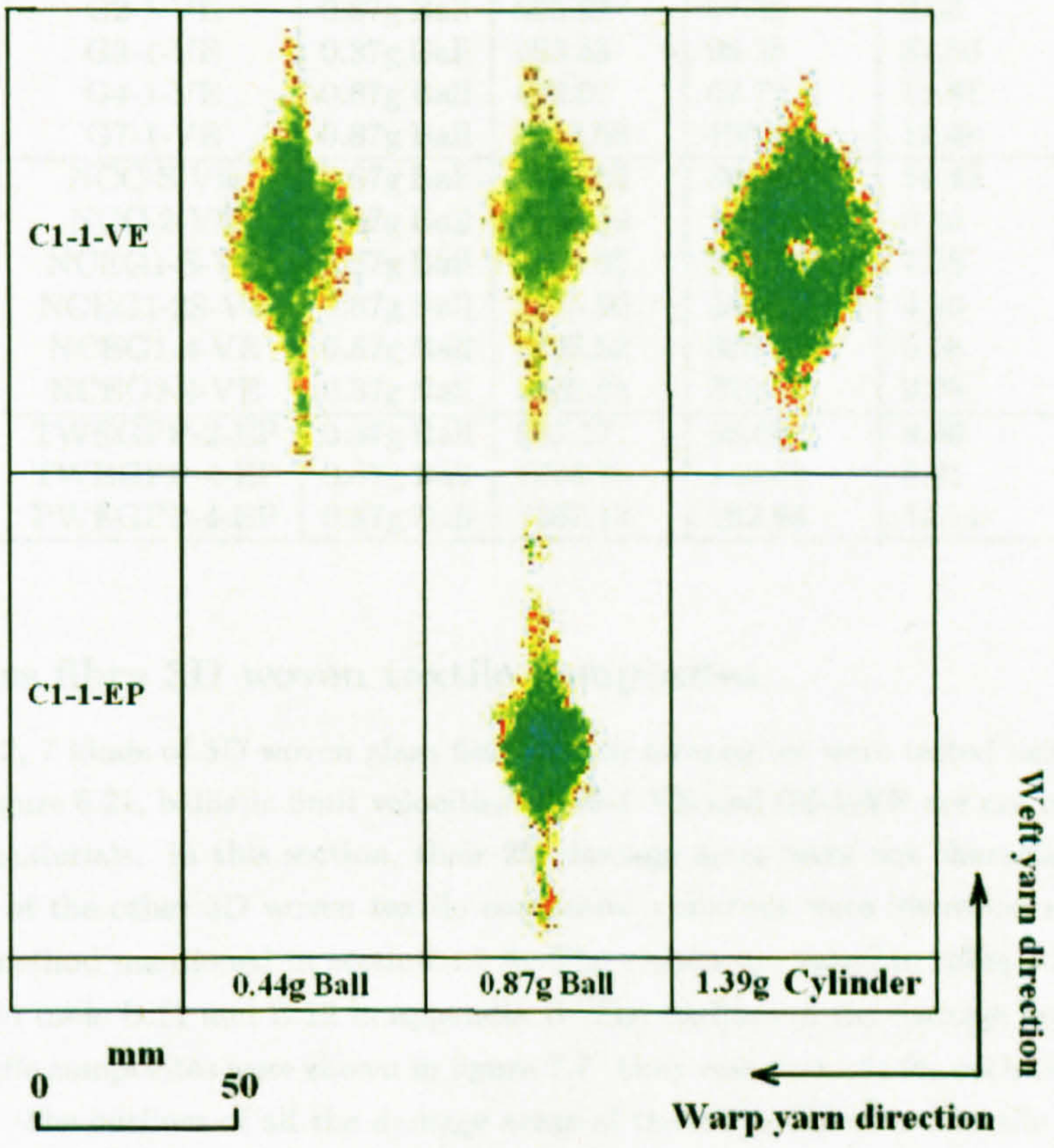

Figure 7.6: **Outline of damages of V_{50} samples of C1-1-VE and C1-1-EP .**

In section 6.3.1, samples of 3D woven textile composite C1-1-VE were impacted by 0.44g, 0.87g steel balls and 1.39g cylinder projectile. Samples of 3D woven textile composite C1-1-EP were impacted by 0.87g steel balls. The damage areas of the 24 samples used for V_{50} calculation were investigated using ultrasonic c-scan. The results were listed in table 7.2. More details can be found in table B.8, table B.9 and table B.10 in appendix B. Examples of damage images were shown in figure 7.6. More images can be found in figure C.9 in appendix C.

Table 7.2: Damage areas of V_{50} samples of new materials

Group	Material	Projectile	Average damage areas (mm^2)	Standard deviation (mm^2)	Coefficient of variation (%)	Areal density (kg/m^2)
3D woven	C1-1-VE	0.44g Ball	972.79	124.88	12.84	3.26
	C1-1-VE	0.87g Ball	743.22	92.02	12.38	3.26
	C1-1-VE	1.39g Cylinder	1570.26	201.21	12.81	3.26
	C1-1-EP	0.87g Ball	808.78	92.89	11.48	3.58
	G1-1-VE	0.87g Ball	527.85	54.61	10.35	4.95
	G2-1-VE	0.87g Ball	635.02	57.36	9.03	5.48
	G3-1-VE	0.87g Ball	293.53	98.35	33.50	4.84
	G4-1-VE	0.87g Ball	452.07	62.71	13.87	6.83
	G7-1-VE	0.87g Ball	1552.58	193.77	12.48	8.93
Non-crimp	NCC-S-VE	0.87g Ball	2090.62	301.41	14.42	4.95
	NCC-2-VE	0.87g Ball	2890.09	186.63	6.46	4.59
	NCEG1-S-VE	0.87g Ball	4425.45	348.58	7.88	2.19
	NCEG1-2S-VE	0.87g Ball	5285.90	242.50	4.59	4.30
	NCEG1-4-VE	0.87g Ball	5836.52	325.49	5.58	4.32
	NCEG2-4-VE	0.87g Ball	3329.85	329.11	9.88	3.56
Co-mingled	TWEGPP-2-EP	0.87g Ball	983.17	88.08	8.96	2.82
	TWEGPP-4-EP	0.87g Ball	1664.78	146.63	8.81	5.52
	PWEGPP-4-EP	0.87g Ball	1367.14	192.86	14.11	5.33

7.2.7 Glass fibre 3D woven textile composites

In section 6.3.2, 7 kinds of 3D woven glass fibre textile composites were tested using the gas gun. As shown in figure 6.21, ballistic limit velocities of G5-1-VE and G6-1-VE are not as good as those of baseline 3 materials. In this section, their 2D damage areas were not characterized. The 2D damage areas of the other 3D woven textile composite materials were identified using the visual examination method mentioned in section 4.3.4. The results are listed in table 7.2. More details can be found in table B.11 and B.12 in appendix B. The outlines of the damage areas of these five 3D woven textile composites were shown in figure 7.7. Only one example for each textile composite is shown here. The outlines of all the damage areas of these five 3D woven textile composites can be found in figure C.10 in appendix C.

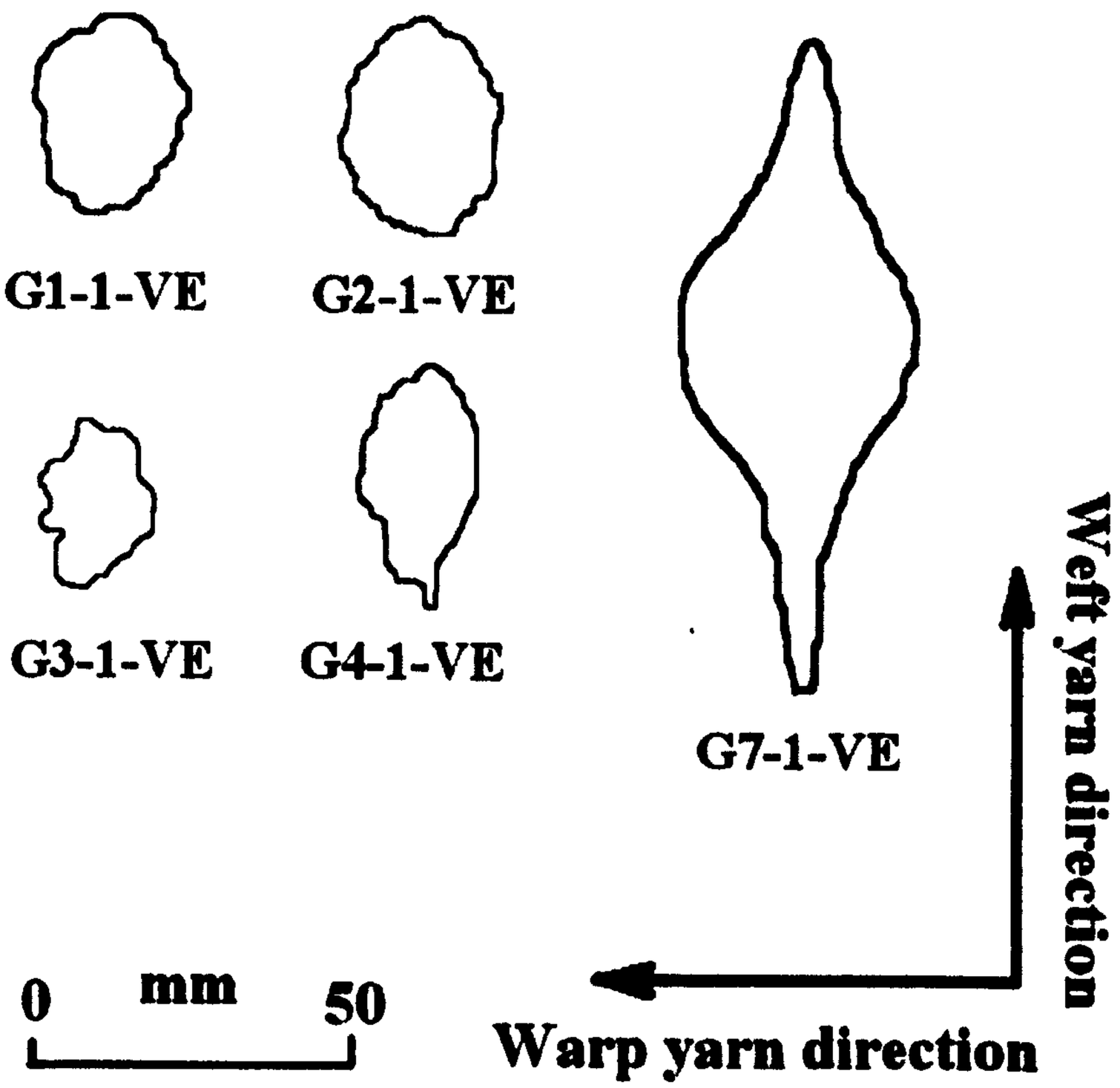

Figure 7.7: **Outline of damages of V_{50} samples of 3D E-glass woven textile composites .**

7.2.8 Non-crimp carbon textile composites

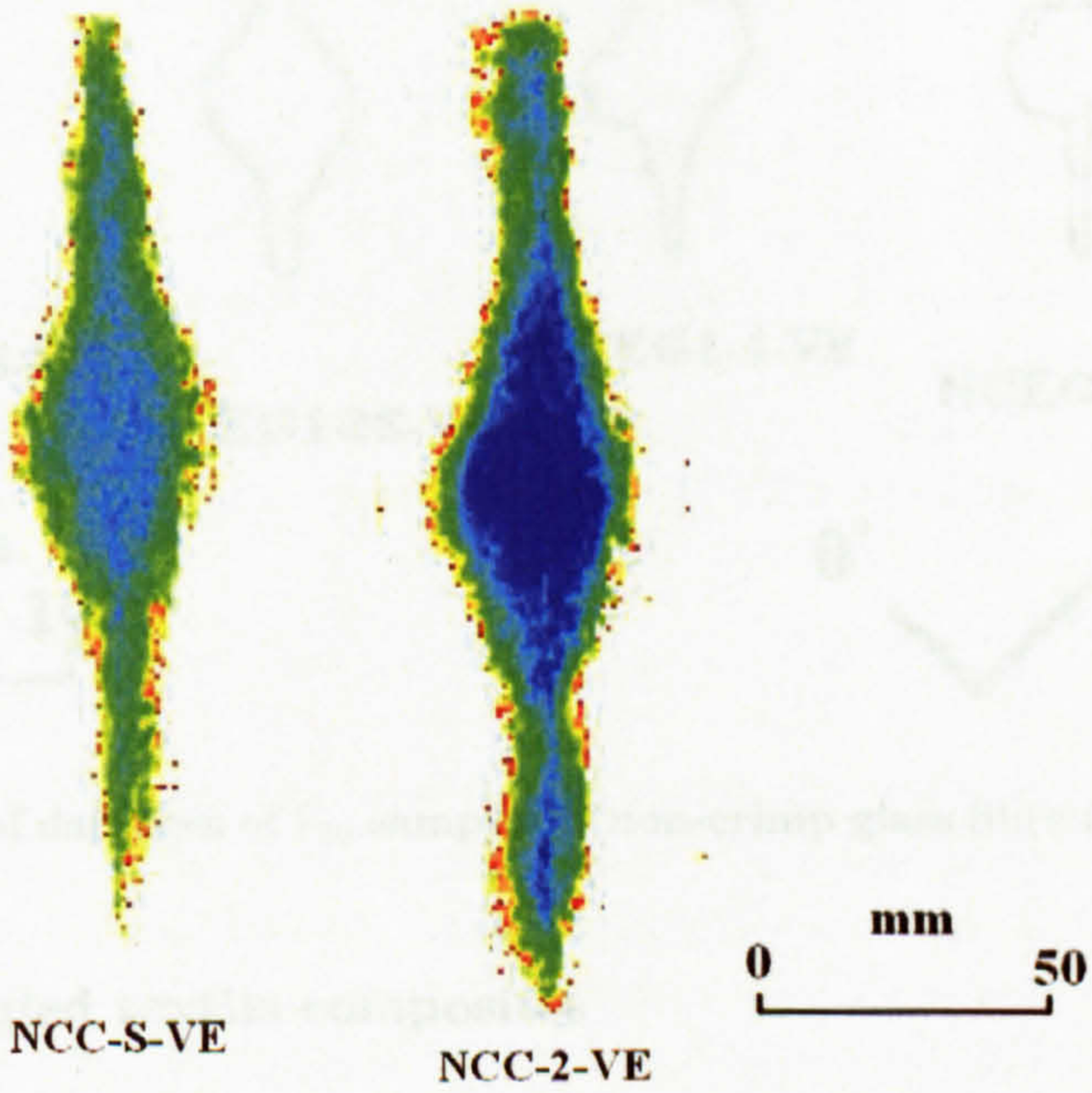

Figure 7.8: **Outline of damages of V_{50} samples of NCC-S-VE and NCC-2-VE .**

In section 6.4.1, two kinds of non-crimp carbon fibre textile composites were tested, i.e. NCC-S-VE and NCC-2-VE. In this section, damage areas of the 12 samples used for the calculation of the ballistic limit were investigated using ultrasonic c-scan machine. The results are shown in table 7.2. Damage areas of all samples can be found in table B.13 in appendix B. Examples of the outlines of the damage areas are shown in figure 7.8. The outlines of all 12 samples are shown in figure C.11 in appendix C.

7.2.9 Non-crimp E-glass textile composites

In section 6.4.2, four kinds of non-crimp textile composites were impacted by 0.87g steel balls. In this section, the damage areas of their samples used for the calculation of ballistic limit velocities were investigated using visual examination method described in section 4.3.4. The results are shown in table 7.2. Damage areas of all samples can be found in table B.14 in appendix B. Examples of the outlines of the damage areas are shown in figure 7.9. The outlines of these 24 samples are shown in figure C.12 in appendix C.

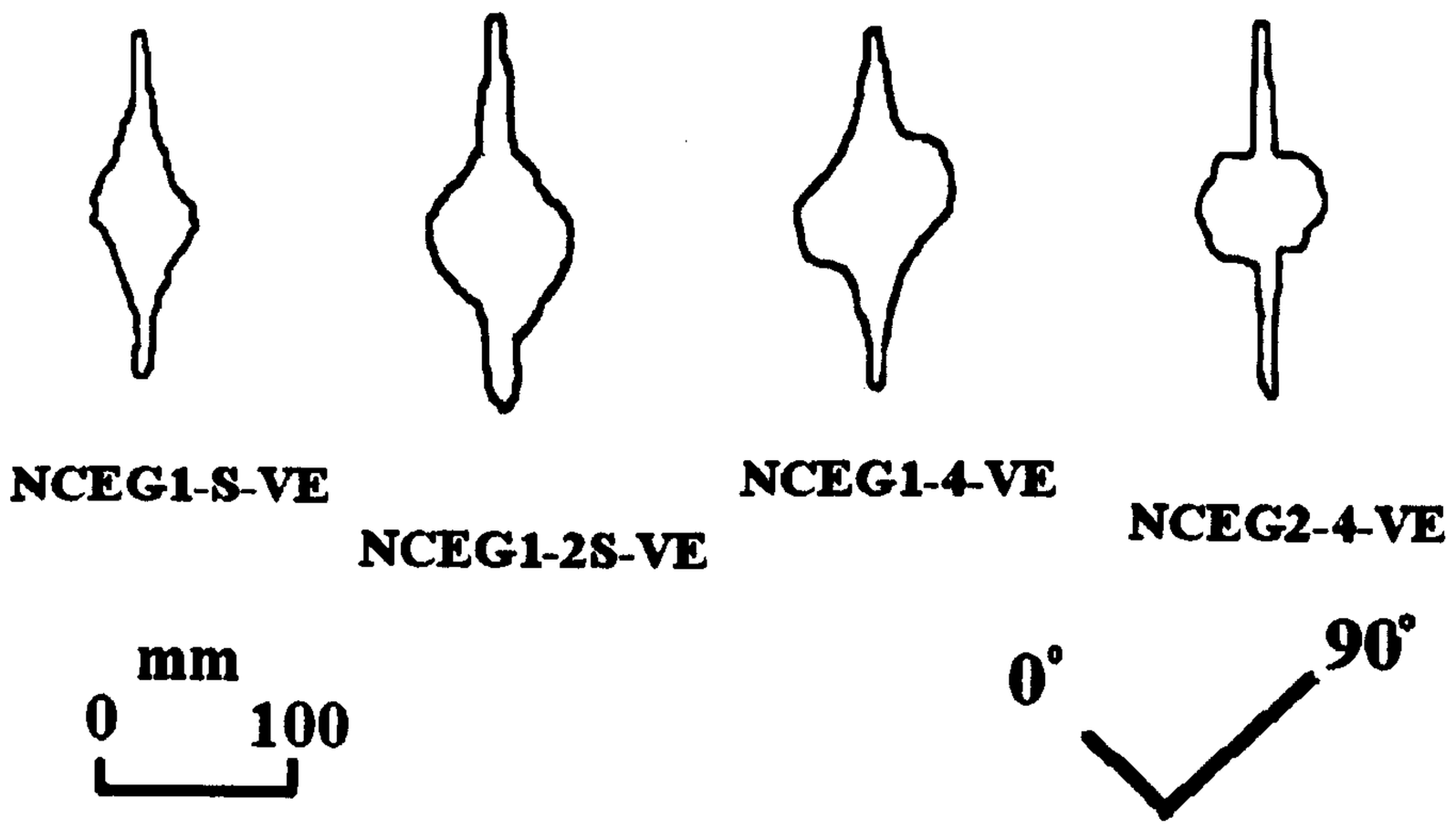

Figure 7.9: **Outline of damages of V_{50} samples of non-crimp glass fibre textile composites .**

7.2.10 Co-mingled textile composites

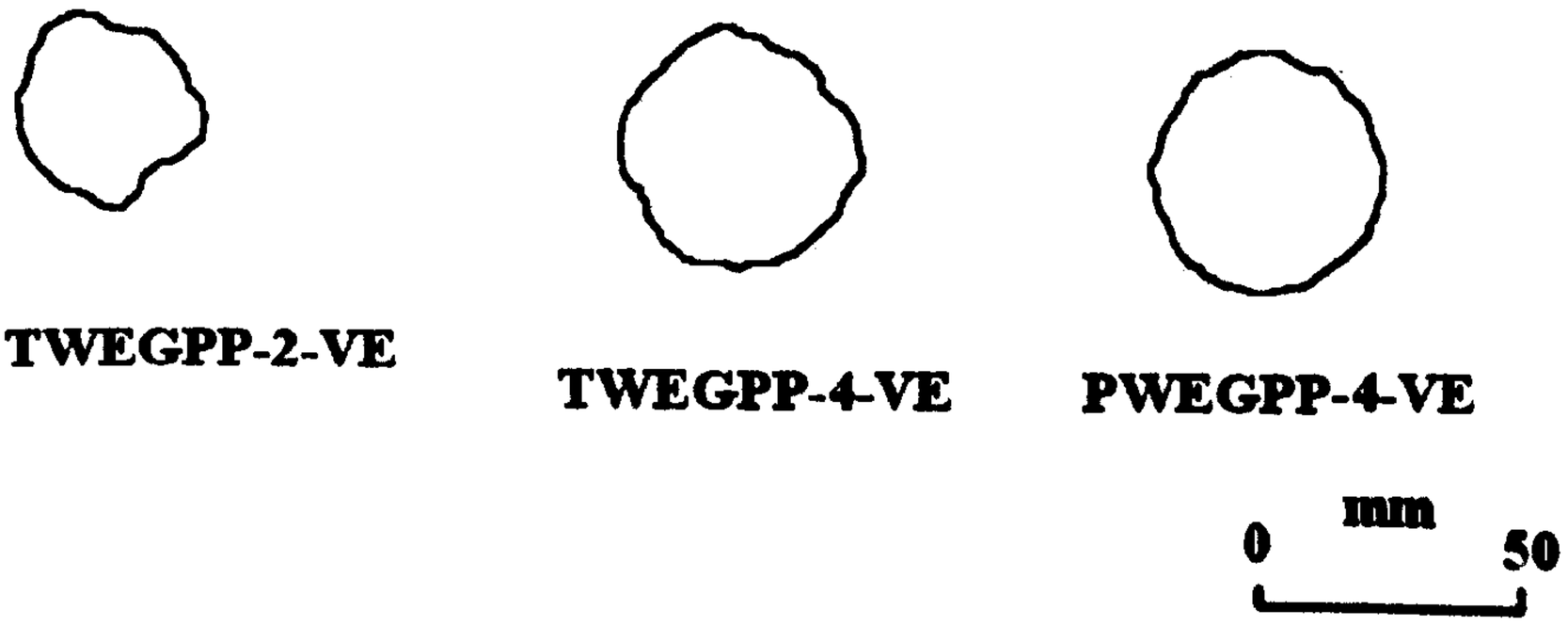

Figure 7.10: **Outline of damages of V_{50} samples of textile composites with co-mingled yarns .**

In section 6.5.2, four kinds of textile composites with co-mingled E-glass and polypropylene fibres were tested. In these section, samples of all the four composite materials used for V_{50} calculation were characterized using visual examination method described in section 4.3.4. The results are shown in table 7.2. Damage areas of all samples can be found in table B.15 in appendix B. Examples of the outlines of the damage areas are shown in figure 7.10. The outlines of these 24 samples are shown in figure C.13 in appendix C.

7.3 Discussion of results

7.3.1 Repeatability of 2-D damage area results

As mentioned in chapter 6, inherent repeatability of experimental results is an important issue. Recalls in section 6.6.2, 28 pairs of ballistic impacts with near identical impacting velocities were observed. 2-D damage areas of 20 out these 28 pair of ballistic impacts have been determined. It has been observed that there were 10 pairs of ballistic impacts with difference in 2-D damage areas smaller than 7%. Thus overall the repeatability of 2-D damage area results was not worse than that of gas gun test results. The worst repeatability of 2-D damage area results were observed in the case of 3D textile composites where 4 out 6 pairs of ballistic impacts with difference in 2-D damage areas higher than 20%.

7.3.2 *EAD* and *SAD*

As mentioned in section 7.1, damage resistance of textile composites can be evaluated as the dependence of the damage area on the impact energy. E_{50} results calculated in chapter 6 can be seen as perforation energies. Ballistic impact damage resistance can be evaluated by plotting damage areas of textile composites against perforation energies of textile composites. Composites with various areal densities have been used in this study. Due to the limited data points available, only a few direct comparisons of damage resistance of textile composites with the same areal density are possible. This is due to the difficult of controlling the thickness of the composite panel during the resin infusion process. In order to include the effect of areal density on both perforation energy and damage area, two new parameters EAD and SAD were introduced. EAD is equal to E_{50}/AD where AD is the areal density of a textile composite. SAD is equal to S/AD where S is the damage area of a textile composites after ballistic impact. In this study, ballistic impact damage resistance will be evaluated by plotting SAD result of textile composite against EAD result of textile composite. An ideal material will maximise EAD and minimise SAD. In the figures below, $1/SAD$ and EAD were used as x-axis and y-axis respectively. Thus the material with best damage resistance will be located in the up-right corner of the chart.

7.3.3 Databases

The damage areas of textile composites in database 1, 2, 3 and 4 shown in table 7.1 were plotted against the areal densities of the textile composites in figure 7.11 and figure 7.12. Standard deviations were used as error bar. It can be seen that the variation of the data is much bigger than that of E_{50} results discussed in the last chapter. In addition, the fact that the damage area values measured by C-scan may be different from the damage area values measured by visual examination maks it not feasible to comapre the results of carbon fibre textile composties and E-glass textile composites. Thus studies of the effect of material variables, and projectile types on damage areas of textile composites were not be carried out unless there was clear difference.

It can be seen in figure 7.12 that the damage areas of PWEG2-6-EP is much smaller than that of textile composites in database 2. Recall in figure 6.12 in chapter 6 that the V_{50} values was on the trendline fitted to V_{50} results of textile composites in database 2, i.e. PWEG2-6-EP has similar perforation energy as textile composites in database 2. Thus PWEG2-6-VE has better damage

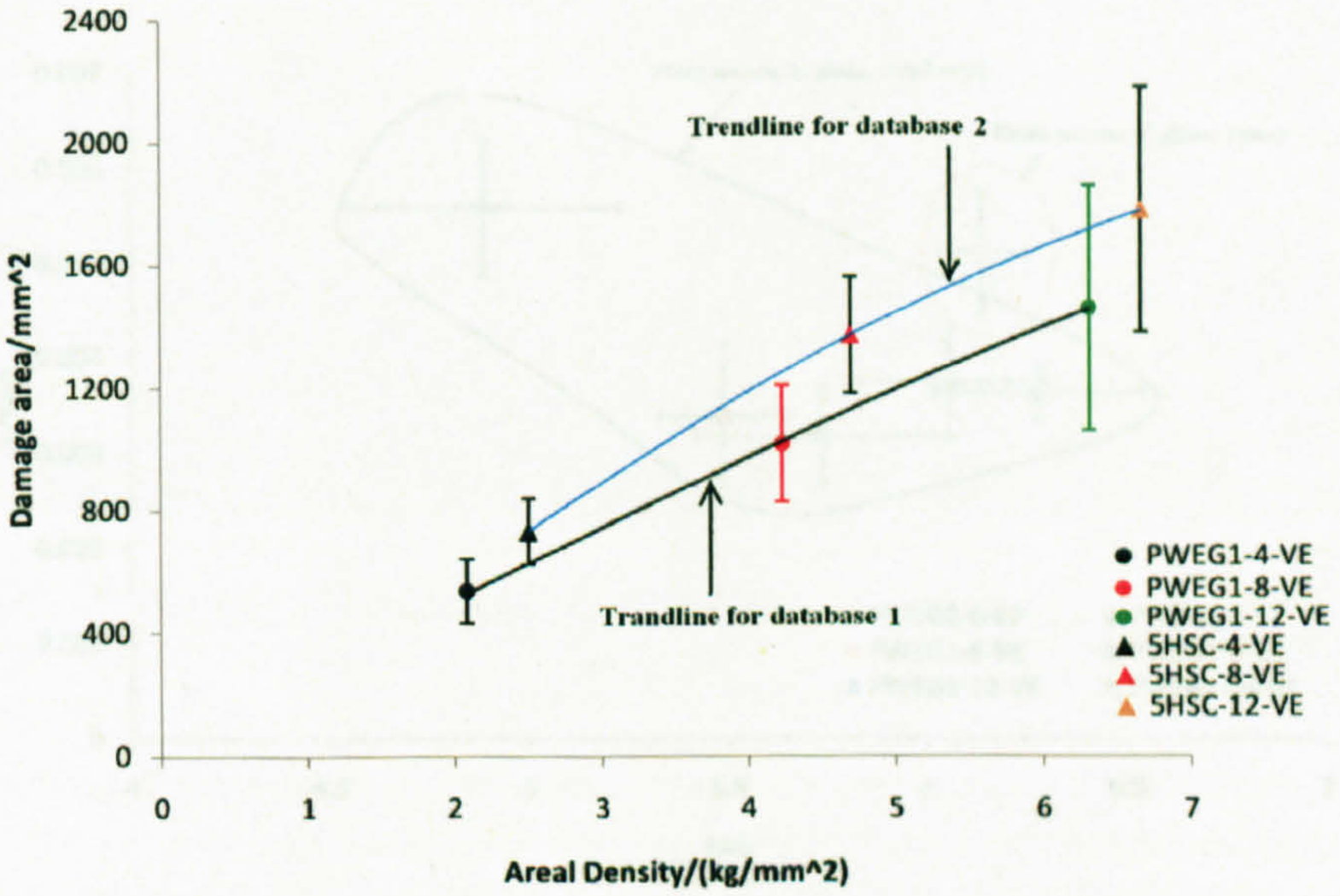

Figure 7.11: **Damage areas of textile composites in databases 1 and 2 impacted by 0.44g steel balls .**

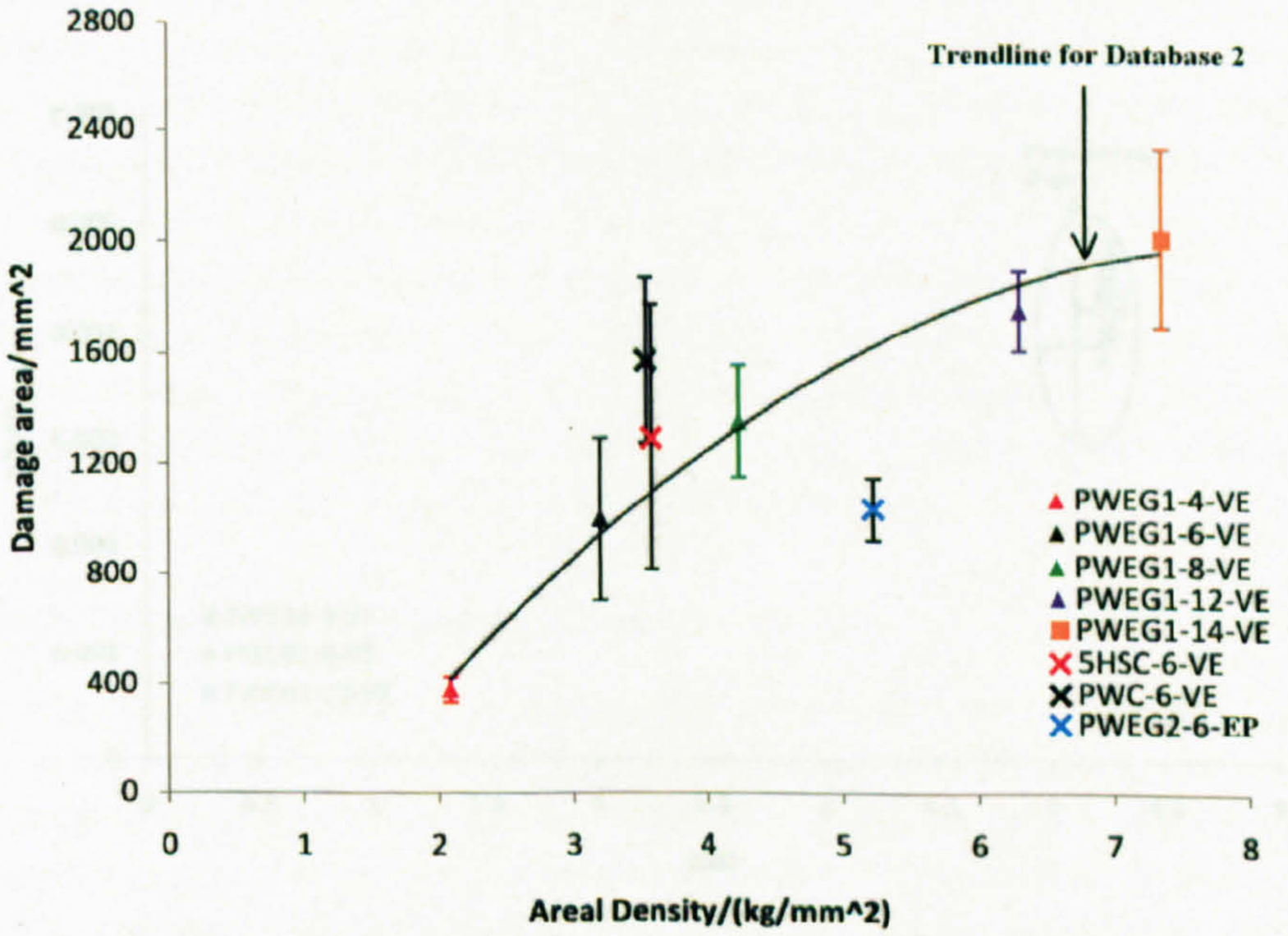

Figure 7.12: **Damage areas of textile composites in databases 1, 2, 3 and 4 impacted by 0.87g steel balls .**

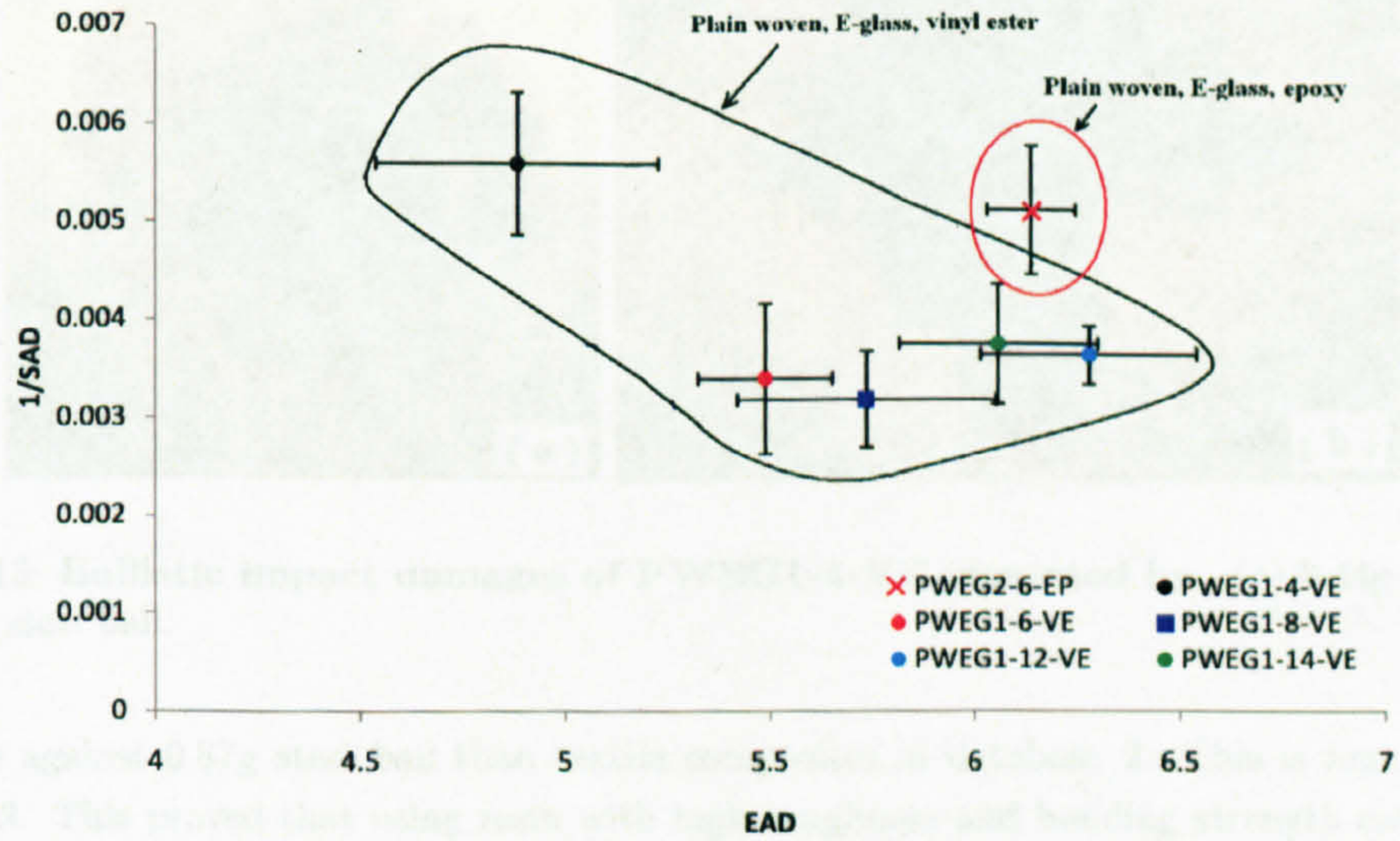

Figure 7.13: *EAD* **versus** *SAD* **of textile composites in databases 2, 3 and 4 impacted by 0.87g steel balls .**

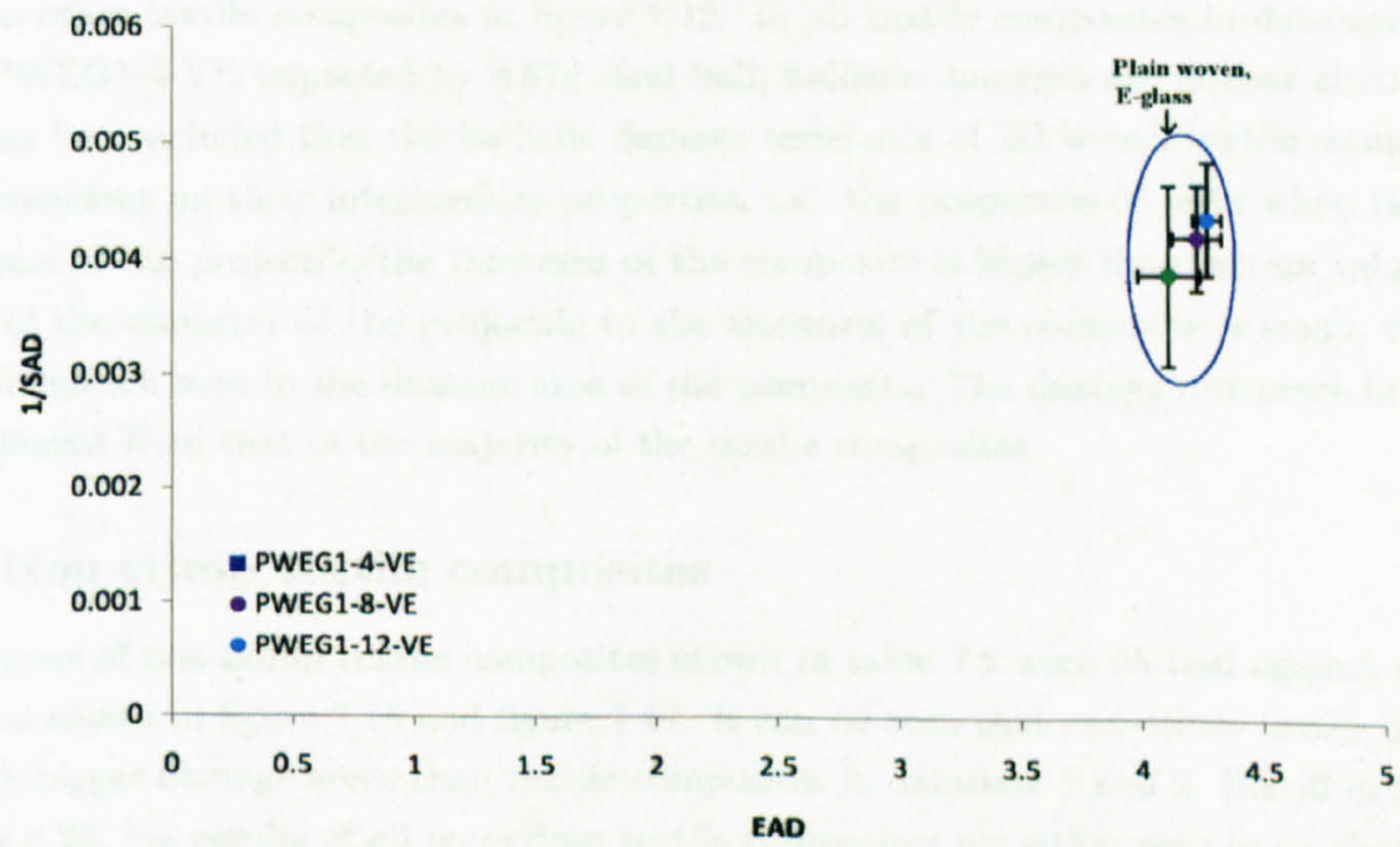

Figure 7.14: *EAD* **versus** *SAD* **of textile composites in database 1 and 2 impacted by 0.44g steel balls .**

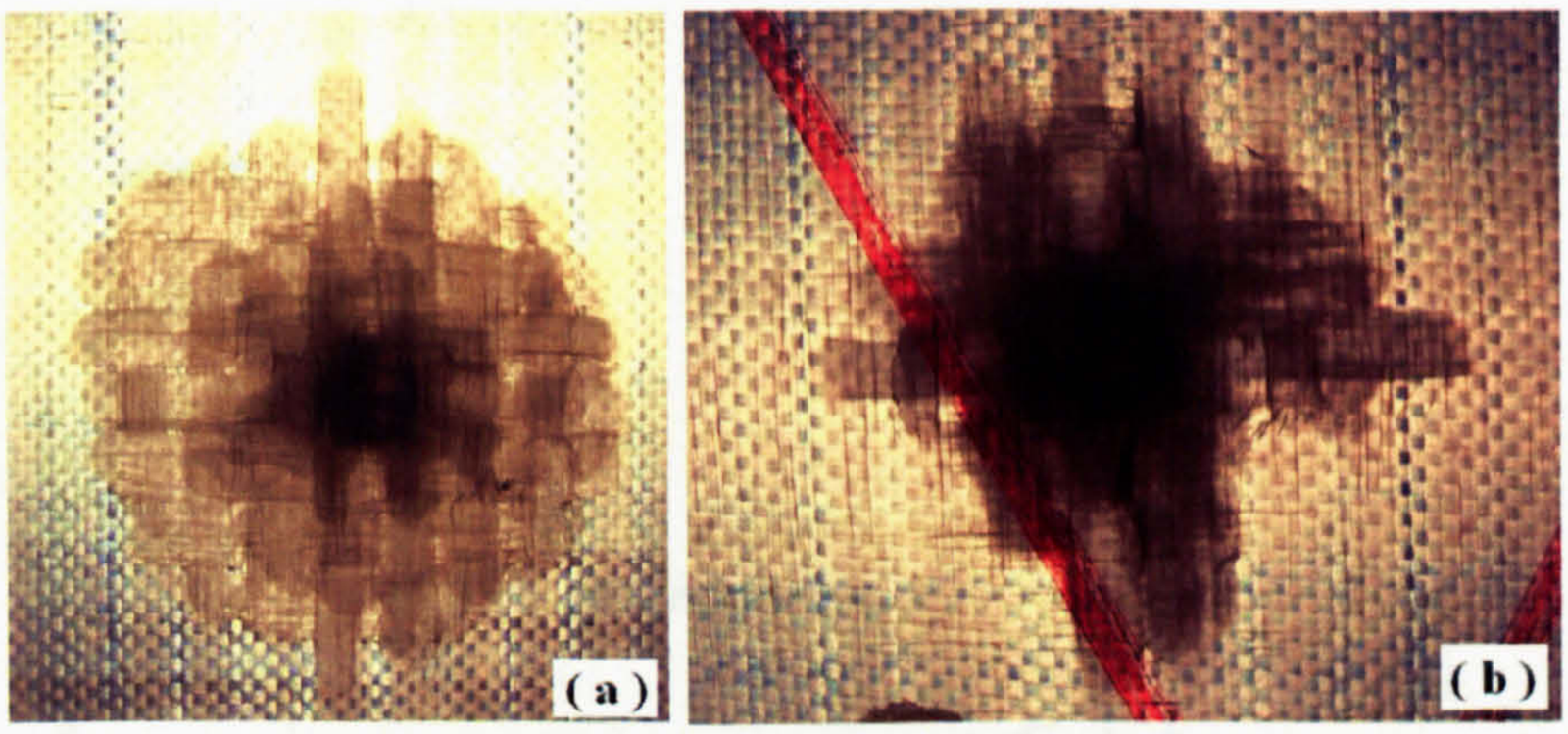

Figure 7.15: **Ballistic impact damages of PWEG1-4-VE impacted by** - (a) 0.44g steel ball; (b) 0.87g steel ball.

resistance against 0.87g steel ball than textile composites in database 2. This is highlighted in figure 7.13. This proved that using resin with high toughness and bonding strength can increase ballistic impact damage resistance of 2D textile composites. It was also noticed that in figure 7.13 that damage resistance of PWEG1-4-VE is very different from other textile composites in database 2. PWEG1-4-VE behaved just normally when impacted by 0.44g steel balls as shown figure 7.14. Figure 7.4 shows that damage areas of all textile composites in database 2 have near circular shape except that of PWEG1-4-VE impacted by 0.87g steel ball. Figure 7.15 shows the ballistic impact damages of PWEG1-4-VE impacted by both 0.44g and 0.87g steel balls. The most significant difference between the figure 7.15 -(a) and (b) is the big area of delamination in figure 7.15 -(a). It suggested that the lack of big delamination is the reason for the different behaviour of PWEG1-4-VE from other textile composites in figure 7.13. In all textile composites in database 2 except that of sPWEG1-4-VE impacted by 0.87g steel ball, ballistic damages are in near circular shape. Thus it can be concluded that the ballistic damage resistance of 2D woven textile composites are mainly dependent on their interlaminar properties, i.e. the properties of resin when the ratio of the diameter of the projectile/the thickness of the composite is bigger than certain values. When the ratio of the diameter of the projectile to the thickness of the composite is small, there is no large delamination area in the damage area of the composite. The damage resistance in such case is very different from that of the majority of the textile composites.

7.3.4 Non-crimp textile composites

Damage areas of non-crimp textile composites shown in table 7.2 were plotted against their areal densities as shown in figure 7.16 and figure 7.17. It can be seen that non-crimp textile composites have much bigger damage areas than textile composites in database 1 and 2. Recall in figure 7.16 and figure 6.26, V_{50} results of all non-crimp textile composites are either near or on the trendlines fitted to textile composites in database 1 and 2. Thus the damage resistance of non-crimp textile composites are much worse than that of textile composites in database 1 and 2. This is highlighted by figure 7.18 and figure 7.19. Figure 7.8 and figure 7.9 show that the shape of the damage areas of non-crimp textile composites are very different from that of textile composites in databases. Figure 7.20 reveals that one reason for the huge size of damages in 90° direction in a non-crimp textile

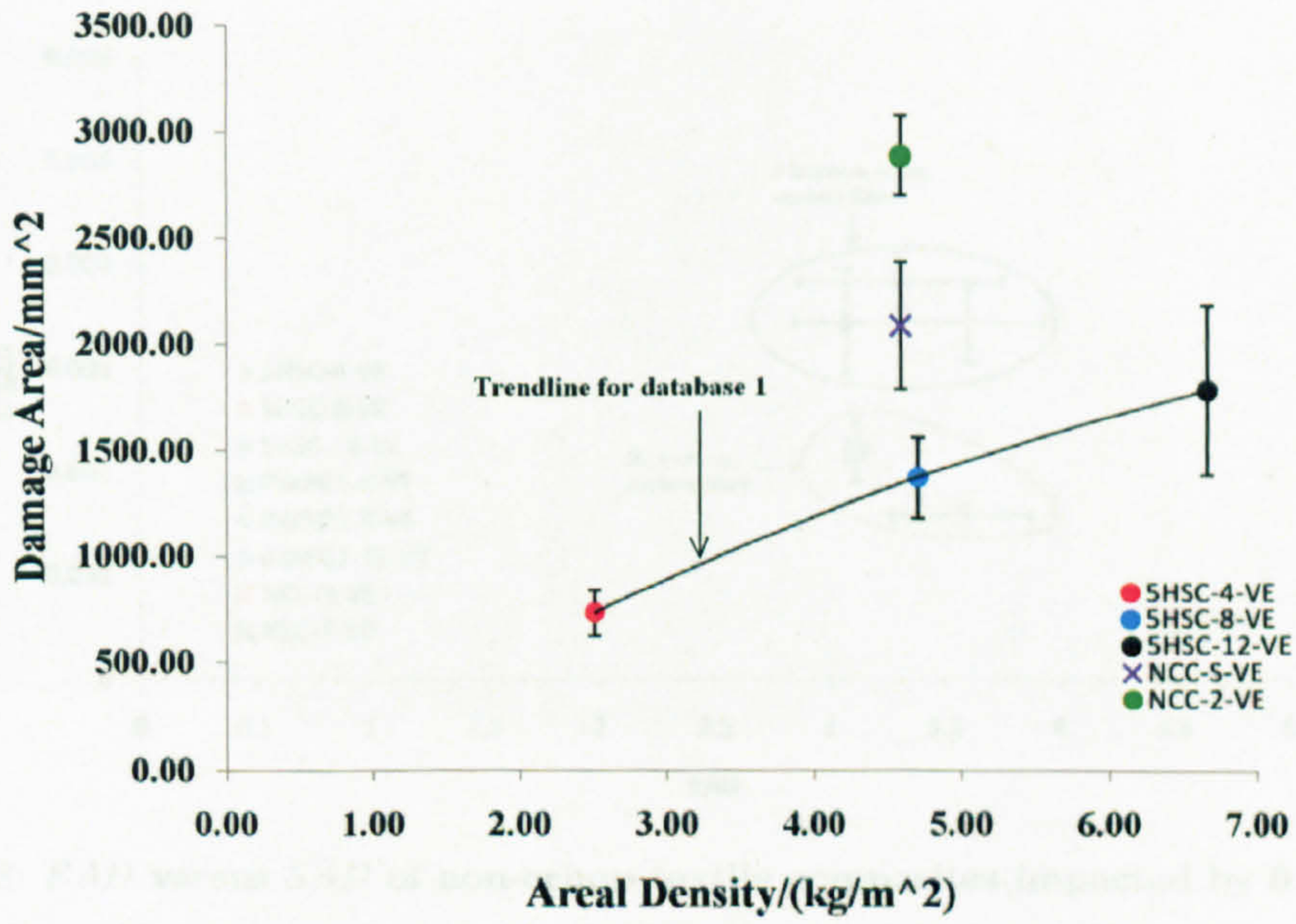

Figure 7.16: **Damage areas of non-crimp textile composites impacted by 0.44g steel balls .**

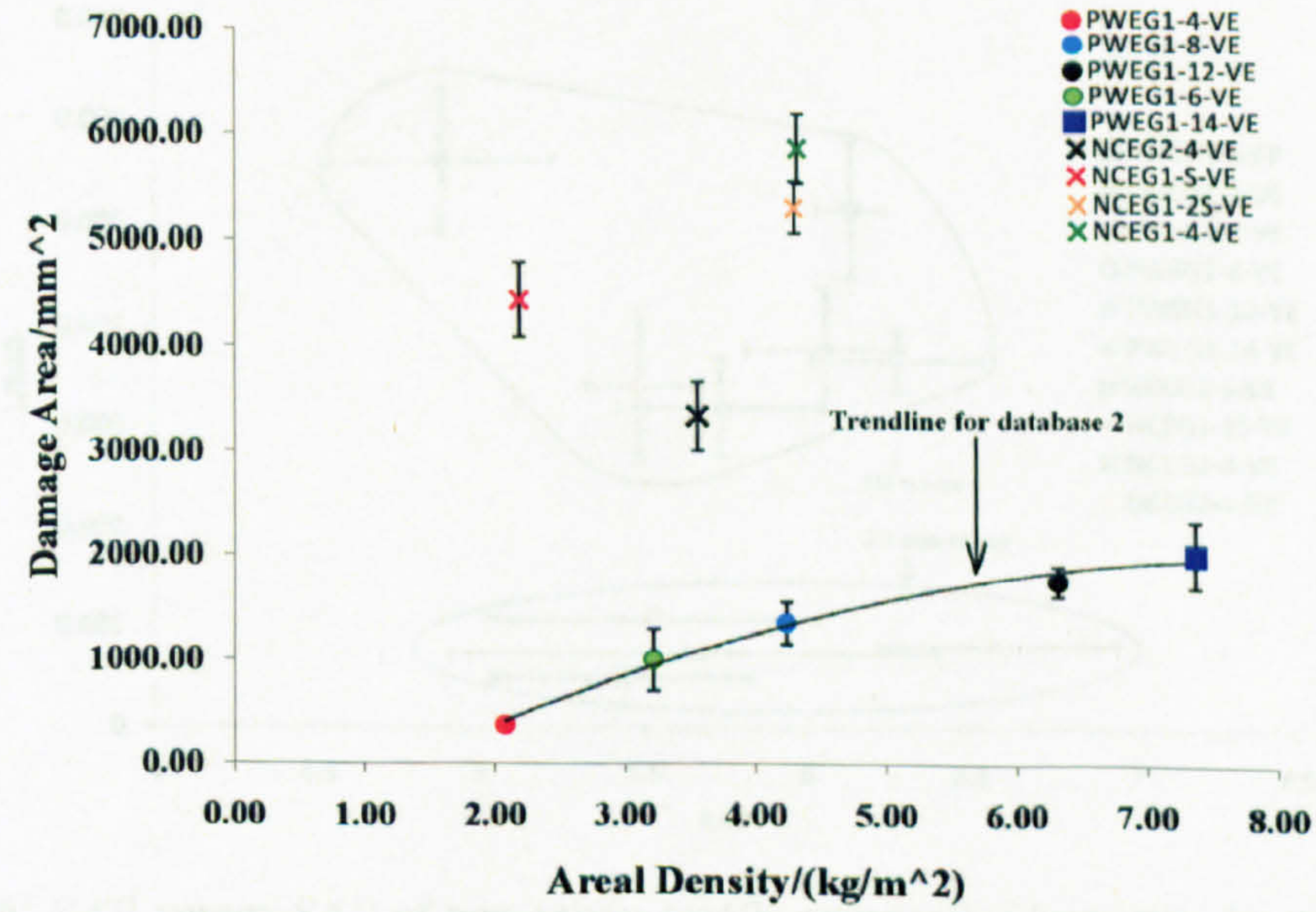

Figure 7.17: **Damage areas of non-crimp textile composites impacted by 0.87g steel balls .**

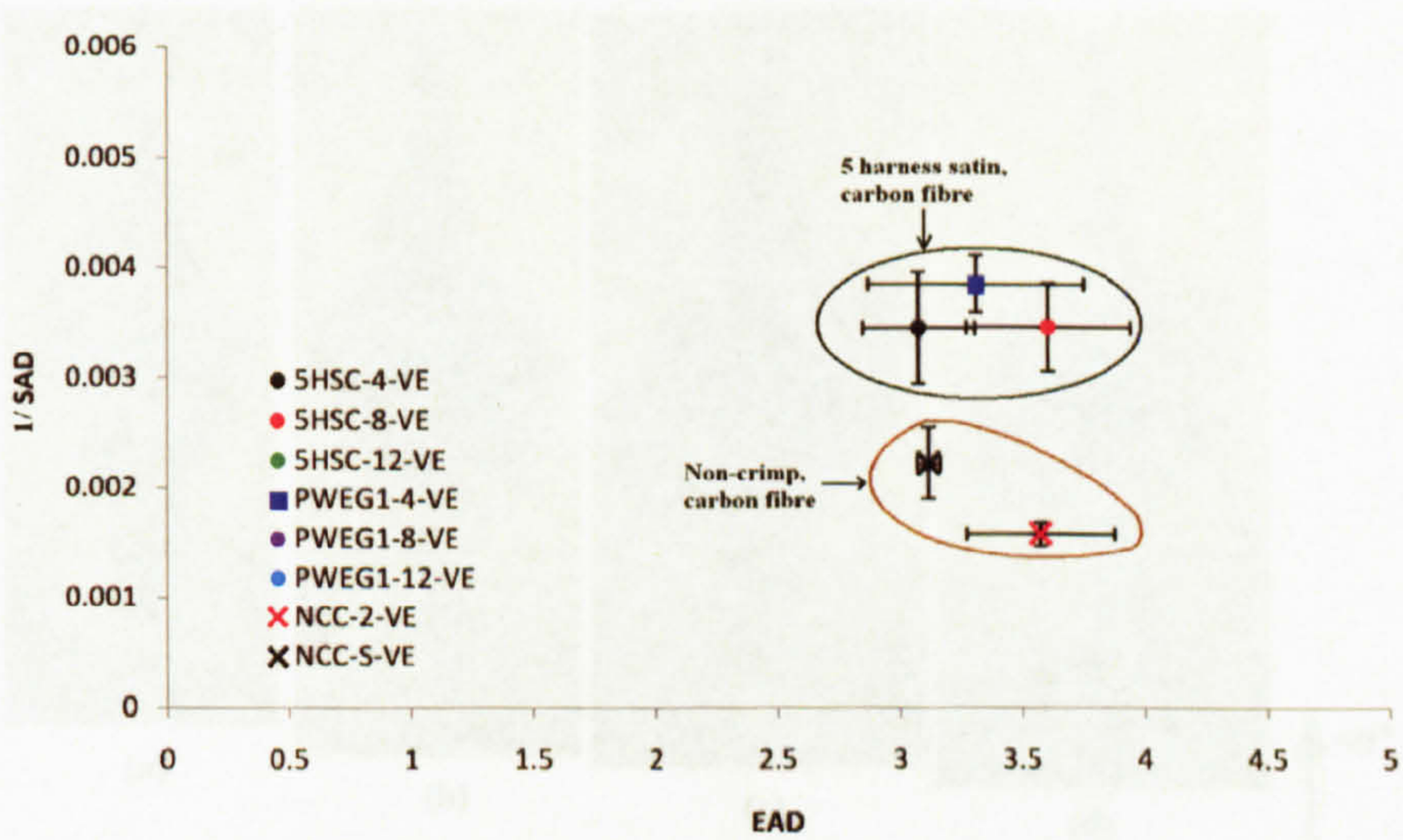

Figure 7.18: *EAD* **versus** *SAD* **of non-crimp textile composites impacted by 0.44g steel balls .**

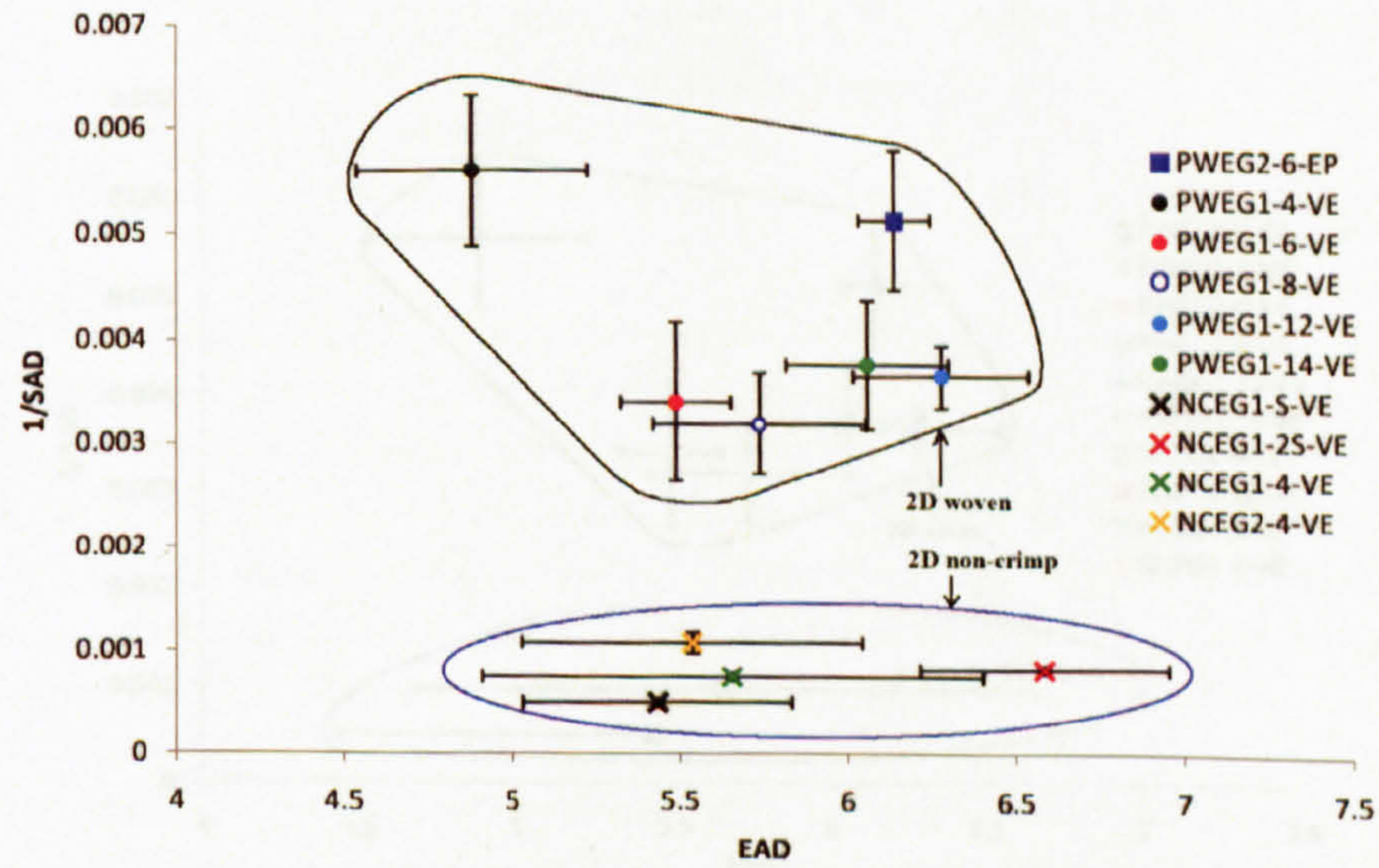

Figure 7.19: *EAD* **versus** *SAD* **of non-crimp textile composites impacted by 0.87g steel balls** - including peel-off of yarns in the rear sides of the composites .

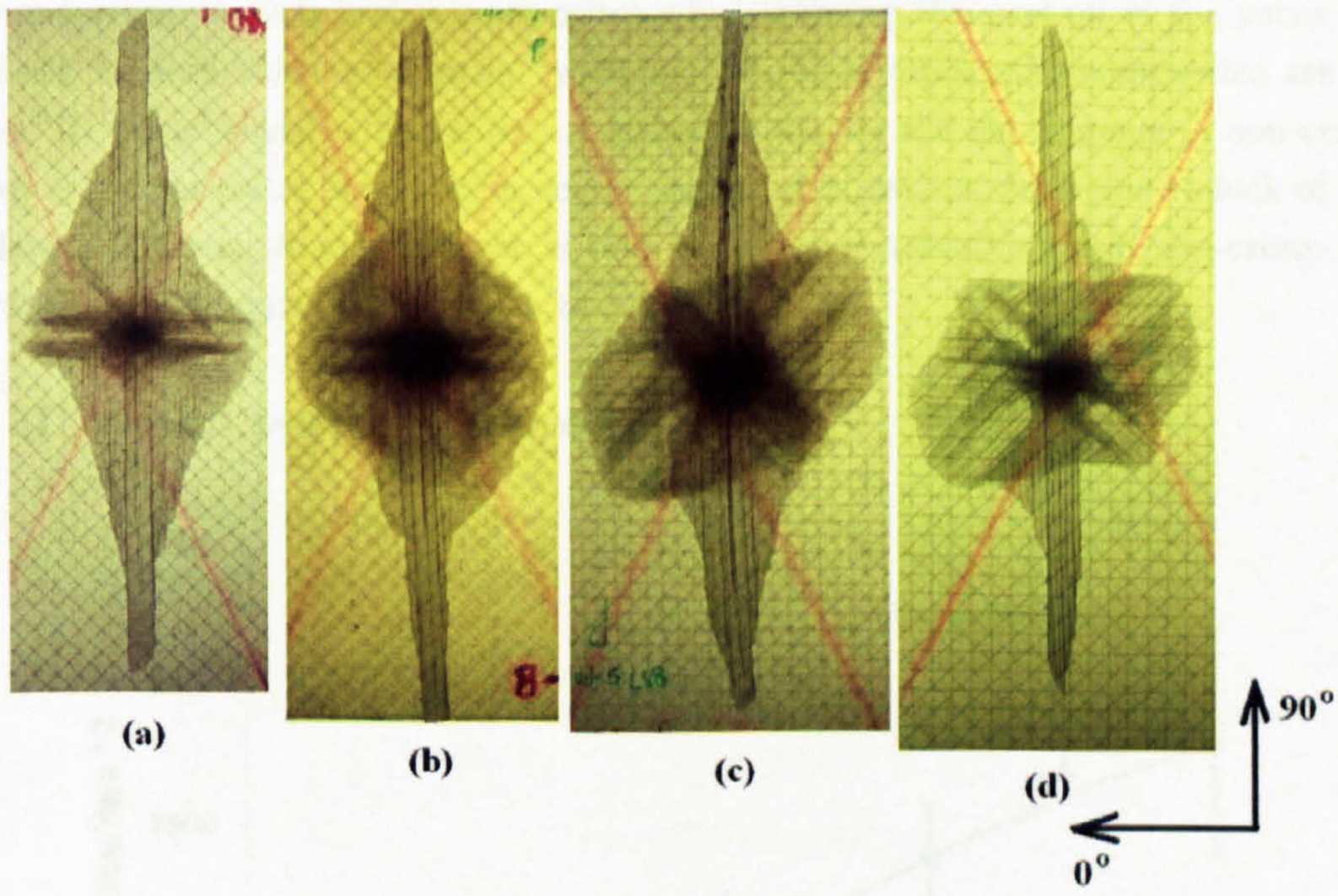

Figure 7.20: **Non-crimp textile composites after ballistic impact tests** - (a) NCEG1-S-VE; (b) NCEG1-2S-VE; (c) NCEG1-4-VE; (d) NCEG2-4-VE.

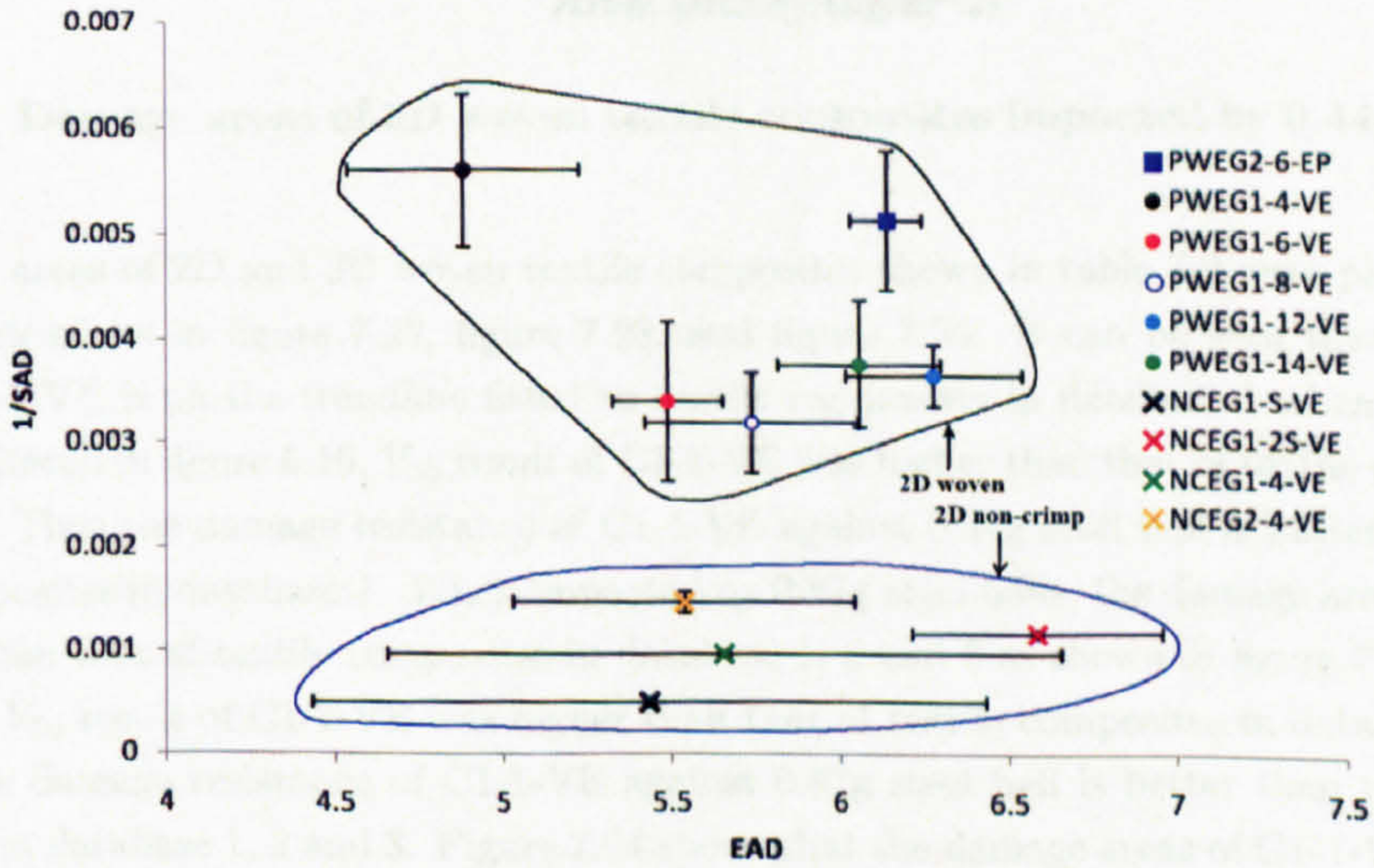

Figure 7.21: *EAD* **versus** *SAD* **of non-crimp textile composites impacted by 0.87g steel balls** - excluding peel-off of yarns in the rear sides of the composites .

composite is the peel-off of the yarns in rear sides of the composite panels. The shapes main body of the damage areas were dependent on fibre lay-up. Figure 7.21 investigates the damage resistance of all the non-crimp E-glass textile composites when ignoring the peel-off of the yarns mentioned above. It can be seen that the damage resistance of non-crimp textile composites are still much worse than 2D woven textile composites. Another reason for the big damage of non-crimp textile composites is the generator strip phenomenon described in section 2.6.4 due to lack of interlacing between layers of yarns. Another reason is that stress waves travel faster in non-crimp yarns than crimped warp or weft yarns in 2D woven textile composites.

7.3.5 3D woven textile composites

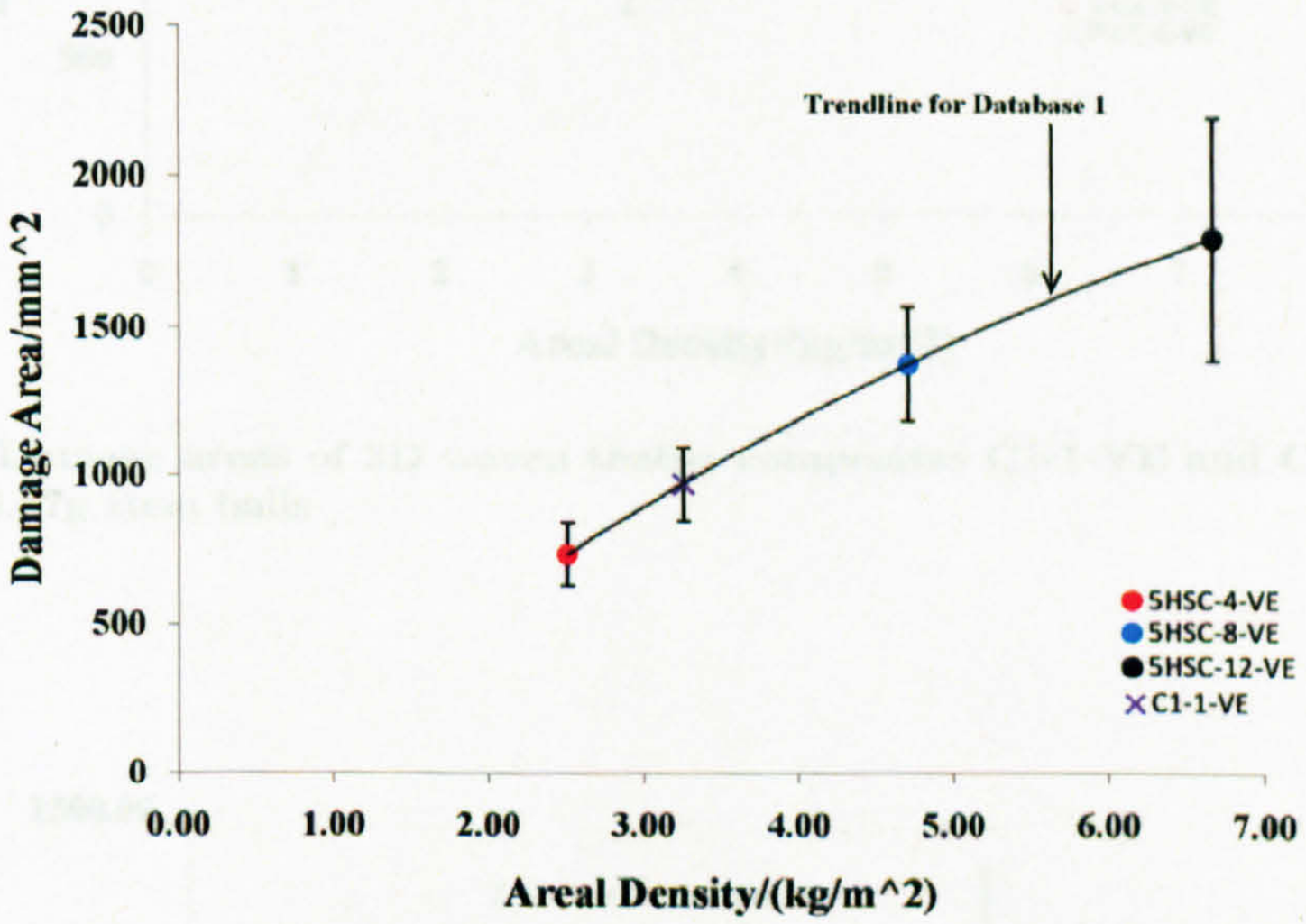

Figure 7.22: **Damage areas of 3D woven textile composites impacted by 0.44g steel balls**

Damage areas of 2D and 3D woven textile composites shown in table 7.2 were plotted against their areal densities in figure 7.22, figure 7.23, and figure 7.24. It can be seen that the damage areas of C1-1-VE is on the trendline fitted to textile composites in database 1 when impacted by 0.44g ball. Recall in figure 6.16, V_{50} result of C1-1-VE was higher than that of textile composites in database 1. Thus the damage resistance of C1-1-VE against 0.44g steel ball is better than that of textile composites in database 1. When impacted by 0.87g steel balls, the damage area of C1-1-VE is smaller than that of textile composites in database 1, 2 and 3 as shown in figure 7.23. Recall in figure 6.18, V_{50} result of C1-1-VE was higher than that of textile composites in database 1, 2 and 3. Thus the damage resistance of C1-1-VE against 0.87g steel ball is better than that of textile composites in database 1, 2 and 3. Figure 7.24 shows that the damage areas of G1-1-VE, G2-1-VE, G3-1-VE, G4-1-VE and G7-1-VE are much smaller than the damage areas of the textile composites in database 2. Recall in figure 6.21, the V_{50} results of G1-1-VE, G2-1-VE, G3-1-VE, G4-1-VE and G7-1-VE are on the same level as composites in database 2. Thus the damage resistance of G1-1-VE, G2-1-VE, G3-1-VE, G4-1-VE and G7-1-V are better than composites in database 2. The good damage resistance of all 3D textile composites were highlighted in figure 7.25, figure 7.26 and

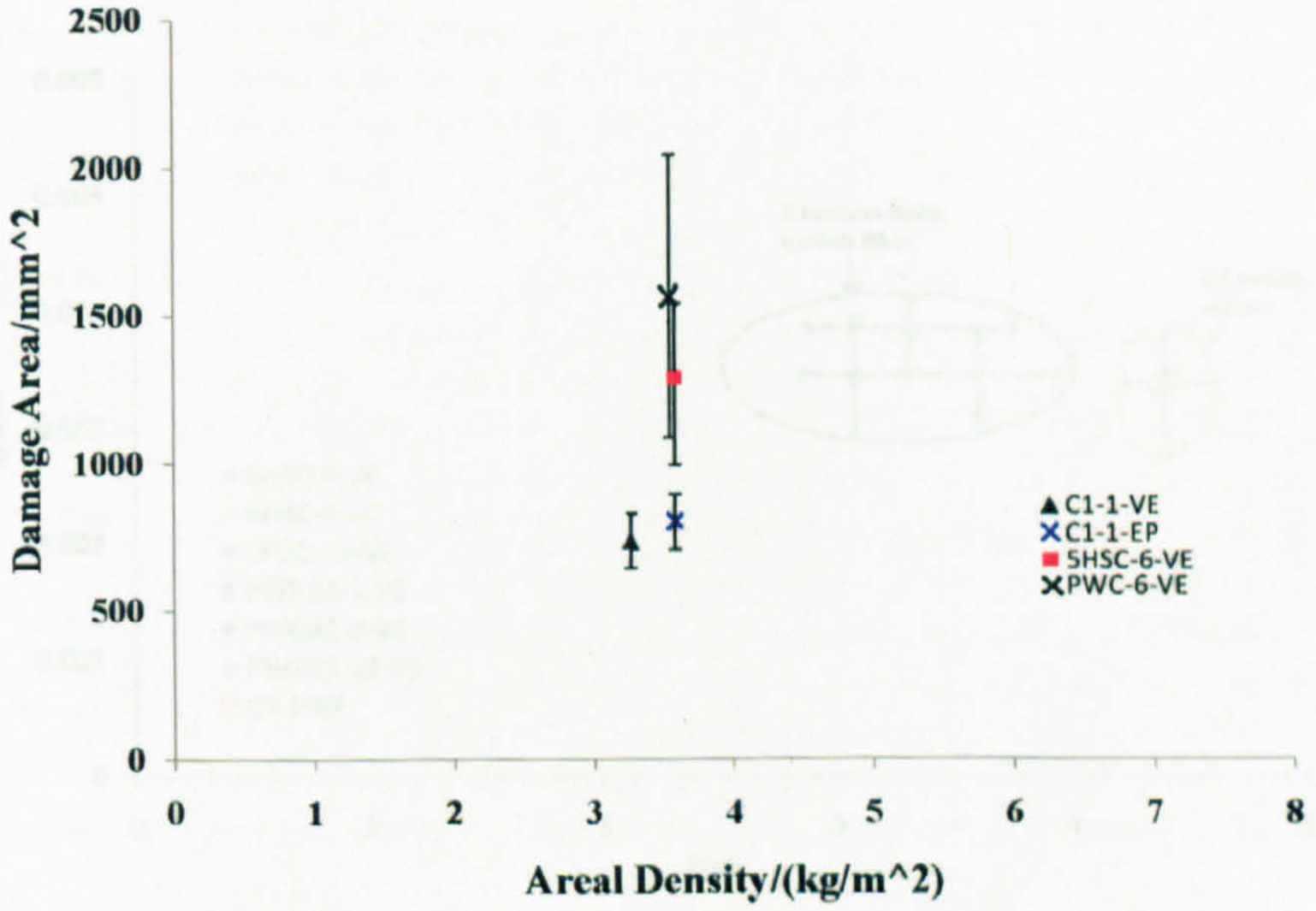

Figure 7.23: **Damage areas of 3D woven textile composites C1-1-VE and C1-1-EP impacted by 0.87g steel balls .**

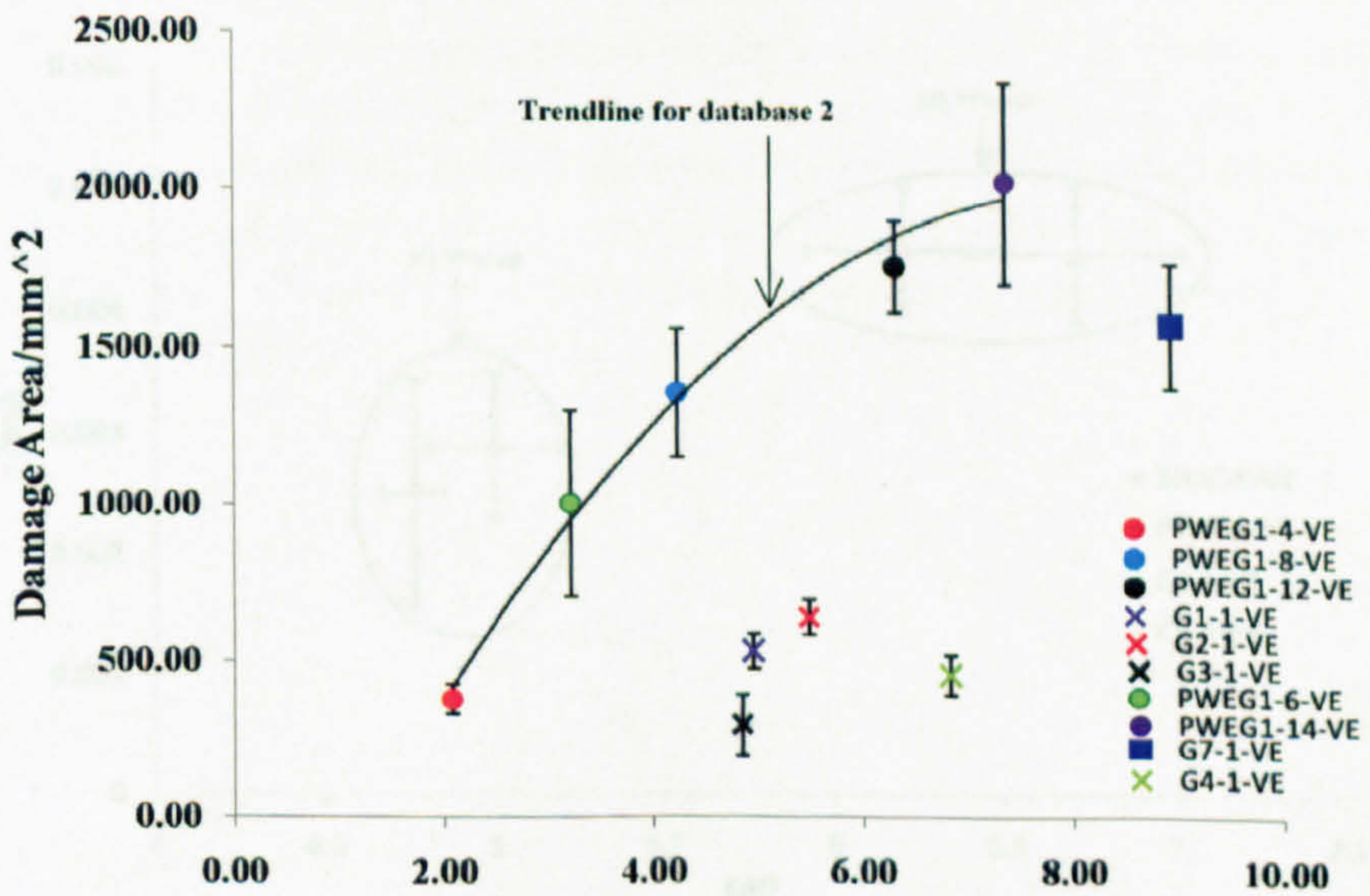

Figure 7.24: **Damage areas of 3D woven E-glass textile composites impacted by 0.87g steel balls .**

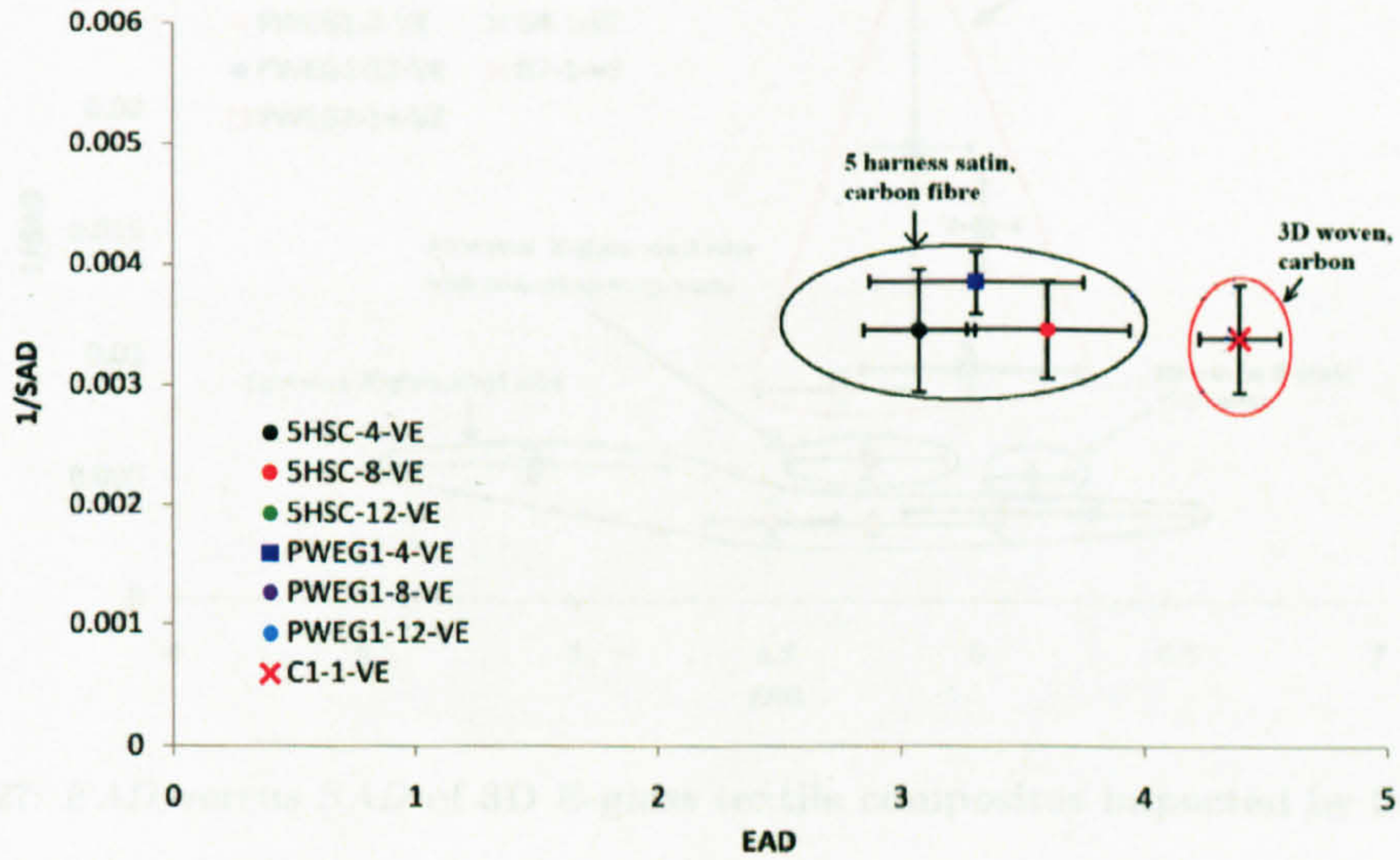

Figure 7.25: EAD **versus** SAD **of 3D textile composites impacted by 0.44g steel balls .**

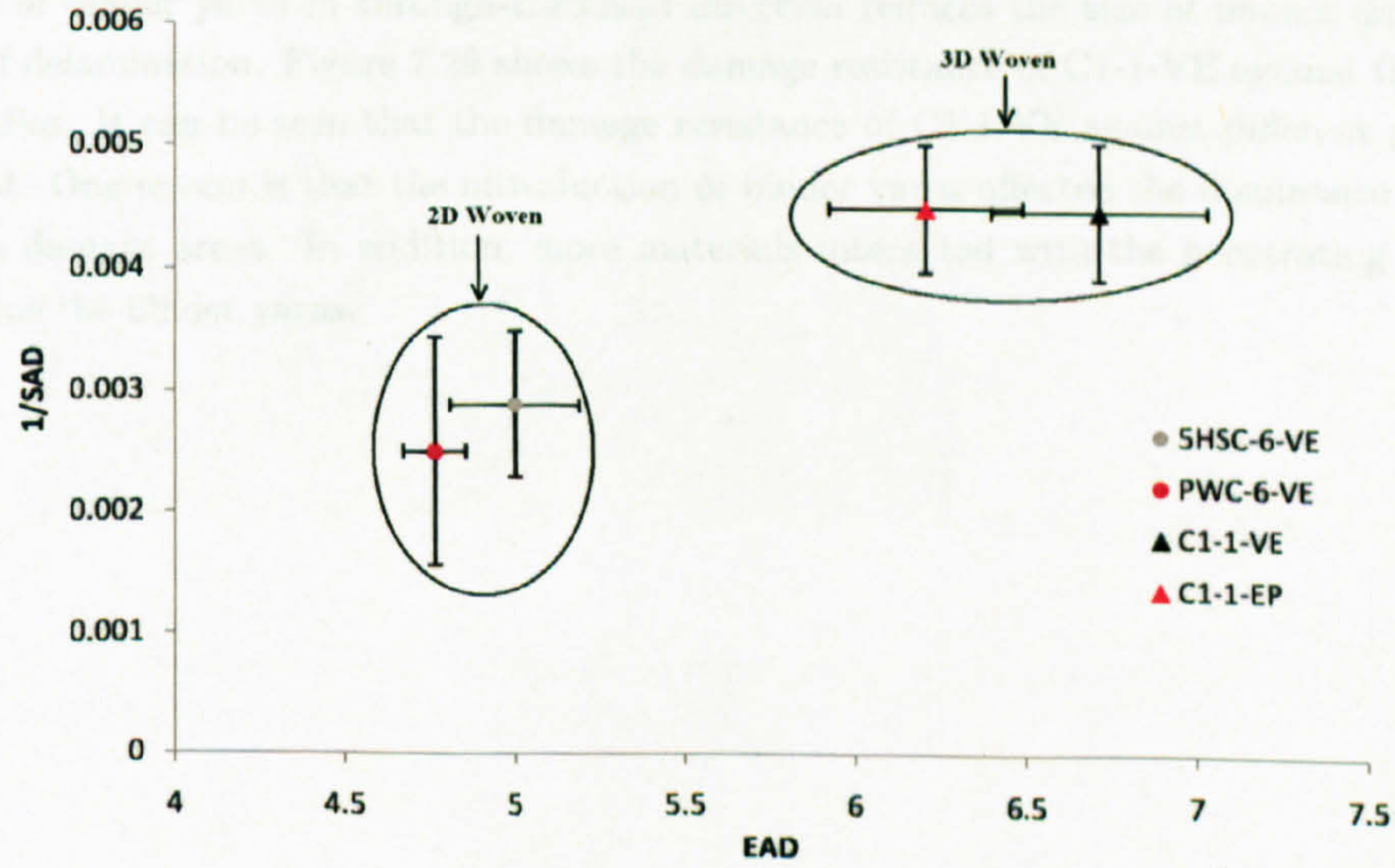

Figure 7.26: EAD **versus** SAD **of 3D carbon textile composites impacted by 0.87g steel balls .**

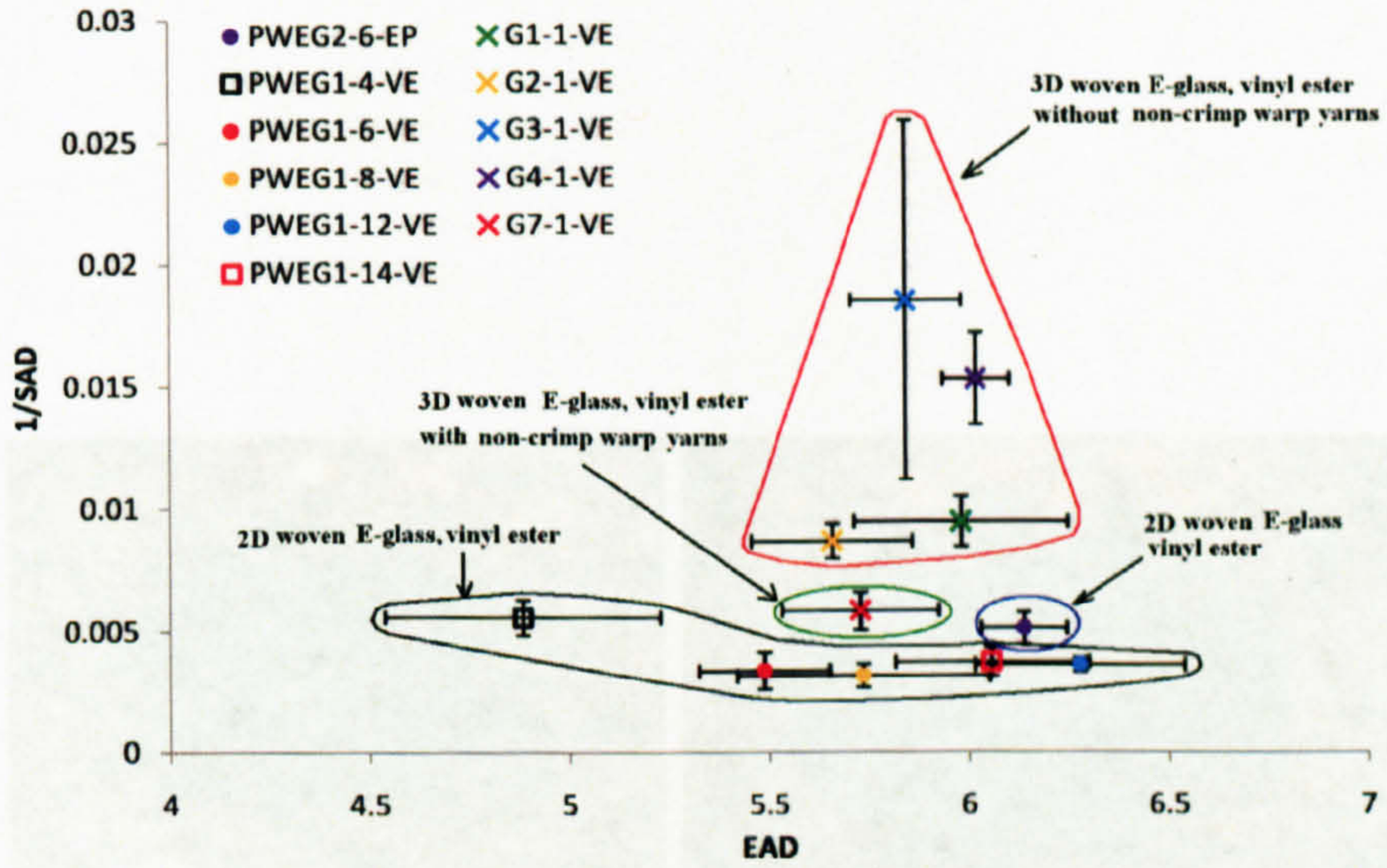

Figure 7.27: *EAD* **versus** *SAD* **of 3D E-glass textile composites impacted by 0.87g steel balls** .

figure 7.27. Figure 7.7 shows that the outlines of G1-1-VE, G2-1-VE, G3-1-VE, and G4-1-VE are not circular. Figure 7.28 shows that big delamination area was only observed in G2-1-VE. This suggests that the good damage resistances of G1-1-VE etc are due to the reducing or eliminating of big delamination areas.

The majority of yarns in C1-1-VE are non-crimp yarns. Compared with non-crimp textile composites, C1-1-VE has much better damage resistance as shown in figure 7.30. This proved that the introduce of binder yarns in through-thickness direction reduces the size of impact damage, i.e. the size of delamination. Figure 7.29 shows the damage resistance of C1-1-VE against three kinds of projectiles. It can be seen that the damage resistance of C1-1-VE against different projectiles is different. One reason is that the introduction of binder yarns affected the dominance of delamination in damage areas. In addition, more materials interacted with the penetrating projectile directly due the binder yarns.

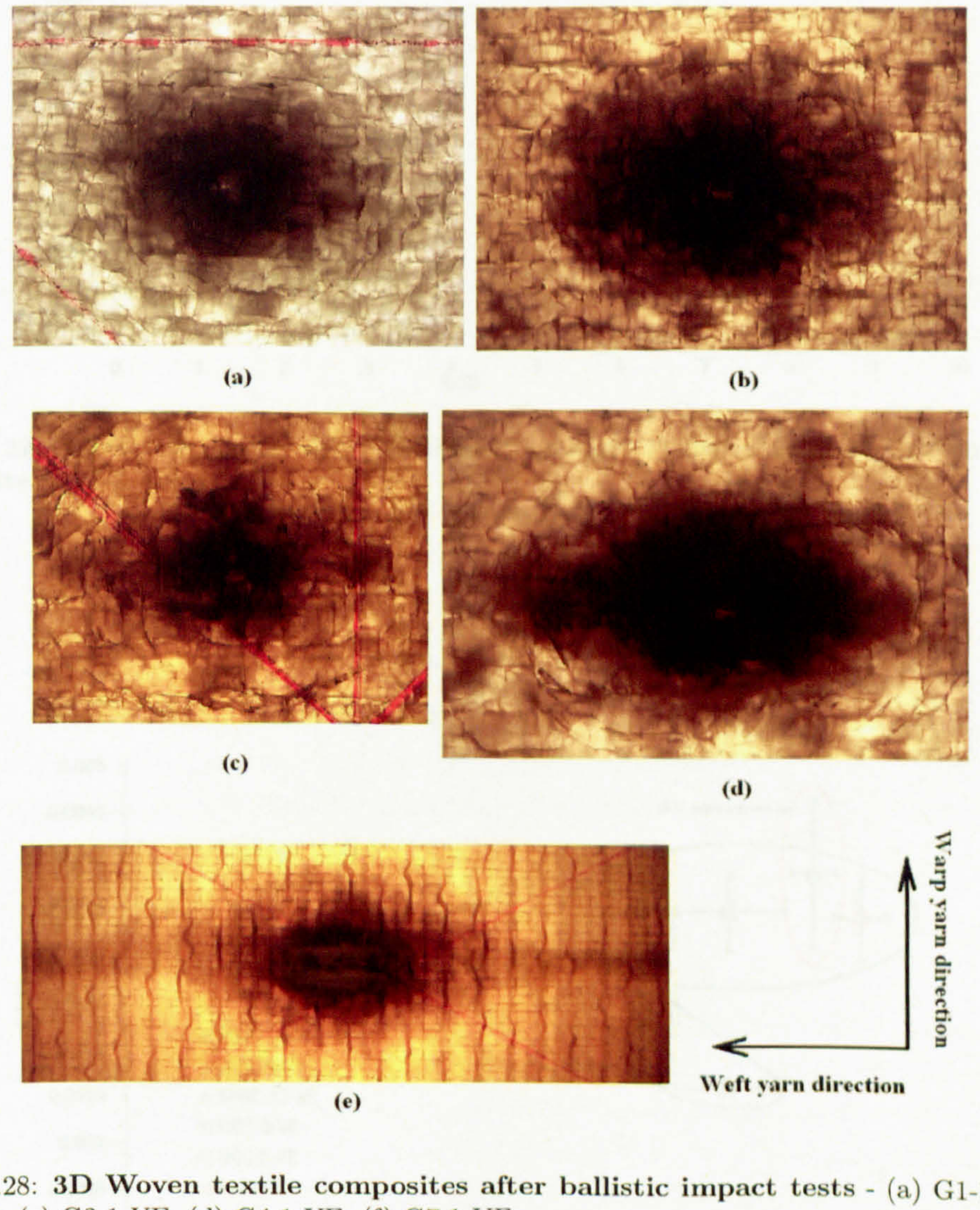

Figure 7.28: **3D Woven textile composites after ballistic impact tests** - (a) G1-1-VE; (b) G2-1-VE; (c) G3-1-VE; (d) G4-1-VE; (f) G7-1-VE.

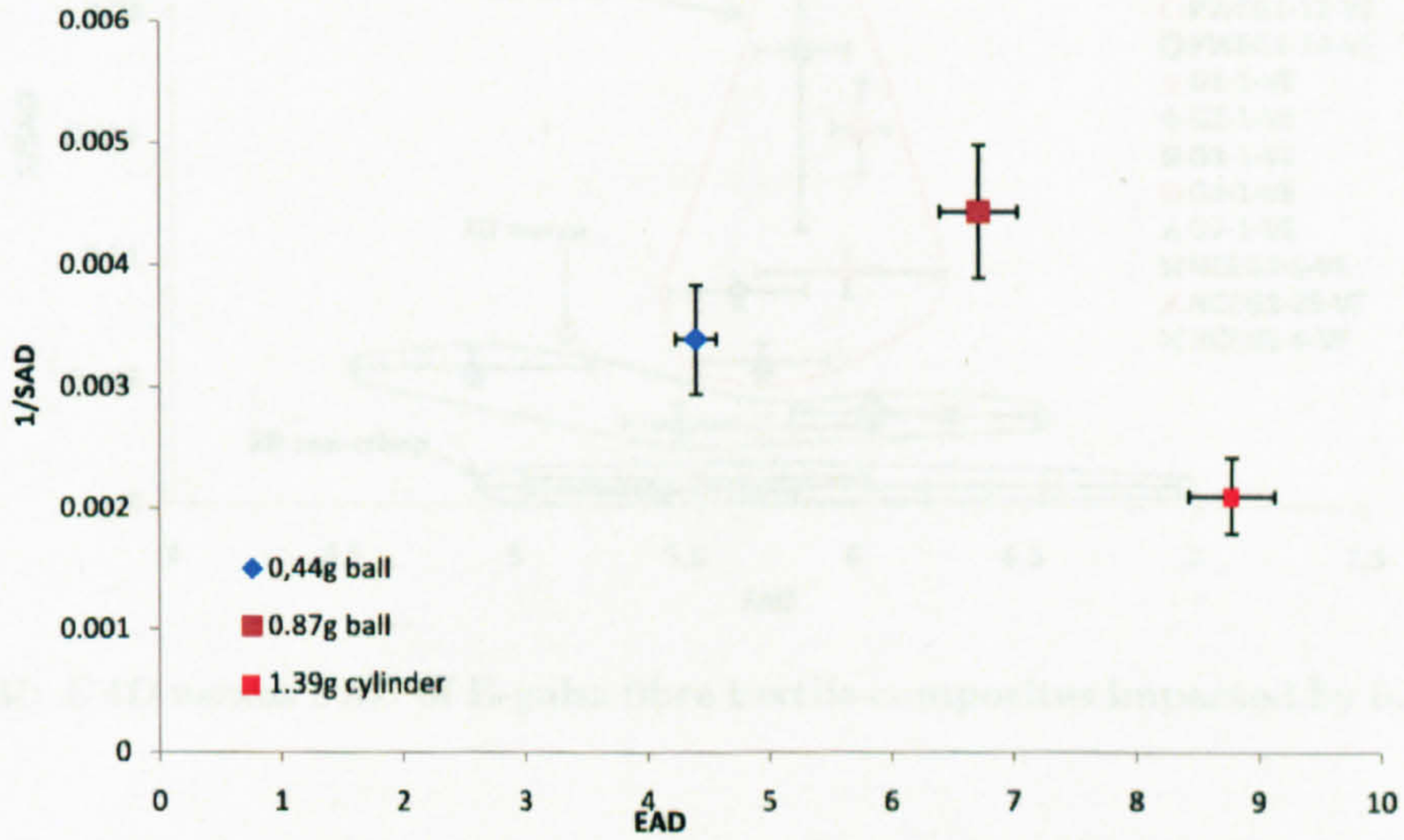

Figure 7.29: **Effect of projectile on ballistic damage resistance of 3D woven textile composites** - C1-1-VE .

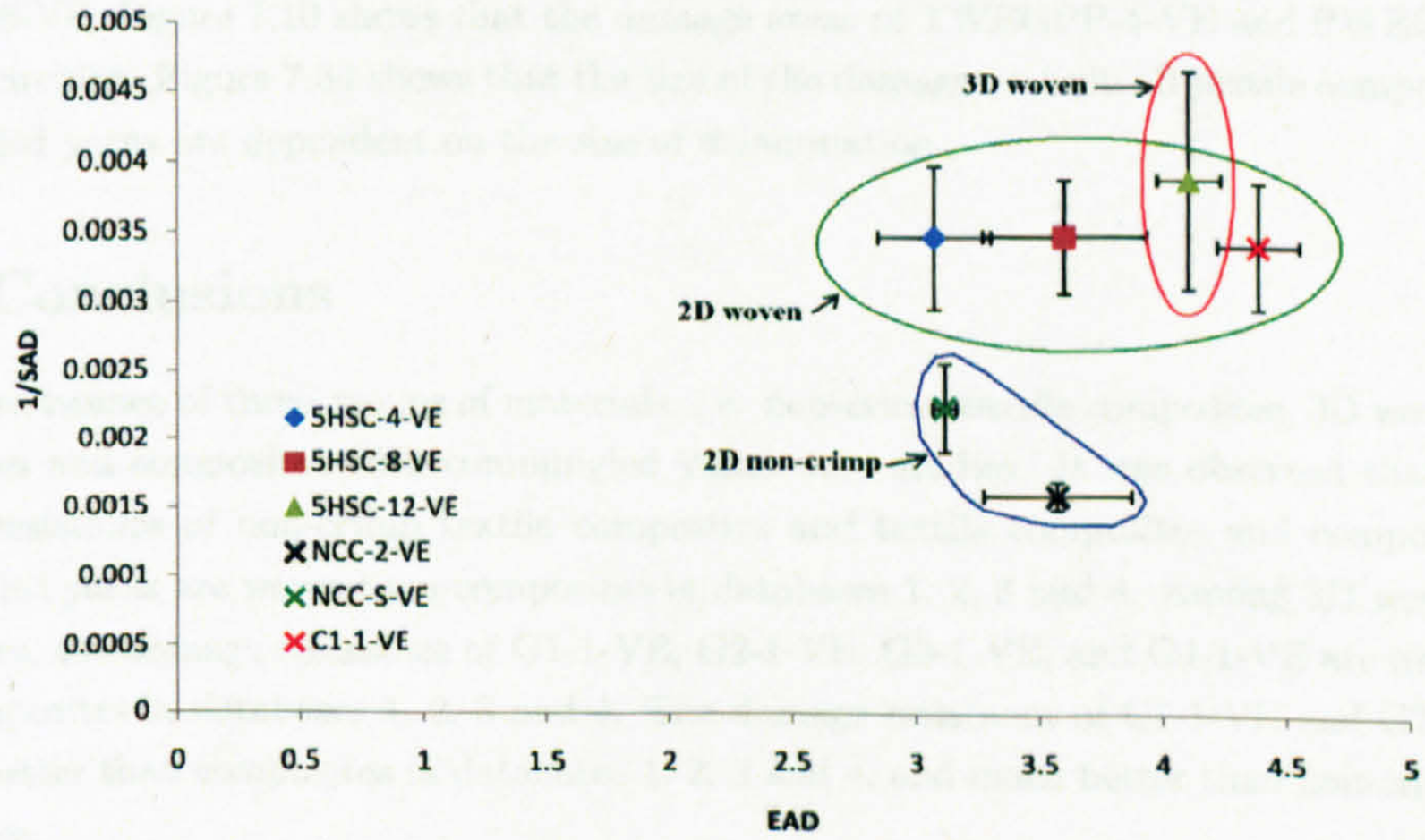

Figure 7.30: EAD **versus** SAD **of carbon fibre textile composites impacted by 0.44g steel balls** - 2D woven, 3D woven and 2D non-crimp textile composites .

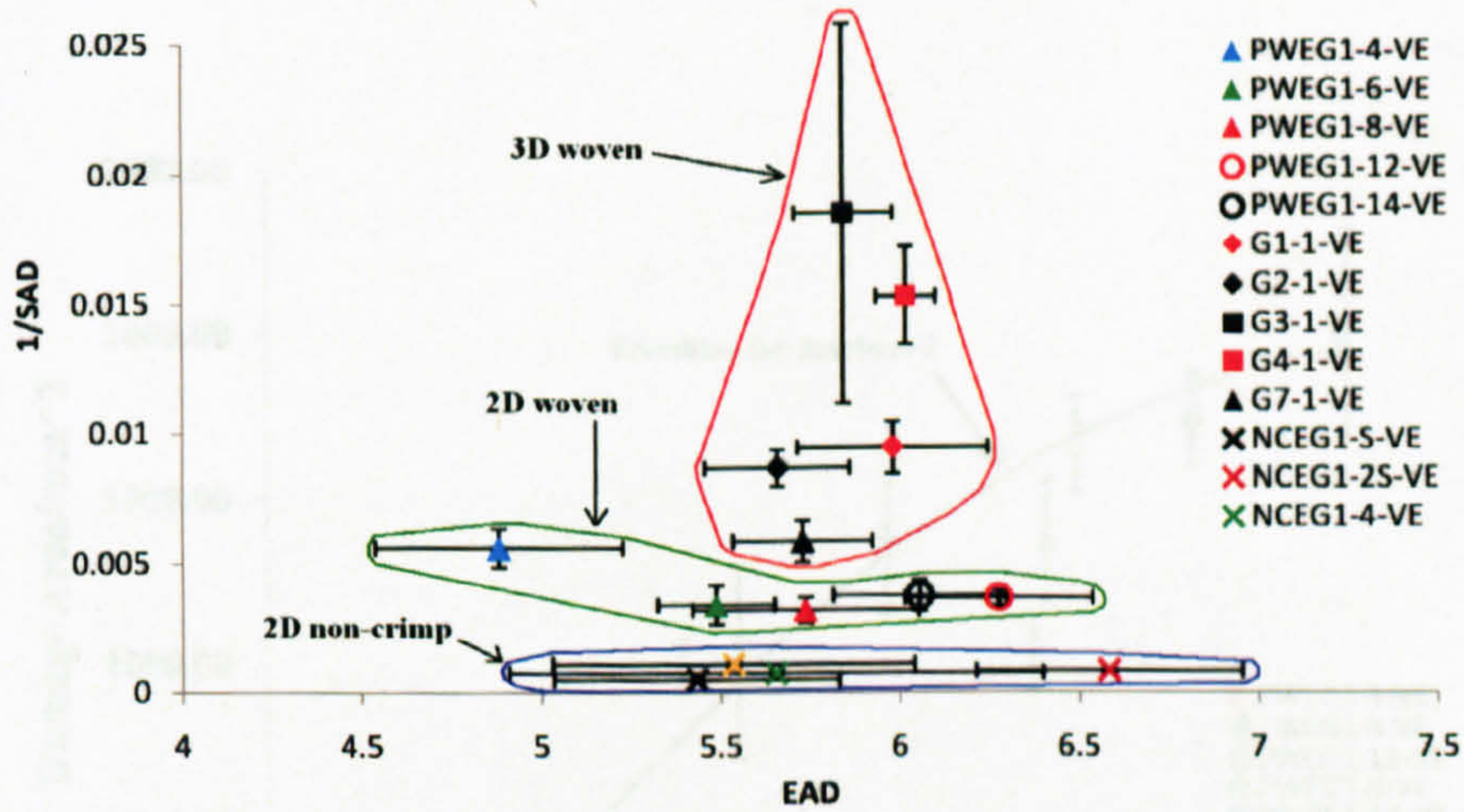

Figure 7.31: *EAD* **versus** *SAD* **of E-galss fibre textile composites impacted by 0.87g steel balls .**

7.3.6 Textile composites with commingled yarns

Damage areas of textile composites with commingled yarns shown in table 7.2 were plotted against their areal densities as shown in figure 7.32. It can be seen that the damage area of TWEGPP-2-VE is above the trendline fitted to composites in database 2. The damage areas of TWEGPP-4-VE and PWEGPP-4-VE are bigger than that of PWEG2-6-VE. Recall in figure 6.29, V_{50} results of TWEGPP-2-EP,TWPEGPP-4-VE and PWEGPP-4-VE are similar to that of composites in database 2. Thus the damage resistance of TWEGPP-2-EP is not as good as composites in database 2. The damage resistance of TWEGPP-4-EP and PWEGPP-4-EP are worse than that of PWEG2-6-VE. Figure 7.10 shows that the damage areas of TWEGPP-4-VE and PWEGPP-4-VE are near circular. Figure 7.34 shows that the size of the damage areas in all textile composites with commingled yarns are dependent on the size of delamination.

7.4 Conclusions

Damage resistance of three groups of materials, i.e. non-crimp textile composites, 3D woven textile composites and composites with commingled yarns were studies. It was observed that only the damage resistance of non-crimp textile composites and textile composites and composites with commingled yarns are worse than composites in databases 1, 2, 3 and 4. Among 3D woven textile composites, the damage resistance of G1-1-VE, G2-1-VE, G3-1-VE, and G4-1-VE are much better than composites in databases 1, 2, 3 and 4. The damage resistance of C1-1-VE and G7-1-VE are slightly better than composites in databases 1, 2, 3 and 4, and much better than non-crimp textile composites.

In composites in database 1, 2, 3 and 4 if there is delamination the damage area of the textile composite is dependent on the size of the delamination. For those textile composites, the effect of the projectile on *SAD* value is very small. Using of resin with high toughness and high bonding strength such as epoxy can reduce the size of the damage area. Delaminations in non-crimp textile composites are much bigger than 2D woven textile composites in database 1, 2, 3 and 4. This is due

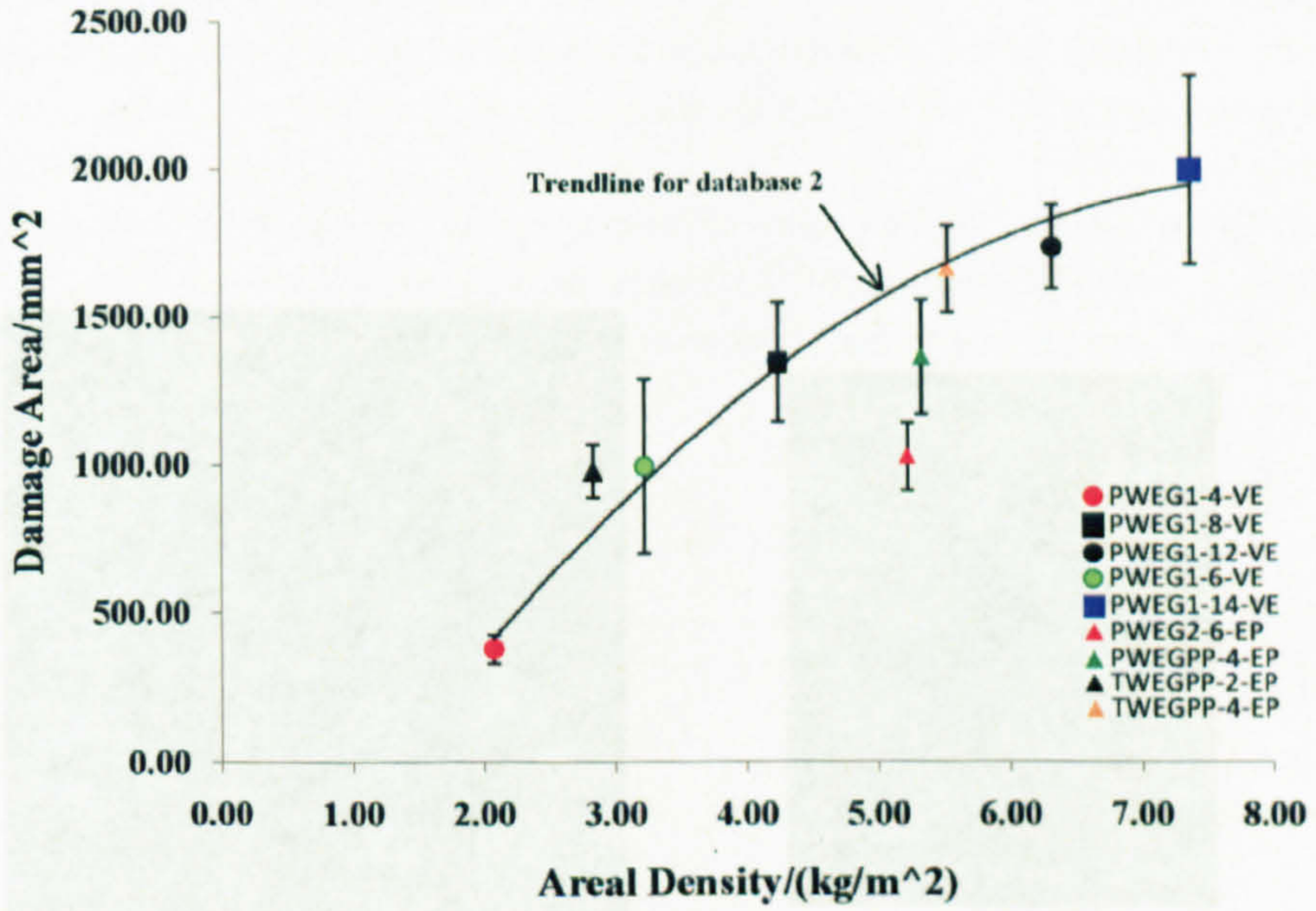

Figure 7.32: **Damage areas of textile composites with comingled yarns impacted by 0.87g steel balls .**

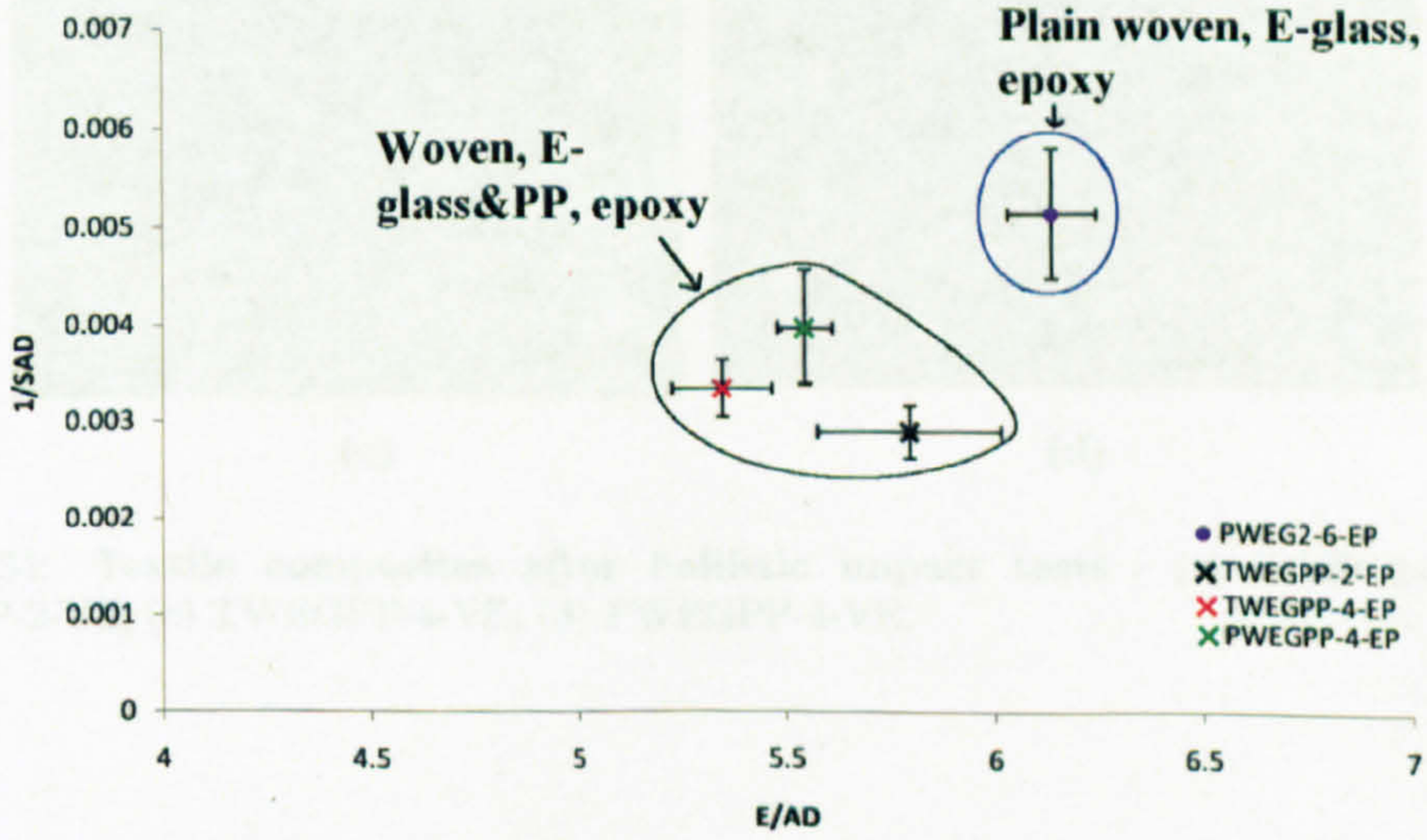

Figure 7.33: EAD **versus** SAD **of co-mingled textile composites impacted by 0.87g steel balls .**

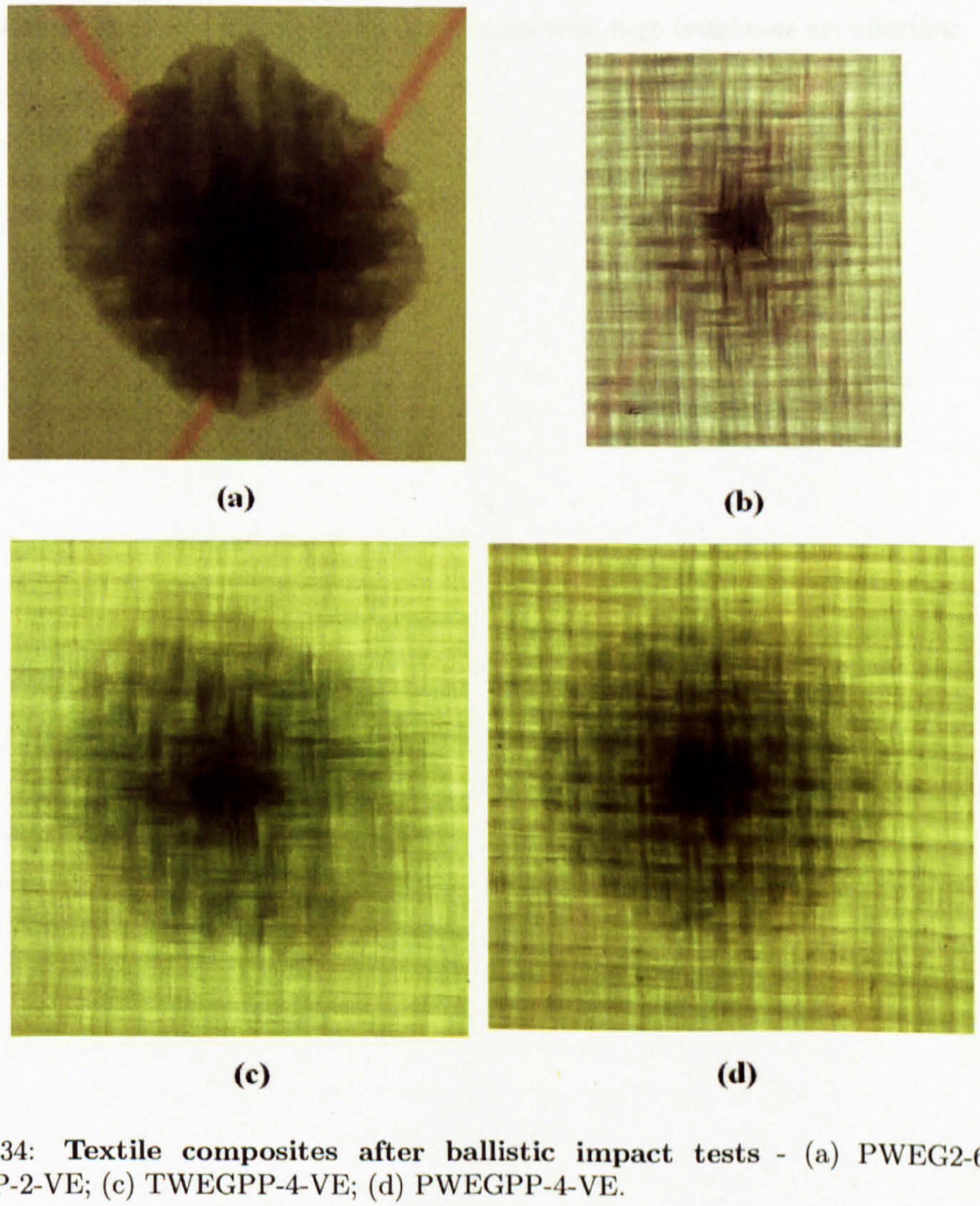

Figure 7.34: **Textile composites after ballistic impact tests** - (a) PWEG2-6-EP; (b) TWEGPP-2-VE; (c) TWEGPP-4-VE; (d) PWEGPP-4-VE.

to the generator strip phenomenon and the faster speed stress waves can travel at in non-crimp yarns. The delaminations in C1-1-VE and G7-1-VE are much smaller than that of non-crimp textile composites. This is due the introduction of binder yarns in the through-thickness direction. It was observed that using high strength yarns such as Kevlar as binder yarns can reduce the size of the damage further. Most other 3D woven textile composites don't have big delamination areas except G2-1-VE.

So far it can be concluded that ballistic impact damage resistance of textile composites can be improved by reducing or eliminating delamination areas. Two methods including introduction of yarns in through-thickness direction and use of resin with high toughness are effective.

Chapter 8

Ballistic impact damage mechanisms in 2D and 3D textile composites

8.1 Introduction

During the characterization of the damage areas of textile composites after ballistic impacts, various types of fracture events such as delamination, matrix cracking etc were treated equally. In addition, the extents of the damage in different regions inside the damage areas were not taken into consideration by the damage areas results. Information of this type is however very important for analyzing both V_{50} results and damage area results.

Failure mechanisms in 2D textile composites subjected to ballistic impacts were reviewed in section 2.5. Damage patterns including delamination, shear plug, transverse fibre fracture, fibre-matrix debonding, matrix cracks, tensile fibre fracture, fibre spallation, stretching of fibres, melting of fibres were mentioned in [17, 20, 25, 32, 28, 48, 74, 77]. In different textile composites, combinations of various damage types form a damage zone. Each damage type may occur at different stages during the penetration of the projectile and at different position within the damage zone. It is impossible to record real-time damage progress during a ballistic impact test. But the status of all damage patterns after penetration positions can be characterized by constructing a 3D model of the damage zone using the computer simulation method described in section 4.3.7. Modelling of the whole damage zone requires thousands of optical microscope images. 2D textile composites such as plain woven and satin textile composites are quasi-isotropic materials, so simulation of the whole damage zone is not necessary. An image of the cross-section that is perpendicular to warp or weft yarns and across the impacting point is sufficient to illustrate damage mechanisms and their locations. The 3D textile composites used in this study are not quasi-isotropic materials. But the methods used for 2D textile composites to determine the position of different damage types were also used for 3D textile composites. Only one image of a cross-section for each 3D woven textile composite was used. Full pictures of the damage zones in the 3D woven textile composites may not be reviewed. This is due to the fact that different types of multi-layer locking yarns are mixed in the weft yarn direction. One cross-section may not include all the multi-layer locking yarns in a

3D woven textile composite. In the sections below, focus will be on finding the distinctive damage mechanisms in 3D woven textile composites. In addition to the computer simulation as described in section 4.3.7, visual inspection of the front and back surfaces of the composite panels were also carried out.

In chapter 6, it was observed that the damage resistance of non-crimp textile composites and composites with commingled yarns are not as good as textile composites in databases. Due to the limitation of time and materials, damage mechanisms in the non-crimp textile composites and composites with commingled yarns studied in the last chapter will not be characterized. Only 3D woven textile composites and composites in database 1 and 2 will be used.

8.2 Results - failure mechanisms of V_{50} Samples

8.2.1 Database 1

8.2.1.1 5HSC-4-VE

One penetrated V_{50} Sample of 5HSC-4-VE was used. Its close-up images of both front and back were taken using a digital camera. The images are shown in figure 8.1 (*a*) and (*b*). Fibre fractures were observed on both front and back surface in the route of the flying projectile. The specimen was then cut along a line near the line A-A as shown in figure 8.1 (*a*). The new surface, i.e. one cross-section of 5HSC-4-VE specimen was polished until reaching line A-A. The cross-section was examined using an optical microscope. Images with magnification of x5 were taken and joined together using imaging software. The final cross-section image is shown in figure 8.1 (*c*) and figure 8.2. Damages observed in the cross-section image include shear plug, delamination, fibre fracture, and matrix cracking. Shear plug and fibre fractures occurred in or near the region of the path of the projectile. Tensile failure of fibre bundle was observed near the back of the specimen (figure 8.2 (a). Delamination was observed between every two adjacent laminate in the resin rich areas. Both the diameter of both shear plug and delamination increased through the thickness. Extensive matrix cracks were observed near the delamination region (Figure 8.2 (*c*)).

8.2.1.2 5HSC-8-VE

One non-penetrated V_{50} sample of 5HSC-8-VE was used. Same methods described used for 5HSC-4-VE specimen were used here. In the 5HSC-4-VE specimen studied above, the steel ball was not captured which makes polishing of the specimen easy. In the non-penetrated sample of 5HSC-8-VE used here, the steel ball was captured as shown in figure 8.3 (*a*). After cutting, the part of the steel ball left in the specimen was taken out leaving an empty hole in the specimen as shown in figure 8.3 (*c*) and figure 8.4 (*a*). It can be seen in figure 8.4 (*a*) that the size of the hole was smaller than the diameter of the projectile. This was because of the fact that the line A-A in figure 8.3 (*a*) was not crossing the centre of the captured projectile. It can also be seen in figure 8.4 (*a*) that the fractured fibres near the impacting surface of the specimen felt down on the empty hole. This could have been prevented by putting specimens into a pool of resin after ballistic impact testss. After the curing of the resin, the damages in the original specimens were "frozen".

Damages observed in in figure 8.3 and figure 8.4 include shear plug, delamination, fibre fracture, matrix crack. Fibre fracture was observed in both front view and back views, and in the shear plug

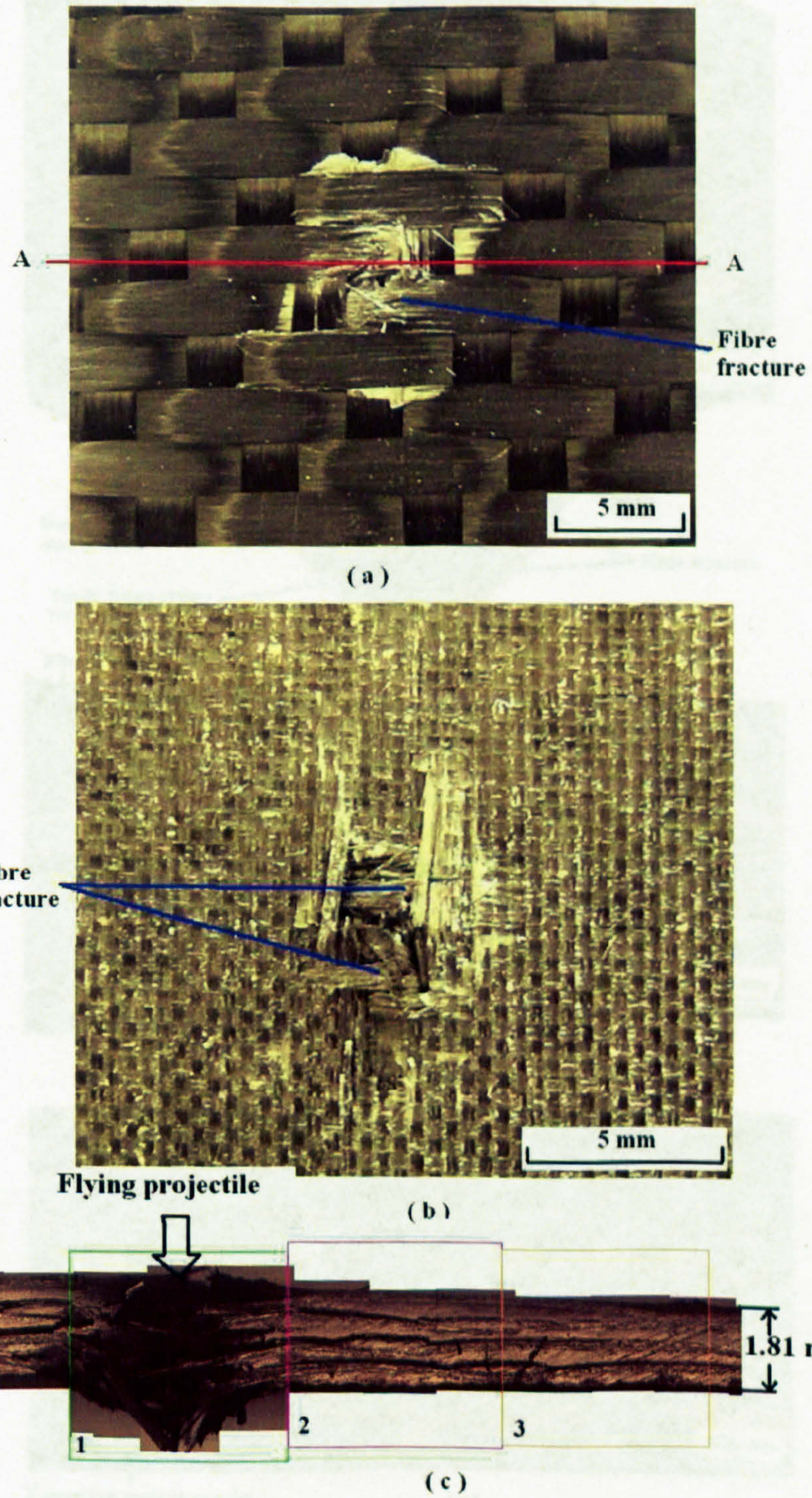

Figure 8.1: **Damage patterns in one penetrated V_{50} sample of 5HSC-4-VE impacted by 0.44g steel ball -Part I** - (a) front view; (b) back view; (c) part section A-A.

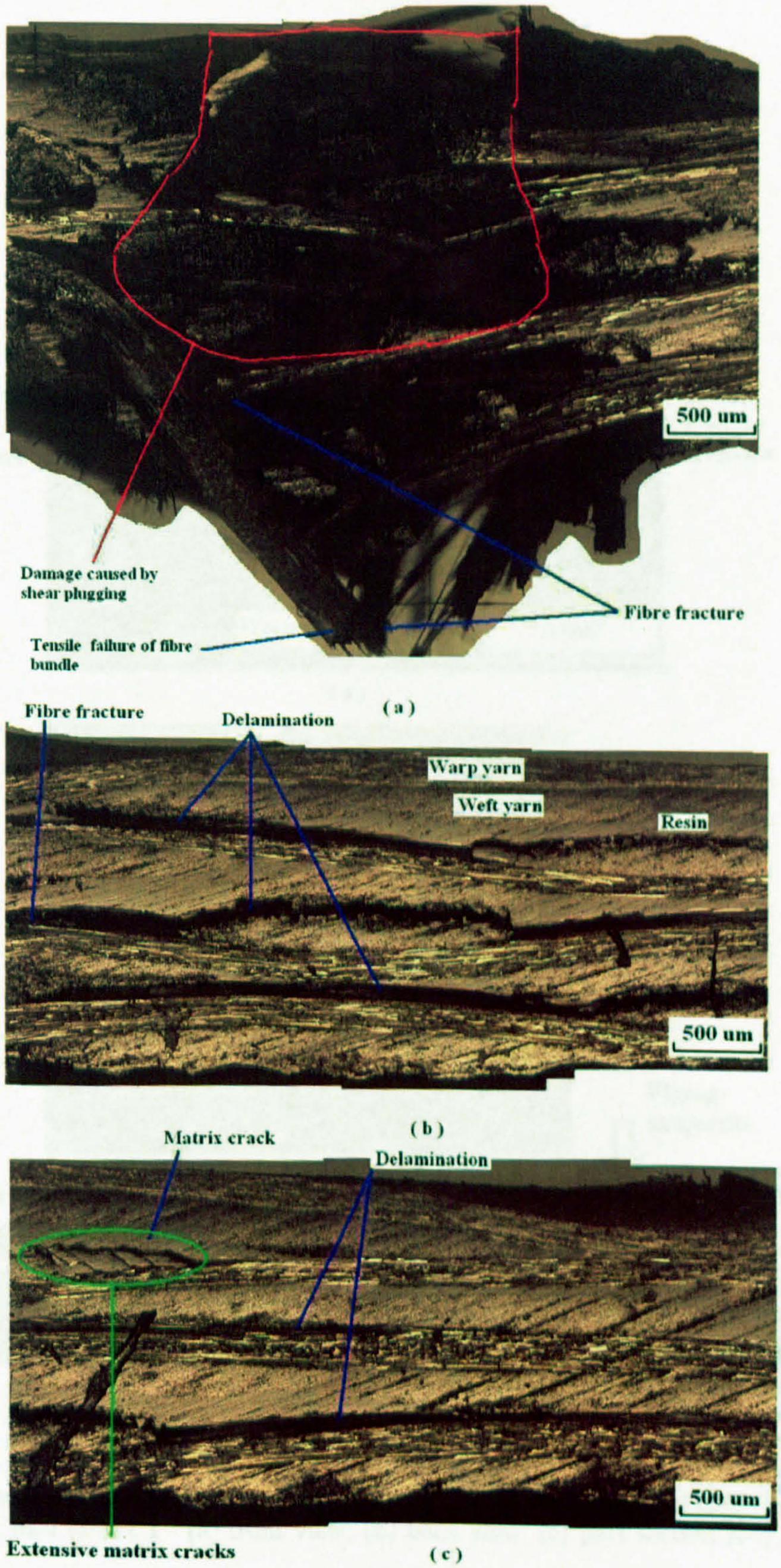

Figure 8.2: **Damage patterns in one penetrated V_{50} sample of 5HSC-4-VE impacted by 0.44g steel ball -Part II** - (a) part 1 in figure 8.1 (*c*); (b) part 2 in figure 8.1 (*c*); (c) part 3 in figure 8.1 (*c*) .

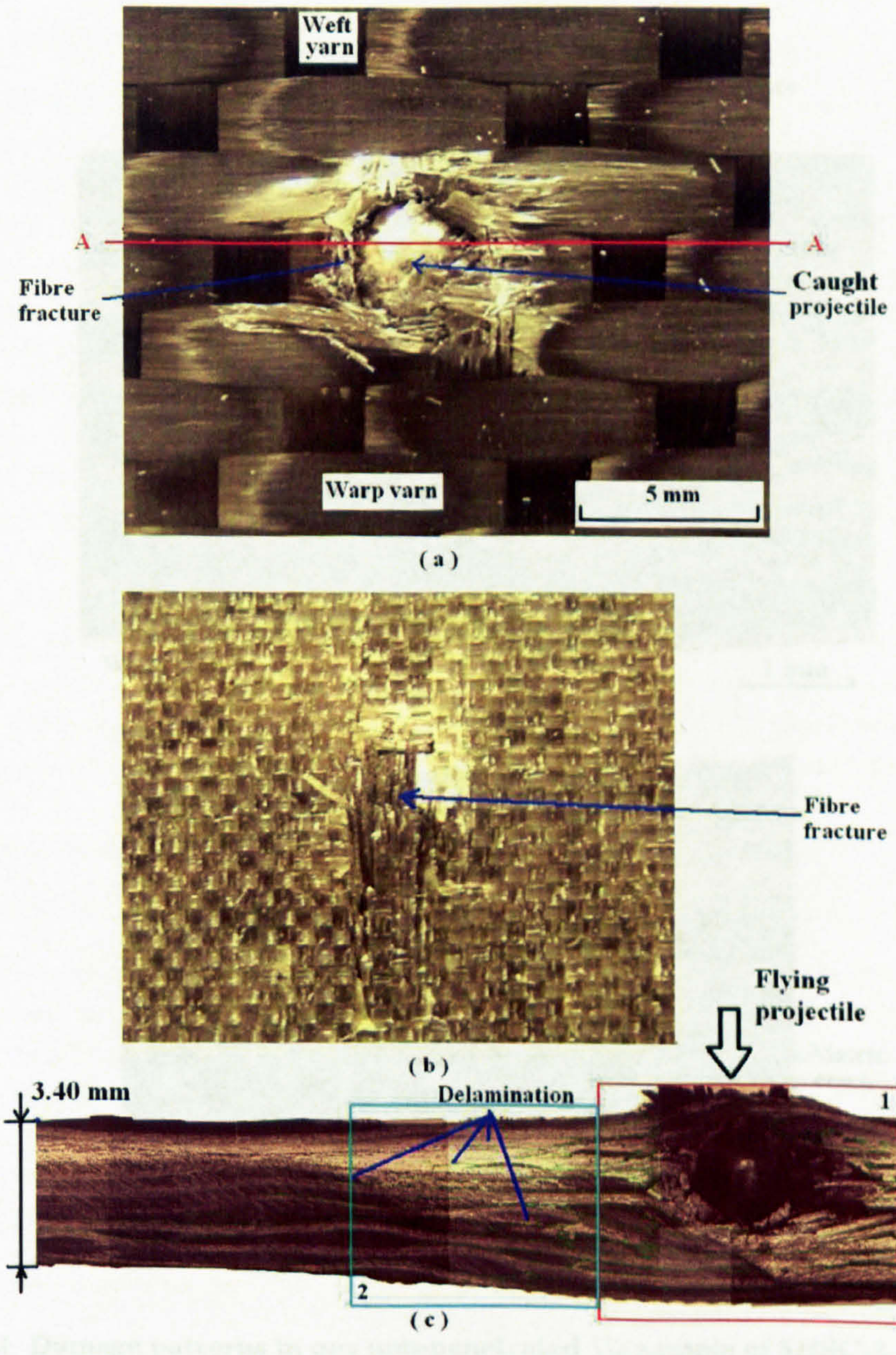

Figure 8.3: **Damage patterns in one non-penetrated V_{50} sample of 5HSC-8-VE impacted by 0.44g steel ball -Part I** - (a) front view; (b) back view; (c) part section A-A.

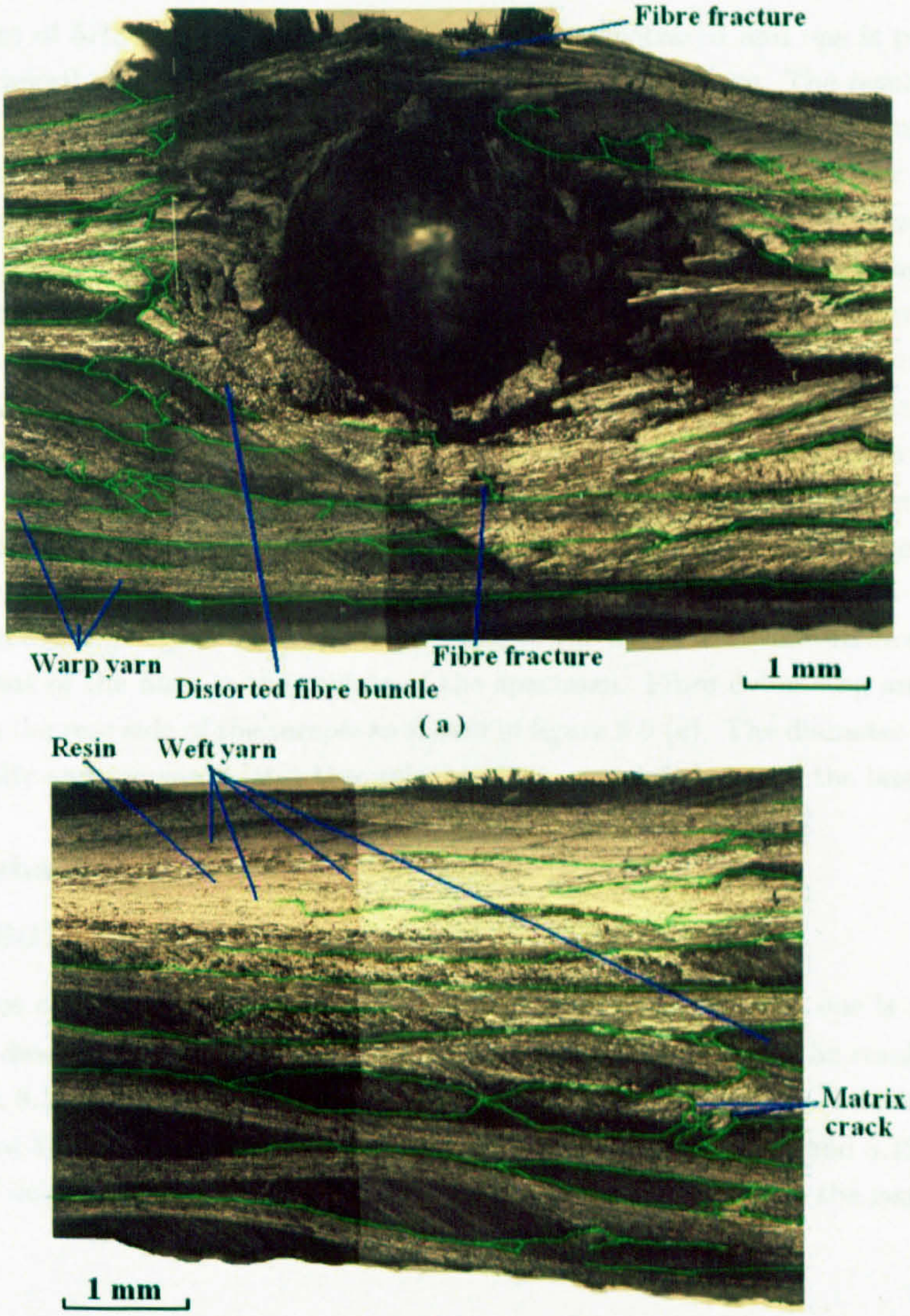

Figure 8.4: **Damage patterns in one non-penetrated V_{50} sample of 5HSC-8-VE impacted by 0.44g steel ball -Part II -** (a) part 1 in figure 8.3 (c); (b) part 2 in figure 8.3 (c).

region and in front of the captured projectile. Distorted fibre bundles were observed surrounding the captured projectile. Matrix cracks were observed in both resin rich areas and across the fibre bundle, i.e. transverse matrix crack. The diameter of delaminations increased through the thickness apart form those between the last two laminates.

8.2.1.3 5HSC-12-VE

Two V_{50} samples of 5HSC-12-VE were used. One is non-penetrated and one is penetrated. The same methods described used for 5HSC-4-VE specimen were used here. The resulting images are shown in figure 8.5 to figure 8.8. Damage observed in the cross-section image includes shear plug, delamination, fibre fracture, matrix crack. In the penetrated V_{50} sample, the clear cuts of fibres in the shear plug is more significant than in the 5HSC-4-VE specimen as shown in figure 8.8 (a). In the non-penetrated V_{50} sample, serious distortion of fibre bundles were observed in the region around the captured projectile as shown in figure 8.8. Figure 8.9 shows scanning electronic microscope (SEM) pictures of fibre fractures in different position through the thickness of the non-penetrated V_{50} sample. In figure 8.9 (a), only shear cut of fibres can be seen. This indicates that fibres were subjected to only transverse shear stresses. In figure 8.9 (b), shear cut fibres still dominates. But fibres with uneven cross-sections were observed which indicates that fibres were subjected to mixture of transverse shear stresses and tensile stresses. In the region near the bottom of the specimen, more fibres with uneven cross-sections were observed. In some region no shear cut of fibres were observed, e.g. figure 8.9 (c). The surfaces of the fibres with uneven cross-sections were rougher than that of the fibre in the middle of the specimen. Fibre debonding and pull-out were also observed in the rear side of the sample as shown in figure 8.9 (e). The diameter of delamination decreased initially and increased later through the thickness until between the last two laminates.

8.2.2 Database 2

8.2.2.1 PWEG1-12-VE

Two V_{50} samples of PWEG1-12-VE was used. One is non-penetrated and one is non-penetrated. Same methods described used for 5HSC-4-VE specimen were used here. The resulting images are shown in figure 8.10 to figure 8.13. It can be seen that damage in PWEG1-12-VE specimens is similar to that of 5HSC-12-VE specimens discussed above. Figure 8.10 (a) and 8.12 (a) shows that the diameter of delamination increases through the thickness until between the last two laminates.

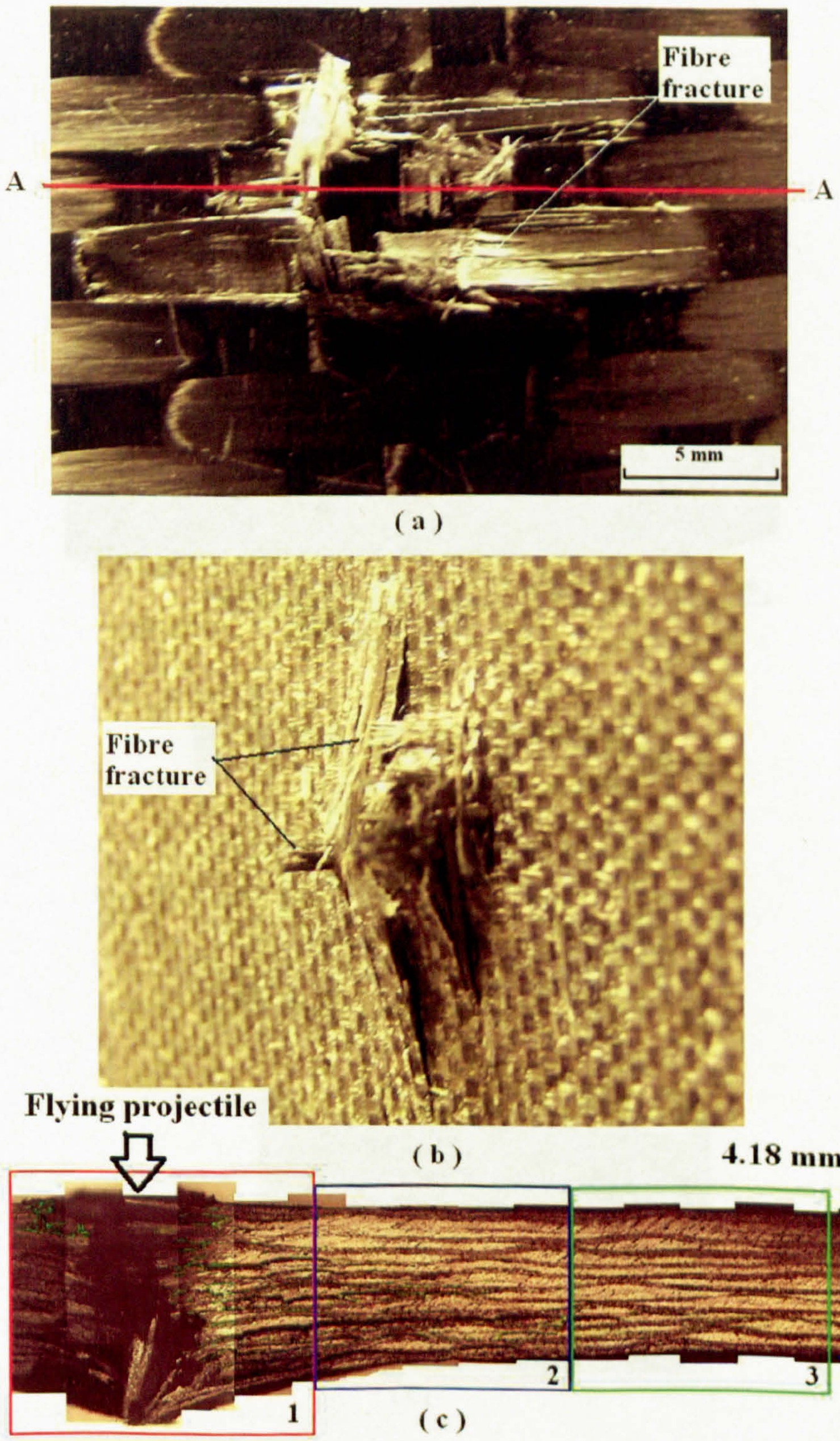

Figure 8.5: **Damage patterns in one penetrated V_{50} sample of 5HSC-12-VE impacted by 0.44g steel ball -Part I** - (a) front view; (b) back view; (c) part section A-A.

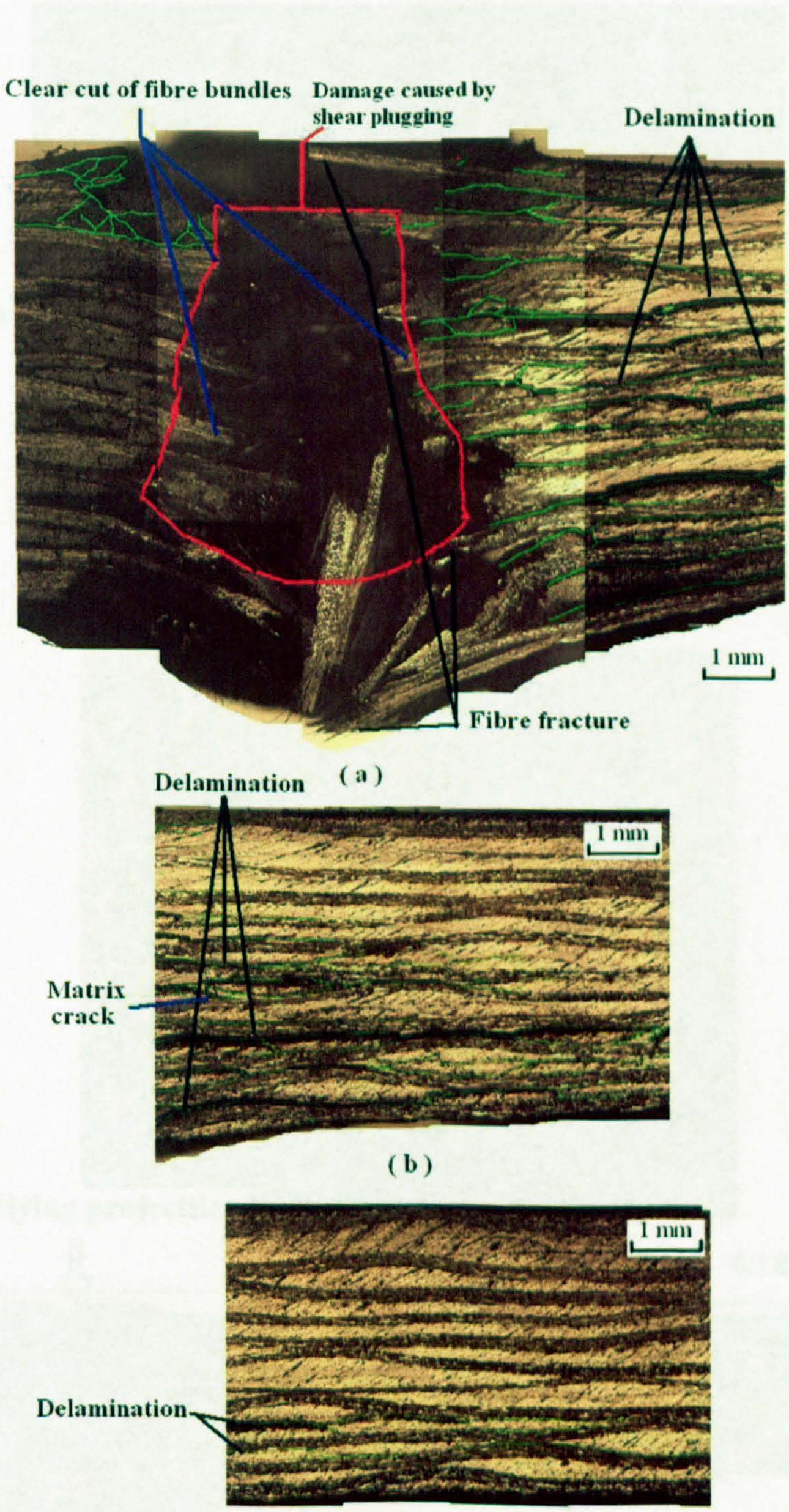

Figure 8.6: **Damage patterns in one penetrated V_{50} sample of 5HSC-12-VE impacted by 0.44g steel ball -Part II -** (a) part 1 in figure 8.1 (*c*); (b) part 2 in figure 8.1 (*c*).

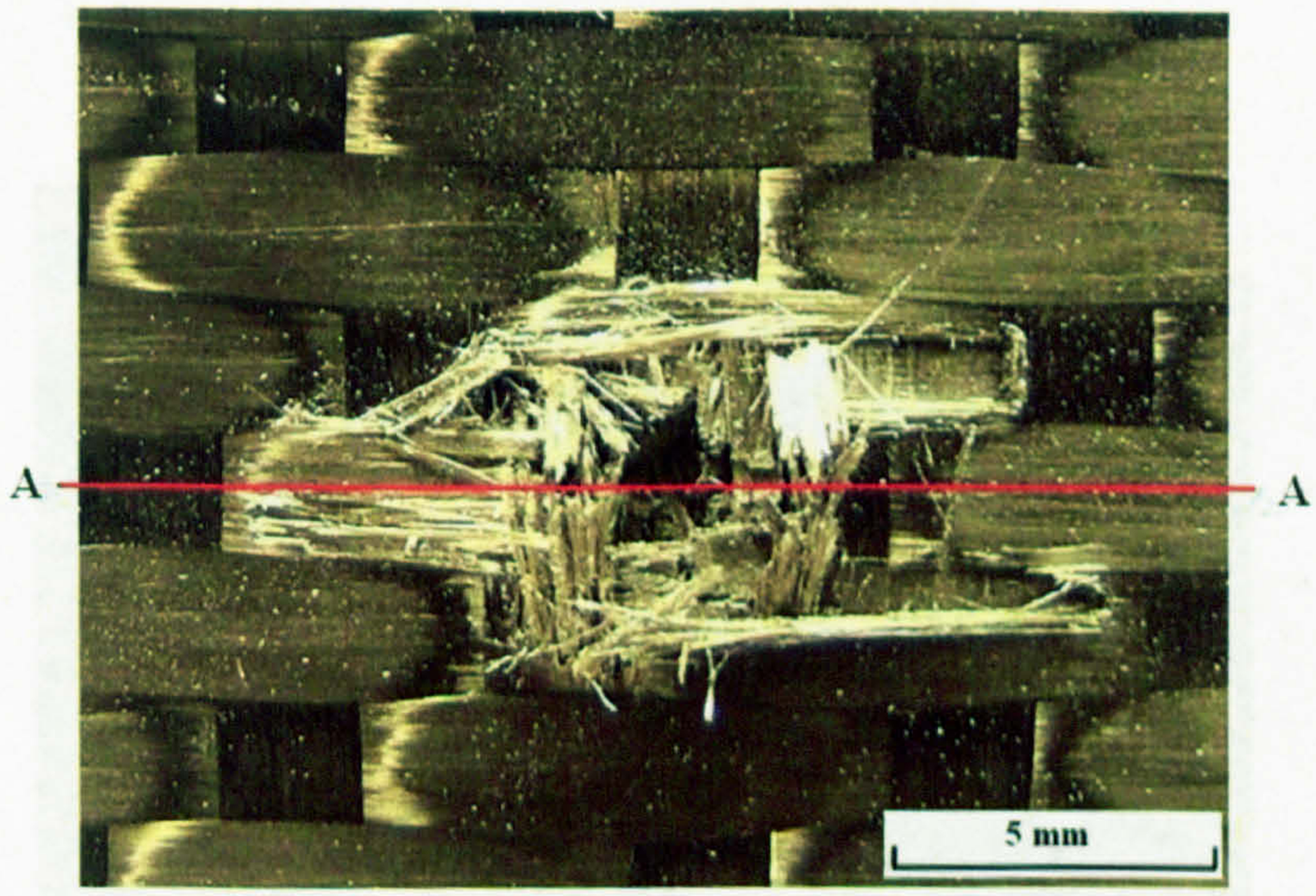

(a)

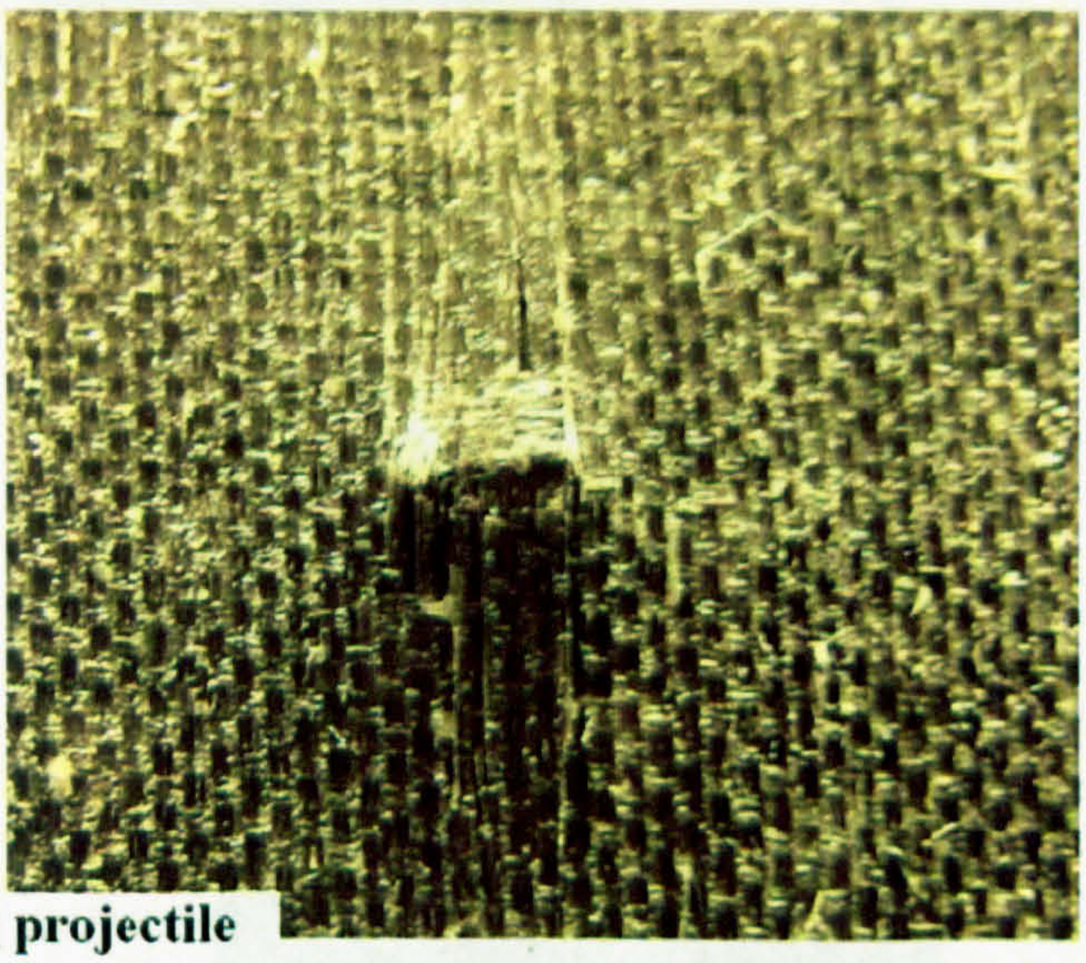

Flying projectile

(b)

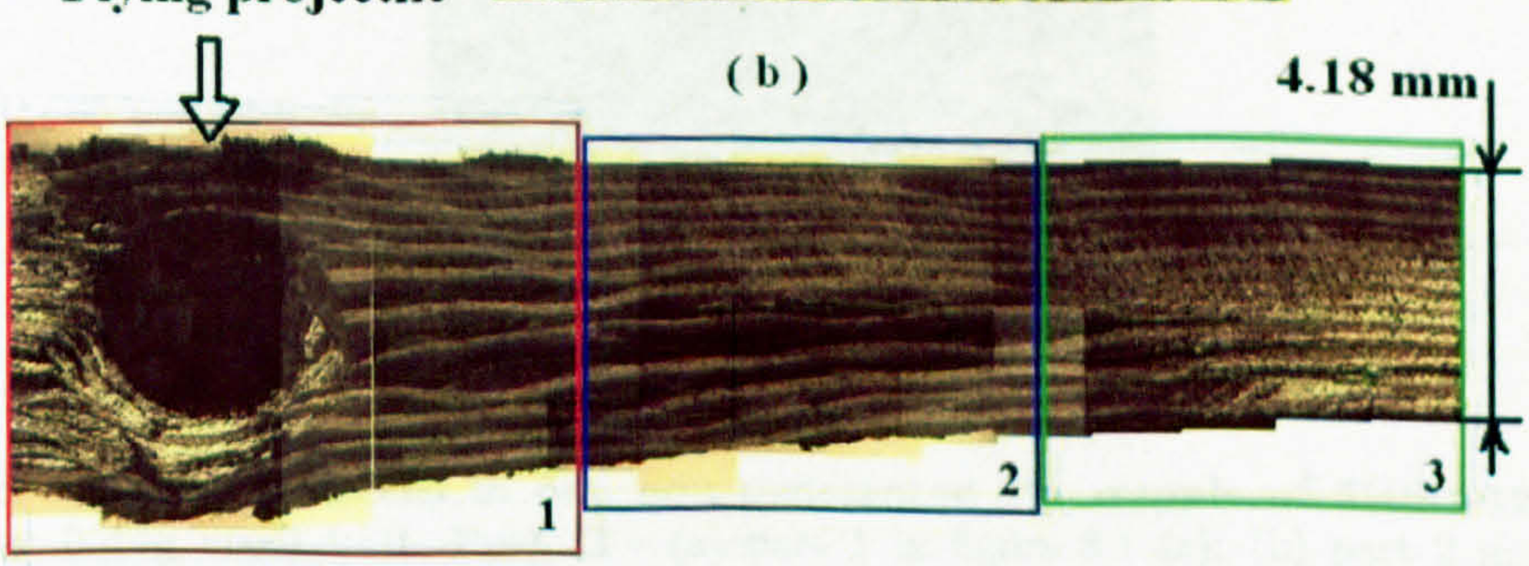

(c)

Figure 8.7: **Damage patterns in one non-penetrated V_{50} sample of 5HSC-12-VE impacted by 0.44g steel ball -Part I** - (a) front view; (b) back view; (c) part section A-A.

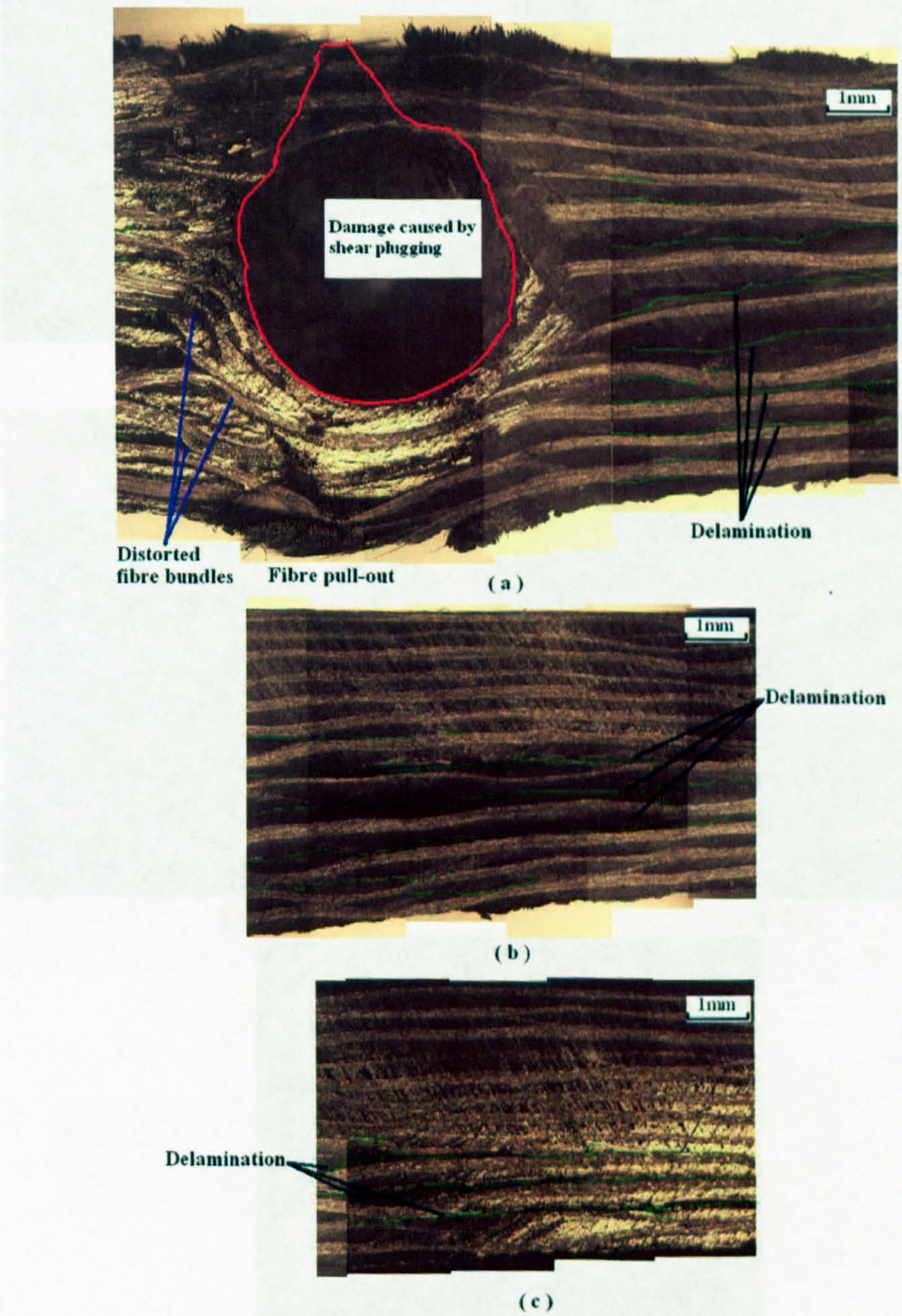

Figure 8.8: **Damage patterns in one non-penetrated V_{50} sample of 5HSC-12-VE impacted by 0.44g steel ball -Part II** - (a) part 1 in figure 8.1 (*c*); (b) part 2 in figure 8.1 (*c*).

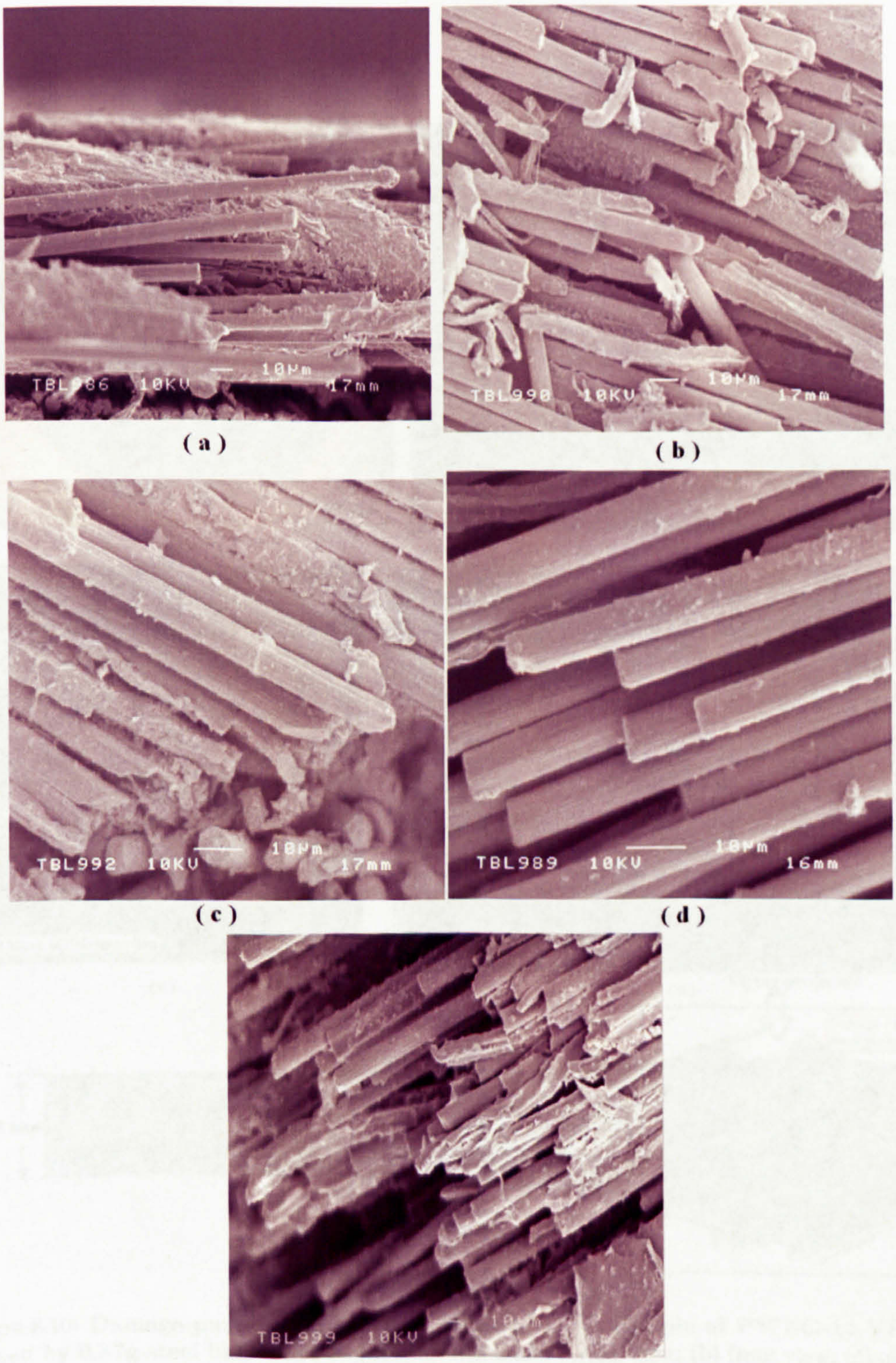

Figure 8.9: **SEM images of fibre fractures in one non-penetrated V_{50} sample of 5HSC-12-VE impacted by 0.44g steel ball** - (a) Fibre failures at the top surface of sample 12; (b) Fibre failures in the middle of sample 12; (c) Fibre failures near bottom of sample 12; (d) Fibre failures on the back of sample 12; (e) Fibre failures on the back of sample 10.

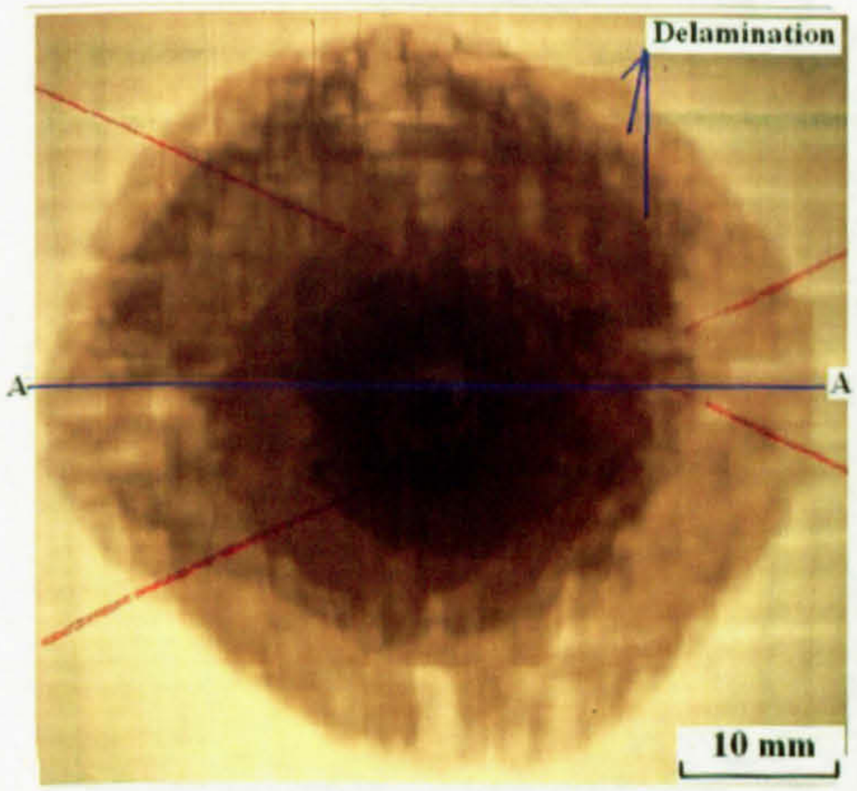

(a)

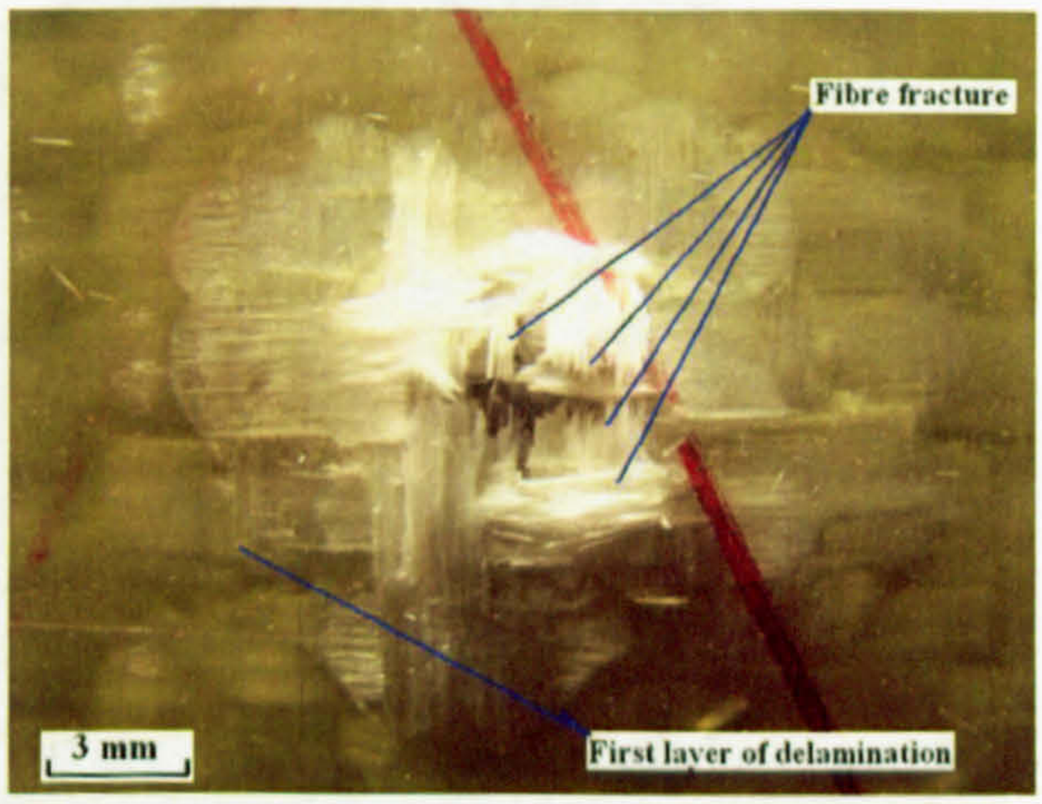

(b)

(c)

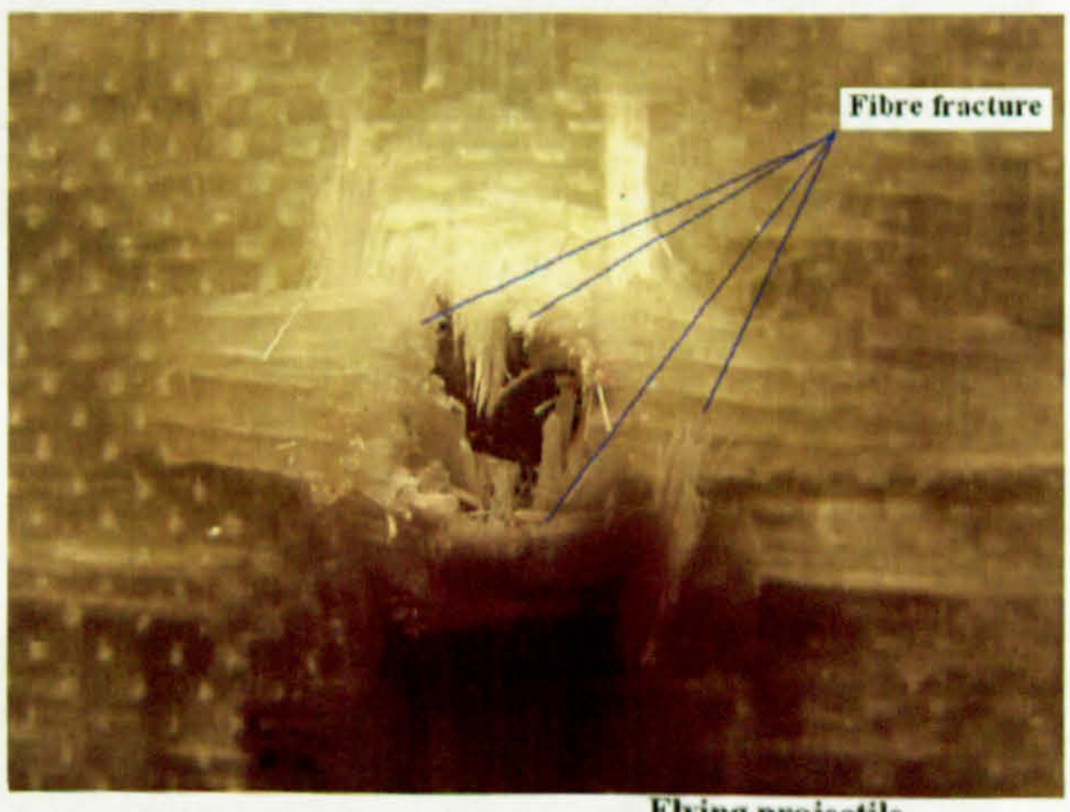

(d)

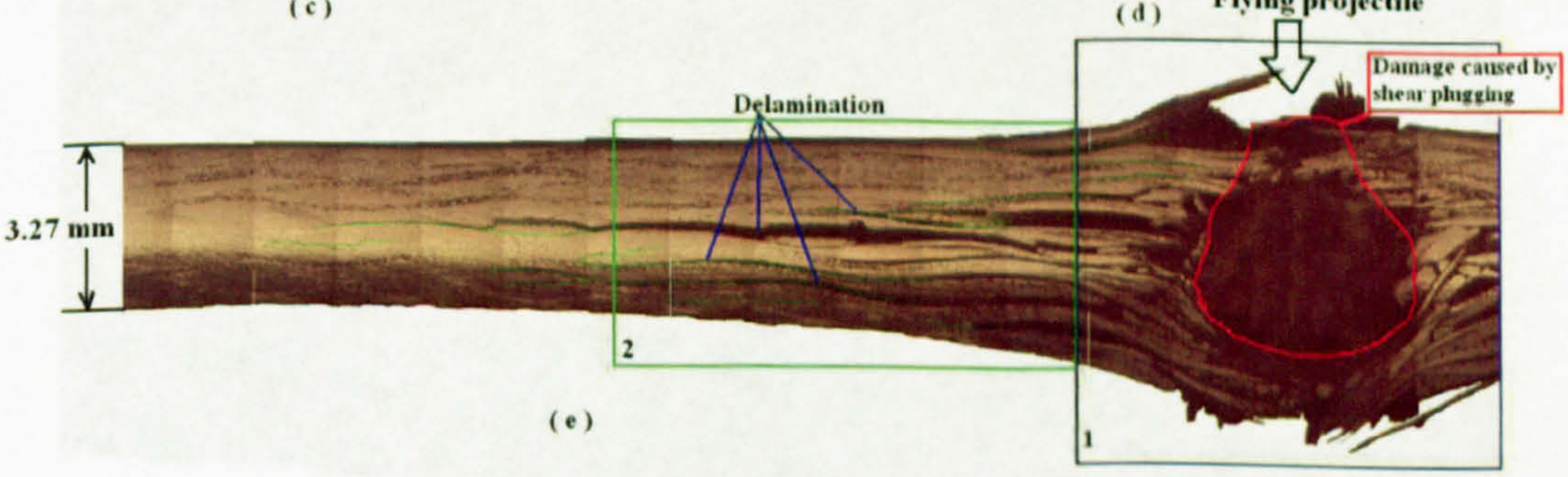

(e)

Figure 8.10: **Damage patterns in one non-penetrated V_{50} sample of PWEG-12-VE impacted by 0.87g steel ball -Part I** - (a) specimen under strong light; (b) front view; (c) oblique view of back face; (d) back view; (e) part section A-A.

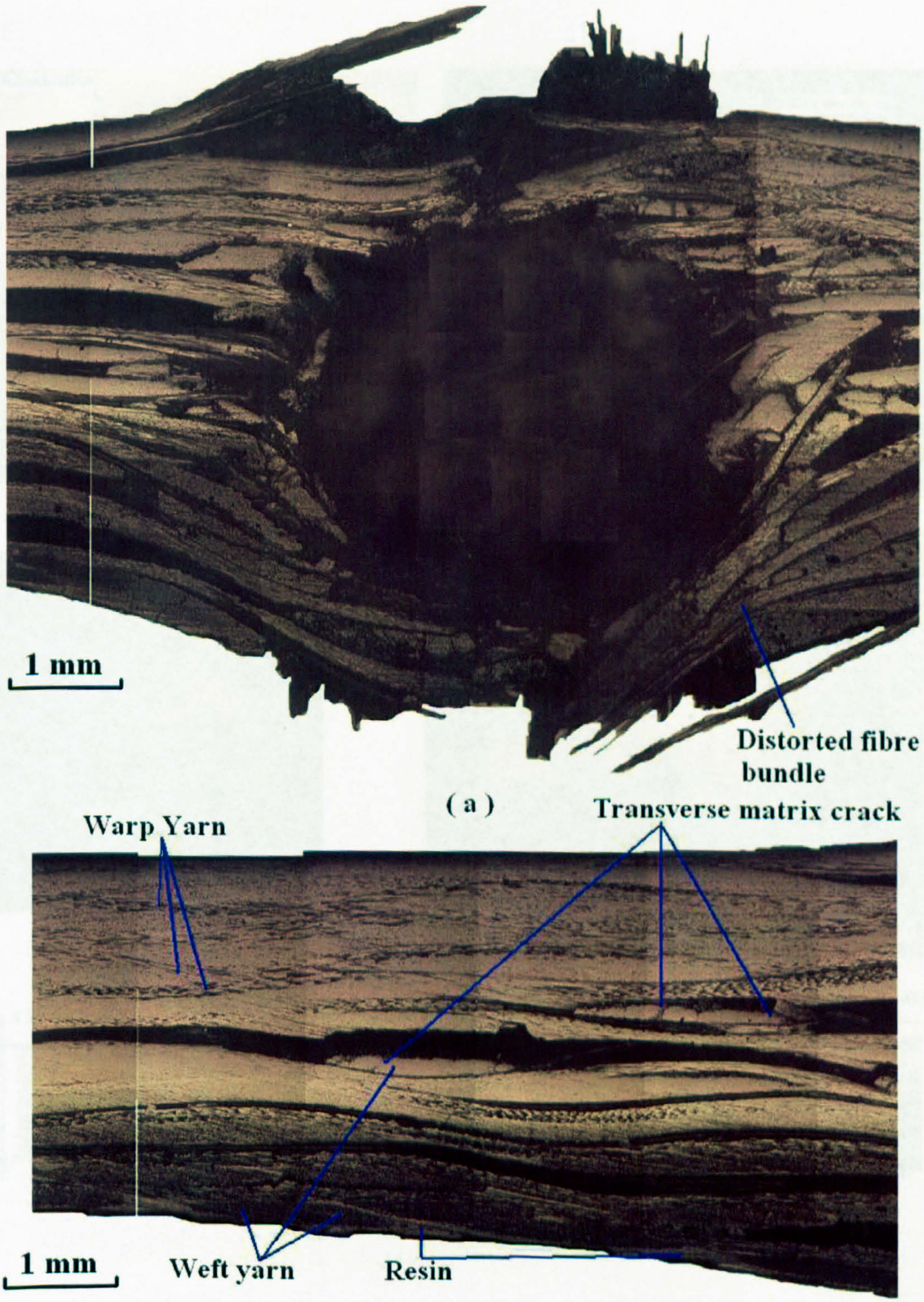

Figure 8.11: **Damage patterns in one non-penetrated V_{50} sample of PWEG-12-VE impacted by 0.87g steel ball -Part II** - (a) part 1 in figure 8.10 (*c*); (b) part 2 in figure 8.10 (*c*).

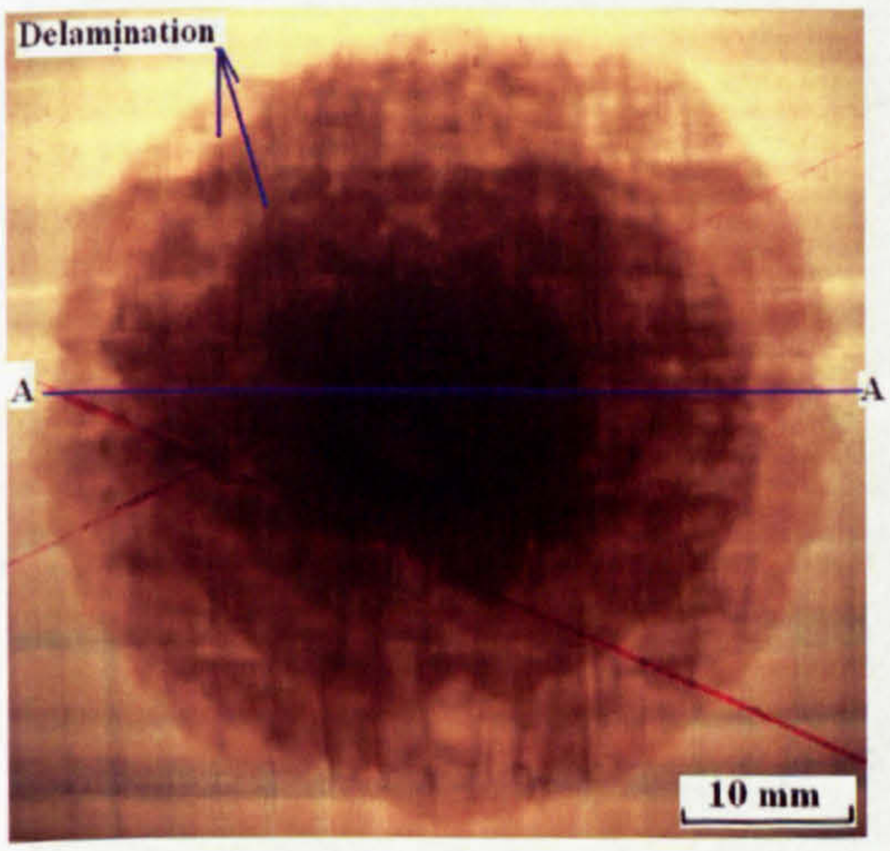

(a)

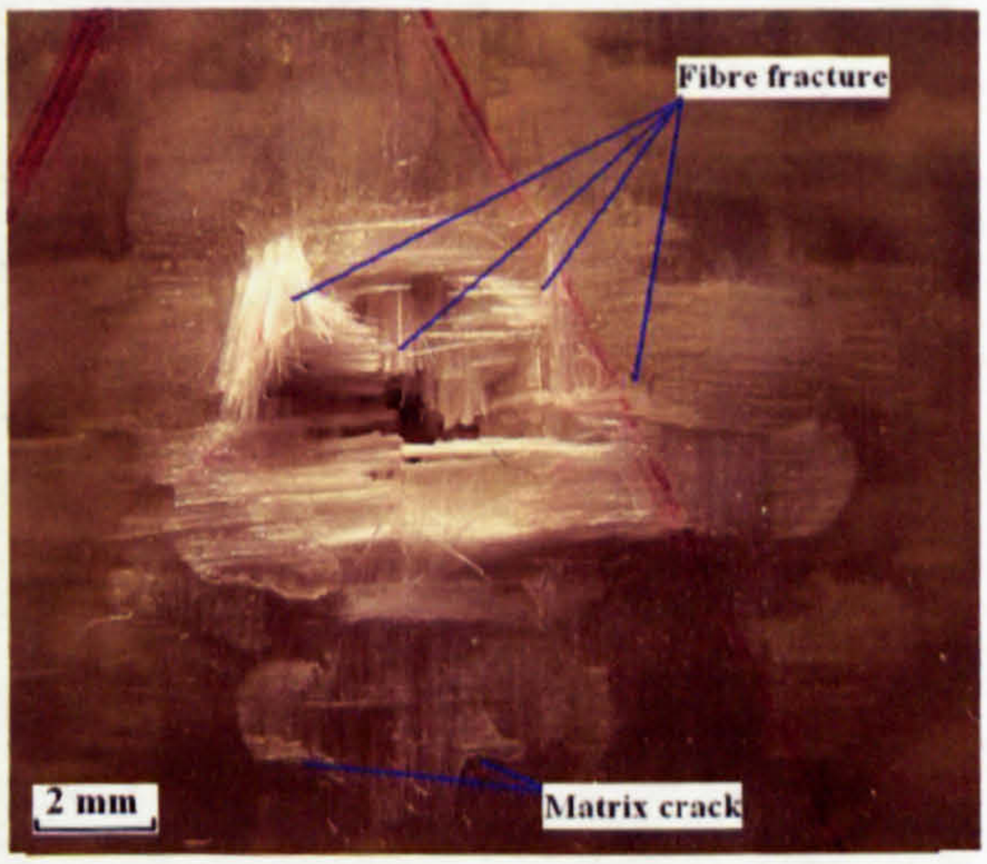

(b)

(c)

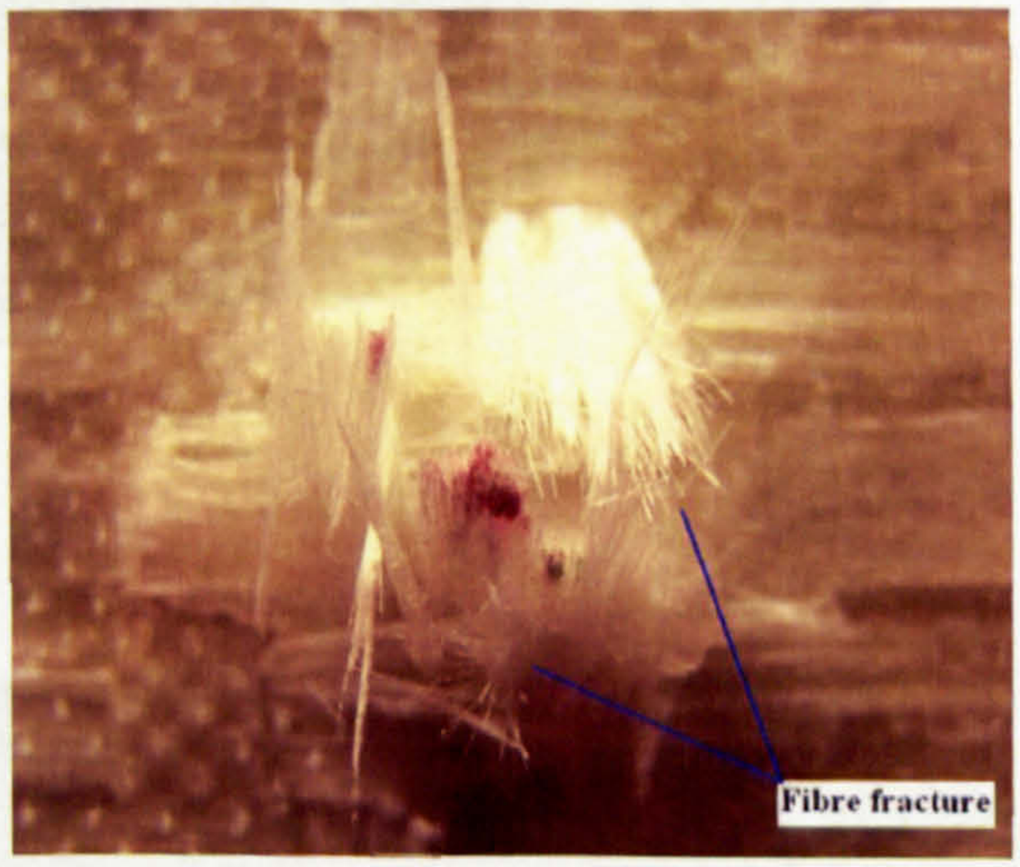

(d)

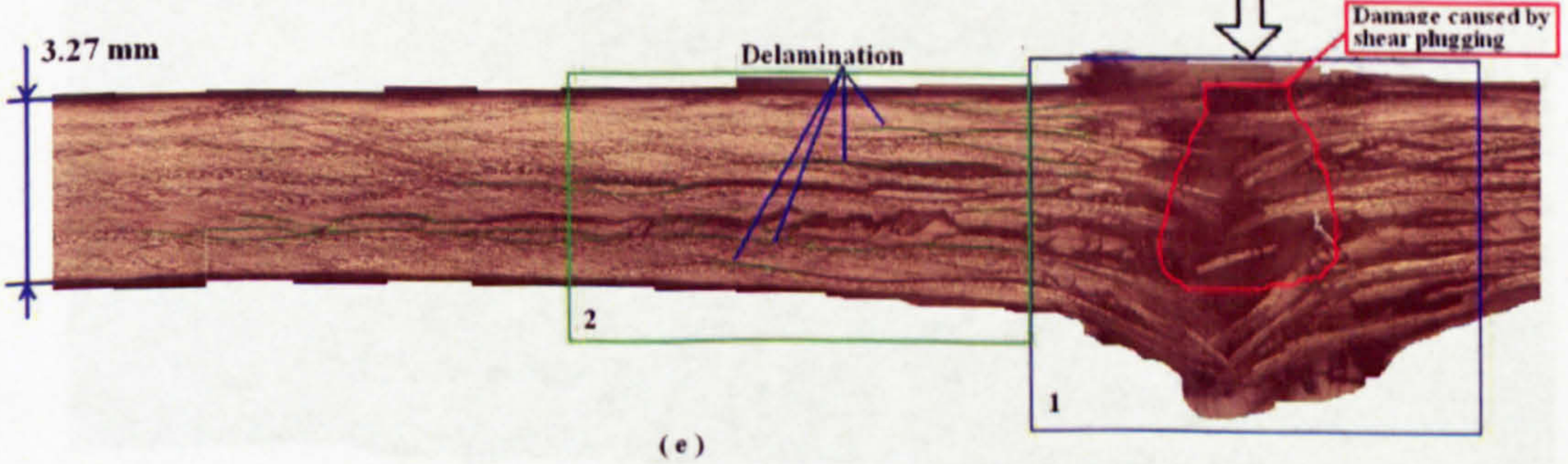

(e)

Figure 8.12: **Damage patterns in one penetrated V_{50} sample of PWEG-12-VE impacted by 0.87g steel ball -Part I** - (a) specimen under strong light; (b) front view; (c) oblique view of back face; (d) back view; (e) part section A-A.

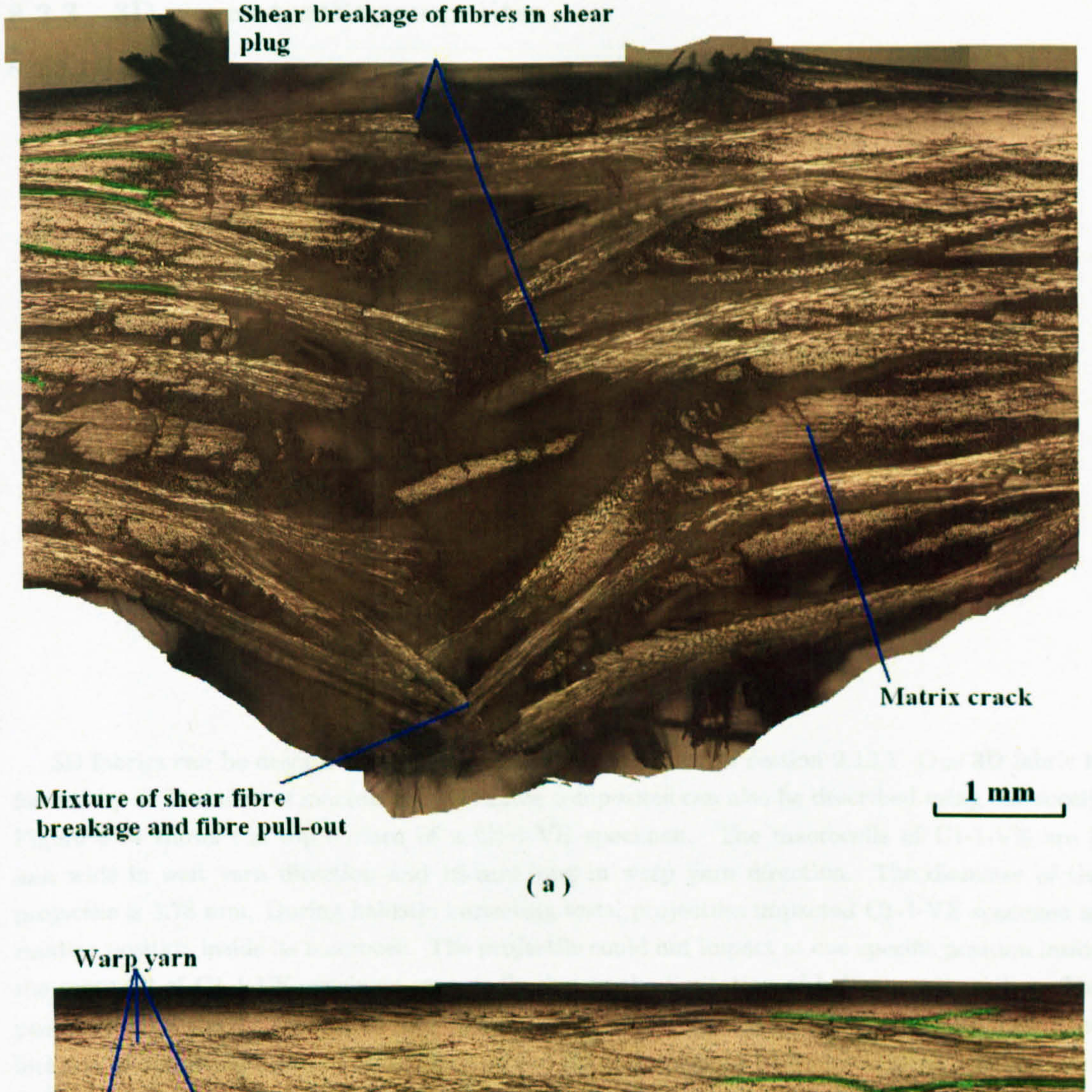

Figure 8.13: **Damage patterns in one penetrated V_{50} sample of PWEG-12-VE impacted by 0.87g steel ball -Part II** - (a) part 1 in figure 8.12 (*c*); (b) part 2 in figure 8.12 (*c*).

8.2.3 3D woven textile composites

8.2.3.1 C1-1-VE

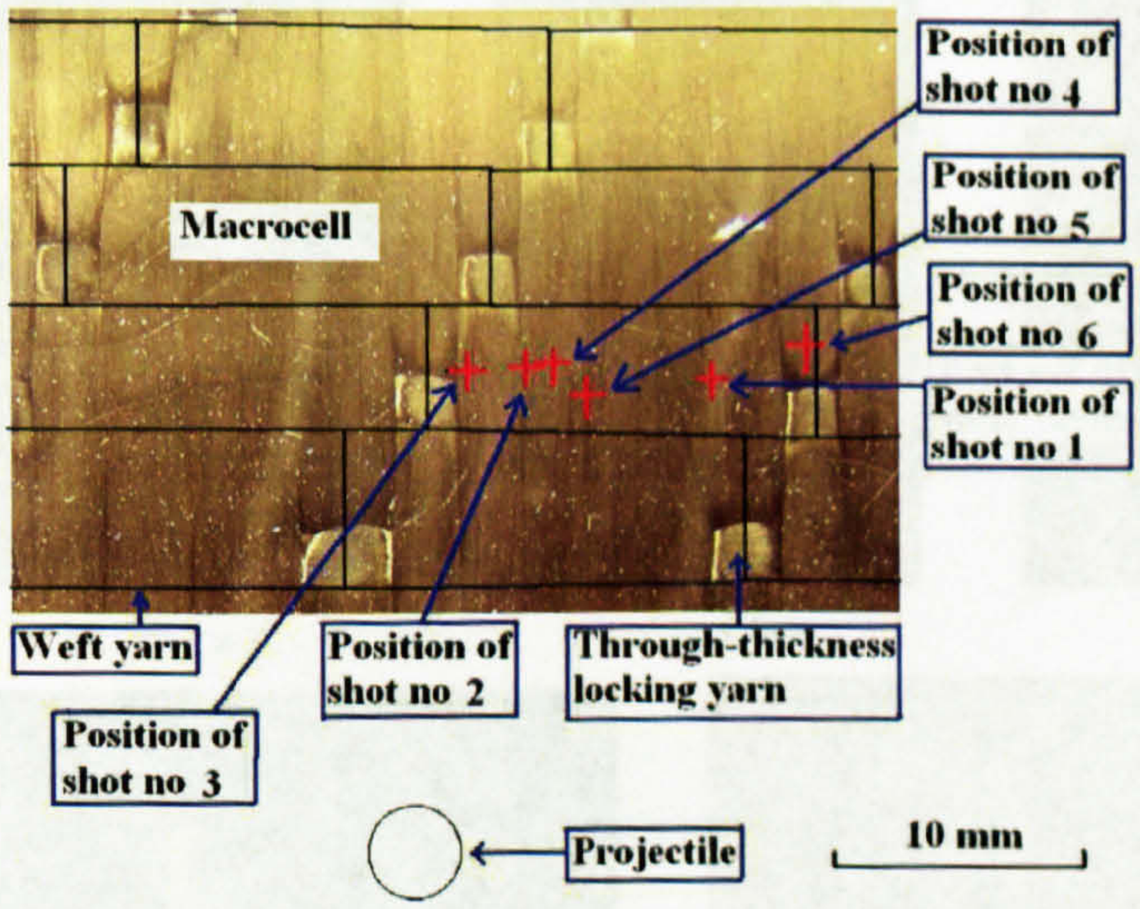

Figure 8.14: **Undamaged C-1-VE specimen .**

3D fabrics can be described using a macrocell as described in section 2.12.1. One 3D fabric is formed by an assembly of macrocells. 3D textile composites can also be described using macrocell. Figure 8.14 shows the top surface of a C1-1-VE specimen. The macrocells of C1-1-VE are 5 mm wide in weft yarn direction and 16 mm long in warp yarn direction. The diameter of the projectile is 3.78 mm. During ballistic impacting tests, projectiles impacted C1-1-VE specimen at random position inside its macrocell. The projectile could not impact at one specific position inside the macocell of C1-1-VE specimen repeatedly due to the limitation of ballistic test facility. The positions of all the six shots used for V_{50} calculation were shown in figure 8.14. It seems that the location of impacting does not affect the shape of 2D damage areas of C1-1-VE specimens as shown in figure C.8 in appendix C. One effect it has is the fracture of binder yarn. Images of sample 1, 3, 6 have different impacting locations. Their front and back surface images after impacting are shown in figure 8.15. It can be seen that in sample 2 and 3 where the projectiles had direct contact with the binder yarns. This resulted in fractures of binder yarns in the front surface. Fracture of binder yarns occurred on the rear side of specimens occurred whether the projectile hit the binder yarns in the front surface or not. Another distinctive damage modes observed in C1-1-VE specimens is the peel-off of the weft yarns in the rear side of the specimen. This was due to the existence of a large quantity of non-crimp weft yarns. More damage including delamination and shear plug was observed through the thickness of the specimen as shown in figure 8.16. Fracture of binder yarns in the middle of the specimen through thickness was observed in a specimen impacted by velocity below ballistic limit velocity as shown in figure 8.17. In some region, bridging of delaminatons by binder yarn was observed.

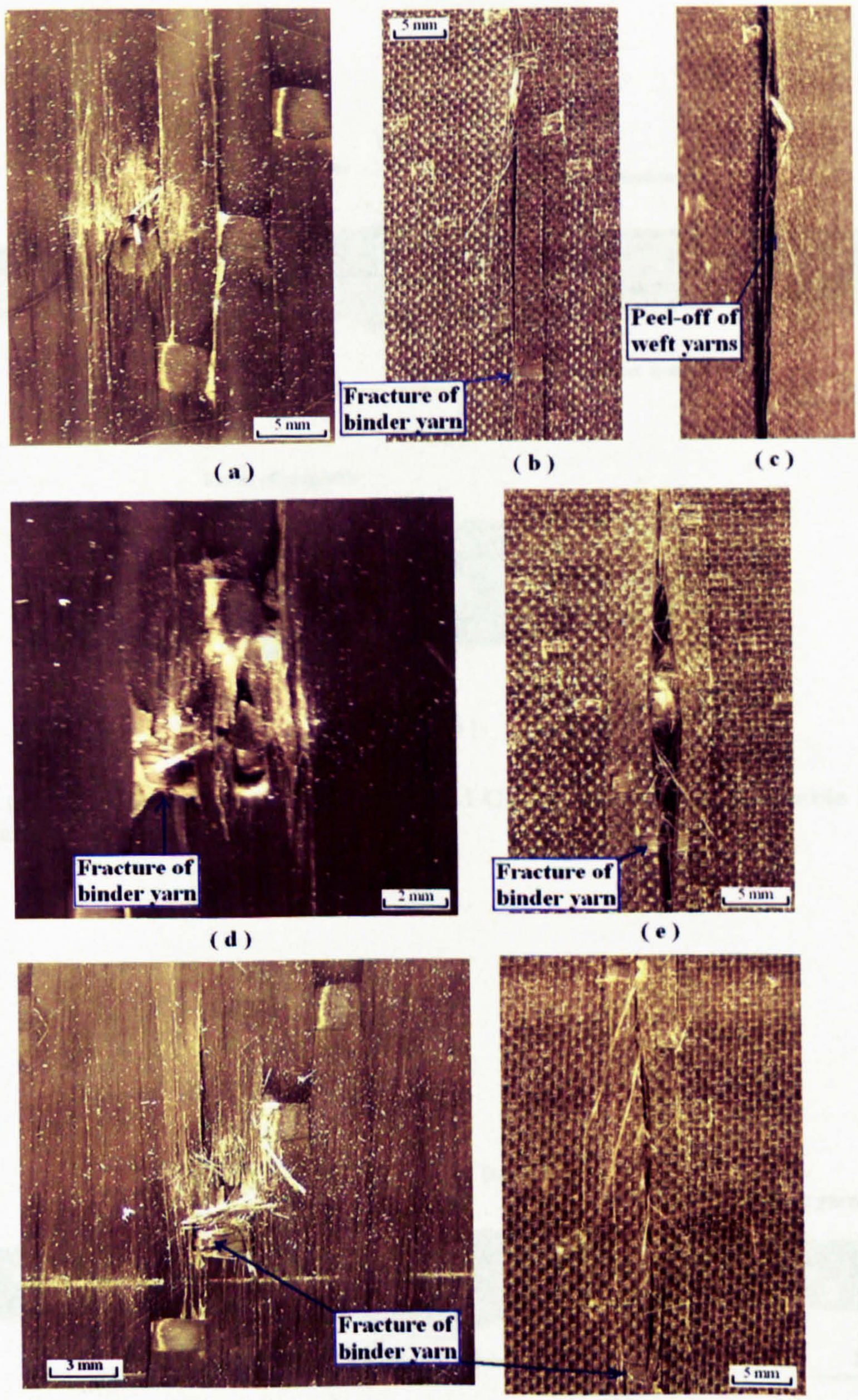

Figure 8.15: **Damages in C1-1-VE specimens** - (a) front view of sample 1 in table B.8;(b) back view of sample 1 in table B.8; (c) corner view of sample 1 in table B.8; (d) front view of sample 3 in table B.8; (e) back view of sample 3 in table B.8; (f) front view of sample 6 in table B.8; (g) front view of sample 6 in table B.8.

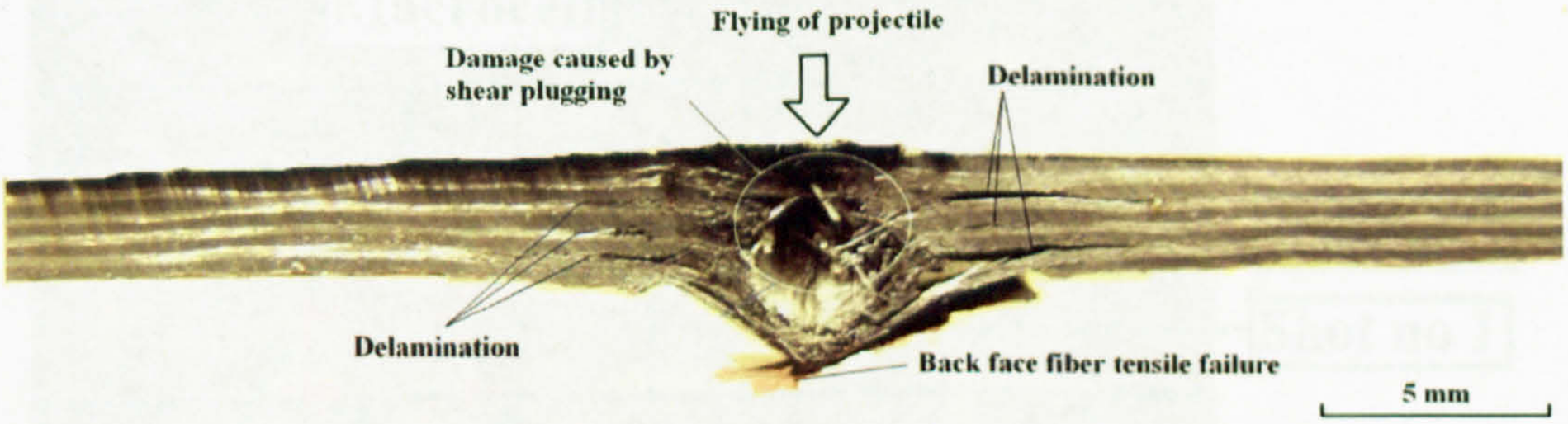

Figure 8.16: **Cross-section of ballistic impacted C1-1-VE specimen 3 in table B.8.** - (a) in weft yarn direction; (b) in warp yarn direction.

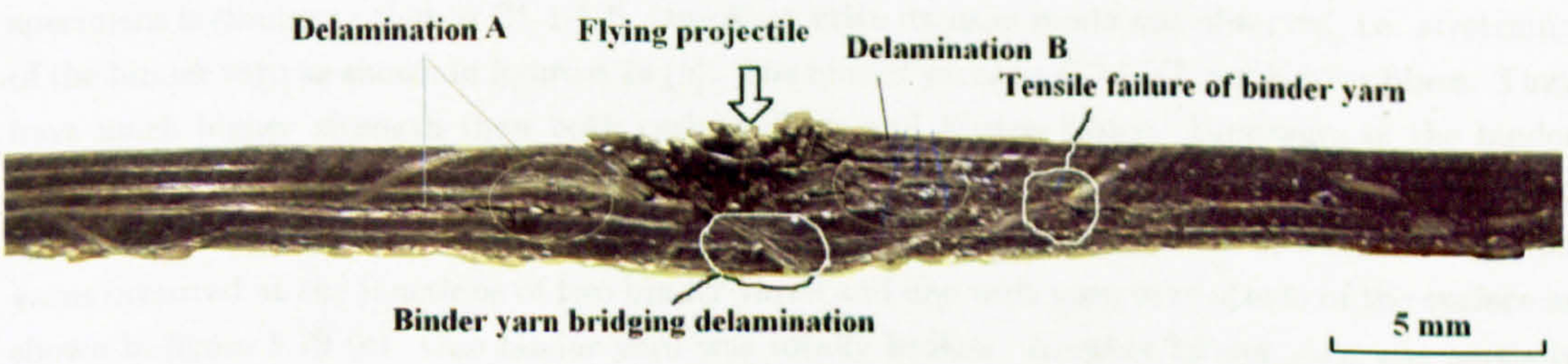

Figure 8.17: **Cross-section in weft yarn direction of ballistic impacted C1-1-VE specimen** - below ballistic limit.

8.2.3.2 G7-1-VE

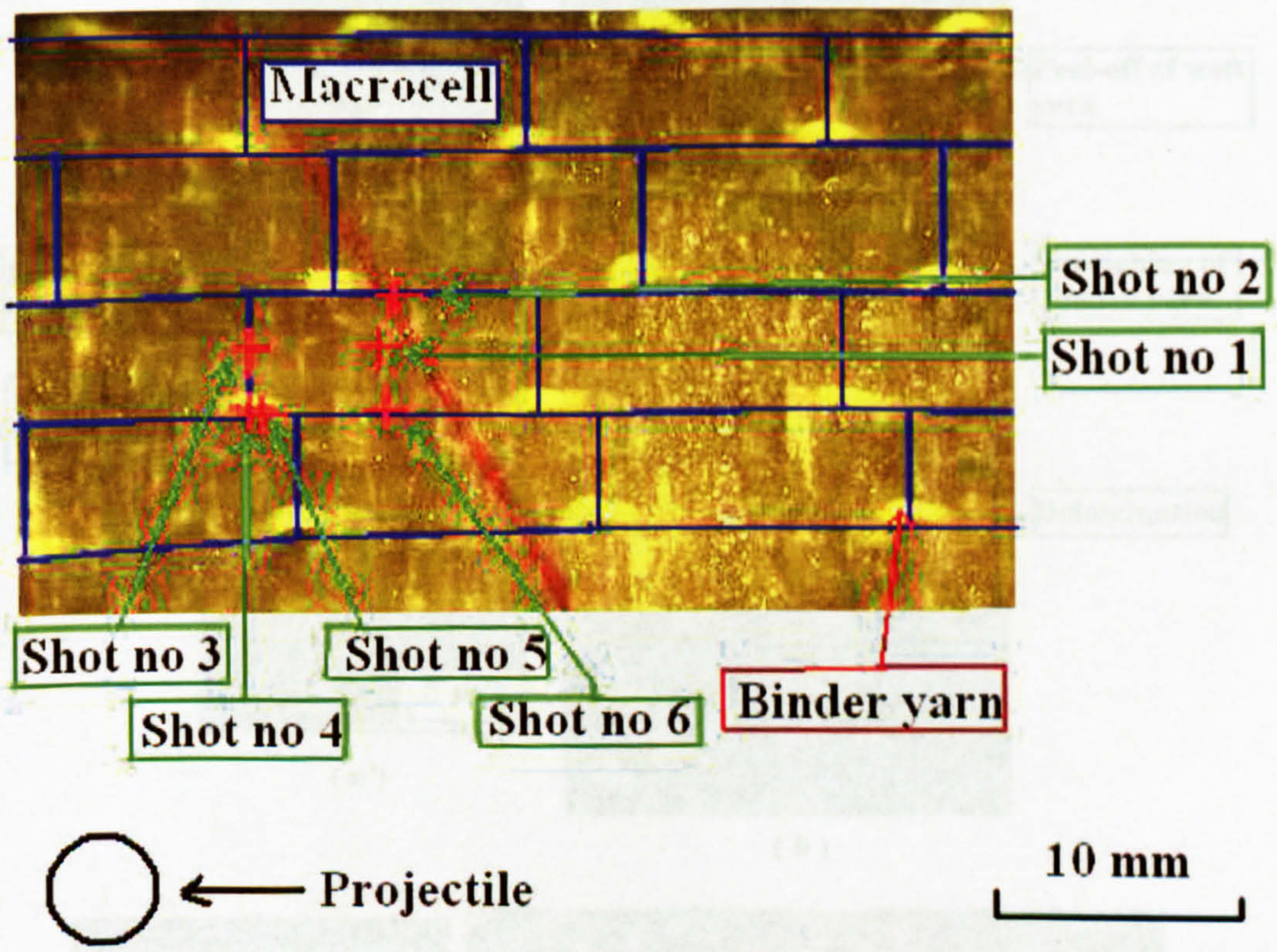

Figure 8.18: **Undamaged G7-1-VE specimen.**

As shown in table 4.1, 3D fabrics G7 and C1 have same fabric architecture, i.e. through-thickness interlocking structure. Figure 8.18 shows the front surface of a G7-1-VE specimen where the macrocells and the locations of the six shots used for V_{50} calculation were shown. The macrocells of G7-1-VE is 4.6 mm wide in the weft yarn direction and 12.5 mm long in the warp yarn direction. The diameter of the projectiles is 4.75 mm. The effect of the impacting location in G7-1-VE specimens is similar to that in C1-1-VE. One distinctive damage mode was observed, i.e. stretching of the binder yarn as shown in figure 8.19 (*b*). The binder yarns in G7-1-VE are Kevlar fibres. They have much higher strength than both carbon fibres and E-glass fibres. Breakages of the binder yarns in the rear side the specimens in G7-1-VE specimens occurred not as often as in C1-1-VE specimens. It was only observed in shot number 6 in figure 8.18. In shot no 6, fracture of binder yarns occurred at the junctions of two binder yarns and one weft yarn in rear side of the surface as shown in figure 8.19 (*c*). One binder yarn was totally broken. Another binder yarn was partially broken. The former was in the pass of the flying projectile. More damages including delamination, shear plug were observed through the thickness of the specimen as shown in figure 8.20.

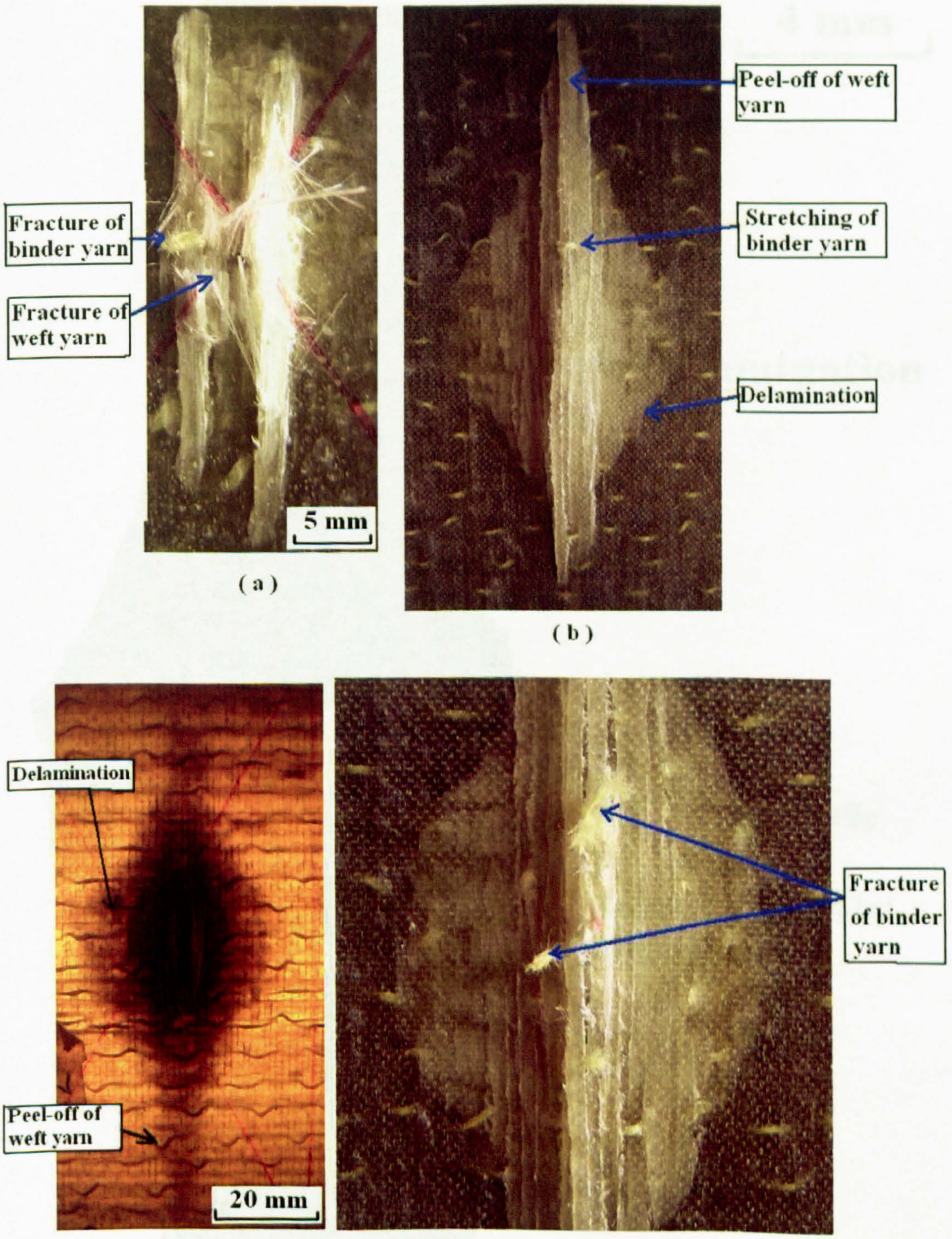

Figure 8.19: **Damages in G7-1-VE specimens** - (a) front view of sample 5 in table B.11;(b) back view of sample 2 in table B.11; (c) sample 2 in table B.11 under strong light; (d) front view of sample 6 in table B.11.

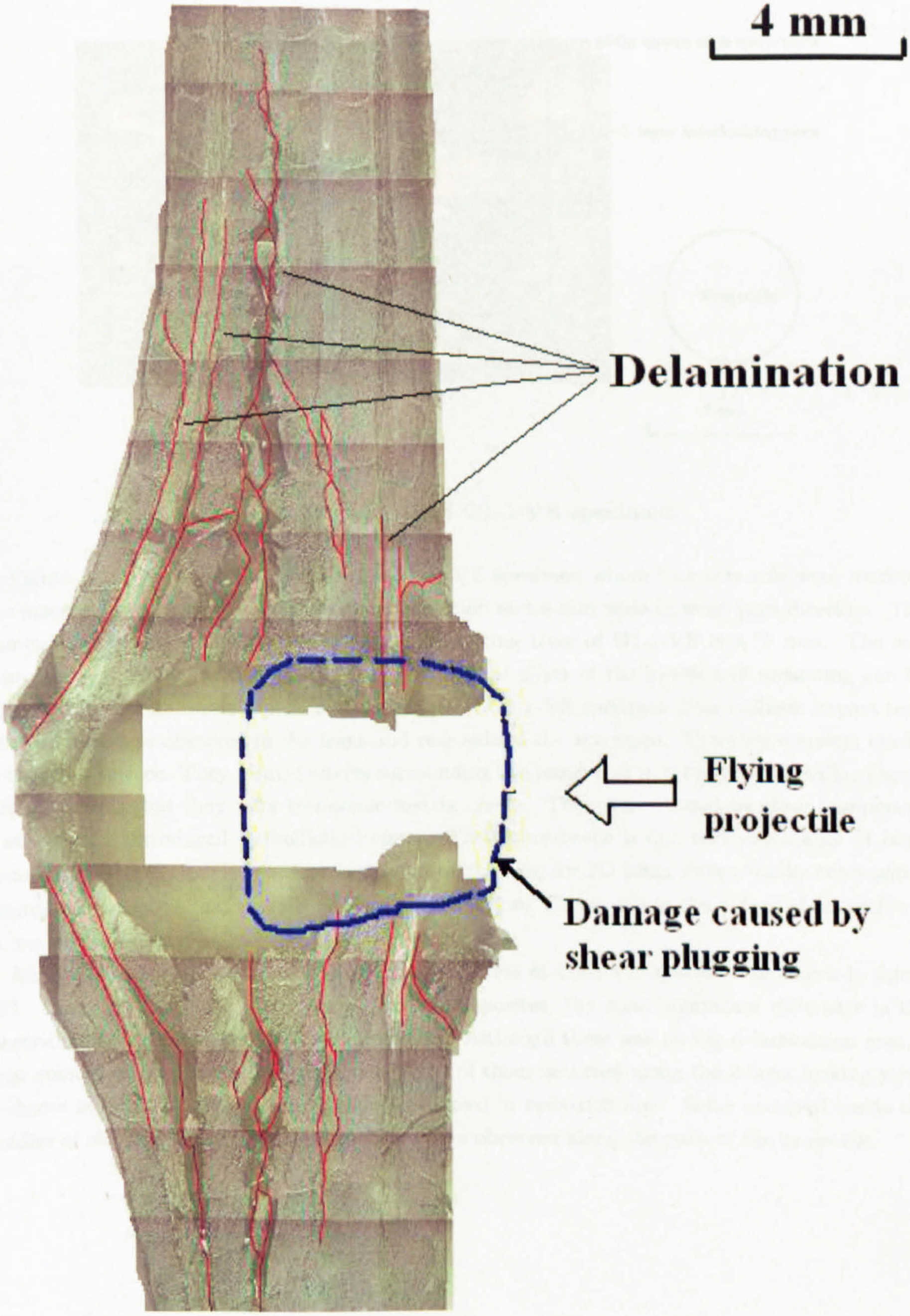

Figure 8.20: **Cross-section in weft yarn direction of ballistic impacted G7-1-VE specimen.**

8.2.3.3 G1-1-VE

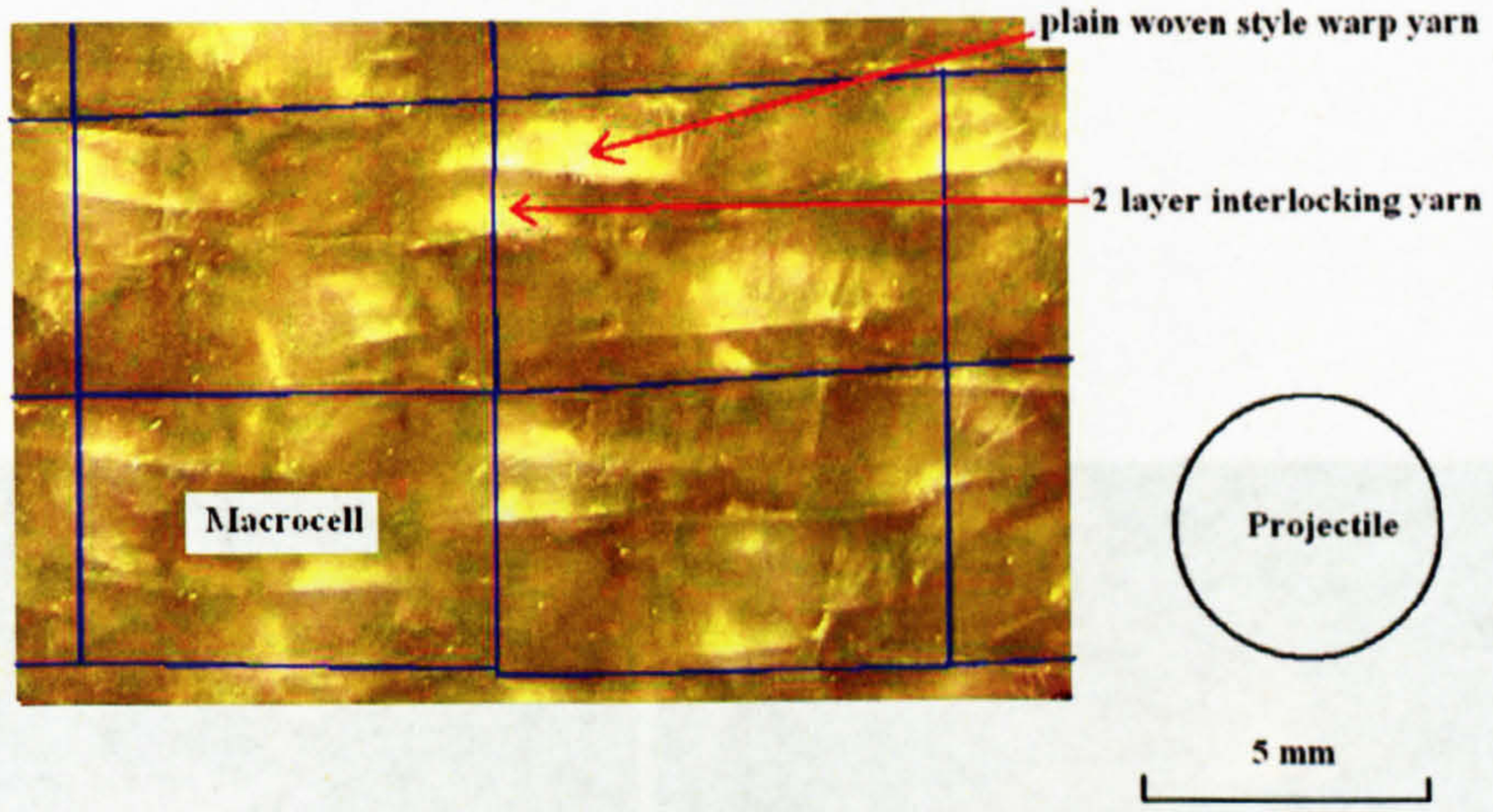

Figure 8.21: **Undamaged G1-1-VE specimen.**

Figure 8.21 shows the top surface of a G1-1-VE specimen where its microcells were marked. The macrocells are 5 mm wide in weft yarn direction and 8 mm wide in warp yarn direction. The diameter of the projectiles used in ballistics impacting tests of G1-1-VE is 4.75 mm. The size of projectile is similar to the size of macrocell. So the effect of the location of impacting can be ignored. Figure 8.22 shows typical surface images of G1-1-VE specimen after ballistic impact test. Fibre fracture was observed in the front and rear side of the specimen. There were matrix cracks on the front surface. They formed circles surrounding the impacting point of the projectile. Figure 8.22 (*c*) reveals that they were transverse matrix cracks. They were caused by shear component of stress wave introduced by ballistic impact. Their occurrence is due to the presence of large resin-rich area in G1-1-VE specimen which is not the case for 2D plain woven textile composites. Figure 8.22 (*d*) shows that there is no large delamination. This is due to the nature of G1 preform, i.e. no large laminate.

More damages were observed through the thickness of G1-1-VE specimen as shown in figure 8.23. Compared with 2D plain woven textile composites, the most significant difference is the absence of big delamination area and shear plug. Although there was no big delamination area, a large amount of matrix cracks still exited. Some of them occurred along the 2-layer locking yarns as shown in figure 8.23 (position 2). Some occurred in resin-rich area. Some occurred inside the bundles of the weft yarns. Fractures of fibres were observed along the path of the projectile.

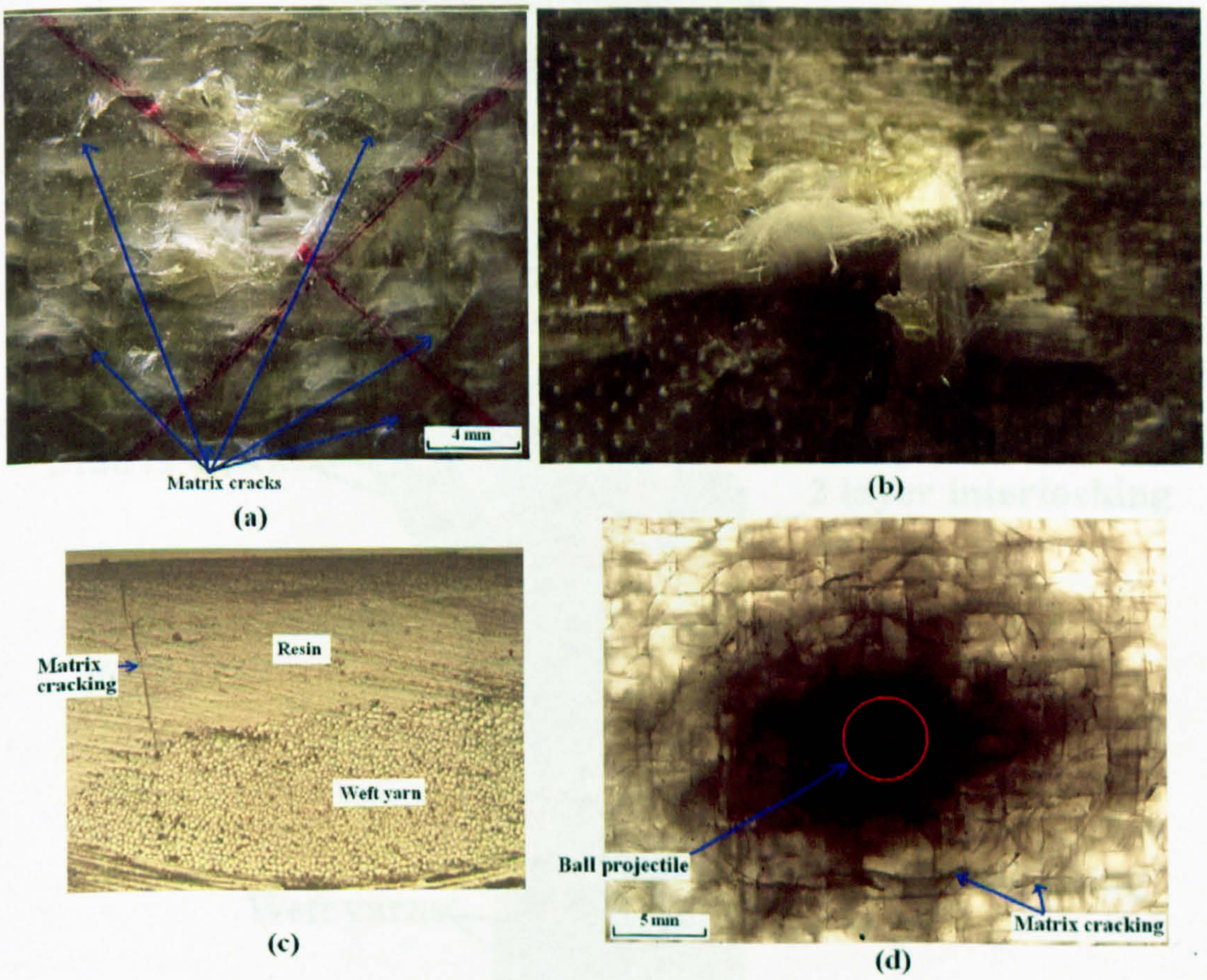

Figure 8.22: **G1-1-VE specimen after ballistic impacts** - (a) front view; (b) back view; (c) cross-section view; (d) spcimen under strong light.

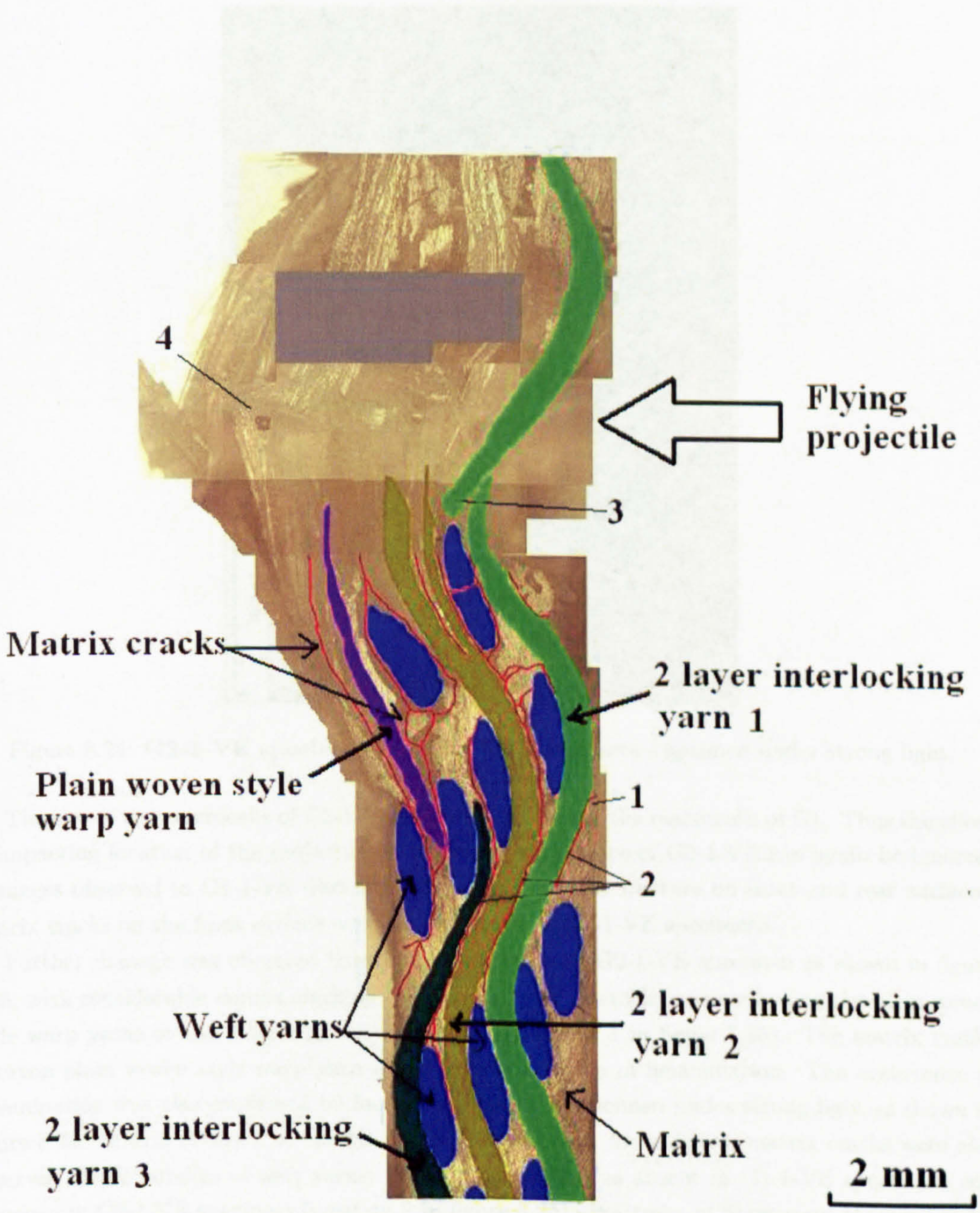

Figure 8.23: **Cross-section in weft yarn direction of ballistic impacted G1-1-VE specimen.**

8.2.3.4 G2-1-VE

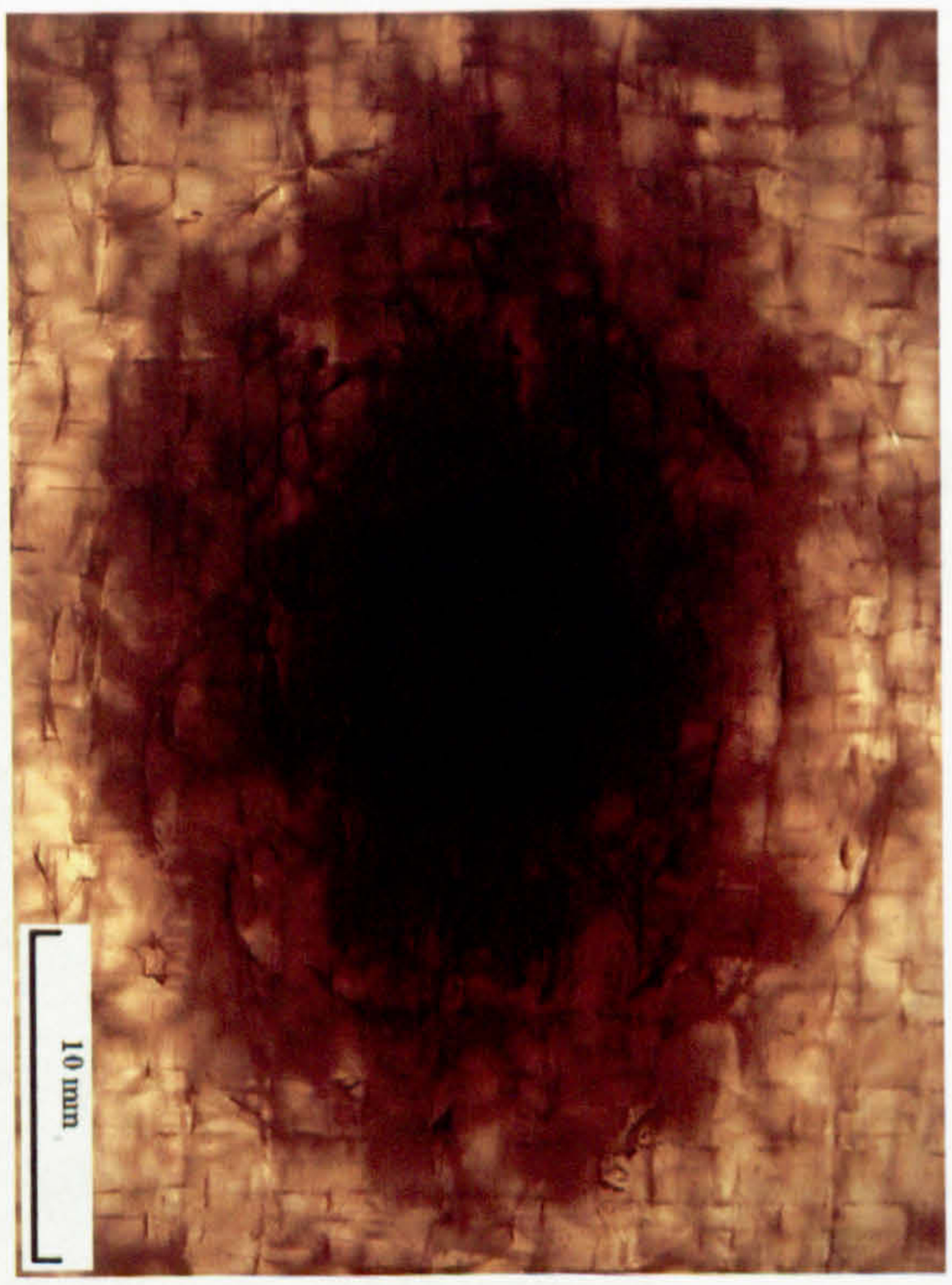

Figure 8.24: **G2-1-VE specimen after ballistic impacts** - spcimen under strong light.

The size of the macrocells of G2-1-VE is similar to that of the macrocells of G1. Thus the effect of impacting location of the projectile on ballistic performance of G2-1-VE can again be ignored. Damages observed in G1-1-VE discussed above such as fibre fracture on front and rear surfaces, matrix cracks on the front surface were also observed in G2-1-VE specimens.

Further damage was observed through the thickness of G2-1-VE specimen as shown in figure 8.25, with considerable matrix cracking. Most of the matrix cracks occurred along the plain woven style warp yarns or the 2 layer interlocking yarns (position 1 in figure 8.25). The matrix cracks between plain woven style warp yarn 1 and 2 form a region of delamination. The occurrence of delamination was also confirmed by looking at G2-1-VE specimen under strong light as shown in figure 8.24. Matrix cracks also observed in resin rich areas. In addition, matrix cracks were also observed inside bundles of weft yarns. Shear plug which was absent in G1-1-VE specimens was observed in G2-1-VE specimen (position 2 in figure 8.25). Fractures of fibres were observed along the path of the projectile.

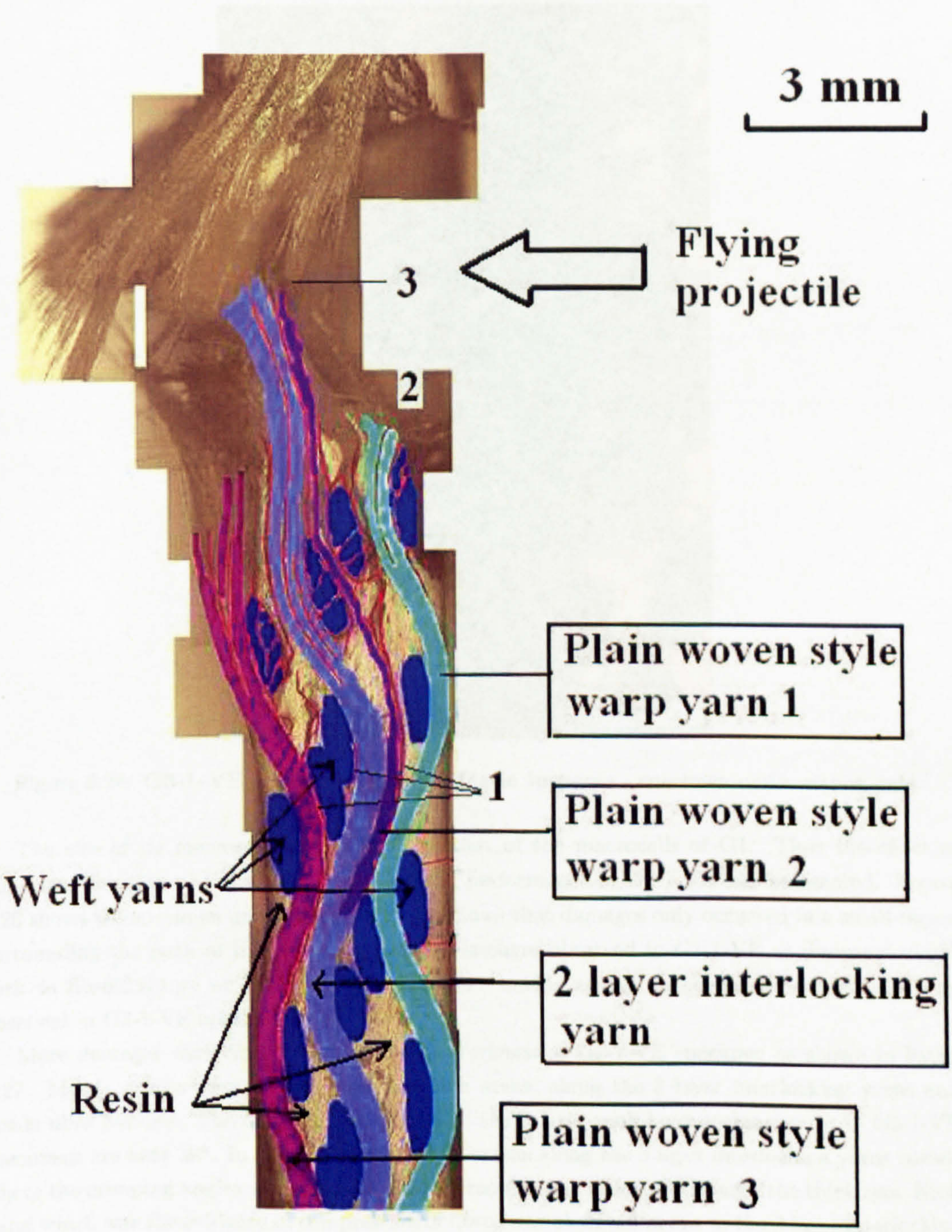

Figure 8.25: **Cross-section in weft yarn direction of ballistic impacted G2-1-VE specimen.**

8.2.3.5 G3-1-VE

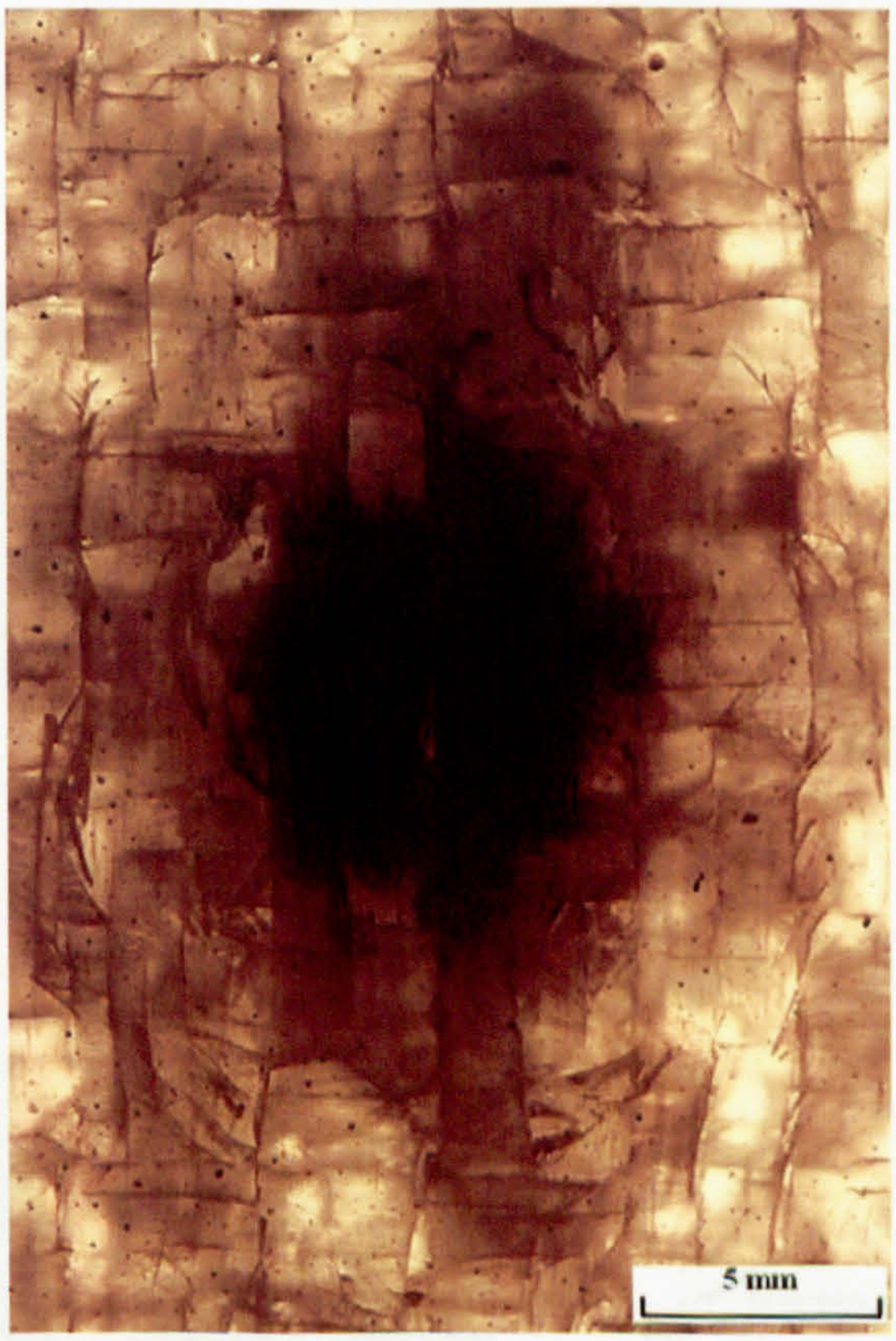

Figure 8.26: **G3-1-VE specimen after ballistic impacts** - specimen under strong light.

The size of its macrocells is smaller than that of the macrocells of G1. Thus the effect of impacting location of the projectile on ballistic performance of G2-1-VE can be ignored. Figure 8.26 shows the specimen under strong light. It shows that damages only occurred in a small region surrounding the path of the flying projectile. Damages observed in G1-1-VE as discussed above such as fibre fracture on front and rear surfaces, matrix cracks on the front surface were also observed in G3-1-VE specimens.

More damages were observed through the thickness of G2-1-VE specimen as shown in figure 8.27. Matrix cracks were observed at resin-rich areas, along the 3 layer interlocking yarns and inside fibre bundles. The crimp angles of part of the 3 layer multilayer locking yarns in G3-1-VE specimens are near 30°. In figure 8.27 all matrix cracks along the 3 layer interlocking yarns ceased where the crimping angles were near 30°. Fibre fracture was observed through the thickness. Kink band which was the evidence of compression of fibres was observed in one of the 3 layer interlocking yarns as shown in figure 8.28. No major delamination was observed.

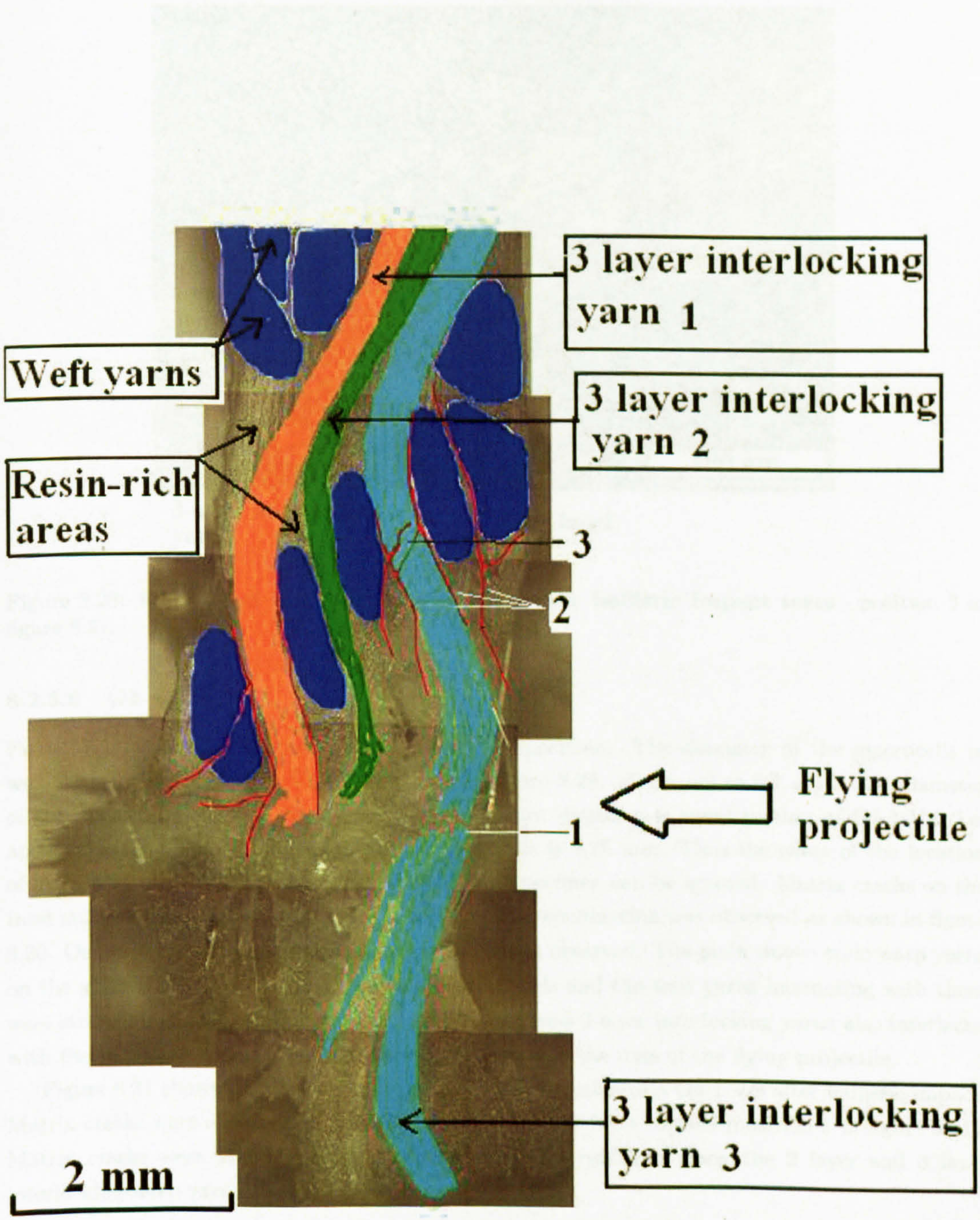

Figure 8.27: **Cross-section in weft yarn direction of ballistic impacted G3-1-VE specimen.**

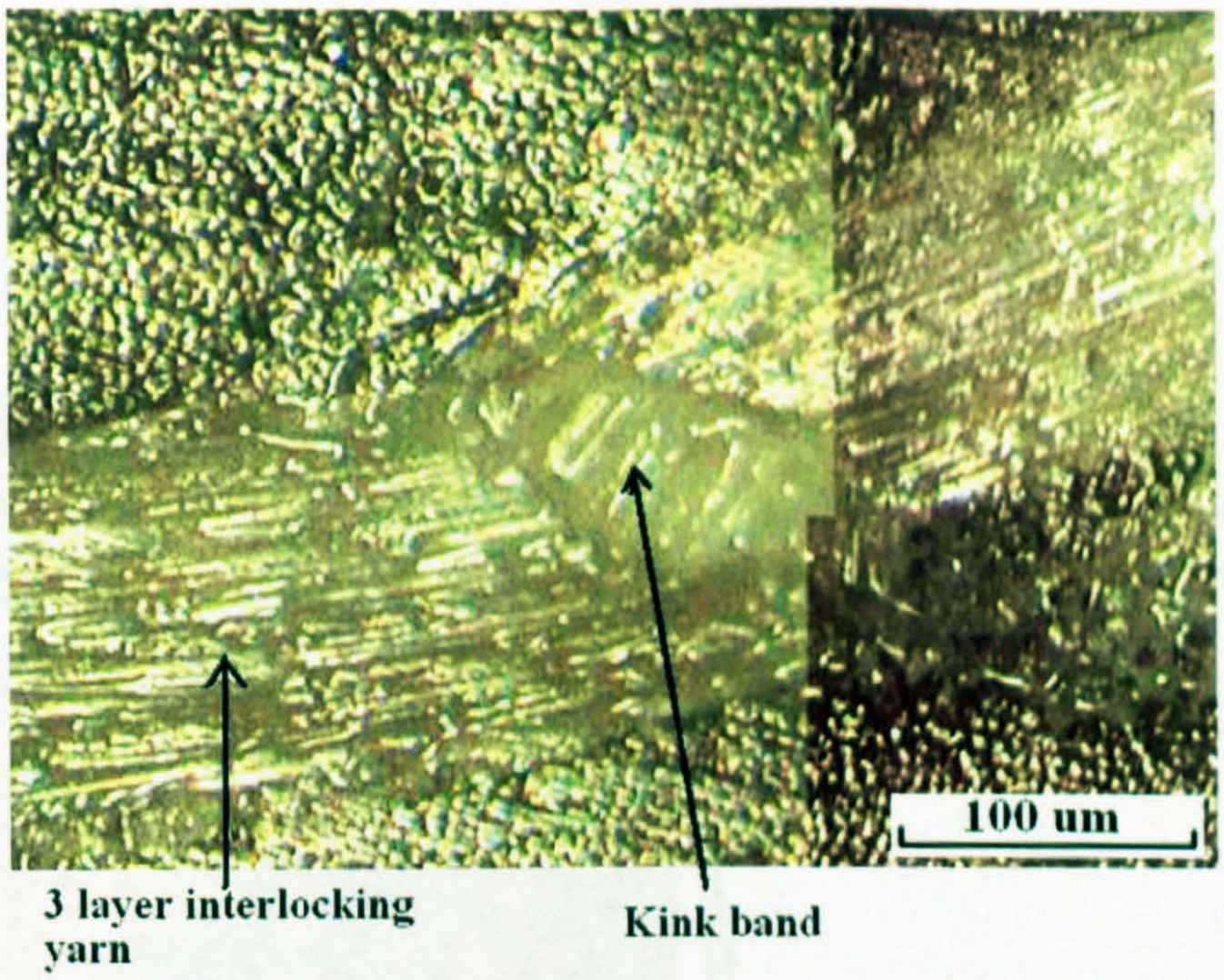

Figure 8.28: **Kink band in G3-1-VE specimen after ballistic impact tests** - position 3 in figure 8.27.

8.2.3.6 G4-1-VE

Figure 8.29 shows the top surface of a G4-1-VE specimen. The diameter of the macrocells in weft yarn direction of G4-1-VE is equal to a in figure 8.29. a is equal to 5.7 mm. The diameter of the macrocells of G4-1-VE specimen in warp yarn direction is equal to that of G1-1-VE, i.e. approximately 8 mm. The diameter of the projectile is 4.75 mm. Thus the effect of the location of impacting on ballistic performance of G4-1-VE specimen can be ignored. Matrix cracks on the front surface were observed in G4-1-VE specimens. Delamination was observed as shown in figure 8.30. One distinctive damage pattern in G4-1-VE was observed. The plain woven style warp yarns on the surface of the rear side of the composite panels and the weft yarns interacting with them were stretched, peeled off and broken. Some 2-layer and 3-layer interlocking yarns also interlaced with the same weft yarns. But they were only broken in the pass of the flying projectile.

Figure 8.31 shows the cross-section in warp yarn direction of a G4-1-VE after ballistic impact. Matrix cracks were observed at the resin rich area on the front surface (position 1 in figure 8.31). Matrix cracks were also observed in other resin rich areas and along the 2 layer and 3 layer interlocking warp yarns.

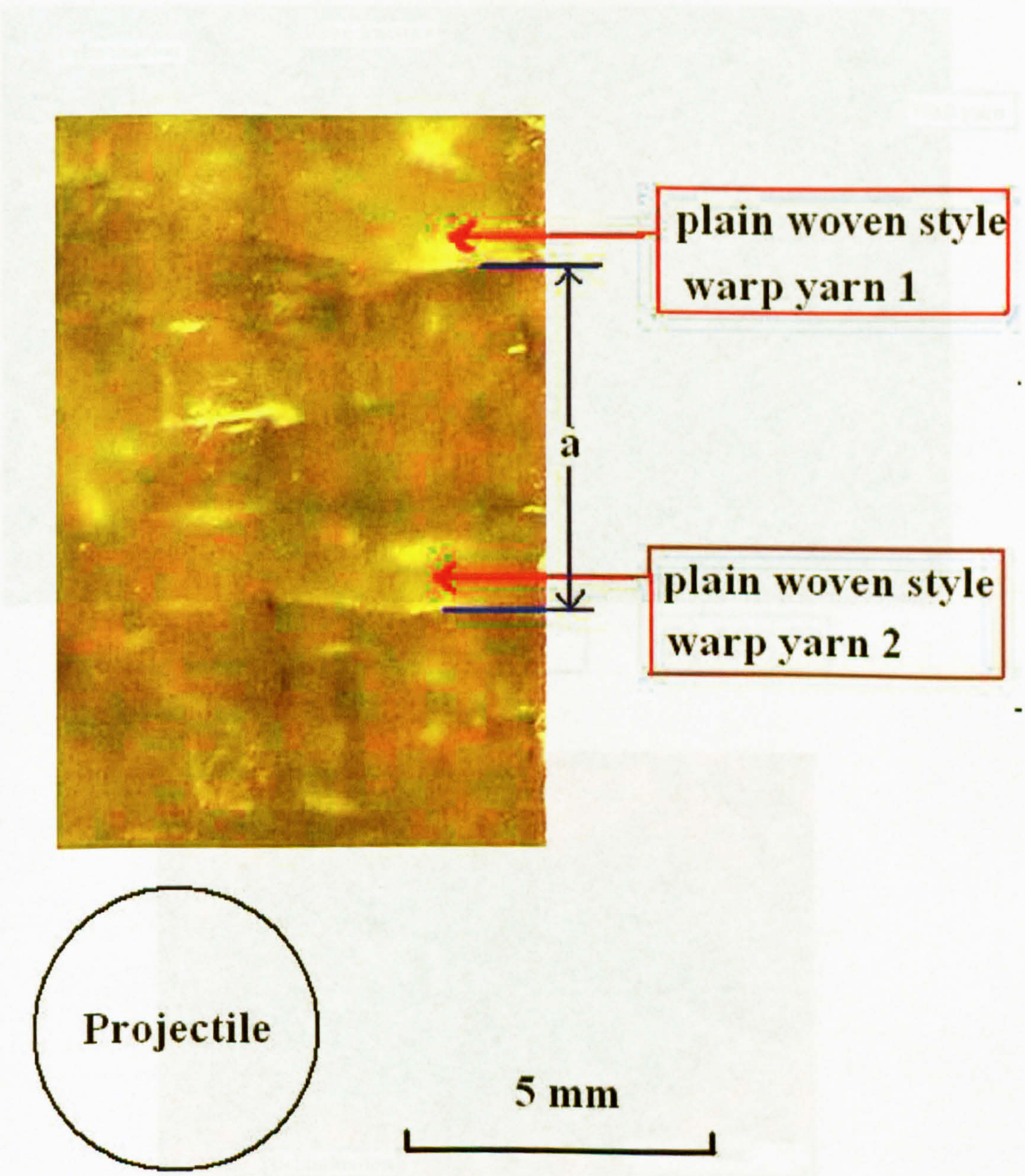

Figure 8.29: **Undamaged G4-1-VE specimen .**

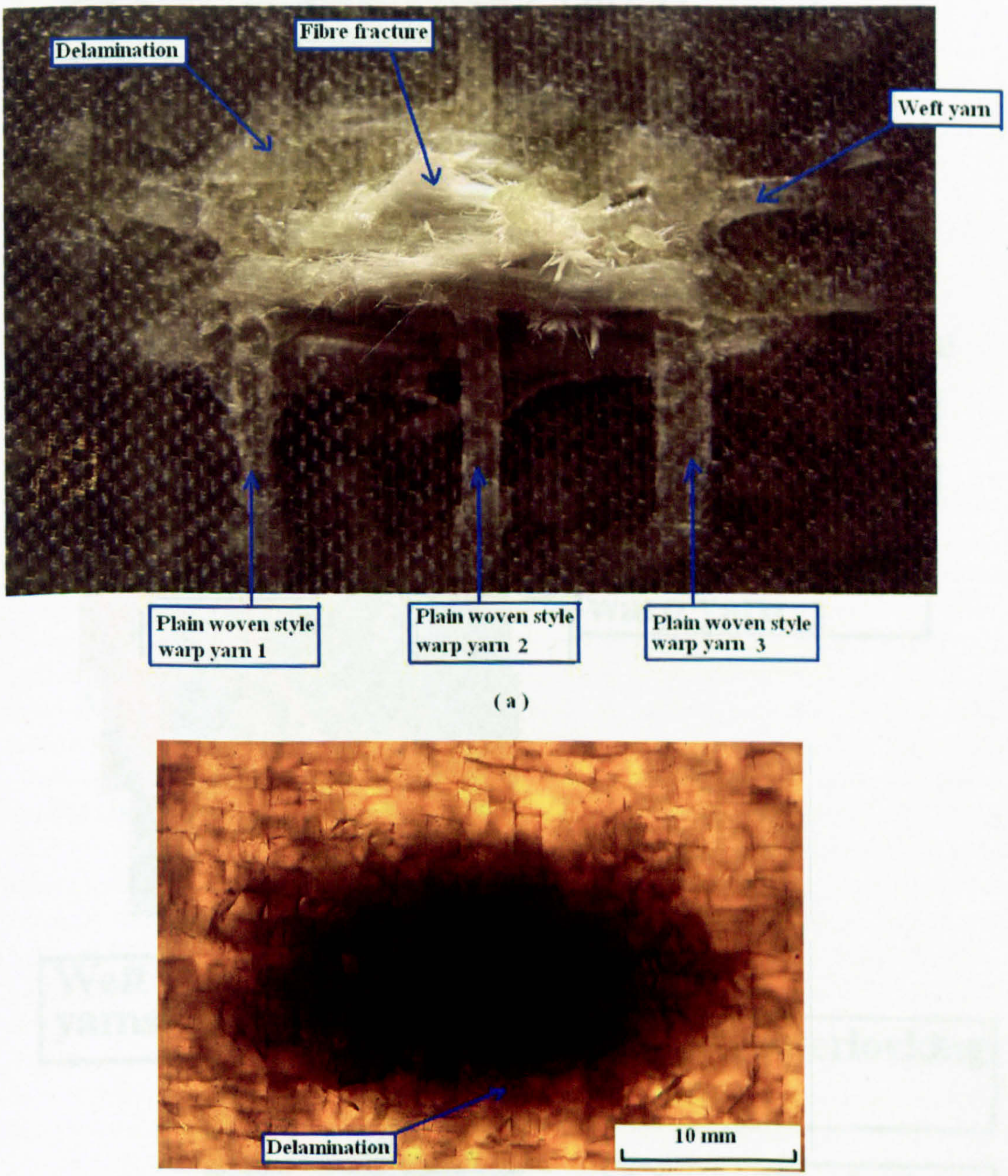

Figure 8.30: **G4-1-VE specimen after ballistic impact** - (a) back view; (b) under strong light.

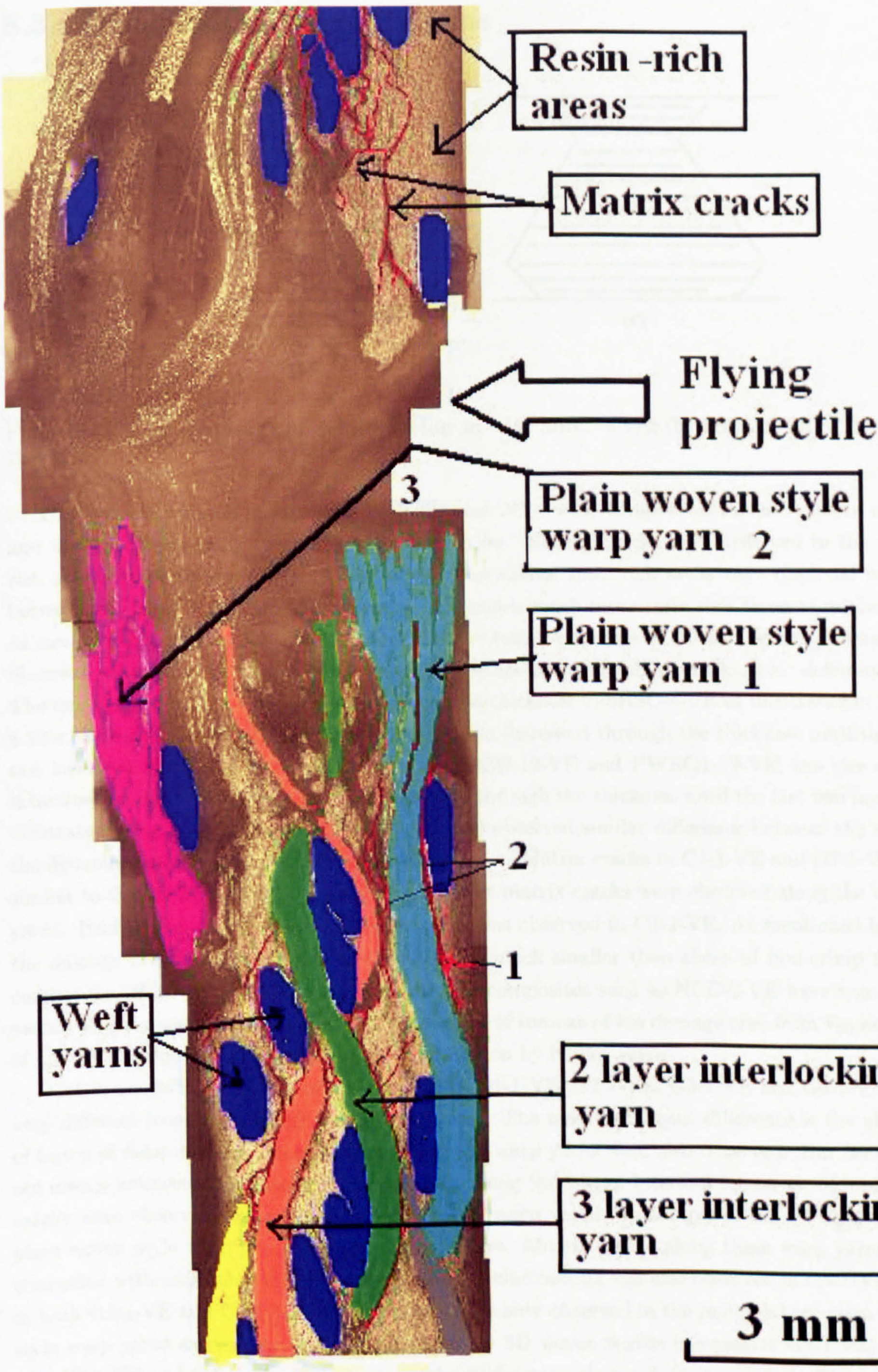

Figure 8.31: **Cross-section in weft yarn direction of ballistic impacted G4-1-VE specimen.**

8.3 Discussion and conclusions

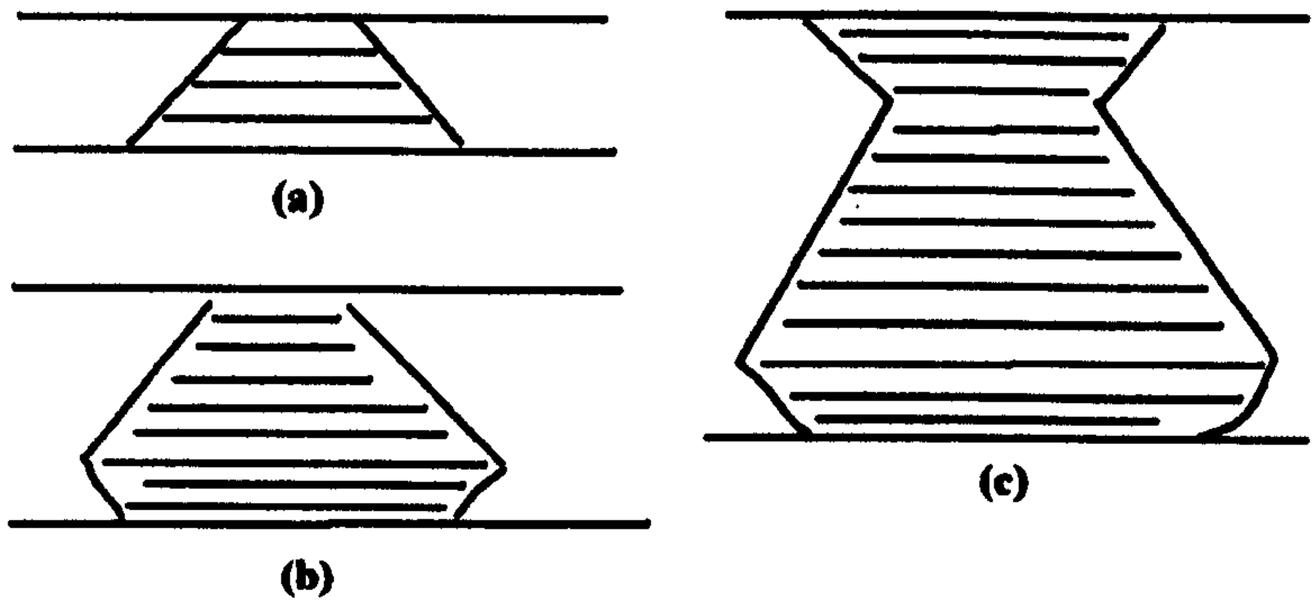

Figure 8.32: **The diameter of delamination in** - (a) 5HSC-4-VE; (b) 5HSC-8-VE; (C) 5HSC-12-VE.

Damage mechanisms observed in both 2D and 3D textile composites include matrix cracks and fibre fractures along the path of the projectiles. Matrix cracks were observed in the resin-rich areas, inside fibre bundles. In 2D textile composites, resin-rich areas were observed mainly between two layer of fabrics. In 3D textile composites much more resin-rich areas were observed as mentioned in section 5.3. Matrix cracks in the resin-rich areas of 2D textile composites were observed connected with each other forming continuous interlaminar cracks, i.e. delamination. The size of the delamination increased through the thickness in 5HSC-4-VE as illustrated in figure 8.32-*a*. But in 5HSC-8-VE, the size of delamination increased through the thickness until the last two layers as illustrated in figure 8.32 (*b*). In 5HSC-12-VE and PWEG1-12-VE, the size of the delamination decreased firstly and then increased through the thickness until the last two layers as illustrated in figure 8.32 (*c*). Gellert et al [38] also observed similar difference between the size of the delamination of thin and thick textile composites. Matrix cracks in C1-1-VE and G7-1-VE are similar to that of 2D textile composites except that matrix cracks were observed along the binder yarns. Bridging of delamination by binder yarns was observed in C1-1-VE. As mentioned before, the damage areas of V_{50} samples of C1-1-VE are much smaller than those of non-crimp textile composites. Both C1-1-VE and non-crimp textile composites such as NCC-2-VE have non-crimp yarns. This suggested that the significant reduction of the size of the damage area from V_{50} samples of C1-1-VE is due to the suppressing of delamination by binder yarns.

Matrix cracks in 3D woven textile composites G1-1-VE, G2-1-VE, G3-1-VE and G4-1-VE were very different from those of 2D textile composites. The most significant difference is the absence of layers of delamination. Matrix cracks along the warp yarns were also observed. But they were not always connected with each other, especially along the 3-layer interlocking yarns. More matrix cracks were observed along the plain woven style warp yarns. In sample of G2-1-VE, there are plain woven style warp yarns through the thickness. Matrix cracks along these warp yarns were connected with each other forming delamination. Delamination was also observed in G4-1-VE. But in both G2-1-VE and G4-1-VE, delaminations were only observed in the region where plain woven style warp yarns existed through the thickness. In 3D woven textile composites G1-1-VE, G2-1-VE, G3-1-VE and G4-1-VE, transverse matrix cracks were observed on the surface. They formed circles surrounding the impacting point of the projectile. They were caused by shear component

of stress wave introduced by ballistic impact.

Fibre fractures in 2D textile composites were only observed along the path of the projectile. Shear cut fibre bundles were observed firstly in the through-thickness direction. Then distortions of fibre bundles were observed in non-penetrated samples. In penetrated samples, fracture of fibre bundles continued. No shear cuts were observed. Fibre debonding and fibre pull-out were observed suggesting that the projectile started to penetrate by breaking fibres rather than producing shear plug. SEM images show that there are differences in the shape of the cross-section of the broken fibres through the thickness. Shear cut fibres dominated in the front and middle of the region of broken fibres. This suggested the dominance of shear stress. Fibres with uneven fracture surface were observed in the region near the rear side of the composite panels. This suggested that fibres in the rear side of the composite panels were subjected to mixture of shear and tensile stresses.

Fibre fractures in 3D woven textile composites were not only restricted to the path of the projectile. In samples of C1-1-VE, fractures of binder yarns were observed on front surface, back surface and in the middle of the composite. Fractures in the binder yarns on the back surface and in the middle of the composite were not the in path of the projectile. The former happened due to the peel-off of the weft yarns in the rear side of the composite panel. The later happened to the delamination in the middle of the composite panel. In samples of G7-1-VE, stretching of binder yarns were also observed. This is due to the fact that Kevlar fibres used in G7-1-VE have high strength and tensile failure strain. As mentioned in section 2.11, the fracture energy of fibres is much higher than that of pure resin. The introduction of binder yarns in the through thickness direction caused more fibre fractures. Thus fewer delaminations were needed to absorb the kinetic energy of the projectile.

Fibre fractures in 3D woven textile composites G1-1-VE, G2-1-VE, G3-1-VE, G4-1-VE were different to those of 2D textile composites. No shear cut of fibre bundles were observed except G2-1-VE. In G2-1-VE, clear cut plain woven style warp yarn was observed. Warp yarns in G1-1-VE etc have bigger crimping angles than warp yarns in 2D textile composites. This caused the fibres subjected to mixture of shear and tensile force. In extreme case, fibres were subjected to compressive stress, e.g. the 3-layer locking yarns in G3-1-VE. As we know, composites are strong when subjected to tensile stress in the fibre direction. But they are weak when subjected to transverse shear stress. It can be concluded that the use of multi-layer locking yarns reduced transverse fracture of composites and caused more tensile and compressive fracture of composites. Thus less fibre fracture and matrix cracks were needed to absorb the kinetic energy of the projectile.

Chapter 9

Energy absorption of 2D and 3D textile composite in drop weight impacts

9.1 Introduction

As described in chapter 3, the purpose of drop weight impact testing is to assess the composite's ability to absorb energy during high energy low velocity impacts. The drop weight impact test facility used in this study was more advanced than the ballistic impact test facility. The histories of force, velocity and displacement can be recorded. Thus it is possible to identify a penetrating impact with zero residual velocity. The impacting energy of this impact can be taken as the perforation energy. The impacting velocity of this impact will be names as V_{50} drop mass. Sufficient numbers of samples were needed to identify this impact.

So far, it have been observed that 3D woven textile composite C1-1-VE has higher single hit V_{50} than 2D textile composites in databases. 3D woven textile composite G1-1-VE, G2-1-VE, G3-1-VE, G4-1-VE have much better damage resistance than 2D textile composites in databases. All these five composites are worth further assessment. But due to the limitation of materials available, only the perforation energy of C1-1-VE was characterized. For the purpose of comparison, perforation energies of textile composites in database 1 were also characterized.

The term high energy impact was defined here as impact test where the incident energy of the striker was more than the penetration energy, therefore all the tested specimens were perforated. The impact response of 2D plain woven carbon and glass fibre textile composites were investigated using the CEAST machine described in chapter 4.

9.2 Results - V_{50} drop mass of 2D and 3D textile composites

9.2.1 5HSC-4-VE, 5HSC-8-VE and 5HSC-12

5HSC-4-VE, 5HSC-8-VE and 5HSC-12-VE are manufactured using carbon fibre five harness satin weaves. They are materials of baseline 1 in ballistic impact tests. Table 9.1, table 9.3 and table

Table 9.1: Drop weight impact tests of 5HSC-4-VE specimens

Sample No	Weight of the impactor/kg	Impacting velocity/(m/s)	Impacting energy/J	Peak Force/N	E_0 /J	Status
1	15.7	2.08	33.87	5717.25	35.77	Non-penetrated
2	15.7	2.12	35.41	5100.15	37.68	Penetrated
3	15.7	2.12	35.41	5553.90	37.34	Non-penetrated
4	15.7	2.17	36.88	6769.95	38.39	Non-penetrated
5	15.7	2.17	36.95	5953.20	39.20	Penetrated
6	15.7	2.17	36.95	4991.25	39.09	Penetrated
7	15.7	2.17	36.95	5789.85	39.08	Non-penetrated
8	15.7	2.21	38.49	4882.35	40.21	Penetrated
9	15.7	2.21	38.49	5100.15	40.80	Penetrated
10	15.7	2.34	43.11	4918.65	44.83	Penetrated
11	15.7	2.51	49.27	6788.10	48.45	Penetrated
12	15.7	2.58	52.35	5753.55	45.81	Penetrated
13	15.7	2.66	55.43	5390.55	39.47	Penetrated
14	15.7	2.69	56.97	5898.75	44.91	Penetrated
15	15.7	2.69	56.97	5608.35	43.27	Penetrated
16	15.7	2.73	58.51	5789.85	45.64	Penetrated
17	15.7	3.07	73.90	5662.80	38.52	Penetrated
18	22.5	6.26	441.30	5445.00	36.71	Penetrated
19	22.5	6.26	441.30	5553.90	35.41	Penetrated
20	22.5	6.26	441.30	5572.05	37.42	Penetrated

Table 9.2: Drop weight impact tests of 5HSC-8-VE specimens

Sample No	Weight of the impactor/kg	Impacting velocity/(m/s)	Impacting energy/J	Peak Force/N	E_0 /J	Status
1	15.7	3.82	114.46	15209.70	116.47	Non-penetration
2	15.7	3.86	117.01	13576.20	119.79	Non-penetration
3	15.7	3.86	117.01	15300.45	119.21	Non-penetration
4	15.7	3.89	118.55	13884.75	121.45	Penetration
5	15.7	3.89	118.55	13376.55	120.97	Penetration
6	22.5	6.26	441.30	13013.55	110.01	Penetration
7	22.5	6.26	441.30	13721.40	114.00	Penetration
8	22.5	6.26	441.30	14501.85	110.57	Penetration

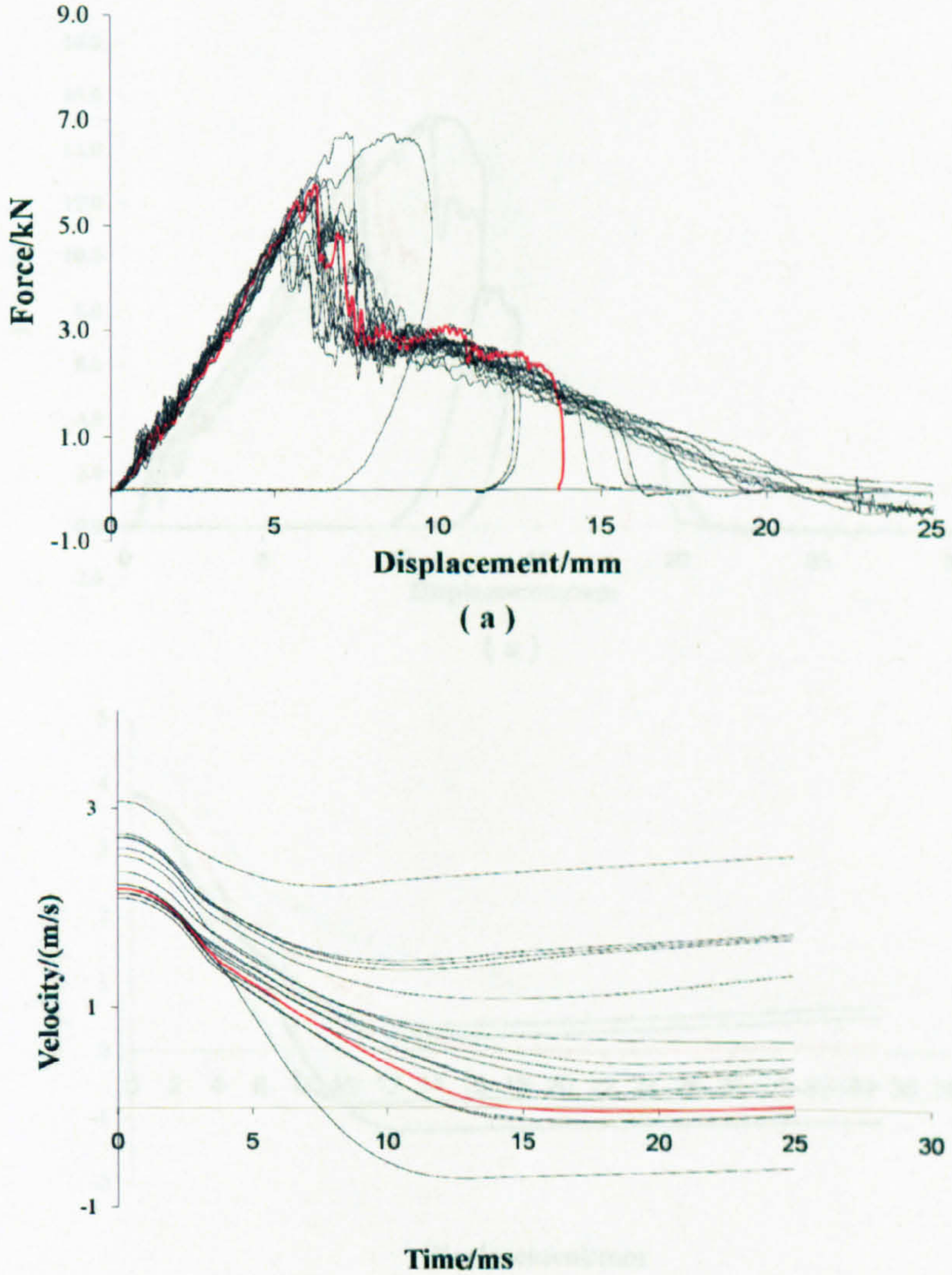

Figure 9.1: **Results of 5HSC-4-VE specimens impacted by 15.7kg impactor droped from various heights** - (a) Force versus displacement curves; (b) Velocity versus time curves.

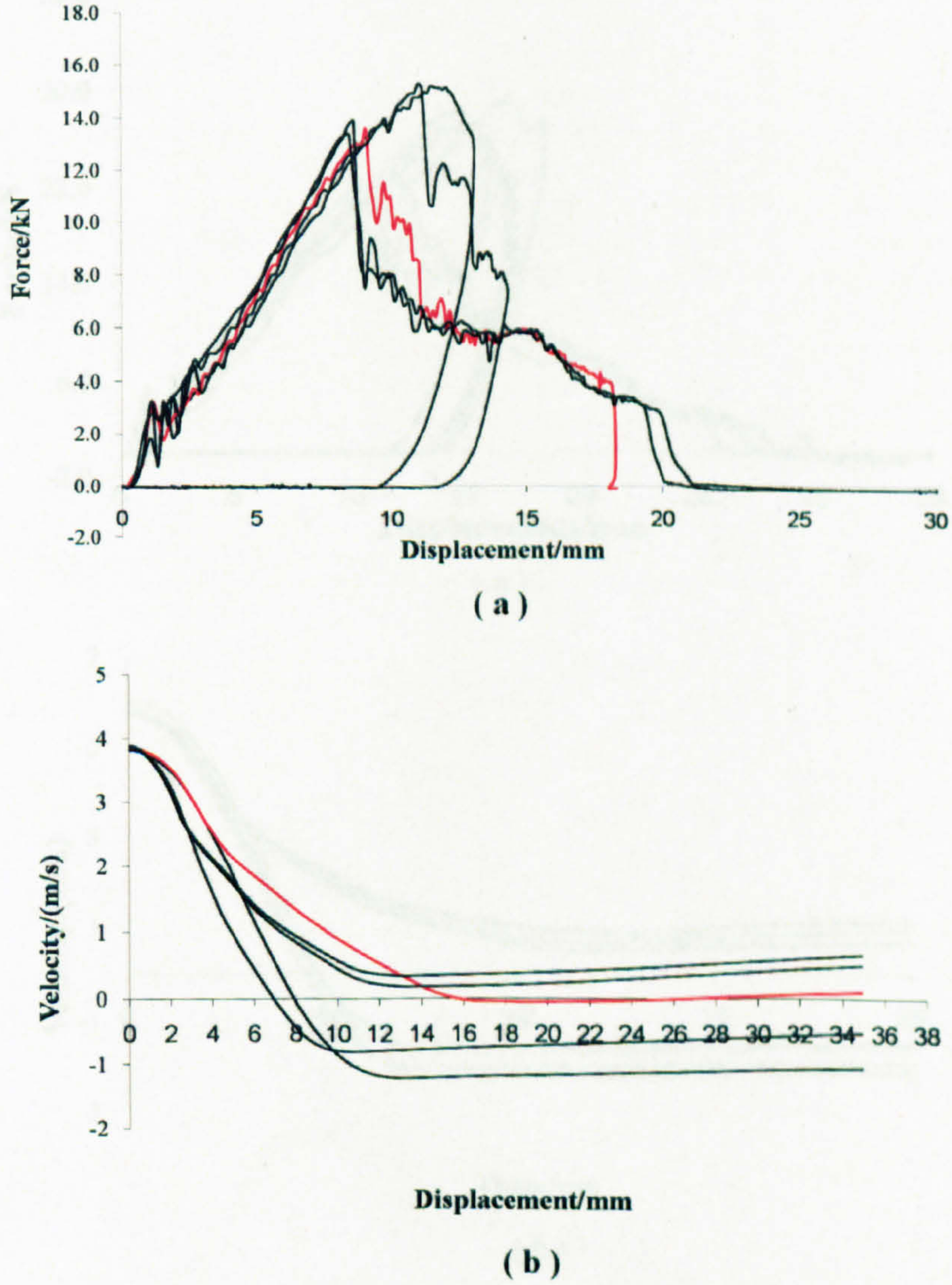

Figure 9.2: **Results of 5HSC-8-VE specimens impacted by 15.7kg impactor droped from various heights** - (a) Force versus displacement curves; (b) Velocity versus time curves.

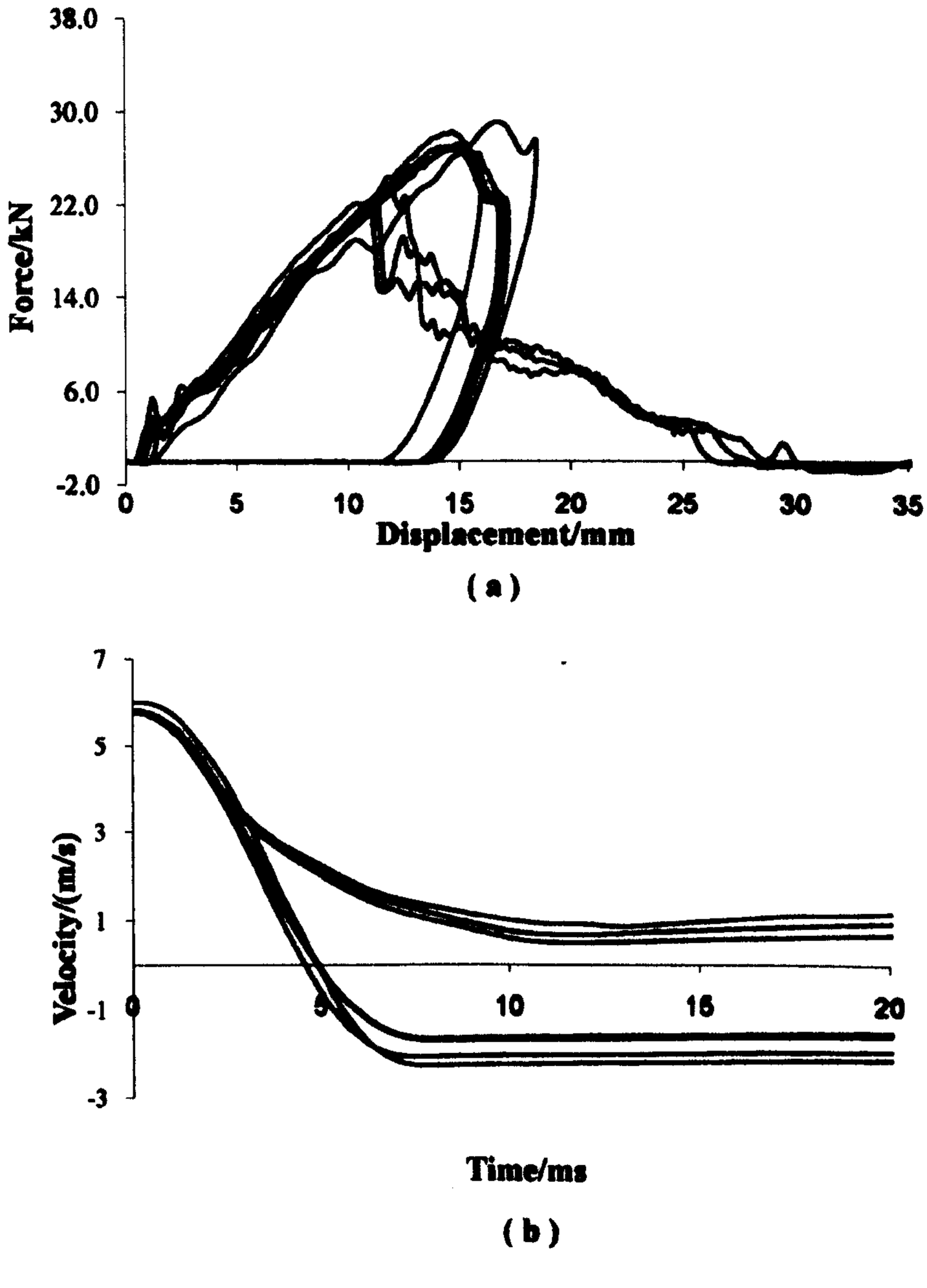

Figure 9.3: **Results of 5HSC-12-VE specimens impacted by 15.7kg impactor droped from various heights** - (a) Force versus displacement curves; (b) Velocity versus time curves.

Table 9.3: Drop weight impact tests of 5HSC-12-VE specimens

Sample No	Weight of the impactor/kg	Impacting velocity/(m/s)	Impacting energy/J	Peak Force/N	E_0 /J	Status
1	15.7	5.77	261.74	28350.30	264.18	Non-penetration
2	15.7	5.79	263.28	22469.70	265.34	Penetration
3	15.7	5.79	263.28	26753.10	265.86	Non-penetration
4	15.7	5.79	263.28	26880.15	265.88	Non-penetration
5	15.7	5.81	264.82	22034.10	265.50	Penetration
6	15.7	5.81	264.82	27297.60	267.45	Non-penetration
7	15.7	5.83	266.36	27043.50	268.93	Non-penetration
8	15.7	5.83	266.36	23232.00	265.17	Penetration
9	15.7	6.01	283.29	29040.00	285.71	Non-penetration
10	18.5	6.01	333.82	33214.50	337.06	Non-penetration
11	20.5	6.01	369.91	33359.70	373.85	Non-penetration
12	22.5	6.01	406.00	33759.00	386.76	Penetration
13	22.5	6.26	441.30	36245.55	422.12	Penetration
14	22.5	6.26	441.30	20328.00	235.92	Penetration
15	22.5	6.26	441.30	24575.10	245.56	Penetration
16	22.5	6.26	441.30	25900.05	272.64	Penetration
17	22.5	6.26	441.30	31744.35	386.96	Penetration

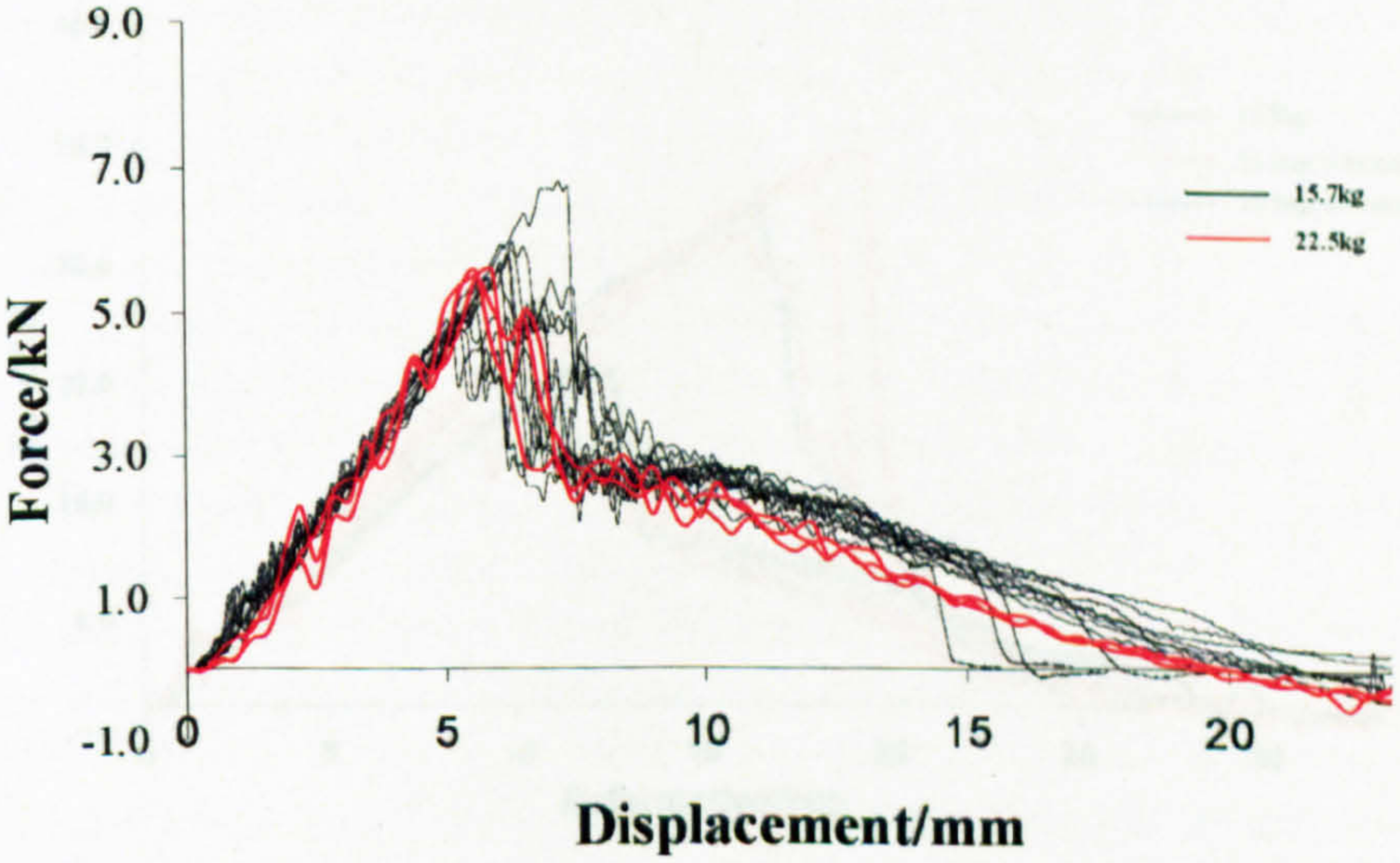

Figure 9.4: **Results of 5HSC-4-VE specimens impacted by 22.5kg impactor .**

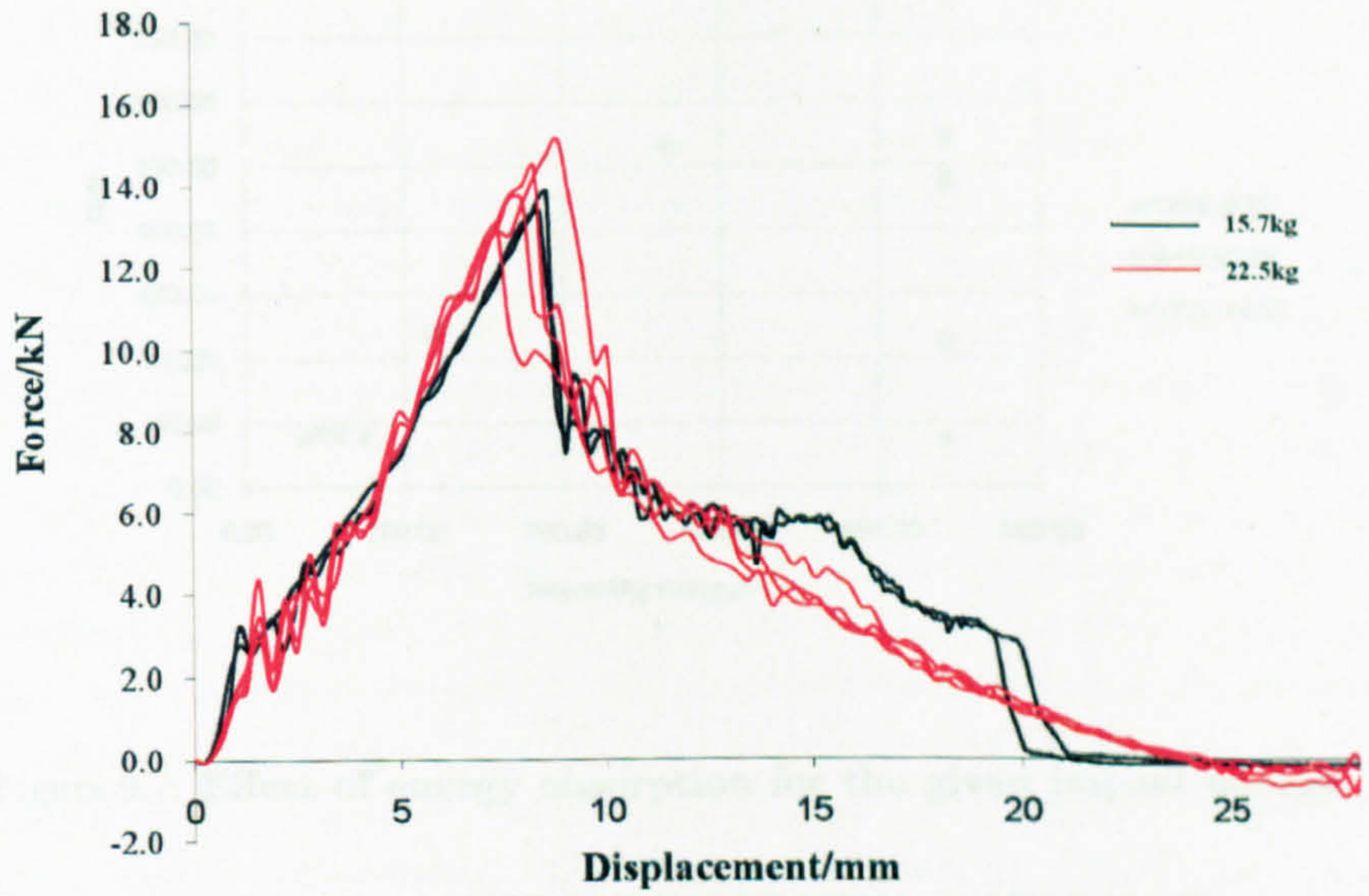

Figure 9.5: **Results of 5HSC-8-VE specimens impacted by 22.5kg impactor .**

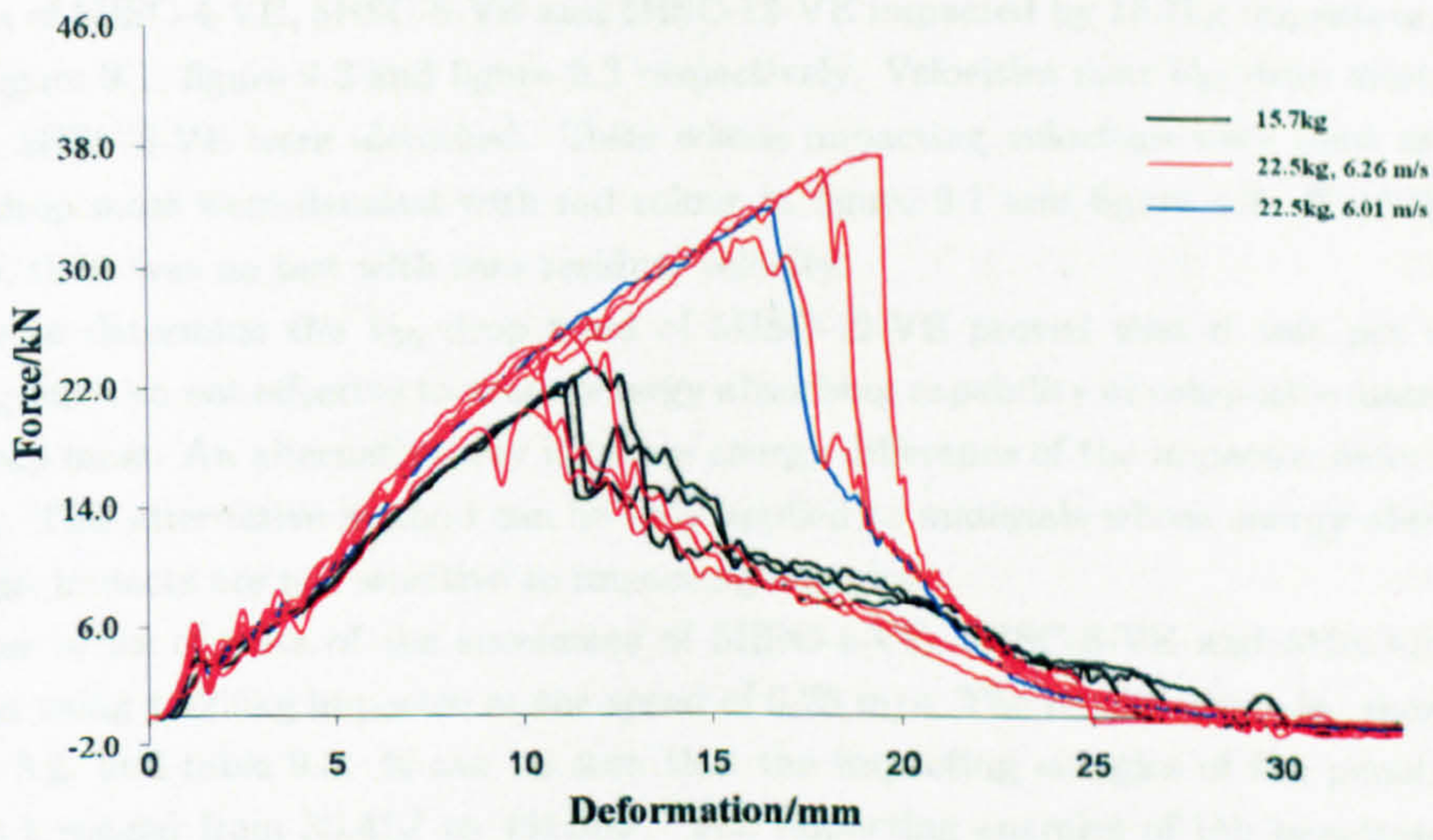

Figure 9.6: **Results of 5HSC-12-VE specimens impacted by 22.5kg impactor .**

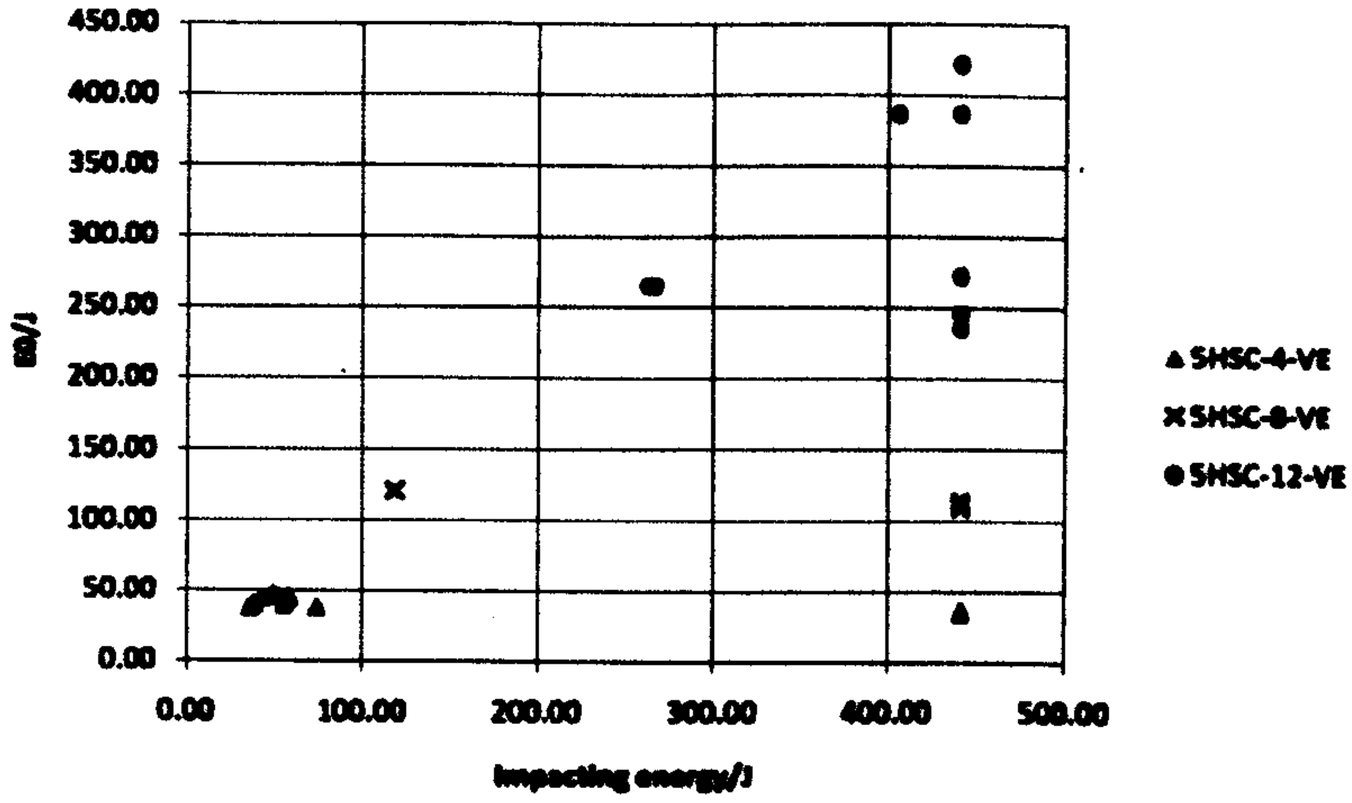

Figure 9.7: **Effect of energy absorption for the given impact energy** .

9.2 list the experimental details of 5HSC-4-VE, 5HSC-8-VE and 5HSC-12-VE respectively. Tests of all these specimens can be divided into two groups according to the weight to the impactor. When impactor with weight of 15.7kg was used, various impacting velocities were used. This was achieved by lifting the impactor to various heights. All these tests aimed to determine an impacting velocity named V_{50} drop mass which is similar to the ballistic limit velocity in ballistic impacting tests, i.e. at which the 15.7kg impactor was just able to perforate the specimen. This velocity was identified by looking at the velocity history of all the tests. If a test with zero residual velocity can be identified then its impacting velocity was near V_{50} drop mass of the composite material tested.

Results of 5HSC-4-VE, 5HSC-8-VE and 5HSC-12-VE impacted by 15.7kg impactors are shown in figure figure 9.1, figure 9.2 and figure 9.3 respectively. Velocities near V_{50} drop mass of 5HSC-4-VE and 5HSC-8-VE were identified. Tests whose impacting velocities were used as velocities near V_{50} drop mass were denoted with red colour in figure 9.1 and figure 9.2. For 5HSC-12-VE specimens, there was no test with zero residual velocity.

Failure to determine the V_{50} drop mass of 5HSC-12-VE proved that it was not only time-consuming but also not effective to access energy absorbing capability of composite materials using the V_{50} drop mass. An alternative way is to use energy difference of the impactor before and after impacting. This alternative method can be only applied to materials whose energy absorptions in drop weight impacts are not sensitive to impacting energies.

Another series of tests of the specimens of 5HSC-4-VE, 5HSC-8-VE and 5HSC-12-VE were carried out using a 22.5kg impactor at the speed of 6.26 m/s. The results were also shown in table 9.1, table 9.2, and table 9.3. It can be seen that the impacting energies of the penetrated tests in table 9.1 ranged from $35.41J$ to $441.30J$. The impacting energies of the penetrated tests in table 9.2 ranged from $118.55J$ to $441.30J$. The impacting energies of the penetrated tests in table 9.3 ranged from $263.28J$ to $441.30J$. This series of tests aimed to study the effects of impacting energies on energy absorptions of 5HSC-4-VE, 5HSC-8-VE and 5HSC-12-VE. The results were shown in figure 9.4, figure 9.5 and figure 9.6. It can be seen that the difference between the force

versus displacement curves of 5HSC-4-VE and 5HSC-8-VE when impacted by 15.7kg impactor and by 22.5kg impactor is very small. This is confirmed by their maximum energy absorption values E_0 as shown in figure 9.7.

Compared with 5HSC-4-VE and 5HSC-8-VE, 5HSC-12-VE reacted differently. When impacted by 22.5kg impactor at $6.26m/s$, 6 specimens produced two groups of results. One group of 3 specimens have similar forces versus displacement curves to that of specimens impacted by 15.7kg impactor. The other group have significantly larger maximum force than the first group. One specimen was impacted by 22.5kg impactor at 6.01 m/s. Its force versus displacement curve is similar to the second group when impacted at 6.26 m/s as shown in figure 9.7. One possible reason for this difference was the big thickness of the samples of 5HSC-12-VE. The thickness of 5HSC-4-VE, 5HSC-8-VE and 5HSC-12-VE are $1.8mm$, $3.4mm$ and 4.2 mm respectively. The diameter of the hole of the clamping plate was $40mm$ as shown in figure 4.28. The diameter of the hemispherical impactor was $20mm$. Clamping forces were not fixed due to the limitation of the testing facilities. For thin specimens such as 5HSC-4-VE and 5HSC-8-VE, the effect of clamping force was very small, because their stiffness were small. The global deformation during the impacting process was small compared to the diameter of the hole in the clamping plate. This was not the case for 5HSC-12-VE specimens where global deformation reached the part of composite clamped by clamping plate. Sliding of specimens was observed in some tests. So far it can be concluded that the clamping fixture used here are not suitable for the tests of 5HSC-12-VE specimens at speed around $6m/s$. The major reason for this difference was due to the fact that the CEAST impactor machine used in this study was poorly designed. As mentioned in section 7.1, absorbed energy is a second-order compound parameter whose accuracy completely depends on the accuracy of impact force in the low-velocity impacts. Thus the absorption energy results of low-velocity impacts were not as good as that in his ballistic impacts in this study.

9.2.2 C1-1-VE

C1-1-VE is manufactured using 3D woven carbon fabrics. The same impactors used in the tests of 5HSC-4-VE, 5HSC-8-VE and 5HSC-12-VE were used. The results are shown in table 9.4. The tests using 15.7kg impactor are aiming to determine a impacting velocity named V_50 drop mass. The force versus displacement and velocity versus time curves of these tests are shown in figure 9.8. No test with zero residual velocity was found. But sample 6 and 8 have near zero residual velocities. They are denoted using blue and red colour in figure 9.8. Their force versus displacement curves show that the impactor was stopped in both tests. Short distance of rebound of the impactor occurs in the test of sample 6. During the rebound the velocity of the impactor decreased due to two factors. One is the friction force between the steel rod in the impactor and composite sample. Another one is the force of gravity. When the velocity of the impactor reaches zero the friction force change direction from downwards to upwards. Because the force of the gravity was equal to the friction force, the impactor stopped. Similar events happened in the test of sample 8. But the force of gravity was bigger than the friction force. The impactor started to penetrate the specimen again before being stopped. Although no test with zero residual velocity was found. It is believed that V_{50} drop mass is between the velocities in the tests of sample 6 and 8.

In order to study the effect of impacting energy on energy absorption, another impactor of 22.5kg was also used. Impacting velocity of 6.26 m/s was used. The results are shown in figure

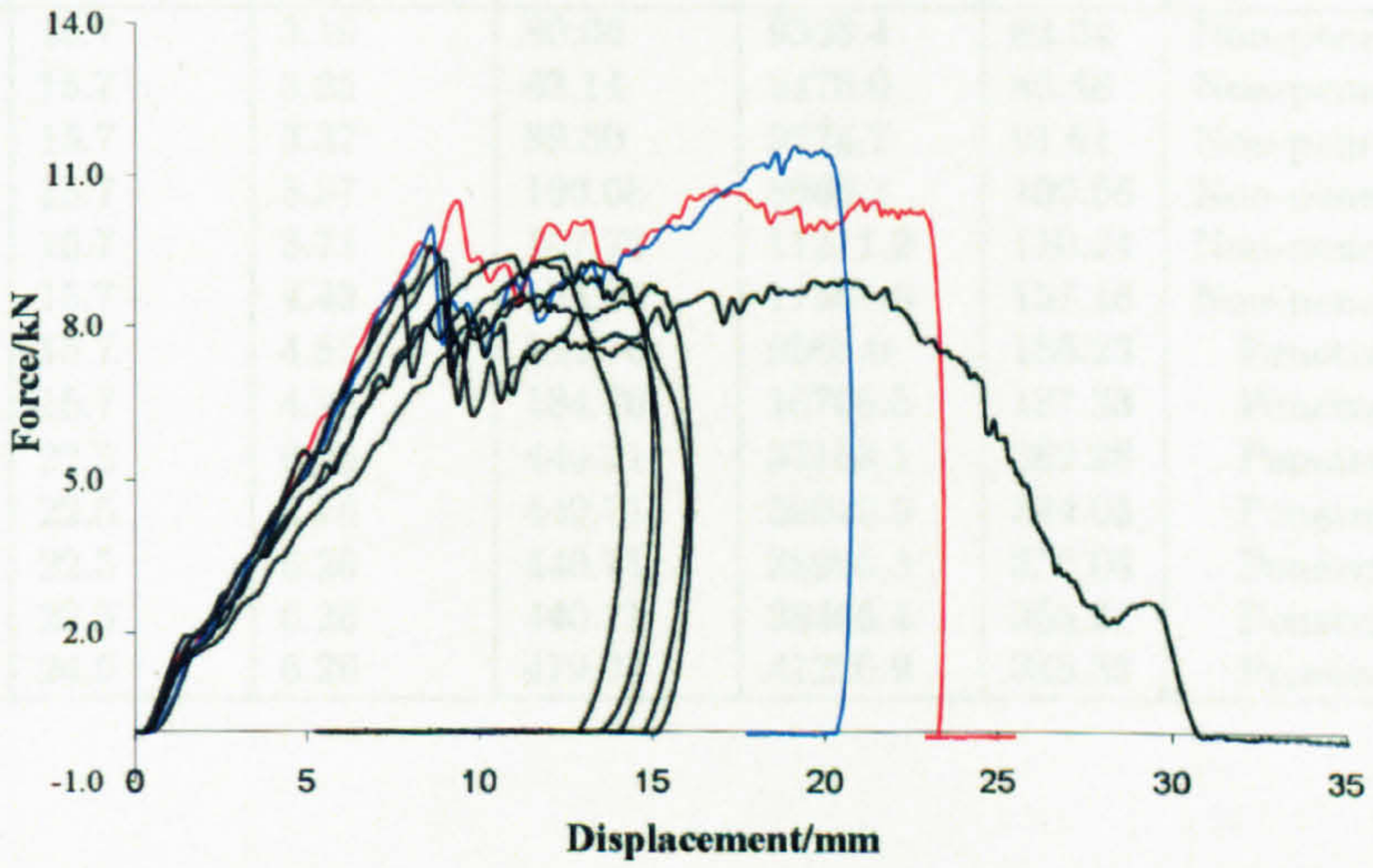

(a)

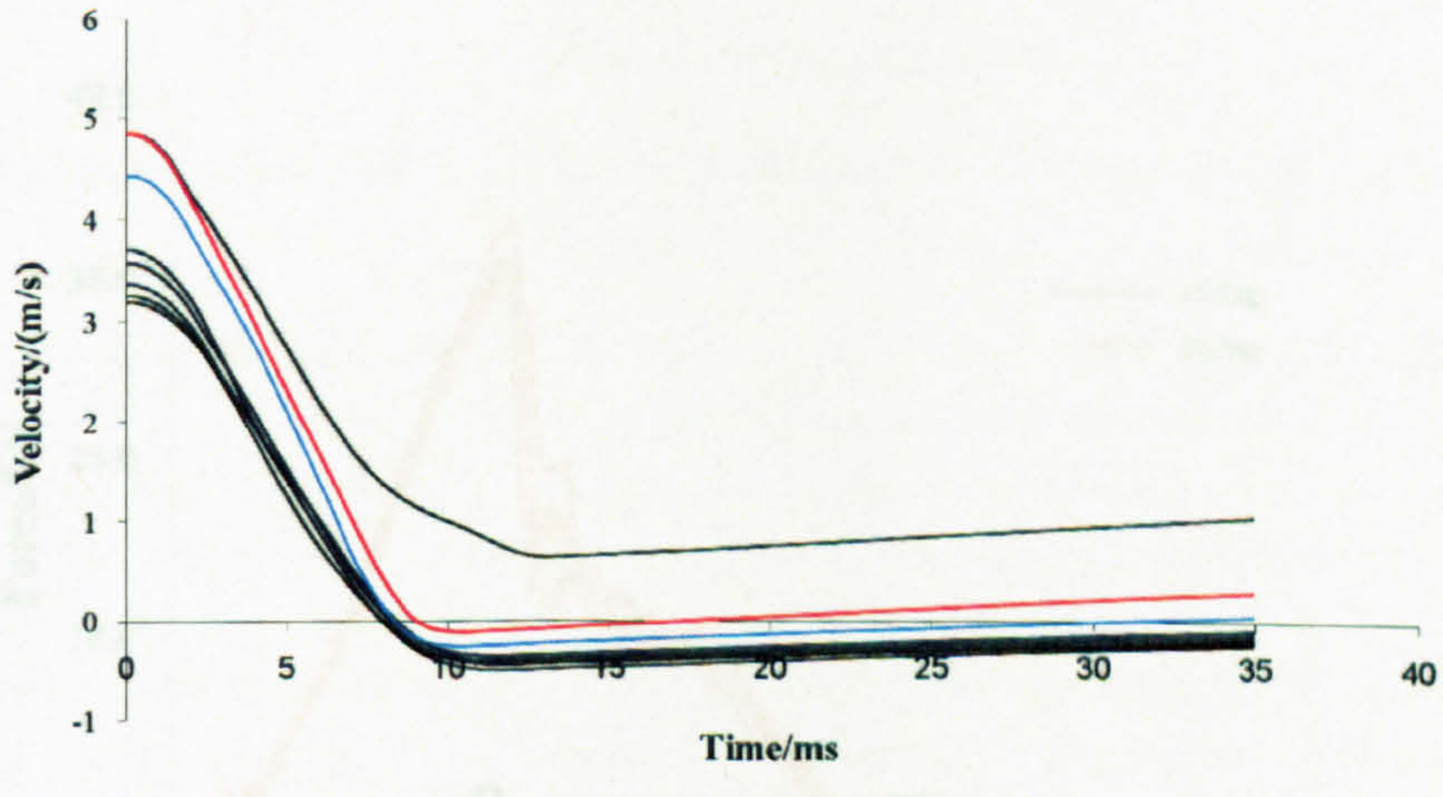

(b)

Figure 9.8: **Results of C1-1-VE specimens impacted by 15.7kg impactor** - (a) Force versus displacement curves; (b) Velocity versus time curves.

Table 9.4: Drop weight impact tests of C1-1-VE specimens

Sample No	Weight of the impactor/kg	Impacting velocity/(m/s)	Impacting energy/J	Peak Force/N	E_0 /J	Status
1	15.7	3.19	80.06	9365.4	82.24	Non-penetration
2	15.7	3.25	83.14	8476.0	85.48	Non-penetration
3	15.7	3.37	89.30	9274.7	91.61	Non-penetration
4	15.7	3.57	100.08	8966.1	102.56	Non-penetration
5	15.7	3.71	107.78	11271.2	110.24	Non-penetration
6	15.7	4.43	153.96	11561.5	157.16	Non-penetration
7	15.7	4.85	184.76	9565.0	186.23	Penetration
8	15.7	4.85	184.76	10708.5	187.33	Penetration
9	22.5	6.26	440.71	37153.1	362.28	Penetration
10	22.5	6.26	440.71	39070.9	344.03	Penetration
11	22.5	6.26	440.71	38990.3	336.03	Penetration
12	22.5	6.26	440.71	38466.4	355.51	Penetration
13	24.5	6.26	479.94	41226.9	345.33	Penetration

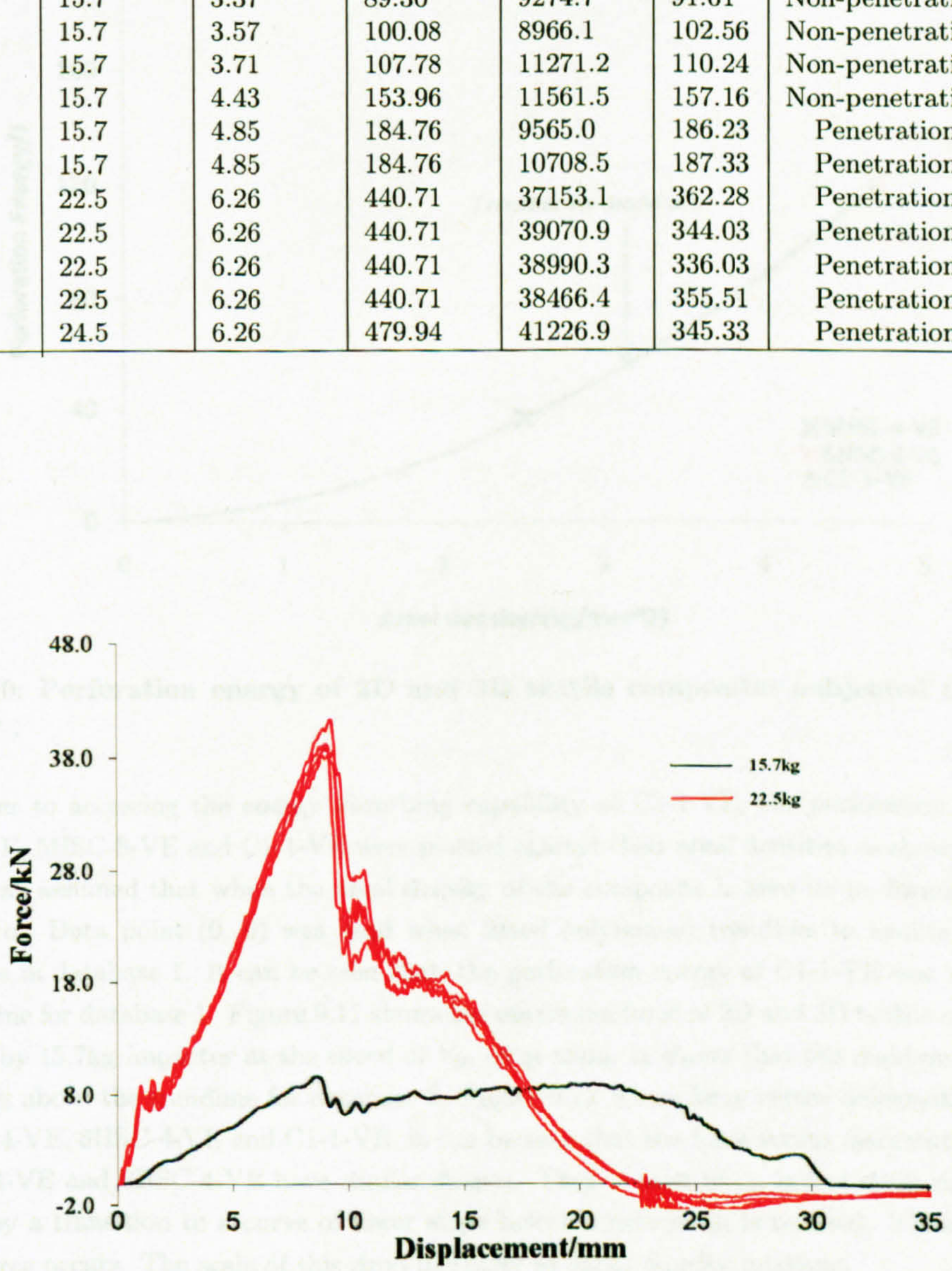

Figure 9.9: **Force versus displacement curves of C1-1-VE specimens impacted by different impacting energies .**

9.9. Huge difference was observed between the results of 15.7kg impactor and 22.5kg impactor. The later have much higher maximum force and E_0. So the energy absorptions of C1-1-VE in penetrated drop weight impacts were affected by impacting energies.

9.3 Discussion and conclusions

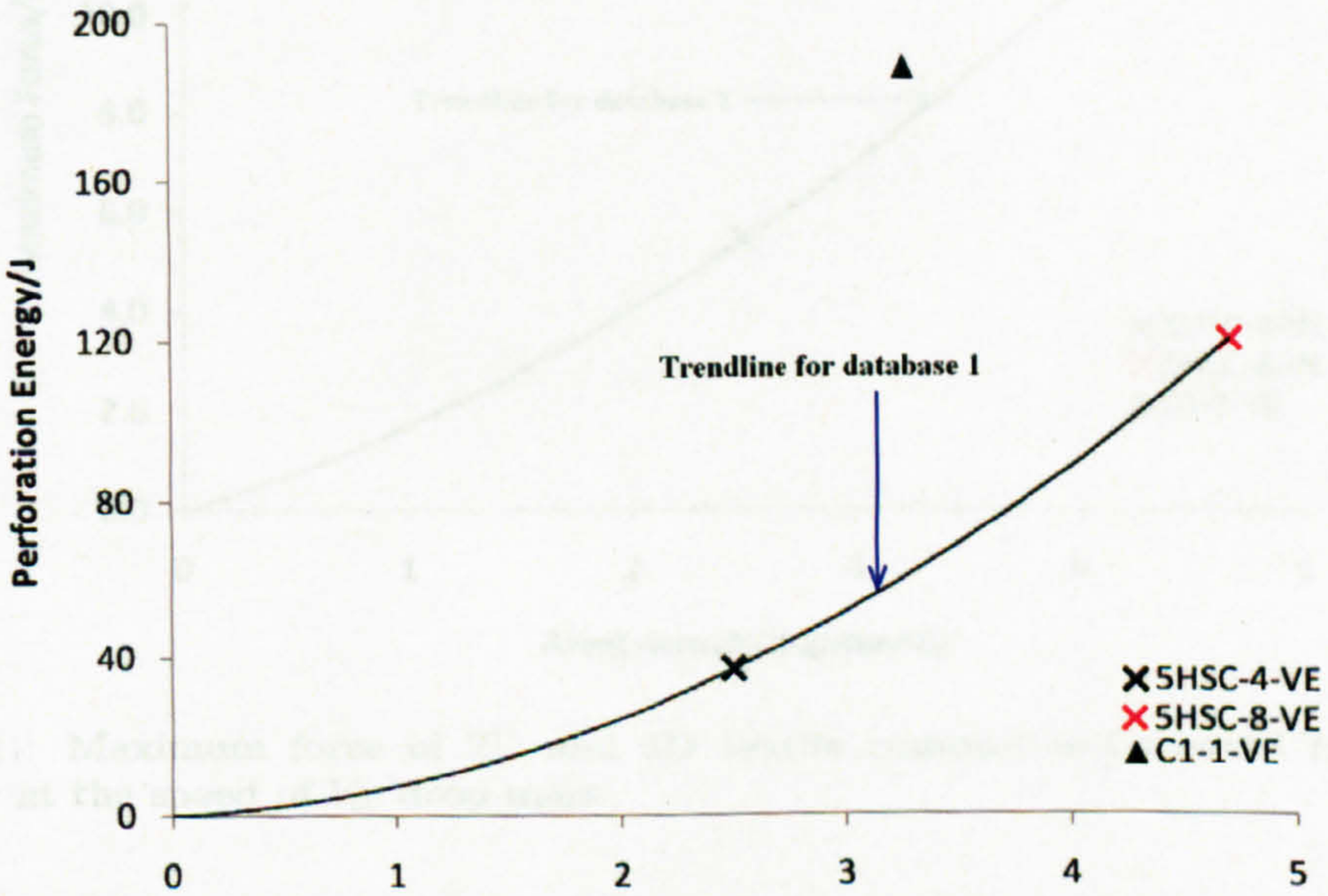

Figure 9.10: **Perforation energy of 2D and 3D textile composites subjected to 15.7kg impactor .**

In order to accessing the energy absorbing capability of C1-1-VE, the perforation energy of 5HSC-4-VE, 5HSC-8-VE and C1-1-VE were plotted against their areal densities as shown in figure 9.10. It was assumed that when the areal density of the composite is zero its perforation energy is also zero. Data point (0, 0) was used when fitted polynomial trendline to results of textile composites in database 1. It can be seen that, the perforation energy of C1-1-VE was well above the trendline for database 1. Figure 9.11 shows the maximum force of 2D and 3D textile composites impacted by 15.7kg impactor at the speed of V_{50} drop mass. It shows that the maximum force of C1-1-VE is above the trendline for database 2. Figure 9.12 shows force versus deformation curves for 5HSC-4-VE, 8HSC-4-VE and C1-1-VE. It can be seen that the force versus deformation curves of 5HSC-4-VE and 8HSC-4-VE have similar shapes. They consist of an initial steep rise portion followed by a transition to a curve of lower slope before a maximum is reached. Then a sudden drop of force occurs. The scale of this drop increases as aerial density increases.

The force versus deformation curve of C1-1-VE is different to that of 5HSC-4-VE and 5HSC-8-VE. There is no initial drop of force and there is a plateau between the maximum force point and the sudden drop of force. The initial drop of force at characteristic load points P_i in the force versus deformation curves of 5HSC-4-VE and 5HSC-8-VE was caused by delamination or debond at the initial stage of impact [51]. In C1-1-VE, there is no such initial drop of force. But there

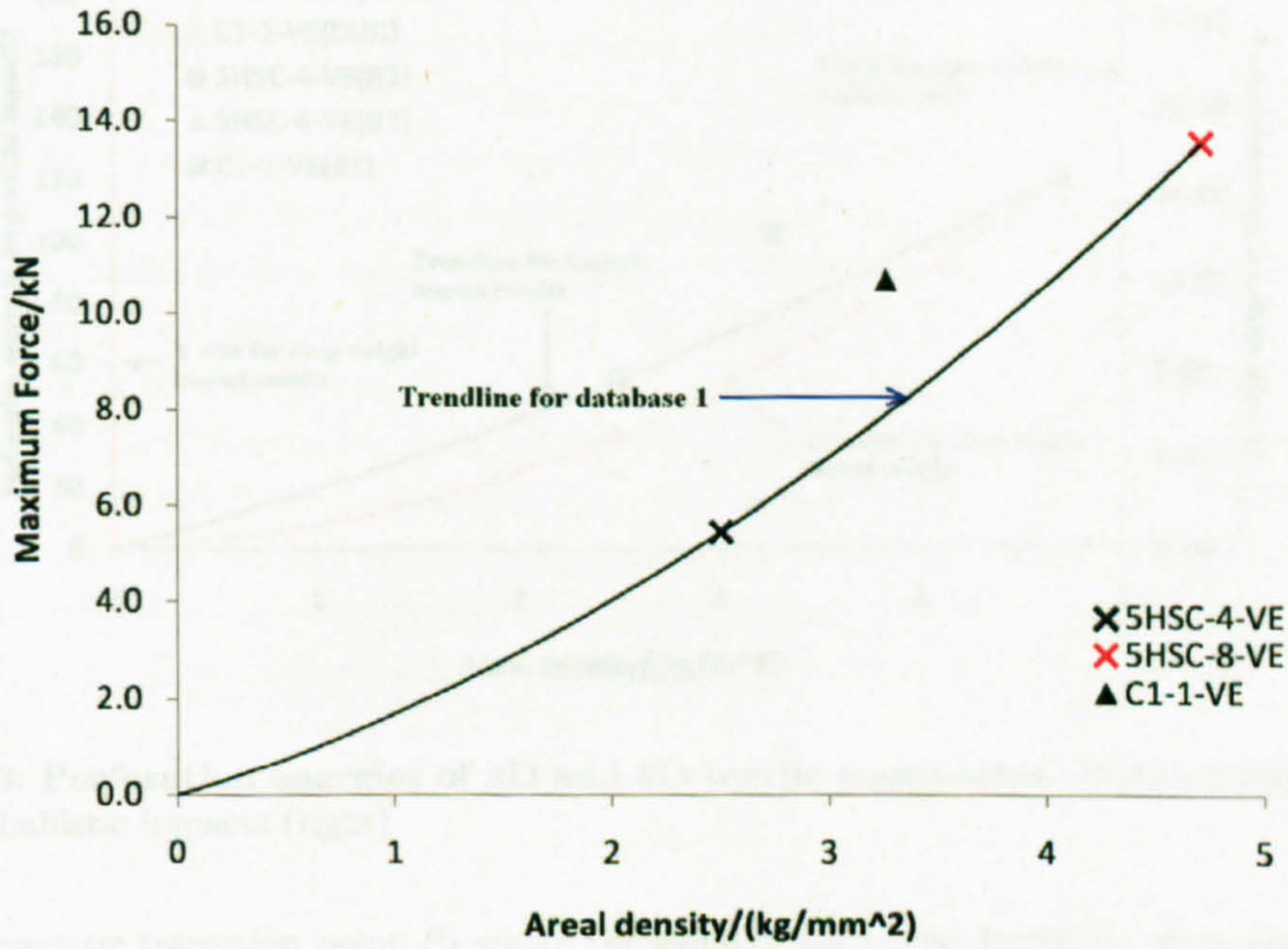

Figure 9.11: **Maximum force of 2D and 3D textile composites impacted by 15.7kg impactor at the speed of V_{50} drop mass .**

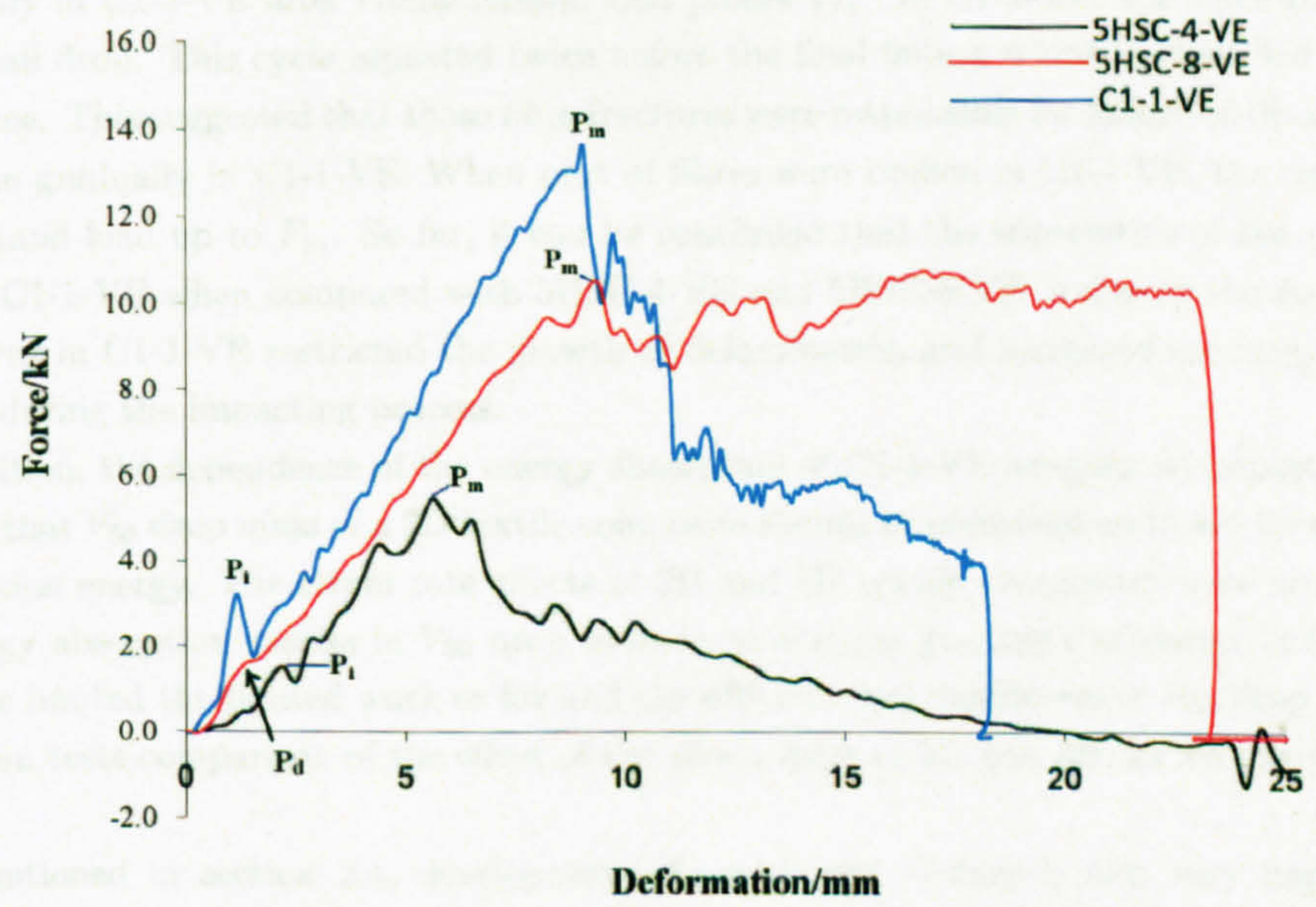

Figure 9.12: **Force versus deformation curves of 2D and 3D textile composites impacted by 15.7kg impactor at the speed of V_{50} drop mass .**

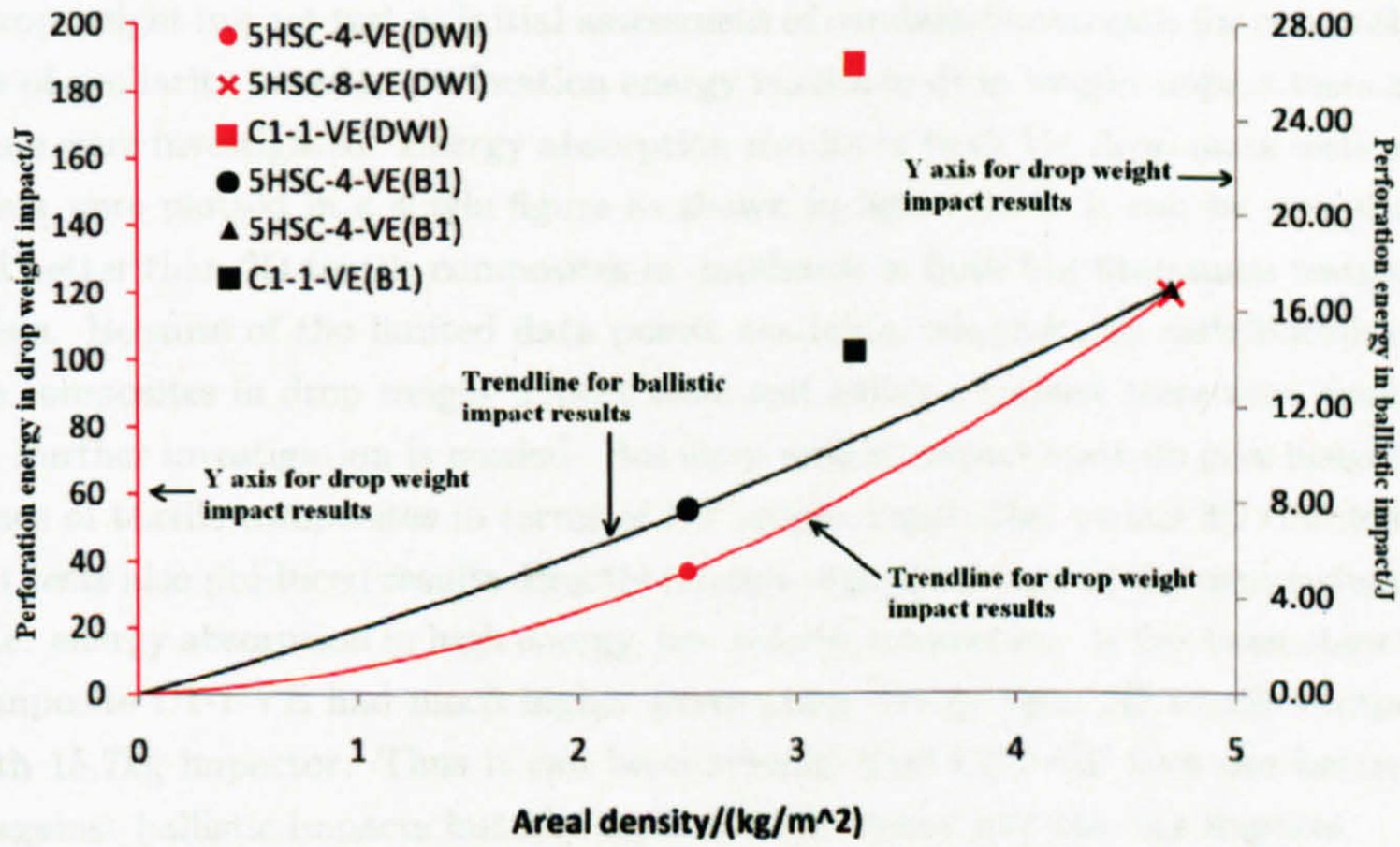

Figure 9.13: **Perforation energies of 2D and 3D textile composites** - in drop weight impacts (left) and ballistic impacts (right)

is a characteristic transition point P_d where the slope of the curve decreases. It proves that the use of binder yarns in through thickness direction successfully prevented the initial drop of force due to delamination. The characteristic load points P_m in 5HSC-4-VE, 5HSC-8-VE and C1-1-VE represent the load that delamination can stand before major damage [51]. C1-1-VE has higher P_m than materials in database 1. This is one reason why the perforation energy of C1-1-VE is higher than materials in database 1. Unlike in 5HSC-4-VE and 5HSC-8-VE, the force didn't drop dramatically in C1-1-VE after characteristic load points P_m. In C1-1-VE, the force raised again after a small drop. This cycle repeated twice before the final failure which is identified as sudden drop of force. This suggested that those fibre fractures were responsible for failure of the composites taken place gradually in C1-1-VE. When part of fibres were broken in C1-1-VE, the rest of fibres can still stand load up to P_m. So far, it can be concluded that the superiority of the perforation energy of C1-1-VE when compared with 5HSC-4-VE and 5HSC-8-VE is due to the fact that the binder yarns in C1-1-VE restricted the growth of delamination and increased the integrity of the materials during the impacting process.

In addition, the dependence of the energy absorption of C1-1-VE samples on impacting energy suggested that V_{50} drop mass of a 3D textile composite should be identified and used for calculation of perforation energy. The strain rate effects of 2D and 3D textile composites were studied using their energy absorption results in V_{50} drop mass tests and gas gun tests as shown in figure 9.13. Due to the limited the limited work so far and the different test conditions in V_{50} drop mass tests and gas gun tests comparison of the effect of the strain rates of 2D and 3D textile composites was difficult.

As mentioned in section 2.1, development of assessment system is also very important for development of new composite armour. Ballistic gas gun tests involve high speed movement of projectile and release of highly compressed gas. Great efforts are needed for both safety issues and accuracy issues. In contrast, drop weight impact tests are well developed. They can be easily carried out precisely with commercial available instrument. Thus in order to assess the feasibility

of using drop weight impact test as initial assessment of candidate materials for composite armours, the degree of similarity between perforation energy results in drop weight impact tests and ballistic impact tests were investigated. Energy absorption results in both V_{50} drop mass tests and ballistic impact tests were plotted in a single figure as shown in figure 9.13. It can be seen that C1-1-VE performed better than 2D textile composites in databases in both V_{50} drop mass tests and ballistic impact tests. Because of the limited data points available, whether the distribution of results of 2D textile composites in drop weight impact tests and ballistic impact tests were similar or not is not clear. Further investigation is needed. But drop weight impact tests do give insight of ballistic performance of textile composites in terms of 2D textile composites versus 3D textile composites.

Impact tests also produced results directly related to performance of the composite materials as armour, i.e. energy absorption in high energy, low velocity conditions. It has been observed that 3D textile composite C1-1-VE had much higher perforation energy than 2D textile composites when tested with 15.7kg impactor. Thus it can be concluded that C1-1-VE provides better protection not only against ballistic impacts but also against high energy low velocity impacts.

Chapter 10

Discussions and Conclusions

10.1 Overview of experiments

A series of test methods have been used to form an assessment system for material selection for composite armours. Because there is very limited data related to the ballistic performance of textile composites published, brand new ballistic performance databases were built using 2D woven textile composites. The materials used in of these databases are listed below:

- single hit V_{50} database
  - Database 1 materials: 5HSC-4-VE, 5HSC-6-VE, 5HSC-8-VE, 5HSC-12-VE
  - Database 2 materials: PWEG1-4-VE, PWEG1-6-VE, PWEG1-8-VE, PWEG1-12-VE, PWEG1-14-VE
  - Database 3 materials: PWC1-6-VE, PWC1-6-EP
  - Database 4 materials: PWEG2-6-EP
- damage area database
  - Database 1 materials: 5HSC-4-VE, 5HSC-6-VE, 5HSC-8-VE, 5HSC-12-VE
  - Database 2 materials: PWEG1-4-VE, PWEG1-6-VE, PWEG1-8-VE, PWEG1-12-VE, PWEG1-14-VE
  - Database 3 materials: PWC1-6-VE
  - Database 4 materials: PWEG2-6-EP
- V_{50} drop mass database
  - Database 1 materials: 5HSC-4-VE, 5HSC-8-VE

In addition to the three databases listed above, damage mechanisms in database 1 and 2 materials including 5HSC-4-VE, 5HSC-8-VE, 5HSC-12-VE and PWEG1-12-VE were characterized. No database materials were used in manufacturability study. This is due to the fact that manufacturing of 2D woven textile composites using vacuum assistant resin infusion method has been widely studied. Most importantly, the main part of manufacturability study is simulation of the architecture of the preform after manufacturing using optical microscope. The small change of the layered structure of the preform in 2D woven textile composites can be ignored.

Three groups of new materials have been assessed, i.e. 3D woven textile composites, non-crimp textile composites and composites with comingled yarns. Details of the assessments of these materials are listed below:

- manufacturability study
  - 3D woven: C1-1-VE, G1-1-VE, G2-1-VE, G3-1-VE, G4-1-VE, G5-1-VE, G6-1-VE, G7-1-VE TWEGPP-4-VE
- single hit V_{50} database
  - 3D woven: C1-1-VE, G1-1-VE, G2-1-VE, G3-1-VE, G4-1-VE, G5-1-VE, G6-1-VE, G7-1-VE
  - non-crimp: NCC-S-VE, NCC-S-VE, NCEGE1-S-VE, NCEG1-2S-VE, NCEG1-4-VE, NCEG2-4-VE
  - co-mingled: PWCPET1-2-VE, PWCPET1-4-VE, PWCPET2-2-VE, PWEGPP-4-VE, TWEGPP-2-VE, TWEGPP-4-VE
- damage area database
  - 3D woven: C1-1-VE, G1-1-VE, G2-1-VE, G3-1-VE, G4-1-VE, G5-1-VE, G6-1-VE, G7-1-VE
  - non-crimp: NCC-S-VE, NCC-S-VE, NCEGE1-S-VE, NCEG1-2S-VE, NCEG1-4-VE, NCEG2-4-VE
  - co-mingled: PWEGPP-4-VE, TWEGPP-2-VE, TWEGPP-4-VE
- damage mechanisms study
  - 3D woven: C1-1-VE, G1-1-VE, G2-1-VE, G3-1-VE, G4-1-VE, G7-1-VE
- V_{50} drop mass
  - 3D woven: C1-1-VE

As can be seen, the further the assessment method progressed along the flow chart in figure 3.1 the less materials were assessed. This is due to the fact that new materials that didn't perform as well as materials in databases were omitted for the purpose of saving time and materials.

10.2 Results and discussions

10.2.1 Databases

The main aim of the tests of materials in database 1, 2, 3 and 4 is to form the basis for quantitative assessments of new materials. They also gave insight into issues such as damage mechanisms, effect of projectiles, and effect of resin materials etc. For example, it has been observed that perforation energy of a textile composite in databases is dependent on the type of projectiles used in ballistic impact tests, and the effect of the projectile weight in drop weight impact tests of materials in databases can be ignored. The effect of the type of the projectile on the damage

area in ballistic impact is not clear. This is due to the big variation in damage area results, and no significant difference has been observed between damage areas of a composite in databases impacted by different projectiles. Damage mechanism studies revealed that the damage area of a textile composite in databases was dependent on the size of its biggest delamination, while V_{50} of a textile composite was decided by the energy absorbed in the forms of fibre fracture, delamination, matrix cracking etc. A parameter UI was found to be able to incorporate the effect of the type of projectiles.

The effect of the resin on the ballistic performance of textile composites in the databases has been studied. It was observed that the use of high toughness and high bonding strength resin such as epoxy did not increase the V_{50}, but reduced the 2D damage areas of the E-glass textile composites in the databases. For carbon fibre textile composites in the databases, lower V_{50} was observed for composites with epoxy resin than composites with vinyl ester resin. In damage area studies of carbon fibre textile composites with epoxy resin, ultrasonic c-scan image showed that the diameters of the damage areas of PWC-6-EP samples were only around 4 times of the size of the projectiles. In contrast, the diameters of the damage areas of PWC-6-VE samples were around 10 times of the size of the projectiles. Furthermore, visual inspection showed failure mechanism of petaling in the rear side of the composite panels. The above observations suggest that combination of high bonding strength of epoxy resin and low failure strain of carbon fibre is not good for ballistic impact applications.

The effect of fibre material on ballistic performance of textile composites in databases has been studied. It has been observed that plain woven carbon and glass fibre textile composites have similar V_{50} when compared based on the areal densities of the preforms other than the areal densities of the whole textile composites. Although more tests are still needed, this proves that the parameter developed by Cunniff [26] as defined in equation 2.11 may be used to assess fibre materials for composite armours if only the areal densities of the preforms were used as bases for assessments. The study of the effect of fibre material on damage area of textile composites in databases has not been done. Because it has been observed that damage area results of a textile composite in databases generated using ultrasonic c-scan machine were different from that generated using visual examination. The later was bigger than the former. Ultrasonic c-scan machine failed detecting matrix cracking in the edge of the damage areas.

The effect of thickness (or areal density) on ballistic performance of textile composites in databases has been studied. A linear relationship was observed between perforation energies E_{50} and areal density for database 2 materials, i.e. plain woven E-glass textile composites as shown in figure 6.9. The relationship between E_{50} and areal densities was not linear in database 1 materials, i.e. 5 harness satin weaves as shown in figure 6.8. Damage area studies revealed that for both database 1 and 2 materials, the damage area increased as the areal density increased. Damage mechanism studies revealed that the size of the delamination increased through the thickness in 5HSC-4-VE. But in 5HSC-8-VE, the size of delamination increased through the thickness until the last two layers. In 5HSC-12-VE and PWEG1-12-VE, the size of the delamination decreased firstly and then increased through the thickness until the last two layers. Other damage mechanisms commonly observed in 5HSC-4-VE, 5HSC-8-VE and 5HSC-12-VE include fibre fractures in region surrounding the path of the projectile, shear plug formed by clear-cut of fibre bundles along the path of the projectile and serious fibre distortion in non-penetrated V_{50} samples. Inside the shear plug, fibre fractures were due to transverse shear stress. After the shear plug, the failure fracture

due to mixture of shear and tensile stress were observed.

The effect of weaving structure on ballistic performance of textile composites in databases has also been studied. It has been observed that V_{50} of 2D plain woven textile composite PWC-6-VE were the same as that of satin woven textile composite 5HSC-6-VE. This proves that the small change of crimping angles of yarns in PWC-6-VE and 5HSC-6-VE didn't affect the energy absorbing capability of the composite, because it didn't affect the two main energy absorbing mechanisms, i.e. fibre fracture and delamination.

The single-hit V_{50}, damage areas, and V_{50} drop mass results of the 2D woven textile composites in databases laid the foundation of this study. The use of these results should not be restricted to this study, especially, some findings discussed above were not used in assessments of new materials in this study. They may be used together with further investigations to form a comprehensive understanding of ballistic performance of textile composites.

10.2.2 Assessments of 3D woven fabrics

The first group of new materials assessed was 3D woven fabrics. This group had 8 kinds of 3D woven monoliths with 7 kinds of weaving structures. These 3D woven fabrics differed from each other in terms of fibre materials, number of the layers of weft yarns, and most importantly the arrangments of multi-layer locking warp yarns as discussed in section 4.1.2. Before gas gun tests of these 3D textile composites, computer simulation method described in section 4.3.7 was used to examine the similarity between the ideal yarn arrangement and the real yarn arrangement in these 3D woven textile composites. Although the manufacturability of these textile composites are not as important as other properties such as ballistic impact properties, but knowing the real yarn arrangements in these 3D textile composites was as important as measuring single-hit V_{50} or damage areas of these 3D textile composites. Because without knowing the degree of distortion of the ideal architectures in these 3D textile composites, wrong judgements of the relationships between the experimental results and the yarn arrangements in 3D textile composites may be made.

In terms of manufacturability, 3D woven textile composites did not perform as well as 2D textile composites in databases. This was because of the serious distortion of yarn arrangements in some 3D textile composites such as G5-1-VE. In 3D textile composites including C1-1-VE and G7-1-VE, the distortion of yarn arrangement was small. Wet-out of fibres in 3D woven textile composites was as good as in the textile composites in databases. After comparing the distortions of ideal yarn arrangements in different 3D textile composites, it was concluded that in order to have good closeness between ideal yarn arrangement and real yarn arrangement a 3D woven textile composite should use yarn coating method as illustrated in figure 4.1, use more straight and plain woven style warp yarns, use even rows of weft yarns, mix of different kinds of multi-layer locking yarns, and avoid using 3 or more layer locking yarns.

Ideally computer simulation of 3D textile composites under ballistic impacts should be done in order to get the full picture of what happen during ballistic impacts of 3D textile composites. But due to the huge amount of images needed to generate simulations of the 3D textile composites and the limited time available, computer simulations of 3D textile composites after ballistic impacts were not pefomred in this study. Instead, one cross-section image for each 3D textile composite and visual inspections were used to characterize damage mechanisms in these 3D textile composites.

Although it was not clear whether all damages in 3D textile composites after ballistic impacts have been identified or not, the findings in damage mechansim studies of 3D textile composites in study were important. Because it minimized the chance of wrong judgements of the relationship between experimental results and architectures of 3D textile composites. Together with computer simulations of 3D textile composites, damage mechanism studies formed the basis for understanding and explaining experimental results as illustrated in the discussions below.

It has been observed that 3D woven textile composite C1-1-VE performed better than textile composites in databases in ballistic impact tests, and performed as well as textile composites in databases in damage resistance assessments. It has also been observed that 3D woven textile composites G1-1-VE, G2-1-VE, G3-1-VE, G4-1-VE and G7-1-VE performed as well as textile composites in databases in ballistic impact tests, and performed much better than textile composites in databases in damage resistance assessments. However 3D woven textile composites G5-1-VE and G6-1-VE performed not as well as textile composites in databases in ballistic impact tests.

The results of 3D woven textile composites C1-1-VE proved that the introduction of the through-thickness binder yarns may have resulted in increase of the capability of energy absorption of textile composites in ballistic impacts. Damage mechanism studies revealed that tensile fibre fractures occurred in the rear side of panels of C1-1-VE, and binder yarns bridged delaminations. Although C1-1-VE had similar size of damage area to 2D woven textile composites in databases, it had much smaller damage area than non-crimp textile composites. Both C1-1-VE and non-crimp textile composites have non-crimped yarns in both warp and weft yarn directions. As we know, textile composites with non-crimped fibres could have higher compression after impact strength than textile composites with crimped fibre such as plain woven textile composite. High compression after impact strength is also an important character a good candidate material for composite armour should have. Thus C1-1-VE is very suitable for composite armour applications.

3D woven fabric G7 has the same yarn arrangement as C1. Weft and warp yarns in G7-1-VE were wrapped with nylon fibres. This prevented weft yarns or warp yarns from merging with each other when binder yarns were not present. Thus the thickness of G7-1-VE was much bigger than C1. This resulted in inferiority of G7-1-VE compared to textile composites in databases in terms of fibre volume fraction and number of laminates. Because textile composites in databases with similar areal density to G7-1-VE had as many as 17 layers of 2D fabrics, while G7-1-VE has only 4 layers of non-crimped warp yarns and 5 layers non-crimped weft yarns. The majority of yarns in G7-1-VE were non-crimp yarns. Damage mechanism study of G7-1-VE revealed that only 3 or 4 layer of delaminations were observed in G7-1-VE after ballistic impacts. Fractures of binder yarns in G7-1-VE was uncommon. They only occurred when binder yarns were in or very close to the paths of the flying projectiles. This is not good for the multi-hit impact properties of G7-1-VE. Because the main aim of the use 3D woven fabrics in armour applications is to promote failure mechanisms with high energy absorbing capability such as tensile failure of fibres and fibre pull-out so as to reduce the size of the delamination areas. So far it can be concluded that although the use of nylon coating yarns was good for manufacturability, it was not good for the multi-hit ballisitc performance of 3D textile composites. In addition, yarns with medium strength should have been used as binder yarns in 3D textile composties.

Damage mechanisms studies revealed that there were no fundamental difference between failures of 3D textile composites C1-1-VE, G7-1-VE and 2D woven textile composites in databases. Damages mechanisms commonly observed in 2D woven textile composites after ballistic impacts

such as delamination, shear plug and shear cut of fibre bundles were also observed in C1-1-VE and G7-1-VE. Fibre debonding and pull-out were only observed in the rear side of composite panels, and in some binder yarns. Energy absorptions in C1-1-VE and G7-1-VE were still not very efficient. This was not the case for other six 3D woven textile composites where multi-layer locking yarns provided the majority of the weft yarns. Computer simulations of these six 3D textile composites revealed the degree of crimping of the warp yarns in these six 3D textile composites as high as 32°. Damage mechanisms studies reviewed that the damage morphologies in these six 3D woven textile composites were very different from that of 2D woven textile composites in databases, C1-1-VE and G7-1-VE. The most significant difference was the reduction of large delamination areas commonly observed in 2D textile composites. Matrix crackings were observed along the multi-layer locking yarns, but unlike in 2D textile composites they were not connected to each other forming delaminations. Unlike 2D textile composites, C1-1-VE and G71-1-VE, shear cut of fibre bundles which formed shear plugs was rarely observed. Mixture of shear and tensile fractures of fibres dominated damage characteristics in these six 3D textile composites. Extensive fibre debonding and pull-out were observed. In G3-1-VE, compressive fibre failures were observed. It seems that the energy absorptions in these six textile composites were very efficient. But the perforation energies of G1-1-VE, G2-1-VE, G3-1-VE and G4-1-VE were not higher than those of the textile composites. Computer simulations of these textile composites exposed big resin-rich areas in these 3D textile composites. It has been observed that the fibre volume fractions in these six 3D textile composites were much lower than in composites in databases. Thus methods which can increase the fibre volume fractions of a textile composite such as using small tow size, with more non-crimp yarns etc should be used in further investigations of the ballistic impact performances of 3D textile composites with architectures similar to these size textile composites. So far, it can be concluded that reduced large delaminations and high percentage of tensile fibre fractions were responsible for the good damage resistance of 3D textile composites G1-1-VE, G2-1-VE, G3-1-VE, G4-1-VE.

Damage mechanisms studies also revealed that 3D textile composites G1-1-VE etc also differred from each other in terms of damage mechanisms and ballistic impact properties. It has been observed that G1-1-VE performed better than G2-1-VE in ballistic impact tests. This is due to the fact that all the plain woven style warp yarns in G1-1-VE only interlaced with the out most layer of weft yarns. It resulted in higher fibre volume fraction in the region near the surface of the textile composites. This could have reduced the occurrence of transverse matrix crackings in the region near the surface of the textile composites caused by shear stress waves under high speed impacts, and eliminated the occurrence of large delaminations due to the presence of plain woven style yarns in the middle of the textile composites. In addition, shear plug formed by shear cuts of fibre bundles was not observed in the cross-section image of G1-1-VE, but was observed in the cross-section image of G2-1-VE. G5-1-VE didn't perform as well as G3-1-VE and G4-1-VE in ballistic impact tests. It has been observed that this was largely due to its fibre volume fraction being lower than that of G3-1-VE and G4-1-VE. This suggested that mixture of warp yarns with different multi-layer locking structures only in weft yarn direction may have resulted in low fibre volume fractions. Computer simulation of G5-1-VE revealed that distortion of the arrangement of weft yarns was the most serious among all 3D wove textile composites used in this study. This resulted in the looser distribution of warp yarns in G5-1-VE than in G1-1-VE etc. Loose distribution of yarns were also observed in weft yarns of G6-1-VE. It has been observed that G6-1-VE also did not performed as well as G1-1-VE etc. Computer simulation studies revealed

that the distortion of ideal architecture in G6-1-VE was the most serious among all 3D woven textile composites. Based on the discussions above, it can be concluded that when using 3D woven textile composites in ballistic applications, plain woven style yarns should be placed in the region near the surface of the textile composites, and mixture of multi-layer locking yarns in only weft yarn direction and non-even arrangement of weft yarns should be avoided.

10.2.3 Assessments of other materials

Non-crimped textile composites and textile composites with comingled yarns are the other two kinds of candidate materials assessed in this study. It has been observed that all non-crimp textile composites didn't preformed as well as composites in databases. This is due to the generator strip phenomenon and the fact that stress waves travelled faster in non-crimped yarn than in crimped yarn along the axial direction which resulted in much bigger damage areas in non-crimped textile composites than in composites in databases.

During assessments of textile composites with comingled yarns, it has been observed that textile composites with comingled carbon and PET fibres had much lower perforation energies than textile composites in databases. This is due to the low strength of the PET fibres. It has also be observed that textile composites with comingled E-glass/PP fibres performed worse than composites in databases. This is due to the lower damage resistance of composites with comingled E-glass/PP fibres.

10.2.4 Assessing system

Another major aim of this study is to develop an assessment system for composite armours. An assessing system including ballistic gas gun tests, damage area measurements, and computer simulation of yarn arrangement in textile composites has been developed. It involves assessments of single-hit V_{50}, damage resistance and manufacturability. Drop weight impact tests of both the baseline materials and new materials were also carried out in an attempt to assess the feasibility of using it for initial selection of candidate materials, because high speed impact tests were complex and not as mature as drop weight impact tests. In addition, high perforation energy in low velocity, high energy impacting conditions was also desirable for composite armours. It has been observed that C1-1-VE performed better than materials in databases in both ballistic impact tests and V_{50} drop mass tests. Further investigations are needed to assess the accuracy of using drop weight impact tests for initial selection of candidate materials. During the drop weight impact tests, it was also observed that the weight of the projectiles affected the energy absorption in penetration tests of C1-1-VE, while it had little effect on the energy absorption in penetration tests of 2D woven textile composites 5HSC-4-VE and 5HSC-8-VE. Thus the energy absorption of C1-1-VE is dependent on the impact energy in low velocity high energy impact. This suggested that the perforation energy of 3D woven textile composites in ballistic impact tests should be characterized using methods similar to the method used in this study. Perforation energies of textile composites measured by measuring the impacting velocity and the exit velocity of the projectile may not revealed the energy absorbing capability of 3D textile composites correctly.

10.3 Conclusions

Single-hit ballistic limited velocity (V_{50}) databse, two-dimentional damage area database and database of energy absorption in drop weigth impacts of 2D woven textile composites have been set-up based on the experimental results of 2D woven textile composites. The following conclusions have been made based on observations of these databases: the effect of the projectile weight in drop weight impact tests of materials in database 1 can be ignored; in most 2D woven textile composites, the damage areas were dependent on the size of their biggest delaminations, while their V_{50}s were decided by the energy absorbed in the forms of fibre fracture, delamination, matrix cracking etc; the use of high toughness and high bonding strength resin such as epoxy did not increase the V_{50}, but reduced the 2D damage areas of the E-glass textile composites; combination of high bonding strength of epoxy resin and low failure strain of carbon fibre resulted in poor ballistic peformance of carbon textile composites with epoxy resin; a linear relationship was observed between perforation energies and areal densities of plain woven E-glass textile composites; the variation of the size of the delaminations in the through-thickness direction of a 2D woven textile composite was dependent on the its thickness; fibre fractures, shear plug, serious fibre distortion was observed in 2D textile composites under ballistic impacts; small change of crimping angles of yarns in PWC-6-VE and 5HSC-6-VE didn't affect the energy absorbing capabilities of the composites;

After the assessments of the eight 3D woven textile composites, the following conclusions have been made: although the replacements of 2D woven textile with 3D woven textile didn't result in big increase of the ballistic impact performance of textile composites, it did lead to improvements in durability of textile composites when subjected to ballistic impacts; in some cases, 3D textile composites also had higher ballistic impact performance than 2D textile composites; 3D textile composites provided better protection in service against low velocity high energy threats; visualizations of the real yarn arrangements in 3D textile composites were essential in assessing the ballistic performances of 3D textile composites; information obtained by it such as resin-rich areas, packingess of yarns were must for robust explanation of the ballistic tests results; If using the theoretical yarn arrangements alone, some explanation of the experiment results may be wrong; the use of nylon coating yarns was good for manufacturability, but it was not good for the ballisitc performance of 3D textile composites; yarns with medium strength should have been used as binder yarns in 3D textile composties; reduced amount of large delaminations and high percentage of tensile fibre fractions were responsible for the good damage resistance of 3D textile composites G1-1-VE, G2-1-VE, G3-1-VE, G4-1-VE; when using 3D woven textile composites in ballistic applications, plain woven style yarns should be placed in the region near the surface of the textile composites, and mixture of multi-layer locking yarns in only weft yarn direction and non-even arrangement of weft yarns should be avoided.

After the assessments of the four non-crimped textile composites, the following conclusions have been made: the generator strip phenomenon and the fact that stress waves travelled faster in non-crimped yarn than in crimped yarn along the axial direction caused the poor damage resistance of non-crimped textile composites.

Chapter 11

Implications of This Work and Suggestions for Future Work

11.1 Implications of This Work

Research in the field of ballistics were highly complicated because of the requirements of monitoring events happened in micro-seconds. Considerable amount of efforts are need to ensure that the research activities in this field are safe, cost-effective and most importantly be able to produce meaningful results. Nowadays most research activities in the field of ballistics are carried out by organizations related to military departments in various countries. Because of the place of the applications for ballistic research, i.e. in battlefield, direct use of results of ballistic research will need the involvement of the highest level of the government of a country. Thus direct use of results of ballistic research without modification was very rare.

This work proved that research in the field of ballistic carried out in University laboratories with small budget can produce meaningful results. The following results can be used directly when design composite armours:

- Ballistic test results of various 2D and 3D textile composites
- Some 3D textile composites such as C1-1-VE have been proved to have better ballistic performance than 2D textile composites. They can be used as new materials for composite armour directly.
- Some characteristics of the yarn arrangements in 3D textile composites have been proved to be good for ballistic performance of 3D textile composites, such as more plain woven style yarns on the surfaces of 3D fabrics. Those characteristics of yarn arrangements can be used in developments of 3D fabrics for composite armours directly. 3D textile composites with all the good characteristics mentioned in this study are recommended.

There are some findings in this study that may not be used directly when design composite armours, but may provide insight into armour design as summarised below:

- The amount of fibre materials is the most important parameter governing the single-hit ballistic performance of textile composites.

- In 2D textile composites, the fabric architecture has limited effects on the single-hit ballistic performance. In 3D textile composites, the fabric architecture affects the single-hit ballistic performance.

- Carbon fibres should not be used together with resins with high bonding strength such as epoxy. The damage resistance of E-glass textile composites can be increased by using epoxy resin rather than vinyl ester resin.

11.2 Suggestions for Future Work

In chapter 4 it was noted that there are a large number of testing variables related to the gas gun tests. A natural progression of the work reported in this thesis would be to investigate the effect of some of these variables. For example investigation into the effect of obliquity and sample support would provide useful information, both for a better simulation of real ballistic impact. In addition, a further study of the effect of the variables of a projectile such as shape, weight, and materials is also required.

In section 2.13.2.3, visualization of the yarn architecture of 3D woven textile composite by X-ray computed tomography (CT) has been described. Visualization of the yarn architecture of 3D woven textile composite by computer simulation method used in this study was a time-consuming process. From the work reported in this thesis here there are strong indications that visualization of the yarn architecture of 3D woven textile composite before and after impact is necessary for fully understanding the ballistic impact events of 3D woven textile composites. A further progression of the work reported in this thesis would be visualization of the yarn architecture of 3D woven textile composite before and after ballistic impact by X-ray computed tomography (CT) which is far more efficient than the computer simulation method used in this study.

In addition, investigations into the improvements of assessment system for composite armours are also needed. Improvements may be achieved by characterizing other material properties that are in the performance matrices of composite armours but not studied in this work. For example, compression after ballistic impact test can be used to study the damage tolerance of 3D textile composite.

Apart from investigations into test methods, further investigations into improvements of the materials are needed. Improvements may be made by studying the ballistic performances of more 3D textile composites with structural characters identified in the work of this thesis to be suitable for armour applications. For example, work is required for investigations into the effect of putting more yarns in surface region of a 3D textile composite and the effect of the tow size of binder yarns in 3D textile composites. Improvements may also be made by broadening the selection of materials for 3D fabrics and matrix. For example, effort is needed in investigations into the effect of the materials for binder yarns in 3D textile composites.

Bibliography

[1] S Adanur and C A Tam. On-machine interlocking of 3d laminate structures for composites. *Composites Part B: Engineering*, 28(5-6):497 – 506, 1997.

[2] B Anctil. *Ballistics 2005: 22nd International Symposium on Ballistics*, chapter Performance evaluation of multi-threat body armour systems, pages 1071–1078. DEStech Publications, Inc, Vancouver, BC, Canada, November 14-18 2005.

[3] F J Arendts, K Drechler, and J Brandt. Advanced textile structural composites- status and outlook. In *Proceedings of International Conference on Advanced Composite Material*, pages 406 – 409, 1993.

[4] Zleyha Aslan, Ramazan Karakuzu, and Buket Okutan. The response of laminated composite plates under low-velocity impact loading. *Composite Structures*, 59(1):119 – 127, 2003.

[5] M. Bannister, I. Herszberg, A. Nicolaidis, F. Coman, and K. H. Leong. The manufacture of glass/epoxy composites with multilayer woven architectures. *Composites Part A: Applied Science and Manufacturing*, 29(3):293 – 300, 1998.

[6] J. N. Baucom and M. A. Zikry. Evolution of failure mechanisms in 2d and 3d woven composite systems under quasi-static perforation. *Journal of Composite Materials*, 37(18):1651–1674, 2003.

[7] J.N. Baucom and M.A. Zikry. Low-velocity impact damage progression in woven e-glass composite systems. *Composites Part A: Applied Science and Manufacturing*, 36(5):658 – 664, 2005.

[8] Giovanni Belingardi and Roberto Vadori. Low velocity impact tests of laminate glass-fiber-epoxy matrix composite material plates. *International Journal of Impact Engineering*, 27(2):213 – 229, 2002.

[9] K. Berketis, D. Tzetzis, and P.J. Hogg. The influence of long term water immersion ageing on impact damage behaviour and residual compression strength of glass fibre reinforced polymer (gfrp). *Materials & Design*, 29(7):1300 – 1310, 2008.

[10] G. A. Bibo and P. J. Hogg. Influence of reinforcement architecture on damage mechanisms and residual strength of glass-fibre/epoxy composite systems. *Composites Science and Technology*, 58(6):803 – 813, 1998.

[11] R A Blake. *Delaware Composites Design Encyclopedia: Test Methods*, volume Volume VI, chapter ULTRASONIC NONDESTRUCIVE EVALUATION TECHNIQUES FOR COMPOSITE MATERIALS, pages 57 – 109. CRC Press, University of Delaware, USA, 1989.

[12] D. J. Boll, W. D. Bascom, J. C. Weidner, and W. J. Murri. A microscopy study of impact damage of epoxy-matrix carbon-fibre composites. *Journal of Materials Science*, 21(8):2667–2677, August 1986.

[13] J. Brandt, K. Drechsler, and F. J. Arendts. Mechanical performance of composites based on various three-dimensional woven-fibre preforms. *Composites Science and Technology*, 56(3):381 – 386, 1996.

[14] D S Brookstein, J Skelton, J R Dent, R W Dent, and D J Rose. Solid braid structure. In *Unitied States Patent (535783)*. United States Patent and Trademark Office, Alexandria, Virginia, USA, 1994.

[15] Joon-Hyung Byun and Tsu-Wei Chou. Process-microstructure relationships of 2-step and 4-step braided composites. *Composites Science and Technology*, 56(3):235 – 251, 1996.

[16] JOON-HYUNG BYUN and TSU-WEI CHOU. Mechanics of textile composites. In Anthony Kelly and Carl Zweben, editors, *Comprehensive Composite Materials*, pages 719 – 761. Pergamon, Oxford, 2000.

[17] W J Cantwell. *Impact damage in carbon fibre composites.* PhD thesis, Imperical College, London, 1986.

[18] W. J. Cantwell and J. Morton. The influence of varying projectile mass on the impact response of cfrp. *Composite Structures*, 13(2):101 – 114, 1989.

[19] W.J. Cantwell. Geometrical effects in the low velocity impact response of gfrp. *Composites Science and Technology*, 67(9):1900 – 1908, 2007.

[20] W.J. Cantwell and J. Morton. The impact resistance of composite materials – a review. *Composites*, 22(5):347 – 362, 1991.

[21] Bryan A. Cheeseman and Travis A. Bogetti. Ballistic impact into fabric and compliant composite laminates. *Composite Structures*, 61(1-2):161 – 173, 2003. Impact on Composites 2002.

[22] Wing L. Cheng, Scott Langlie, and Shigeru Itoh. High velocity impact of thick composites. *International Journal of Impact Engineering*, 29(1-10):167 – 184, 2003. Hypervelocity Impact.

[23] Ernest S. C. Chin. Army focused research team on functionally graded armor composites. *Materials Science and Engineering A*, 259(2):155 – 161, 1999.

[24] Chitrangad. Aramid ballistic structure. In *United States Patent (6030683)*. United States Patent and Trademark Office, Alexandria, Virginia, USA, 2000.

[25] N Cristescu, L E Malvern, and R L Sierakowski. *Foreign Object Impact Damage To Composites*, chapter Failure Mechanisms in Composite Plates Impacted by Blunt-Ended Penetrators, pages 159 – 171. AMERICAN SOCIETY FOR TESTING AND MATERIALS, North Wales, Pa. January 1975, 1975.

[26] P M Cunniff. Dimensionless parameters for optimization of textilebased body armor systems. In *Proceedings of the 18th International Symposium on Ballistics*, San Antonio, Texas, 1999.

[27] G. J. Czarnecki. Estimation of the v50 using semi-empirical (1-point) procedures. *Composites Part B: Engineering*, 29(3):321 – 329, 1998.

[28] I M Daniel and T Liber. Wave propagation in fiber composite laminates, part 2. Technical Report IITRI-D6073-3-PT-2; NASA-CR-135086, NASA, Jun 1976.

[29] G. A. O. Davies, D. Hitchings, and G. Zhou. Impact damage and residual strengths of woven fabric glass/polyester laminates. *Composites Part A: Applied Science and Manufacturing*, 27(12):1147 – 1156, 1996.

[30] F. Desplentere, S.V. Lomov, D.L. Woerdeman, I. Verpoest, M. Wevers, and A. Bogdanovich. Micro-ct characterization of variability in 3d textile architecture. *Composites Science and Technology*, 65(13):1920 – 1930, 2005.

[31] DAVID W. DWIGHT. Glass fiber reinforcements. In Anthony Kelly and Carl Zweben, editors, *Comprehensive Composite Materials*, pages 231 – 261. Pergamon, Oxford, 2000.

[32] Roger L Ellis. Ballistic impact resistance of graphite epoxy composites with shape memory alloy and extended chain polyethylene spectra hybrid components. Master's thesis, Virginia Polytechnic Institute and State University, 1996.

[33] B K Fink, A M. Monib, and J W Gillespie. Damage tolerance of thick-section composites subjected to ballistic impact. Technical Report ARL-TR-2477, U.S.Army Research Laboratory (ARL), May 2001.

[34] B K Flink. Performance metrics for composite integral armor. Technical Report ARL-RP-8, U.S.Army Research Laboratory (ARL), Department of Chemistry, Oklahoma State Univ., Stillwater, OK, October 2000.

[35] Keisuke Fujii, Motokazu Aoki, Noriyuki Kiuchi, Eiichi Yasuda, and Yasuhiro Tanabe. Impact perforation behavior of cfrps using high-velocity steel sphere. *International Journal of Impact Engineering*, 27(5):497 – 508, 2002.

[36] Bazle A. Gama, Travis A. Bogetti, Bruce K. Fink, Chin-Jye Yu, T. Dennis Claar, Harald H. Eifert, and John W. Gillespie Jr. Aluminum foam integral armor: a new dimension in armor design. *Composite Structures*, 52(3-4):381 – 395, 2001.

[37] E P Gelert, S D Pattie, and R L Woodward. Energy transfer in ballistic perforation of fibre reinforced composites. *Journal of Materials Science*, 33(6):1845–1850, 1 April 1998.

[38] E. P. Gellert, S. J. Cimpoeru, and R. L. Woodward. A study of the effect of target thickness on the ballistic perforation of glass-fibre-reinforced plastic composites. *International Journal of Impact Engineering*, 24(5):445 – 456, 2000.

[39] J W Gillespie, A M Monib, and L A Carlsson. Damage tolerance of thick-section s-2 glass fabric composites subjected to ballistic impact loading. *Journal of Composite Materials*, 37(23):2131–2147, 2003.

[40] Werner Goldsmith, C K Dharan, and Hui Chang. Quasi-static and ballistic perforation of carbon fiber laminates. *International Journal of Solids and Structures*, 32(1):89 – 103, 1995.

[41] M. Grujicic, G. Arakere, T. He, W.C. Bell, B.A. Cheeseman, C.-F. Yen, and B. Scott. A ballistic material model for cross-plied unidirectional ultra-high molecular-weight polyethylene fiber-reinforced armor-grade composites. *Materials Science and Engineering: A*, 498(1-2):231 – 241, 2008. International Conference on Recent Advances in Composite Materials (ICRACM 2007).

[42] Valrie A Gunon, Tsu Wei Chou, and John W Gillespie. Toughness properties of a three-dimensional carbon-epoxy composite. *Journal of Materials Science,*, 24:4168 – 4175, 1989.

[43] Y. M. Gupta and J. L. Ding. Impact load spreading in layered materials and structures: concept and quantitative measure. *International Journal of Impact Engineering*, 27(3):277 – 291, 2002.

[44] R. I. Hammond, W. G. Proud, H. T. Goldrein, and J. E. Field. High-resolution optical study of the impact of carbon-fibre reinforced polymers with different lay-ups. *International Journal of Impact Engineering*, 30(1):69 – 86, 2004.

[45] A K Harry. Lightweight armor material. In *United States Patent (3722355)*. United States Patent and Trademark Office, Alexandria, Virginia, USA, March 1973.

[46] Paul J. Hogg. Toughening of thermosetting composites with thermoplastic fibres. *Materials Science and Engineering: A*, 412(1-2):97 – 103, 2005. International Conference on Recent Advances in Composite Materials.

[47] M. V. Hosur, U. K. Vaidya, C. Ulven, and S. Jeelani. Performance of stitched/unstitched woven carbon/epoxy composites under high velocity impact loading. *Composite Structures*, 64(3-4):455 – 466, 2004.

[48] M. J. Iremonger and A. C. Went. Ballistic impact of fibre composite armours by fragment-simulating projectiles. *Composites Part A: Applied Science and Manufacturing*, 27(7):575 – 581, 1996.

[49] B James and S Howlett. Enhancement of post impact structural integrity of gfrp composite by though-thickness reinforcement. presented in the 2nd European Fighting Vehicle Symposium, Shrivenham, UK, 1997.

[50] S.T. Jenq, S.B. Wang, and L.T. Sheu. A model for predicting the residual strength of gfrp laminates subject to ballistic impact. *Journal of Reinforced Plastics and Composites*, 11(10):1127–1141, 1992.

[51] Jang-Kyo Kim, Man-Lung Sham, Min-Seok Sohn, and Hiroyuki Hamada. Effect of hybrid layers with different silane coupling agents on impact response of glass fabric reinforced vinylester matrix composites. *Polymer*, 42(17):7455 – 7460, 2001.

[52] Wen-Shyong Kuo, Tse-Hao Ko, and Cheng-Po Chen. Effect of weaving processes on compressive behavior of 3d woven composites. *Composites Part A: Applied Science and Manufacturing*, 38(2):555 – 565, 2007.

[53] R C Laible. *Ballistic Materials and Penetration Mechanics.* Elsevier, North-Holland, 1980.

[54] Fritz Larsson and Lars Svensson. Carbon, polyethylene and pbo hybrid fibre composites for structural lightweight armour. *Composites Part A: Applied Science and Manufacturing*, 33(2):221 – 231, 2002.

[55] B. L. Lee, J. W. Song, and J. E. Ward. Failure of spectra polyethylene fiber-reinforced composites under ballistic impact loading. *Journal of Composite Materials*, 28(13):1202–1226, 1994.

[56] B. L. Lee, T. F. Walsh, S. T. Won, H. M. Patts, J. W. Song, and A. H. Mayer. Penetration failure mechanisms of armor-grade fiber composites under impact. *Journal of Composite Materials*, 35(18):1605–1633, 2001.

[57] SHAW MING LEE and PAUL ZAHUTA. Instrumented impact and static indentation of composites. *Journal of Composite Materials*, 25:204 – 222, 1991.

[58] K. H. Leong, B. Lee, I. Herszberg, and M. K. Bannister. The effect of binder path on the tensile properties and failure of multilayer woven cfrp composites. *Composites Science and Technology*, 60(1):149 – 156, 2000.

[59] J. M. Lifshitz, F. Gov, and M. Gandelsman. Instrumented low-velocity impact of cfrp beams. *International Journal of Impact Engineering*, 16(2):201 – 215, 1995.

[60] W E Lundblad, C Dixon, and H C Ohler. Ballistic resistant article comprising a three dimensional interlocking woven fabric. In *United States Patent (5456974)*. October 1995.

[61] R. McIlhagger, J.P. Quinn, A.T. McIlhagger, S. Wilson, D. Simpson, and W. Wenger. The influence of binder tow density on the mechanical properties of spatially reinforced composites. part 2 - mechanical properties. *Composites Part A: Applied Science and Manufacturing*, 39(2):334 – 341, 2008.

[62] F A Milton. Army after next proposal for ground combat vehicles. presented at Army Science Conference, Norfolk, VA, USA, June 1998.

[63] T. Mitrevski, I.H. Marshall, and R. Thomson. The influence of impactor shape on the damage to composite laminates. *Composite Structures*, 76(1-2):116 – 122, 2006. Fifteenth International Conference on Composite Materials - ICCM-15.

[64] T.G. Montgomery, P.L. Grady, and C. Tomasino. The effects of projectile geometry on the performance of ballistic fabrics. *Textile Research Journal*, 52(7):442–450, 1982.

[65] A. P. Mouritz, M. K. Bannister, P. J. Falzon, and K. H. Leong. Review of applications for advanced three-dimensional fibre textile composites. *Composites Part A: Applied Science and Manufacturing*, 30(12):1445 – 1461, 1999.

[66] Cox B. N. and Flanagan G. Handbook of analytical methods for textile composites. Technical report, 1997.

[67] L. M. Nunes, S. Paciornik, and J. R. M. d'Almeida. Evaluation of the damaged area of glass-fiber-reinforced epoxy-matrix composite materials submitted to ballistic impacts. *Composites Science and Technology*, 64(7-8):945 – 954, 2004.

[68] D.C. Prevorsek, H.B. Chin, and A. Bhatnagar. Damage tolerance: design for structural integrity and penetration. *Composite Structures*, 23(2):137 – 148, 1993.

[69] J.P. Quinn, A.T. McIlhagger, and R. McIlhagger. Examination of the failure of 3d woven composites. *Composites Part A: Applied Science and Manufacturing*, 39(2):273 – 283, 2008.

[70] A D Resnyansky. The impact response of composite materials involved in helicopter vulnerability assessment: Literature review - part 2. Technical Report DSTO-TR-1842 Part 2, Australian Covernment, Departments of Defence, Defense Science and Technology Organisation (DSTO), April 2006.

[71] S. Rudov-Clark and A.P. Mouritz. Tensile fatigue properties of a 3d orthogonal woven composite. *Composites Part A: Applied Science and Manufacturing*, 39(6):1018 – 1024, 2008.

[72] G M Savage. Fabric and fibre reinforced laminate armours. *Metals and Materials*, pages 285 – 290, 1989.

[73] G. A. Schoeppner and S. Abrate. Delamination threshold loads for low velocity impact on composite laminates. *Composites Part A: Applied Science and Manufacturing*, 31(9):903 – 915, 2000.

[74] B R Scott. The penetration of compliant laminates by compact projectiles. In *Proceedings of the 18th International Symposium on Ballistics*, pages 1184–1191, 1999.

[75] R G Shephard. The use of polymers in personal ballistic protection. presented in International Conference on Polymers in Defence, Dragonara Hotel, Bristol. UK, March 1987.

[76] A. SHINDO. Polyacrylonitrile (pan)-based carbon fibers. In Anthony Kelly and Carl Zweben, editors, *Comprehensive Composite Materials*, pages 1 – 33. Pergamon, Oxford, 2000.

[77] R L Sierakowski and N Takeda. *Composite Materials (Proceeding of Japan-U.S. Conference)*, chapter An investigation of in-plane failure mechanisms in impacted fiber reinforced plates, pages 12–21. 1981.

[78] Robert L Sierakowski and Shive K Chaturvedi, editors. *Dynamic Loading and Characterization of Fiber-Reinforced Composites*. John Wiley & Sons, 1997.

[79] Fredrik Stig and Stefan Hallstrm. Assessment of the mechanical properties of a new 3d woven fibre composite material. *Composites Science and Technology*, In Press, Corrected Proof:–, 2008.

[80] F R Sullivan. Reinforced plastic turret for m2/m3. Technical Report MTL TR 87-39, U.S.Army Materials Technology Laboratory, 1987.

[81] John Summerscales, editor. *Non-destructive testing of fibre-reinforced plastics composites*. Springer, New York, NY, USA, 1990.

[82] I Susuki and T takatoya. Impact damage properties of 3-d carbon/bismaleimide composites. In *Proceedings of the 5th Japan Int. SAMPE Symposium*, Tokyo, Japan, 1997.

[83] V. B. C. Tan, C. T. Lim, and C. H. Cheong. Perforation of high-strength fabric by projectiles of different geometry. *International Journal of Impact Engineering*, 28(2):207 – 222, 2003.

[84] Yasuhiro Tanabe, Motokazu Aoki, Keisuke Fujii, Hideaki Kasano, and Eiichi Yasuda. Fracture behavior of cfrps impacted by relatively high-velocity steel sphere. *International Journal of Impact Engineering*, 28(6):627 – 642, 2003.

[85] C. Ulven, U. K. Vaidya, and M. V. Hosur. Effect of projectile shape during ballistic perforation of vartm carbon/epoxy composite panels. *Composite Structures*, 61(1-2):143 – 150, 2003. Impact on Composites 2002.

[86] I. VERPOEST. Composite preforming techniques. In Anthony Kelly and Carl Zweben, editors, *Comprehensive Composite Materials*, pages 623 – 669. Pergamon, Oxford, 2000.

[87] S Voss, A Fahmy, and H West. Impact tolerance of laminated and 3-dimentionally reinforced graphite-epoxy panels. In *Proceedings of the International Conference on Advanced Composite Materials*, University of Wollongong, Australia, 1993. Warrendale, Pa. : TMS, c1993.

[88] Paul Wambua, Bart Vangrimde, Stepan Lomov, and Ignaas Verpoest. The response of natural fibre composites to ballistic impact by fragment simulating projectiles. *Composite Structures*, 77(2):232 – 240, 2007.

[89] B. Wang and S. M. Chou. The behaviour of laminated composite plates as armour. *Journal of Materials Processing Technology*, 68(3):279 – 287, 1997. Superplasticity and Superplastic Technology in Japan.

[90] X. Wang, B. Hu, Y. Feng, F. Liang, J. Mo, J. Xiong, and Y. Qiu. Low velocity impact properties of 3d woven basalt/aramid hybrid composites. *Composites Science and Technology*, 68(2):444 – 450, 2008.

[91] D E Weerth. Composite infantry fighting vehicle. Technical Report MTL TR 89-23, U.S.Army Materials Technology Laboratory, 1995.

[92] S. Yadav, D.R. Chichili, and K.T. Ramesh. The mechanical response of a 6061-t6 al/al2o3 metal matrix composite at high rates of deformation. *Acta Metallurgica et Materialia*, 43(12):4453 – 4464, 1995.

[93] Hung Man Yang. Aramid fibers. In Anthony Kelly and Carl Zweben, editors, *Comprehensive Composite Materials*, pages 199 – 229. Pergamon, Oxford, 2000.

[94] R H Zee, C J Wang, A Mount, B Z Jang, and C Y Hsieh. Ballistic response of polymer composites. *Polymer Composites*, 12(3):196–202, 1991.

[95] Ralph H. Zee and Chung Y. Hsieh. Energy absorption processes in fibrous composites. *Materials Science and Engineering A*, 246(1-2):161 – 168, 1998.

[96] G. Zhou. The use of experimentally-determined impact force as a damage measure in impact damage resistance and tolerance of composite structures. *Composite Structures*, 42(4):375 – 382, 1998. International Workshop on Experimental Techniques in the Analysis of Composite Structures.

Appendix A

Figures of gas gun shots and V_{50}

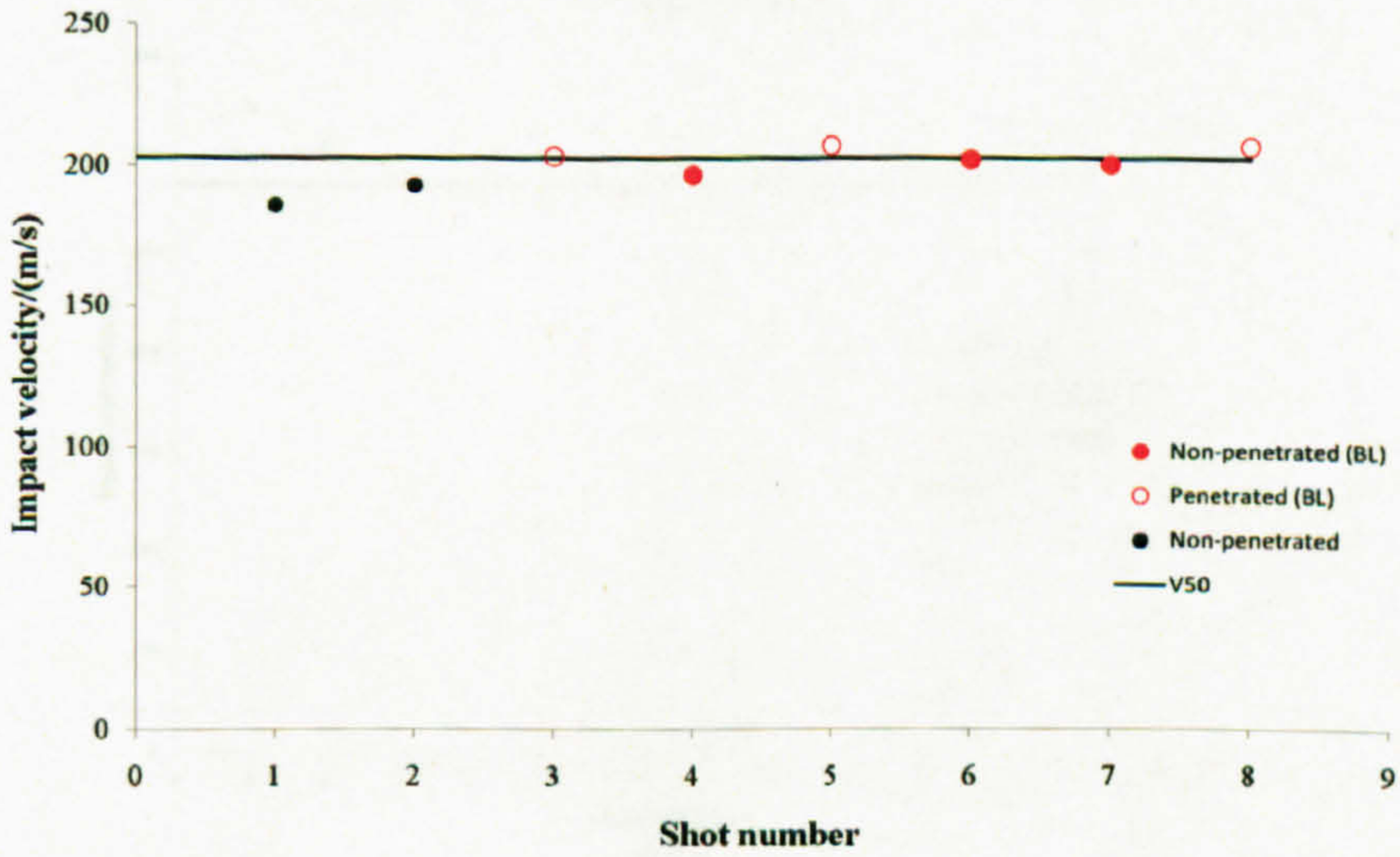

Figure A.1: **Gas gun test results of materials in database 1 using 0.87g steel balls - 5HSC-6-VE**

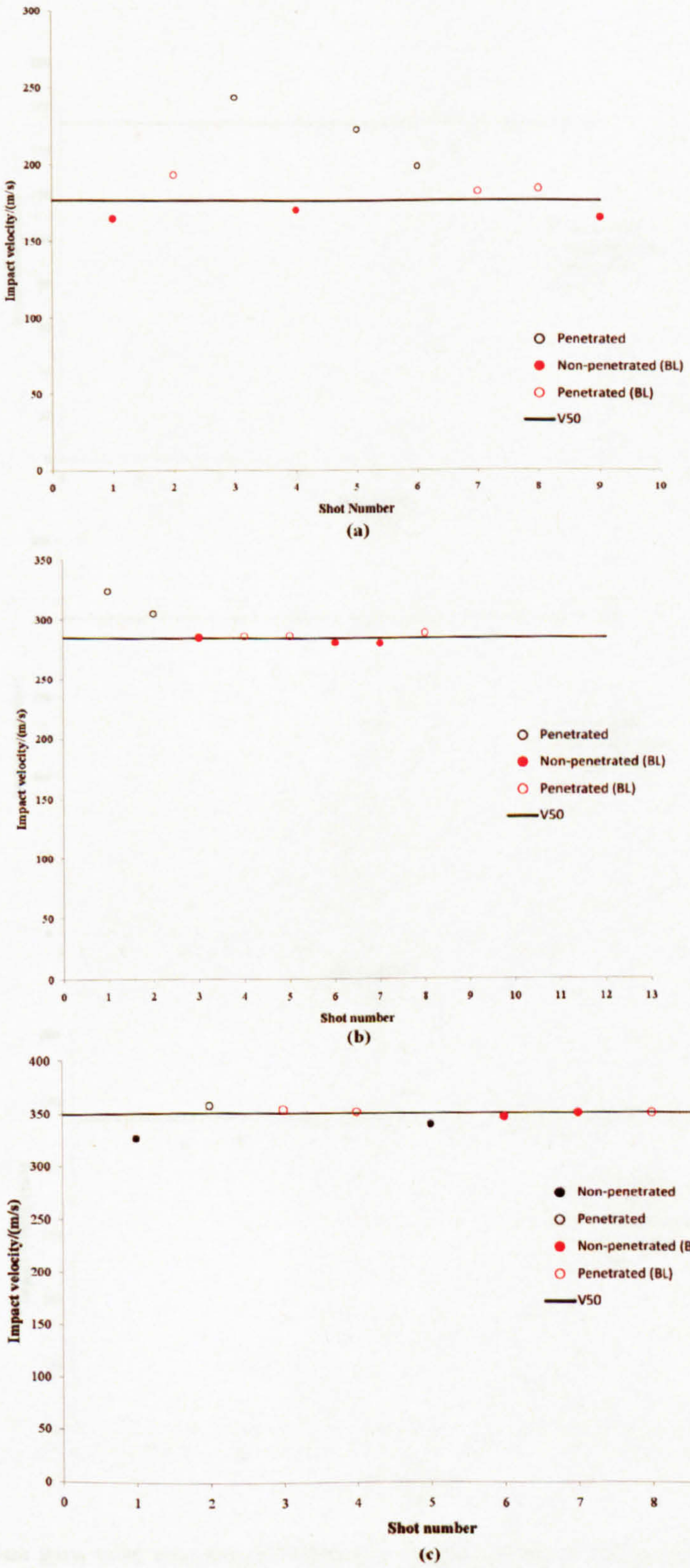

Figure A.2: **Gas gun test results of materials in database 2 using 0.44g steel balls** - (a) PWEG1-4-VE; (b) PWEG1-8-VE; (c) PWEG1-12-VE.

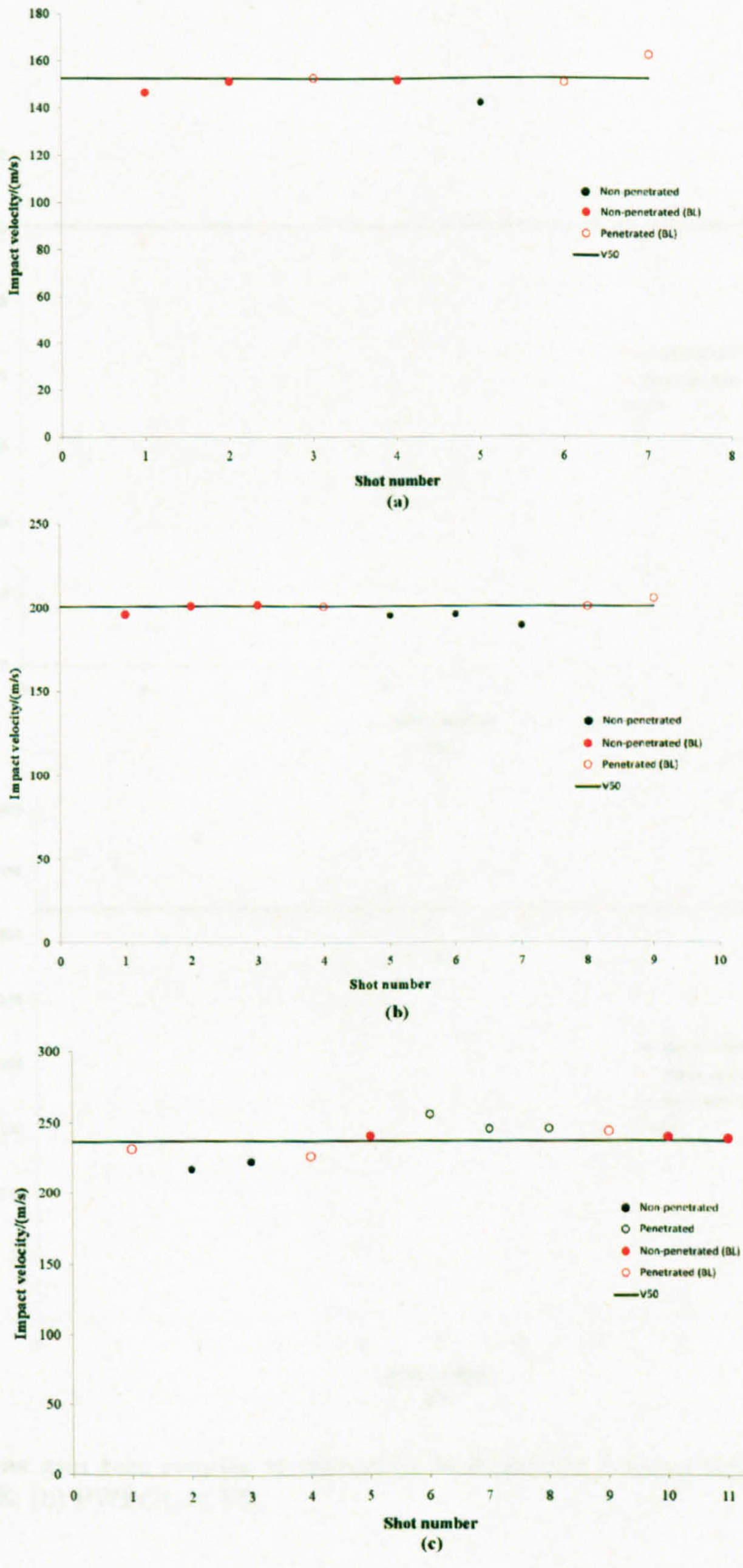

Figure A.3: **Gas gun test results of materials in database 2 using 0.87g steel balls** - (a) PWEG1-4-VE; (b) PWEG1-6-VE; (c) PWEG1-8-VE.

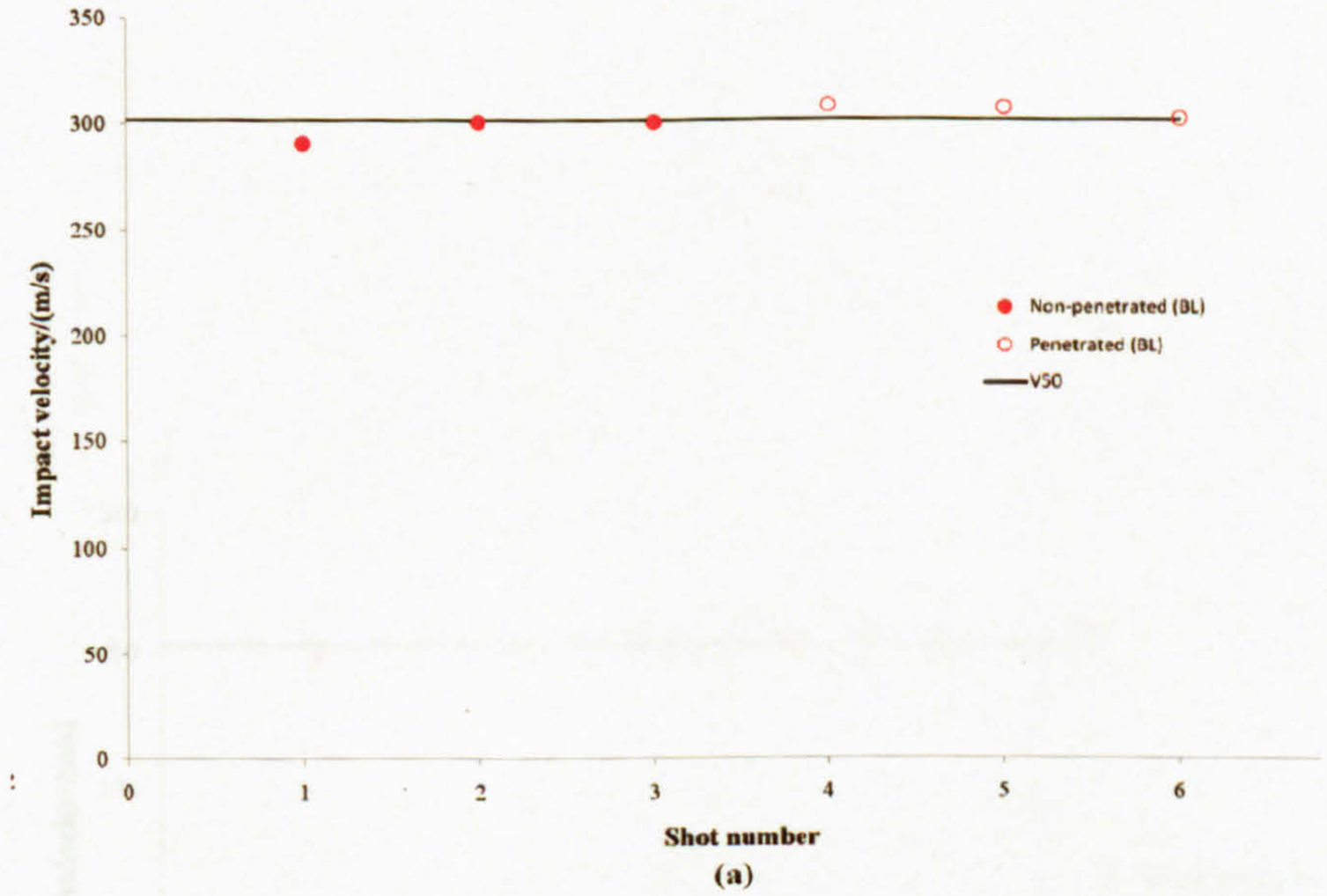

(a)

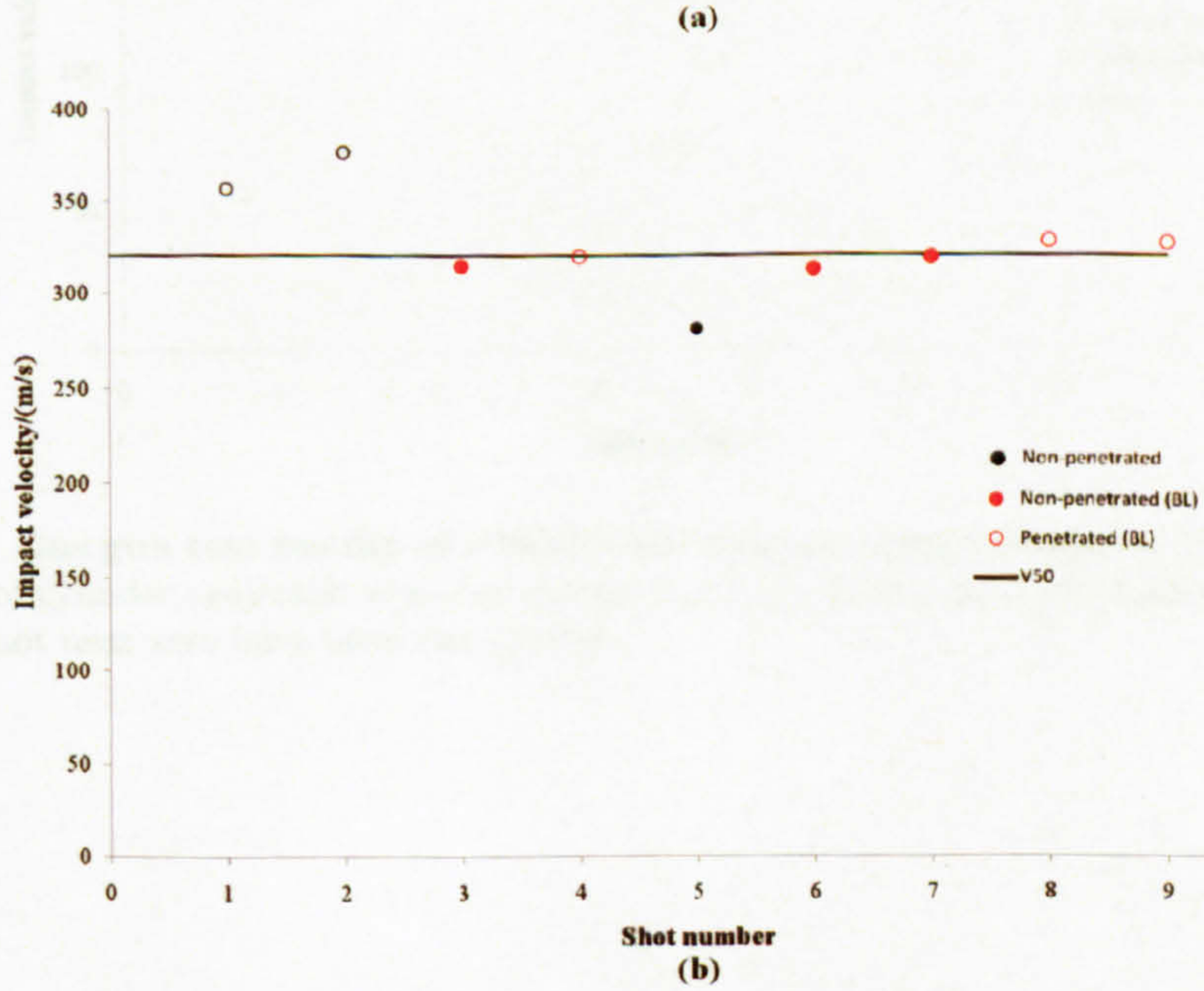

(b)

Figure A.4: **Gas gun test results of materials in database 2 using 0.87g steel balls** - (a) PWEG1-12-VE; (b) PWEG1-14-VE.

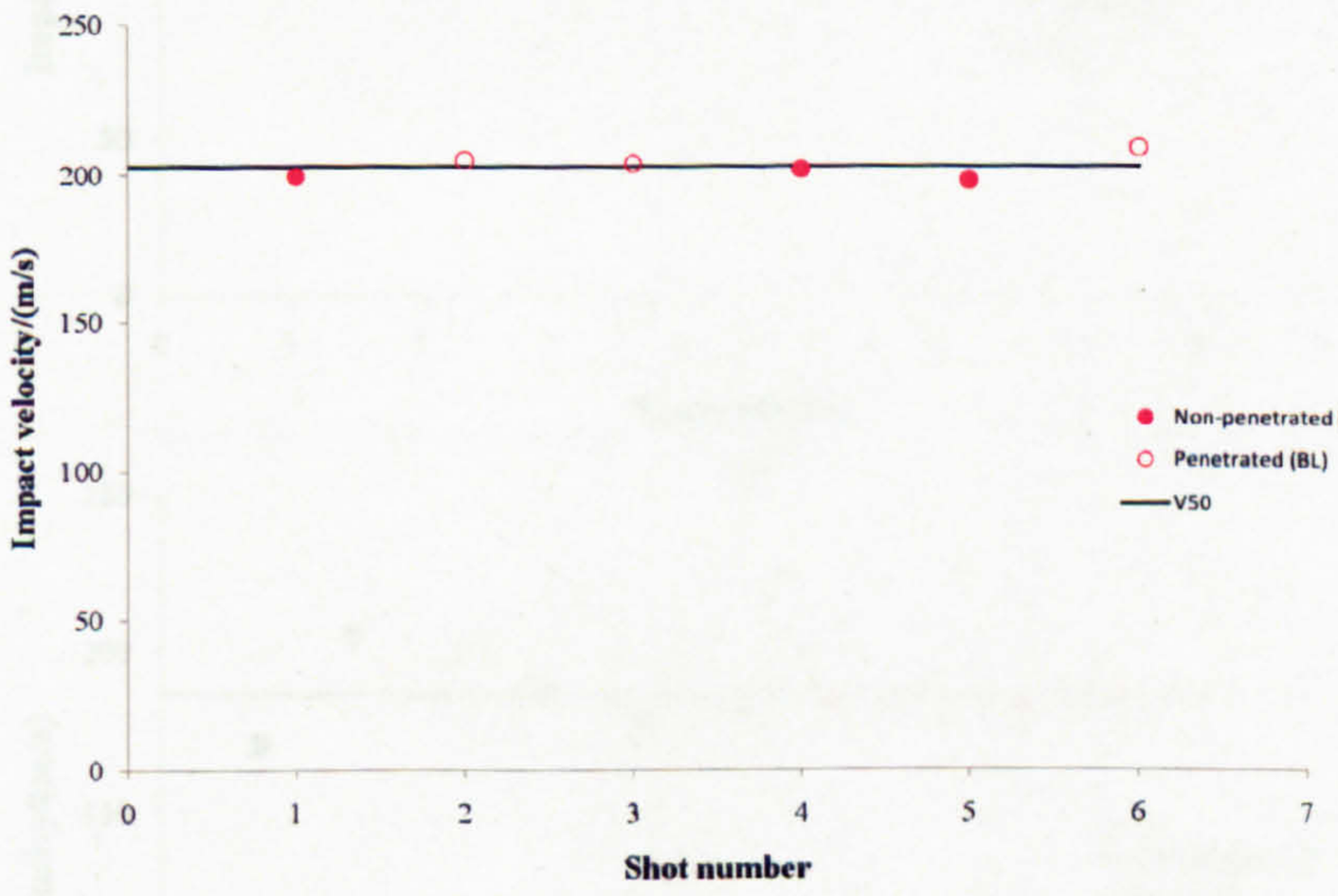

Figure A.5: **Gas gun test results of PWEG-8-VE using 1.39g cylinders** - Yaw (as defined in figure 2.3) of cylinder projectile was characterized by high speed strobe photography; shots whose yaws were not near zero have been disregarded

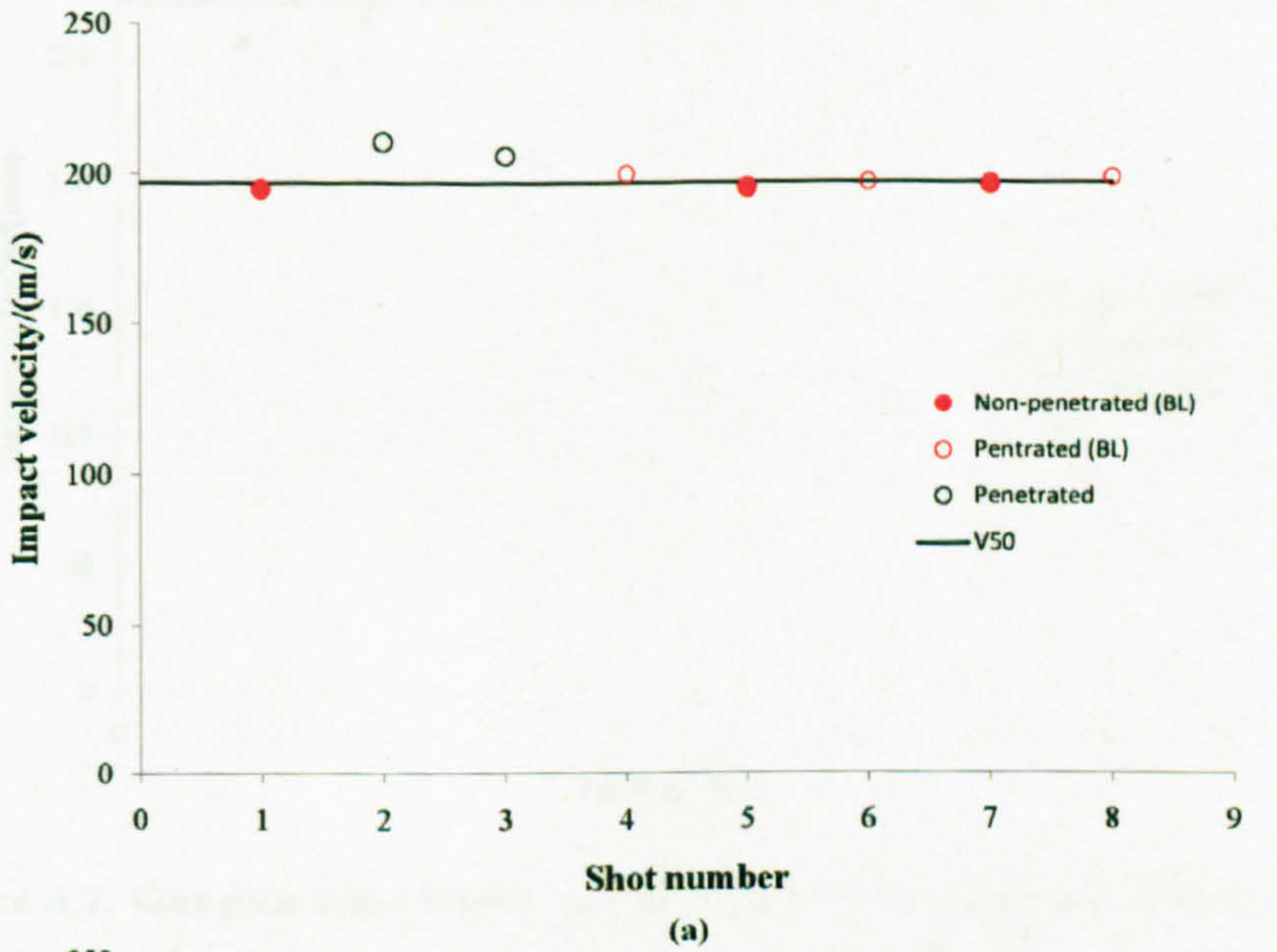

Figure A.6: **Gas gun test results of materials in database 3 using 0.87g steel balls** - (a) PWC-6-VE; (b) PWC-6-EP.

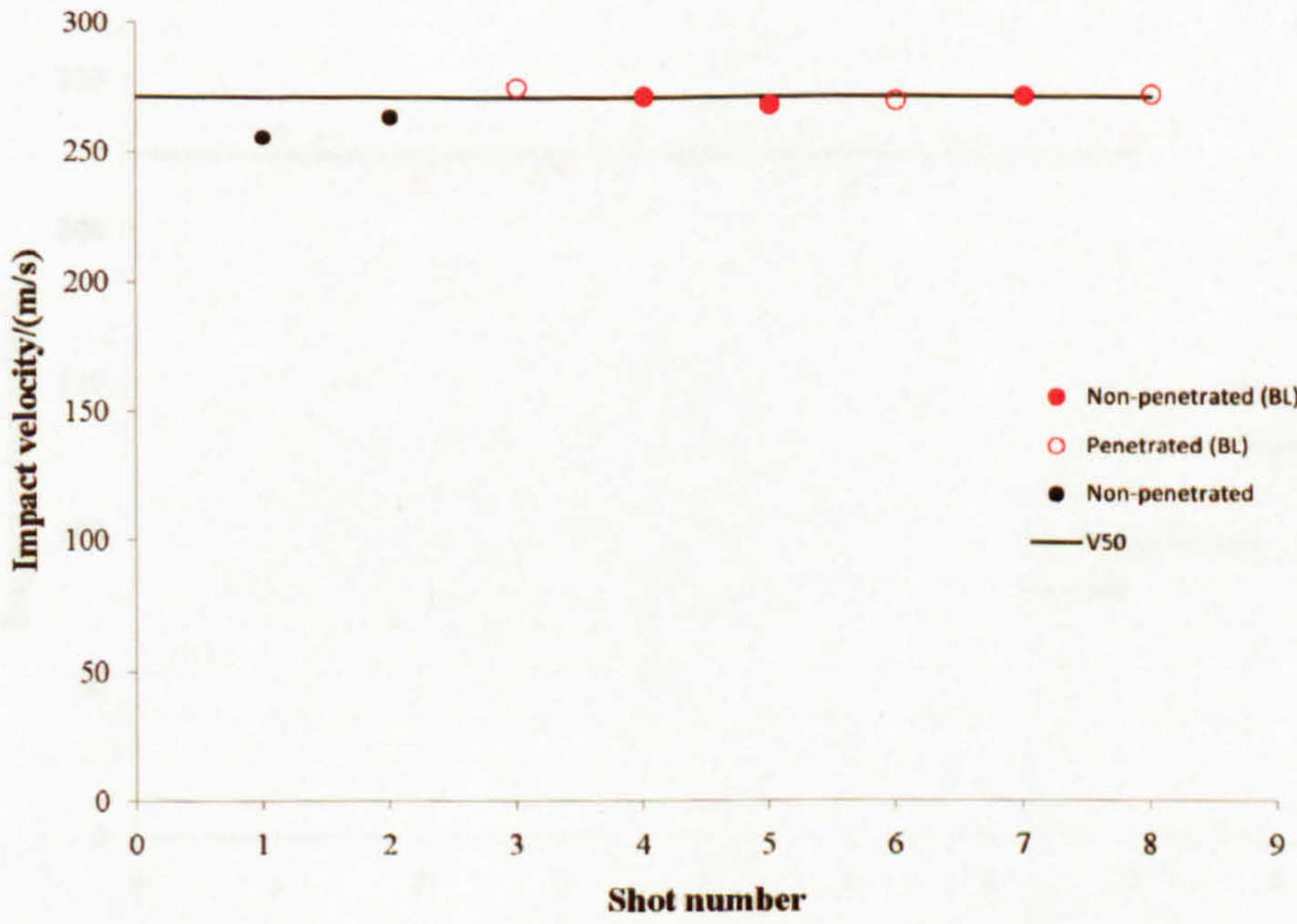

Figure A.7: **Gas gun test results of PWEG2-6-EP using 0.87g steel balls -**

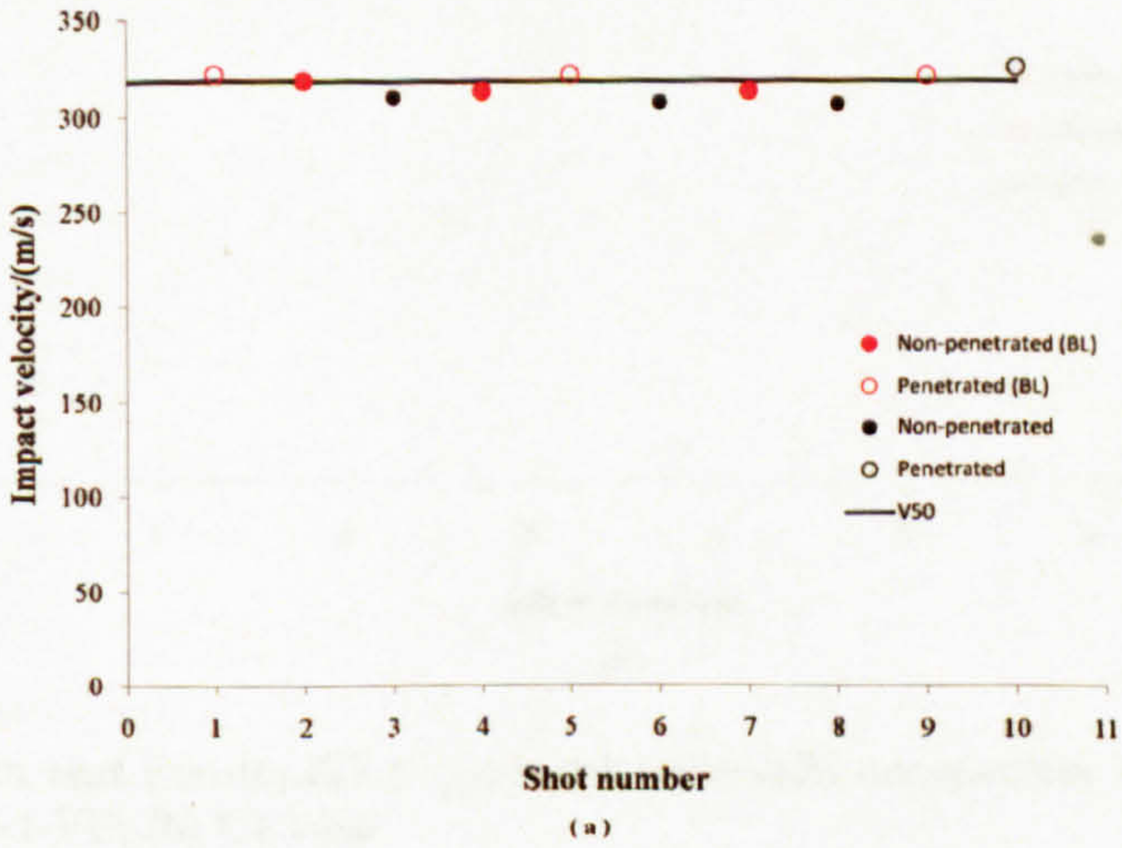

Figure A.8: **Gas gun test results of C1-1-VE against 0.44 gram steel balls -**

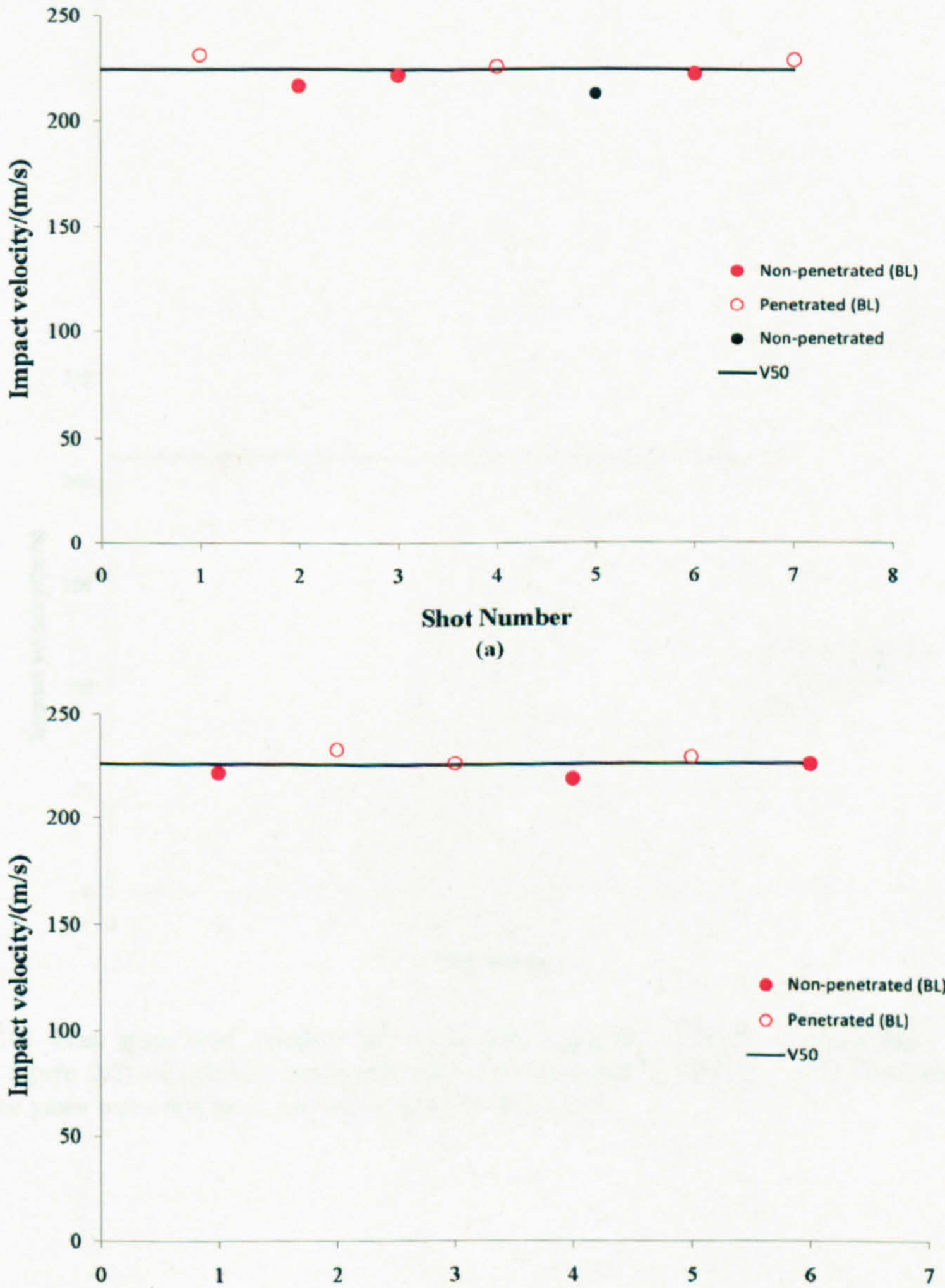

Figure A.9: **Gas gun test results 3D carbon woven textile composites against 0.87 gram steel balls** - (a) C1-1-VE; (b) C1-1-EP

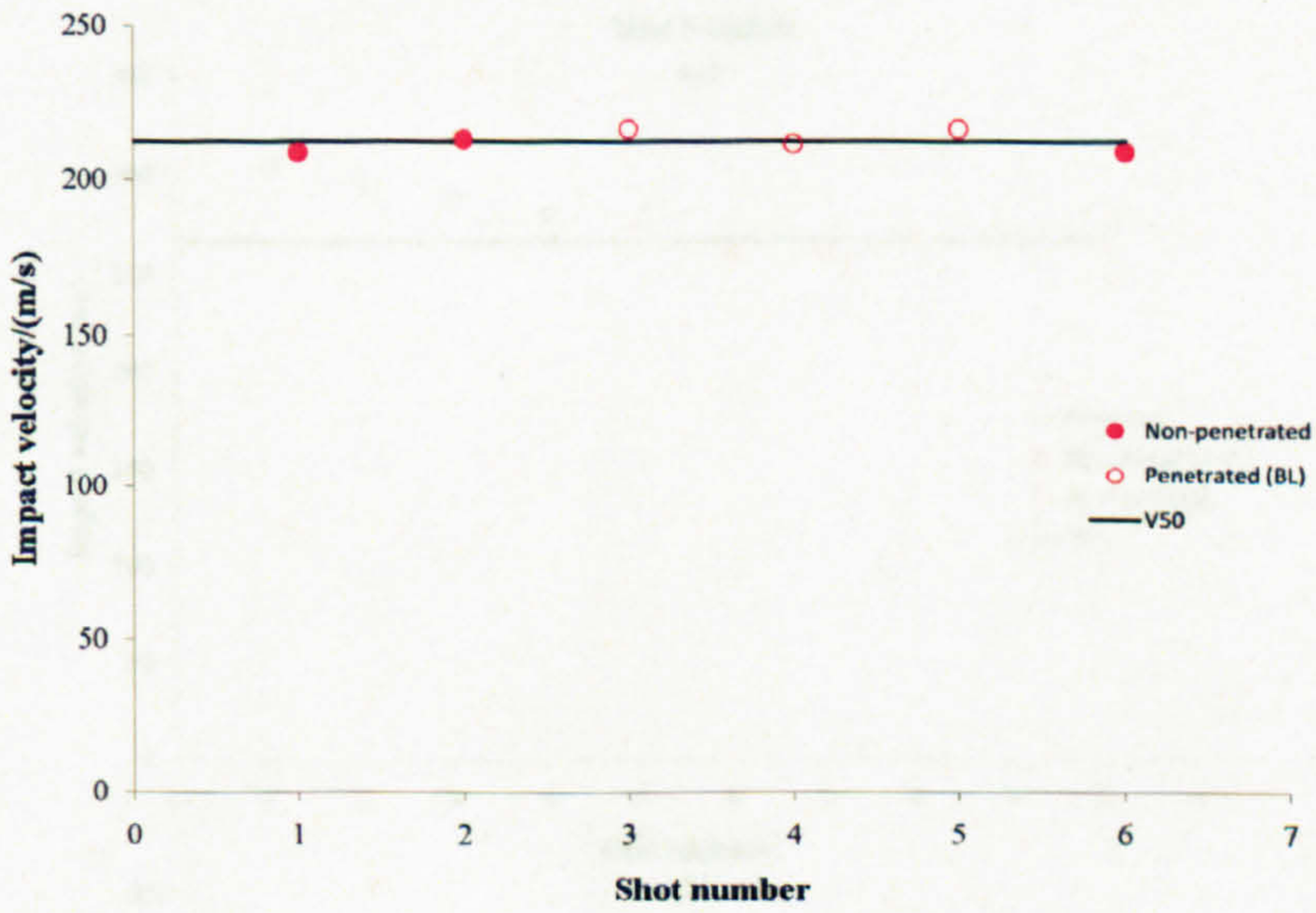

Figure A.10: **Gas gun test results of C1-1-VE against 1.39 gram cylinders** - Yaw (as defined in figure 2.3) of cylinder projectile was characterized by high speed strobe photography; shots whose yaws were not near zero have been disregarded

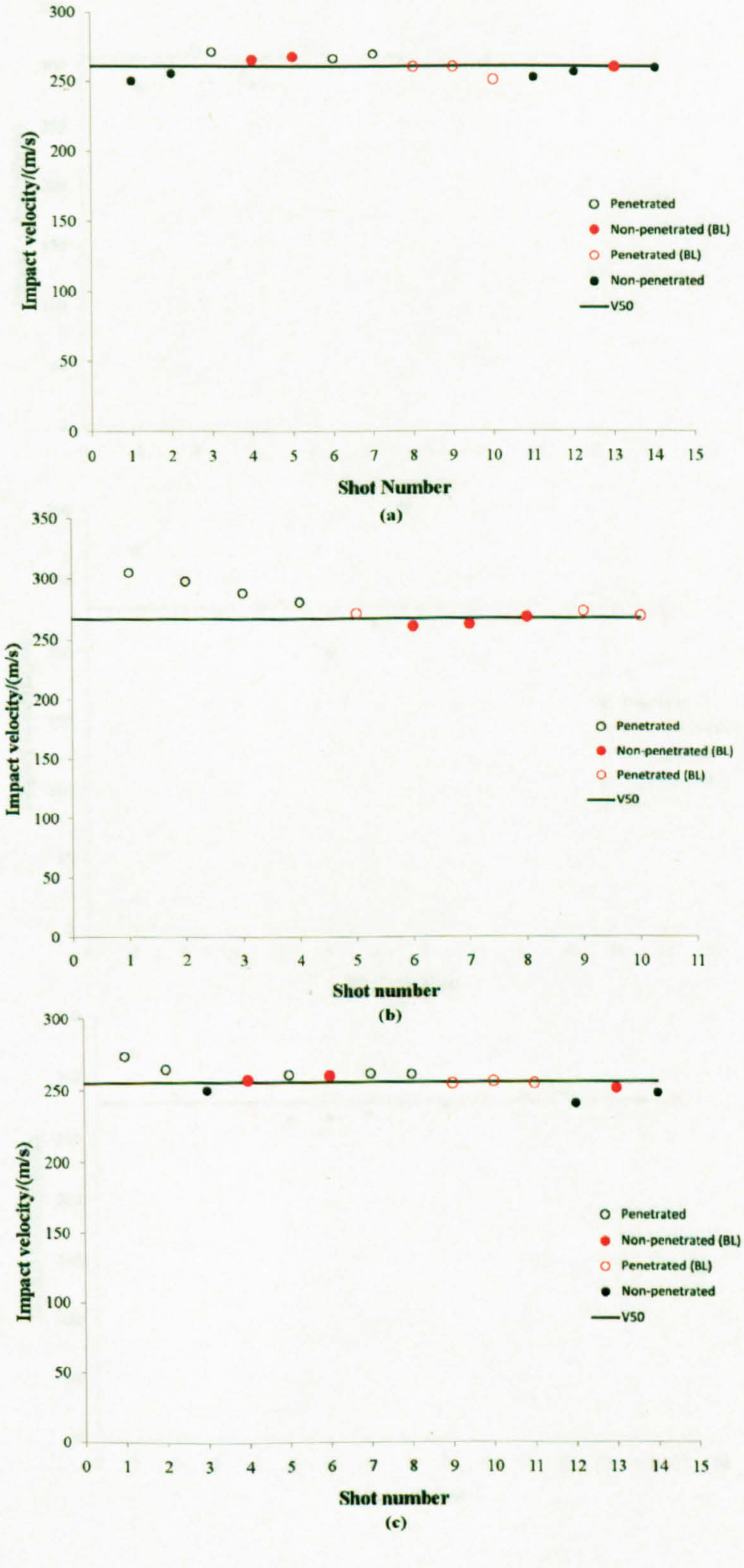

Figure A.11: **Gas gun test results of 3D E-glass woven textile composites against 0.87 g steel balls.** - (a) G1-1-VE; (b) G2-1-VE; (c) G3-1-VE.

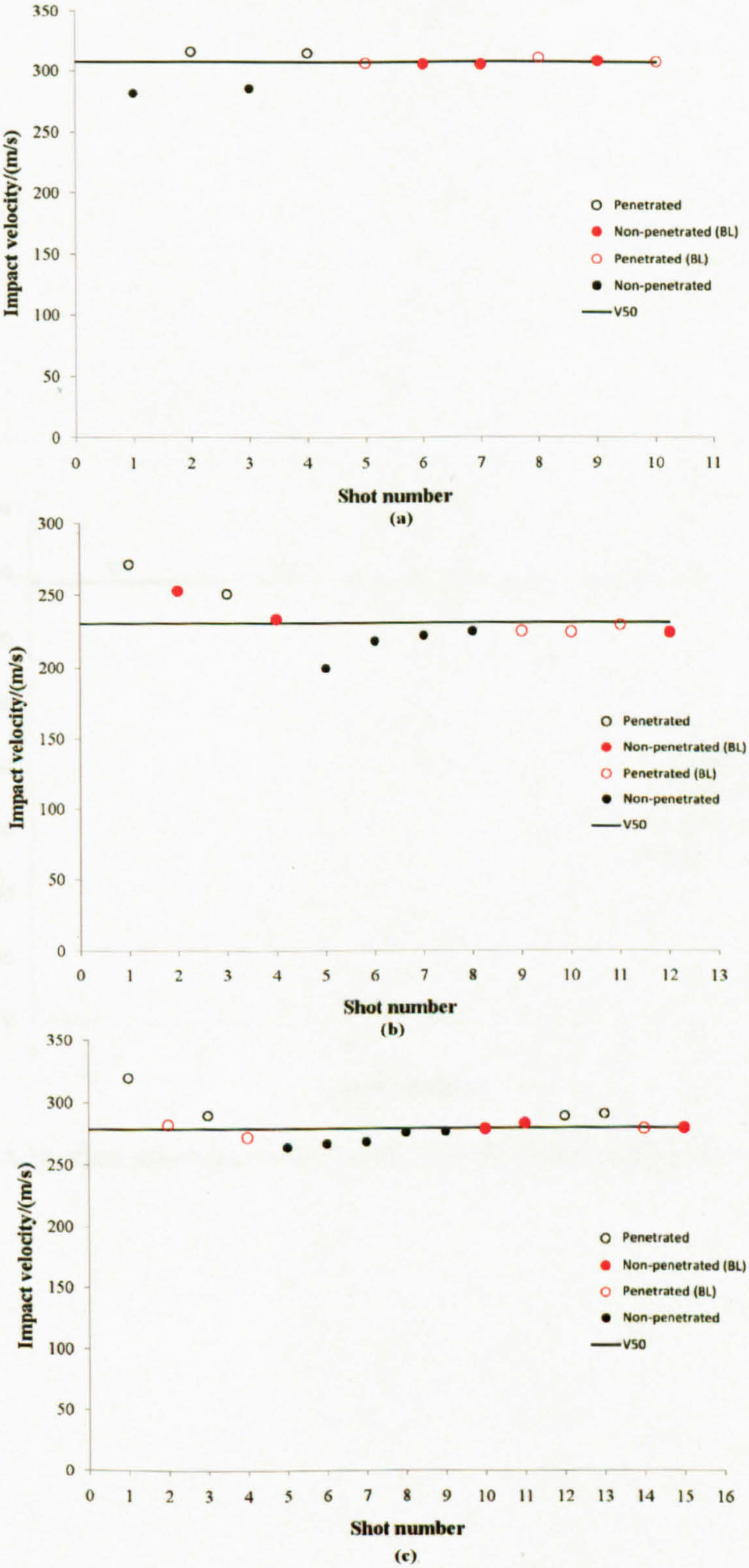

Figure A.12: **Gas gun test results 3D E-glass woven textile composites against 0.87 g steel balls.** - (a) G4-1-VE; (b) G5-1-VE; (c) G6-1-VE.

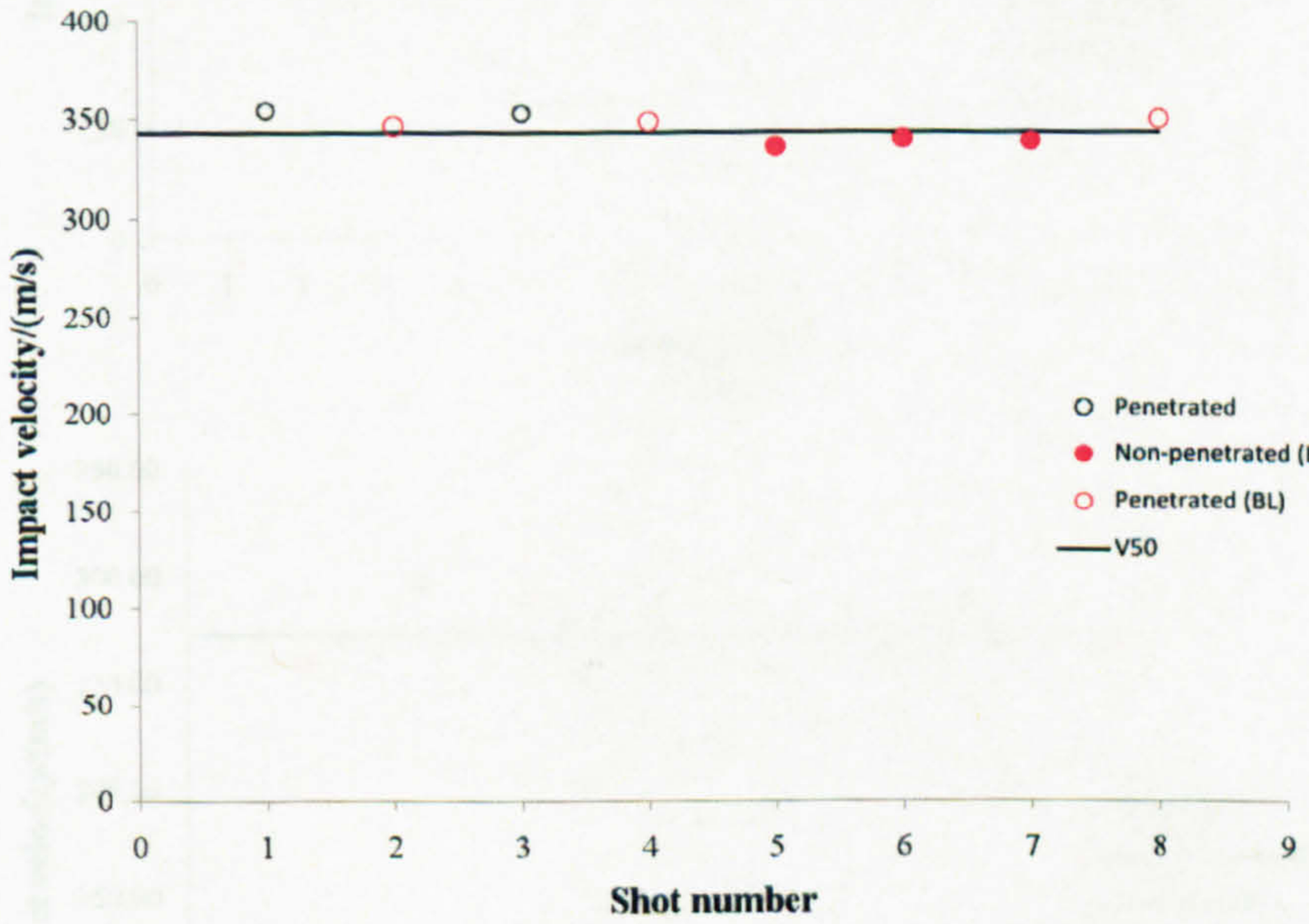

Figure A.13: **Gas gun test results of G7-1-VE against 0.87 g steel balls -**

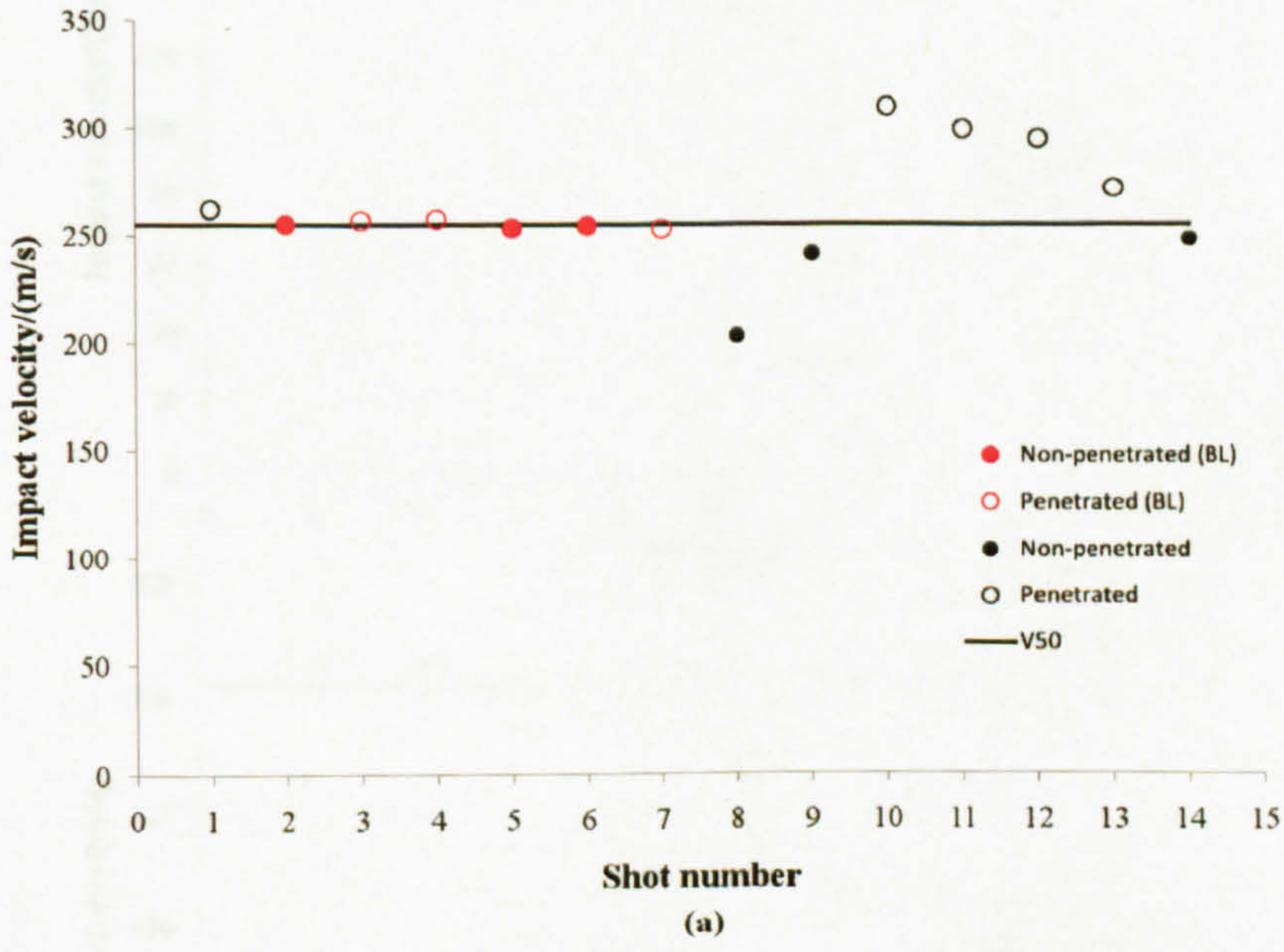

(a)

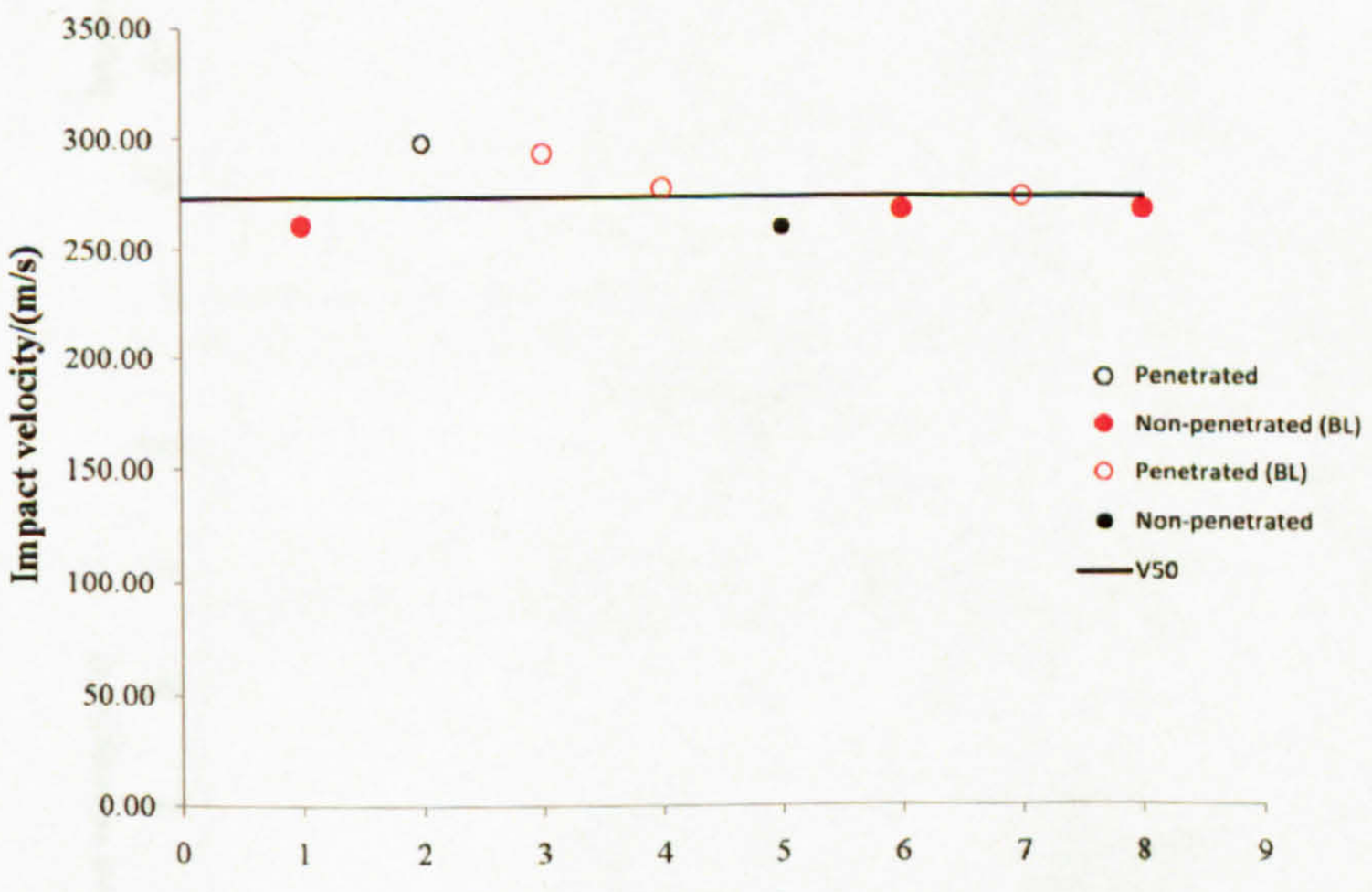

(b)

Figure A.14: **Gas gun test results of carbon fibre non-crimp textile composites against 0.44 g steel balls** - (a) NCC-S-VE; (b) NCC-2-VE.

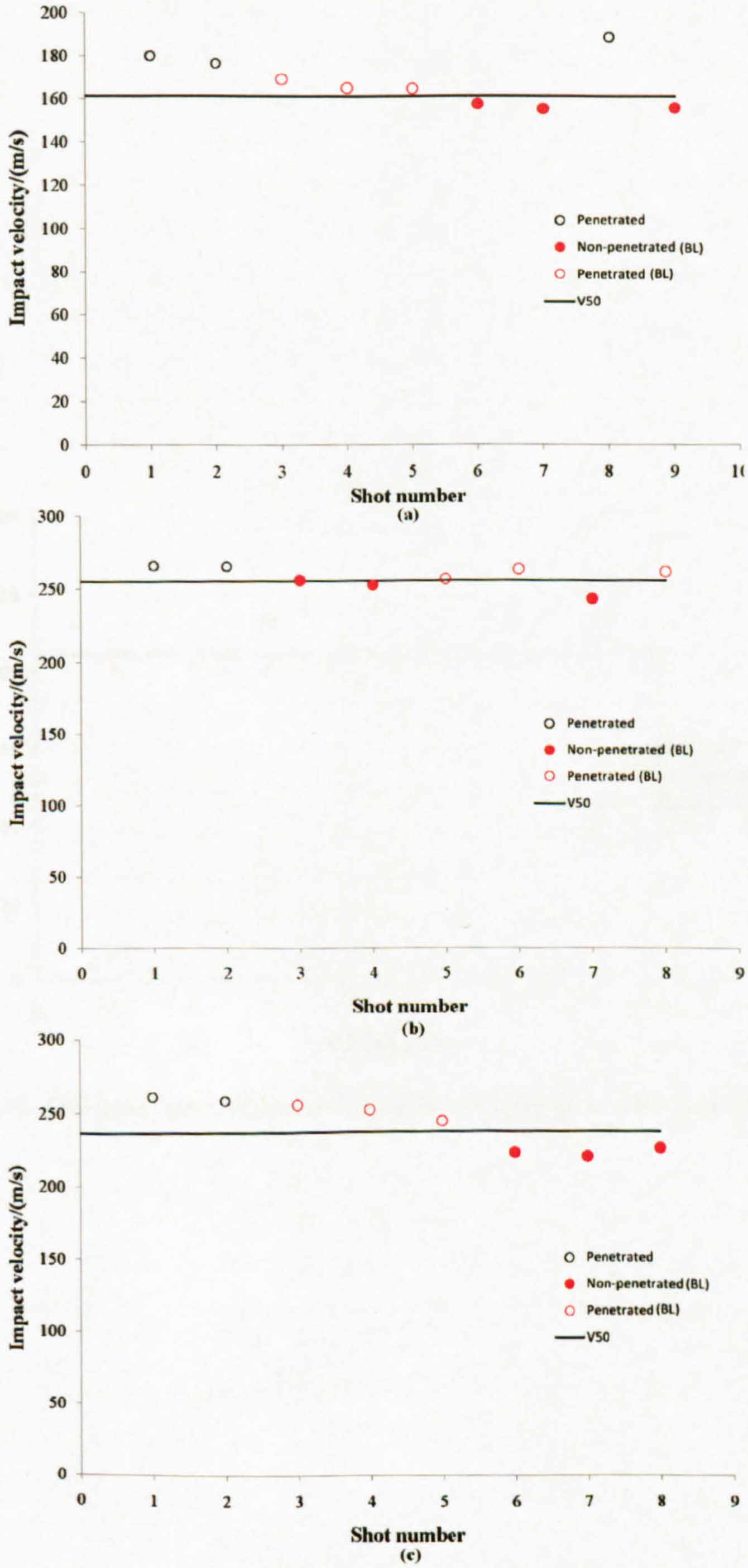

Figure A.15: **Gas gun test results of E-glass fibre non-crimp textile composites against 0.87 g steel balls** - (a) NCEG1-S-VE; (b) NCEG1-2S-VE; (c) NCEG1-4-VE.

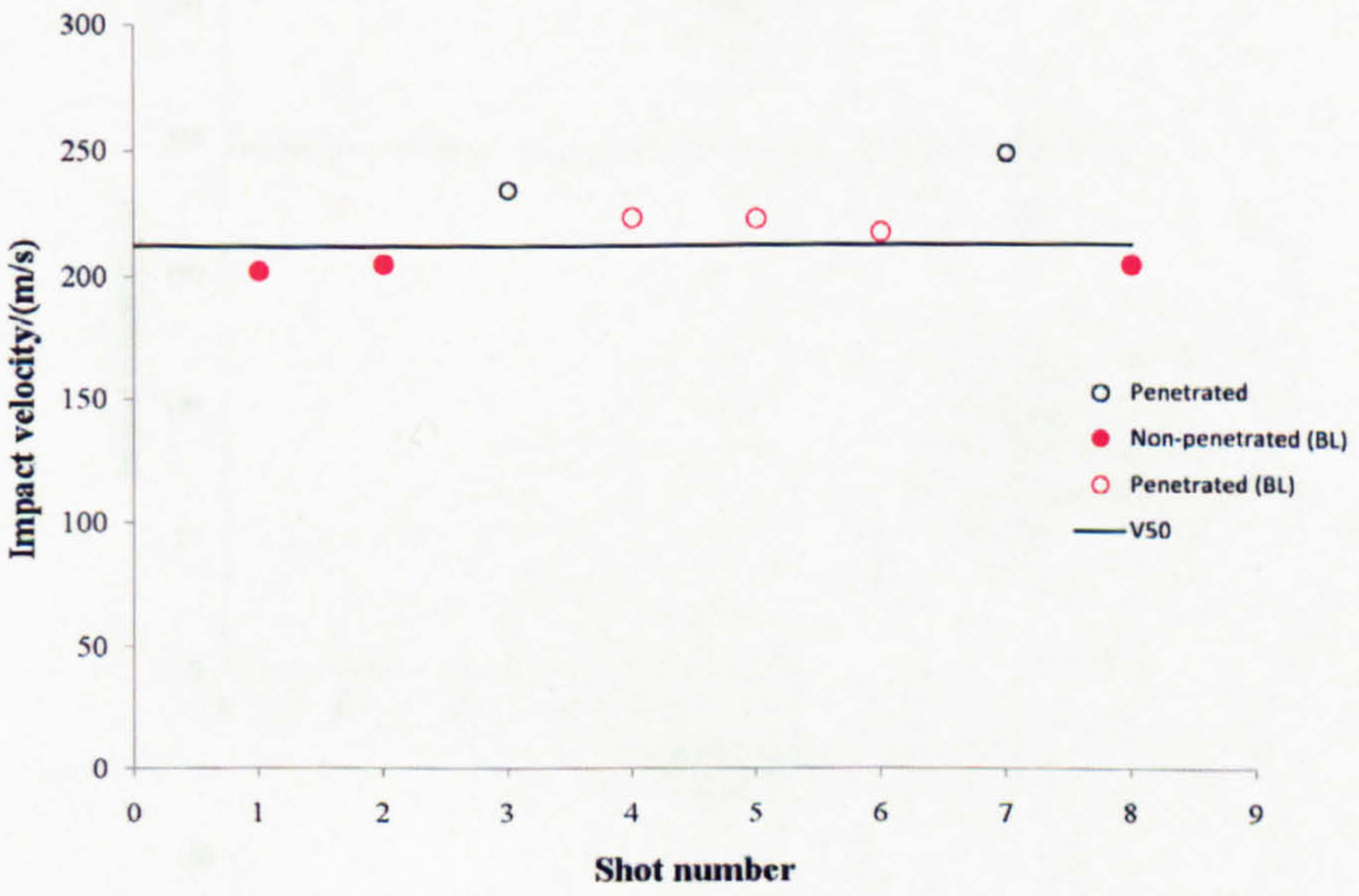

Figure A.16: **Gas gun test results of NCEG2-4-VE against 0.87 g steel balls -**

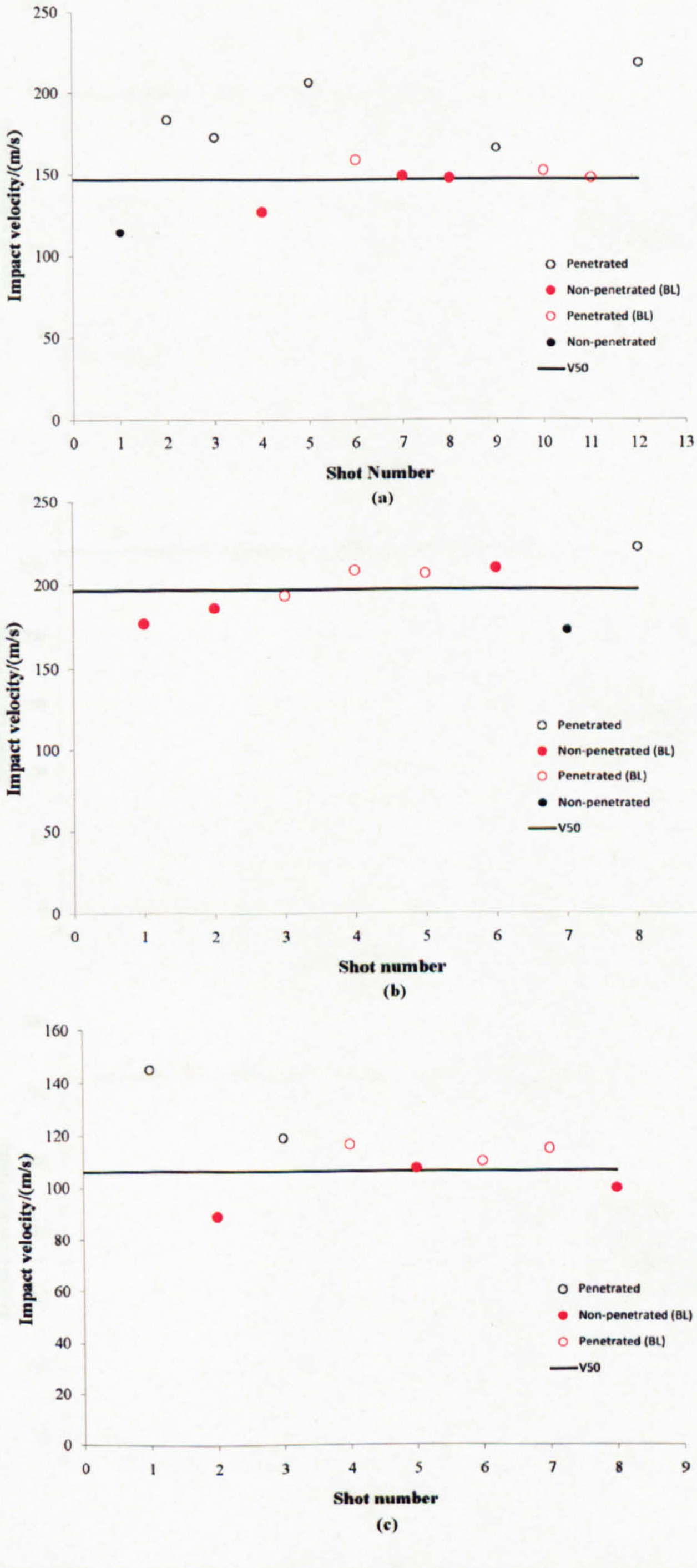

Figure A.17: **Gas gun test results of carbon PET fibre commingled textile composites against 0.44 g steel balls.** - (a) PWCPET1-2-VE; (b) PWCPET1-4-VE; (c) PWCPET2-2-VE.

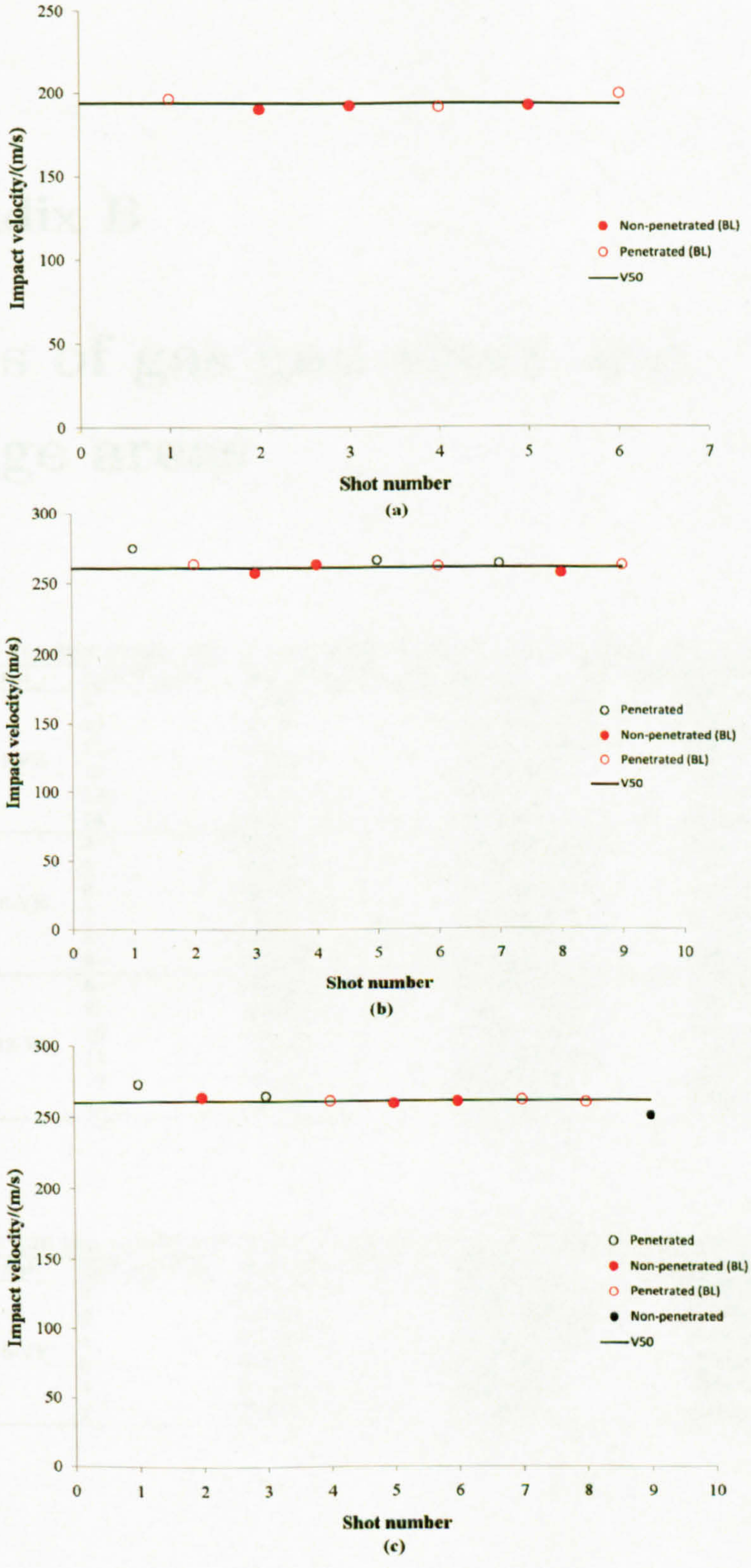

Figure A.18: **Gas gun test results of E-glass PP fibre commingled textile composites against 0.87 g steel ball.** - (a) TWEGPP-2-EP; (b) TWEGPP-4-EP; (c) PWEGPP-4-EP.

Appendix B

Tables of gas gun shots and damage areas

Table B.1: Gas gun test results and damage areas of materials in database 1 using 0.44g steel balls

Material	Shot Number	Shot Velocity/m/s)	Status	Damage area/mm^2
5HSC-4-VE	9	180.44	Non-penetrated	827.98
	10	181.39	Non-penetrated	600.97
	11	184.86	Non-penetrated	644.98
	12	185.71	Penetrated	877.98
	13	190.77	Penetrated	771.96
	14	198.79	Penetrated	699.97
5HSC-8-VE	4	267.31	Non-penetrated	1294.00
	5	268.28	Non-penetrated	1754.93
	6	268.71	Non-penetrated	1348.95
	7	278.81	Penetrated	1330.99
	8	280.72	Penetrated	1301.96
	9	300.26	Penetrated	1223.96
5HSC-12-VE	8	346.89	Non-penetrated	2485.88
	9	346.92	Penetrated	1605.96
	10	350.15	Non-penetrated	1927.92
	11	355.21	Non-penetrated	1855.02
	12	356.83	Penetrated	1457.3
	13	364.43	Penetrated	1402.08

Table B.2: Gas gun test results and damage areas of materials in database 1 using 0.87g steel balls

Material	Shot Number	Shot Velocity (m/s)	Status	Damage area/mm^2
5HSC-6-VE	1	196.81	Non-penetrated	1784.00
	2	200.65	Non-penetrated	1185.00
	4	202.20	Non-penetrated	1202.00
	6	203.30	Penetrated	1156.00
	3	206.81	Penetrated	954.00
	7	207.02	Penetrated	1483.00

Table B.3: Gas gun test results and damage areas of materials in database 2 using 0.44g steel balls

Material	Shot Number	Shot Velocity (m/s)	Status	Damage area/mm^2
PWEG1-4-VE	9	164.41	Non-penetrated	555.04
	10	170.35	Non-penetrated	580.44
	11	165.20	Non-penetrated	520.34
	12	193.30	Penetrated	576.48
	13	182.18	Penetrated	490.11
	14	183.89	Penetrated	518.49
PWEG1-8-VE	4	280.48	Non-penetrated	953.67
	5	281.15	Non-penetrated	1251.22
	6	285.63	Non-penetrated	1035.77
	7	286.82	Penetrated	906.07
	8	288.95	Penetrated	1027.22
	9	286.54	Penetrated	950.25
PWEG1-12-VE	8	346.25	Non-penetrated	1523.44
	9	348.23	Penetrated	1450.20
	10	349.82	Non-penetrated	1319.58
	11	349.61	Non-penetrated	1376.95
	12	350.89	Penetrated	1809.08
	13	353.29	Penetrated	1333.01

Table B.4: Gas gun test results of and damage areas materials in database 2 using 0.87g steel balls

Material	Shot Number	Shot Velocity (m/s)	Status	Damage area/mm^2
PWEG1-4-VE	1	146.58	Non-penetrated	308.06
	2	151.39	Non-penetrated	375.52
	4	152.03	Non-penetrated	426.48
	6	150.85	Penetrated	433.69
	3	152.89	Penetrated	363.85
	7	162.58	Penetrated	350.26
PWEG1-6-VE	1	196.14	Non-penetrated	918.86
	2	200.86	Non-penetrated	1025.80
	3	201.44	Non-penetrated	1573.90
	4	200.56	Penetrated	910.21
	8	200.74	Penetrated	784.85
	9	205.60	Penetrated	780.57
PWEG1-8-VE	11	237.71	Non-penetrated	1360.78
	10	238.99	Non-penetrated	1390.99
	5	240.12	Non-penetrated	1659.24
	4	225.55	Penetrated	1208.50
	1	230.98	Penetrated	1066.59
	9	243.26	Penetrated	1419.68
PWEG1-12-VE	1	290.72	Non-penetrated	1916.81
	2	300.56	Non-penetrated	1589.66
	3	300.78	Non-penetrated	1855.16
	6	302.21	Penetrated	1603.39
	5	307.45	Penetrated	1657.10
	4	308.37	Penetrated	1829.83
PWEG1-14-VE	6	312.42	Non-penetrated	2114.26
	3	314.31	Non-penetrated	1765.44
	7	318.97	Non-penetrated	2432.86
	4	319.80	Penetrated	1581.42
	9	327.05	Penetrated	2249.76
	8	327.84	Penetrated	1877.14

Table B.5: Gas gun test results and damage areas of materials in database 2 against 1.39 gram cylinder

Material	Shot Number	Shot Velocity (m/s)	Status	Damage area/mm^2
PWEG1-8-VE	1	198.03	Non-penetrated	1255.80
	2	199.43	Non-penetrated	1497.50
	4	201.81	Non-penetrated	1380.00
	6	203.76	Penetrated	1393.43
	3	204.92	Penetrated	1377.26
	7	209.18	Penetrated	1229.86

Table B.6: Gas gun test results and damage areas of materials in database 3 using 0.87 g steel ball

Material	Shot Number	Shot Velocity (m/s)	Status	Damage area/mm^2
PWC-6-VE	1	194.86	Non-penetrated	1883.96
	2	195.16	Non-penetrated	1790.00
	4	196.17	Non-penetrated	1958.00
	6	196.78	Penetrated	1881.90
	3	198.49	Penetrated	987.00
	7	199.70	Penetrated	933.00
PWC-6-EP	1	184.25	Non-penetrated	
	2	185.17	Non-penetrated	
	4	190.13	Non-penetrated	
	6	185.96	Penetrated	
	3	187.76	Penetrated	
	7	188.95	Penetrated	

Table B.7: Gas gun test results PWEG2-6-VE against 0.87 g steel ball.

Material	Shot Number	Shot Velocity (m/s)	Status	Damage area/mm^2
PWEG2-6-EP	1	268.25	Non-penetrated	1095.58
	2	271.52	Non-penetrated	1088.56
	4	271.73	Non-penetrated	1046.75
	6	269.53	Penetrated	1129.76
	3	272.13	Penetrated	814.21
	7	275.08	Penetrated	1010.44

Table B.8: Gas gun test results and damage areas of C1-1-VE against 0.44 g steel ball

Material	Shot Number	Shot Velocity (m/s)	Status	Damage area/mm^2
0.44g Ball	1	248.81	Non-penetrated	1135.98
	2	252.68	Non-penetrated	1055.86
	4	253.32	Non-penetrated	931.97
	6	255.33	Penetrated	871.96
	3	256.70	Penetrated	1036.99
	7	263.07	Penetrated	803.99

Table B.9: Gas gun test results and damage areas of C1-1-VE and C1-1-EP against 0.87 g steel ball

Material	Shot Number	Shot Velocity (m/s)	Status	Damage area/mm^2
0.87g Ball	1	216.47	Non-penetrated	795.00
	2	221.59	Non-penetrated	688.00
	4	222.14	Non-penetrated	841.3
	6	225.55	Penetrated	643.00
	3	228.81	Penetrated	837.99
	7	230.98	Penetrated	654.00
C1-1-EP	1	218.88	Non-penetrated	817.00
	2	221.65	Non-penetrated	689.98
	4	225.70	Non-penetrated	732.95
	6	226.85	Penetrated	935.86
	3	229.18	Penetrated	786.98
	7	233.35	Penetrated	889.92

Table B.10: Gas gun test results and damage areas of C1-1-VE against 1.39 gram cylinder

Material	Shot Number	Shot Velocity (m/s)	Status	Damage area/mm^2
1.39g Cylinder	1	208.67	Non-penetrated	1792.92
	2	208.73	Non-penetrated	1206.91
	4	212.72	Non-penetrated	1677.93
	6	211.10	Penetrated	1537.96
	3	215.95	Penetrated	1547.91
	7	215.98	Penetrated	1657.92

Table B.11: Gas gun test results and damage areas of 3D E-glass woven textile composites against 0.87 g steel ball - Part I

Material	Shot Number	Shot Velocity (m/s)	Status	Damage area/mm^2
G1-1-VE	1	260.21	Non-penetrated	560.00
	2	265.57	Non-penetrated	584.41
	4	267.77	Non-penetrated	525.82
	6	250.85	Penetrated	467.53
	3	260.24	Penetrated	456.85
	7	260.33	Penetrated	572.51
G2-1-VE	1	260.42	Non-penetrated	589.29
	2	261.98	Non-penetrated	610.35
	4	267.77	Non-penetrated	598.14
	6	268.25	Penetrated	746.15
	3	270.88	Penetrated	628.97
	7	272.40	Penetrated	637.21
G3-1-VE	1	250.36	Non-penetrated	173.95
	2	256.52	Non-penetrated	244.75
	4	259.38	Non-penetrated	336.30
	6	254.05	Penetrated	304.26
	3	254.11	Penetrated	369.26
	7	255.57	Penetrated	403.44
G4-1-VE	1	305.04	Non-penetrated	466.61
	2	305.68	Non-penetrated	568.85
	4	308.49	Non-penetrated	404.36
	6	306.60	Penetrated	396.73
	3	307.82	Penetrated	431.82
	7	310.90	Penetrated	444.03

Table B.12: Gas gun test results and damage areas of of 3D E-glass woven textile composites against 0.87 g steel ball - Part II

Material	Shot Number	Shot Velocity (m/s)	Status	Damage area/mm^2
G5-1-VE	1	224.52	Non-penetrated	
	2	233.23	Non-penetrated	
	4	252.62	Non-penetrated	
	6	223.91	Penetrated	
	3	224.06	Penetrated	
	7	224.55	Penetrated	
G6-1-VE	1	277.83	Non-penetrated	
	2	278.19	Non-penetrated	
	4	282.03	Non-penetrated	
	6	271.70	Penetrated	
	3	277.58	Penetrated	
	7	281.57	Penetrated	
G7-1-VE	1	335.46	Non-penetrated	1326.60
	2	338.39	Non-penetrated	1704.71
	4	339.49	Non-penetrated	1284.79
	6	346.25	Penetrated	1682.43
	3	348.26	Penetrated	1622.92
	7	349.58	Penetrated	1694.03

Table B.13: Gas gun test results and damage areas of carbon fibre non-crimp textile composites against 0.44 g steel ball

Material	Shot Number	Shot Velocity (m/s)	Status	Damage area/mm^2
NCC-S-VE	1	253.32	Non-penetrated	2338.90
	2	254.36	Non-penetrated	2213.00
	4	255.21	Non-penetrated	2485.00
	6	252.71	Penetrated	1930.00
	3	256.85	Penetrated	1705.90
	7	257.56	Penetrated	1870.90
NCC-2-VE	1	260.30	Non-penetrated	3113.90
	2	266.76	Non-penetrated	2917.97
	4	267.22	Non-penetrated	2728.89
	6	272.83	Penetrated	2821.90
	3	277.06	Penetrated	3093.90
	7	292.88	Penetrated	2664.00

Table B.14: Gas gun test results and damage areas of E-glass fibre non-crimp textile composites against 0.87 g steel ball.

Material	Shot Number	Shot Velocity (m/s)	Status	Damage area/mm^2
NCEG1-S-VE	1	154.99	Non-penetrated	4526.06
	2	155.46	Non-penetrated	4603.246
	4	157.28	Non-penetrated	4674.07
	6	164.62	Penetrated	4376.53
	3	164.99	Penetrated	3746.34
	7	169.10	Penetrated	4626.46
NCEG1-2S-VE	1	242.56	Non-penetrated	5677.49
	2	252.07	Non-penetrated	5177.31
	4	255.61	Non-penetrated	5081.48
	6	256.00	Penetrated	5025.02
	3	261.12	Penetrated	5342.10
	7	262.77	Penetrated	5411.99
NCEG1-4-VE	1	220.10	Non-penetrated	5789.23
	2	222.78	Non-penetrated	5879.52
	4	225.60	Non-penetrated	5689.26
	6	243.78	Penetrated	5404.97
	3	251.80	Penetrated	6399.84
	7	255.27	Penetrated	5856.32
NCEG2-4-VE	1	202.54	Non-penetrated	3214.42
	2	204.30	Non-penetrated	3125.47
	4	205.19	Non-penetrated	2999.88
	6	217.54	Penetrated	3646.24
	3	222.87	Penetrated	3163.45
	7	223.48	Penetrated	3829.65

Table B.15: Gas gun test results of carbon PET fibre commingled textile composites against 0.44 g steel ball.

Material	Shot Number	Shot Velocity (m/s)	Status
PWCPET1-2-VE	1	126.80	Non-penetrated
	2	147.37	Non-penetrated
	4	148.80	Non-penetrated
	6	147.76	Penetrated
	3	151.85	Penetrated
	7	158.65	Penetrated
PWCPET1-4-VE	1	176.75	Non-penetrated
	2	185.84	Non-penetrated
	4	209.25	Non-penetrated
	6	192.97	Penetrated
	3	205.98	Penetrated
	7	207.87	Penetrated
PWCPET2-2-VE	1	88.94	Non-penetrated
	2	99.33	Non-penetrated
	4	107.17	Non-penetrated
	6	109.82	Penetrated
	3	114.51	Penetrated
	7	116.37	Penetrated

Table B.16: Gas gun test results and damage areas of E-glass PP fibre commingled textile composites against 0.87 g steel ball.

Material	Shot Number	Shot Velocity (m/s)	Status	Damage area/mm^2
TWEGPP-2-EP	1	190.10	Non-penetrated	1082.76
	2	192.42	Non-penetrated	965.58
	4	192.54	Non-penetrated	923.46
	6	191.38	Penetrated	1021.73
	3	196.29	Penetrated	848.69
	7	199.95	Penetrated	1056.82
TWEGPP-4-EP	1	256.67	Non-penetrated	1707.15
	2	256.79	Non-penetrated	1601.87
	4	262.71	Non-penetrated	1592.71
	6	261.24	Penetrated	1828.92
	3	262.10	Penetrated	1812.13
	7	263.04	Penetrated	1445.92
PWEGPP-4-EP	1	258.78	Non-penetrated	1329.96
	2	260.27	Non-penetrated	1566.16
	4	263.23	Non-penetrated	1513.67
	6	259.42	Penetrated	1506.96
	3	260.88	Penetrated	1185.00
	7	261.15	Penetrated	1101.07

Appendix C

Figures of the outlines of the damages in V_{50} specimens

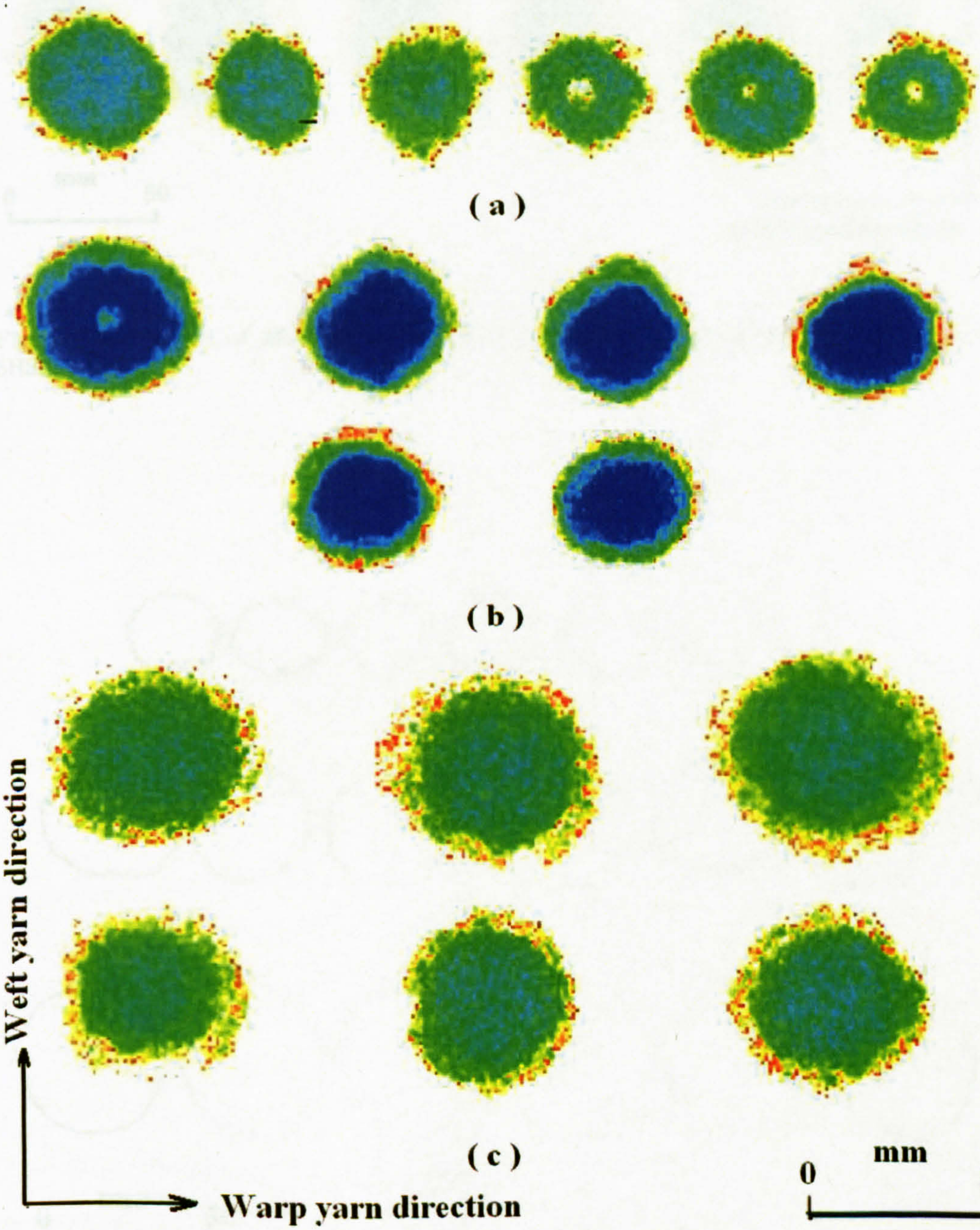

Figure C.1: **Shapes of 2D damage areas of V_{50} specimens in database 1 -Part I -** (a) 5HSC-4-VE; (b) 5HSC-8-VE; (c) 5HSC-12-VE.

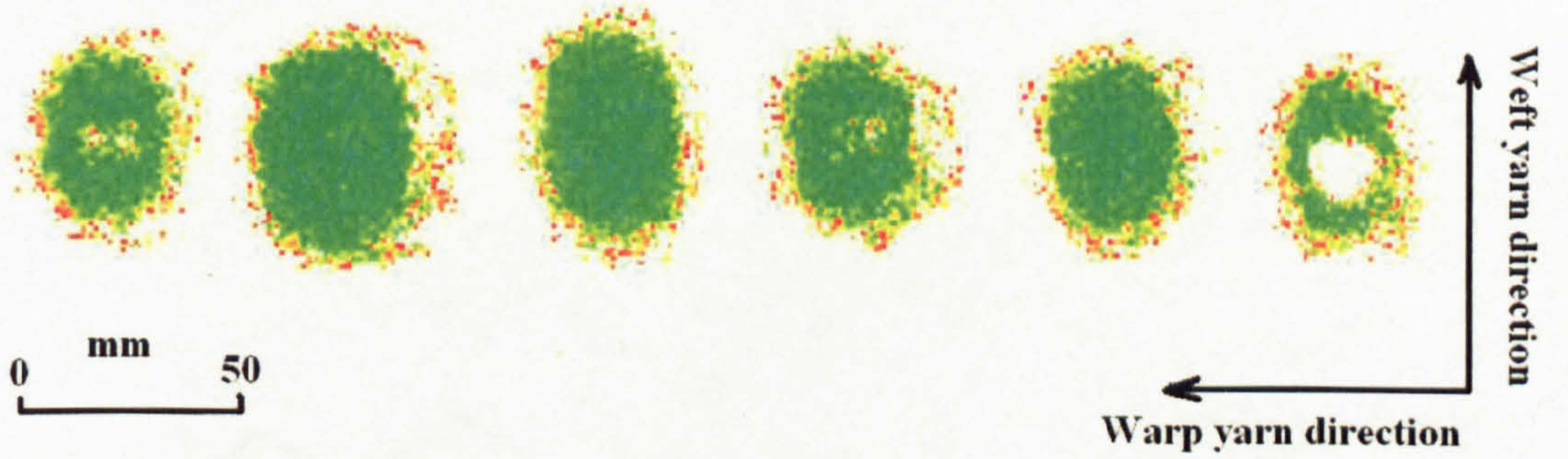

Figure C.2: **Shapes of 2D damage areas of V_{50} specimens in database 1 -Part II** - (a) 5HSC-6-VE.

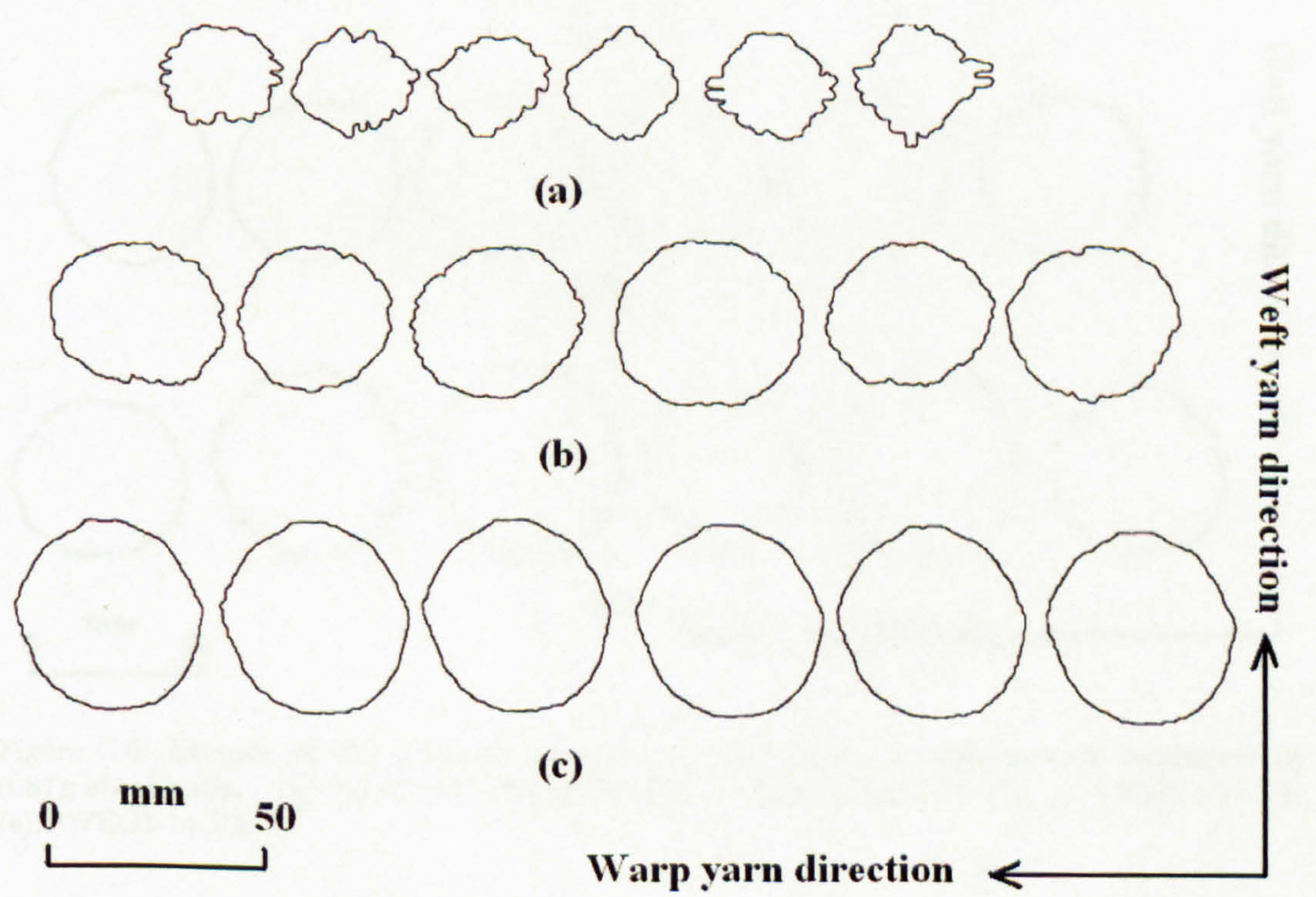

Figure C.3: **Shapes of 2D damage areas of V_{50} specimens in database 2 impacted by 0.44g steel balls.** - (a) PWEG1-4-VE; (b) PWEG1-8-VE; (c) PWEG1-12-VE.

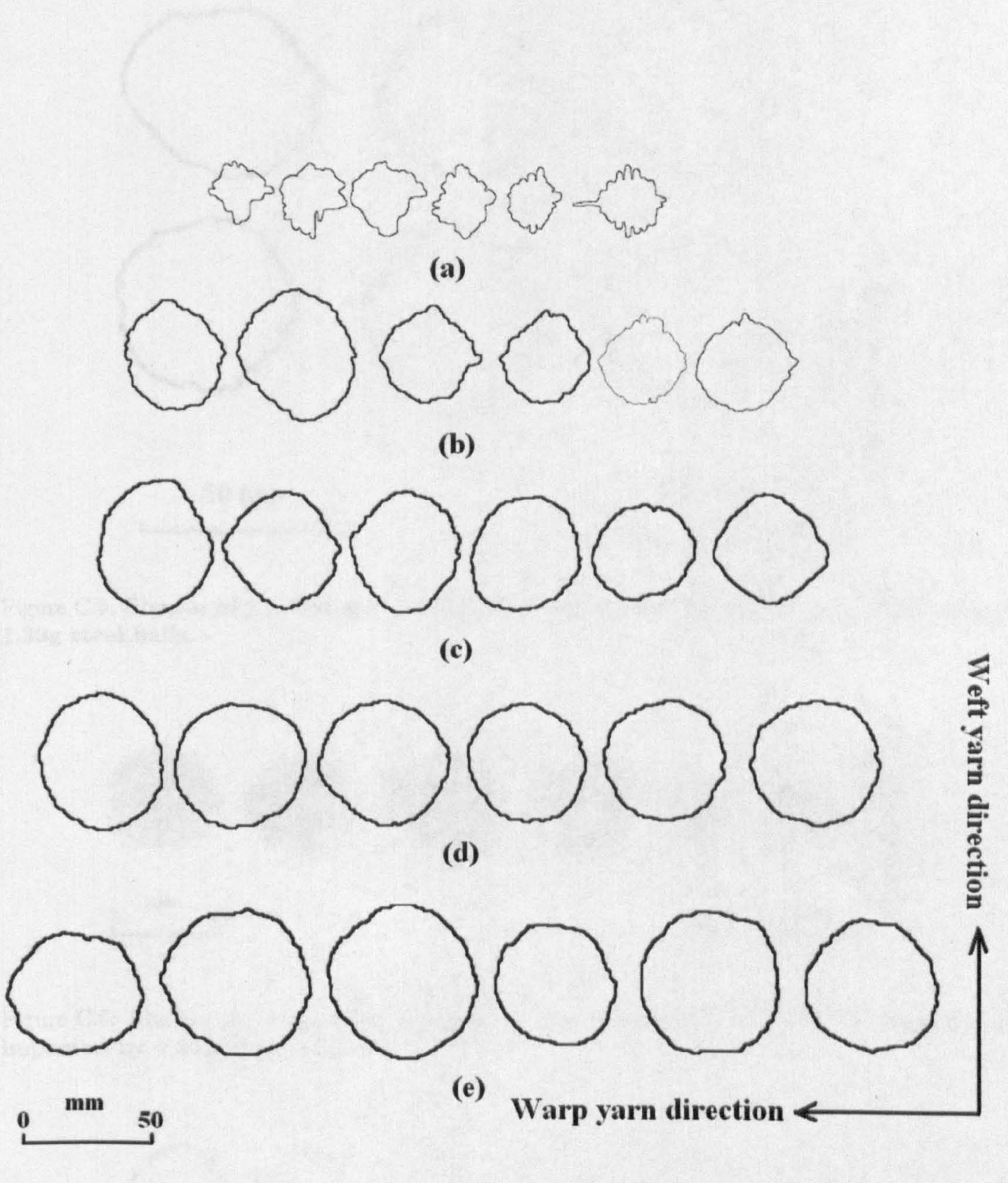

Figure C.4: **Shapes of 2D damage areas of V_{50} specimens in database 2 impacted by 0.87g steel balls.** - (a) PWEG1-4-VE; (b) PWEG1-6-VE; (c) PWEG1-8-VE; (d) PWEG1-12-VE; (e) PWEG1-14-VE.

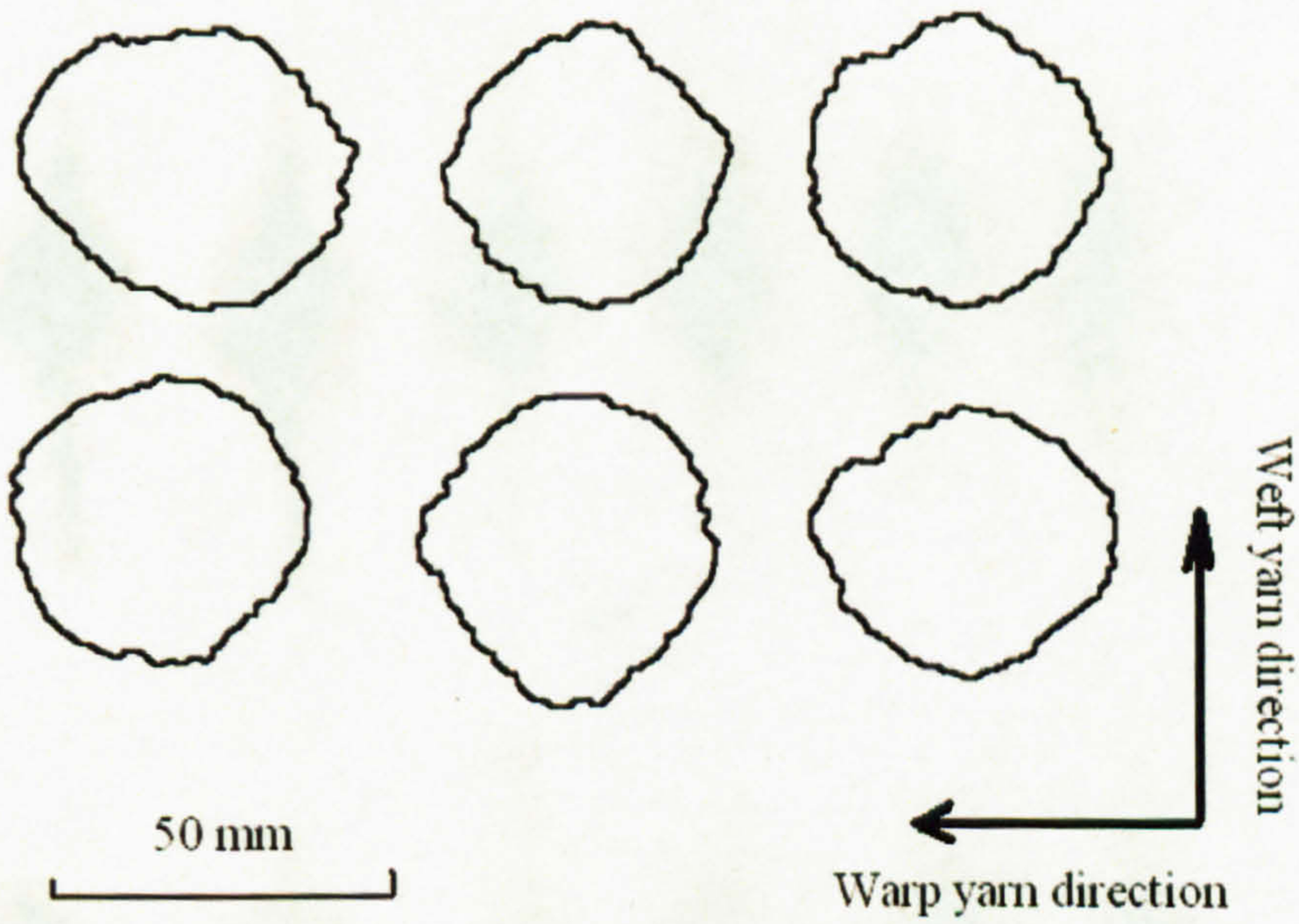

Figure C.5: **Shapes of 2D damage areas of V_{50} specimens of PWEG1-8-VE impacted by 1.39g steel balls.** -

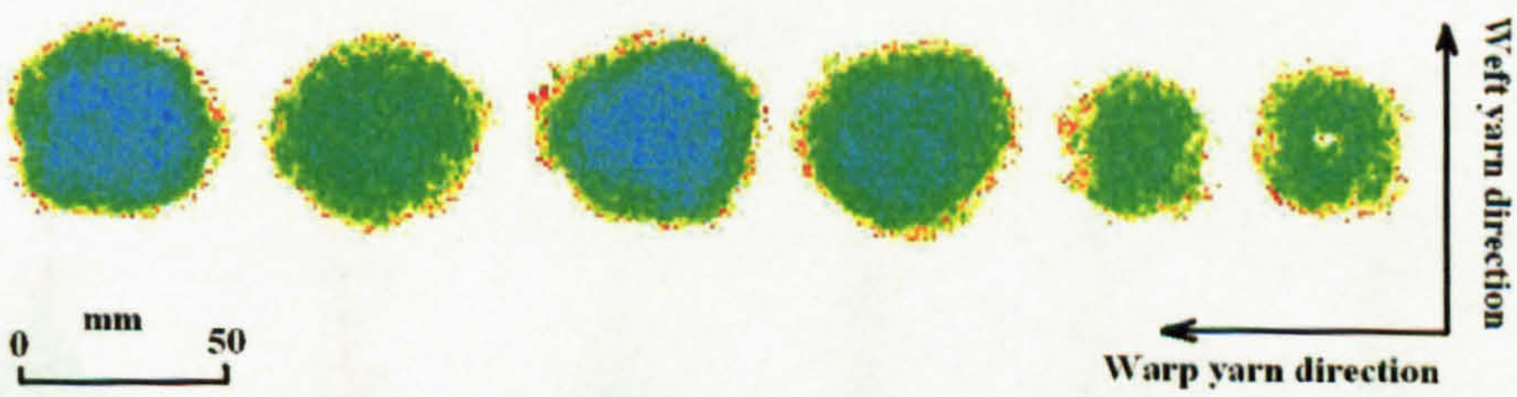

Figure C.6: **Shapes of 2D damage areas of V_{50} specimens of PWC-6-VE in database 3 impacted by 0.87g steel balls.** -

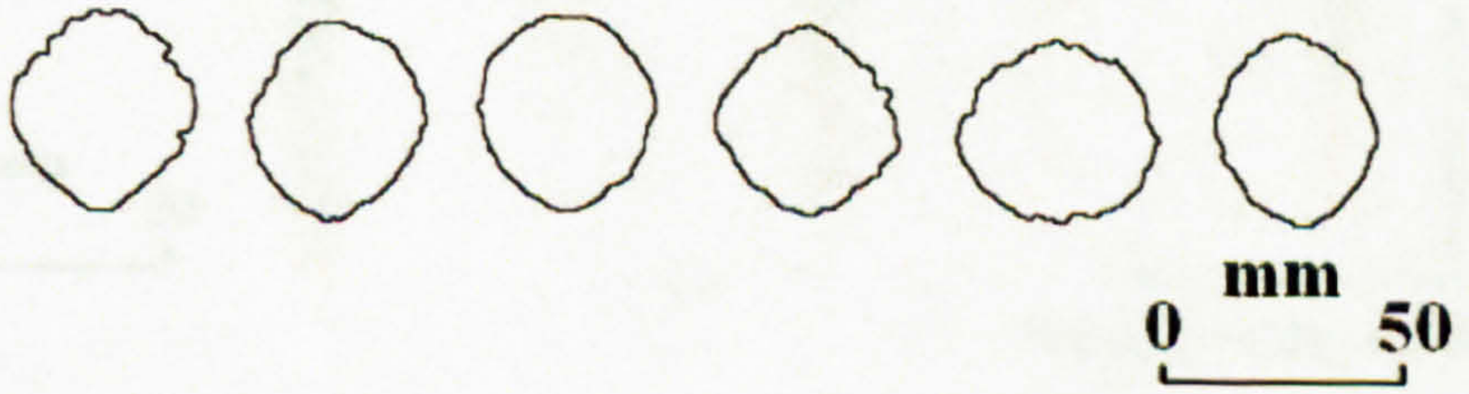

Figure C.7: **Shapes of 2D damage areas of V_{50} specimens of PWEG2-6-VE in database 3 impacted by 0.87g steel balls.** -

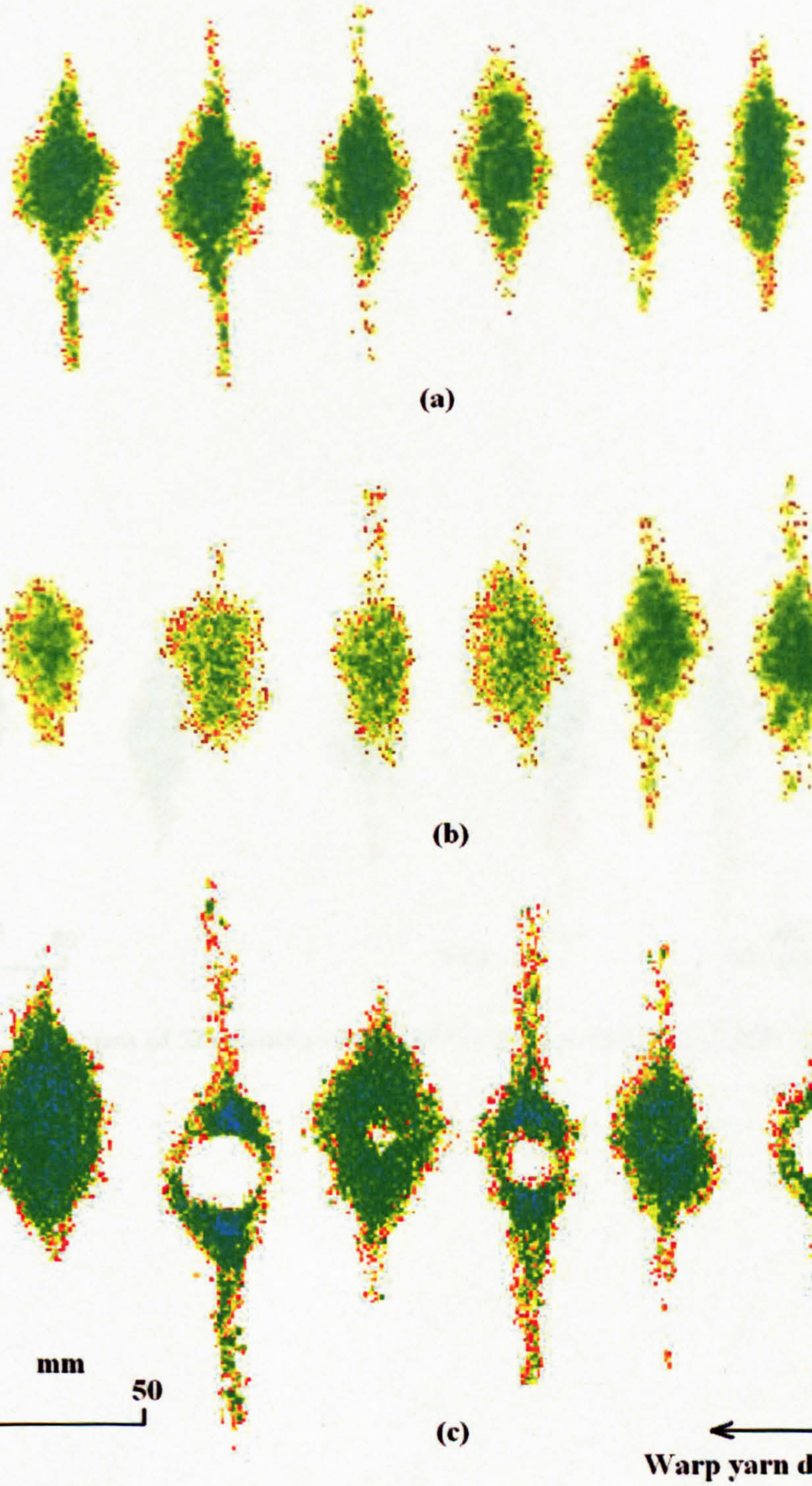

Figure C.8: **Shapes of 2D damage areas of V_{50} specimens of C1-1-VE impacted by** - (a) 0.44g steel ball; (b) 0.87g steel ball; (c) 1.39g steel ball.

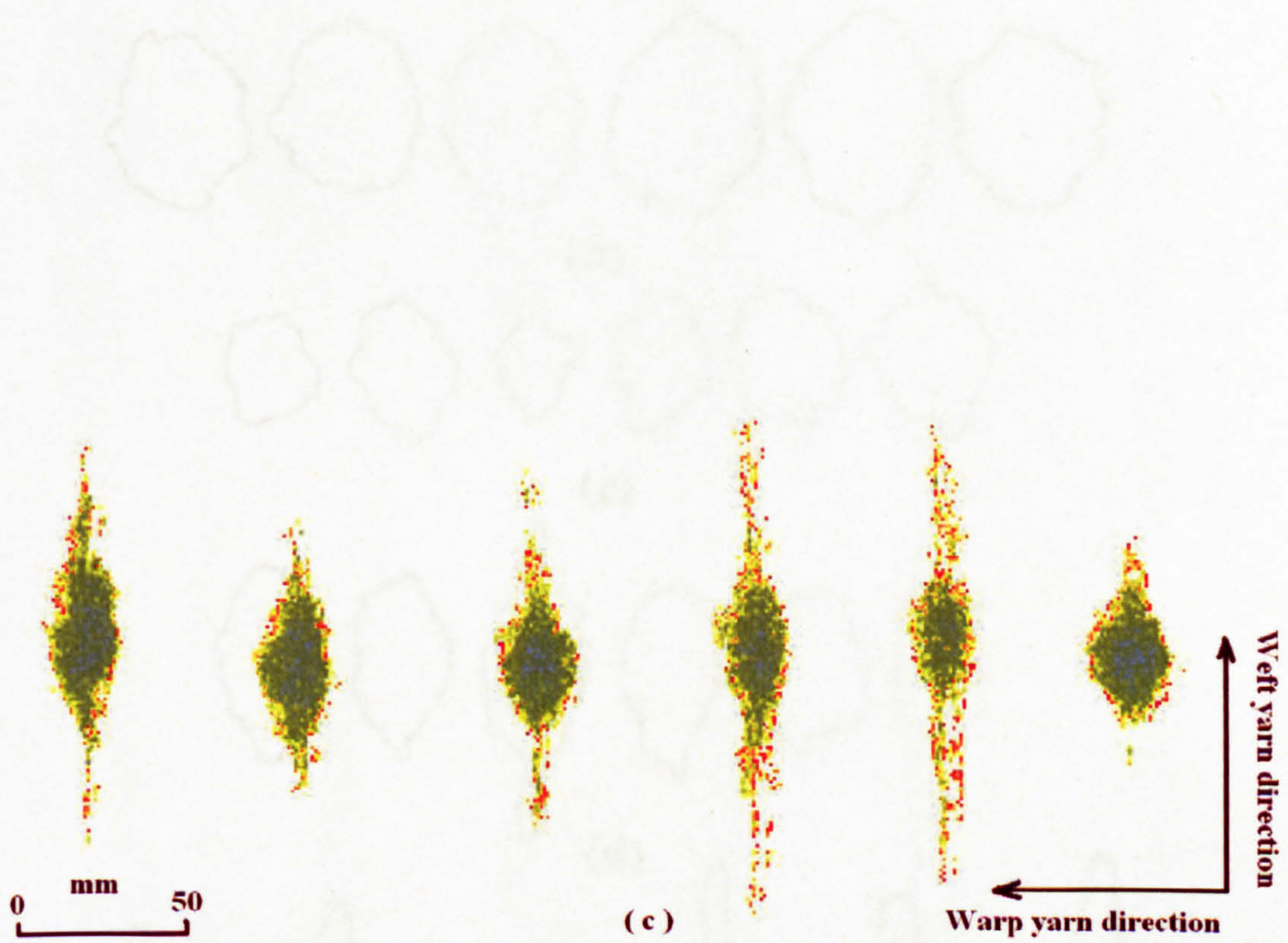

Figure C.9: **Shapes of 2D damage areas of V_{50} specimens of C1-1-EP impacted by 0.87g steel balls -**

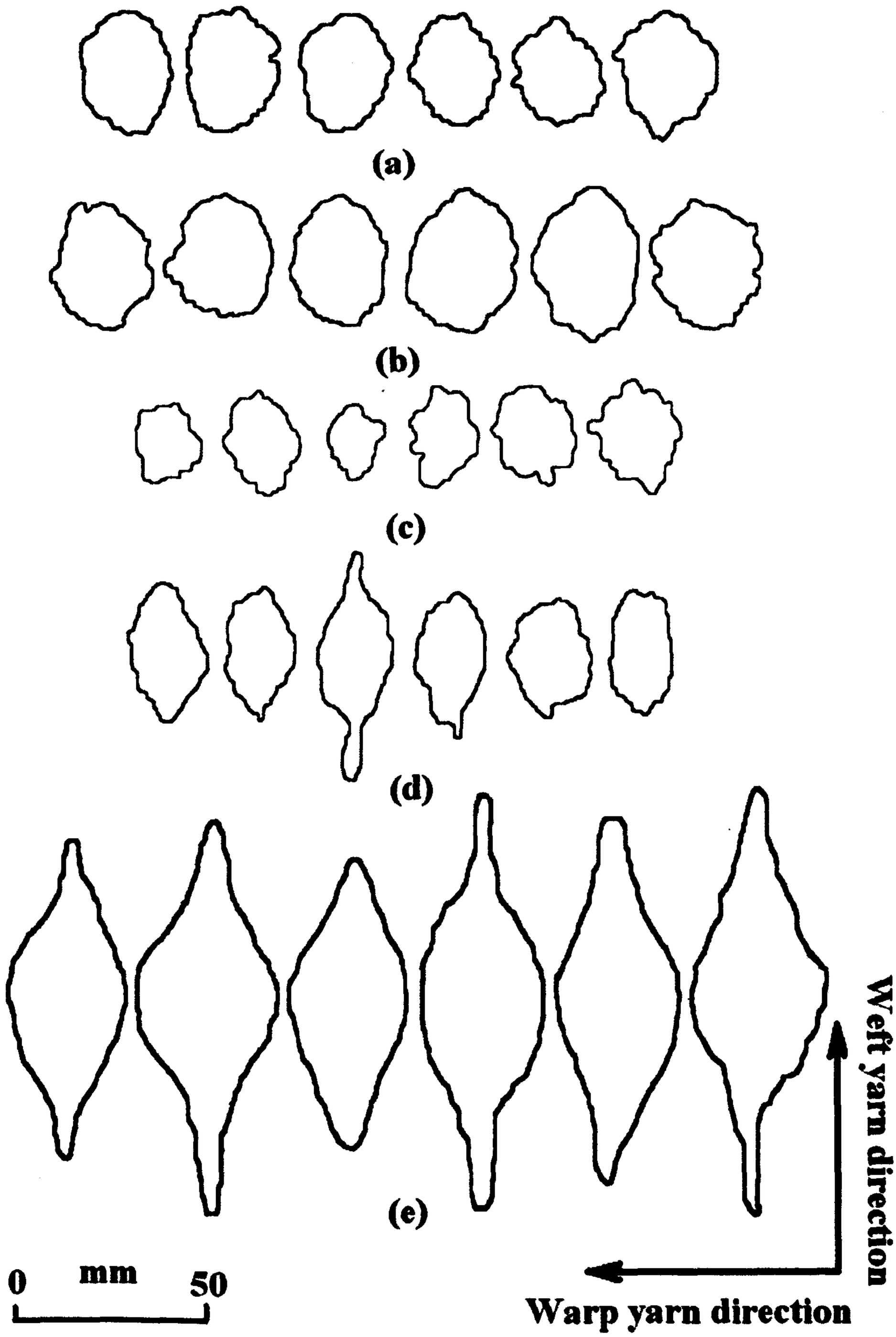

Figure C.10: **Shapes of 2D damage areas of V_{50} specimens of 3D woven glass fibre textile composites impacted by 0.87g steel ball** - (a) G1-1-VE; (b) G2-1-VE; (c) G3-1-VE; (d) G4-1-VE; (e) G7-1-VE.

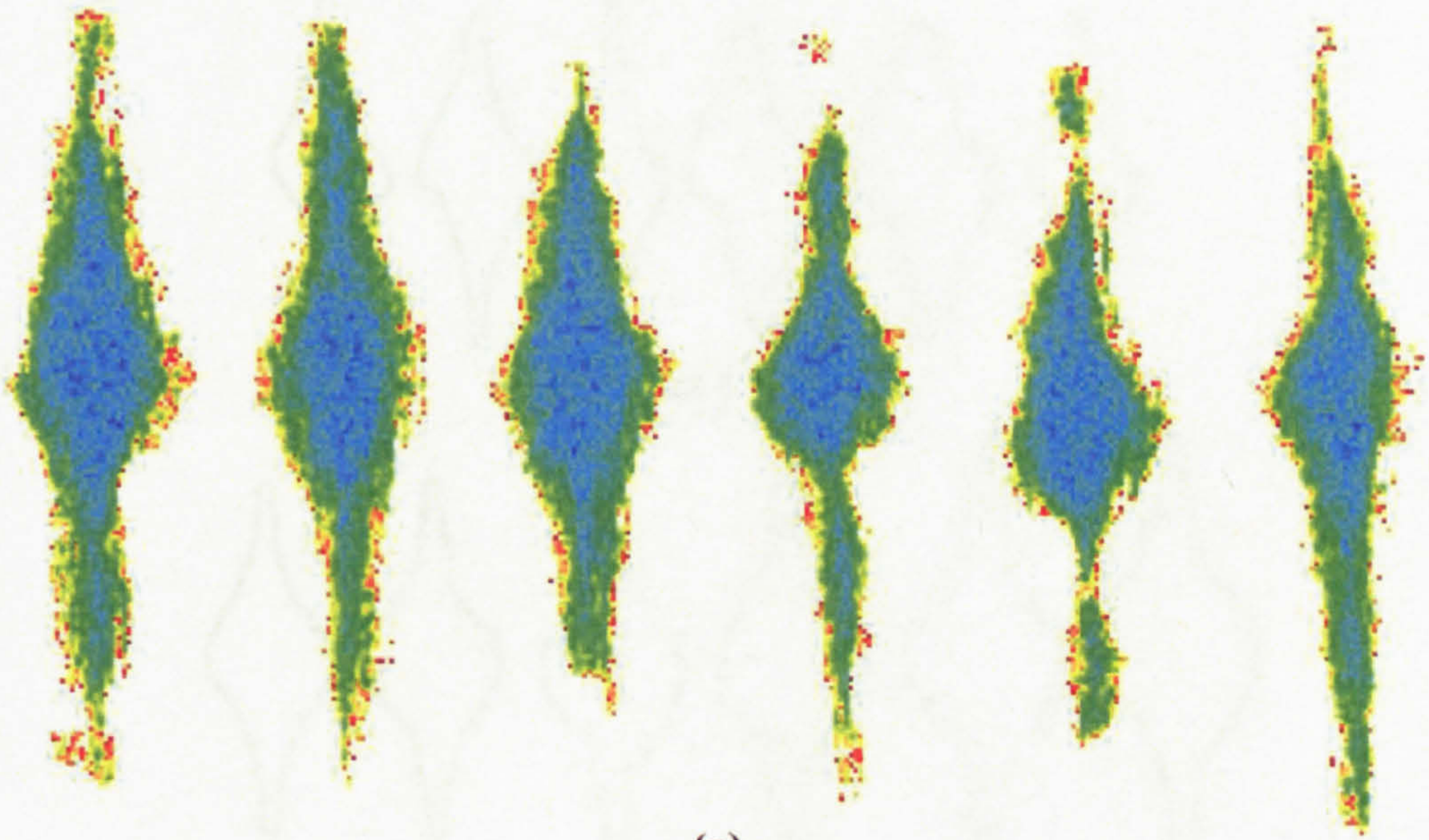

(a)

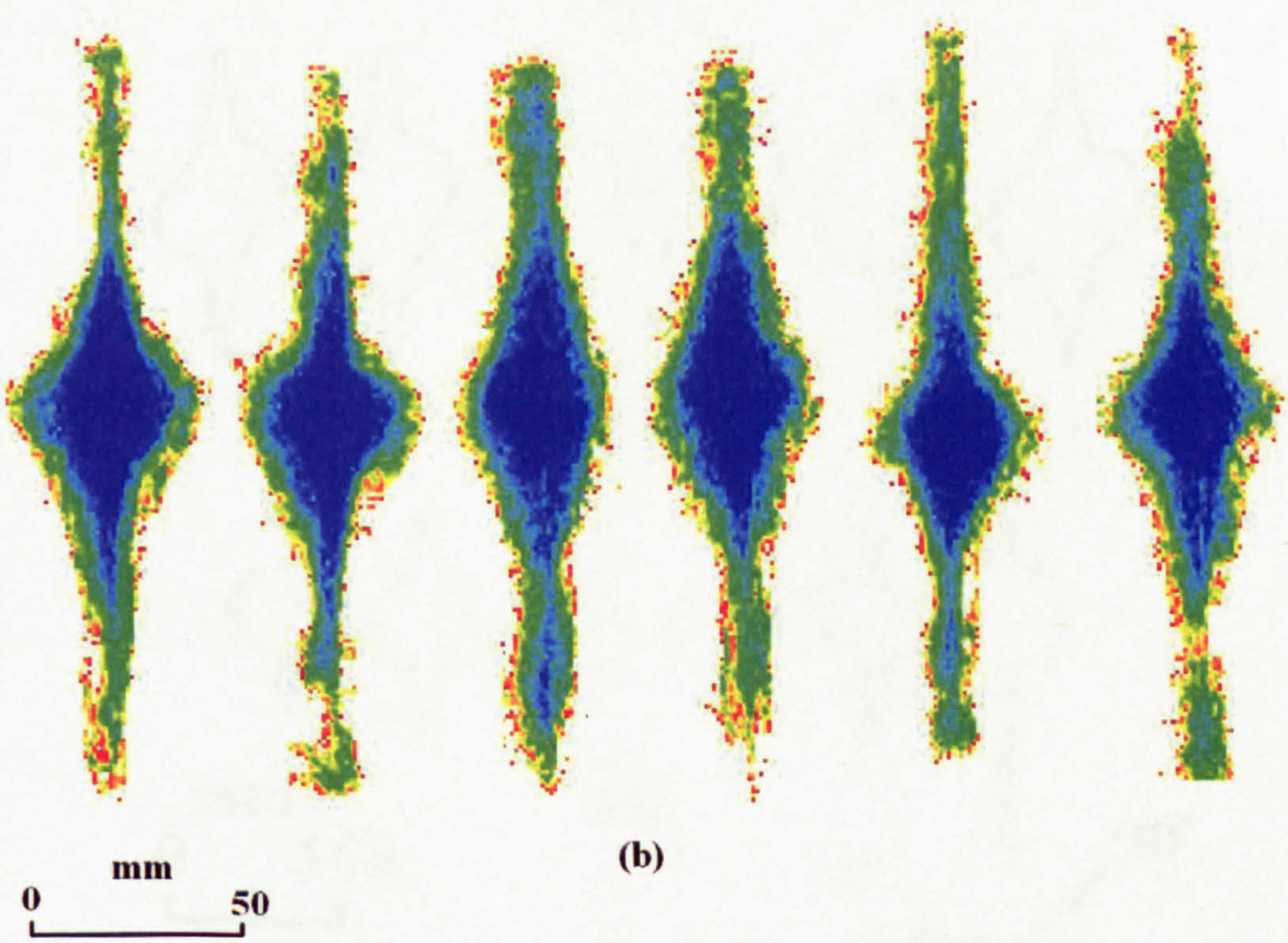

(b)

Figure C.11: **Shapes of 2D damage areas of V_{50} specimens of carbon fibre non-crimp textile composites** - (a) NCC-S-VE; (b) NCC-2-VE.

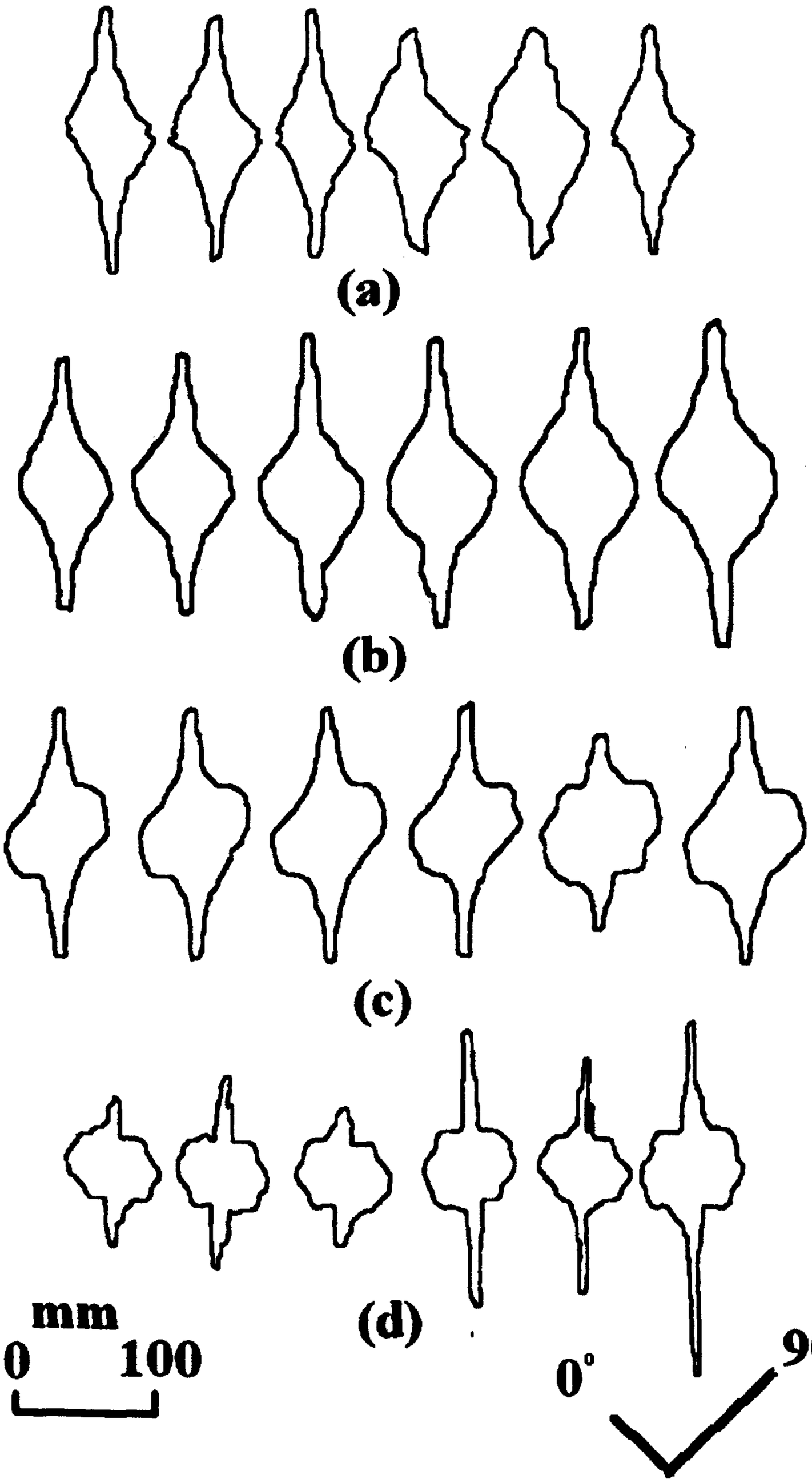

Figure C.12: **Shapes of 2D damage areas of V_{50} specimens of glass fibre non-crimp textile composites** - (a) NCEG1-S-VE; (b) NCEG1-2S-VE; (c) NCEG1-4-VE; (d) NCEG2-4-VE.

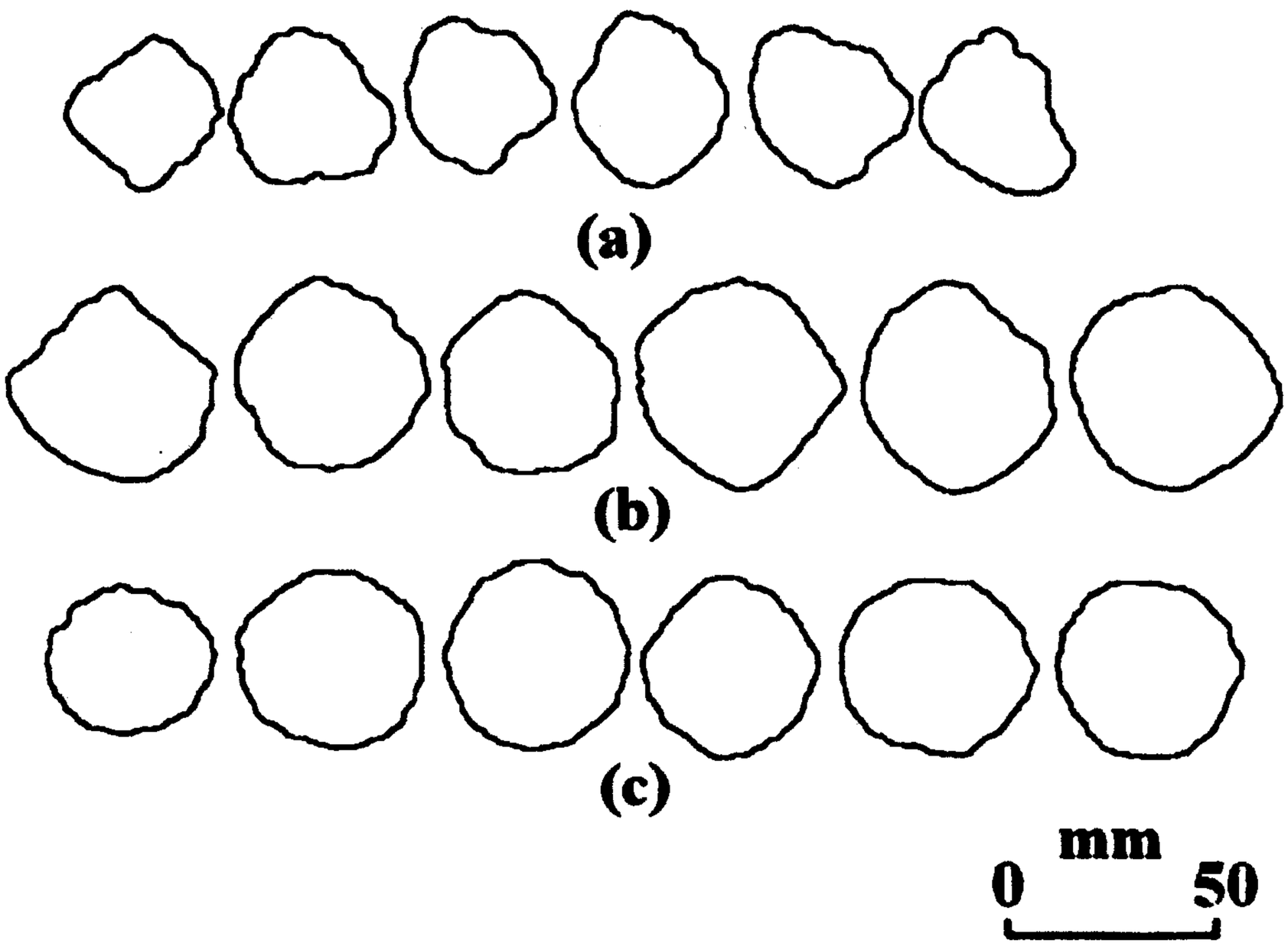

Figure C.13: **Shapes of 2D damage areas of V_{50} specimens of co-mingled textile composites** - (a) TWEGPP-2-VE; (b) TWEGPP-4-VE; (c) PWEGPP-4-VE.